Academic Press Rapid Manuscript Reproduction

SOLAR MATERIALS SCIENCE

edited by

Lawrence E. Murr

Department of Metallurgical and Materials Engineering
New Mexico Institute of Mining and Technology
Socorro, New Mexico

CONTRIBUTORS

Numbers in parentheses indicate the pages on which authors' contributions begin.

Richard H. Bube (585), *Department of Material Science and Engineering, Stanford University, Stanford, California*

Robert A. Buhrman (277), *School of Applied and Engineering Physics, Cornell University, Ithaca, New York*

Barry L. Butler (3), *Materials Branch, Solar Energy Research Institute, 1536 Cole Boulevard, Golden, Colorado*

M. A. Butler (619), *Solid State Materials, Division 5154, Sandia Laboratories, Albuquerque, New Mexico*

Richard S. Claassen (3), *Materials and Process Sciences, Organization 5800, Sandia Laboratories, Albuquerque, New Mexico*

H. G. Craighead (277), *Bell Telephone Laboratories, Holmdel, New Jersey*

A. W. Czanderna (93), *Materials Branch, Solar Energy Research Institute, 1536 Cole Boulevard, Golden, Colorado*

David Ginley (619), *Solid State Materials, Division 5154, Sandia Laboratories, Albuquerque, New Mexico*

Richard W. Griffith (665), *Department of Energy and Environment, 480, Brookhaven National Laboratory, Upton, New York*

Alex Ignatiev (151), *Department of Physics, University of Houston, Central Campus, Houston, Texas*

Osman T. Inal (53), *Department of Metallurgical and Materials Engineering, New Mexico Institute of Mining and Technology, Socorro, New Mexico*

Lawrence Kazmerski (489, 551), *Photovoltaics Branch, Solar Energy Research Institute, 1536 Cole Boulevard, Golden, Colorado*

Raymond W. Mar (439, 459), *Exploratory Chemistry, Divison 1-8313, Sandia Laboratories, Livermore, California*

L. E. Murr (53, 735, 761), *Department of Metallurgical and Materials Engineering, New Mexico Institute of Mining and Technology, Socorro, New Mexico*

Richard B. Pettit (171, 199), *Thermophysical Properties, Division 5842, Sandia Laboratories, Albuquerque, New Mexico*

Steve Pohlman (319), *Materials Branch, Solar Energy Research Institute, 1536 Cole Boulevard, Golden, Colorado*

E. P. Roth (171, 199), *Thermophysical Properties, Division 5842, Sandia Laboratories, Albuquerque, New Mexico*

C. H. Seager (619), *Solid State Materials, Division 5154, Sandia Laboratories, Albuquerque, New Mexico*

A. J. Sievers (229, 255), *Laboratory of Atomic and Solid-State Physics, Cornell University, Ithaca, New York*

Maria Telkes (377, 405), *Solar Thermal Storage Development, The American Educational Complex, American Technological University, P.O. Box 1416, Killeen, Texas*

PREFACE

Solar energy has been described as a limitless, cheap, and clean energy source of the future rivaling fusion power. However, like many other technologies, it is today undeveloped and inefficient in large measure. Development requires the use of specialized materials and materials that are abundant, cheap, and reliable enough to render the process cost effective or profitable. In a large sense, solar efficiencies and solar technology applications are currently materials limited. However, the science of materials has made large strides in the past two decades. Properties of materials in particular are becoming understandable and predictable on the basis of structure and microstructure, and the application of materials science has led in some cases to materials design criteria based on fundamental microstructural manipulations that include defect chemistry.

One of the principal drawbacks in the development of contemporary solar and other related energy technologies has been the lack of professionals, trained or expert, in these specialized areas or able to immediately apply their particular skills or professional training and experience. This can be rectified in the long term by alterations in curricula and the establishment of new curricula to address a particular energy technology area, while in the short term continuing education approaches are the more expedient routes. The lecture series upon which this book is based, sponsored by the New Mexico Joint Center for Materials Science, sought to serve both these approaches and at the same time provide for an overview of the state-of-the-art in specific solar technology areas. This book is therefore intended as a timely exposition of the materials aspects of contemporary and future solar energy development. In general, the major objectives are to provide advanced undergraduate and beginning graduate students with a formal vehicle introducing basic concepts of materials science, demonstrating their utilization in solar technology, and providing contemporary and state-of-the-art examples of this utilization and the technology; and to provide a basis for continuing education in the general area of solar materials science, and a concept of the application of materials science and related skills of technical or professional people to the development of a viable solar technology.

The subject matter addressed by the post-introductory chapters is divided into three categories: (1) solar collector (photothermal) materials; (2) solar storage and photochemical materials; and (3) solar conversion (photovoltaic) materials. Lectures originally composing the series upon which this book is based were organized to present an introduction to a topic, or an overview of a solar materials area, and then to present a state-of-the-art description of a research topic in this area, or

encompassing the particular phenomena discussed in the overview. Thus, while this book is not specifically intended as an introduction to solar materials science, it does, in many areas, contain a significant, if not sufficient, level of introductory or background information, and can indeed serve as an introduction to solar materials science. To a large extent, this book depicts the theme of application of materials science and engineering in solar energy and solar technology development. It is, as was the original lecture series, intended as a single semester course for upper division undergraduates and graduate students in a wide range of curricula and programs, including metallurgy, metallurgical and materials engineering, materials science, electrical and mechanical engineering, engineering science, solid-state physics and chemistry, and other related areas and disciplines. Its organization is also intended to serve as a self-study guide and reference for a wide range of researchers and other professionals and for continuing education use. An extensive list of problems keyed to the chapters, and each containing a list of reference readings, along with a special section on problem solutions and discussion are intended to extend the topic coverage, and provide a mechanism for emphasizing and reinforcing the applications of materials science principles in solar energy research and development. The presentation assumes some background in the materials sciences as well as mathematics (through differential equations), chemistry, and physics (through modern or introductory solid-state physics). Introductory chapters provide some review of the necessary background or suggest adequate reference sources that may be consulted. In addition, the original lectures were video-taped in order to provide additional circulation of the program, and to aid in self-paced or independent study programs. These tapes are available through the New Mexico Joint Center for Materials Science by contacting the editor.

The New Mexico Joint Center for Materials Science sponsored the Distinguished Lecture Series, which composes this volume as a continuing education and engineering curriculum enrichment program for both upper division and graduate credit in the Fall, 1979 academic semester. It is a pleasure to acknowledge the financial support of the federal laboratory members: Sandia Laboratories, the Air Force Weapons Laboratory, and Los Alamos Scientific Laboratory. The facilities and participation made available through the University of New Mexico and the New Mexico Institute of Mining and Technology are also gratefully acknowledged. Finally, the typing of front matter and other sections of the complete camera-ready manuscript and the related editorial assistance of Lorraine Valencia were an important and very much appreciated contribution to the final composition of this book.

LAWRENCE E. MURR
Socorro, New Mexico
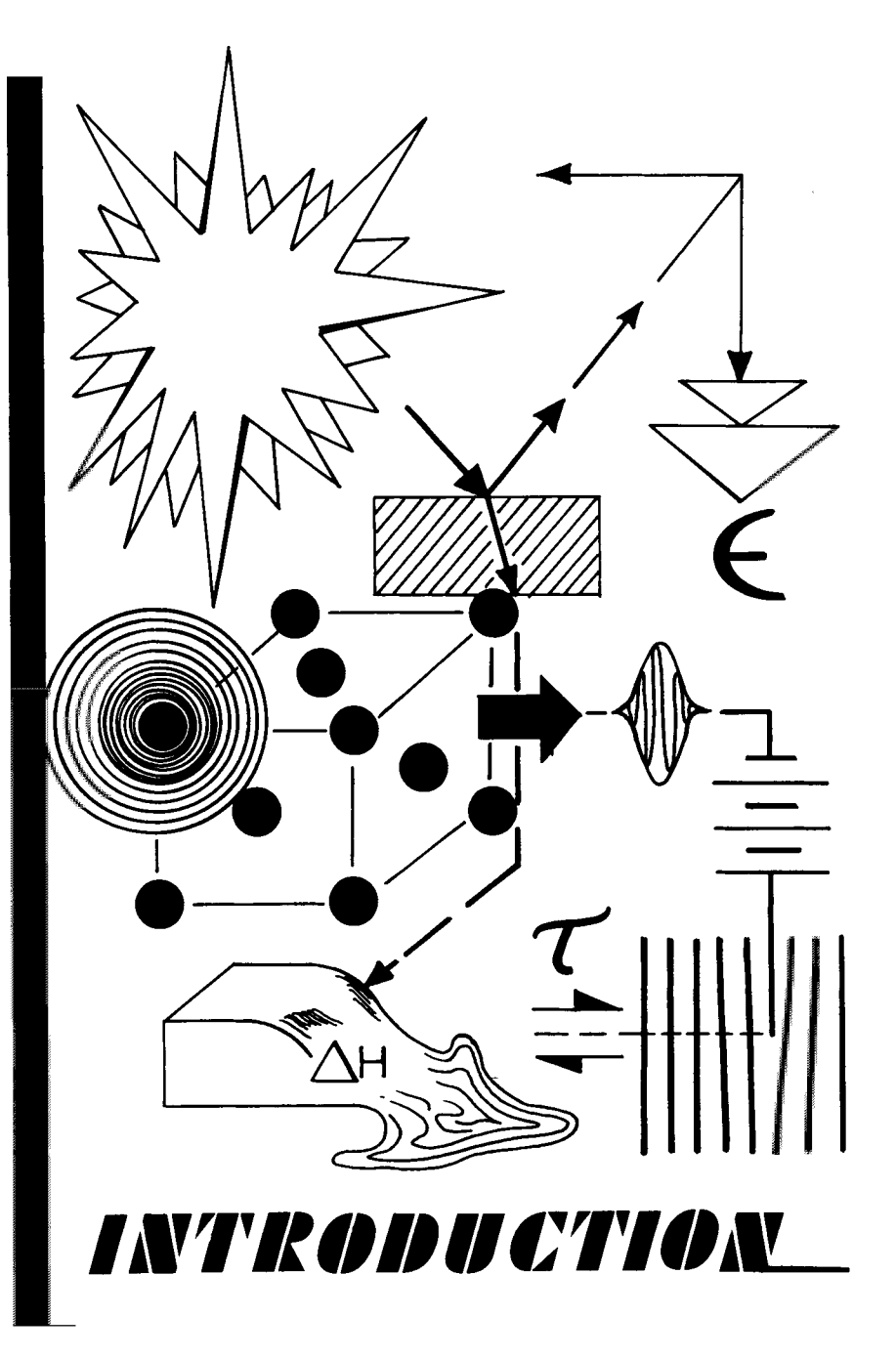
INTRODUCTION

"As for the supplies of mechanical power, it is axiomatic that the exhaustion of our coal and oil-fields is a matter of centuries only. As it has often been assumed that their exhaustion would lead to the collapse of industrial civilization. I may perhaps be pardoned if I give some of the reasons which lead me to doubt this proposition.

Water-power is not, I think, a probable substitute on account of its small quantity, seasonal fluctuation, and sporadic distribution. It may perhaps, however, shift the centre of industrial gravity to well-watered mountainous tracts such as the Himalayan foothills, British Columbia, and Armenia. Ultimately we shall have to tap those intermittant but inexhaustible sources of power, the wind and the sunlight. The problem is simply one of storing their energy in a form as convenient as coal or petrol. If a windmill is one's back garden could produce a hundred weight of coal daily (and it can produce its equivalent in energy), our coalmines would shut down. Even tomorrow a cheap, foolproof, and durable storage battery may be invented, which will enable us to transform the intermittent energy of the wind into continuous electric power." [From J.B.S. HALDANE, "Daedalus or Science and The Future" (A paper read to the Heretics, Cambridge, on February 4, 1923)]

In the first of three introductory chapters, the enormous distortions in the predictions relating to world energy posture noted above by Haldane are made self evident, but the conclusions he arrives at some fifty-five years ago are unalterably reinforced. More importantly, the dependence of solar energy implementation, and its success as a viable energy alternative upon the science of materials is demonstrated. The range of solar energy systems is outlined and the materials problems as well as materials utilization in these systems is illustrated with specific examples. The overwhelming theme of this chapter is that materials along with design criteria pervade all aspects of the solar materials problems in the United States, and that there is a need for confidence in reliable performance and system lifetime projections, which can only be obtained through a knowledge of materials and materials problems. The second chapter provides for a review of crystal structure and crystal defects as well as an overview of the structure-property relationships which can be considered to figure prominently in the selection and performance of materials for specific solar energy applications. This chapter also provides for a fundamental understanding of solar materials microstructures as well as examples of principal techniques for their observation and analysis. The third and final chapter in this introductory section outlines the analytical approaches for the elucidation and study of surface and interfacial phenomena crucial to all solar materials systems to be described in three principal sections of this book. Some selected examples of current solar materials problems are also presented to emphasize the application of the techniques described.

CHAPTER 1

INTRODUCTION TO SOLAR MATERIALS SCIENCE[1]

Richard S. Claassen

Sandia Laboratories[2]
Albuquerque, New Mexico

Barry L. Butler

Solar Energy Research Institute[2]
Golden, Colorado

I. INTRODUCTION

Solar radiation can be converted to forms of energy which man
finds useful through a number of natural phenomena or by the use
of technology. A broad program is underway to understand and
exploit the natural phenomena as well as to develop and improve
the full range of technologies needed to make solar energy a sig-
nificant contributor to our national energy supply. One impor-
tant aspect of the technology development is materials. The pur-
pose of this series is to present an up-to-date report on the
status of materials research and development which will play a
major role in the more promising approaches to converting solar

3

radiation to other useful energy forms.

It is convenient to view the entire solar energy program from two broad frames of reference; the first programmatic, the second technical. The national solar program in the United States has been organized according to the conversion paths indicated in Figure 1 (1). This series of lectures will focus on the technological side of Figure 1 where materials science and engineering have the greatest opportunity to influence program success. From a conceptual, or technical viewpoint, it is appropriate to divide all solar systems into two broad classes as illustrated in Figure 2 (2); 1) those in which the primary interaction is a discrete quantum process, and 2) those in which the primary process is production of heat.

This series has necessarily been limited to three principle areas, namely, solar collector materials, photochemical conversion and storage, and solar conversion materials. Although many important elements of the solar program have been left out, the examples covered will illustrate the central importance of materials development and will indicate the challenges to the materials community. The next section provides a general framework in which materials development can be considered starting with emphasis on performance, life, and cost and ending with a strong recommendation for systems studies prior to expending effort on materials development. The third section discusses optical elements which are common to both thermal and quantum conversion processes. The fourth section identifies examples of problems in conversion processes. The final section is a brief summary of our viewpoint.

II. FRAMEWORK FOR MATERIALS DEVELOPMENT IN SOLAR ENERGY

A. *Principle Issues*
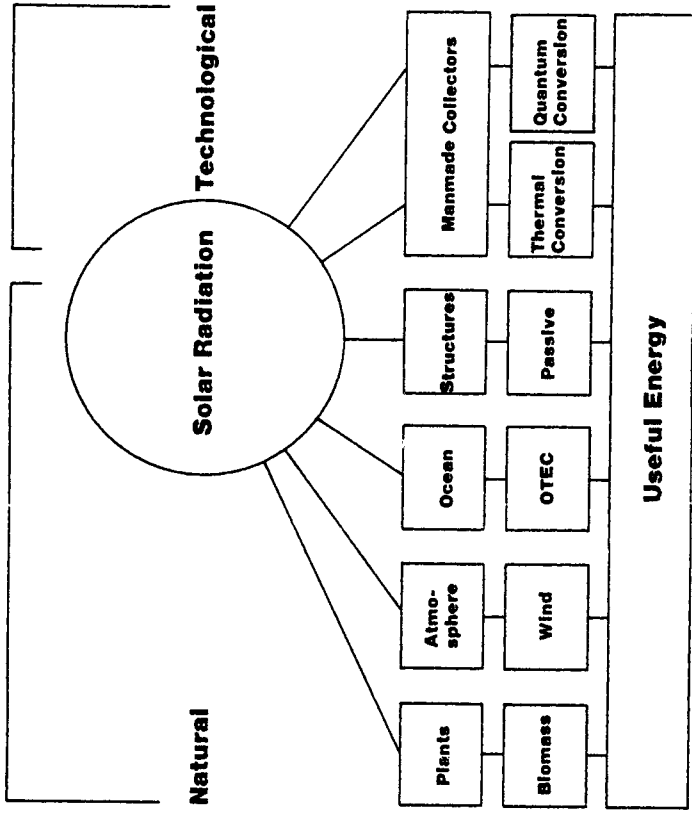
Figure 1. Solar Energy Conversion Paths
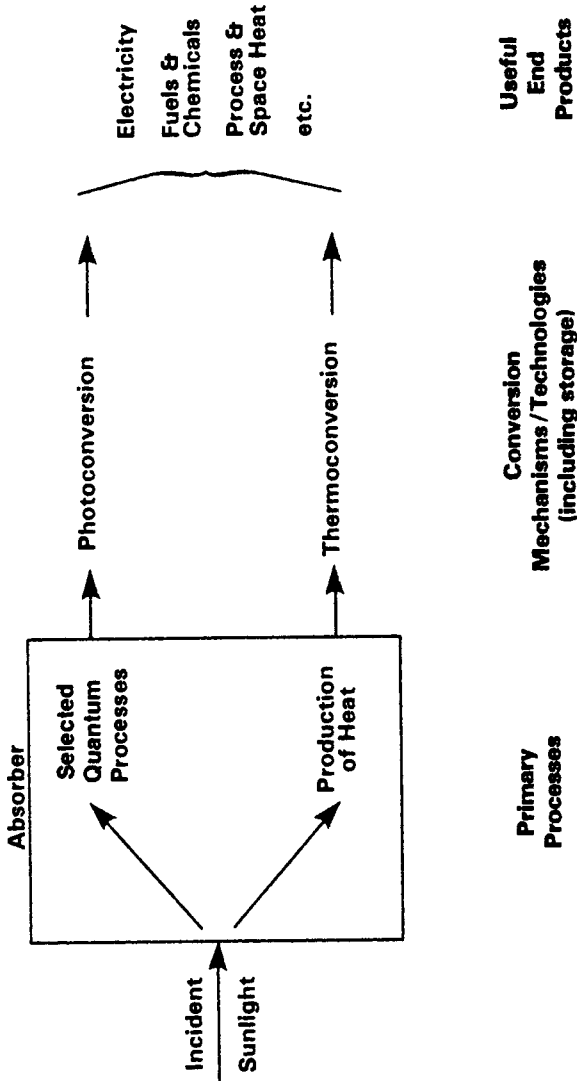
FIGURE 2. *Solar Energy Conversion Processes (2)*

It must be understood clearly that the principle issues in
the development of solar energy are neither scientific proofs nor
engineering feasibility demonstrations. We know that solar
energy will work. What remains to be established is acceptable
performance, adequate life, and low enough cost to enable wide-
spread use.

At first glance it might seem that materials performance in
solar devices would be modest, but in many cases, the requirements
on materials are quite demanding. A concentrator, for example,
which focuses the sun on a small receiver must cover large areas
and have accurate optics, high specular reflectance, and long-
term durability in a hostile environment. Photovoltaic devices
(solar cells) must have the maximum possible efficiency to mini-
mize overall systems costs while maintaining long-term durability
in the terrestrial environment.

Although solar energy systems require no fuel, they are char-
acterized by high initial cost. Service life measured in decades
is required to amortize that initial cost at acceptable rates.
Elements which are exposed to the atmosphere such as mirrors or
surface covers (glazings) will be subject to degradation mechan-
isms such as deposition of dust, corrosion by water vapor and chem-
icals in the atmosphere and photochemical degradation. Because
of the daily variation of solar insolation and because of short
term fluctuations resulting from cloud passage some elements of
the solar system will be subject to cyclic fatigue. Problems
such as these must be resolved in advance so that the buying
public can have confidence in the expected lifetimes of the solar
devices.

Cost reduction is an essential element of the solar energy
program. Concern for cost is reflected in considerations of
materials availability, in the development and demonstration of
mass production processes which are inherently inexpensive and in
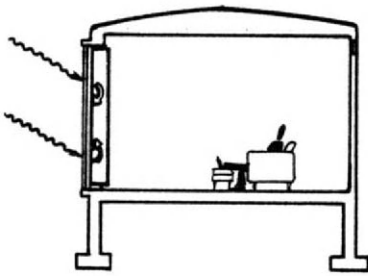
Passive
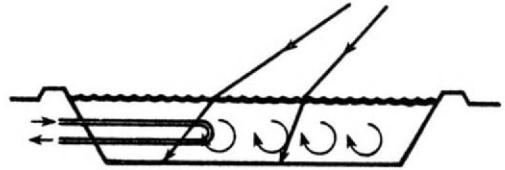
Saltless Solar Pond
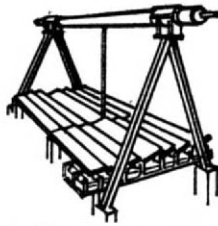
Single Axis Tracking Concentrator

Parabolic Dish

External Central Receiver

FIGURE 3. Solar Energy Collector

the design of solar energy systems of minimum complexity.

Anyone working on materials development for solar energy sy-
stems should frequently check his progress against the dominating
parameters of performance, life, and cost.

B.   *Generic Systems Referred to in this Series*

Figures 3 and 4 provide pictorial illustrations of the prin-
ciple solar energy conversion technologies. This series will
emphasize the lower three optical concentrators shown in Figure
3: namely, the single-axis tracking system and the two-axis
tracking parabolic dish and the central receiver systems. Sec-
ondary solar systems, such as ocean thermal energy conversion and
wind which use the earth as the collector, will not be considered
in this report. In central receiver systems the elevated focal
point is surrounded by a large number of tracking heliostats.
Solar cells or photochemical cells may be deployed in an array as
illustrated in Figure 4 or may be placed at the focal point of
one of the concentrating systems.

C.   *Components, Functions, and Disciplines*

The energy conversion concepts just outlined above require a
broad range of system components shown in Figure 5. These system
components require specific materials functions. The materials
functions can be loosely defined as: optical functions including
reflection, transmission and absorption; energy storage and trans-
fer functions which include the use of energy transfer media and
phase change materials; and finally, the structural functions
which provide the strength and stiffness required. Research
disciplines can be identified with each of these required ma-
terials functions. Specific examples will be cited later in this
lecture series. But to give an example, a transmitting material
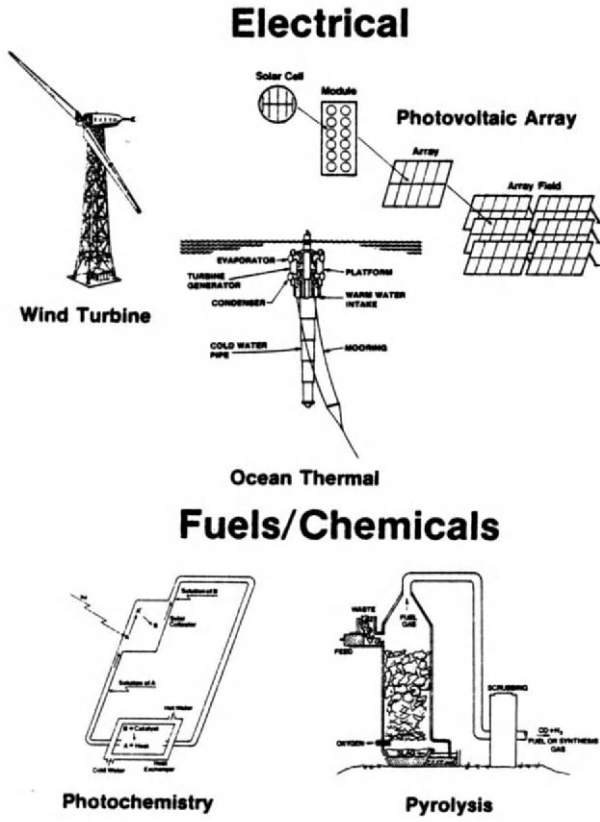
FIGURE 4. Solar and Renewable Energy Collectors

System
Components

Materials Uses
and Functions

Disciplines/Specialties

Concentrators
1X to 2000X

Reflectors

Metals
Glass/Ceramics
Polymers
Composites
Surfaces
Corrosion/Compatibility
Optics

Receivers/Advanced
Converters

Transmitters

Thermal
Converters

Photoconverters

Energy Transfer
Systems

Transfer Fluids
and Chemicals

Melting & Solidification

Containers

Optical, OTEC &
Wind Structures

Shape/Stiffness

Support/Strength

FIGURE 5.   Relation of materials research to system
components.

would require the disciplinary studies of optics, solid state
chemistry, glass and polymers. These studies would be aimed at
understanding the optical transmittance of these materials as a
function of material chemistry, radiation environment, and ter-
restrial environment. The output of this materials research
would be a basic understanding which could lead to improved
transmittance, longer life, or a materials processing break-
through which could yield lower capital cost. Thus, the materials
research to support the solar conversion technologies will pro-
vide the basis for improving the elements of life cycle costs.

D.   Discipline Relationships

   The problems posed by using materials in solar energy con-
version systems are approached from a disciplinary point of view
because they are similar to problems found with the application
of materials to other areas of technology. Studying the basic
materials properties and structures property relationships of
certain materials such as metals, ceramics, polymers, composites,
etc., allows the understanding generated in one technology to be
applied to another. Disciplinary research will aid in the de-
velopment and tailoring of materials for solar energy systems.

   In general materials in solar applications must perform in
the terrestrial environment for a long time without degradation.
In all systems which either use a glazing or a reflecting surface
or refracting optics, dust and dirt attachment and adhesion to
the mirror, glazing or lens will decrease the transmitted or re-
flected light which the converter can utilize. Refurbishing or
cleaning can be a major expense in a large area solar array.
Thus, materials research in the area of dust adhesion to glasses
and plastics is an area which is of generic importance to the
optical collecting system. Once the solar optical materials
needs are identified the heat transfer and energy transfer needs

come next. The major concern in the area of energy transfer is the fluid and container compatibility which will limit system life. Compatibility of materials used in photovoltaic device electrical contacts and optical encapsulating materials is another concern. Containment contamination or poisoning of quantum processes which would hinder the conversion of light to chemical energy is also important in photochemical conversion systems. In the area of non-optical collecting systems such as wind and OTEC, the major issues respectively are fatigue life of the turbine blades as well as their costs and in OTEC systems it is the performance degradation due to corrosion and biofouling which will take place over the life of the plant.

The materials program that must be developed in support of solar energy requires both the ability to select the materials with the right properties and also to develop basic supporting understandings of these materials. The material selection requires the applications of solid state physics and chemistry and chemical engineering. For example, the selection of the right material for a photovoltaic device would require an understanding of solid state physics. The understanding of a material for a photochemical process would require a basic understanding of the interaction of light and chemicals. For energy transfer systems, one would need to know which chemical reactions to select and under what types of conditions they would operate. Physics and chemical engineering support the materials selection for the conversion process and materials engineering would support materials selection for the more classical stress, strain and corrosion and compatibility conditions.

Once the materials are identified for each of the areas of technology, then the supporting disciplines of metallurgy, ceramics, polymers, and surface science come into play to understand the material properties and their interactions with each

other in the system environment. By way of example, Table I has
been included to indicate where costs, performance, and life im-
provements could result from research in various materials
disciplines.

E. Identifying Critical Materials Issues

   A critical materials issue is one that limits the cost, per-
formance, life or availability of a material or a particular so-
lar energy conversion system. Before expending development
effort on particular material problems, it is necessary to de-
velop a perspective of the importance of that problem in the over-
all solar energy program. A system study can provide that per-
spective. Because the materials requirements are system specific
a series of examples will be used to illustrate the systems
approach to identify the critical materials areas. The first ex-
ample is a broad study of materials availability; the second ex-
ample traces all the important parameters in a specific collector
design; and the third which appears in the subsequent section
treats the absorber material.

   Ray Watts, et. al., at Battelle Pacific Northwest Laboratory,
have developed a methodology for identifying material constraints
in the photovoltaic program (3). Their analysis places emphasis
on material supply and cost. They then apply the general concept
to specific designs for silicon and gallium arsenide cells. One
output of this study is the identification of aluminum, antimony,
copper, and gallium as significant material availability problems.
Ways are suggested to mitigate material supply problems using the
framework of the study.

   George Treadwell of Sandia Laboratories has made a systems
analysis of a parabolic-cylindrical solar collector (4). The
study is a design tradeoff of the many parameters involved;
namely, the rim angle, the receiver tube size, asymetries in the

TABLE I. *Impacts of Materials Research on Life Cycle Cost Elements*

	Performance Changes	Cost	Life
Metallurgy Containment Cyclic Loading	Lower Corrosion Rates Higher Temperatures	Thinner Walls Lower Alloy Additions	Predictable Lives More Cycles to Failure
Reflectors	Ag—Alloys (Al) Increase Reflectance	Same as Ag	More Atmospheric Resistance
Polymers Encapsulants Transmitters	Lower Permeability Higher Solar Transmittance	Thin Films Thin Films	UV Resistance UV Resistance
Ceramics/Glass Transmitters Absorbers	Lower Fe^{+2} Ion Content Higher Temperatures	Thin Sections Cheap Raw Materials	Very Stable Thermal Shock Resistance
Surface Science Optical Degradation of Mirrors	Higher Reflectivity of Ag	Processing	Atmospheric Resistance
Absorbers	Higher α and Lower ε	Processing	Collector Environment Resistance
Catalysis	Higher Reaction Rates	Thin Films	Low Poisoning

collector, reflection and transmission properties of the mirror
and receiver tube envelope respectively, and the optical absorp-
tion and infrared emittance of the coating on the receiver tube.
In addition, the questions of whether to have a glass jacket a-
round the receiver tube is addressed as is the gap between the
jacket and receiver. Energy balance calculations are used to
test the sensitivity of the overall system performance to each
of the above parameters. A number of conclusions can be drawn.
For example, rim angles beyond 90° do not add much to system
performance. On the other hand, considerable gain can be a-
chieved by increasing the transmission of the glass jacket be-
yond that of conventional glass. Anti-reflection coatings on the
glass surface make an important improvement in system performance.

III. OPTICAL ELEMENTS

Our definition for this topic can be stated: optical elements
interact with incoming light by transmission, reflection, and
absorption but do not in themselves produce useful output energy.
For convenience we include support structures in this category.
This section will highlight important materials problems in
trough structures, selective absorbers, transmitters, and re-
flectors. Tables II, III, and IV give nominal optical properties
and durability data for a wide range of materials (5).

A. *Collector Types*

The solar conversion systems that we will be dealing with are
nonconcentrating systems, single axis concentrating systems and
two axis concentrating systems. The nonconcentrating systems in-
clude some photovoltaic devices, shallow solar ponds, passive
applications and thermal flat plate applications. The nonconcen-

TABLE II. *Properties of Selected Solar Absorber Surfaces (6)*

Material	Technique	Supplier (S)/ Developer (D)	α_s	$\varepsilon_t(T)$	T Stability** (°C)
Black Chrome	electro-deposited	Many	0.94-0.96	0.05-0.10(100) o.20-0.25(300)	300
Pyromark	paint	Tempil	0.95	0.85(500)	<750
S-31 (nonselective)	paint	Rockwell International	0.8-0.85	0.8-0.85	>550
SOLARTEX	electro-deposited	Dornier (W. Germany)	0.93-0.96	0.14-0.18(310)	700
SOLAROX (proprietary)	"	"	0.92	0.20	200
Black Epoxy	paint	Amicon Corp.	NA	NA	NA
436-3-8	"	Bostik (U.S.M. Corp.)	0.90	0.92	NA
Enersorb	"	Desoto	0.96	0.92	NA
7729	"	C. H. Hare	0.96	0.90-0.92	NA
R-412	"	Rusto-leum Co.	0.95	0.87	NA
5779	"	"	0.95	0.90	NA
Nextel (nonselective)	"	3-M	0.97-0.98	>0.90	150
NOVAMET 150 (proprietary)	"	Ergenics	0.96	0.84	800 (1 hr)
MAXORB	(Proprietary)	Ergenics	0.97(±.01)	0.10(±.03)	150(20 wks) <400(1 hr)
Tabor Black (NiS/2nS)	electrodeposited + overcoat	Miromit	0.91	0.14	

TABLE III.   *Thermal and Optical Properties of Cover Plate Materials (7)*

Material	Index of Refraction	Normal Incident Short-wave Transmittance ($\lambda=0.4$-2.5μ)	Normal Incident Long-wave Transmittance ($\lambda=2.5$-40μ)	Thickness* (m)	Density (kg/m^3)	Specific Heat (J/°K-kg)	Thermal** Capacity (W-hr/°K-m^2)	References
Glass	1.518	0.840	0.020	3.175×10^{-3}	2.489×10^3	0.754×10^3	1.659	(8)
Fiberglass Reinforced Polyester (Sunlite)	1.540	0.870	0.076	6.350×10^{-4}	1.399×10^3	1.465×10^3	0.361	(8)
Acrylic (Plexiglas)	1.490	0.900	0.020	3.175×10^{-3}	1.189×10^3	1.465×10^3	1.534	(8)
Polycarbonate (Lexan)	1.586	0.840	0.020	3.175×10^{-3}	1.199×10^3	1.193×10^3	1.260	(8)
Polytetrafluoroethylene (Teflon)	1.343	0.960	0.256	5.080×10^{-5}	2.148×10^3	1.172×10^3	0.036	(8,9)
Polyvinyl Fluoride (Tedlar)	1.460	0.920	0.207	1.016×10^{-4}	1.379×10^3	1.256×10^3	0.049	(8)
Polyester (Mylar)	1.640	0.870	0.178	1.270×10^{-4}	1.394×10^3	1.046×10^3	0.051	(8)
Polyvinylidene Fluoride (Kynar)	1.413	0.930	0.230	1.016×10^{-4}	1.770×10^3	1.256×10^3	0.063	(10)
Polyethylene (Marlex)	1.500	0.920	0.810	1.016×10^{-4}	0.910×10^3	2.302×10^3	0.059	(8, 11)

*These values correspond to the thickness associated with the stated transmittances. They were used in the simulations to compute thermal capacity and are representative of commercially available film thicknesses.

**Thermal capacity = (Thickness) (Density) (Specific heat)

Material	Supplier	Estimates of Solar Weighted Reflectance[b] at Receiver Acceptance Angle τ			
		τ=4mr	10mr	18mr	$R_s(2\pi)$
I. Second-Surface Glass					
(a) Laminated Float Glass – 2.7mm thick –silvered	Carolina Mirror Co.	0.83	0.83	0.83	0.83
(b) Laminated Low-Iron Sheet Glass – 3.35mm thick – silvered	Gardner Mirror Co.	0.90	0.90	0.90	0.90
(c) Corning Silvered Microsheet Co.-0.114 mm thick- Mounted on optically flat plate	Corning Glass	0.76	0.87	0.92	0.95
(d) Corning 0317 Glass – 1.5 mm thick – Evaporated silver	Corning Glass	0.95	0.95	0.95	0.95
II. Metallized Plastic Films					
(a) 3M Scotchcal 5400 Laminated to backing sheet	3M Company	0.60	0.84	0.85	0.85
(b) 3M FEK-163 Laminated to backing sheet	3M Company	0.83	0.85	0.85	0.85
(c) Aluminized 2 mil FEP Teflon (G405600) Laminated to backing sheet	Sheldahl	0.70	0.81	0.82	0.87
(d) Silvered 2 mil FEP Teflon (G400300) Mounted on Optically Flat Plate	Sheldahl[a]	0.73	0.82	0.90	0.96
(e) Silvered 5 mil FEP Teflon (G401500) Mounted on Optically Flat Plate	Sheldahl[a]	0.77	0.83	0.89	0.95
(f) Front Surface Aluminized Mylar (200XM648A) stretched membrane	Boeing	0.88	0.88	0.88	0.88
III. Polished, Bulk Aluminum					
(a) Alzak Type I Specular	Alcoa				0.85
Perpendicular to rolling marks		0.61	0.68	0.76	
Parallel to rolling marks		0.68	0.76	0.83	
(b) Kinglux No. C4	Kingston Ind.				0.85
Perpendicular to rolling marks		0.67	0.71	0.75	
Parallel to rolling marks		0.69	0.71	0.75	
(c) Type 3002 High Purity Al – Buffed and Bright Anodized	Metal Fabrications, Inc.[a]	0.44	0.60	0.71	0.84

a) Experimental materials not produced in high production, so cost information is lacking.
b) Estimated from $\approx$500 nm specularity data (Ref. 12) and solar weighted total hemispherical reflectance data. Standard deviation of the estimates is about 2%.

trating systems usually require a glazing which allows the
light to reach the absorber/converter element and may be
called upon to minimize heat loss from that element.   In
most cases, the transmitting glazing protects the components
from the harsh terrestrial environment.   Nonconcentrating
systems also require a large area of an absorber/converter
which could be a photoconversion device or a thermal conver-
sion device.

Single axis concentrating systems such as parabolic troughs
or linear fresnel lenses concentrate light onto a line where the
photo or thermal conversion functions take place.   Figure 6 shows
a typical trough.   These concentrating systems require either a
high performance optical reflector which has both high lens focal
quality and also high reflectance or a high quality transmitting
lens.   The converter system is now much reduced in size to as
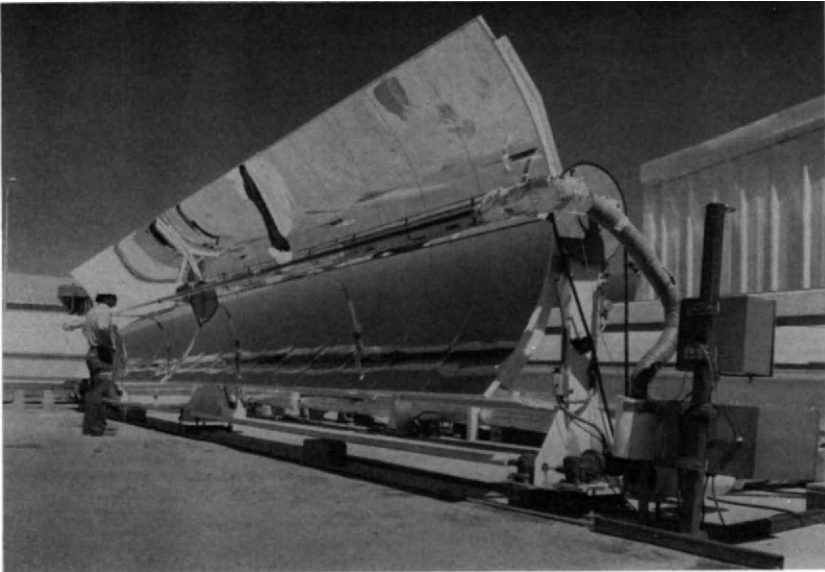
FIGURE 6.   A parabolic-cylindrical collector system.

little as 1/20th to 1/100th of what would have been needed in a
flat plate system of the same aperture area. The operating tem-
peratures of such systems can approach 300°C. The materials prob-
lems generated by this type of optical concentrator include the
design of low cost stable structures to form the focusing reflect-
ing or refracting optical elements, corrosion resistant mirror ma-
terials to reflect the solar energy, stable lens materials, re-
ceiver heat transfer materials which can stand high temperatures
and high rate of change of temperature produced when the sun is
obscured by a cloud. These systems also offer the potential for
quantum optical reactions to take place at the focus which may
require the transfer of solar energy directly to a photochemical
or photobiological process or to a photovoltaic device which under
these circumstances would probably need to be cooled.

As is true for all solar energy technology, there is great
pressure to reduce the cost of the structure for a trough. Since
cost correlates with weight, we desire a lightweight structure
fabricated from low-cost raw material. The performance require-
ments for the trough are: 1) to provide the correct optical
shape to the reflective surface; 2) to maintain this shape with-
in specified tolerances during operation; 3) to survive and pro-
tect the reflective surface under extreme weather conditions; 4)
to withstand long-term exposure to the environment. The first
item is conveniently treated in terms of the slope error at each
point on the mirror. Biggs and Vittitoe have developed a
stochastic methodology for deducing system performance from ex-
perimental measurements of geometrical errors (13). Accelerated
aging tests have shown that materials have a strong influence on
the degradation of the focal image quality with time.

An engineering estimate suggests that three pounds per
square foot is a practical target for a lightweight structure of
minimum cost which will minimize structural loads on the base

support. The structure must have adequate stiffness to retain
its optical shape. Of particular importance is adequate flex-
ural rigidity to withstand wind loading. An engineering esti-
mate for this value is 0.5 x 10^6 pound-inch. Using the concepts
of low aerial density and flexural rigidity a figure of merit
may be developed to compare various material candidates (14).

$$\Lambda \approx \frac{E}{\rho^3 (1 - \nu^2)}$$

where E is Young's modulus, ρ is density and ν is Poisson's ra-
tio. For the above values $\Lambda_{min} = 231\frac{Nm^7}{kg^3}$. Table V shows that
for simple slab construction some of the obvious material can-
didates fall short of the minimum figure of merit. By going to
more sophisticated structures, at least two promising candidates
have been identified. They are a trough structure section fabri-
cated from sheet molding compound with an integral rib structure
(Figure 7) and steel bonded to aluminum honeycomb (15).

TABLE V. Figure of Merit for Slab Type Mirror Structures (14)

Material	Density gm/cm^3	Poisson's ratio ν	Modulus E GPa	Figure of Merit Λ $\frac{Nm^7}{kg^3}$
Steel	7.80	0.30	199.9	.5
Aluminum	2.77	0.33	68.9	3.6
Sheet Molding	1.80	0.32	12.4	2.4
Plywood (fir)	.55	0.30	7.6	50.2
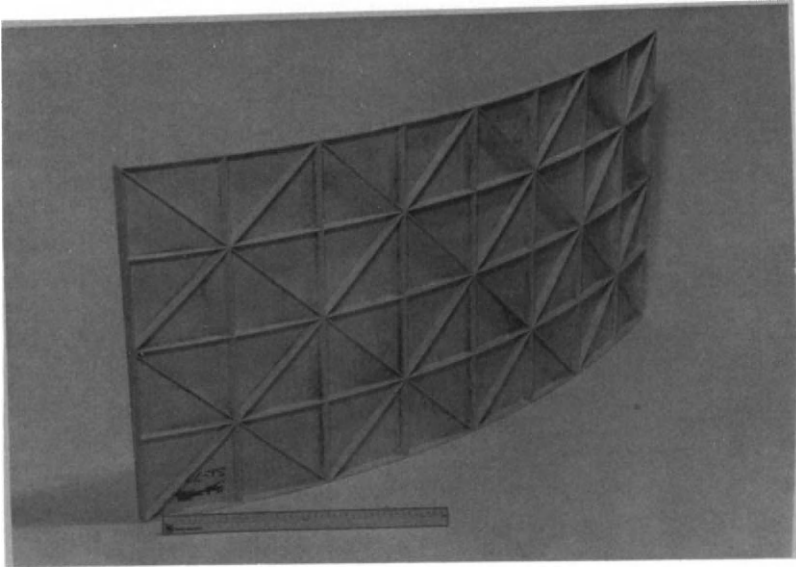
FIGURE 7. Parabolic reflector molded with ribs from sheet moulding compound.

Double axis concentrators such as parabolic dishes, circular Fresnel lenses, or central receiver systems provide concentration ratios much higher than can be achieved with single-axis concentrators, sometimes with ratios exceeding 2000. As the concentration ratio increases for both single and two-axis focusing systems the accuracy of the lens system must be improved because the equivalent system F number keeps increasing. In addition, the receiver temperatures can go as high as 600 to 1000°C causing many high temperature materials problems and in particular, a severe thermal shock problem when a cloud passes over. As the concentration ratio and power density increase so does the amount of area covered by the optical concentrator. This requires very large areas of high quality, high accuracy mirror or lens to be deployed. The problems associated with maintaining and servicing a large mirror field require that very high reliability long life components be used.

B. Selective Absorbers

For thermal conversion systems it would be desirable to have
all of the incident light absorbed by the heat transfer surface
while a minimum of energy is reradiated. Properties of typical
commercial materials are listed in Table II. Figure 8 illustrates
why it may be possible to approach this goal while Figure 9,
drawn to the same scale, illustrates that strong selectivity in
the right wavelength range is provided by black chrome on nickel
(16). Note that a material, Pyromark® (Tempil Corporation) paint,
designed to be highly absorptive in the visible region also has
high absorption and therefore high emittance in the infrared.
The improvement which can be achieved by selective absorbers is
strongly dependent on specific design. Figure 10 shows the
difference in efficiency for a flat-plate, double-glazed collector
covered with a selective absorber and one with a non-selective
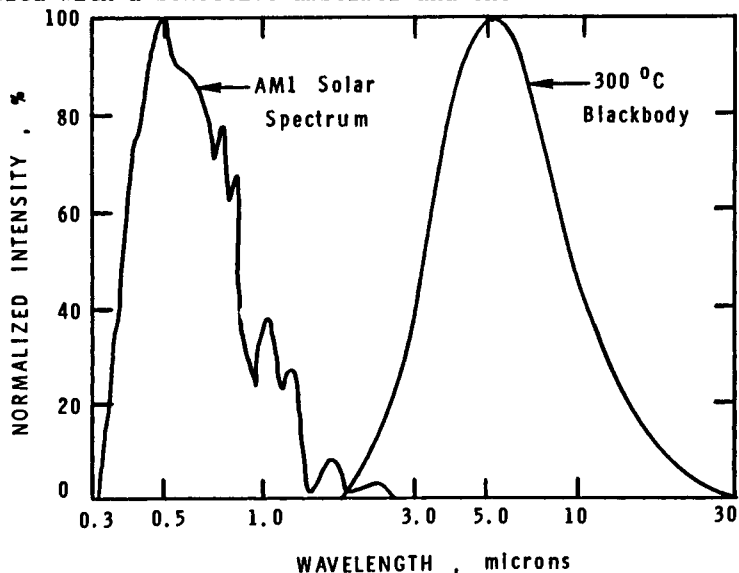
*FIGURE 8. Normalized intensity versus wavelength for solar
radiation which has passed through one atmosphere and for a black
body radiating at 300°C. The almost complete separation of spec-
tra makes selective absorber effective.*
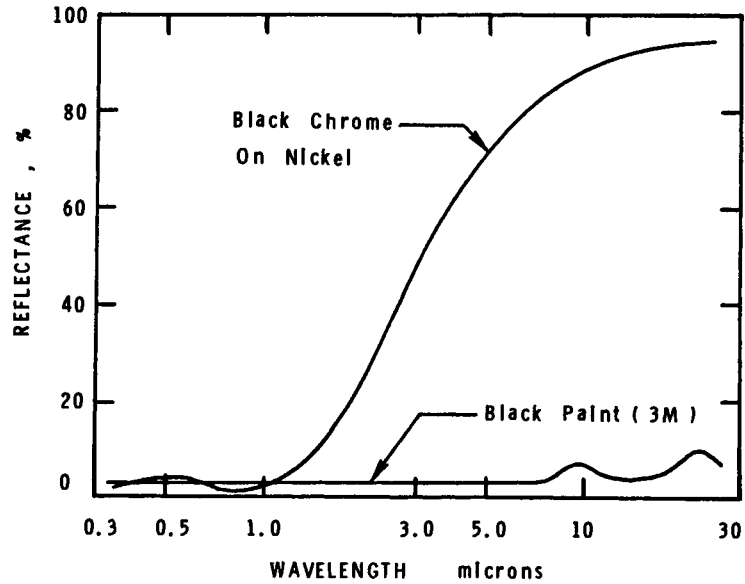
FIGURE 9. *Reflectance versus wavelength for two materials of widely different optical characteristics. The solar absorption coefficient, α_s, for the black chrome is 0.95; the emittance, ε, at $300^\circ C$ is 0.25 (16).*
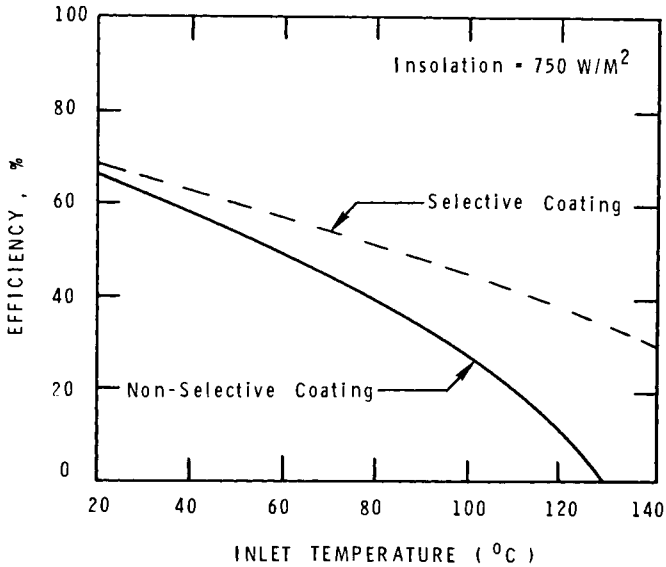
FIGURE 10. Double glazed flat plate collector efficiency as a function of fluid inlet temperature for a specific set of conditions given in the reference (17). The nonselective coating has an emissivity ε of 0.95, the selective coating an ε of 0.10.

absorber (17). Note that for low temperatures appropriate to space heating there is little gain from the selective absorber but at the higher temperatures needed for air conditioning machines the advantage is substantial. (A. Siever treats the subject of absorption, emission, and selectivity in a later chapter).

With linear concentrating collectors the influence of selective absorbers is significant. Figure 11 illustrates this influence of selective absorption on collector efficiency for a system typical of a trough collector. Note that for operating temperatures of 300°C efficiency is improved from 16 to 42% by use of a selective coating (18).

For a central receiver, higher operating temperatures can be used to provide greater thermodynamic efficiency in electric generation. The higher flux on the receiver tends to mask the importance of the power being reemitted. On the other hand, the
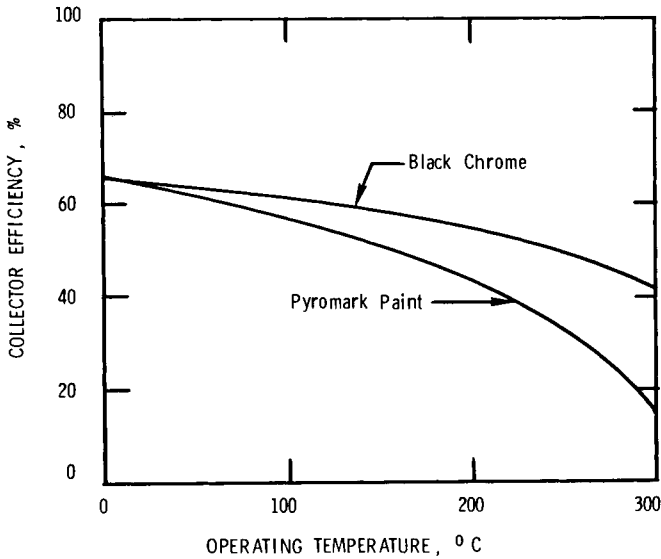
*FIGURE 11.   Collector efficiency as a function of fluid op-
erating temperature for a parabolic-cylindrical collector (18).*

higher receiver temperatures increase the emittance proportional
to T^4.   The relative importance of these two trends is highly
specific to the design and to the operating parameters. Some
feeling for these tradeoffs may be gained from Figure 12 which
indicates the improvement in efficiency which might be gained by
going from a nonselective absorber to an ideal selective coating.
Note that a plant would be operated to provide a constant temper-
ature working fluid.   That means that a vertical trajec-
tory on the graph will be followed as the sun goes through its
daily cycle. A selective absorber which contributes little at
noon time may still be significant in the morning and afternoon.
We do not presently have selective absorbers which are stable at
temperatures above $400^{\circ}C$.   (R. A. Buhrman discusses cermet films
for high temperature selective absorbers in a later chapter).
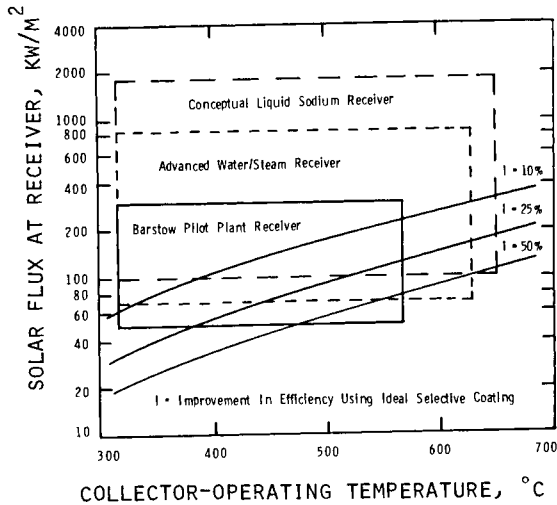
FIGURE 12. A parametric display of improvement in solar flux to thermal energy efficiency in changing from nonselective to ideally selective absorbers. A practical system will probably operate at constant temperature so that the greater improvement at lower fluxes will be important during early and late daylight hours (19).

C. Transmitters

Transmitting materials are required to separate sensitive components from ambient atmosphere and to block re-radiation of long wavelength thermal energy. The chosen materials should have the highest possible transmission in the solar spectrum, but that desirable attribute is degraded by reflection at the front and back surfaces and absorption in the body of the trans-mitting material. Typical transmitting materials are listed in Table III. In most mirror designs the light passes through the transmitter twice, thereby doubling the losses by absorbtion.

Reflection at the surface is caused by the difference in in-dex of refraction of the two media. The fraction reflected is given by the following formula:

$$\frac{I}{I_o} = (\frac{\eta_1 - \eta_2}{\eta_1 + \eta_2})^2$$

Where I and I_o are the incident and reflected intensity, and the indexes of refraction of air and glass are η_1 and η_2. For ordinary glass and air, the total reflection loss from the front and back surfaces is about 8%. It has been shown that a thin layer on the surface with an intermediate index of refraction can reduce reflection losses to about ½%. Beauchamp has shown that a silica film produced by precipitation can affect this improvement (20). The precipitation process, however, is expensive and is difficult to control in production. A practical, inexpensive process for producing the intermediate index of refraction layer would make an important contribution to the solar program.

Absorbtion in glass has been viewed as a potential problem. The best mirrors, from a geometric point of view, are made from float glass. In the final stage of production of float glass, the glass floats on a pool of tin which is stabilized by a reducing atmosphere. The iron impurity present in most common glass is reduced to Fe^{++} in the reducing atmosphere. Fe^{++} has a broad absorbtion band around 1000 nm. The marked effect can be seen in the solid curve of Figure 13. The process for glass production can be changed so that the iron impurity is either eliminated or oxidized to the Fe^{+++} state in the glass. The remaining absorbtion is then almost negligible as indicated by the dashed curve of Figure 13. Other transmitters such as polymers or other glasses will need measurement to be sure that absorbtion is not a problem.

Probably the most important questions about transmitters concern life and cleaning procedures. Dust accumulation on the first surface causes absorbtion and scattering. How quickly this degrades system performance depends on system design. Scattering is particularly important in collectors which depend on accurate
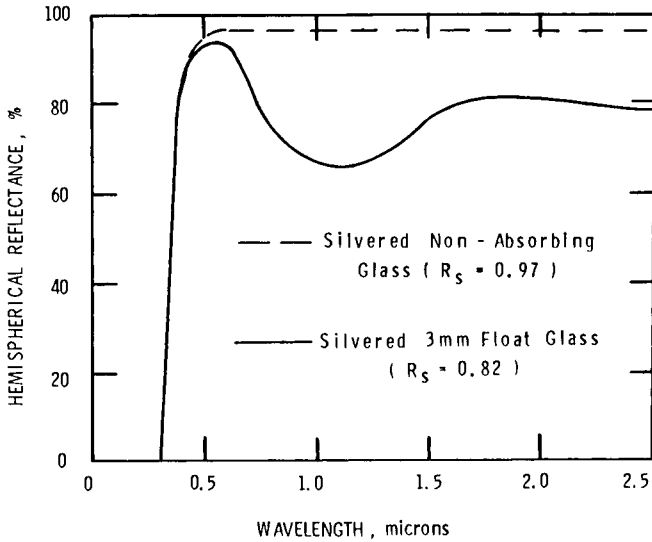
FIGURE 13. The hemispherical reflectance of glass silvered on the back surface. The principal absorbtion in the float glass is due to an iron impurity in the Fe^{++} state (21).

focusing. Cleaning procedures are being studied but those in-
vestigated to date are expensive and may scratch the front sur-
face which in turn will degrade performance. Degradation due to
accumulation of dirt is an important problem. Local environment
tests at Albuquerque have indicated that 5% reduction in reflec-
tion is a typical loss in a two-month exposure (22). The actual
degradation is highly variable depending on local rain or snow
precipitation. This great variability adds to the difficulty of
estimating system performance. The problem of dust accumulation
is discussed in later chapters by P. Roth and R. B. Pettit.

D. Reflectors

    The principle use of reflectors is in concentrators which
multiply the solar flux on a receiver. Typical reflector mate-
rial systems are given in Table IV. Diffuse reflection does not
contribute significantly so it is the specular reflectance which
must be maximized. Figure 14 illustrates specular reflectance as

SPECULAR BEAM PROFILE

R_1 = 0.73
σ_1 = 1.4 mrad
R_2 = 0.15
σ_2 = 12.1 mrad
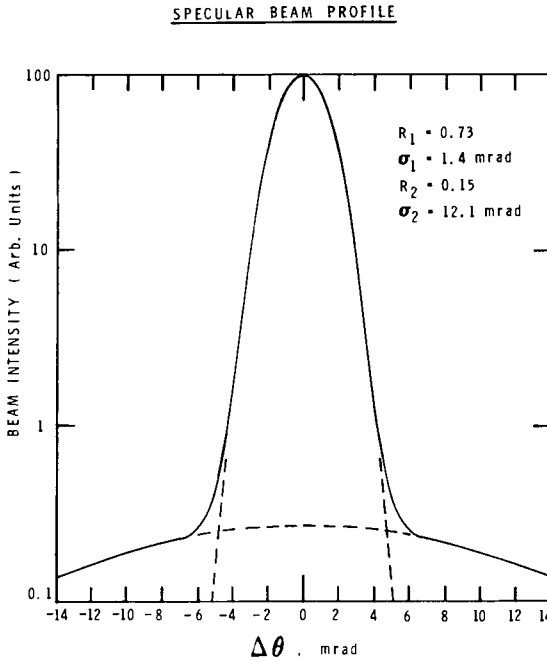
*FIGURE 14. Bidirectional reflection intensity for alumi-
nized teflon plastic film illustrating two components of specu-
lar reflection. Note logarithmic scale (23).*

measured by a bidirectional reflectometer (23). The material for
this illustration is aluminized teflon, chosen because it has
two components of the reflected beam, namely a narrow specular
reflectance and a diffuse component scattered hemispherically.
Note that the beam intensity is displayed on a logarithmic
scale which exaggerates the width of the beam profiles.
Specular reflectance can be characterized by two parameters,
R_s the fraction of energy reflected in the specular beam, and
σ the standard deviation in the beam profile. A high-quality
reflector for concentrator use should have a high R_s and a
low σ. An example of system sensitivity to specular re-
flectance is provided by a reference design for a central re-

ceiver in the 25 to 300 MWe range utilizing an advanced sodium
receiver (24). The system study uses the technique of determin-
ing the break-even cost for a given component as the quality of
that component is reduced. It computes the required reduction in
component cost to maintain the same overall expense of producing
electric energy. Figure 15 displays the break even cost (value)
for various values of the specular reflectance of the heliostat
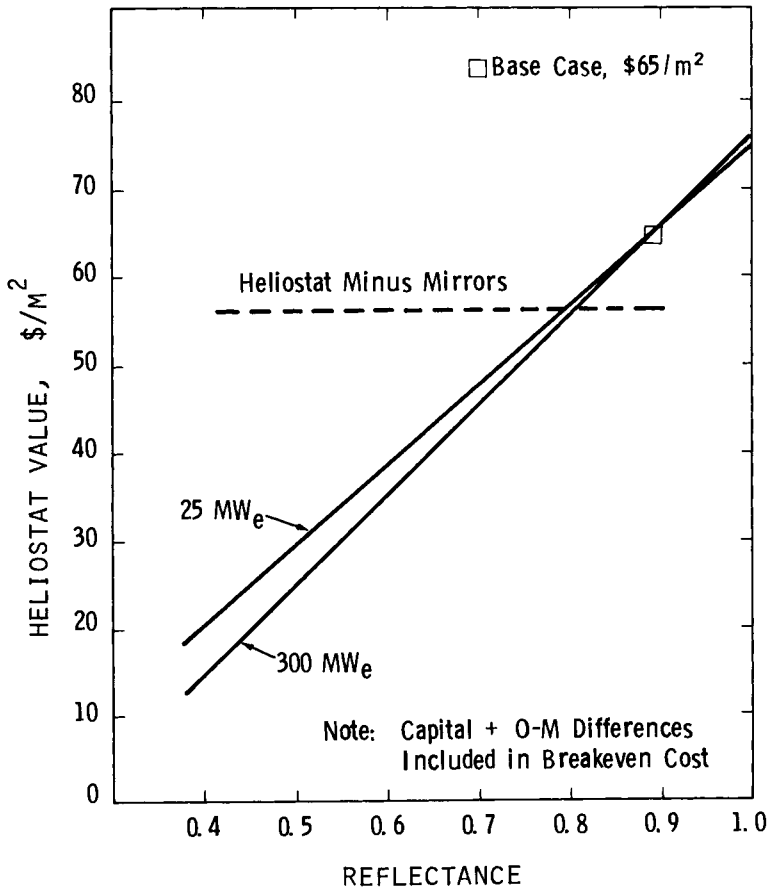
FIGURE 15. Sensitivity of heliostat value to mirror re-
flectance. The value is based on a full economic analysis of a
central receiver solar power plant (24).

mirrors. Note that the cost of the mirrors themselves would have
to drop drastically if reflectance falls a few percentage points
below the reference design of 0.90.

The importance of angular distribution may be considered in
the same way although the calculation of sensitivity to angular
error has actually been done for tracking errors in the heliostat.
Figure 16 indicates than an upper limit for σ is about 2 millirads.
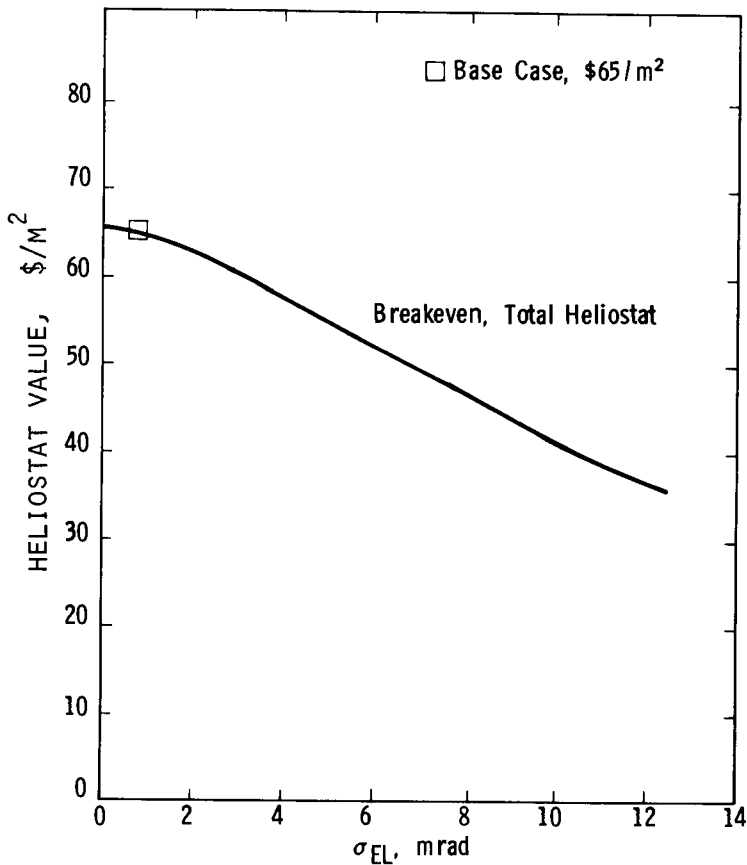
FIGURE 16. Heliostat value vs. standard deviation in angu-
lar accuracy for a central tower receiver (24).

Fortunately silvered glass mirrors can be held well within this
limit. Wren, however, points out that the importance of specu-
larity is highly design specific (25).

IV. CONVERSION PROCESSES

A. *Thermal Processes*

A detailed framework of thermoconversion paths is presented
in Figure 17 (2). Selective absorbtion, an important step in the
conversion of insolation to heat, has already been discussed in
the preceding section. Additional areas of technical interest
and technological importance are containment and thermochemical
storage materials.

1. *Heat Transfer Materials.* Virtually all solar systems for
direct conversion to heat require a heat transfer material to
separate the working fluid from the atmosphere or other incompa-
tible environments. A particularly difficult example is posed by
the Barstow Central Receiver Pilot Plant. The heat transfer fluid
is water/steam operating at high internal pressure which means
that the receiver tubes must be thick-walled. Incoloy 800 has been
selected as the base line material. Problems include creep at the
$550°C$ operating temperature, and low-cycle fatigue induced by the
diurnal cycle and by random clouds. Departure from nucleate boil-
ing will cause high cycle fatigue of the nickel alloy. The com-
bination of these degradation mechanisms over the 30-year life
of the system creates a creep-fatigue interaction mode with
which we have little experience. This application for alloys is
subject to the boiler code which presently qualifies only Incoloy
800 and 2-1/4 chrome 1 moly alloy. If these two alloys prove in-
adequate for the severe stresses of the central receiver applica-
tion, then an extensive characterization program extending over
several years will be required to qualify a new alloy.

Primary Products	Conversion Mechanism Technology	Useful End Products
Ocean Thermal Gradients	Closed and Open Cycle Heat Engines	Electricity Shaft Horsepower
Hot Liquids, Solids, Gases (May require Solar Concentrators)	Thermomechanical Effect	Shaft HP
	Thermoelectric Effect	Electricity
	Various Heat Engines	Electricity, Shaft HP
	Direct Heat Transfer	Process & Space Heat
Atmospheric Winds	Wind Turbines	Electricity, Shaft HP
Evaporation/ Precipitation	Hydroelectric	Electricity

Production of Heat →

Thermoconversion

Primary Process	Primary Products	Conversion Mechanism Technology	Useful End Products

FIGURE 17. Detailed framework for thermal conversion paths (2).

2. *Thermochemical Storage.* Thermochemical storage refers to
the use of reversible chemical reactions with high heat of re-
action to store thermal energy. It offers a number of advantages
such as high energy density in the storage medium, and long-term
storage at ambient temperatures. Thermochemical storage systems
offer a wealth of material problems because the most attractive
materials in terms of specific energy density are also very
corrosive or chemically aggressive. The highest temperatures
and therefore the most corrosive environment are generally found
in the most complex and expensive components of the system,
namely, the reactor/heat exchangers. Side reactions, even at
very low rates, can destroy the reversibility of the chemical
reactions over many cycles. Many of the reactions of interest
for thermochemical storage require a catalyst in one or both
directions so that detailed knowledge must be obtained on catalyst
lifetime, degradation, and poisoning.

Ray Mar will discuss the broad subject of thermochemical
storage in a later chapter. To illustrate the challenge for ma-
terial development, we provide one example now. The reaction

$$2SO_3 = 2SO_2 + O_2$$
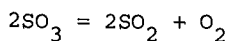
is attractive because of the high heat of reaction of 98.3 kilo-
joules/mole. For practical rates of reaction in either direction,
catalysts are required although an inexpensive V_2O_5 based catalyst
is available for the lower temperature exothermic reaction (from
right to left in the above equation). The endothermic reaction
takes place at temperatures ($>1000°K$) exceeding the melting point
of V_2O_5. Other transition metal oxides are candidates for de-
velopment.

B. Quantum Processes

The detailed framework for photoconversion paths is shown in
Figure 18 (2). Note that direct conversion of sunlight to a
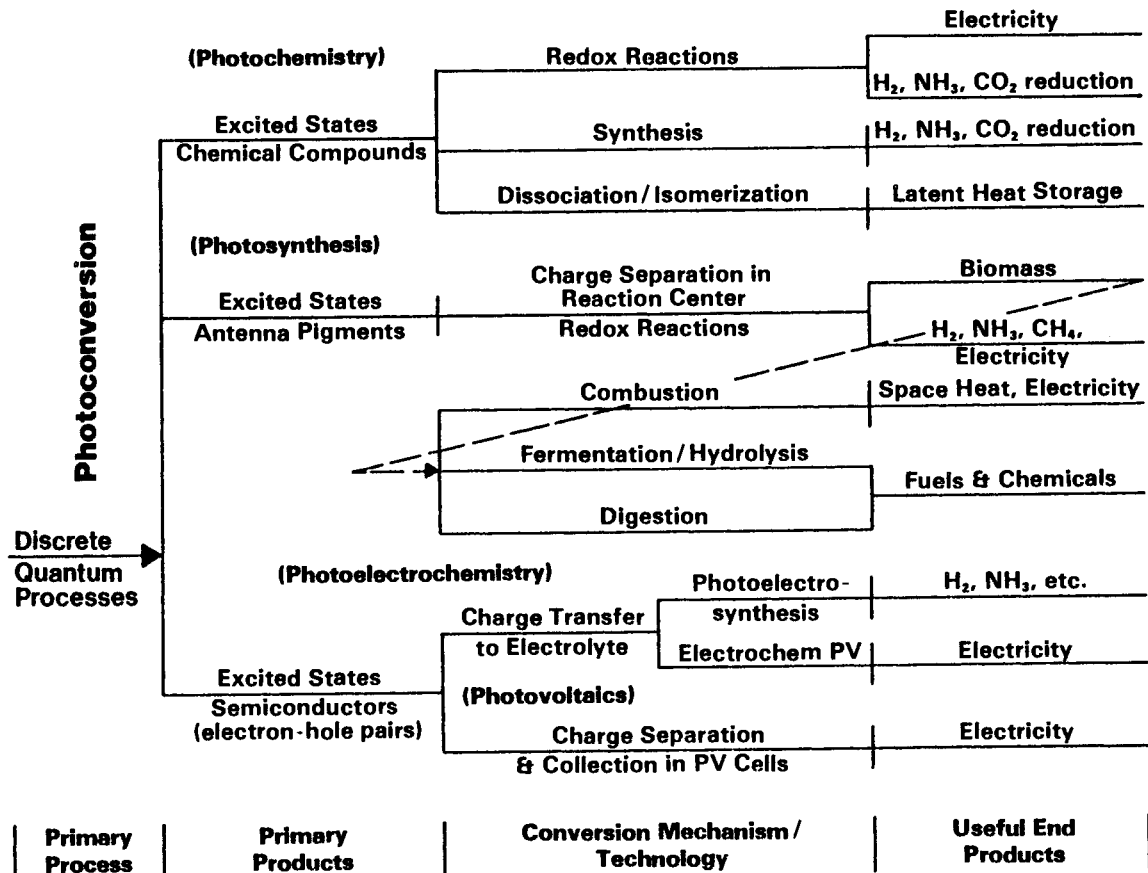
FIGURE 18. Detailed framework for photoconversion paths (2).

chemical or electrical product is a newer technology than thermal
conversion, it can be seen that the conversion technology is not
nearly as well developed. Photoconversion processes are mate-
rials specific. Photovoltaics and photochemistry require semi-
conductors or compounds with appropriate band gaps and configura-
tions to produce charge separation of an electron and a hole that
have been generated by the interaction of a solar photon with the
material. It should be noted that not all photochemistry in-
volves charge-separation, for example, charge separation does not
take place in unimolecular storage and homolytic and hetrolytic
dissociations (see Figure 4). In the area of photosynthesis, the
materials which take part in the reactions, and also the material
used to modify or digest primary photosynthetic products are of
critical importance to this conversion technology. The materials
challenges posed by these conversion technologies require a defini-
tive understanding of the interaction of light with materials in
the solid and liquid states in both inorganic and organic materials
and possibly in the living biological environment.

   1. Efficiency by Concentration. Efficiency is of obvious
importance in all quantum processes. Because solar systems are
subject to cost pressure, system efficiency may be achieved with
concentrating collectors. For such concentrator systems, cost
may be less important than efficiency. Burgess has provided an
example by calculating system costs for photovoltaics used in
simple arrays compared to photovoltaics used in combination with
focusing collectors (26). Figure 19 is a display of the array
cost for the cells, structure, and directly associated equipment
as a function of the cell cost per unit area. The sharply curved
line is for a simple array fixed in orientation. The other two
curves for sun tracking collectors indicate that the array cost
is nearly independent of cell cost out to approximately $1000 per
square meter. The important point to observe in this figure
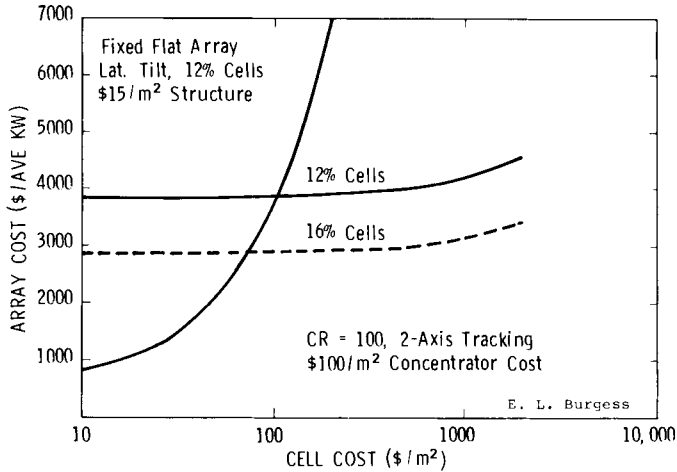
FIGURE 19. The total array cost per average power vs. photo-voltaic cell cost for a fixed flat array and for a concentrator system of 100X for two cell efficiencies. For concentrators, the cost is relatively insensitive to cell cost even at $200/m^2, the minimum present cost (26).

is that an increase of cell efficiency is directly reflected in lower array cost. We will consider ways to increase efficiency in photovoltaics in the next section.

  2. *Photovoltaic Systems*. Silicon solar cells have per-formed admirably in our space program. High fabrication cost has prevented the transfer of this capability to widescale terrestrial use. Materials development has focused on high leverage problems identified by systems analysis.

  The cost of silicon solar cells is being reduced in a step-by-step approach which addresses every element of cost. This program which lacks a single dramatic breakthrough is appealing because of the tremendous advantage of silicon technology. Ex-tensive experience in working with silicon has been gained by the semiconductor industry. The basic physics and chemistry of silicon have been explored in minute detail. Successful large-

scale manufacturing takes place in many locations. The dramatic
cost reductions for solar cells do appear possible. Such reduc-
tion may be achieved by the economy of scale up to large produc-
tion coupled with new technologies. Today silicon solar arrays
cost in the neighborhood of $20 per peak watt. The Department
of Energy target for 1986 is $0.50 per peak watt in 1978 dollars.

Table VI displays the cost goals for the several steps in pro-
ducing silicon solar cell arrays (27). Note that in 1976 every
step was equal or greater in cost than the entire goal for 1986.
Each step or element of the manufacturing process must be re-
duced significantly in order to achieve the ultimate goal. Ma-
terials technology will play a central role in every step. Me-
tallization provides a typical example. The 1976 technology
used silver for the electrical conductors deposited on the front
surface of the cell. The cost of the metal alone was more than
the total cost goal for solar cells. Alternative metallization
materials must be developed which contain little or no precious
metal. A nickel palladium alloy and screened aluminum conductors
are being investigated for this program.

TABLE VI. Department of Energy Goals for Manufacturing Costs
for Silicon Solar Cell Arrays in 1978 Dollars (27)

		Calendar Year					
		76	78	80	82	84	86
Silicon Material	¢/W	190	110	65	9	5	3
Ingot/Sheet Growth Value added	¢/W	480	210	160	190	52	14
Ingot Slicing Value added	¢/W	370	60	50	1	0	0
Cell Manufacture Materials	¢/W	80	40	35	20	8	7
Value added	¢/W	430	120	85	25	9	6
Array Fabrication Materials	¢/W	50	50	30	10	8	8
Value added	¢/W	400	110	80	45	18	12
Array Price Goals	$/W	20	7	5	3	1	0.50

Unresolved problems identified by the Jet Propulsion Labora-
tory are in the area of electrical contacts are: 1) improved
understanding of process limitations and required controls and
the development of low-cost processes that will repeatedly yield
quality contacts (there are a large number of chemical and
physical interactions that today are not predictably controlled);
2) Verification of long-life contacts. This requires definition
and understanding of the interactions of contacts with encapsu-
lants; such as, moisture resistant contacts versus hermetic seals,
and encapsulated module life testing and field demonstrations.

Solar cells can be made from III-V compounds for which
gallium arsenide is the model. These more complex cells are of
interest because of the limitations on silicon cells. Silicon
has a band gap of about 1.1 eV. Photons with energy below that
are not absorbed and photons with energy appreciably above that
lose the excess energy in heat which does not contribute to cell
output. A more general perspective is presented in Figure 20
which shows the various contributions to inefficiency in graphi-
cal form (28). For air mass 0, that is, insolation above the
atmosphere, about 56% of the loss is due to wavelength mismatch.
The remainder is due to practical limits within the cell. The
cell inefficiency is more complicated than indicated by the dia-
gram because the factors are influenced by cell temperature and
by concentration of sunlight.

Inefficiency due to wavelength mismatch can be reduced by
multiple or cascade cells as illustrated in Figure 21 (29). The
best match to the solar spectrum is achieved for the lower band
gap E_{G2} of about 1 eV and the upper band gap E_{G1} of about 1.7 eV.
A dichroic mirror scheme is easier to construct. E. W. James,
et. al., at Varian have constructed an experimental cell using a
dichroic mirror and silicon for the lower band gap material (30).
The higher band gap is provided by $(Al_{0.93}Ga_{0.07})As/(Al_{0.17}Ga_{0.83})As$
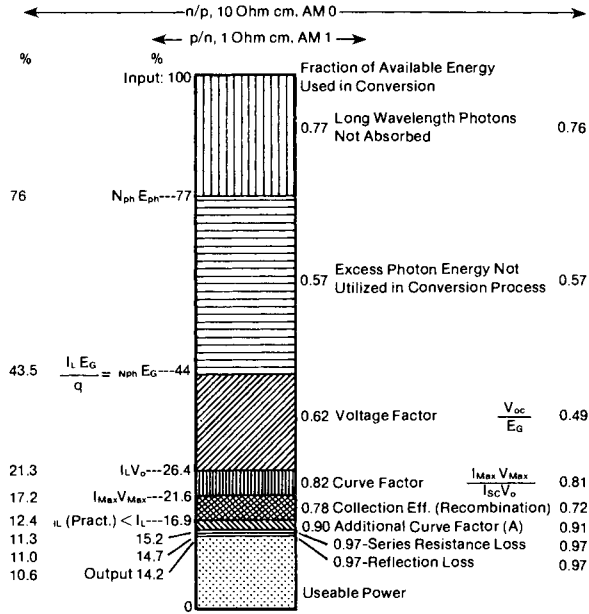
FIGURE 20. Bar chart of distribution of energy losses in the 1-Ω-$cm\rho$-on-η and the 10-Ω-$cm\eta$-on-ρ silicon solar cell under air mass one and air mass zero sunlight, respectively (28).
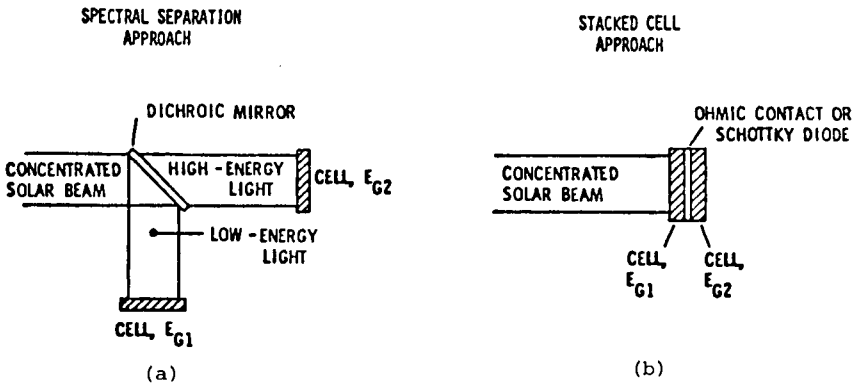
FIGURE 21. Two ways to implement the concept of spectral splitting to achieve higher cell efficiency. The bandgap E_{G1} is lower than E_{G2} (29).

which has a value of 1.65 eV.   Figure 22 shows the high

efficiency of this experimental cell for a range of solar flux.

The figure also displays the contributions to efficiency made by

each of the cells.

One way in which materials technology might dramatically re-

duce the cost of solar cells is by providing mass production

techniques which are inherently inexpensive. One approach under

study is the direct deposition of silicon onto a substrate by

vapor deposition or evaporation which produces a thin film of

polycrystalline silicon. If successful this would bypass a very

expensive part of silicon cell production. Note that in Table

VI the cost goals for growing and slicing single crystal silicon

are more than half of the total cost. The problem with poly-
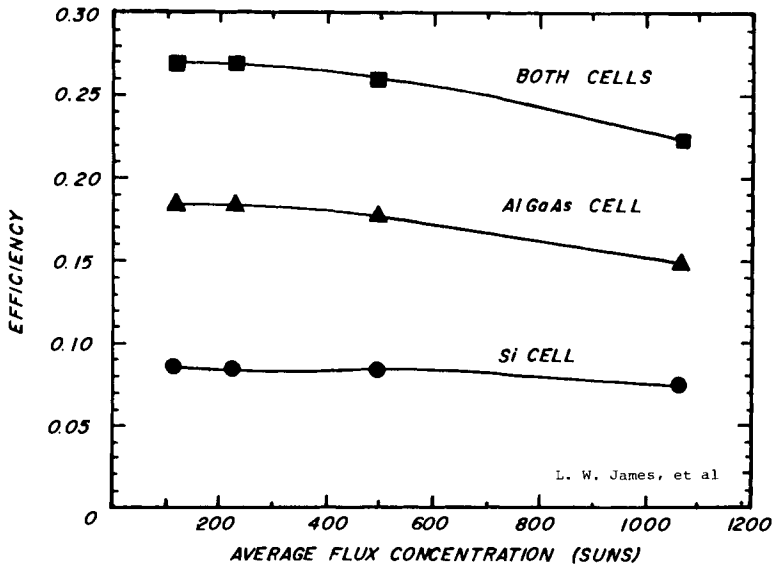
FIGURE 22. The efficiency of a spectral splitting cell
constructed of silicon and $A\ell_{0.99}Ga_{0.07}As/A\ell_{0.17}Ga_{0.83}As$
for a range of solar concentrations. Contributions from cell
are indicated (30).

crystalline silicon cells is a severe performance penalty be-
cause of carrier trapping at the grain boundaries. Chemical va-
por deposition of silicon p-n layer on graphite substrate gave
an average size crystallite of 20-30 microns which resulted in a
cell efficiency of about 1.5% (31). Techniques are now being
developed for passivating grain boundaries so that charge mo-
bility in polycrystalline silicon will be nearly equal to that in
single crystal silicon which in turn should enable high cell
efficiencies. Grain boundary passivation will be discussed by
D. Ginley in his chapter and amorphous seminconductors by R. W.
Griffith in his chapter.

   3. Photoconversion. Photoconversion includes chemical and
biological processes in which radiant energy is converted directly
via quantum processes into other forms of energy (such as chemi-
cal feedstocks, liquid and gaseous fuels, and electricity). The
solar program includes basic research in photochemical, photo-
electrochemical, and photobiological conversion of solar energy.
Photochemistry deals with the effects of light in producing
chemical change. The synthesis of photochemical model systems
that convert light energy into chemical potential (e.g., charge
separation) for processes such as CO_2-reduction or N_2-fixation
is an example of a solar energy application. Photoelectrochem-
istry is the interface between chemistry and solid-state physics.
Its solar applications include the production of chemicals or
electricity at a semiconductor-electrolyte interface. Photo-
biology encompasses the effects of light either in living systems
or in high molecular weight complexes isolated from living sys-
tems. Understanding the primary processes of photosynthesis holds
the key for potential applications in this area (22).

   Although photoconversion mechanisms are capable of relatively
high theoretical conversion efficiencies (20% to 30%), photocon-
version technology is in its infancy. Basic research is needed

in order to design and characterize new molecular systems and to identify limitations of known systems. In all cases, a fundamental understanding of the relevant molecular processes is required to devise more efficient and controllable routes for direct production of fuels, chemicals and electricity from available sunlight.

Photochemical processes are attractive for conversion and storage of solar energy because the sun's energy corresponds to about one to three electron volts per photon, which is in the same range as the chemical bonds in a wide variety of materials (32). Photochemical processes for solar energy conversion are presently the furthest from commercial application because there does not exist a purely synthetic, operable photochemical system However, there does exist a great deal of flexibility vith chemical systems which would allow greater opportunity to assemble and "tune" the components to specific systems requirements (33).

For example, three potentially useful solar-driven reactions are:

$$2H_2O \rightarrow 2H_2 + O_2$$
$$N_2 + 3H_2O \rightarrow 2NH_3 + 3/2 \, O_2$$
$$CO_2 + 2H_2O \rightarrow CH_4 + 2O_2$$
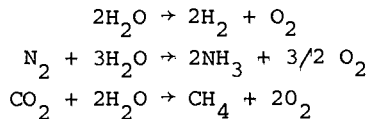
As written, these are 4-, 6-, and 8-electron processes, for which the respective Gibbs free-energy requirements are, on the average, 1.23, 1.17, and 1.06 eV/electron. Assuming that each electron transfer is initiated by sequential absorption of one photon, and taking the energy loss to be 0.8 eV/photon (34), we see that these processes can, in principle, be driven by light in the 600-660 nm range. If the energy loss were, say, 0.5 eV/ photon, light of 710-790 nm would be sufficiently energetic to initiate the reactions.

It is unlikely, however, that any two electrons in such a sequential process will be transferred at the same potential. For

example, in the case of Co_2 reduction, it appears that the first step would occur closer to the redox potential of CO_2/CO_2^- (2.2 eV) (35) than to the average value of 1.06 eV. Thus, a spectrum of reduction potentials will probably be required. If specific, stepwise electron transfer from excited states can be effected, then for each step, it would be possible to determine the optimum wavelengths of light needed to initiate the processes. In this way, the complete solar spectrum might be utilized for photochemical generation of ammonia or methane from renewable resources (33).

Photoelectrochemical energy conversion is based on photoactive semiconductor electrodes that absorb visible light, thereby creating electron/hole pairs which separate in the space-charge layer produced at a semiconductor/liquid electrolyte interface. These separated electrons and holes are subsequently injected into the electrolyte to drive chemical reduction and oxidation reactions.

Photoelectrochemical cells can be configured to produce electricity or to drive chemical reactions (36). The emphasis of the program is on the latter systems. Chemical reactions driven uphill in energy (endoergic) produce fuels (for example, splitting of H_2O into H_2 and O_2); chemical reactions can also be driven downhill in energy (exoergic) and produced useful chemicals (for example, reduction of H_2 to NH_3). For the endoergic case, solar energy is converted into chemical energy, while for the exoergic case, solar energy provides the activation energy for the chemical reaction. The production of hydrogen by photoelectrochemical water splitting (photoelectrolysis) is a primary objective of the program.

Photoelectrochemical systems have high theoretical conversion efficiency (about 25%); they can be operated with inexpensive polycrystalline and/or amorphous electrodes without drastic loss

of efficiency; and simple and inexpensive photochemical reactor
systems based on photochemical diodes in a slurry or colloidal-
type system can be utilized. However, the major problem pre-
venting the implementation of these advantages is the lack of
sufficient chemical stability in the semiconductor electrode
materials that have band gaps in the optimum range (1.0 eV to
2.0 eV) in the electrolyte solutions. D. Ginley discusses
photoelectrochemistry in a later chapter.

The main emphasis of the photobiological efforts are in the
production of hydrogen from the interaction of light with bio-
logical materials (37). A number of biological systems will pro-
duce hydrogen when irradiated with solar radiation. These include
a number of green algaes and a number of photosynthetic micro-
organisms and photosynthetic bacteria. The goal of the re-
searchers in this area is the production of photobiological so-
lar cells. Because of the complexity of the reactions involved
in the absorption of light and long chain molecules, it is suggest-
ed that the reader study a recent review of this field for fur-
ther details (38).

V. SUMMARY

In summary we would like to emphasize that materials along
with design pervade all aspects of the solar energy program. We
have provided examples where materials development can have a
large leverage on system costs. For solar energy to have a large
impact not only must acceptable cost be achieved but the public
must have confidence in the product and its performance over
the design lifetime. That means that we in the technical com-
munity need confidence in reliable performance and confidence in
our life projections. Confidence must be based on a thorough
knowledge of the materials and their properties in the intended

use environment.   The materials community is responsible for that
knowledge.

ACKNOWLEDGMENTS

REFERENCES

1. *Solar Thermal Power Systems Program.*   January 1978, DOE/ET-
    0018/1.

2. Grosskreutz, J.C., *Private Communication.*

3. Lichfield, J.W., et al., "A Method for Identifying Material
    Constraints to Implementation of Solar Energy Technologies",
    PNL-2711, July 1978.

4. Treadwell, G.W., "Design Considerations for Parabolic-
    Cylindrical Solar Collectors", SAND76-0082, July 1976.

5. Butler, B.L., Call, P.J., Jorgensen, G.L., and Pettit, R.B.,
    "Solar Reflectance, Transmittance and Absorptance of Common
    Materials", October 1979, Proceedings of the Solar Indus-
    trial Process Heat Conference, Oakland, California, November
    1979.

6. Call, P.J., "Applications of Passive Thin Films", Chapter 9,
    *Properties of Polycrystalline and Amorphous Thin Films and
    Devices,* L.L. Kazmerski, Editor; Academic Press (1979).

7. Jorgensen, G.L., "Long-Term Glazing Performance", Proceed-
    ings of Solar Glazing: 1979 Topical Conference, Mid-Atlan-
    tic Solar Energy Association, June 1979.   (SERI/TP-31-193)

8. Ratzel, A.C., and Bannerot, R.B., "Commercially Available
    Materials for Use in Flat-Plate Solar Collectors",

Proceedings of 1977 Flat-Plate Solar Collector Conference, CONF-770253, 387 (1978).

9. Eidin, F.E., and Whillauer, D.E., "Plastic Films for Solar Energy Applications", *Proceedings of the United Nations Conference on New Sources of Energy,* Vol. 4, Rome, August 21-31, 519 (1961).

10. *Kynar 500. Polyvinylidene Fluoride for Architectural Finishes.* Pennwalt Corporation, Plastics Department, Three Parkway, Philadelphia, Pennsylvania. Brochure PL138-677-5M-B.

11. Hummel, D.O., *Infrared Analysis of Polymers, Resins and Additives, an Atlas,* Vol. 2, Part 2, Wiley-Interscience, New York (1969).

12. Butler, B.L., and Pettit, R.B., "Optical Evaluation Techniques for Reflecting Solar Concentrators", *SPIE 114,* 43 (1977).

13. Biggs, F., and Vittitoe, C., "The Helios Model for the Optical Behavior of Reflecting Solar Concentrators", SAND76-0347, March 1979.

14. Reuter, R.C., Jr., and Allred, R.E., "Structural and Material Optimization for Solar Collectors", Proceedings of 1979 International Congress of the International Solar Energy Society, May 28 - June 1, 1979.

15. Reuter, R.C., Jr., "Weight Minimization of Sandwich Type Solar Collector Panels", Proceedings of the 14th Intersociety Energy Conversion Engineering Conference, Vol. I, p. 1, August 5-10, 1979.

16. McDonald, G.E., "Spectral Reflectance Properties of Black Chrome for Use as a Solar Selective Coating", NASA TMX-71596, August 1974.

17. Duffie, J.A., and Beckman, W.A., *Solar Energy Thermal Processes,* John Wiley & Sons, Inc., 1974.

18. Treadwell, G.W., McCulloch, W.H., and Rusk, R.S., "Test Results from a Parabolic-Cylindrical Solar Collector",

SAND75-5333, July 1975.

19. Abrams, M., "The Effectiveness of Spectrally Selective Surfaces for Exposed, High-Temperature Solar Absorbers", SAND-75-8300, January 1978.

20. Beauchamp, E.K., "Low Reflection Film for Solar Collector Cover Plates", SAND75-0035, 1975.

21. Vitko, J., "Optical Studies of Second Surface Mirrors Proposed for Use in Solar Heliostats", SAND78-8228, April 1978.

22. Freese, J.M., "Effects of Outdoor Exposure on the Solar Reflectance Properties of Silvered Glass Mirrors", SAND78-1649, September 1978.

23. Pettit, R.B., "Characterization of the Reflected Beam Profile of Solar Mirror Material", *Solar Energy 19*, 733, 1977.

24. Fish, J.J., and Dellin, T.A., "Heliostat Design Cost/Performance Tradeoff", SAND79-8248, November 1979.

25. Wren, L., *J. Energy 3*, 82, 1979.

26. Burgess, E.L., Proceedings of the Society of Photo-Optical Instrumentation Engineers, August 24-25, 1976.

27. Excerpted from First Annual Report, Low-Cost Silicon Solar Array, ERDA/JPL 1012-76/5.

28. "Solar Cells: Outlook for Improved Efficiency", Published by an Ad Hoc Panel on Solar Cell Efficiencies, National Research Council, National Academy of Sciences, Washington, D.C., 1972.

29. Hovel, H.J., *IBM J. Res. Devel. 22*, 112-121, 1978.

30. James, L.W., VanderPlas, H.A., and Moon, R.L., "Novel Solar Cell Concentrator Photovoltaic Converter System", Varian Associates, SAND79-7048.

31. Chu, T.L., et al., *Solar Energy 17*, 229, 1975.

32. Milne, T.A., Connolly, J.S., Inman, R.E., Read, T.B., and Seibert, M., "Research Overview of Biological and Chemical Conversion Methods and Identification of Key Research Areas for SERI", SERI/TR-33-067, 1978.

33. Connolly, J.S., "Solar Photochemistry", Solar Energy Sympo-
     sia of the 1978 Annual Meeting, American Section of the
     International Solar Energy Society, H.W. Boër and A.F.
     Jenkins, Eds., Part I, p. 2-5, 1978.

34. Bolton, J.R., *Science 202,* 705-711, 1978.

35. Jordan, J., and Smith, P.T., *Proc. Chem. Soc.,* 246-247,
     1960.

36. Nozik, J., "Photoelectrochemistry: Applications to Solar
     Energy Conversion", *Annual Review of Physical Chemistry,*
     Vol. 29: 1978, p. 189.

37. Weaver, P., Lien, S., and Seibert, M., "Photobiological
     Production of Hydrogen--A Solar Energy Conversion Option",
     Solar Energy Research Institute, SERI/TR-33-122, 1979.

38. Seibert, N., Connolly, J.S., Milne, T.A., and Reed, T.B.,
     "Biological and Chemical Conversion of Solar Energy at
     SERI", *AICHE Symposium Series, Vol. 74,* No. 181, p. 42,
     1978.

CHAPTER 2

INTRODUCTION TO THE ROLE OF CRYSTAL
DEFECTS IN SOLAR MATERIALS[1]

L.E. Murr
O.T. Inal

Department of Metallurgical and Materials Engineering
New Mexico Institute of Mining and Technology
Socorro, New Mexico

I. INTRODUCTION

To a large extent, the science of materials is dominated by
the role of imperfections in determining or controlling the
properties of materials - physical, chemical, mechanical, elec-
trical, etc. Conversely, the characterization of materials im-
perfections has led to a basic understanding of many properties,
the selective control of imperfections, and as a consequence,
many instances of selective control of residual properties of
materials, or the "tailor making" of materials to accommodate
specialized property requirements, including particular operating
environments. Solar materials are, in the broadest sense, any
materials selected to meet specific requirements involved in
solar applications, which can include collection, conversion,
storage, and transmission or distribution of energy from the sun.
Specific properties of interest can therefore involve optical and
thermal response, corrosion, erosion, and related degradation
resistance, electrical or electronic properties, thermal and

electrical conduction, as well as mechanical properties including
hardness, strength, ductility, etc. In certain cases, one or
many of these properties may be required, while many systems will
consist of an integrated system or composite of many materials
and properties to facilitate a specified function. In such cases,
properties desirable in one portion of the system, which result
by the presence of selective imperfections, may be incompatible
with those required in another portion. That is, imperfections
required to achieve one property may be noticeably detrimental to
another. Consequently, some sort of compromise or optimization
may be required. This can mean a very delicate variation or
control of internal structure, or the number and kind of imper-
fections which must be achieved through changes in crystal
structure, chemical composition, or both.

   Crystal defects, or imperfections, in crystalline materials
are now well documented (1-4). In general, they are grouped into
regimes of zero-dimensional (or point) defects, one-dimensional
(or line) defects, two-dimensional (or planar) defects, and
three-dimensional (or volume) defects. Vacancies, interstitials,
and substitutional impurities constitute the more common point
defects (5) while charge balance requirements in ionic solids
require pairs of such defects to be formed, or some other
charge-compensating mechanism, such as the formation of a color
center where an electron is trapped by an anion vacancy (6).
Dislocations constitute the more common line defects (2), while
interfaces such as grain and phase boundaries, and free surfaces
(the solid-vapor or liquid-vapor interfaces) are characteristic
of planar imperfections (7,8). Point defect aggregates or other
larger voids account for the major types of volume defects (9).
The way in which such defects are formed or interact is an impor-
tant part of understanding how they will effect residual materi-
als properties (3,10). In addition, the amorphous state, charac-
terized by a general lack of structural order, is also of some
practical importance because residual properties are also very

much dependent upon the degree of disorder, or the number and
kind of crystal defects.

II.   CRYSTAL STRUCTURES AND ORDER-DISORDER PHENOMENA

   Crystal defects are characterized as regular types of devia-
tions from (or alterations of) perfect, periodic arrangements of
atoms in a crystal lattice array.   In describing such defects, it
is therefore necessary at the outset to define perfect lattice
arrays.   Such arrays can be characterized by the fourteen differ-
ent Bravais lattices illustrated in Fig. 1.   Solid materials
which are composed of periodic arrays of such lattices (having
unit cell dimensions a, b, c as shown) are called crystalline
materials while solids which do not possess any of the identifi-
able unit cell structures shown in Fig. 1 are called non-crystal-
line or amorphous materials.   In some respects, amorphous solids
might be considered to be characterized by a defect continuum
because there is no periodic reference regime.   However, even
amorphous solids can contain geometric units such as silicate
tetrahedra composing common glass, which is perhaps the most
common example of an amorphous solid.   Crystalline materials can
be described by either long-range or short-range order (or atomic
lattice periodicity) while an amorphous solid exhibits complete
disorder.   Since lattice disorder is a state of high entropy, it
is not a minimum energy configuration and as a consequence all
materials will, under certain conditions, crystallize; forming a
periodic lattice array of either short-range or long-range order;
which can include a superlattice (4).   Many solids which are
non-crystalline (disordered) will therefore slowly crystallize
(or become ordered) when energy (especially thermal energy) is
supplied to drive such a process.
   While all truly non-crystalline solids are disordered, not
all crystalline solids are ordered in the sense that an ordered,
solid solution superstructure is created (4).   An order-disorder
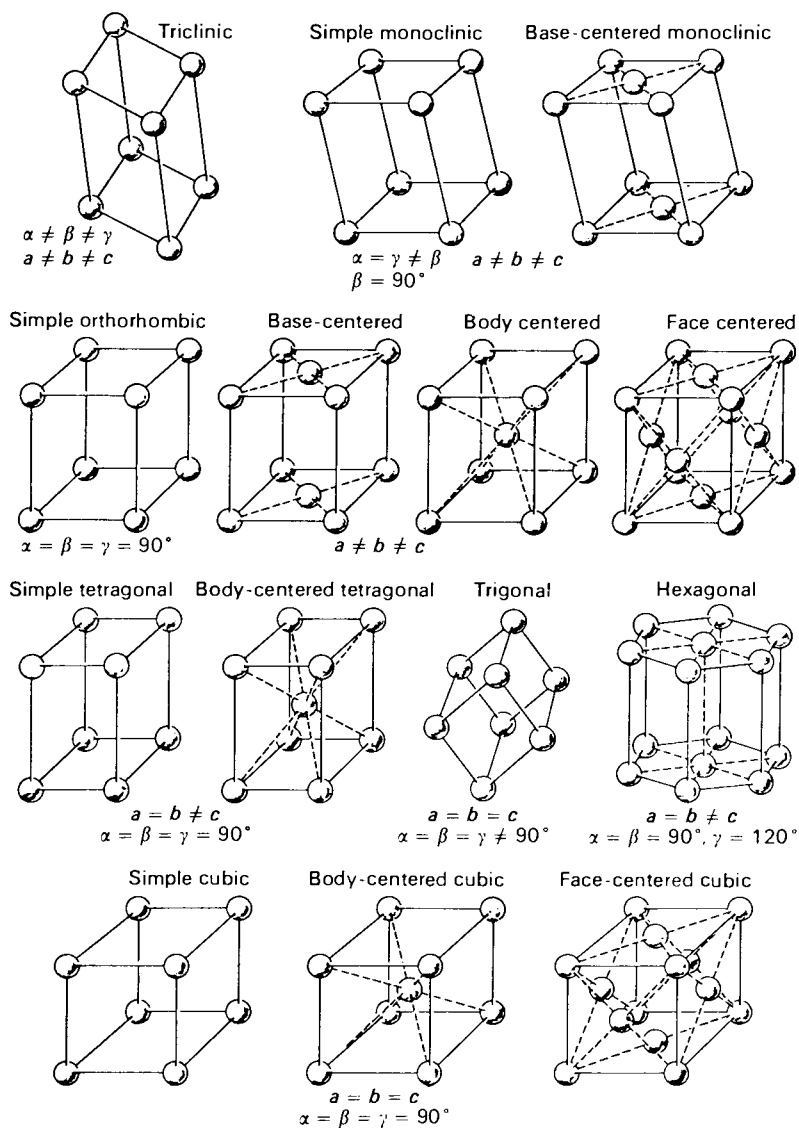
FIGURE 1.   Fourteen Bravais lattices composing seven differ-
ent crystal systems. Each lattice represents a particular unit cell
in a periodic atomic arrangement.   α, β, and γ are the vertex
angles; a, b, c are the unit cell dimensions or lattice parameters.

transition can occur for crystalline solids as illustrated in
Fig. 2, and this rearrangement of atomic species into specific
periodic, lattice positions can have a profound effect on both
the physical and mechanical properties of solid-state material.
Figure 3 illustrates the perfect, periodic atomic structure
characterizing the packing of iridium atoms in an oriented (001)
face-centered cubic crystal lattice array accommodating an equi-
librium-related, pseudo-hemispherical geometry of a needle-pointed
end-form which is observed in a field-ion microscope (7,11,12).
Figure 4 illustrates the crystalline-non-crystalline regimes and
shows the disorder (non-crystalline)-to-order (crystalline)
transition which occurs in a so-called glassy metal or alloy.
The appearance of very short-range crystalline regions in the
glassy structure is especially noticeable by the appearance of
plane-edge "rings" of clusters of iron atoms shown in Fig. 4(d);
especially apparent when these image features are phenomenologi-
cally compared with those of the much larger, perfect crystal
surface shown in the field-ion image of Fig. 3.

It should be apparent from an inspection of Figs. 2 and 4
that temperature is an important factor in the determination of
specific phase equilibria as well as order-disorder phenomena,
and can have a profound effect on the structure and properties of
solar materials, especially at higher temperatures (300 - 600°C)
These effects can be predicted to some extent from phase diagrams,
as illustrated in Fig. 5 showing compound formation in a two-
component (binary) alloy system (13,14).

To a large extent, Fig. 4(a) and (b) are indicative of the
extremes in solid lattice energies which can characterize a
perfectly ordered crystal lattice and a non-crystalline, dis-
ordered array respectively composed of the same number of specific
atoms. A perfect crystal is a minimum energy configuration (8),
while any deviation from this configuration constitutes a degree
of disorder which requires additional energy, or is characteris-
tic of a higher-energy state. Consequently, a higher-energy state
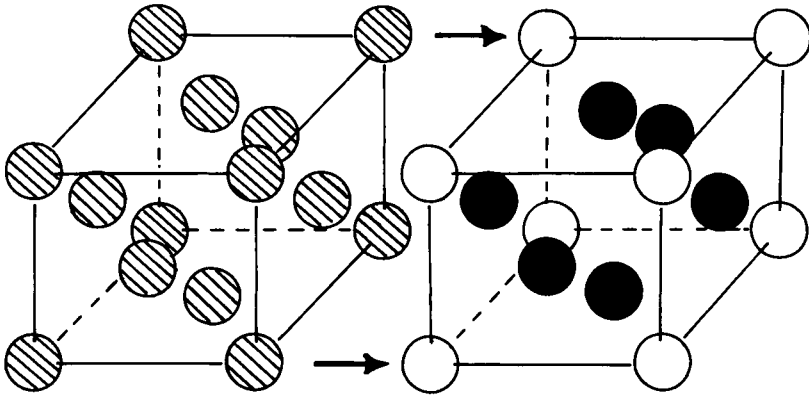
FIGURE 2.   Disorder-to-order transition in a face-centered
cubic A_3B crystal unit cell such as Cu_3Au forming superlattices.

(a)   (b)
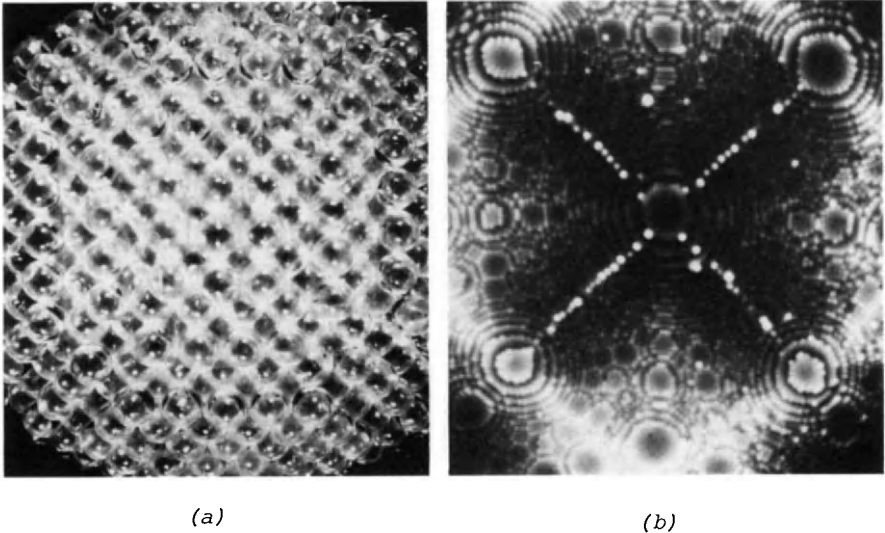
FIGURE 3.   Perfect crystal packing of atoms to accommodate a
pseudo-hemispherical end form in the [001] direction.   (a) Ball
model.   (b) Field-ion image of iridium [001] end form showing
atomic structure.   Note that the [001] direction is normal to the
page.   The symmetries observed arise from plane-packing and
crystal plane symmetries which are apparent from a [001] stereo-
graphic projection.   Individual image dots are single iridium
atoms.

(a)   (b)

(c)   (d)
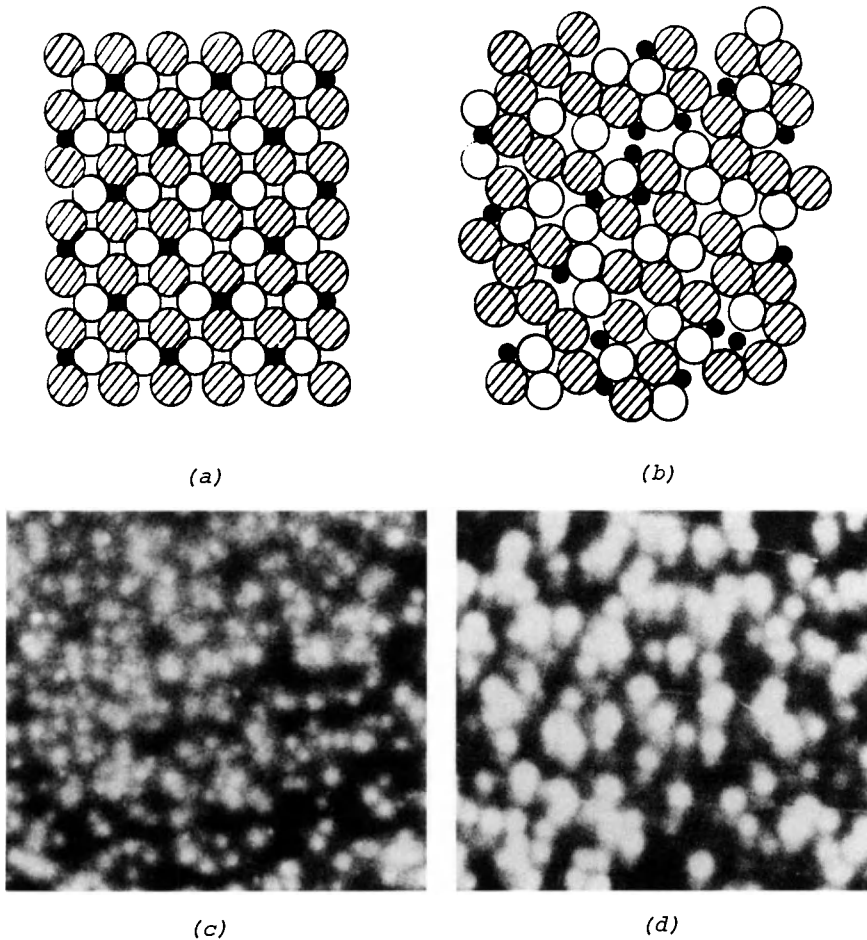
FIGURE 4. Lattice order-disorder phenomena. (a) Perfect
cubic lattice with long-range order. (b) Completely disordered
structure in (a). There is no recognizable unit cell or unit cell
periodicity. (c) Disordered (amorphous) $Fe_{80}B_{20}$ alloy surface
observed in the field-ion microscope. (d) Same $Fe_{80}B_{20}$ as in (a)
after partial ordering and segregation at $780°C$. The image is
dominated by clusters of iron. Fe_2B and Fe_3B phases are only
weakly imaged and suppressed in the background.

will, given the opportunity, revert to a minimum energy config-

uration, and such intrinsic instabilities suggest that essen-

tially all materials are, to some degree, unstable. Consequently,

their structures and properties can be expected to change with
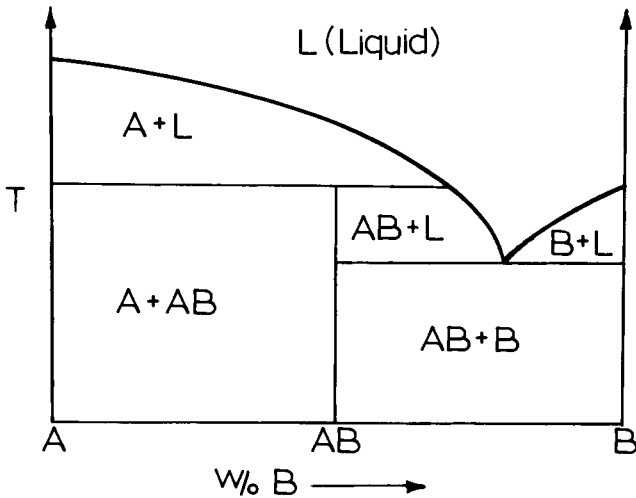
FIGURE 5. Compound formation in a binary system of elements A and B as a function of temperature and composition.

time and exposure to environments which provide an energy-related mechanism for driving the system toward a lower energy state. This can be achieved by alterations in the range of order or variations in defect density and arrangement, or the degree of disorder, and can include the imposition of temperature, pressure (stress), and compositional changes as a result of environmental reactions.

III. CRYSTAL LATTICE DEFECTS AND SOLAR-RELATED MATERIALS STRUCTURES

With reference to the perfect, ordered crystal regime shown in Figs. 2-4, the amorphous as well as the disordered regimes are defect states. However, these defects are not readily defined as systematic variations in the three-dimensional space lattices shown in Fig. 1. Such variations can be geometrically character- ized by variations in single atom periodicity or other interrup- tions within the lattice as a result of the insertion of single atoms, variations in linear arrays or chains of atoms, variations

in the periodicities over an area or plane of atoms or of the
coincidence of separate crystals, and three-dimensional inter-
ruptions in atomic periodicity.

A.   Point (Zero-Dimensional) Defects

Point defects occur in a space lattice when atom positions
are vacant (vacancies) (or anion-cation vacancy pairs in ionic
solids in order to maintain charge neutrality), when atoms occur
within the lattice interstices (interstitials), when (especially
in ionic solids where charge neutrality must be preserved) a
vacancy-interstitial pair is formed, or when a foreign or impurity
atom substitutes for a normal lattice atom (substitutional impur-
ity). The substitutional impurity can also be the same atom
having a different valence, and an interstitial impurity can also
be an atom of a different species or of different valence. An
additional, basic modification of the vacancy in an ionic crystal
can also occur when instead of forming a vacancy-interstitial
pair, an electron is trapped at the site of an anion vacancy,
thereby maintaining charge neutrality. Such a defect is referred
to as a color center (or F-center) because of its selective effect
upon optical absorption causing coloring in transparent crystals.
Figure 6 illustrates the appearance of these different point
defects in a simple cubic-crystal lattice section.

Point defects of the type shown in Fig. 6 can arise during
growth and solidification, in response to energetic radiation of
various types, and through diffusion. Their effects on a variety
of electrical, optical, mechanical and other properties can be
visualized to some extent by considering the effect they would
have on an electron or related electromagnetic wave propagating
through the lattice, and the variations such defects would
impose upon lattice atom cohesion and coordination.
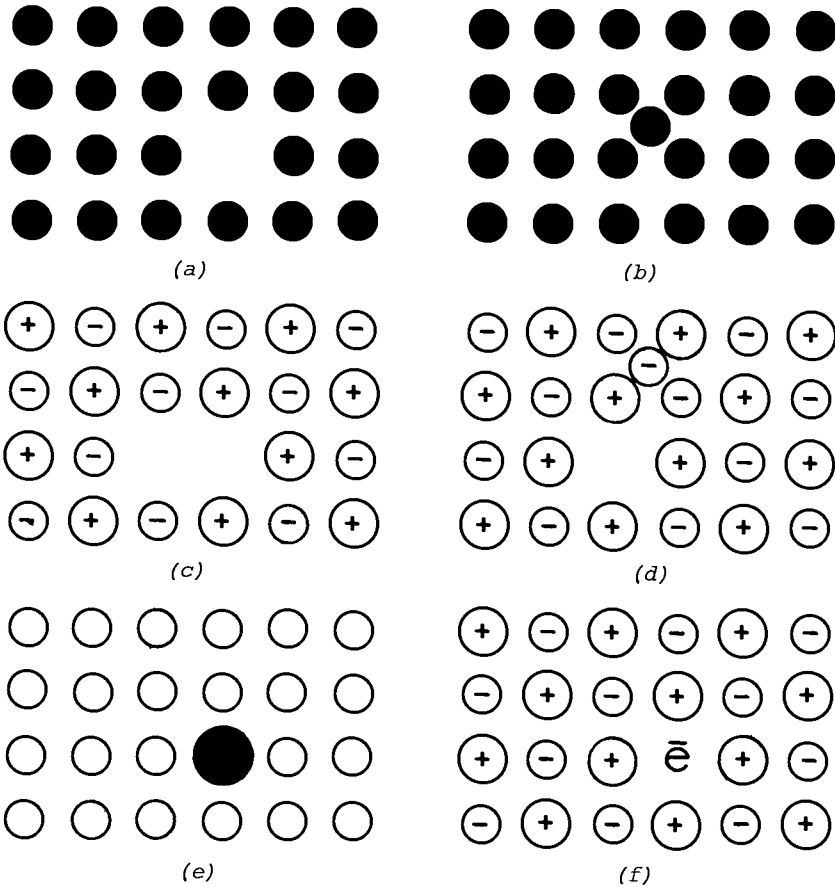
FIGURE 6. Point defects. (a) Vacancy. (b) Interstitial.
(c) Cation-anion vacancy pair maintaining charge neutrality.
(d) Vacancy-interstitial pair maintaining charge neutrality.
(e) Substitutional impurity. (f) Color center (anion vacancy
site occupied by an electron, $\bar{e}$).

B. Line (One-Dimensional) Defects

Figure 7 illustrates the simplest type of Volterra (15) or
line defects, consisting of an extra half-plane in the same
simple cubic crystal lattice section shown in Fig. 6(a). Crystal
lattice line defects are referred to as dislocations, and Fig. 7
shows an edge-type dislocation which has the property of glide on
a close-packed plane or slip plane, thereby accommodating lattice
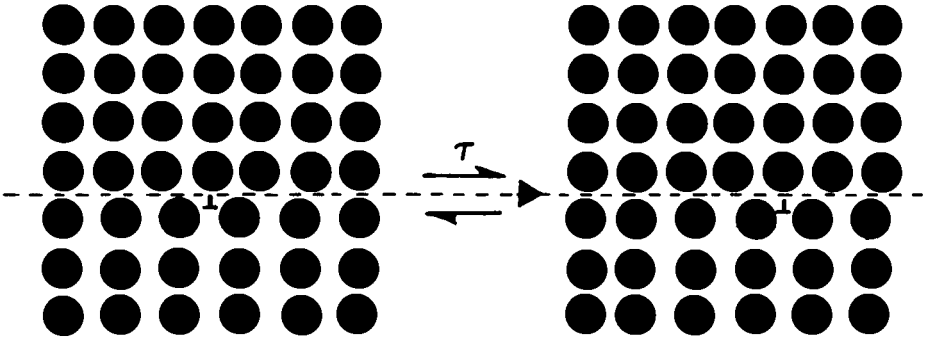
FIGURE 7. Shear-induced motion of a simple edge dislocation.
The shear stress is denoted by τ.

shear. Dislocations of the type shown in Fig. 7 allow for slip
as a systematic lattice translation which can be visualized by
the motion of the dislocation line, which is perpendicular to the
page in Fig. 7(a) and (b). It can be observed in Fig. 7 that if
the dislocation line were to continue moving to the right (by
successive lattice atom translations) a step (slip step) would be
created. Similarly, if a perfect crystal section is cut and
systematically sheared as shown in Fig. 8, an edge dislocation is
created within the lattice section and is connected with a screw
dislocation by a continuous dislocation line shown dotted. The
lattice distortion creating the dislocation line is characterized
by a Burgers vector which is perpendicular to the edge disloca-
tion line and parallel to the corresponding screw dislocation
line in Fig. 8. Moving away from the two surfaces in Fig. 8 upon
which the edge or screw dislocation lines emerge (dislocation
lines are normal to the corresponding surfaces) results in a
systematic variation in dislocation type from pure edge (where
$\underset{\sim}{b}$, the Burgers vector is perpendicular to the dislocation line)
to pure screw (where $\underset{\sim}{b}$ is parallel to the dislocation line) (3).
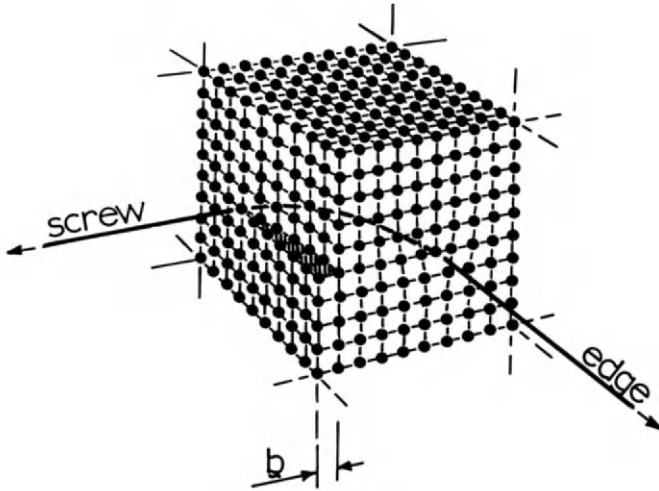
FIGURE 8. Total dislocation (having edge and screw-type character) in a section of a simple cubic crystal lattice.

Since dislocations, as shown in Figs. 7 and 8, are associated with stress (deformation), it is perhaps readily apparent that they arise in crystals in response to deformation, or accommodate externally applied stresses. Furthermore, it can be visualized from both Figs. 7 and 8 that because of the plane bending to accommodate the dislocation within the crystal lattice, a region of localized stress (or strain) occurs along the dislocation line. This disturbance would also be expected to have an effect upon wave propagation or the behavior of electrons in a crystal lattice section, and their movement could allow them to interact with the point defects shown in Fig. 6. Such interactions could impede the motion of the dislocation line, or allow for absorption of point defects or arrays of point defects along the dislocation line, within the so-called "core" region. For example, impurity atoms absorbed along a dislocation line would transform this linear array into a special regime which could profoundly effect physical and mechanical properties. In addition to the ability of dislocations to glide along a slip plane as illustrated

in Fig. 7, the selective absorption of vacancies at a dislocation core can allow for the motion of a dislocation line in a direction normal to the slip plane shown, giving rise to a process called climb. Since vacancy motion can occur by diffusion resulting by thermal activation, climb is normally considered to be associated with hot environments. Consequently, the application of both heat and stress can allow for alterations in dislocation arrangement in crystals as a result of both glide and climb processes. The motion of dislocations can be impeded by interactions with other dislocations and therefore as the density of dislocations (line length per unit volume of crystal expressed as cm^{-2}) increases, there is a marked effect upon deformation. This gives rise to an increase in yield stress and ultimate tensile stress, as well as hardness; and physical and mechanical properties of all crystalline materials are related to dislocation density. Consequently, the mechanical properties of solar-related support materials are, as is well known, markedly influenced by dislocations; especially fatigue, creep, and other modes of deformation leading to eventual failure (3,5,10,15).

Dislocations in face-centered cubic materials are characterized by Burgers vectors of the type $\frac{a}{2}$ <110>, where a is the lattice parameter. The dislocation line is characterized by glide upon {111} planes in specific <110> directions. The energy associated with the formation of a unit length of dislocation line is proportional to the square of the Burgers vector and as a consequence can be lowered by selective adjustments in lattice translations (3). This process creates partial dislocations which result by the systematic splitting up of total dislocations into two partials having Burgers vectors different from the total dislocation; resulting in a lower total energy. The partials so created are connected by a region of systematic lattice distortion which is coincident with the slip plane, and which, as a consequence, forms a planar (or two-dimensional) defect having an area equal to the product of the dislocation length and the
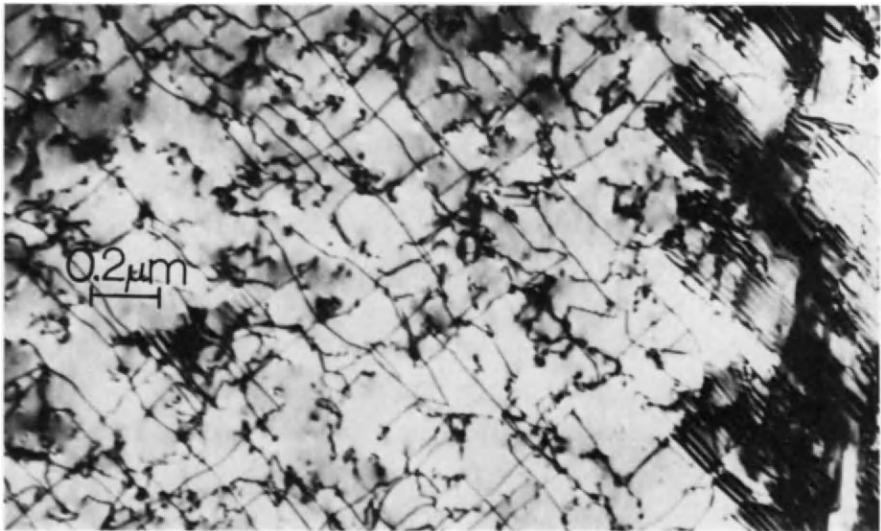
*FIGURE 9.   Dislocations in a 0.1 μm thick nickel electrode-
posited layer.   The dislocations appear as black lines in the
bright-field electron transmission image because plane bending
around the dislocation core as shown in Figs. 7 and 8 causes
electrons diffracted in this regime to be systematically excluded
in the image.   Stacking fault and microtwin fringes are also
observed in the image area.*

distance separating the partials, or the area enclosed by a dis-
location loop. Dislocations in crystals either terminate upon
themselves (forming a dislocation loop), another dislocation
(which can lead to the formation of networks), or at a free sur-
face or interface. Dislocation lines do not end within a volume
of perfect crystal. These features are now well known and well
documented (2,3,15). Figure 9 shows dislocations in a thin
electrodeposit of nickel observed by transmission electron
microscopy (12).

     In addition to applied stresses, dislocations (and stacking
faults) can arise in response to internal stresses or they can
accommodate stresses which arise in solids during growth and
related processes of lattice accommodation. Dislocations can
also be regarded as regions of different stoichiometry in many

solid crystalline materials, and can be altered in form to main-
tain charge neutrality in ionic solids. Because the stoichiom-
etry (or charge regime) in the vicinity of a dislocation line
emerging on a surface can be different from the surrounding
matrix, and as a consequence of differences in local lattice
energy in the dislocation core (at the point where a dislocation
line emerges on a free surface), dislocations can act as prefer-
ential sites for incipient process initiation such as corrosion
(dissolution or solubilization) and related surface reactions; or
nucleation and growth. This is especially true for screw dislo-
cations which, as shown in Fig. 8, give rise to a spiral ramp
allowing for crystal growth in the direction of the screw dislo-
cation line by a spiral growth around the dislocation line. In
most cases, however, dislocations have little effect upon growth
processes such as the deposition and growth of one material upon
another in processes like vacuum vapor deposition, vacuum sput-
tering, or electrodeposition. Such processes of film growth upon
a substrate are mainly characterized by two-dimensional (layer)
growth and are controlled primarily by crystallographic orienta-
tion - initially that of the substrate, and then as the influence
becomes rapidly weaker as a result of continuing growth away from
the substrate, that of the overgrowth itself; including recrys-
tallization (16,17). These features are illustrated in Fig. 10
which shows the growth of a nickel electrodeposit upon a poly-
crystalline copper substrate at various overgrowth thicknesses.

C.   Planar (Two-Dimensional) Defects

We have briefly described one of the simplest types of planar
defects in crystalline materials in the discussion of stacking
faults above (Sect. III B). Stacking faults are by their nature
prominent in materials where the stacking-fault free energy is
low because dislocations are widely separated in such materials
and cannot cross-slip easily (move from one slip plane to another,
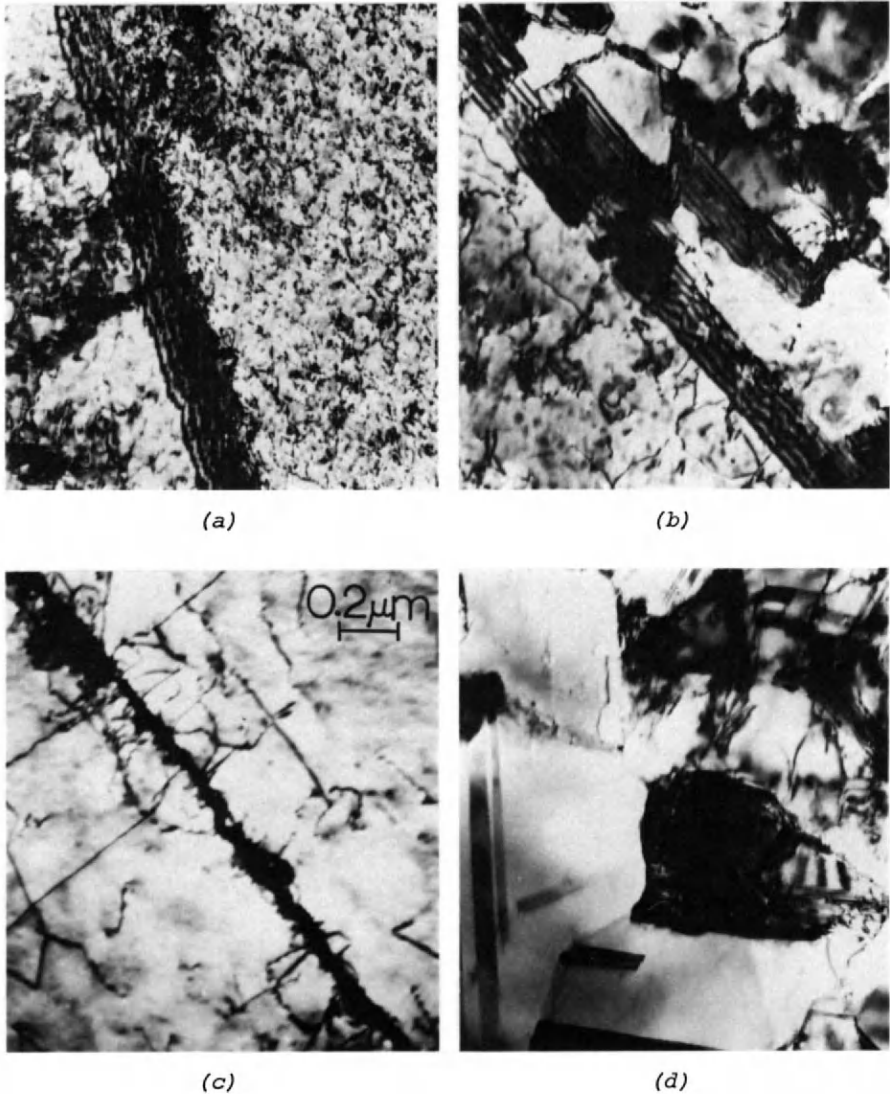
FIGURE 10.   Sequence of bright-field electron micrographs
showing the development of microstructure in electrodeposited
nickel overgrowths upon annealed, polycrystalline copper. (a)
0.1 μm Ni overgrowth. Note different dislocation arrangements
and density on either side of the grain boundary. (b) 0.5 μm Ni
overgrowth showing stacking faults and twins developing. (c) 5
μm Ni overgrowth showing a reduction in dislocation density and a
variation in grain and grain boundary structure. (d) 25 μm Ni
overgrowth showing recrystallization phenomena.

(a)   (b)
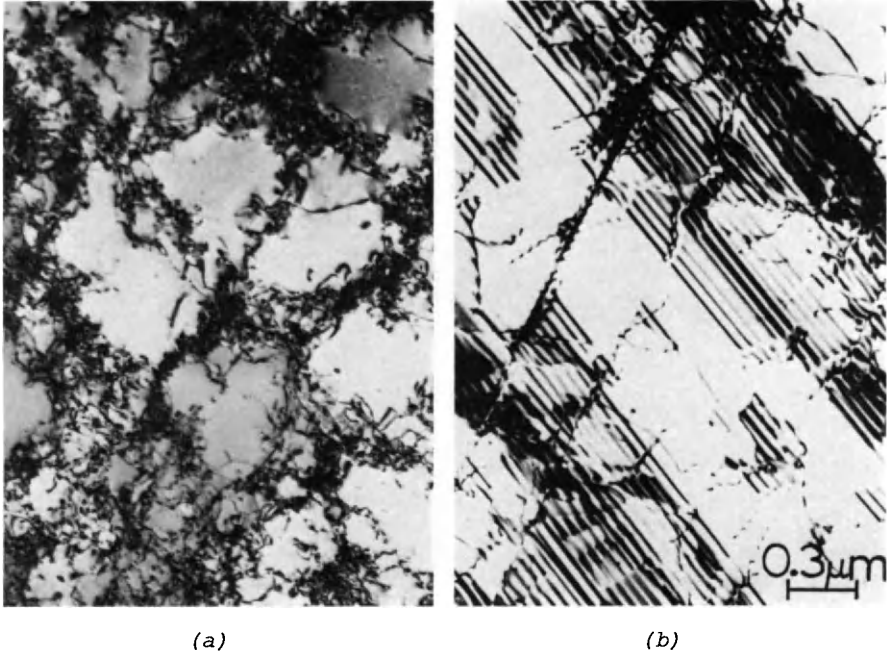
FIGURE 11. Residual microstructures resulting from differ-
ences in stacking-fault free energy, which governs the ability of
dislocations to extend forming stacking faults, or cross-slip.
(a) Dislocation cells in nickel resulting by extensive cross-slip
of dislocations. (b) Planar dislocation arrays and stacking
faults in stainless steel where cross-slip is effectively pro-
hibited. Both materials in sheet form were subjected to a shock
stress of 15 GPa magnitude and 2 μs duration.

parallel slip plane). Consequently, materials with a high stack-
ing-fault free energy respond very differently to deformation:
those with high stacking-fault free energy forming complex dislo-
cation arrays as a consequence of prominent cross-slip, as com-
pared to those with low stacking-fault free energy forming
primarily planar dislocation arrays or stacking faults. These
features are illustrated in Fig. 11 for nickel (having a stacking-
fault free energy of 128 mJ/m^2) and type 304 stainless steel
(having a stacking-fault free energy of 21 mJ/m^2), subjected to
exactly the same deformation (3,8,15).
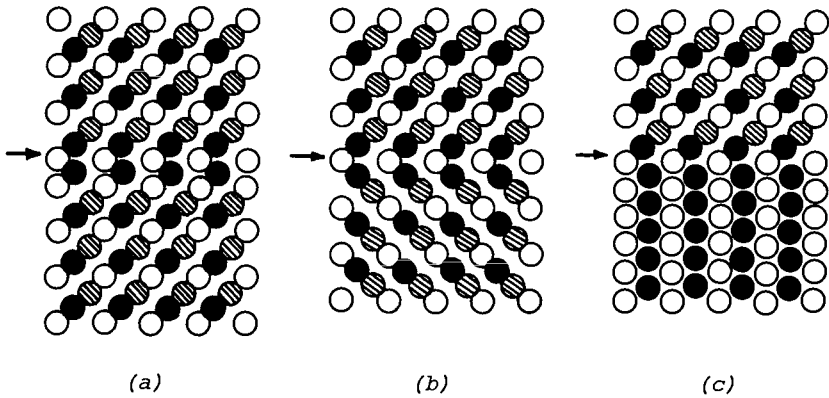
FIGURE 12.   Schematic view of planar shear interfaces formed in {111} planes of a face-centered cubic lattice having perfect atomic packing periodicities A, B, C, denoted ○ , ● , ◍ . *(a) Single intrinsic stacking fault (arrow). (b) Overlapping stacking faults (on every {111} plane) producing a twinned region separated by planar interfaces (arrow).   (c) Systematic stacking-fault formation and shear adjustments producing a new phase separated by planar interfaces (phase boundaries) (arrow).*

Figure 12 shows some simple schematic diagrams for the formation of stacking faults and related planar defects in face-centered cubic materials by the systematic shearing of {111} planes through the propagation of partial dislocations.   Deformation twins are observed to result by the formation of intrinsic stacking faults on every (111) plane while more selective shear operations result in a hexagonal close-packed regime with planar interfaces separating the hcp phase from the unaltered fcc phase. Such solid interfaces, separating twinned regions or different phases (having differences in crystal structure, composition, or both), are also planar defects because they interrupt the periodicity of any specific phase, and act as a region of transition from one structure to another.

1. *Grain Boundaries.* When crystals of the same material are
joined together, the interface characterizing the transition from
one orientation to the other is called a grain boundary. Essen-
tially all useful engineering materials are polycrystalline and
therefore contain grain boundaries separating the individual
grains or crystallites. In general, a grain boundary can be
characterized by five degrees of freedom (8,18). In the case of
very elementary boundaries characterized by only one symmetrical
rotational parameter, or the angle of misorientation between two
identical lattices, the boundary can be regarded simply as a
regular array of edge dislocations accommodating the lattice mis-
match. This dislocation concept of a grain boundary usually
applies strictly to low angles of misorientation ($\Theta \leq 5°$), how-
ever regularly spaced dislocations can be shown to characterize
the intrinsic or equilibrium structure of even larger-angle
boundaries. For symmetrical, low-angle boundaries, the disloca-
tion spacing is given approximately by the ratio of the Burgers
vector to the misorientation angle (in radians) ($d \cong |\underset{\sim}{b}|/\Theta$).
Consequently, for very small misorientations the spacing can be
large (hundreds or thousands of nanometers) while for large mis-
orientations, the spacings become very small. In addition, the
energy per unit area of a grain boundary is proportional to the
angle of misorientation for a simple, symmetrical boundary, and
increases rapidly with increasing misorientation between zero and
roughly $15°$ (8).

Figure 13 demonstrates some of these features and shows
several, more realistic examples of grain boundaries. Figures
13(a) and (b) show the idealized grain boundary structures des-
cribed above while Fig. 13(c) shows a surface view of the atomic
features of a non-symmetric, large-angle grain boundary in irid-
ium as observed in the field-ion microscope (8,11,12). By sys-
tematically removing successive atom layers of the iridium end
form in Fig. 13(c) by field evaporation (11,12), the detailed
structure of the grain boundary plane can be reconstructed. It

(a)

(b)

(c)

(d)
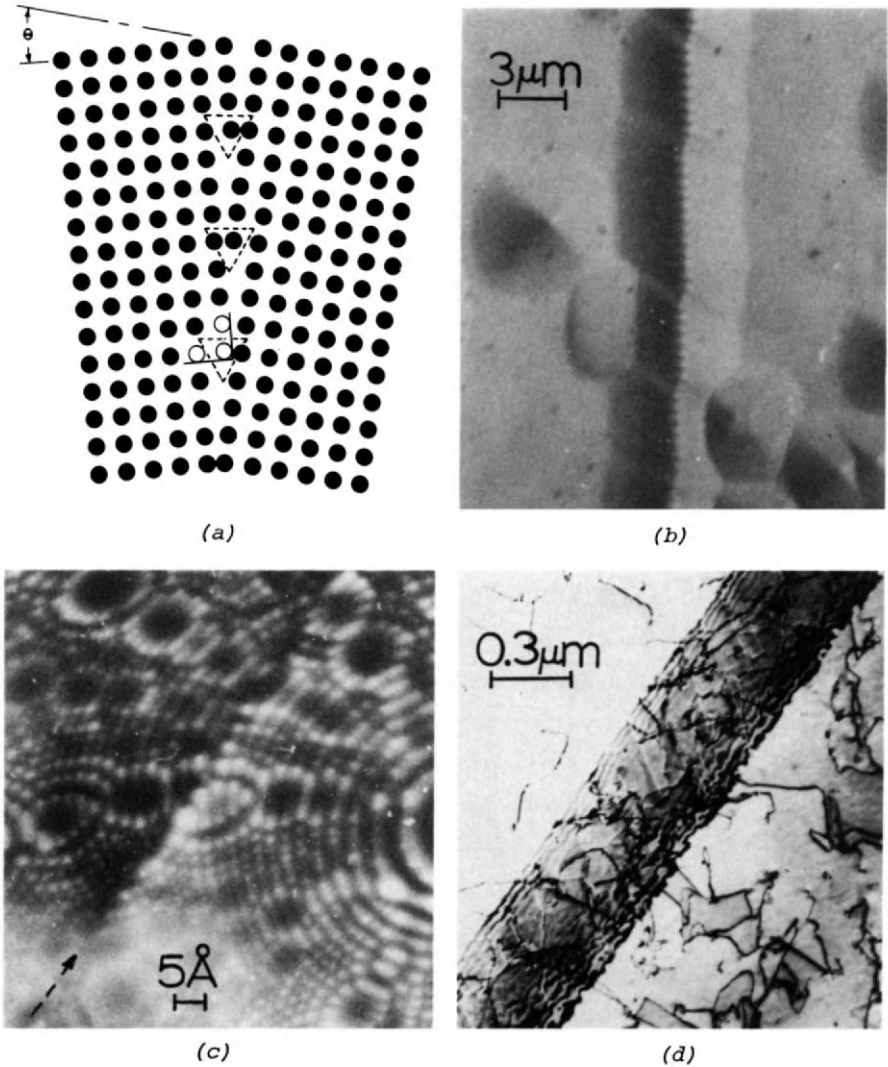
FIGURE 13. Examples of grain boundary structure. (a) Simple
(symmetrical) grain boundary schematic showing intrinsic disloca-
tion structure (dotted triangles) which can also be regarded as
primitive ledges (open circles). The grain misorientation is
denoted by θ. (b) Low-angle grain boundary in LiF characterized
by regularly spaced dislocation etch pits observed by optical
microscopy. (c) Asymmetrical grain boundary in an iridium field-
emission end form. The arrow denotes the interface. (d) Grain
boundary projection from a thin section in an electrodeposited Ni
film showing dislocations and more complex structure characteriz-
ing the interface. Bright-field transmission electron micrograph.

must be recognized that the area might only be 0.01 μm on a side.
By comparison, grain boundaries can be observed in projection by
electron transmission through thin polycrystalline films, and
this technique can allow for a complete characterization of many
representative grain boundaries in a specific solid-state mater-
ial as illustrated in Fig. 13(d). It is especially significant
to observe that while the intrinsic dislocation structure is not
visible in Fig. 13(d), other so-called extrinsic dislocations are
visible within the boundary, and dislocations are observed to
terminate on the boundary plane as described previously. Extrin-
sic dislocation structures can accommodate deviations from ideal-
ized coincidence arrays (low energy configurations) or allow for
other structural phenomena. Extrinsic grain boundary dislocations
can also be regarded as ledges upon the boundary plane or bound-
ary "surface", and can actually take the form of large steps
having a height of many matrix dislocation Burgers vectors. To
some extent, the concept of interfacial structural steps or ledges
is even apparent in Fig. 13(a), but extrinsic dislocations or
ledges are usually not associated with the equilibrium boundary
structure. Figures 14 and 15 illustrate some of the features of
intrinsic and extrinsic grain boundary dislocation structure
alluded to above, and Fig. 15 shows the interaction of the extrin-
sic structure (ledges) with the equilibrium dislocation structure
of a grain boundary in molybdenum. Figure 15(b) convincingly
demonstrates the very specific step character of large grain
boundary ledges as evidenced by the contrast fringe displacements
along particular ledge portions.

Grain boundaries, because of their regular dislocation arrays
(intrinsic grain boundary dislocations) and other more complex
extrinsic or ledge structures become very prominent regimes ad-
sorbing or absorbing impurities, creating a transitional or inter-
facial phase region which can have a profound effect upon the
physical and mechanical properties of solar materials. Figure 16
shows a more complete view of grain boundary structure which is
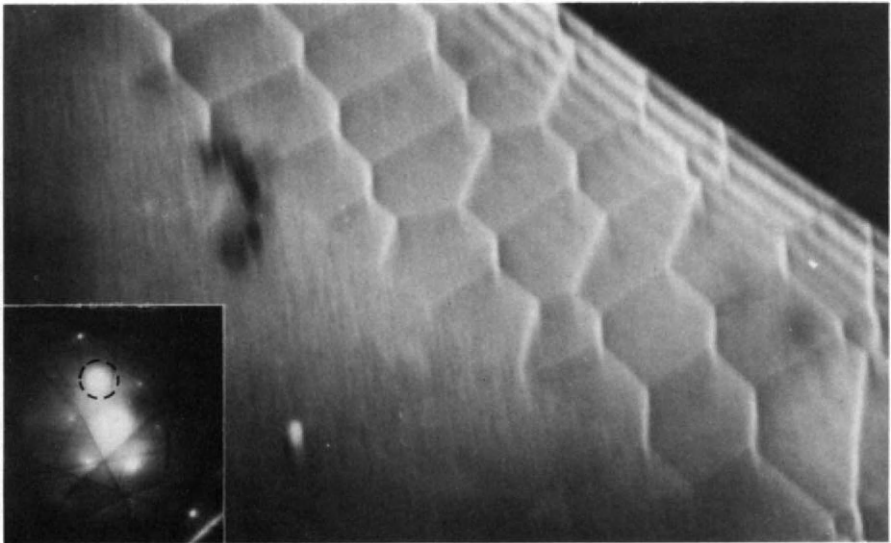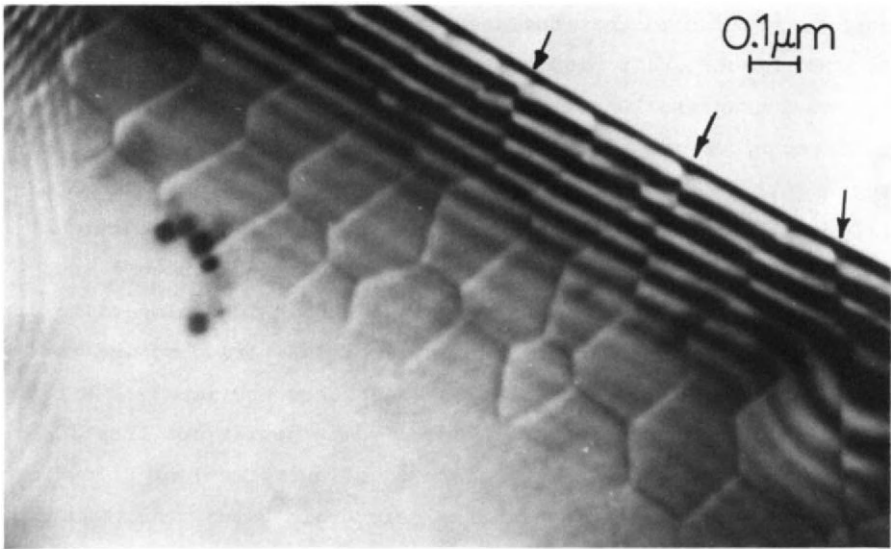
(b)

FIGURE 14. Grain boundary dislocation networks forming ledges
on the interfacial planes as evidenced by the boundary contrast
fringe displacements indicated by the arrows. (a) Bright-field
electron transmission image in 304 stainless steel. (b) Dark-
field image utilizing strong reflection shown circled in the
selected-area electron diffraction pattern insert.
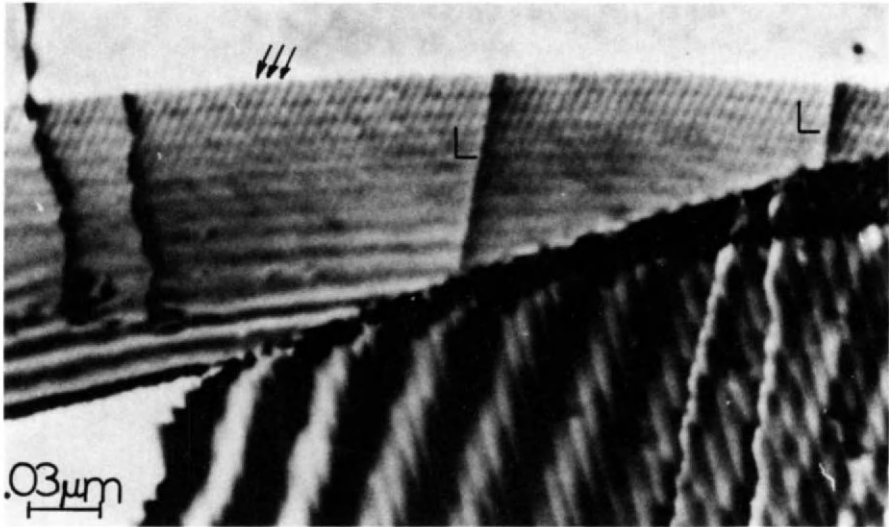
(a)
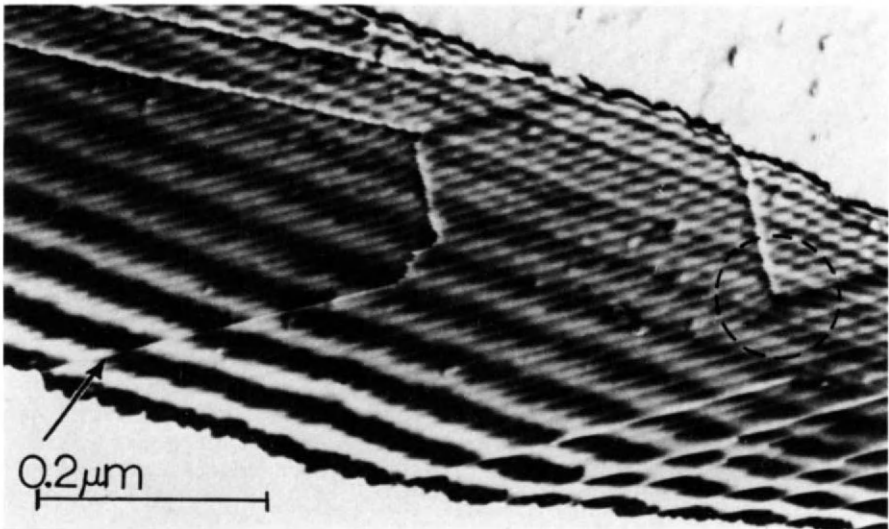
(b)

FIGURE 15.   Intrinsic (equilibrium) and extrinsic (ledge)
grain boundary dislocation (GBD) structure in molybdenum thin
films.   (a) Regularly-spaced intrinsic GBD's (arrows) and ledges
(L).   (b) Interaction of intrinsic and extrinsic GBD's (within
dotted area) and large ledge portions causing boundary contrast
fringe displacements (arrow).   (a) and (b) are bright-field
electron transmission micrographs.
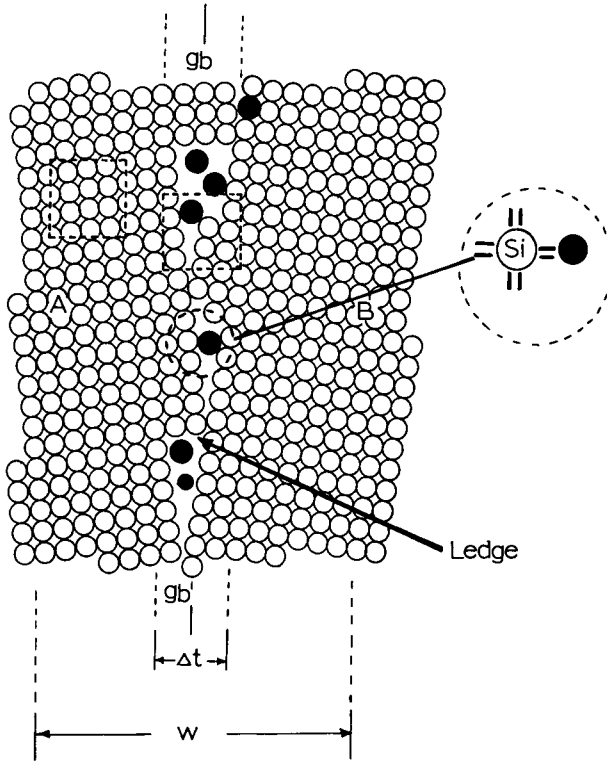
*FIGURE 16. General grain boundary schematic showing struc-
tural features (especially larger ledges), impurity segregation,
and passivation effects in covalent semiconductors such as Si.
The grain boundary plane or Gibbs dividing surface is denoted gb
while the interfacial phase is denoted by Δt. W denotes the
range of space-charge region which can be associated with semi-
conductor interfaces. Dotted boxes in the upper portion illus-
trate variations in density, structure, and composition which can
be characteristic of a specific volume of the interfacial phase
as compared to the grain structure in perfect crystal portions A
or B.*

nonetheless a very simplified schematic depicting only a somewhat

idealized, two-dimensional section. It is especially significant

to note, as discussed extensively by Murr (8,19,20), that grain

boundary ledges, because of their obvious, localized stress con-

centration are sources of dislocations when an external stress is

applied, allowing for translations and rotations of individual
grains in a polycrystalline regime, which Ashby (21) has described
as giving rise to non-homogeneous plastic deformation gradients.
These deformation gradients assume a periodicity or wavelength
equal to the grain size, D, so that residual yield stress, σ, for
polycrystalline metals and alloys can be expressed as

$$\sigma = \sigma_o + kD^{-1/2} \tag{1}$$

where σ_o is a strain-dependent term which includes the so-called
friction stress, and k is a materials constant which can depend
upon the stacking-fault free energy or the grain boundary struc-
ture (8,22). Equation (1) is usually somewhat historically
referred to as a Hall-Petch law, but in a more general form we
can write

$$\sigma = \sigma' + k\lambda^{-n} \tag{2}$$

where σ' is a strain-dependent term, λ is the deformation gradi-
ent wavelength (21), and n can vary between approximately 0.25
and 1, depending upon the nature of the microstructural units.
For example, if a polycrystalline material is further sub-refined
by the formation of additional interfaces having structural pro-
perties similar to grain boundaries, then it might be expected
that the yield stress could be expressed by a relationship simi-
lar to Eq. (1). Indeed, this is exactly what has been observed
for the formation of deformation twins in shock-deformed poly-
crystalline metals and alloys (23,24). Figure 17 illustrates
this phenomena for shock-loaded type 304 stainless steel sheet.
If the deformation twin spacing is Δ, the yield stress can be
expressed by

$$\sigma = \sigma' + k'\Delta^{-1/2} + kD^{-1/2} \tag{3}$$

or if we let $\sigma_o = (\sigma' + k'\Delta^{-1/2})$, then Eq. (3) is identical to
Eq. (1). The friction stress also includes of course the imped-
ance to dislocation motion caused by the presence of the
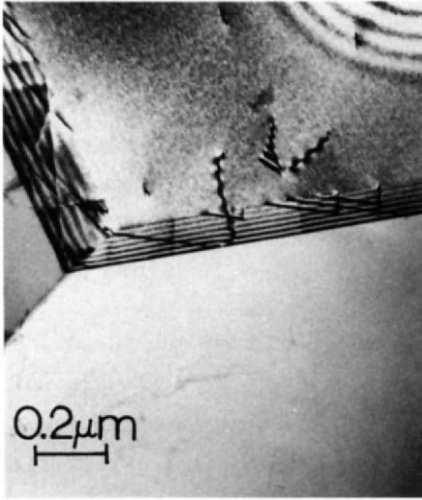
(a)

(b)
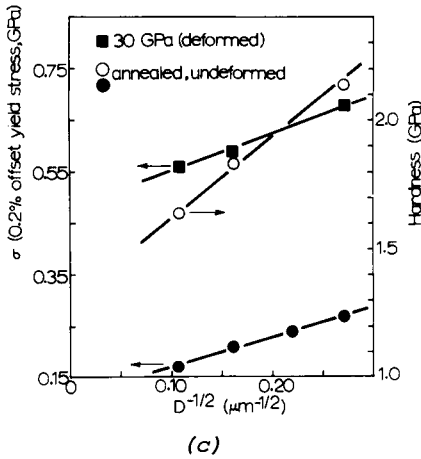
(c)
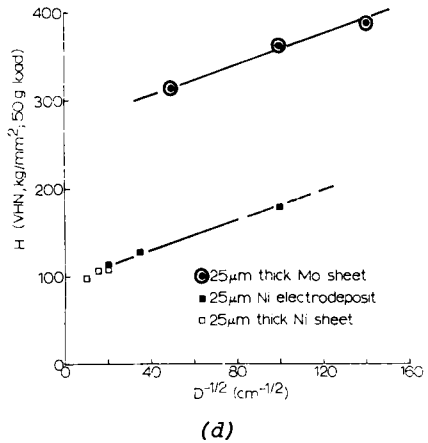
(d)

FIGURE 17.   Effect of grain size and grain-refinement-producing substructure on the mechanical properties (yield strength and hardness) of thin metallic sheets and coatings.   (a) Annealed 304 stainless steel grain structure (28 μm grain size, D).   (b) Systematic deformation twin formation in (a) in response to shock deformation at 30 GPa peak pressure (2 μs pulse duration).   The effective twin boundary spacing, Δ is much less than the original grain size, D.   (c) Residual yield stress and microhardness for various grain sizes of annealed and shock-deformed 304 stainless steel sheets as shown in (a) and (b).   (d) Hardness versus reciprocal square root of the residual grain size in thin metal sheets and electrodeposits.

shock-induced deformation twins.   These new interfaces also pro-
vide for additional ledge sources for dislocations when a stress
is applied.   Since hardness is usually simply related to yield
stress (8), there is a similar dependence of hardness on the de-
formation gradient wavelength (or grain size) as shown in Fig.
17(c) and (d).   Figure 17(d) suggests, on comparison with Fig. 10,
that not only would the mechanical properties of solar-related
overgrowths vary with thickness as a consequence of variations in
grain size with thickness, but optical properties might also be
expected to vary because electromagnetic wave interactions will
change with changes in the volume fraction of interfacial surface,
variations in interfacial thickness, and alterations in inter-
facial structure.   This is also true of free electron interac-
tions in metals, and these features are illustrated in Fig. 18.
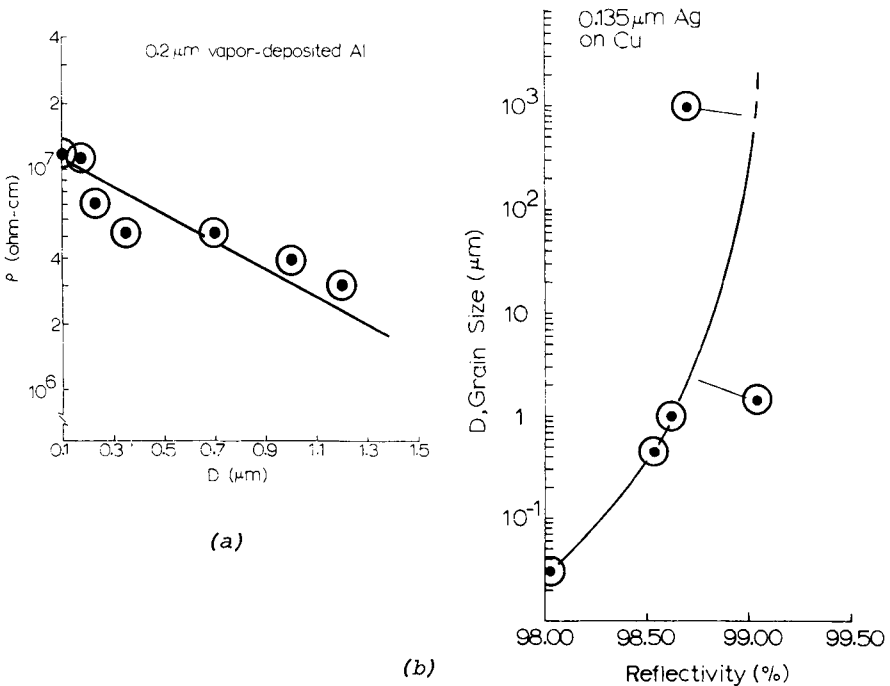
FIGURE 18.   (a) Resistivity (d.c.) versus grain size in vapor-
deposited aluminum films.   (b) Reflectivity (at 10.6 μm) versus
grain size for silver films vapor-deposited upon polished, poly-
crystalline copper substrates.

   2. Phase Boundaries and Related Interfaces. In Fig. 12,
only the twin boundary shown schematically in Fig. 12(b) is a
grain boundary while the stacking fault is a special intrinsic
interface and the boundary shown in Fig. 12(c) is a phase bound-
ary. Interfaces separating precipitates or dispersed phases in
solid matrices are also phase boundaries, and interfaces can also
be described as domain boundaries separating polarized or magne-
tized regimes (as in ferroelectric and ferromagnetic materials,
respectively), or as domain boundaries separating an ordered
regime from a disordered regime, or different arrangements of
superlattices (with reference to Fig. 2) (4). Interfaces can
also separate phase regions such as solid from liquid [although
this is sometimes a comparatively thick interfacial phase region
(8)], and a free surface can also be considered as an interface
separating the solid and vapor phases. In many respects, a free
surface (solid-vapor interface) is another special case of a
planar defect, however, surface structure can complicate this
rather idealized concept. Surfaces and surface structure are,
nonetheless, of major importance in the fabrication and utiliza-
tion of a great variety of solar materials because most solar
coatings – absorbers, reflectors, photovoltaic conversion films –
are grown upon substrates, either structural members or other
types of deposits. Having formed a deposit, the substrate/deposit
interface then can be characterized as a special type of phase
boundary. Interfaces or grain boundaries in semiconductors or
photovoltaic heterojunctions are not only structurally very
important but also electrically important. While the interface
phase or geometrical and crystallographic structure can be de-
fined within an interface phase region having a thickness Δt, the
electronic phase region associated with the interface is charac-
terized by the width of the space-charge region having a dimen-
sion W as shown in Fig. 16. Figure 19 illustrates the idealized
structure of a free surface. It should be noted that if either
grain A or B in Fig. 16 is viewed separately, the "surface"
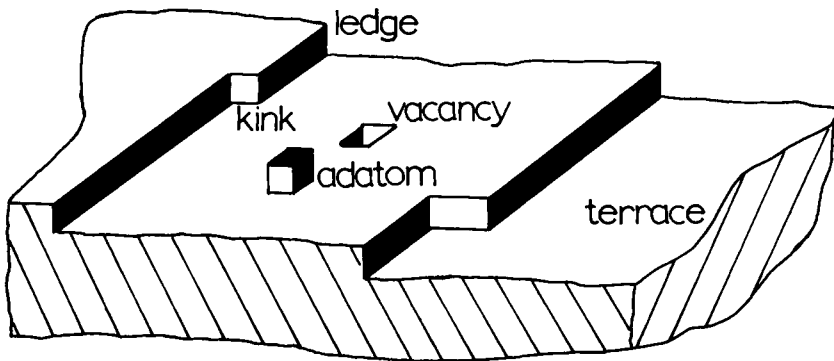
FIGURE 19. Schematic view of idealized surface structure (solid-vapor interface). The terrace planes are parallel to (001).

structure at the interface will be identical to Fig. 19, and the only significant differences are the coordination, bonding, and associated relaxations. The absorption of certain atoms such as hydrogen at grain boundaries in semiconductors can have a passifying effect with regard to recombination and trapping of electrons at "dangling bonds" as shown in Fig. 16, and this phenomenon can have important implications in the development of more efficient solar cells, to be discussed in more detail in subsequent chapters (c.f. chapters by Ginley and others).

Murr and Annamalai (25) and Murr and Inal (26) have recently demonstrated that not only are dislocations in substrates of little consequence in influencing the structure of an overgrowth (as shown in Fig. 10), but also grain boundaries are also not prominent in promoting specific features of nucleation and growth of a deposited layer. This particular feature is illustrated in Fig. 20. In Fig. 20(a) it can be observed that while very thin films are not strongly influenced by the grain boundary intersecting the surface, the grain orientations, as mentioned earlier, have a very significant influence on the overgrowth structure. Figure 20(b) shows that even in the initial stages of nucleation,

30μm

0.5μm

0.1μm
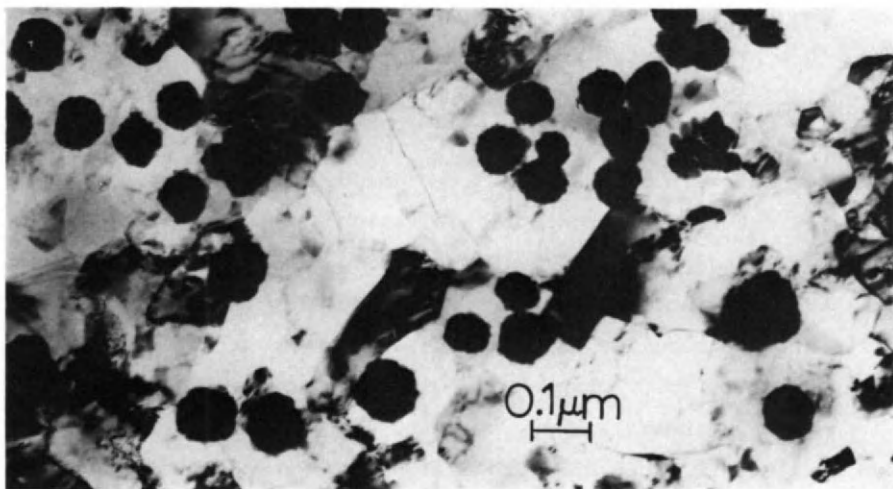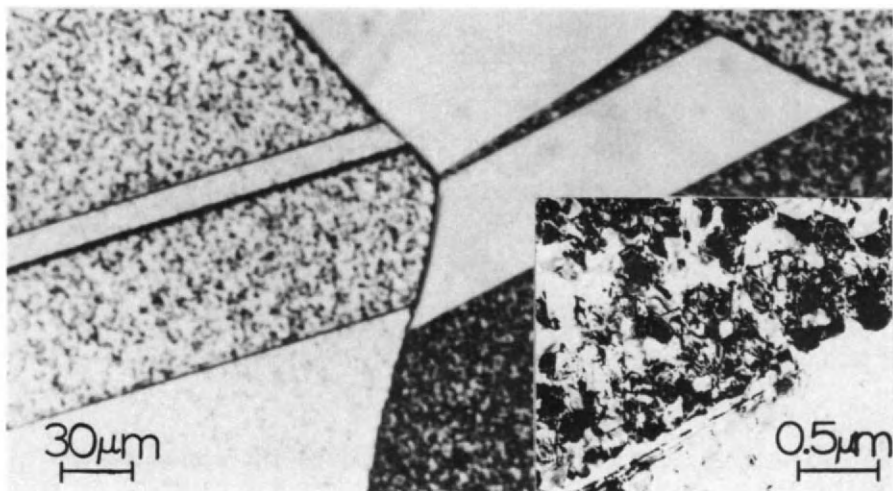
(b)

FIGURE 20. Microstructural features of deposit growth upon
a substrate. (a) Optical microscopic view of 1 μm thick nickel
electrodeposit upon a polycrystalline copper substrate. The in-
sert shows a magnified view of a 0.1 μm thick Ni overgrowth in a
twinned orientation as observed in the transmission electron mi-
croscope. (b) Auto-electrodeposited copper nuclei (primarily
single-crystal clusters) on a polycrystalline thin-film aluminum
substrate observed in the transmission electron microscope.
There is no systematic or preferred coincidence of the copper
nuclei (black) with the substrate grain boundary planes which
intersect the substrate surface.

grain boundaries are not preferred sites, and nucleation occurs
somewhat heterogeneously over the surface. Nucleation and growth
of a deposit initially occurs epitaxially, and in the first few
atom layers even pseudomorphically (where the deposit atoms
are in exact registry with the substrate atoms) (26,27). Epitax-
ial growth is illustrated in the observations of copper electro-
deposited upon a tungsten single-crystal field-emission end form
in Fig. 21(a) and (b). While, as shown in Fig. 20(b), many
initial nuclei are single crystals which assume some minimum
energy, faceted shape, many are initially short-range ordered and
actually composed of clusters of very small grains or crystalline
regions which pack as spherical or hemispherical clusters. This
is especially true in deposition processes involving complex
chemical reactions typical of most electrodeposition processes.
Figure 21(c) and (d) illustrate these features for very small
electrodeposited clusters upon field-emission end forms. Such
structures, like those described recently for very fine, poly-
crystalline iron whisker deposits (28) can incorporate oxides and
other reaction products, producing a kind of microstructural com-
posite with metallic clusters surrounded by or imbedded in oxides
or other compounds which may be crystalline (with very short-range
order) or non-crystalline (amorphous). To a large extent, these
structures and microstructural composites can be altered by a
host of deposition parameters including chemical composition of
the bath in electrodeposition, the temperature (also of the sub-
strate), rate of deposition (and current density in electrodepo-
sition), substrate orientation and grain size, and overgrowth
thickness. Indeed, as we have discussed earlier, grain size and
related microstructural dimensions are altered with deposit thick-
ness. Figure 22 illustrates some of these effects in relation to
residual absorptivity (α) for electrodeposited black-chrome
selective absorber deposits on polycrystalline nickel.
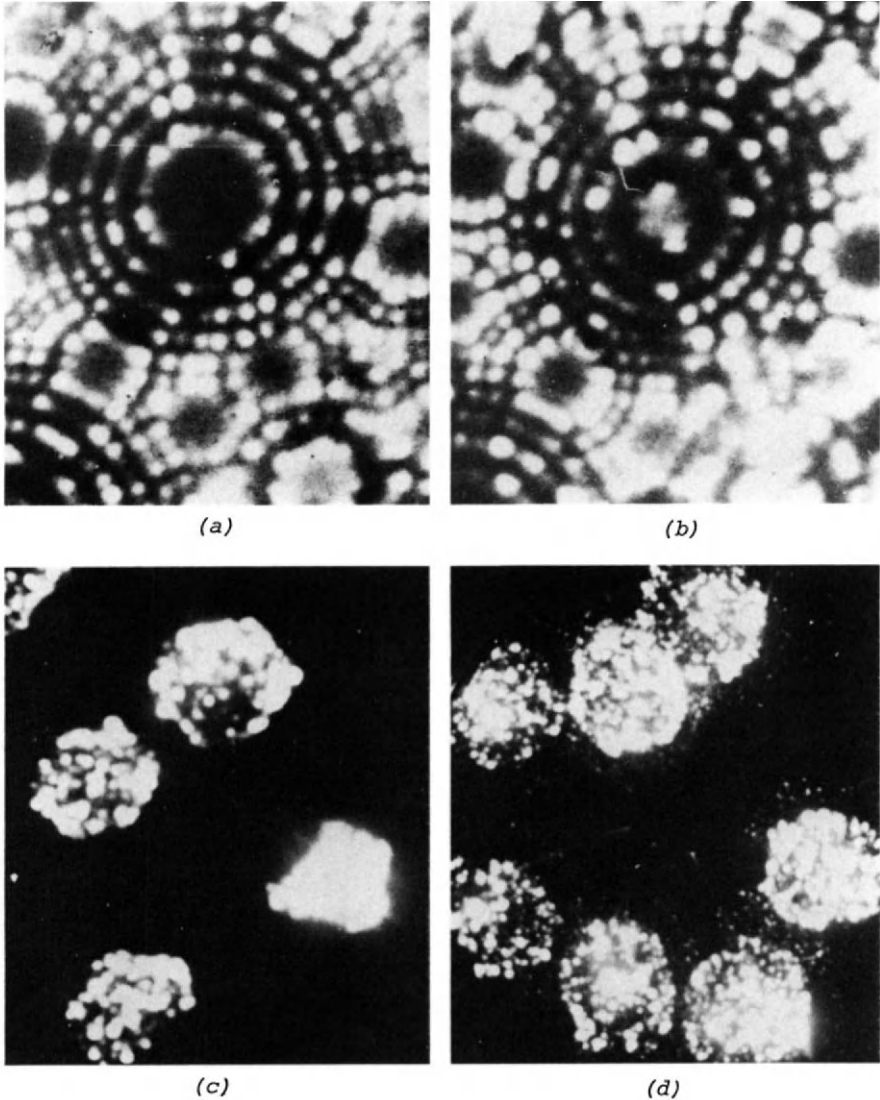
FIGURE 21. Nucleation and initial deposit growth on a sub-
strate surface. (a) Perfect [011] oriented tungsten end form
observed in the field-ion microscope. (b) Same surface as (a)
following epitaxial growth of a few layers of copper upon the sur-
face by auto-electrodeposition (electrochemical displacement re-
action). (c) Partially ordered clusters of Ni electrodeposited
upon a 304 stainless steel substrate observed in the field-ion
microscope. (d) Partially ordered clusters of black chrome
electrodeposited upon a nickel substrate (field-ion image).
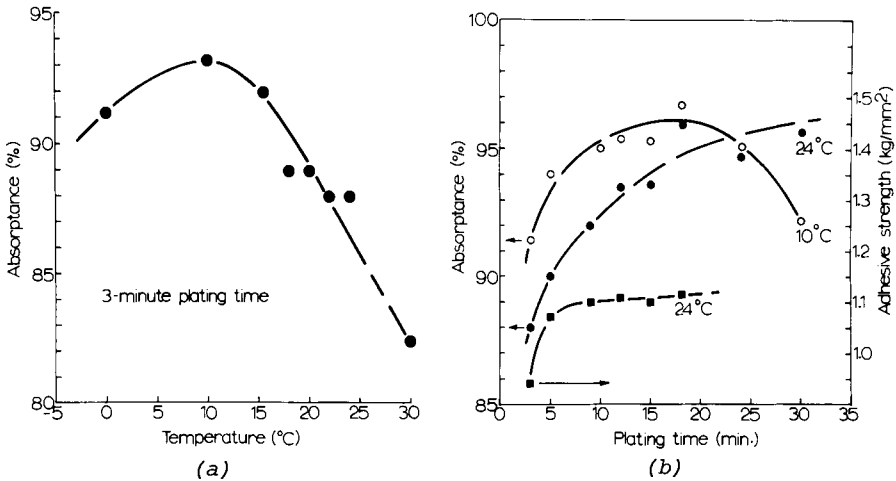
FIGURE 22.   (a) Absorptance of black chrome electrodeposits on plane nickel substrates as a function of bath temperature during electrodeposition.   Constant plating time assures essentially identical deposit thickness of ~ 2 μm.   (b) Absorptance and adhesive strength of black chrome electrodeposits on plane nickel substrates at different (constant) bath temperatures as a function of plating time, which corresponds to varying deposit thicknesses.

D.   Volume (Three-Dimensional) Defects

When individual point defects such as those illustrated in Fig. 2 agglomerate in a solid material, a three-dimensional defect arises.   This can take the form of a vacancy cluster or void, a region of altered chemistry in the case of an element-rich cluster or impurity cluster, precipitates or agglomerated dispersed phases, vacancy discs which allow for lattice relaxation to produce a dislocation loop as referred to briefly above; and related defects, including metal colloids, F-aggregate centers, and the like.   Such defects can have a marked effect on physical and mechanical properties and optical properties as well by altering electromagnetic wave propagation.   For example, the distribution and size of metal colloids can have a significant effect on optical absorption and this is also true of color-center aggregates as recently discussed by Murr (29,30), and Birsoy and

Murr (31). Furthermore, the production of complex color centers
by elemental substitutions and valence changes can have a signi-
ficant effect on selective absorption of light in transparent
crystals (31). Figure 23 illustrates some of these defects.

Szilva and Murr (32) have demonstrated that void density in
thin, vapor-deposited, polycrystalline silver films strongly in-
fluences reflectivity (at $\lambda = 10.6\,\mu m$); reflectivity decreases
with an increase in void density. Furthermore, void density has
been shown to be temperature dependent in thin, vapor-deposited
silver films (32).

Void structures, such as those shown in Fig. 23(c) can form
during deposit growth by exclusion of certain crystal orientations
which are rapidly enveloped in the growing deposit. In addition,
porous structures can arise by variations in deposit growth mor-
phologies and the development of crystallographic orientations.
This can lead to dendritic structures or columnar growth, botry-
oidal morphologies, and the like in deposits for specific solar
applications. These deposit structures, illustrated in Fig. 24,
are highly selective with regard to the absorption or reflection
of optical waves, and can, as noted earlier, be altered by alter-
ing reaction chemistries or other deposition or deposition-rela-
ted parameters.

IV. SUMMARY

After having defined crystal lattice arrays and described the
concepts of order, disorder, and the so-called amorphous state of
atomic structure, we have endeavored to systematically and chron-
ologically define and illustrate the principal crystal defects in
the context of their recognized and anticipated influence on a
variety of properties associated with solar materials performance,
properties, and utilization. The implications are that solar
materials science is simply an area of specialization within the
broadest framework of materials science, and that there exists a
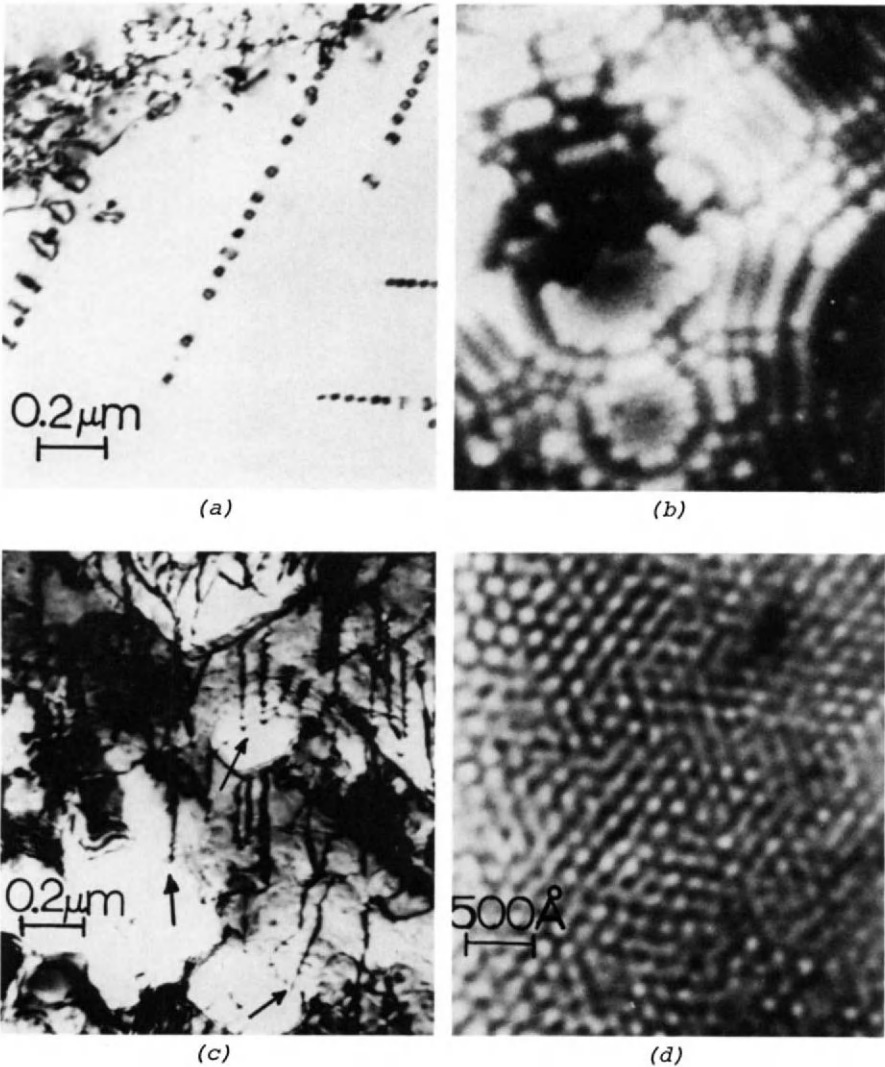
FIGURE 23. Examples of three-dimensional crystal lattice de-
fects (voids). (a) Dislocation loops (vacancy cluster discs) in
rapidly quenched nickel observed in the transmission electron mi-
croscope. (b) Large vacancy disc or void layer in (102) plane of
vapor-deposited platinum observed in the field-ion microscope.
(c) Voids in electrodeposited nickel film observed in the trans-
mission electron microscope. Note dislocations terminating on
the void surfaces (arrows). (d) F-aggregate centers (forming a
special void lattice structure) in electron irradiated CaF_2. The
(111) plane is parallel to the image surface (bright-field elec-
tron transmission image).
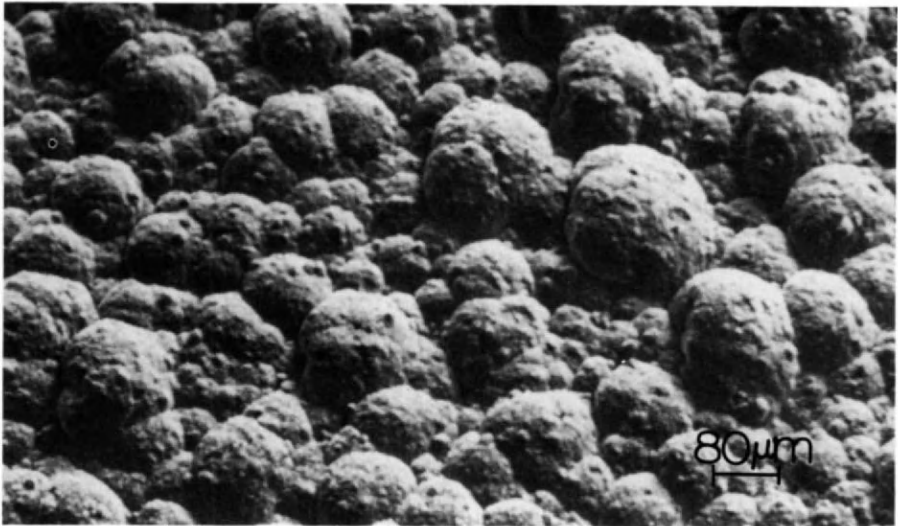
(a)
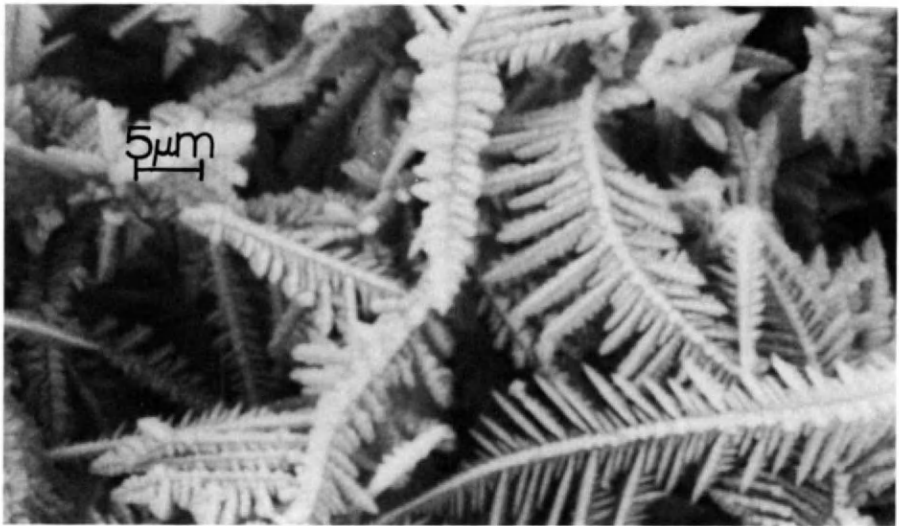
(b)

FIGURE 24. Thick, auto-electrodeposited (electrochemical displacement reaction) overgrowths of copper on iron (a) and aluminum (b) substrates observed in the scanning electron microscope. (a) Shows botryoidal growth morphology resulting from crystal agglomeration while (b) shows dendritic crystal morphologies. (a) corresponds to deposition from a $CuSO_4$ solution at $30^{\circ}C$, pH 2.2. (b) Corresponds to deposition from a $CuSO_4$ solution at $50^{\circ}C$, pH 3.2.

very obvious relationship between crystal structure, particularly
defect microstructure, and the performance of materials in solar
applications. We have also briefly outlined the basic features
of materials growth and microstructural alterations during growth,
especially in the context of deposits grown upon a suitably de-
fined substrate or polycrystalline support material. It has been
shown that microstructure has a very important if not controlling
effect on optical properties as well as associated physical and
mechanical properties, and that in many instances a compromise in
the microstructural manipulations must be considered in order to
optimize all of the desirable features of a specific solar mater-
ials application. For example, in the case of highly reflecting
films grain size should be large, but the associated mechanical
properties such as tensile strength and hardness decline with in-
creasing grain size. Furthermore, grain size in most overgrowths
will vary with deposit thickness, and this variation can occur in
a complex way, being dependent upon a host of interdependent var-
iables which can include deposit thickness, deposition rate,
temperature, deposition environment parameters such as vacuum or
bath composition, etc. All of these parameters can have a pro-
found effect on the growth and regularity of deposit crystal
structure, perfection, and range of order. However, we have also
demonstrated that in many instances, especially in the growth of
deposits upon a substrate, the defect structure of the substrate
may have little if any effect on the development of deposit mi-
crostructure. Moreover, variations in crystal orientation, es-
pecially surface orientation, is a controlling feature in the
development of an overgrowth upon a substrate.

In describing crystal defects and illustrating their influence
in the structure and properties of solar materials, some instru-
mentation techniques in solar materials research were also illus-
trated with regard to the direct observation of crystal defects,
the range of lattice order or disorder, and related microstruc-
tural phenomena. In some respects it was intended to illustrate

not only specific defect microstructures but to demonstrate the
utility in a varied approach involving several techniques to
directly observe a material's microstructure at different dimen-
sional levels. This interdisciplinary instrumental analysis
approach, involving direct observations of microstructure, can
allow for very precise structure - property relationships to be
established, and for the development of specialized processes for
the efficient and economical manufacture and further development
of materials for specific solar energy applications. A more
general, concise review of instrumentation might be found in the
November 1976 issue of Physics Today. Finally, while we have not
stressed the very complex role crystal defects can have in re-
combination contributing to loss of efficiency in the operation
of solar cells, especially dislocations and grain boundaries,
these features will be described in detail in later chapters. A
recent article by Boer (33) is also recommended.

REFERENCES

1. Damask, A.C., and Dienes, G.J., "Point Defects in Metals",
   Gordon and Breach, Science Publishers, Inc., New York,
   (1971).
2. Amelinckx, S., "Direct Observation of Dislocations", Academ-
   ic Press, Inc., New York, (1964).
3. Hirth, J.P., and Lothe, J., "Theory of Dislocations",
   McGraw-Hill Book Co., New York, (1968).
4. Barrett, C.S., and Massalski, T.B., "Structure of Metals",
   3rd ed., McGraw-Hill Book Co., New York, (1966).
5. Thomas, G., and Washburn, J. (eds.), "Electron Microscopy and
   Strength of Crystals", Interscience, New York, (1963).
6. Seitz, F., *Rev. Modern Phys.*, 26, 7 (1954).
7. Amelinckx, S., Gevers, R., Remaut, G., and VanLanduyt, J.
   (eds.), "Modern Diffraction and Imaging Techniques in Mater-
   ial Science", North Holland/American Elseview, Amsterdam/

New York, (1970).

8. Murr, L.E., "Interfacial Phenomena in Metals and Alloys",
    Addison-Wesley Publishing Co., Reading, Mass., (1975).

9. Arsenault, R.J. (ed.), "Defects and Defect Clusters in B.C.C.
    Metals and Their Alloys", Proceedings of an International
    Conference, Nuclear Metallurgy Vol. 18, National Bureau of
    Standards, Gaithersburg, Marylang, (1973).

10. Kuhlmann-Wilsdorf, D., Interactions Between Vacancies and
    Dislocations, Chap. 7 in "Frontiers in Materials Science",
    Murr, L.E. and Stein, C. (eds.), Marcel Dekker, Inc., New
    York, p. 253, (1976).

11. Müller, E.W., and Tsong, T.T., "Field-Ion Microscopy: Prin-
    ciples and Applications", Elsevier, New York, (1969).

12. Murr, L.E., "Electron Optical Applications in Materials
    Science", McGraw-Hill Book Co., Inc., New York, (1970).

13. Gordon, P., "Principles of Phase Diagrams in Materials Sci-
    ence", McGraw-Hill Book Co., New York, (1968).

14. Staudhammer, K.P., and Murr, L.E., "Atlas of Binary Alloys:
    A Periodic Index", Marcel Dekker, Inc., New York, (1973).

15. Cottrell, A.H., "Mechanical Properties of Matter", J. Wiley
    and Sons, Inc., New York, (1964).

16. VanDerMerwe, J.H., "Single-Crystal Films", Pergamon Press,
    Oxford, (1964).

17. Gündiler, I., and Murr, L.E., *Thin Solid Films,* 37, 387
    (1976).

18. Lange, F.F., *Acta Met.,* 15, 311 (1967).

19. Murr, L.E., *Met. Trans., 6A,* 505 (1975).

20. Murr, L.E., and Venkatesh, E.S., *Metallography,* 11, 61 (1978).

21. Ashby, M.F., *Philos. Mag.,* 21, 399 (1970).

22. McElroy, R.J., and Szkopiak, Z.C., *Int. Metall. Rev.,* 7, 175
    (1975).

23. Moin, E., and Murr, L.E., *Mater. Sci. Engr.,* 37, 249 (1979).

24. Murr, L.E., Moin, E., Wongwiwat, K., and Greulich, F., Effect
    of Grain Size and Deformation-Induced Grain Refinement on

the Residual Strength of Shock-Loaded Metals and Alloys, in
"Strength of Metals and Alloys", Vol. 2, Haasen, P., Gerold,
V., and Kostorz, G., (eds.), Pergamon Press, New York,
p. 801, (1979).

25. Murr, L.E., and Annamalai, V., *Met. Trans., 9B,* 515 (1978).

26. Murr, L.E., and Inal, O.T., *Phys. Stat. Sol. (a),* 51, 345
     (1979).

27. Murr, L.E., Inal, O.T., and Singh, H.P., *Thin Solid Films,*
     9, 241 (1972).

28. Wilsdorf, H.G.F., Inal, O.T., and Murr, L.E., *Z. Metall-
     kunde,* 69, 701 (1978).

29. Murr, L.E., *Phys. Stat. Sol. (a),* 22, 239 (1974).

30. Murr, L.E., Void-Lattice Formation in Natural Fluorite by
     Electron Irradiation, "Proc. Electron Microscopy Society of
     America", Bailey, G.W. (ed.), Claitor's Publishing Div.,
     Baton Rouge, La., p. 614, (1976).

31. Birsoy, R., and Murr, L.E., *Phys. Stat. Sol. (a),* 52, 77
     (1979).

32. Szilva, W.A., and Murr, L.E., *Phys. Stat. Sol. (a),* 40, 211
     (1977).

33. Boer, K.W., "The Physics of Solar Cells", *J. Appl. Phys.,*
     50(8), 5356 (1979).

CHAPTER 3

SURFACE AND INTERFACE STUDIES AND THE STABILITY
OF SOLID SOLAR ENERGY MATERIALS[1]

A.W. Czanderna

Solar Energy Research Institute[2]
Golden, Colorado

I. INTRODUCTION

The purpose of this chapter is to provide an overview of the
extremely important role that surface and interface studies of
solid materials must play if the United States is to achieve wide
scale commercialization and application of the various solar tech-
nologies. After introductory comments are made to provide a gen-
eral perspective of the problems, an overview of surface and inter-
face studies that are immediately applicable to solar energy tech-
nologies will be presented. For conciseness in this chapter, I
shall include both surfaces and interfaces in the term "surface".
Following the overview on surface studies, a number of problems in
solar technologies will be discussed briefly and in a general man-
ner. The examples chosen will be representative, important prob-
lems in solar materials research, but they are not necessarily

those of highest priority and certainly not the only problems that
need to be studied. I will conclude the chapter with some recent
results obtained from studying the enhancement of the thermal
oxidative degradation of isotactic polypropylene on copper oxide
surfaces resulting from the catalytic effect of copper ions.
These results will serve as a detailed example of a problem caus-
ed by a basic incompatibility of two materials. This example will
also demonstrate the extensive prior work that is necessary to
secure an understanding of the problem. Improved materials and
processes can be most readily conceived from an understanding of
degradative processes. Thus, an underlying theme of this entire
chapter will focus attention on the mechanisms of degradation, or
surface reactions that cause a change in the desired properties of
a component of an entire solar energy system.

     As indicated in the chapter by Butler and Claassen, the major
problem is not discovering how to collect radiant energy, but how
to collect it cheaply. The solar flux reaching the earth is low
in energy density, which means very large collection areas will be
required to capture significant amounts of solar energy.

     It will be necessary to deploy large areas of heliostats,
photovoltaic arrays, or flat plate collectors to concentrate the
energy density or convert it into another energy form, as is ac-
complished by photovoltaic materials. The cost of materials util-
ized, production processes, and the operation and maintenance of
systems must be held to a minimum. This requires, for example,
using thin films for mirrors, for photovoltaic systems, for anti-
reflection coating, etc., and that these films be made from inex-
pensive, durable, and easily processed materials. Inexpensive
long-life materials in flat plate collectors and durable, stable
absorber coatings are also necessary.

     In general, the actual or conceptual design of solar collec-
tion systems requires large areas of contact between different

materials, i.e., metals, oxides, polymers, semiconductors, ceram-
ics, composites, and transfer media. Reflectors, transmitters,
absorbers (both thermal and quantum), and heat transfer materials
must have low life cycle cost, reliable and durable performance,
and remarkable long term stability. The latter is apparently
counter to basic physics and chemistry, because atoms at a surface
are necessarily in a higher energy state than if they were in the
bulk. By their very presence, surface materials must be more re-
active and thermodynamically less stable than bulk materials.
Yet, the dilute energy density of solar radiation requires us to
deploy systems with large surface areas! Fortunately, kinetic
limitations frequently retard the effects of a thermodynamic driv-
ing force. Therefore, systems with large areas of different kinds
of materials, can remain stable if they are chosen correctly.

Solar systems are subjected to a unique set of stresses that
may alter their stability and, hence, their performance and life
cycle costs. These stresses include UV, temperature, atmospheric
gases and pollutants, the diurnal and annual thermal cycles, and
in concentrating systems a high intensity solar flux. In addition,
condensation and evaporation of water, rain, hail, dust, wind,
thermal expansion mismatches, etc., may impose additional problems
on the performance of a solar system. These stresses and factors
must be considered not only individually, but also for synergistic
degradative effects that may result from their collective action
on any part of the system. The initiation of many degradative
effects can reasonably be expected to occur at surfaces.

Heat transfer fluids and storage containers offer another set
of problems after the solar energy is collected. While special
factors such as biofouling in OTEC or the diurnal cycle play a
role in some of these cases, there exists a new set of problems
at the fluid/container surface. Again, an interaction at a sur-
face may limit the performance of a component of a solar energy

system.

It is fair to conclude that surface studies are of much greater relative importance in solar materials science than in materials science in general. After studying this chapter, please consider the devices described and the collection processes presented in the remaining chapters, and try to recognize the surface problems that will arise in each case. It is likely that every one of the solar devices or systems described in the following chapters has a surface-related problem, either directly or indirectly.

The editor has demonstrated excellent insight into solar materials science by requesting the preparation of a chapter dealing with surface phenomena. For example, how have you been exposed in your curriculum to the fundamental aspects of surface phenomena? It is likely the bits and pieces of surface phenomena that you have encountered have not been presented in an organized overview course. In different courses, you may have touched on the thermodynamics of interfaces, dislocations at grain boundaries, nucleation and growth phenomena, friction and wear, interfacial diffusion, faceting, grain boundary sliding, thermally activated growth, and adsorption phenomena without really recognizing that these are part of a surface science discipline. You are fortunate if you have had a course on surface physics, surface chemistry, or surface phenomena. There is little question that one of the most active research areas in materials science is the study of surfaces. In the past, proper emphasis has been placed in most materials science curricula on relating the bulk properties to the structure and composition of the solid. In the future, one should expect a similar emphasis to be placed with respect to surfaces, because of the wide scale research efforts that are in progress all over the world in which surface reactivity and stability are being related to the crystallographic

orientation and composition at the surface of the materials. What
part of this type of research is of near-term importance to solv-
ing the surface problems in solar systems? After the discussions
presented in the next two sections, you should be able to answer
this question.

II. SURFACE STUDIES APPLICABLE TO SOLAR MATERIALS

An overview of the most important phenomena in surface
science related to studying solar materials is presented first in
this section. The methods of characterizing surfaces and those
deemed likely to have the largest near-term impact on solving the
problems of surface degradation are then discussed.

If the ionic species in plasmas are neglected, the universe
of interest consists of solid, liquid, and gas phases, none of
which is infinite. The boundary region between these phases,
i.e., the surface phase, has fundamentally different properties
from the bulk. The possible boundaries are the solid/solid,
solid/liquid, solid/gas, liquid/liquid, and liquid/gas surfaces
(interfaces). These boundaries are studied in surface science
to develop an understanding of phenomena and to develop theories
that will permit prediction of future events. Some of the broad
topical areas of study at the five possible surfaces are listed
in Table 1. An understanding of these topics is enhanced by ap-
plying the methodologies of surface science. A list of acronyms
used in this chapter is appended.

The S/S, S/G, and S/L surfaces, in that order, are of great-
est interest to the solar materials scientist. As detailed in
recent books (1-16), the experimental effort for studying these
surfaces is now very extensive; the theoretical treatments are
difficult. In science, it is customary to adopt a model based on
an ideal situation and to compare the behavior of real systems

Table 1. Topical Study Areas at Different Surfaces Between the Solid (S), Liquid (L), and Gas (G) Phases

Surface		Topical Area of Study
Solid A Solid B	S/S	Corrosion, Adhesion, Epitaxial Growth, Friction, Diffusion, Nucleation and Growth, Thin Films, Solid State Devices
Liquid Solid	S/L	Wetting, Lubrication, Friction, Surface Tension, Capillarity, Electrochemical Properties
Gas Solid	S/G	Catalysis, Corrosion, Oxidation, Diffusion Surface states, Electron emission Thin films, Condensation and Nucleation
Gas Liquid	L/G	Diffusion, Surface tension Vapor pressure
Liquid A Liquid B	L/L	Immiscible Phases Spreading of films

with the ideal model. What is a realistic view of the boundary at a solid surface? It is not the ideal plane of infinite dimensions, but on an atomic scale consists of different crystal planes with composition, structure, orientation, and extent that are fixed by the pretreatment of the solid. As shown by Fig. 1, imperfections such as an isolated atom, a hole, an edge, a step, a crevice, a corner, and a screw dislocation may also coexist on the surface. Wide variations in the microscopic topography, as shown in Fig. 2, may also adversely influence the stability of the surface (Figs. 2(a) and (b) or the operation of a device because of voids (Fig. 2(c)).

During pretreatment of a solid, impurities may accumulate at or in the boundary in trace and larger quantities, and drastically alter the behavior of the boundary. The pretreatment of solid surfaces, which may involve outgassing, chemical reduction,
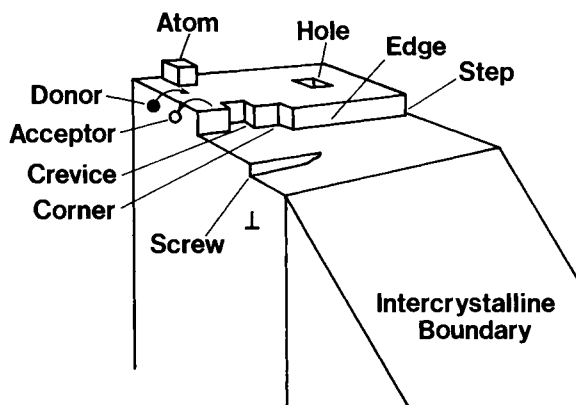
FIGURE 1. The solid surface is not an ideal infinite single crystal.

flashing a filament, ion bombardment, cleavage, field desorption, or depositing a thin film (17), are all made in an effort to minimize the uncertainty about the initial composition of the surface. Following controlled use of the solid, reexamination of the surface permits evaluation of the influence of the use on the measured properties of the surface. Characterization of the surface before, after, and if possible, during use of the material is clearly required.

For an overview of characterizing a solid surface, consider the questions: How much surface is there and where is it located? Is the surface real or clean? What solid form does the surface have? What is its topography and structure? What thermodynamic processes occur? How do surface species migrate? What is the equilibrium shape of surfaces? What is the depth of the surface phase? How much gas or liquid is adsorbed and where? What is the nature of the adsorbate-solid interaction? How should these phenomena be studied? The history of studying these effects in
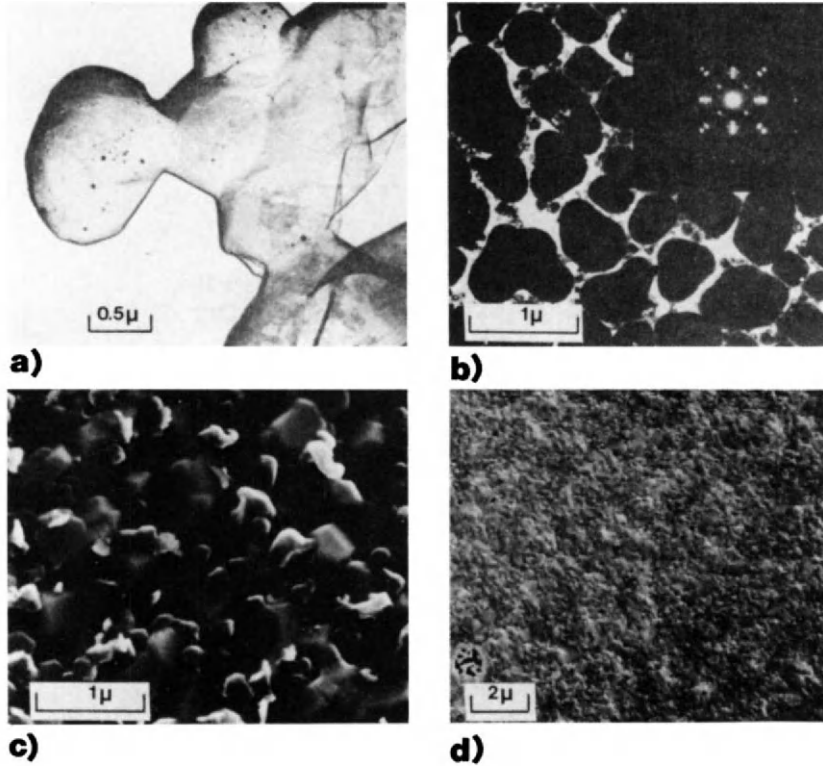
FIGURE 2. Real surfaces: a. Silver powder; b. a partial-
ly oxidized copper film on NaCl; c. sulfided copper film in
H_2S/H_2 at $200°C$; d. as in c but at $73°C$.

gas adsorption on solid surfaces alone leads us to recognize that
careful experimentation is the primary necessity in surface
science. The experimental methods deemed most appropriate for
solar materials will be indicated as each of the characterization
questions are addressed in the following paragraphs.

A. *Surface Area*

Following Langmuir's pioneering work about 70 years ago, in
which the importance of structure, composition and bonding to
chemisorption were demonstrated, Brunauer, Emmett, and Teller
(BET) provided a means for deducing the surface area from multi-
layer physical adsorption isotherms (18). The BET method for
analyzing type II adsorption isotherms is used routinely by hund-
reds of laboratories with commercially available facilities (19).
When the surface is located internally, hysteresis is observed
between the adsorption and desorption branches of the isotherm,
forming type IV isotherms. The hysteresis results from capillary
filling of internal pores. A large number of methods have been
developed to determine the internal surface area from type IV
isotherms (19). An excellent treatise on surface area and poros-
ity of solids is available (20), extensive examples from recent
studies of this subject have been cataloged (21), and the parame-
ters used to differentiate between physical and chemical adsorp-
tion have been tabulated (21).

Visual observation of the topographical features of solids
is possible using electron microscopic (EM) examination of re-
plicas of surfaces, or by using a scanning electron microscope
(SEM). An assessment of the external surface area can be made
from SEM or EM photographs, but obviously the internal area is
not directly observable. Thus, qualitative and quantitative ans-
wers are provided to the questions of how much surface is there
and where is it located, except for the case of S/S.

B. *Real and Clean Surfaces; Solid Forms*

Broadly speaking, real surfaces are those obtained by ordin-
ary laboratory procedures, e.g., mechanical polishing, chemical

etching, etc. Such a surface is covered by chemisorbed material, generally an oxide, and by physically adsorbed molecules from the surrounding environment. Real surfaces have been studied exten- sively because they are easily prepared, readily handled, and amenable to many types of measurements. It is the real surface that is encountered in most practical applications, and this will be particularly the case for solar materials. Figures 1 and 2 are illustrative of real surfaces.

Clean surfaces, which may be obtained by outgassing, chemi- cal reduction, cleaving, field desorption, ion bombardment and annealing, preparing a thin film in ultra high vacuum (UHV) or flashing a filament (17) are more difficult to prepare and keep. Clean surfaces constitute the closest approximation to the true crystalline surface. They can be prepared on ordered single crystals, and can then be perturbed in carefully controlled ex- periments. Fundamental studies on clean well-ordered surfaces are increasing the basic understanding of S/G interactions in the modeling tradition of the kinetic theory, the dilute solution, the point particle, and the harmonic oscillator. Except for materials that can withstand solar concentration factors of about 1000, the large areas required for solar collectors mitigate against using clean single crystal surfaces in devices.

In surface studies, various solid forms are used, such as: (1) powders, (2) foils, (3) vacuum-prepared thin films, (4) coatings, (5) filaments, (6) cleaved solids, (7) field emitter tips, (8) single crystals, and (9) polycrystalline solids. These may be formed from metals, semiconductors, and compounds. The specialization of solid forms (5) through (8) preclude their wide- spread surface study for solar applications. Solid forms (3), (4), and (9) will be used widely in solar systems for reasons given in Section I.

C. *Structure and Topography*

A clear distinction must be made between structure and top-
ography, which are frequently used interchangeably (and incorrect-
ly) in the literature. Topography can be illustrated with a few
SEM photographs showing contouring, hills and valleys, and
superatomistic surface features. Structure refers to the repet-
itive spacing of atoms in a surface grating. The results of sur-
face structural determinations show that the lattice spacing in
the bulk and at surfaces is generally the same. The most common
methods of deducing surface structure are by the diffraction of
low energy electrons, either elastically or inelastically (ELEED
and ILEED), by reflected high energy electrons (RHEED), and by
using the imaging techniques of the field emission (FEM) and
field ionization (FIM) microscopes (1,8-10,12,13). The value of
the techniques of LEED, RHEED, FEM, and FIM to fundamental sur-
face science is evidenced by the extensive results secured using
them and published in the journal, *Surface Science.* The cost
effective deployment of large areas of solar collectors will most
probably be in the form of polycrystalline materials, with all
index planes emerging at the surface. Therefore, it is not ex-
pected that the structural determination of solar materials sur-
faces will be applied except for a few special cases. Rather,
the challenge will be to understand the changes in surface activ-
ity of heterogeneous real surfaces, such as those shown in Figs.
1 and 2.

D. *Surface Composition or Purity*

The useful properties of real surfaces often depend on the
presence of chemical groups, e.g., impurities, that are extraneous
to the bulk composition. These tend to prevent the self-minimi-

zation of the surface energy of the solid. They also influence the growth kinetics, topography, surface diffusion coefficients, and residence time of adsorbed species. Depending on the surface energy, impurities may concentrate at the surface or incorporate themselves into the bulk. These processes involving mass transport to, from, and along the surface may produce significant time-dependent changes in the properties of the material. Therefore, it is extremely important to be able to identify the elemental composition of solid surfaces at various stages of using solar materials.

Until eleven years ago, experimental techniques did not exist for identifying the elements on a surface. Since then, commercial instruments have become readily available and have been developed for the single purpose of measuring the elemental composition of surfaces. The basic principles of the four most widely used methods, Auger electron spectroscopy (AES), X-ray photoelectron spectroscopy (XPS or ESCA), ion scattering spectroscopy (ISS), and secondary ion spectroscopy (SIMS), are compared in Table 2. As is seen, electrons in AES and XPS are energy analyzed, and the scattered or sputtered ions in ISS and SIMS are mass analyzed. As a result, advantages and limitations are imposed on the information that can be secured from each of these techniques. A listing of the most important characteristics of AES, XPS, ISS, and SIMS is given in Table 3.

Although the samples must be analyzed in vacuum in all four cases, the analysis for the accumulation of impurities from the gas and liquid phases can be accomplished using load lock chambers. For the S/S surface, composition profiling can be accomplished by in situ ion etching. For this a 0.5 to 10 keV ion beam is used to bombard a surface. The energy transfer causes particles to be ejected (sputtered) from the surface, thus exposing increasing depths of the solid to probing with surface-

Table 2. Comparisons of Some Categories for Four Methods of Surface Analysis

Method/ Category	AES	XPS(ESCA)	ISS	SIMS
Input "Particle"	Electrons	Photons (x-rays)	0.5-3.0 KeV Ions	0.5-20 KeV Ions
Damage to Sample by input particle	Moderate (focussed ᴇ-beam)	Minimal (x-radiation)	Moderate (defocussed ion beam)	Moderate and variable depending on the sample
Output Particle	Electrons	Electrons	Inert Ions	Secondary Ions
Measured Quantity of Output Particle	Auger Electron Energy	Auger and Core Level Electron Energy	Scattered Ion Energy after Binary Collision	Mess of sputtered surface Ions
Sampled Depth	2-10 Monolayers	2-10 Monolayers	Surface Monolayer	1-2 Monolayers

sensitive analysis techniques. Details of the ion-etching pro-
cesses for probing the composition at increasing depths of the
solid can be secured from a number of sources (22-24). The prin-
cipal factors that influence ion yields during sputtering, i.e.,
energy, number, angle of incidence, and ion used in bombardment,
as well as the binding energy of the solid, have been collected
into a useful set of illustrations (25). The principal limita-
tions result from cratering problems, different crystal faces
having different sputtering yields, sputtering rates depending
on bombardment angles, bombardment damage, and bombardment en-
hanced diffusion.

Further information about ISS   (25-28),   SIMS   (22,23,29),
AES (30-32), and XPS (32-34) is readily available. For compar-
ing these four surface analysis techniques, a continuation of
Table 2 is useful. Factors that need to be compared include the
influence of the sample on the results under such categories as
vacuum worthiness, geometry, solid type (metal, semiconductor,

Table 3. Advantages and Limitations of Using AES, SIMS, ESCA, and ISS Surface Analysis Techniques

Auger Electron Spectroscopy

- is useful for chemical shifts for some elements when in different compounds
- is especially good for CIDP (composition-in-depth analysis)
- is especially sensitive to light elements
- will form carbon from polymers (e-beam cracking)
- has superb lateral resolution (0.2-5.0μ beam)
- is fastest of the methods
- is sensitive to 2-10 monolayers
- may have severe charging problems

Secondary Ion Mass Spectroscopy

- is sensitive to 1-2 monolayers
- can detect isotopes with unit resolution
- can detect H and D present (the only one)
- can be sensitive to 1 ppm
- is especially good for CIDP
- is responsive to chemical matrix effects
- has complex spectra
- has varying elemental sensitivity
- is quantitative with difficulty, at best
- requires destruciton of sample for the analysis

Electron Spectoscopy for Chemical Analysis

- is most quantitative of major techniques
- is especially useful for chemical shifts from the same element in different compounds
- is useful for CIDP
- is especially sensitive to light elements
- is least destructive of all techniques (X-ray excitation)
- has poor lateral resolution
- is sensitive to 2-30 monolayers; metals, oxides, and polymers, in that order

Ion Scattering Spectroscopy

- is sensitive to first monolayer
- can detect isotopes present (O^{16} - O^{18}, N^{14} - N^{15}, S^{32} - S^{34})
- for some elements, may provide chemical information about surtace compounds
- is useful for composition in-depth profiles
- can possibly be quantitative
- is useful for studying ordered surfaces
- has simple spectra
- has poor resolution
- is necessarily destructive

insulator, organic, compound), atomic number, isotopic and matrix
effects, and surface structures. Then, factors should be compar-
ed that influence the results or data acquisition such as sputter
rate, lateral resolution, vacuum requirements, time to obtain a
spectrum, signal to noise, ability to depth profile, elemental
identification, resolution, sensitivity, depth resolution,
chemical effects, information about the matrix, and quantifica-
tion potential.

There are many other methods applicable to surface studies
(35). Some of these include Rutherford back scattering (RBS)
(36), the electron microprobe (37), the atom probe (38), glow
discharge mass spectrometry (GDMS) (39), glow discharge optical
spectroscopy (GDOS) (40), and surface analysis of neutral and ion
impact radiation (SCANIIR) (41). Some of these methods, e.g.,

GDMS, GDOS, and SCANIIR, are not commercially available or are
very expensive, e.g., RBS and atom probe, so are currently of
marginal value for widespread study of solar materials.
The methods of surface analysis mentioned in this section are of
obvious importance to the characterization of solar materials. A
listing of techniques required for characterization studies of
the surfaces of solar materials will be presented at the end of
Section II.

E. *Surface Thermodynamics, Equilibrium Shape, and Diffusion*

Surface atoms are in a markedly different environment than
bulk atoms. They are surrounded by fewer neighboring atoms, which
are in a surface-unique anisotropic distribution, compared to
those in the bulk. The surface phase has higher entropy, internal
energy, work content (Helmholtz energy), and free energy (Gibbs
energy) per atom than when in the bulk phase. For isotropic
solids, surface free energy and surface tension are equivalent

8-10 . At equilibrium, the solid surface will develop the shape
that corresponds to the minimum value of total surface free ener-
gy. The surface free energy of solids can be calculated for sur-
faces of different structures. The relative magnitude of surface
free energy can be deduced from experiments involving thermal
facetting, grain boundary grooving, etc. The low index planes
are the most stable because they have the lowest free energy.
All small particles and all large flat polycrystalline surfaces,
which are characteristic of the the type planned for solar appli-
cations, possess a relatively large surface excess energy and
are thermodynamically unstable.

   Based on calculations made for inert gases (42), ionic hali-
des (43), and semiconductors (44), the depth of the surface phase
may range up to 5 nm. In the latter two cases, substantial devi-
ations of the actual surface structures from those characteristic
of a truncated but otherwise bulk solid have been reported from
theoretical analyses of LEED intensities from single crystals.
The reconstruction or rearrangement of the surface involves move-
ments of up to 0.05 nm in the surface atomic plane and possibly in
the first bulk layer as well (44).

   Surface atoms are restrained from interatomic motion by near-
est neighbor bonding, but these bonds are weaker than for a corre-
sponding position in the bulk. The potential barriers for sur-
face diffusion are lower than for bulk diffusion, so less activa-
tion energy is required to produce surface diffusion processes.
The mechanism of surface diffusion may change with temperature
because the surface population of adions, vacancies, ledges, etc.
or other conditions such as structure and ambient atmosphere may
change.

F. Amount Adsorbed and Nature of Adsorbate/Solid Interactions

This section applies primarily to the G/S surface, although the general concept is valid for the L/S surface. Adsorption is the accumulation of a surface excess of two immiscible phases. Except for multilayer physical adsorption, the forces of interaction limit the amount adsorbed to one atomic layer, i.e., up to a monolayer of chemisorption. For measuring the amount of gas adsorbed directly, mass gain, volumetric, and radiotracer techniques are used. Indirect techniques require relating the amount adsorbed to the increase or decrease in intensity of some "output particle" such as desorbed gas, scattered ions, ejected Auger electrons, or quanta of radiation. The direct techniques are limited in their applicability but there is a danger for the indirect techniques in assuming that the change in signal intensity varies linearly with adsorbate coverage (21).

Adsorbed gases may bind to the surface nondissociatively or dissociatively, remain localized or have mobility, form two dimensional surface compounds, or incorporate themselves into the solid, either as an absorbed entity or as part of a new compound. The interaction between a chemisorbed species and the solid depends on the geometric configuration, fractional coverage, and the electronic interaction. Understanding of the electronic bonding interaction is sought using a wide diversity of measurement techniques, such as infrared spectroscopy, magnetic susceptibility, electron spin and nuclear magnetic resonance, work function, conductance, LEED, impact desorption, FEM, FIM, electron energy loss, ultraviolet photoelectron spectroscopy, etc..

Most of the measuring techniques used to study the chemisorptive interaction require high vacuum or better. This is unfortunate for the solar surface materials scientist. Solar systems are required to operate in real environments at atmospheric pressure. Therefore, the chemisorption phenomena of interest are those that lead to degradation of solar materials surfaces. Thus,

an understanding of the weak co-chemisorption processes (40-150 kJ/mol) on a surface with a prior adsorbed layer, carried out at from sub- to super-atmospheric pressures, will require pushing to the limit the currently available techniques, such as infrared, ellipsometric, microgravimetric, and magnetic measurements. At the same time, innovative methods of detection need to be developed. The problems of studying real surfaces of solar materials are similar to those encountered by corrosion and catalytic scientists.

G.   Methods of Studying Surfaces of Solar Materials

The object of scientific study is to gain understanding by securing control of the variables. As indicated in the chapter by Claassen and Butler, the detailed study of particular solar materials is best undertaken when the selections can be made as a result of other research. The selection of the solid form (e.g., polycrystalline thin films), the specific S/S, S/L, or S/G surface (e.g., silver/glass in mirrors), and the preparation technique will be dictated by the cost and the performance properties of the components. Once the options have been narrowed, it is clear that in-depth, fundamental investigations of the surfaces between the materials need to be carried out. The consumer should be understandably impatient if a degradative failure in a solar system cannot be corrected because the proper long-term applied research has not been carried out to gain the required understanding of the cause. At the same time, only finite resources of research funds and personnel can be made available. What types of surface characterization measurements then are most important and what surfaces should be studied? The latter question will be addressed in Section III.

According to the compilation by Lichtman (35), there were
over 70 methods available in 1974 for relating some measured par-
ameter with a S/G surface. For surfaces as defined in this paper,
the number of techniques one could apply easily exceeds 100 (2,3,
4,11,12). Most of the available methods require some to total
specialization for its use alone. Broad philosophical guidelines
need to be developed in order to narrow the choices of surface
analytical facilities required for general study of solar mater-
ials surfaces. These guidelines should be based on (1) studying
the surfaces of long-term interest to solar energy conversion
systems; (2) studying surfaces under (actual and simulated) con-
ditions as close as possible to those encountered when operating
the system; (3) studying the fundamental processes at the S/S,
S/G, and S/L surfaces that impact (1) and (2); (4) employing,
initially, those methods where equipment is commercially available
or where custom equipment can be used or reproduced quickly be-
cause of available expertise; and (5) selecting facilities that
will have the optimum impact on problems encountered in thermal,
photovoltaic, biochemical, and ocean thermal energy conversion
systems. Since solar materials must remain stable for long per-
iods, the surface properties that provide input data on the re-
activity (and/or degradation) must be specifically studied. These
properties are the surface composition or purity, topography
(including defects and inclusions), structure, area, interaction
with ambient gases or vapors at various pressures and radiation
exposures, and electron energy distribution. The leading experi-
mental methods for characterizing these properties are listed in
Table 4. A number of these, notably LEED, FEM, and FIM are not
practically applicable to the likely use of polycrystalline mat-
erials in mass produced solar systems. Thus, the initial charact-
erization should not attempt to relate reactivity to structural
sensitivity per se, but only to the average structural distribu-

Table 4. Tabulation of Methods for Measuring Important Properties of "Surfaces"

Area	Topography	Purity or Composition	Ambient
Gravimetric	SEM		Atmosphere
Volumetric	EM	AES	UHV
EM	Optical Microscopy	ISS	VHV
	Optical Interferometry	SIMS	Modified Atmosphere
Electron Density of States	**Microdefects**	ESCA	
	EM	RBS	**Structure**
UPS	TED	Atom Probe	LEED
	Optical Microscopy	Electron Microprobe	FIM
			FEM
Amount	**Inclusions**	**Chemical Bonds**	TED
Adsorbed, Film Growth	AES/SAM	IR, FTIR	X-Ray
	ISS/SIMS (Imaging)		
Gravimetric		**Valence State and Coordination**	
Ellipsometry		ESCA	

tion   on a polycrystalline surface.   As the number of problems at the S/L surface increases, some of the methodologies discussed at the recent conference on non-traditional approaches for studying the solid/electrolyte interface will have to be considered (45).

III. SURFACE SCIENCE OF SOLAR MATERIALS SURFACES

In this section, an overview will be provided of the type of surface science research that is important to all energy technologies.   These comments are based in part on a report prepared from 51 authorities in the field (46).   Broad areas of surface science that will impact solar materials research will be indicated.   Some specific problems dealing with layers of supported thin films or coatings in reflectors, absorbers (heat), photovoltaics (quantum

absorbers), and transmitters will then be outlined.

A. *Surface Science in Energy Technologies*

It is clear that surface phenomena play a widespread and dominant role in various energy technologies. Our ability to prepare surfaces with the desired performance properties will exert a major control over the wide range of energy conversion technologies. Most of the problems are long range in nature. An understanding is needed to correlate the molecular properties of surfaces with their behavior in corrosion, grain boundary fracture, adhesion, radiation damage, catalysis, lubrication, and embrittlement. Studies which have been concentrated on the S/G interface must be broadened to the S/L and S/S interfaces. New measuring techniques need to be developed and, when necessary, national centers of surface science research should be established.

To improve communication between scientists, efforts should be made to bring together scientists from different disciplines. Understanding of surface phenomena and its applications require knowledge of physics, chemistry, materials, mathematics, and the various applied engineering sciences. Team research in applied surface science is absolutely necessary because of the enormous background required from the various disciplines. I strongly encourage those who major in materials to secure at least intermediate-level courses in physics, chemistry, and another applied science area. The time spent in broadening your scope with more course work will make you a highly sought member of an interdisciplinary surface science team.

The following are the types of surface science studies that are expected to have the broadest impact on all energy technologies (40).

o   Studies of film growth;

o   Characterization of the compositional, structural, and
    electronic properties that influence behavior,

o   Studies of reaction dynamics and elementary processes (ad-
    sorption, diffusion, bonding, and desorption) at surfaces,
    and related theoretical developments;

o   Development of instrumental methods for studies of exter-
    nal and internal surfaces under operating conditions;

o   Studies of the structure, composition, and electronic
    properties of surfaces between condensed media (S/S, S/L),
    of grain boundaries, and of related theoretical develop-
    ments;

o   Studies of the strength of surfaces, as in adhesion, grain
    boundary cohesion, lubrication, and environmental influ-
    ences;

o   Quantification of surface measurement techniques and meas-
    urement of sputtering yields;

o   Studies of real surfaces, oxides, sulfides, and carbides;

o   Studies of surface modifiers such as implanted species,
    poisons, promotors, and inhibitors for the structural and
    chemical stabilization of surfaces;

o   Studies of the surface properties of new classes of mater-
    ials such as bimetallic clusters, composites, ceramics,
    polymers, ion-implanted materials, intercalation compounds,
    etc.;

o   Search for substitutes of precious metals and other sur-
    face active materials not available in the U.S.; and

o   Characterization of surface defects.

B. *Areas of Surface Science and Solar Energy Technologies*

    It is useful to divide surface science into specific areas

of study to consider how these will apply to solar materials. These study areas are chemisorption and catalysis; semiconductor, thin film and solar device surfaces; electrode, electrocatalysis, and photon-assisted surface regions; corrosion; ion interactions with near-surface regions; and grain, phase, and interfacial boundaries. The impact each of these areas of surface science can make on solar materials is given in the next six subsections.

1. *Catalysis and Chemisorption of Solar Materials.* Catalysis and chemisorption problems are more important in other energy technologies than to solar. However, chemisorption, corrosion, and catalyzed activation in solar device surfaces are of significant short range importance. This is particularly true when the reaction degrades the performance of the solar device. Examples of current problems include the surface reactions of mirrors, thermal absorbers, and photovoltaic materials, such as cuprous sulfide. Mechanisms and dynamics of the reaction must be sought. A specific example is the copper catalyzed thermal oxidative degradation of certain polymers. If the properties of polymers used to protect surfaces are degraded by this type of catalyzed reaction, the surface may not only be left unprotected, but the characteristics of the degraded polymer overlayer may lead to an accelerated reaction at the polymer/solid interface.

There are several longer term problems. The first is concerned with the dynamics of growth and preparation of photoactive surfaces via G/S deposition processes under well defined condi- · tions. Chemical vapor deposition and plasma sputtering processes are included here. Processes of this type can be cost competitive with electrochemical film preparation procedures and avoid the multiprocess steps where introducing undesired contaminants is difficult or costly to control. The second problem involves the photocatalysis of water to produce hydrogen using such compounds as titanium dioxide and strontium titanate.

2. *Thin Film and Semiconductor Surfaces*. Thin films and
semiconductors are especially important in solar energy. Metal-
lization films, protective films, antireflection coatings, chem-
ically passivating films, abrasion resistant coatings, transparent
conducting coatings, and semiconductors for photovoltaics are of
near-term importance. In general, the growth processes of films
and coatings need to be understood. In the solar thermal area,
studies of reflector, transmitter, and absorber surfaces that are
stable under solar stresses are needed. Studies of the effect
of long-term irradiation of light from 300-2600 nm on metal/semi-
conductor, metal/polymer, and semiconductor/polymer surfaces are
needed. There is need to elucidate the chemical and structural
properties at S/S surfaces, and to determine as well the electro-
nic properties for photovoltaic materials. Considerable detail
of long term research needs for reflector surfaces, glass sur-
faces, and absorber coatings is available in recent planning doc-
uments (47-49). The photovoltaic needs are covered adequately
in other chapters of this book. For longer-term photoelectrochem-
ical applications, investigations of stable surfaces for the pho-
toelectrolysis of water for the production of hydrogen are needed.
The selection of specific candidate surfaces for further study
requires more research.

3. *Electrodes, Electrocatalysis, and Photon Assisted Sur-
face Reactions*. The surface research on electrodes and electro-
catalysis will affect solar technologies primarily in studying
fuel cells, storage batteries, industrial electrolytic cells,
and industrial electrocatalysts. All these study areas are also
general to energy since they touch upon conservation, storage,
generation, and use, such as in vehicle propulsion. Many of the
problems in this area are at the electrode surface, e.g., insuf-
ficient catalytic activity, susceptibility to poisoning, and loss

of electrocatalyst area. These are all part of the broad field
of heterogeneous catalysis. As such, impurities on the solid
surface require careful characterization.

The overview of photon assisted surface reactions will be
covered in the chapter on photoelectrocatalysis. This area has
long range promise as a solar energy technology, and it contains
solid surface/electrolyte interface problems. Research is needed
to establish the factors controlling photostable surfaces, sur-
face states, electrode sensitization, and the consequences of
light intensity and temperature. As indicated in the chapter by
Butler and Claassen, this is a long range research area, detailed
surface investigations of materials probably should await a nar-
rower selection of candidate materials. The characterization of
the various interfaces needs to unravel the key problem of elect-
rode stability as a function of potential and temperature. Since
many electrolytes are transmitting, optical spectroscopic tech-
niques (IR, ATR and Raman) are being used to probe in situ the
species attached to the electrode surface. The detection of ele-
ments using ISS, ESCA, AES and SIMS are of obvious importance to
characterizing materials at various stages of use, as are BET
surface area measurements to characterize the area and pore size
distribution.

4. Corrosion. The corrosive degradation of solar material
surfaces at the S/G and S/L surfaces cover broad categories of
applications of surface science. There is obvious overlap be-
tween corrosion and the problems mentioned in the previous three
sections. Fluids used in heat transfer systems, in flat plate
collectors, in storage applications, and in OTEC systems provide
a different class of L/S problems from those encountered in L/S
photoelectrochemical systems. Studies of the degradation of re-
flector and absorber surfaces at atmospheric pressure constitute

a different class of corrosion reactions from those normally en-
countered because of the synergism of UV, diurnal temperature
cycles, and changing atmospheric contaminants. Except for the
reflector surfaces, the change in the heat transfer across the
new interface is of dominant importance in the early stages while
the lifetime of the system can be compromised at later stages.

   The effort in corrosion studies should be concerned with
studying nucleation and growth of the new phases formed on real
surfaces and then studying the structural, reactive, and adhes-
ive properties of the fully developed phase. As the layer grows,
the heat transfer properties will be affected and system perform-
ance may be oscillatory, particularly, if scaling and spalling
occur during diurnal temperature fluctuations. Characterization
of the phases in the early stages of growth for composition,
structure, and defect distribution will assist in deducing the
mechanism of growth; the characterization methods are required
for both the S/L and S/G surfaces. The emphasis of chemisorptive
corrosion studies for metals and polymers should be on the early
monolayer growth stages; whereas, for ceramics, composites, and
glasses, the emphasis should be on the role of the defect struc-
ture after the product layer has been formed. Surface modifica-
tion/protection research should emphasize the compatibility of
coatings and inhibitors on the base material. The coatings re-
search here is similar to that discussed in Section III B. The
gas (or liquid) transport to the surface, diffusion along and
into the surface, and stresses set up in the coating and at the
S/S surface all need to be understood.

   The current techniques of surface studies need to be applied
to a wider range of conditions. For example, the relationship
between structure and reactivity at atmospheric conditions need
to be addressed by combining such techniques as ellipsometry,

LEED, and the surface analysis spectroscopies (ISS, SIMS, AES,
and ESCA). Surface characterization of nonmetallic materials
needs to be done for covalent and ionic solids, oxide semicon-
ductors, as well as complex systems, including polymeric mater-
ials. Finally, studies and new techniques for characterizing
the S/S surface are required if adherent protective coatings are
to be understood.

   *5. Interaction of Ions with Surface and Near-Surface
Regions*. The two major areas of application of ion beams to
surfaces are ion-beam surface modification and ion-beam surface
analysis. Ion implantation can be used to modify the near-surf-
ace region to provide better corrosion protection, erosion and
wear resistance, and solar cell junction performance. Basic
methods or phenomena here include sputtering, diffusion, corros-
ion, simulation of damage by ion beams, effect of ion-damaged
surfaces on chemisorption, and the effect of impurities on sput-
tering. The systematic application of ion beams to surface anal-
ysis is a highly neglected area of research. Both ISS and SIMS
are sensitive to the surface monolayer and to isotopic detection,
but support for their development has been modest compared with
the much better developed electron spectroscopies.

   Modification of solar conversion systems or preparation of
system components will involve the sputter deposition films or
coatings for mirrors, absorbers, photovoltaic junction contracts,
and the formation of passivating layers. The quality of composit-
ional analysis of these components, other thin film stacks, and
of the type of surfaces described in the preceeding sections will
be improved by more research on SIMS and ISS.

   6. Grain, Phase, and Interfacial Boundaries. The most dif-
ficult surface to study is probably the S/S interface. Nondes-
tructive techniques for examining this interface are difficult to

conceive, let alone implement. The underlying scientific prob-
lems are to relate the structure, composition, defects, phases,
and dynamic behavior of interfaces to their structure, strength,
and interaction with various environments; to study the kinetic,
thermodynamic, and structural factors that control segregation
at interfaces; and to determine the effects on surface dissolu-
tion, and boundary decohesion, both at the surface and internally,
on the interaction with various environments. With the expecta-
tion of the deployment of large areas of polycrystalline thin
film systems in solar systems, this area of surface science is
of both short- and long-term interest.

C. Surface Science Applied to Specific Solar Energy Materials

As a broad summary of the two preceding sections, major re-
search efforts should be carried out on surfaces to elucidate
mechanisms of degradation in solar stressed environments, in
order to guide modifications of materials to minimize the effect
of the of the detrimental processes on the performance of the
system; to understand the influences of structure, bonding, and
composition that provide interfacial stability; to devise mater-
ials preparation and fabrication processes that yield the desired
chemical, electronic, physical, or mechanical properties; and
to devise new experimental techniques to study and/or measure the
important properties of surfaces. In the initial work, the most
promising polycrystalline materials should be selected, and en-
hanced stability/reactivity should be studied, when exposed to a
solar-stressed environment and interfacial contact. The work
should strive to elucidate mechanisms of degradation and react-
ions at S/S, S/L, and S/G interfaces, of photoenhanced degrada-
tion of polymers, and of photoenhanced ion transport in trans-
mitting materials. Gas/solid reactions and cochemisorption

processes need to be studied at atmospheric pressure. Diffusion
in coatings and films, including atom transport and accumulation
at grain boundaries, needs to be understood. Studying the struc-
tural, bonding, and compositional influences on adhesion, includ-
ing the interactions between polymer/metal (oxide) surfaces and
between dust and transmitting materials is important. Influences
of interfacial effects on the optical properties and on the nu-
cleation and growth of new phases at interfaces, as both relate
to system performance, need to be assessed.

In the following sections, the component of a solar energy
conversion system, a current surface problem with it, the approach
for studying it, and some recent progress will be discussed.
An overview of the specific materials and problem is provided in
Table 5.

1. *Silver Interfaces*. As indicated in the first chapter,
silver has the most desirable reflectance property of any element
(~97%) and will require the least concentrator area to collect
and concentrate a given amount of solar radiation. Although sil-
ver itself is relatively unreactive, a fractional monolayer of
adsorbed oxygen enhances its reactivity to atmospheric gases,

Table 5. Some Current Problems with Solar Materials

System or Component	Material(s)	Problem
Reflectors	Silver/Glass	Degradation
Absorbers	Black Chrome	Degrades at T>300°C
Polymers (Encapsulant)	Acrylics	Photodegradation
Polymers (Protective)	Copper/Polymers	Catalyzed Reaction
Solar Cell Material	Cu_2S	Degradation
Solar Cooling	Silica Gel, Zeolites	Cycle Times
Thin Film Solar Cell	CdS/Cu_2S	Interdiffusion
OTEC	Titanium	Biofouling

such as water, carbon dioxide, sulfur dioxide, nitric oxide, etc.
(50). At room temperature and atmospheric pressure, nearly one
monolayer of oxygen can always be expected on silver. Therefore,
chemisorption of atmospheric gases initiates corrosive reactions
and a degradation of the reflectance.   The results of
these reactions have yielded visually transparent areas in mirrors
used in demonstration heliostat fields in time spans ranging from
several months to a few years. Current solar economics require
mirror designs to last 30 years.

 The present mirror system in use is a glass second-surface
silver mirror backed with copper and paint, as shown in Fig. 3.
Interfacial degradation reaction may begin at the silver/glass
interface because of impurities at the interface. These may be
residual impurities resulting from the method of preparation, or
the impurities resulting from the method of preparation, or the
impurities may accumulate there because of radiation-induced
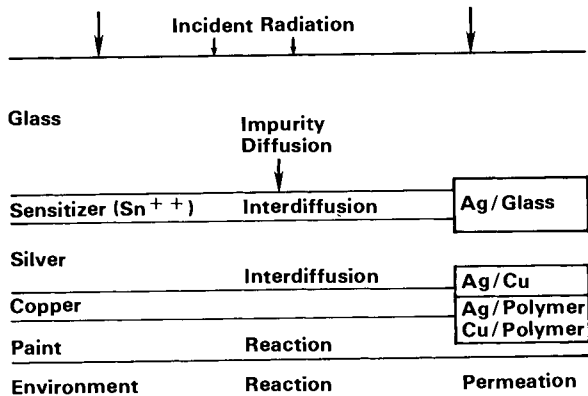
FIGURE 3. *Potential degradation surfaces in a typical
mirror system.*

transport processes of various ions in the glass. Deterioration
of the mirror material may also result from interdiffusion of
copper and silver, and reaction of the copper and then the silver
with atmospheric gases. The rate of permeation of the paint back-
ing by atmospheric gases may increase as the paint weathers in
the sun and elements. For this system, the characterization and
study of the glass/silver, silver/copper, and copper/paint inter-
faces before, and after various stages of use is clearly required.
The methods of characterization outlined in Section II, especially
those of ISS, ESCA, AES, and SIMS, are clearly applicable to this
problem. For solving the mirror degradation problem, it is im-
portant to prepare model mirror systems and secure commercially
made mirrors now in use, and to elucidate the mechanisms of the
reactions that result in deterioration of the reflectance of the
mirror. Characterization of the systems will include using opti-
cal, diffraction, adhesion, and corrosion resistance measurements
in addition to various methods of surface analysis (ISS, ESCA,
AES, SIMS, SEM, IR, etc.). The mechanisms of reactions will be
deduced by measuring the kinetics of pertinent surface reactions
(e.g. $Ag \cdot O_{ads} + SO_2$ (g) + H_2O (v) $\rightarrow AgS_xO_y$), identifying the
sources of contaminants that enhance the degradative reactions,
and carrying out accelerated tests of the interfacial reactions.
Both G/S and L/S interfacial reactions require study as well as
any surface degradation reactions at the polymer/copper (or other
S/S) interface.

Preliminary surface analysis on both polymer coated and un-
coated degraded first-surface silver mirrors shows extensive ac-
cumulation of O, S, and Cl on transparent silver regions and of
O and S on visually reflecting regions (51). The transparent re-
gions also contained silver, showing the corrosion product was
probably a silver oxy-sulfur compound; the shift in the sulfur

ESCA peak indicated the sulfur valence was of the order of +2
rather than the +6 required if silver sulfate were formed.

Extensive detailed study will be required to translate these
initial results into an understanding of the degradation of silver
in mirror systems. However, it is reasonable to anticipate that
a significant improvement in mirror stability will result from
using different glasses and/or backing materials and different
fabrication processes. The modifications of the materials and/or
processes will follow the understanding of the cause of the de-
gradation.

2. *Black Chrome Degradation*. Black chrome has desirable
properties as an absorber coating, as indicated in several chap-
ters in this book and in a recent review article (52). In demon-
stration solar systems, black chrome is overlaid on a nickel/cop-
per/heat exchanger material stack. At temperatures of 250-350°C,
black chrome loses its photothermal absorptivity to become a non-
absorber, but the mechanism of degradation is not known. A number
of studies for improving the stability of black chrome are under-
way (47). A key goal is to determine if the mechanism of degrad-
ation, which is presumably an interface oxidation of chromium par-
ticles in a chromium oxide matrix, is fundamentally different be-
cause of different substrates when overlaid on the heat exchanger
materials or if black chrome itself is kinetically unstable at
about 300°C.

The approach to isolating one possible cause of the degrada-
tion has been to prepare black chrome by reactive evaporation in
oxygen-18 on quartz substrates (53). Microgravimetric techniques
can then be used to measure the time-temperature reactivity of
the material in oxygen-16. Depth profiles using ISS and SIMS,
both of which can detect the presence of the two oxygen isotopes,
can be taken at various stages of the reaction as an additional

aid for elucidating the mechanism of reaction in oxygen.

Changes in the topography (by SEM), in the distribution and amount of Cr° and Cr^{+3} (by ESCA), in the distribution of all elements (by AES), in the distribution of oxygen isotopes (by ISS and SIMS), and in the optical properties (% transmittance and reflectance), can all be correlated with the temperature dependence of the reaction measured microgravimetrically in oxygen and with other gases present. The power of the apparatus described recently (54) for measuring the mass change, optical transmittance and reflectance of thin films is enhanced by auxiliary surface analytical measurements.

In recent preliminary results, it has been shown by ESCA that reactively evaporated black chrome consists of only Cr° and Cr^{+3} and by ISS that the preparation in oxygen-18 yields the desired isotopic labelling (53). Oxidation of black chrome on quartz in oxygen-16 becomes rapid at about 475°C and is completed below 700°C. It is not as yet known if the apparent increased stability (~475 vs 250-350°C) results from the absence of the substrate stack or the preparative process.

3. Polymer/Metal (Oxide) Interfaces.   Polymeric materials are important to solar technologies for use as protective coatings, encapsulants, and backings for mirrors. In each of these cases, the "protected material" is known to degrade when exposed to a solar-stressed environment.

The problem is that the polymer/protected-material interface may experience a degradative reaction. The protective value of the polymer may deteriorate because the UV and/or environmental stresses change the properties of the polymer. The copper ion catalyzed thermal oxidative degradation of polypropylene, which will be discussed in technical detail in Section IV, is an example where the interface and/or material in the interface, e.g., copper,

results in a significant degradative reaction at lower temperatures than normal. Therefore, it is necessary to carry out studies where the synergism of UV, temperature, atmospheric gases, and the interface composition can be assessed.

One approach to studying polymers is to monitor the development of functional groups using an FTIR fitted with an environmental test chamber (ETC) and a UV simulator, as shown in Fig. 4. The sample (1) and blank (2) in an ETC can be subjected to a flow of gases (4) at the same temperature, while only the sample is subjected to a UV flux (3). The IR beam is directed (5) at the sample or reference blank and the reflected beam (6) is focused onto the detector in the FTIR system. The polymer of interest is coated onto both (1) and (2); by proper selection and sequencing the study of the variables, functional groups formed in the polymer can be ascribed to UV, the polymer/S interface, temperature, or a particular gaseous constituent. (A description of the overall apparatus is available [51, p. 7].) The significance of this approach is that the simultaneous or sequential combinations of stresses can cause changes in the important mechanical, chemical, physical, and interfacial properties of the polymer
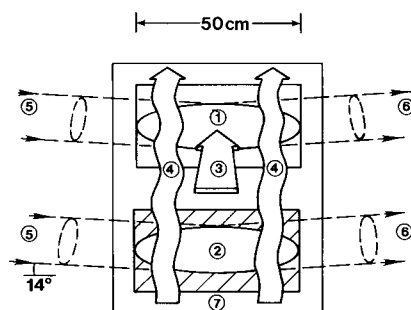
FIGURE 4. Scheme for in-situ photochemical studies using a FTIR.

that adversely affect the functional performance of the component material.

There are other surface and interface problems related to candidate polymers for solar applications. For example, the desirable transmittance of a polymer may be reduced by abrasion from the environment or the adherence of dust. The latter is primarily a problem in surface chemistry. The potential reactivity between a polymer and any other contact surface needs to be studied to determine if an interfacial imcompatibility exists. Reactions at the polymer/S interface may lead to delamination. At the same time, UV enhanced degradation of the bulk polymer may result in adsorption of a corrosive species at the polymer/G interface and permeation of this species through the polymer to the polymer/S interface, where an undesired reaction may actually be accelerated rather than eliminated. The study of thin polymer coatings on metal and metal oxide thin films of candidate solar materials is certainly an area of broad opportunity in surface science.

4. *Water Vapor Sorption by Desiccants.* Desiccant materials have potential applications for solar cooling of buildings by using solar energy to desorb water vapor in regenerating a material used to sorb water vapor. The heat required to vaporize water, which is sorbed by the regenerated desiccant, is extracted from the room to be cooled. The problem is that the rates of sorption and desorption are not known for candidate materials, such as silica gels and zeolites. Furthermore, the effects of several sorption-desorption cycles each day on the rate and amount of water vapor adsorption are also not known. Microgravimetric and chromatographic methods are being used to secure the desired data, which depend critically on the heat of adsorption and on the stability of the internal surface area of porous materials. These methods will permit measuring changes in the surface

area and its location (Section IIA) at various stages of cycling
as a further technique to evaluate the potential of each candidate
desiccant.

The application of microgravimetric materials for studying
the cyclic effects of the reactions of a gas or vapors with a
solid for candidate G/S systems for storage applications is men-
tioned as an aside here. The diurnal solar cycle will subject
storage materials to total cycle times never before studied on
G/S systems. The long-term effects of cyclic de- and rehydration
or de- and re-ammoniation on the rate of reaction needs to be
assessed. Again, potential nucleation and growth problems may
be encountered, but the changes are induced by G/S interactions.

5. *Cuprous Oxide Degradation*. The Cu_2S/CdS system is one of
the leading candidates for the direct photovoltaic conversion of
solar radiation into electrical energy. A cross section of an
assembled solar cell is shown in Fig. 5. First, note the inter-
faces present are CdS/metal, CdS/Cu_2S heterojunction, Cu_2S/grid
material, epoxy/grid material, and epoxy/Mylar. Whether the mat-
erials shown in Fig. 5 actually are the best or not is unimport-
ant for the present discussion. First, the potential number of
interface degradative reactions is important and secondly, one of
the degradative reactions is that between cuprous oxide and
oxygen and/or water vapor. The epoxy and mylar are used to pre-
vent this reaction, but potential interface and bulk polymeric
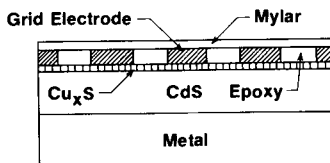
FIGURE 5. *Cross section of a thin film Cu_xS/CdS solar cell.*

reactions may permit both these gases to concentrate at the
Cu_2S/epoxy interface. Therefore, one interfacial study of inter-
est is that of Cu_2S in an oxygen and water vapor environment. It
is known that cell efficiency drops sharply at small departures
from a pure Cu_2S stoichiometry. In his chapter, Dr. Kazmerski
will address another type of interfacial problem of interest,
i.e., changes at the interface because of electron transport
processes.

A viable approach for determining the stability of Cu_2S in
potential reactive gases, and how much of the Cu_2S has reacted,
is to prepare the material and subject it to the degradative
components in situ. A microgravimetric system (54) has been used
for preparing Cu_2S by sulfiding copper films in an H_2S/H_2 atmo-
sphere. Copper films were vacuum deposited onto quartz substrates
and then sulfided to Cu_2S while monitoring the mass gain, trans-
mittance (T), and front-surface reflectance (R). After forming
Cu_2S, the sulfiding atmosphere can be replaced with the desired
reactive atmosphere, and again the mass change, T, and R of the
film can be measured as the reaction proceeds. Auxiliary surface
characterization measurements of the pure films included ESCA,
ISS, AES and SEM. The gravimetric data have shown that stoichio-
metric Cu_2S films 100 to 400 nm thick can be prepared in approp-
riate H_2S/H_2 mixtures and have identified the proper temperatures
and sulfiding times. From SEM data, the films are seen to be
topographically smooth enough (Fig. 2d) to permit using the T and
R data for deducing the optical constants of Cu_2S. These have
been found comparable to those reported by other investigators.
Furthermore, the control of the variables now permits using com-
binations of isotopically labeled oxygen, water, and other gases
for securing a small amount of reaction and confirming it with
ISS and/or SIMS depth profiles.

The critical amount of degradation can be inferred by corre-
lating the extent of the reaction measured with a similar degra-
dation of a functioning heterojunction. Future studies of the
kinetics of degradation in reactive environments should lead to
elucidating the mechanism of degradation and an understanding of
the role of the important Cu_2S/G reactions.

   6.   *Biofouling of Heat Exchanger Surfaces in OTEC Systems.*
The heat exchanger walls in OTEC systems are subjected to a con-
tinuous exposure to a marine environment. One of the key prob-
lems in OTEC systems is to find surfaces that will not permit
the initiation of biological growths, but will withstand the
attack of corrosive sea water. Further elaboration of this prob-
lem is given in the chapter by Pohlman. The approach for study-
ing the L/S interactions and the nucleation and growth of the
species that produces the undesirable biofouling products may
well require employing some of the nontraditional approaches for
studying the L/S interface (45).

IV.   ROLE OF THE POLYPROPYLENE/COPPER OXIDE INTERFACE IN THE
      CATALYZED OXIDATIVE DEGRADATION OF POLYPROPYLENE.

   A number of polymers, e.g., polyethylene and polypropylene,
are known to degrade oxidatively in the presence of copper and
its salts (55). The basic goal in this work was to determine
the role of the polypropylene/copper oxide interface in the cat-
alyzed thermal oxidative degradation of polypropylene. While a
number of different kinds of polymers are proposed for contact
with copper (oxide) in solar conversion systems, this problem
has consequences of a generic nature in energy production and
transmission and in other industrial applications. For example,
it is known that polymer coatings on copper wire, such as poly-
ethylene and polypropylene, degrade and lose their insulating

properties. Failures in electrical and communication network
systems cause problems in civilian and military ground, sea, and
space equipment and vehicles. Therefore, research was carried
out to determine the mechanism of the degradation. From this re-
search, the needs could be determined for improving the lifetime
and stability of systems where polymer/copper oxide interfaces
are encountered. These currently include interconnectors in PV
arrays, paint backing in mirror systems (Fig. 3), and interfacial
contacts in flat plate collectors.

There were two parallel approaches taken during the study
of the catalyzed oxidative degradation of polypropylene. These
were a classical physicochemical approach and a surface analyti-
cal approach for probing the polymer/copper oxide interface.

In the physicochemical approach, 5 μm thick polypropylene
films on different copper oxide (Cu, Cu_2O, $CuO_{0.67}$ and CuO) sur-
faces were heated in oxygen in a quartz spoon gauge reaction ves-
sel. The oxygen consumption was measured as a change in pressure;
the product gases, H_2O and CO_2, were gettered with P_2O_5 and/or
KOH in the reaction vessel. The most important conclusions from
these studies are that the oxygen consumption is fastest for
the polymer on $CuO_{0.67}$ films and that the mechanism of polymer
oxidation is not the same in the absence or in the presence of
the product gases, H_2O and CO_2. The details are available for
the results of oxygen consumption measurements in the presence
and absence of product gas getters for combinations of polyprop-
ylene/glass, polypropylene/copper films, polypropylene/$CuO_{0.67}$
films, and polypropylene/CuO films as well as a discussion of
the mechanisms of degradation (55).

In the surface analytical approach for probing the polypro-
pylene/copper oxide interface, the key question was to determine
if the copper oxide surface actually participated in the reaction

or if it merely served as a source of copper ions that diffuse into the bulk of the polymer for catalytic activity there. Most of the work related to this question has been published (56-59), but an extended summary of it here will emphasize the importance of surface analytical tools for systematically isolating a part of the problem and will show the amount of prior work necessary if an understanding of the problem is to be achieved. For the prior work, the preparation and characterization of $CuO_{0.67}$ films will be discussed first without and then with an oxygen-18 isotopic label. A brief discussion of the preparation of poly-propylene coatings on the isotopically labeled $Cu^{18}O_{0.67}$ films will be followed by a summary of the ISS depth profile analysis of the polypropylene/$Cu^{18}O_{0.67}$ samples.

Copper films, vacuum deposited onto glass substrates up to thicknesses of 108 nm will oxidize in 13.33 kPa of oxygen to form the composition $CuO_{0.67}$ between 108 and 200°C (60). The films have optical and structural properties comparable to Cu_2O; these results combined with the stoichiometric, thickness, and magnetic properties indicate $CuO_{0.67}$ is a gross defect structure of cuprous oxide in which one copper ion, on the average, is missing in each unit cell of the oxide. The oxide, $CuO_{0.67}$, is paramagnetic, indicating that cupric ions or the equivalent are present in it (61). The material is stable in oxygen and air up to to 200°C, but oxidizes to cupric oxide at higher temperat-ures (60). The extensive optical transmittance data obtained during oxidation of copper films 20-165 nm thick can be used as an indicator of complete oxidation of the copper. In the present work, 20-nm copper films, deposited onto glass substrates, were oxidized to 44-nm thick $CuO_{0.67}$ films by heating at 140°C for two hours in air or for eight hours in 1.33 kPa of oxygen-18. Furth-er details of the preparation are available (56,57).

The 44-nm thick $Cu^{18}O_{0.67}$ films were overlaid with polypro-
pylene coatings using a dip coating process. The glass slides
with copper oxide films on both sides were immersed in a solution
of the polymer in p-xylene at 110-120°C under nitrogen and with-
drawn after polymer thicknesses between 40 and 110 nm had been
reached. The thin polymer coatings were desired to reduce the
ion bombardment time for depth profiling to the polymer/copper
oxide interface. Each slide was cut into four pieces for the
experimental work. One was depth profiled as-coated, one was de-
graded in oxygen in the presence of getters, and one was de-
graded in oxygen in the absence of getters. Both degradation re-
actions were carried out at the same temperature. A series of
experiments were carried out at degradation temperatures of 90°,
100°, 110°, and 120°C at an oxygen pressure of 89.3 kPa.

     Composition in depth profiles of the copper, partially
oxidized copper, and completely oxidized copper oxide films on
glass and of the undegraded and degraded polypropylene coatings
on the copper oxide were obtained using a 3-M ISS with a 90°
scattering angle. The details of the data acquisition and
interpretation of the results have been reported (56,58). In the
next three sections, the essence of the ISS results for unlabeled
and labeled copper oxide films is discussed for polypropylene on
copper oxide without degradation, and for degraded polypropylene
both in the presence and absence of getters.

A. ISS Results on $CuO_{0.67}$ and $Cu^{18}O_{0.67}$ Films

     A representative ISS spectrum is shown in Fig. 6 for a 44-nm
$Cu^{18}O_{0.67}$ film on glass after profiling to the oxide/glass inter-
face. The peaks correspond to Cu, $^{16}O, ^{18}O$, Na and K. The appear-
ance of ^{16}O in the isotopically labeled films is a result of the
preparation procedure, as has been discussed (55). Films oxidi-
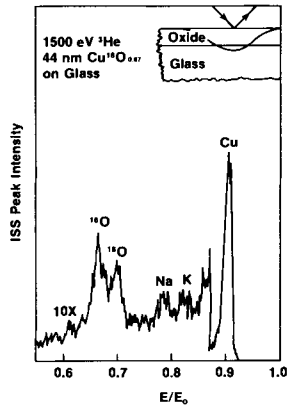
FIGURE 6. ISS spectrum for a $Cu^{18}O_{0.67}$ film at the oxide/ glass interface.

zed in oxygen-16 yield spectra similar to that in Fig. 6, except no oxygen-18 peak is detectable.

The spectrum in Fig. 6 was selected to illustrate the elements detectable at the interface and the ^{16}O-^{18}O peaks. Although the latter overlap, the individual peaks are readily discernible and are separated by 0.030 E/E_0, in agreement with that predicted from the binary collision theory for 90° scattering of ^3He ions. The quantitative potential for ISS has been discussed on the basis of careful analysis of the data (56,57).

Depth profiles of $CuO_{0.67}$ and $Cu^{18}O_{0.67}$ films on glass are shown in Fig. 7. These were obtained by plotting the peak height intensities on spectra [see Fig. 6] taken at various depths of ion milling through the copper oxide. An average Cu/O peak-intensity ratio of 16.7 ± 1.0 was obtained from nine different profiles of $CuO_{0.67}$ films, similar to the one shown in Fig. 7(a), and from partially oxidized copper films on glass substrates. For seven profiles taken with both ^{16}O and ^{18}O present, as illustrated by Fig. 7(b), a Cu/O ratio of 16.3 ± 1.3 was obtained when the contributions from both isotopes were summed to determine an
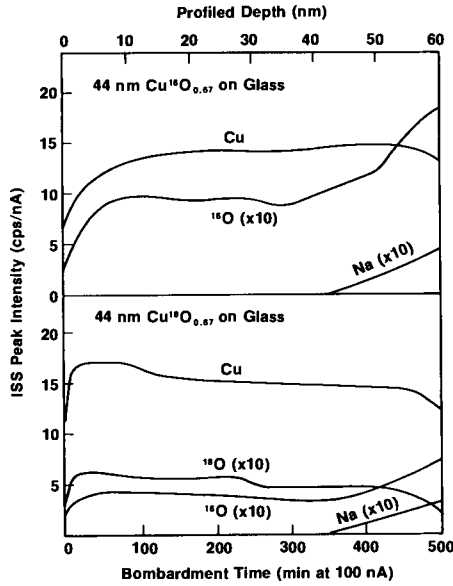
FIGURE 7.   Depth profiles of copper films on glass after complete oxidation in (a) air (^{16}O) and (b) ^{18}O in a stainless steel chamber at approximately $190°C$.

oxygen peak height. The Cu/O ratio for the isotopes was averaged from seven profiles with widely differing concentrations of ^{16}O and ^{18}O. The larger uncertainty for the isotopic mixture results from doubling the possible reading errors when summing the contributions from the two peaks above the base noise level. The possibility of carrying out quantitative ISS studies on a system consisting of oxygen isotopes is supported by these preliminary studies.

Other conclusions reached during the study of copper oxides are: the Cu/O ratio is independent of the substrates used, viz., Au, Pt, or glass (56,58); the Cu/O ratio is slightly different for CuO and $CuO_{0.67}$; and the sputtering rates for $CuO_{0.67}$, CuO,

and Cu films are 0.124 $\pm$ 0.029, 0.076 $\pm$ 0.016, and 0.124 $\pm$ 0.014 nm/min, respectively, when using a 100-nA, 1500-eV, 1-mm (FWHM) ^{3}He primary ion beam at 45° incidence (56,59).

B.   *ISS results for Non-degraded Polypropylene on* $Cu^{18}O_{0.67}$

Originally it was hoped that the effects of the degradations could be studied in a straight forward manner by comparing the depth profiles of polymer coated samples with those of the un-coated copper oxide. However, the depth profiles of the nonde-graded polymer coated copper oxides yielded quite unexpected re-sults, as shown in Fig. 8. (For comparison, see the depth pro-file of the uncoated copper oxide films shown in Fig. 7). It can be noted here that the depth profiles of nearly all the polymer samples, both degraded and nondegraded were qualitatively similar to that illustrated in Fig. 8.

One unexpected characteristic of the polymer depth profiles was the virtual lack of an oxygen signal from the sample until the copper oxide/glass interface was reached by the ion beam. The absolute intensity of the copper signals were 25-35% as large as those obtained from the uncoated oxides, which resulted in disproportionately large Cu/O ratios of 100 to 1 or greater. These Cu/O ratios were five to six times larger than those obtain-ed from the uncoated copper oxide films. This aspect of the depth profiles indicated that meaningful results could not be obtained directly from comparisons between polymer coated and uncoated copper oxide films. Furthermore, minor variations were found in profiles of the nondegraded samples that had been dip-coated for different times (producing different polymer thicknesses). Thus, even comparisons between samples with a similar history but different polymer overlayer thicknesses were

ambiguous. To circumvent these problems, a single glass slide
with a polymer coated copper oxide film was cut into several
pieces. One of the pieces was profiled to act as a control; the
remaining pieces were degraded under various conditions and then
depth profiled. Differences in the depth profiles could now be
attributed to the degradation and not to minor differences in
preparation or storage.

    Though the oxygen signals were small, it was possible to
determine that little if any change occurred in the isotopic
composition of the copper oxide as a result of the dip-coating.
The extent to which the copper oxide might be altered by the
dip-coating process was examined by depth profiling a copper ox-
ide film before dip-coating and after a polymer coating had been
dissolved from the copper oxide film by immersion in boiling
toluene. Only minor differences in the Cu/O ratio were noted
between the two depth profiles of the copper oxide, and it was
concluded that the dip-coating process alone did not signific-
antly affect the copper oxide film. The minor changes in Cu/O
ratios that were observed could be explained by assuming that
the grain boundaries between $CuO_{0.67}$ crystallites of only the
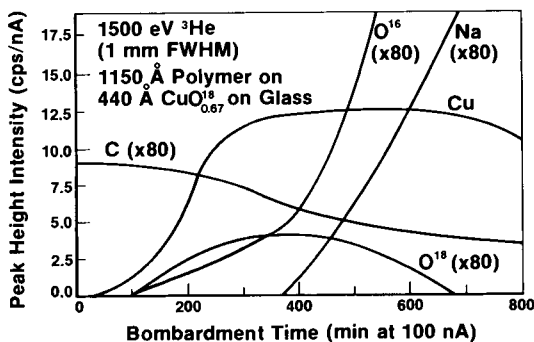
FIGURE 8. Depth profile of 115 nm nondegraded polypropylene
coating on a 44 nm $Cu^{18}O_{0.67}$ film on glass.

atomic layer next to the polymer was reduced to free copper.

C. *ISS results on Degraded Polypropylene on $Cu^{18}O_{0.67}$ Films*

The results for degraded polymer films can be divided into
two categories: those degraded with P_2O_5 and KOH present to get-
ter the reaction product gases and those degraded without the
getters present. The only differences between the preparation
of the two sets of degraded samples was the presence or absence
of the getters. In all but one case, the depth profiles of the
degraded films were similar to the one illustrated in Fig. 8.

The effect of oxidative degradation was determined by com-
paring depth profiles of a nondegraded film with those of degrad-
ed polymers from the same set of samples. However, direct compar-
isons of peak height intensities were found to be less suitable
than comparisons obtained from plotting the Cu/O ratios vs. sput-
tering time. The curves obtained from depth profiles of polymer
samples degraded in the presence of the chemical absorbents P_2O_5
and KOH are illustrated in Fig. 9. The unmarked curve was obtain-
ed from the depth profile of a nondegraded polymer. The remain-
ing curves in Fig. 9 were obtained from depth profiles of degrad-
ed polymers. The times and temperatures used yielded a 10% degra-
tion for curves a and b and 35% for curve c. It can be seen that
the Cu/O ratios for the nondegraded polymer are substantially
lower than those for the degraded polymer samples and that qual-
itatively there are few differences between curves a, b, and c.
The larger Cu/O ratios for the degraded films result from larger
copper concentrations in the "oxide-layer" after the degradation
reaction, i.e., the polymer has reduced the oxide during degrada-
tion. From the actual depth profiles, no change could be seen in
the isotopic composition of the oxide films resulting from the
degradation process, showing that no exchange occurred between
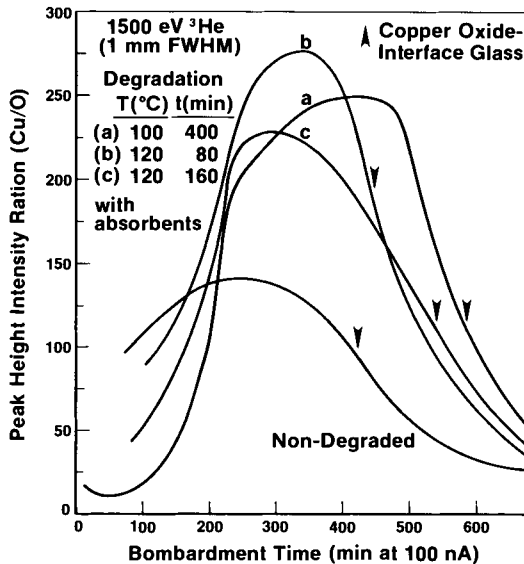
FIGURE 9. Plots of the Cu/O ratios obtained from nonde-graded and degraded polypropylene films after degradation with chemical absorbents present in the reaction vessel.

The oxygen of the degrading atmosphere and that in the copper oxide layer.

Other sets of films were degraded without the presence of P_2O_5 and KOH in the reaction vessel, thereby allowing substantial concentrations of product gases to accumulate in the polymer and in the reaction region during the degradation. The Cu/O curves for these samples also showed that reduction of the polymer occurred (56,59). However, for degradation at 100°C for 400 min., a smaller Cu/O ratio resulted both from a decrease in the copper signals and slightly larger oxygen signals. A depth profile from this degradation sample is shown in Fig. 10. This curve exhibits large differences from all other previously depth profiled polymer coated copper oxide samples. The Cu/O ratio throughout the profile was about 10 to 1, which was not only smaller than those
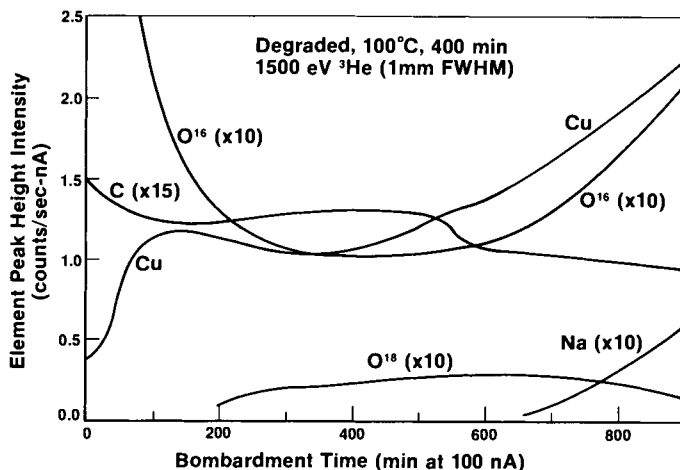
FIGURE 10. *Depth profile of a polypropylene coated copper oxide film that was degraded at 100°C for 400 min without chemical absorbents present in the reaction vessel.*

observed from coated oxides analyzed previously, but it was also smaller than the Cu/O ratios that had been determined for the uncoated oxide films. The small Cu/O ratios resulted from an increase in the absolute oxygen-16 peak intensities and a decrease in the copper peak intensities. Most importantly, there was a marked change in the isotopic composition of the overlayers. The increase in the oxygen-16 in the film compared with the original composition (Fig. 7) is consistent with a process of reduction of the oxide by the polymer followed by reoxidation of the copper by an oxygen-16 environment. Other features in Fig. 10 have been discussed in more detail (56,59).

In conclusion, the ISS studies of polypropylene copper oxide samples show that the polymer/oxide interface participates in the degradative reaction. Reduction of the oxide by the polymer occurs, and, under conditions simulating actual use, copper can be

all or partially reoxidized. The relative importance of the
interface reaction versus the effect of copper ions in the bulk
polymer as catalytic sites is still being pursued.

REFERENCES

1. Hayward, D.O., and Trapnell, B.M.W., "Chemisorption",
    Butterworths, London, 1964; Tompking, F.C., "Chemisorption
    of Gases on Metals", Academic, N.Y., 1978; Rhodin T.N., and
    Ertl, G., "Nature of the Surface Chemical Bond", North-
    Holand, Amsterdam, (1979).
2. Flood, E.A. (ed.), "The Solid Gas Interface", Vols. 1 and 2,
    Dekker, N.Y., (1967).
3. Anderson, R.B. (ed.), "Experimental Methods in Catalytic
    Research", Academic, N.Y., (1968).
4. Green, M. (ed.), "Solid State Surface Science", Dekker, N.Y.,
    (1969).
5. Gould, R.F. (ed.), "Interaction of Liquids at Solid Sur-
    faces", ACS Publications, Washington, D.C., (1968).
6. Anderson, J.R. (ed.), "Chemisorption and Reactions on
    Metallic Films", Vols. I and II, Academic, N.Y., (1969 and
    1971).
7. Chopra, K.L., "Thin Film Phenomena", Krieger, N.Y., (1970).
8. Somorjai, G.A., "Principles of Surface Chemistry", Prentice-
    Hall, Englewood Cliffs, N.J., (1972).
9. Blakely, J.M., "Introduction to the Properties of Crystal
    Surfaces", Pergamon Press, Oxford, (1973).
10. Adamson, A.W., "Physical Chemistry of Surfaces", Wiley-
    Interscience, N.Y., (1976).
11. Kane, P.F., and Larrabee, G.B. (eds.), "Characterization of
    Solid Surfaces", Plenum, N.Y., (1974).
12. Czanderna, A.W. (ed.), "Methods of Surface Analysis",
    Elsevier, Amsterdam, (1975).

13. Hannay, N.B. (ed.), "Treatise on Solid State Chemistry",
     Vols. 6A and 6B, "Surfaces", Plenum, N.Y., (1976).

14. Vanselow, R. (ed.), "Chemistry and Physics of Solid Sur-
     faces", Vols. 1 and 2, CRC Press, Cleveland, (1977 and 1979).

15. Morrison, S.R., "The Chemical Physics of Surfaces", Plenum,
     N.Y., (1977).

16. Baglin, J.E.E., and Poate, R.E. (eds.), "Thin Film Phenom-
     ena-Interfaces and Interactions", Proc. Electrochem. Soc.,
     78-2, (1978).

17. Roberts, R.W., and Vanderslice, T.A., "Ultrahigh Vacuum and
     Its Applications", Prentice-Hall, Englewood Cliffs, N.J.,
     (1963).

18. Brunauer, S., Emmett, P., and Teller, E., *J. Am. Chem. Soc.*
     60, 309 (1938).

19. Robens, E., in Czanderna, A.W. and Wolsky, S.P. (eds.),
     "Microweighing in Vacuum and Controlled Environments",
     Elesevier, Amsterdam, p. 125, (1980).

20. Gregg, S.J., and Sing, K.S.W., "Adsorption, Surface Area and
     Porosity", Academic, N.Y., (1967).

21. Czanderna, A.W., and Vasofsky, R., *Prog. Surface Sci. 9,* 43
     (1979).

22. Honig, R.E., in West, A.R. (ed.), "Advances in Mass Spectro-
     metry", Vol. 6, Elsevier, Barking, England, p. 337, (1974).

23. Winters, H.F., in Kaminsky, M. (ed.), "Radiation Effect on
     Solid Surfaces", Amer. Chem. Soc., Washington, D.C, p. 1,
     (1976).

24. Wehner, G., in ref. 12, p. 1.

25. Czanderna, A.W., Miller, A.C., and Helbig, H.F., in Johari,
     O. (ed.), SEM/1978, Vol. 1, SEM Inc., AMF O'Hare, Il.,
     (1978).

26. Helbig, H.F., and Czanderna, A.W., *JEMMSE, 1,* 379 (1979).

27.   Buck, T.M., in ref. 12, p. 75.

28.   Rusch, T., and Erickson, R.L., in Tolk, N.H., Tully, J.C., Heiland, W., and White, C.W. (eds.), "Inelastic Ion Surface Collisions", Academic, N.Y., p. 73, (1977).

29.   McHugh, J.A., in ref. 12, p. 223.

30.   Joshi, A., Davis, L.E., and Palmberg, P.W., in ref. 12, p. 159.

31.   Sickafus, E.N., *JEMMSE*, *1*, 1 (1979).

32.   Carlson, T.A., "Photoelectron and Auger Spectroscopy", Plenum, N.Y., (1975).

33.   Riggs, W.M., and Parker, M.J., in ref. 15, p. 103.

34.   Brundle, C.R., Baker, A.D. (eds.), "Electron Spectroscopy: Theory, Techniques, and Applications", Vols. 1-3, Academic, N.Y., (1977ff).

35.   Lichtman, D., in ref. 12, p. 39.

36.   Mayer, J.W., and Ziegler, J.F., "Ion Beam Surface Layer Analysis", Elsevier Sequoia, Luasanne, (1974).

37.   Hutchins, G.A., in ref. 11, p. 441.

38.   Müller, E.W., in ref. 12, p. 329.

39.   Coburn, J.W., Taglauer, E., and Kay, E., *J. Appl. Phys. 45*, 1779 (1974).

40.   Greene, J.E., and Whelan, J.M., *J. Appl. Phys. 44*, 2509 (1973).

41.   Tolk, N.H., Simms, D.L., and Foley, E.B., *Radiation Effects 18*, 221 (1973).

42.   Shuttleworth, R., *Proc. Royal Soc. 62A*, 167 (1949).

43.   Benson, G.C., and Yun, K.S., in Flood, E.A. (ed.), "The Solid-Gas Interface", Vol. 1, Dekker, N.Y., p. 227, (1967).

44.   Duke, C., *Crit. Rev. Solid State Matls. Sci. 8*, 69 (1978).

45.   Non-Traditional Approaches to the Study of the Solid-Electrolyte Interface, Snowmass, Co., Sept. 24-27, (1979). Proceedings to appear in a special issue of *Surface Science*.

46. Somorjai, G.A., Yates, J.T., Jr., and Clinton, W., Report
     of the Surface Science Workshop, LBL-6658, Lawrence Berkeley
     Laboratory, U. California, Berkeley, March (1977).

47. Call, Patrick J., National Program Plan for Absorber Surfaces
     R&D, SERI/TR-31-103, January (1979).

48. Solar Optical Materials Program Activity Committee, SERI/
     PR-31-137, July (1979).

49. Solar Glass Mirror Program, SERI/RR-31-145, January (1979).

50. Czanderna, A.W., in Czanderna, A.W. and Wolsky, S.P. (eds.),
     "Microweighing in Vacuum and Controlled Environments",
     Elsevier, Amsterdam, p. 175, (1980).

51. Czanderna, A.W., in Butler, B.L. (ed.), Basic and Applied
     Research Program, SemiAnnual Report, SERI/TR-334-244,
     p. 12, December (1979).

52. Ignatiev, A., O'Neill, P., and Zajac, G., *Solar Energy
     Materials 1,* 69 (1979).

53. Czanderna, A.W., Prince, E.T., and Helbig, H.F., SERI/TP-
     334-352, October (1979).

54. Prince, E.T., Helbig, H.F., and Czanderna, A.W., *J. Vac.
     Sci. Technol. 16,* 244 (1979).

55. Jellinek, H.H.G., Kachi, H., Czanderna, A.W., and Miller,
     A.C., *J. Polymer Sci. 17* 1493 (1979). A detailed list
     of references on the oxidation of polypropylene is given
     in ref. 1 of this paper.

56. Miller, A.C., Ph.D. Thesis, Clarkson College, Potsdam, N.Y.,
     (1977).

57. Czanderna, A.W., Miller, A.C., Jellinek, H.H.G., and Kachi,
     H., *J. Vac. Sci. Technol. 14,* 227 (1977); *Industrial Res.
     20,* 62 (1978).

58. Miller, A.C., and Czanderna, A.W., *Appl. Surface Sci.* (1980).
     In Press. SERI/TR-31-393, July (1979).

59.   Czanderna, A.W., Jellinek, H.H.G., Kachi, H., and Miller,
      A.C., Annual Reports, Incra Project No. 224, July (1974);
      July (1975); July (1977); International Copper Research
      Association, N.Y.
60.   Wieder, H., and Czanderna, A.W., *J. Phys. Chem. 66,* 816
      (1962).
61.   Czanderna, A.W., and Wieder, H., *J. Chem. Phys. 39,* 489
      (1963); *40,* 2044 (1964).

APPENDIX I

AES	Auger Electron Spectroscopy
ATR	Attenuated Total Reflectance
BET	Brunauer, Emmett, and Teller
ELEED	Elastic Low Energy Electron Diffraction
EM	Electron Microscopy
ESCA	Electron Spectroscopy for Chemical Analysis (XPS)
FEM	Field Emission Microscopy
FIM	Field Ion Microscopy
FTIR	Fourier Transform Infrared
GDMS	Glow Discharge Mass Spectroscopy
GDOS	Glow Discharge Optical Spectroscopy
ILEED	Inelastic Low Energy Electron Diffraction
IR	Infrared (Spectroscopy)
ISS	Ion Scattering Spectrometry
LEED	Low Energy Electron Diffraction
RBS	Rutherford Back Scattering (Spectroscopy)
SAM	Scanning Auger Microscopy
SCANIIR	Surface Composition by Analysis of Neutral and Ion Impact Radiation
SEM	Scanning Electron Microscopy
S/G	Solid Gas Interface (G/S)
SIMS	Secondary Ion Mass Spectrometry

S/L   Solid Liquid Interface (L/S)

S/S   Solid Solid Interface (S/S)

TED   Transmission Electron Diffraction

TEM   Transmission Electron Microscopy

TGA   Thermogravimetric Analysis

UHV   Ultra High Vacuum

UPS   Ultraviolet Photoelectron Spectroscopy

VHV   Very High Vacuum

XPS   X-ray Photoelectron Spectroscopy (ESCA)
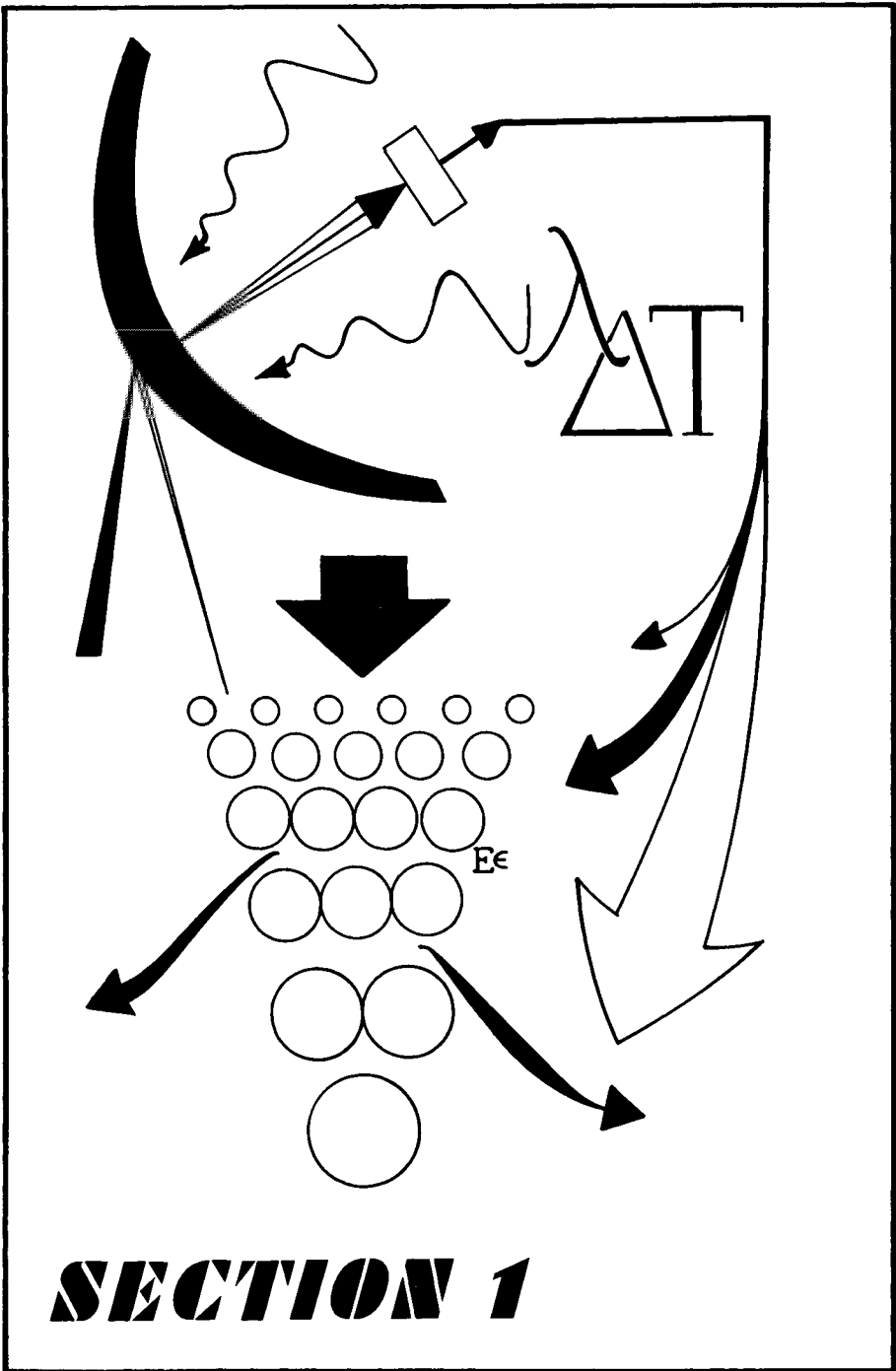
SECTION 1

1. SOLAR COLLECTOR (PHOTOTHERMAL) MATERIALS

The utilization of solar energy ideally begins, in the simplest cases, with a collection scheme in which sunlight is effectively converted to heat. Since this process is the most common and most important feature of home solar passive and active systems, the component materials requirements must ideally involve high efficiency, low cost, and long life. These requirements are certainly not unique to solar energy applications but are requisites in any successful engineering design application. To a large extent, requisite materials properties and performance in solar collection applications can be, or can hope to be, altered by the manipulation of specific microstructural features, even including the development of new materials. In the development of successful solar collectors, the structure, composition, or microstructure of selective absorbers, reflectors, concentrators, and associated support structures must be considered. Specific functional efficiencies, low cost, and long life will depend to a large extent upon structural stability and the interaction of a material with environmental phenomena, including other system components and materials. An understanding of the science of these materials is therefore a prerequisite to successful design implementation. This understanding must also include a knowledge of the relationship of the materials properties to the actual system performance where operationally and environmentally synergistic phenomena are prevalent over long periods of operation.

This section begins with a proposal for tailor-making selective solar absorber coatings based upon the effect of microstructure and microstructural distributions upon optical response, especially absorptivity. Solar mirror materials are discussed, especially their properties and structure, and the performance and degradation of solar mirror materials in the environment (outdoors) are described. Two chapters describe emissivity of metals and the role of emissivity in solar collection. In addition, the effect of microstructure on emissivity is described utilizing the concept of composite materials systems, and one additional chapter describes metal-insulator or metal-oxide composite systems or cermets and the selective manipulation of these microstructures in the development of high-temperature selective absorbers. Finally, the corrosion, erosion, and related degradation of solar collector and related solar materials systems and components are described, beginning with a review of principal corrosion mechanisms in metals and alloys.

The chapters contained in this section are aimed at providing the reader with an overview of solar collector materials, materials problems and design challenges, as well as an understanding of the specific optical features and physical phenomena which control the efficient conversion of sunlight to heat energy. This section is also intended to demonstrate the properties of materials, particularly microstructural properties, which are responsible for their efficient utilization in photothermal processes.

CHAPTER 4

THE OPTICAL PROPERTIES-MICROSTRUCTURE RELATIONSHIP
IN PARTICULATE MEDIA: OPTICAL TAILORING OF
SOLAR ABSORBERS[1]

Alex Ignatiev

Department of Physics
University of Houston
Houston, Texas

I. INTRODUCTION

Historically (1,2) and more recently (3-11) due to revived
interest in solar radiation absorption, studies of solar energy
absorbers have attributed the optical response of absorbers to
be due to the particulate nature of the material. This relation-
ship between optical response and microscopic structure will be
examined in some detail in the following pages, however, it is
informative to first view the basic principles of electromagnetic
radiation absorption by a medium so as to obtain a better con-
ceptual view of solar radiation absorption.

Absorption of electromagnetic radiation in solids is princi-
pally governed by the displacement of charges in the material.
Figure 1 illustrates the main electromagnetic radiation absorp-
tion mechanisms in materials. The principal contributions to
absorption are:

(a) Molecular dipole absorption (microwave region): absorp-
tion due to orientation changes of a polar molecule.
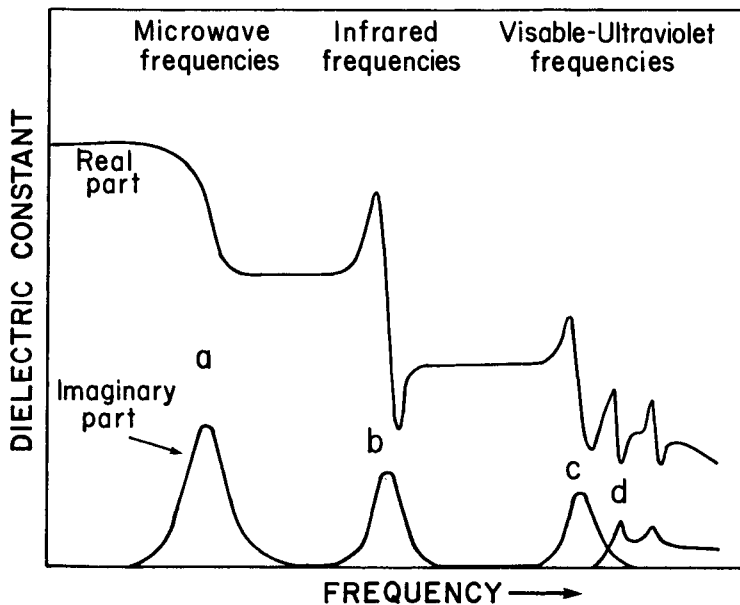
FIGURE 1. Real and imaginary parts of the dielectric response in materials. Note the frequency dependence for the various absorption mechanisms.

(b) Ionic absorption (infrared region): absorption due to the displacement of ions in a material.

(c) Electronic absorption (visible-ultraviolet region): absorption due to the displacement of "free" or weakly bond electrons with respect to nuclear charges.

(d) Interband absorption (visible-ultraviolet region): absorption due to the excitation of electrons in a material to higher energy states.

The absorption of solar radiation (mainly in the visible region) will therefore principally involve mechanisms (c) and (d) and as a result of this and the opening remarks covering particulates the broad conditions for a good solar energy absorber can be defined as:

i.)   The absorber should have a metallic or semimetallic
component.

ii.) The absorber should be composed of small particles.

The understanding of the interaction of an array of small
conducting particles with electromagnetic radiation is therefore
of interest in the study of solar energy absorption.

II.   EFFECTIVE MEDIUM THEORY

The analysis of the interaction of an array of small metal
particles with an electromagnetic (EM) field requires a self
consistant approach for completeness due to the possible multiple
scattering of the incident EM wave by the medium. Within the
restriction of small packing fraction of the particles in the
host medium and small particle size, self consistant analyses of
the multiple scattering have been formulated (12-15) which des-
scibe the response of the particulate medium to be EM field. A
simplified approach to the problem was, however, presented over
70 years ago by Maxwell Garnett (MG) (16). MG equated the inter-
action of an array of small particles with the EM field to the
interaction of a homogeneous "effective medium" with the EM field.
In this approach, the particles are assumed to be small enough
and separated enough that they are not sensitive to the dynamic
characteristics of the incoming wave, i.e., that they exist in a
constant field region in the material. The metallic particles
are taken to be imbedded in a dielectric (Figure 2) and the con-
stant effective field in the material $\bar{E}$ is taken as the volume
average of the induced field in the particles E_i, and the field
in the host dielectric E_m;

$$\bar{E} = fE_i + (1 + f)E_m \tag{1}$$

where f is the packing fraction of the particles in the dielec-
tric. The effective polarization field in the medium can
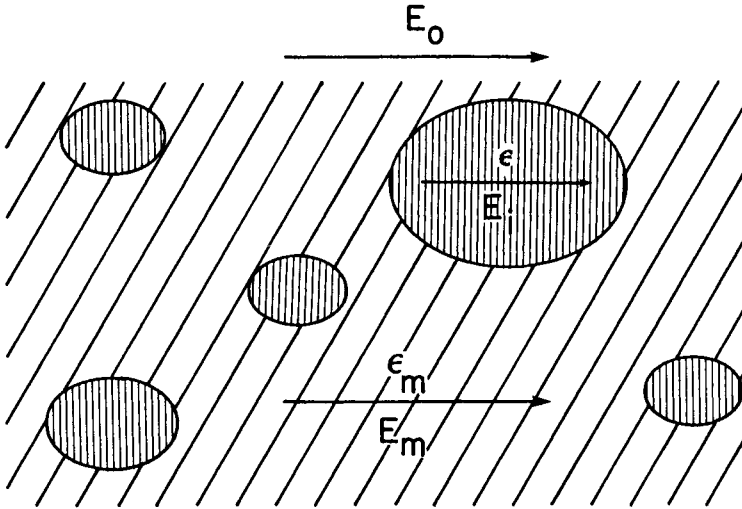
FIGURE 2. Structural model of a particulate analyzed by Effective Medium Theory--Maxwell Garnett approach.

therefore be written as

$$4\overline{P} = (\overline{\varepsilon} - 1)\overline{E} = f(\varepsilon - 1)E_i + (1 - f)(\varepsilon_m - 1)E_m .$$
(2)

Under the assumption of spheroidal particles oriented with respect to the field

$$E_i = \frac{\varepsilon_m}{L_\varepsilon + (1 - L)\varepsilon_m}$$
(3)

where L is a depolarization factor (17) corresponding to a specific shape and orientation spheroid. The depolarization factor defines the polarizability of the spheroid in question.

It is well to note that for a spherical particle L = 1/3 and thus Equation (3) reduces to the well known Clausius-Mossotti

equation for the field in a spherical particle.

Systematic reduction of Equation (2) under the assumption of spherical particles gives the MG expression:

$$\bar{\varepsilon} = \varepsilon_m \frac{\varepsilon(1 + 2f) + 2\varepsilon_m(1 - f)}{\varepsilon(1 - f) + \varepsilon_m(2 + f)} \ . \tag{4}$$

Generalizing Equation (2) to spheriodal particles, however yields

$$\bar{\varepsilon} = \varepsilon_m \frac{(1 + 2/3 \ f\alpha)}{(1 - 1/2 \ f\alpha)} \tag{5}$$

where

$$\alpha = \frac{1}{3} \sum_{i=1}^{3} \frac{(\varepsilon - \varepsilon_m)}{\varepsilon_m + L_i(\varepsilon - \varepsilon_m)} \tag{6}$$

with L_i the depolarization factors for given shape spheroids aligned along three orthogonal directions to the electric field.

Although MG is the most widely used effective medium theory, others have been produced by Bruggeman (14) and by Hunduri (15). Both of these are self consistant in that in expressions similar to (6) ε_{me} is replaced by $\bar{\varepsilon}$. They also have their basis in topological similarities between the particles in the medium and the host dielectric. This results for the case of spherical particles, such particles imbedded in a dielectric composed also of spherical particles. Such topological restrictions lend to limited applicability of these approaches in defining optical properties of particulares (3,18).

The applicability of the effective medium approach in general has certain restrictions which historically were defined by a rule of thumb:

$$ka \ll 1.0 \quad \text{and} \quad f \ll 1 \tag{7}$$

where $k = 2\pi/\lambda$ and a = particle radius.

This would restrict the use of EMT in analyzing solar absorbing particulates to those with particle sizes less than ~ 100 Å. EMT seems, however, to have applicability to systems with much larger particle sizes (19). Such results have led to a recent reevaluation of EMT applicability criteria to particulates by Smith (18). His analysis is based not so much on the requirement of a uniform field at the particle, but on the requirement of *no scattering* of the incident wave by the particle plus an envelope of medium surrounding and correlated with the particle. His results yield the expanded EMT applicability criteria of:

$$a \lesssim 0.2\,\lambda$$

and   (8)

$$(ka)f^{1/3} \sim 1.0 \ .$$

This means that for solar absorbing particulates, EMT can safely be applied to absorbers with particle sizes of ~ 1000 Å and packing fractions of ~ 0.5, e.g., the majority of currently relevant solar absorbers.

The above noted EMT formalism has been given for the general case of spheroidal particles imbedded in a dielectric. That this assumption of spheroidal particles is realistic is, however, yet to be established. Recent scanning and transmission electron microscopy (SEM and TEM) studies (3-11,20-22) on several different particulate solar absorbers (both vacuum evaporated and electrodeposited) have indicated that the absorbers are in fact composed of small particles (Figure 3). The particles in most cases do well approximate oblate and/or prolate spheroids, and in some cases chains of particles have been observed which can be approximated by large eccentricity prolate spheroids, e.g., sausages (Figure 4). The spheroid approximation is therefore acceptable and although it cannot cover all possibilities of particle shape, it can cover the possibilities ranging from platelet to sphere to rod.
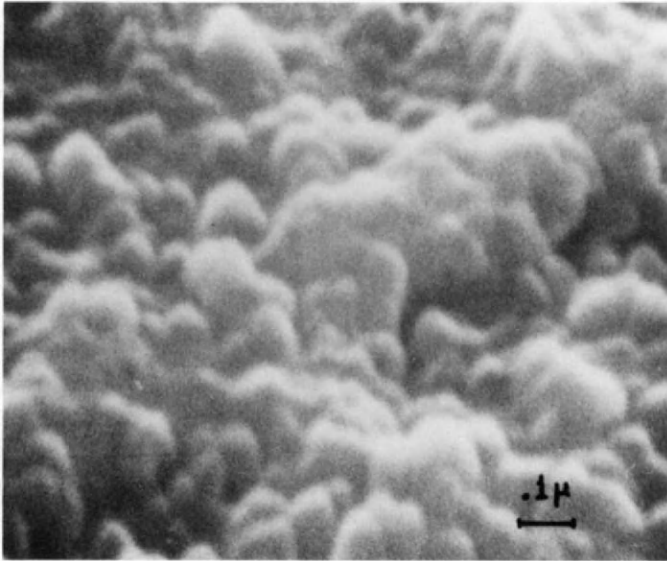
FIGURE 3. Scanning electron micrograph of electrodeposited black chrome after the removal by sputter etching of several hundred angstroms of material. Note the various particle shapes.

In real particulate absorbers, micrograph observations (Figure 3) indicate not only that the particles are well approximated by spheroids, but that under this assumption one would require a distribution of spheroid shapes to approximate the actual particulate structure of most absorbers. The power of the spheroid approximation for the analysis of the optical response of such real absorbers can now readily be seen since the possibility exists in the approximation for the use of a distribution of spheroid shapes to model the distribution of particle shapes observed in real absorbers. This approach has been adopted by several authors to analyze the optical response of particulate gold (20,23), chromium (4,24), nickel (24) and gold cermet (25) vacuum deposited films and black chrome (3,7)
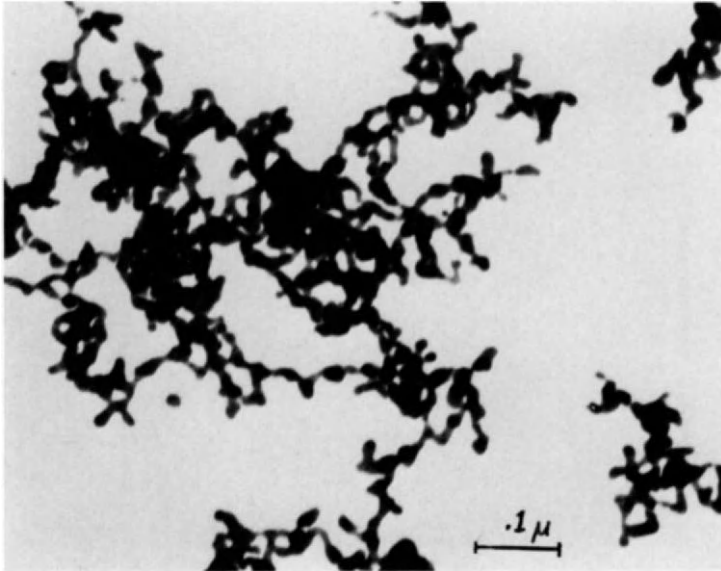
FIGURE 4. Transmission electron micrograph inert-gas evapor-ated gold black. Note the spherical particles linked together in chain-like fashion.

electrodeposited films. The approach of O'Neill and Ignatiev (26) will be expanded upon here to illustrate the applicability of defining distributions of spheroidal particles in the modeling of the optical response of particulate films.

III. SPHEROID MODEL

Within the EMT approach of O'Neill and Ignatiev, the "effec-tive" dielectric permeability of a particulate material with a specific distribution $\rho(m)$ of randomly oriented prolate spheroids with semimajor to semiminor axis ratio m, $(m = b/a)$, is given by:

$$\bar{\varepsilon} = \frac{\varepsilon_{me}(1 - f) + \varepsilon \frac{f}{3} \sum_m g(m)\rho(m) \Delta m}{(1 - f) + \frac{f}{3} \sum_m g(m)\rho(m) \Delta m} \tag{9}$$

where

$$g(m) = \sum_i \frac{1}{1 + [\varepsilon/\varepsilon_{me} - 1]L_i(m)} \tag{10}$$

with $L_i(m)$ = depolarization factor for spheroids of axis ratio m aligned in three orthogonal directions with respect to the incident electric field (Figure 5) to stimulate random orientation of spheroids.
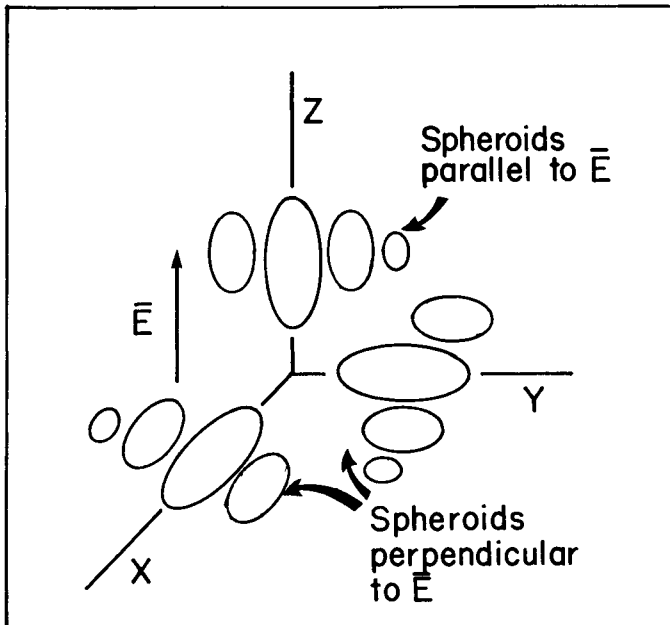
FIGURE 5. *Structural model for spheroid orientation in the Spheroid Model analysis.* *Averaging over spheroids aligned in three orthogonal directions simulates random orientation of spheroids.*

Here ε_{me} is the dielectric permeability of the host dielec-
tric and ε is the permeability of the metallic particles.

It should be realized that $\bar{\varepsilon}$ will be complex since in general
ε_{me} and ε are complex, and that $\bar{\varepsilon}$ will be a function of both λ
and m.

Under the conditions of $f << 1$ which is satisfied for many
solar blacks, Equation (9) reduces to:

$$\bar{\varepsilon}_1 \simeq 1$$

$$\bar{\varepsilon}_2 \simeq \varepsilon_2 \frac{f}{3} \sum_m [g_{||}(m) + 2g_{\perp}(m)]\rho(m)\ \Delta m \tag{11}$$

where $\bar{\varepsilon} = \bar{\varepsilon}_1 + i\ \bar{\varepsilon}_2$ and $g_{||}(m)$ and $g_{\perp}(m)$ are the functions of
Equation (10) for spheroids oriented parallel and perpendicular
to the electric field, respectively.

The absorption coefficient for electromagnetic radiation is
defined by:

$$\alpha(m,\lambda) = \frac{2\pi}{\lambda}\ \bar{\varepsilon}_2(m,\lambda) \tag{12}$$

and under the conditions of Equation (11) the transmittance
through the particulate film can be defined by:

$$T = e^{-\alpha(\lambda)t} \tag{13}$$

where t is the film thickness and

$$\alpha(\lambda) = \sum_m \alpha(m,\lambda). \tag{14}$$

It should now be pointed out that not only is the absorption
coefficient dependent on m and λ, but it is also governed by
material dependent quantities such as free electron density and
interband absorption which affect ε and ε_{me}. These effects on
$\alpha(m,\lambda)$ can be readily seen in Figs. 6 and 7 which compare $\alpha(m,\lambda)$
for low density nickel and chromium particulates.
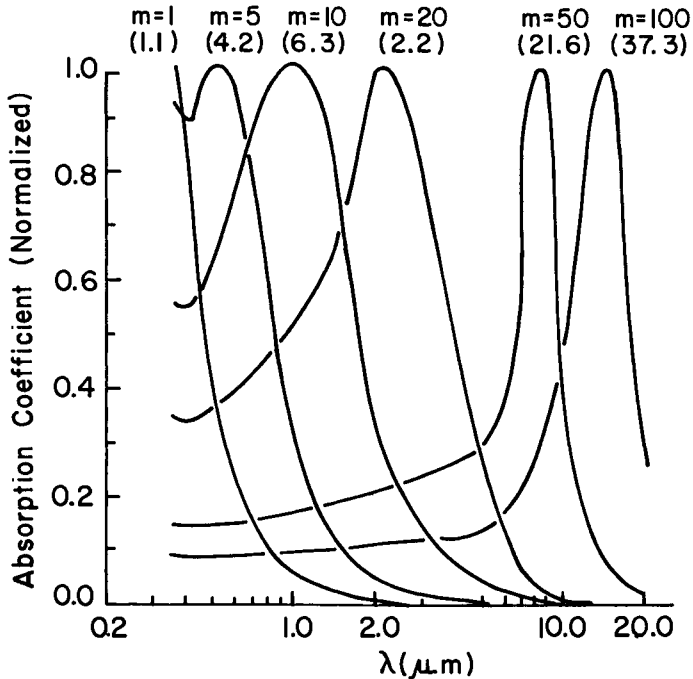
FIGURE 6. Normalized absorption coefficient $\alpha(m,\lambda)$ as a function of m factor and wavelength for particulate nickel.

The applicability of the Spheroid Model to various particu-
late media has been previously shown (7,26) and can be seen in
Figs. 8 and 9. Figure 8 gives the correspondence between
Spheroid Model calculations for the transmittance of an inert
gas evaporated particulate chromium black and experiment. The
particle shape distribution for the black has been defined as
log-normal (26) with thickness and packing fraction measured.
Figure 9 gives the correspondence between Spheroid Model calcu-
lations for the reflectance of electrodeposited black chrome and
experiment (7). The particulate structure used in the calcula-
tions was determined by scanning electron microscopy (SEM) and
X-ray photoemission spectroscopy (XPS) and principally involves
one to several layers of ~ 1000 Å chromium particles on the
substrate. The good agreements in Figs. 8 and 9 between
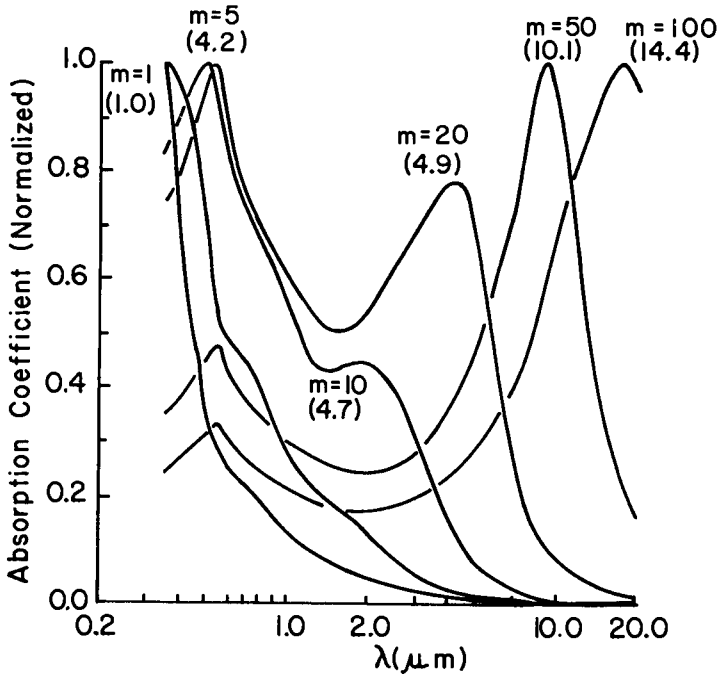
*FIGURE 7. Normalized absorption coefficient α(m,λ) as a
function of m factor and wavelength for particulate chromium.*

calculations and experiments indicate direct applicability of
the Spheroid Model to the analysis of the optical response of
particulates.

IV.   OPTICAL TAILORING

Reexamination of Figs. 6 and 7 reveals that the absorption
coefficients $\alpha(m,\lambda)$ are peaked with peak positions and intensi-
ties very strongly dependent not only on wavelength, but on
spheroid shape (m factor). The wide spectral range of the
absorption peaks resulting from the shape dependence (m depen-
dence) clearly indicates the possibility that almost any spectral
response can be obtained for a particulate absorber through a
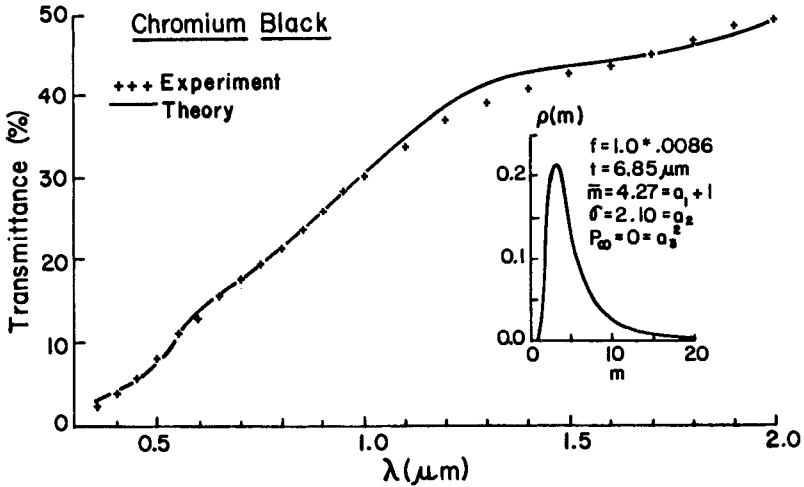
FIGURE 8. Comparison of transmittance from Spheroid Model calculations and experiment for a particulate inert gas evaporated chromium black.

judicious choice of particle shapes comprising the material.
That is, the optical properties of a particulate medium can be
manipulated through the choice of a specific particle shape
distribution, i.e., modification of the microscopic structure
of the particulate.

Modification of the optical response of a material has been
long sought after and has at best been only achieved through
interference effects due to the application of antireflection
coatings to optical systems. Figure 1 indicates that additional
methods for altering optical response could include electron
density modification and band structure modification. Except
for semiconductors, these possibilities have not proven very
successful (27) and it is of interest to see if modification of
the microscopic structure of a particulate could result in the
manipulation of its optical properties.
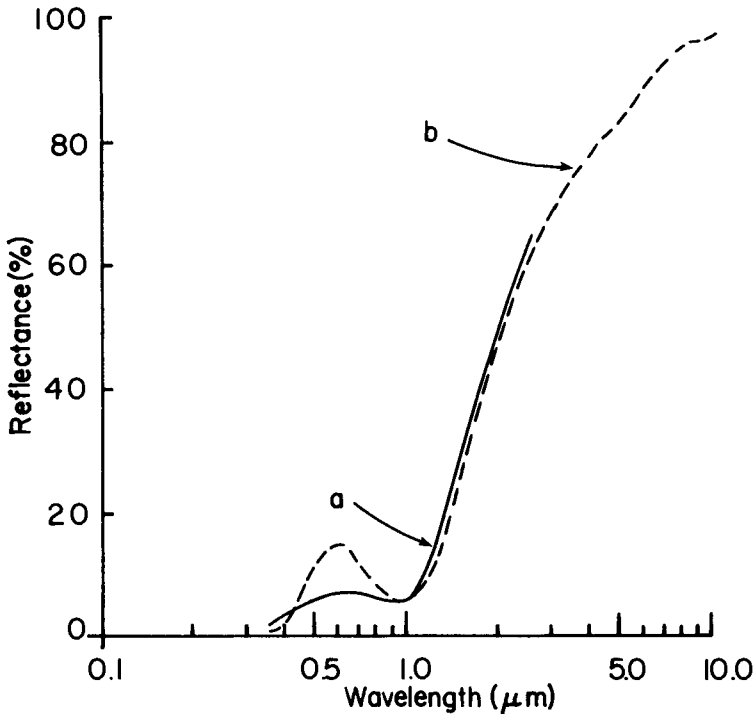
FIGURE 9. Comparison of hemispherical reflectance from Spheroid Model calculations (b) and experiment (a) for a particulate electrodeposited black chrome film.

To investigate this point, the Spheroid Model has been used in a procedure aimed to modify the absorptance of a particulate film to approach that of the optimal solar selective step function absorptance. The procedure minimizes the difference between the absorptance of the film and the solar selective step function absorptance by varying the particle shape distribution in the film. The step function is set at 3 μm for operation of the absorber at a nominal 120°C. The step function cannot be a sharp step as depicted in most previous literature, but must be sigmoid shaped due to the fact that thermal broadening of the absorptance profile will exist (28) (Figure 10).

SOLAR SELECTIVE STEP FUNCTION

(Thermally Broadened 393°k)
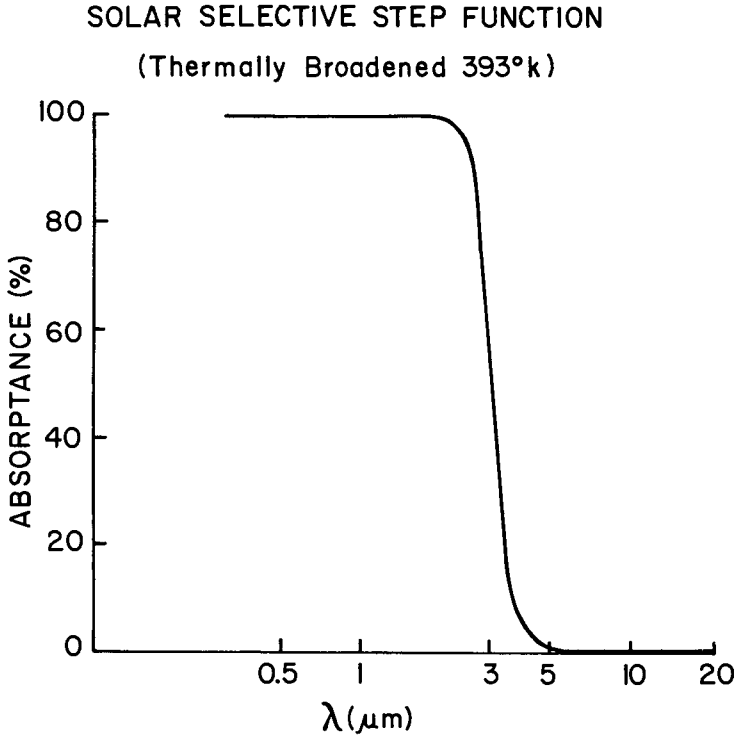
FIGURE 10. *Optimal solar selective step function response for the absorptance of a material. The step is thermally broadened due to the finite temperature of operation of the absorber (120°C in this example) of each Gaussian.*

A least square approach was taken for the minimization pro-
cedure where J was minimized in the expression involving the
absorptance $A(\lambda)$:

$$J = \sum_{\lambda} \left[A(\lambda)_{IDEAL} - A(\lambda)_{CALC} \right]^2. \tag{15}$$

Under the assumption of a perfectly reflecting substrate for the
absorbing film

$$A = 1 - T^2. \tag{16}$$

Therefore, the following J was minimized by the optimization of a particle distribution ρ(m) in the film.

$$J = \sum_{\lambda} \left[(1 - T^2_{IDEAL}) - (1 - T^2_{CALC}) \right]^2 \tag{17}$$

For simplification of the minimization procedure and since it is not clear whether the $\alpha(m,\lambda)$'s are linearly independent for each m, three Gaussians were used to depict the particle distribution instead of a histogram element for each m value present in the distribution. The first Gaussian was centered at m = 1, the third at m = cutoff value with no intensity above the cutoff. The cutoff value of m for each material studied (gold, nickel, and chromium) was arbitrarily defined as the largest m for which the absorption coefficient at 3 μm (the step position in the absorptance) was 10% of its peak value. The second Gaussian was centered between the first and third with the standard deviation σ of the Gaussians defined such that under the condition of equal intensities, the Gaussians would overlap at half their peak values.

The particulate films modeled were composed of small particles of either gold, nickel, or chromium imbedded in air with packing fractions of 0.06. The thicknesses of the films were defined in the absorptance optimization procedure by the conservation of particles criterion:

$$\sum_{m} \rho(m) \Delta m = 1 \tag{18}$$

and the absorptance was optimized to approach the solar selective thermally broadened step function by varying the intensities of the three Gaussians.

Figure 11 gives the results of the optimization. It is seen that absorptances approaching the step function response are obtained and that the particle shape distributions required for
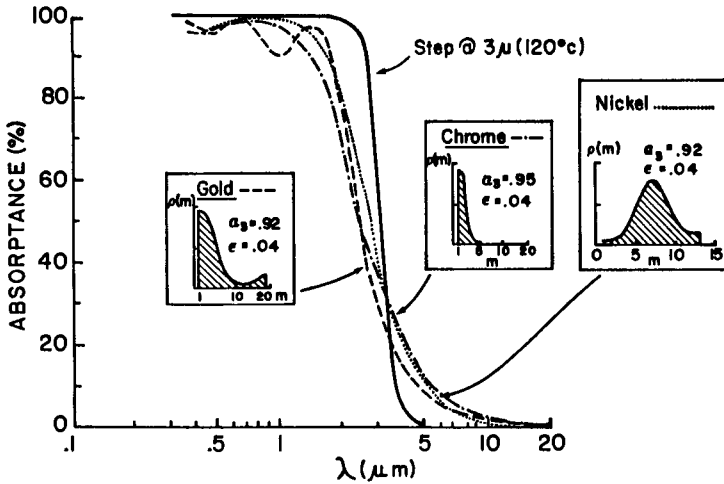
FIGURE 11.   Optimized selective absorptance of particulate
gold, nickel, and chromium films obtained by varying particle
shape distributions.

the three metals are quite different. This latter point is
principally due to the differences in interband and free electron
absorption in the three materials. As can be noted, solar ab-
sorptances of 0.92 to 0.95 (AMII) are realized with infrared
emittances of ~ 0.04 obtained. The solar absorptance values
though not extremely high, are significantly higher than the 0.6
to 0.7 values for equivalent density *non-particulate metallic*
films. It is not clear from this exercise that solar selectivity
can be induced in a material by the modification of its micro-
scopic structure.

V. CONCLUSIONS

    In conclusion, the main points resulting from the above noted
work are that a) through effective medium theory it has been
clearly shown that the optical response of solar absorbers is
strongly dependent on the microscopic structure of the absorber;

and b) that as a result of a), optical tailoring of a material could be accomplished through the manipulation of its microscopic structure.

As to how the manipulation of microstructure is to be accomplished on the required ~ 1000 Å size scale is currently being studied. Electrodeposition, surface damage by ions or other projectiles, and evaporation are being considered as possible techniques which may yield the required particle distributions. If such distribution modification can be generated, it will still be left to see how thermally and photothermally stable such particulate coatings are. This brings up the final point which is that the current understanding of a material's response to concentrated solar radiation is wanting. Since energy materials research is in its very infancy, it is clear that there is still much to be done in this research area before our base of understanding will be expanded to the point where systematic development of new energy materials can be undertaken.

ACKNOWLEDGMENTS

REFERENCES

1. Harris, L., "The Optical Properties of Metal and Carbon Black", (Epply Foundation, 1967).

2. Pfund, A.H., *J. Opt. Soc. Am., 23,* 275 (1933).

3. Window, B., Ritchie, I., and Gathro, K., *Applied Optics, 17,* 2637 (1978).

4. Grandqvist, C.G., and Hunderi, O., *J. Appl. Phys., 50,* (1978).

5. Inal, O.T., and Torma, A.E., *Thin Sol. Films, 54,* 161 (1978).

6. Pettit, R.B., and Sowell, R.R., *J. Vac. Sci. Technol., 13,* 596 (1976).

7. Ignatiev, A., O'Neill, P., and Zajac, G., *Sol. Energy Mat., 1,* 69 (1979).

8. Doland, C., O'Neill, P., and Ignatiev, A., *J. Vac. Sci. Technol., 14,* 259 (1977).

9. Sievers, A.J., in "Solar Energy Conversion: Topics in Applied Physics", Seraphin, B.O. (ed), 31, 57, (1979).

10. Craighead, H.G., and Buhrman, R.A., *J. Vac. Sci. Technol., 15,* 269 (1978).

11. Lampert, C.M., and Washburn, J., *Sol. Energy Mat., 1,* 81 (1979).

12. Smith, G.B., *J. Phy. D., 10,* 139 (1977).

13. Wood, D.M., and Ashcroft, N.W., *Phil. Mag., 35,* 269 (1977).

14. Bruggman, D.A.G., *Ann. Phys. (Leipz.), 24,* 636 (1935).

15. Hunderi, O., *Phys. Rev. B, 7,* 3419 (1973).

16. Maxwell Garnett J.C., *Philos. Trans. Roy. Soc. Long., 203,* 385 (1904), *205,* 237 (1906).

17. Stratton, J.A., "Electromagnetic Theory", McGraw-Hill, New York, Chap. 3, (1941).

18. Smith, G.B., *Appl. Phys. Letters,* (1980).

19. Ignatiev, A., O'Neill, P., Doland, C., and Zajac, G., *Appl. Phys. Letters, 34,* 42 (1979).

20. Zajac, G., and Ignatiev, A., *J. Vac. Sci. Technol., 16,* 233 (1979).

21. Zajac, G., Doland, C., and Ignatiev, A., (to be published).

22. Pettit, R.B., and Sowell, R.R., Proc. 2nd Conf. on Absorber Surfaces for Solar Receivers, (SERI, Boulder, 1979).

23. Norrman, S., Anderson, T., and Grandqvist, C.G., *Phys. Rev. B, 18,* 674 (1978).

24. Zajac, G., and Ignatiev, A., *Sol. Mat.,* (1980).

25. Grandqvist, C.G., *J. Appl. Phys.,* (1979).

26. O'Neill, P., and Ignatiev, A., *Phys. Rev. B, 18,* 6540 (1978).

27. Enrenreigh, H., and Seraphin, B.O., Report on Symp. on
    Fundamental Optical Properties of Solids Relevant to Solar
    Energy Conversion, (Tucson, 1975).

28. Sievers, A.J., Proc. 25th Jubilee ISES, (Atlanta, 1979).

CHAPTER 5

SOLAR MIRROR MATERIALS: THEIR PROPERTIES AND
USES IN SOLAR CONCENTRATING COLLECTORS[1]

R.B. Pettit
E.P. Roth

Sandia Laboratories[2]
Albuquerque, New Mexico

I. INTRODUCTION

    Solar mirror materials are used in a variety of solar collec-
tors in order to redirect the incident sunlight onto a receiver
surface. Applications range from augmented flat plate collectors
to high concentration tracking parabolic dish concentrators (1).
The primary advantage in using solar mirrors to concentrate sun-
light is either to increase the system efficiency (e.g. by re-
ducing thermal losses) or to reduce the system cost where rela-
tively expensive receiver materials are utilized (e.g. photo-
voltaic cells). In most applications, the total mirror surface
area deployed is large; thus the mirrors must be manufactured at
a relatively low cost. Because of the variety of solar applica-
tions, the optical requirements of solar mirrors vary greatly.
All applications are sensitive to the solar averaged reflectance
properties, R_s, which should be as close to unity as possible.
However, the requirements on the distribution of the reflected
sunlight (defined as specularity) can span a wide range from
very diffuse all the way to highly specular depending upon the

171

application. Because of these variations in the required op-
tical properties, it is important that optical characterization
of solar mirrors be consistent with the intended application.

    Because all mirror materials must be supported or held in
a particular orientation with respect to the receiver, the
effect of the supporting structure on the reflected beam loca-
tion (focal point) must also be carefully considered. The
shape of the mirror surface can be either flat as in a helio-
stat, curved with one dimensional curvature as in a parabolic
trough, or with two dimensional curvature as in a parabolic
dish. Any change in the reflectance properties of the material
due to manufacturing, processing, or forming to the desired
shape must also be determined.

    In addition to the reflectance properties, there are many
other important properties of mirrors when used in solar con-
centrators. Of primary importance is the environmental
stability of the material. This includes resistance to ultra-
violet radiation, moisture, temperature cycling, abrasion,
etc. Another important factor is the resistance of the mirror
and support structure to hail impact unless special storage
configurations have been designed (2). The accumulation of
dust particles and other particulates on the mirror surface
can drastically change the reflectance properties; details of
this subject are covered in the next paper in this text. Other
properties of importance include the mirror cost, mechanical
properties, manufacturing tolerances, etc.

    The purpose of this paper is to review the current state of
mirror materials with application to solar concentrators. After
specular reflectance is defined, the optical measurement tech-
niques developed specifically for these materials are discussed.
Next, the solar reflectance properties of mirror materials,
divided into categories of glass, metallized plastics, polished

aluminum, and protective coatings, are summarized. Finally,
current problem areas and future areas of research are discussed.

II.   OPTICAL MEASUREMENTS

Loss of redirected sunlight from a solar mirror can result
from surface contour variations (sometimes called slope errors)
and from scattering due to the mirror material (3). Both effects
are due to surface irregularities at the mirror surface. For the
purposes of this paper, scattering from surface variations with a
characteristic spacing less than approximately 1 mm will be re-
ferred to as the surface "specularity" (sometimes referred to as
specular reflectance properties). On the other hand, the effect
of the surface contour variations on a scale greater than approxi-
mately 10 mm will be referred to as the surface "figure." Contour
variations typically result from local deviations in the surface
normal about the ideal surface shape (see Fig. 1). Thus the sur-
face figure determines the direction of the reflected radiation
while the surface specularity determines the angular spread and
intensity of this radiation.

Because of the large difference between the scales of these
surface variations, two separate and distinct measurement tech-
niques have been used for their determination. Currently a laser
ray trace technique is used for the surface figure measurements
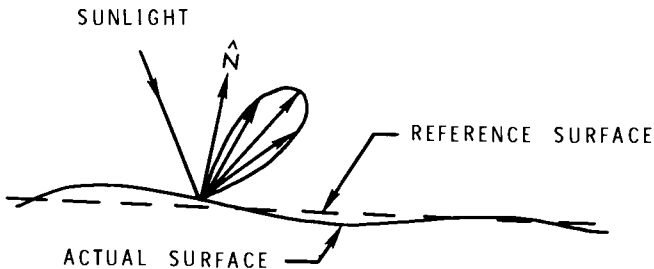
FIGURE 1.   Schematic representation of a mirror surface
showing the difference between slope errors and the mirror
specularity.

while a bidirectional reflectometer is used to measure the specu-
larity (3,4). The overall quality of the particular reflector
surface is obtained by combining these two results.

A measurement of the surface specularity is determined by
irradiating a small area of a flat mirror with a collimated beam
of light and measuring the amount of energy reflected into a
specified solid angle (angular aperture) centered around the
specular beam direction (4). The area irradiated depends upon the
characteristics of the instrumentation, but is typically 1-5 cm^2.
Surface variations with a scale in the range 1-10 mm may affect
either the surface figure or the surface specularity or both
depending upon the details of the measurement technique utilized.
Therefore, care must be exercised when surface irregularities
within this range are present. For curved surfaces (e.g. para-
bolic troughs), any effect of the surface curvature must be
removed from the specularity measurements. Because of these
problems, current measurement techniques used for surface specu-
larity and figure determinations may need additional refinement
either in the type of instrumentation or data analysis procedures
used.

Besides the specularity, another optical quantity of interest
is the hemispherical reflectance (5), which measures all of the
reflected radiation from a surface independently of its angular
distribution. This measurement is typically performed as a func-
tion of wavelength from 350-2500 nm using an integrating sphere
reflectometer (6) (see Fig. 2). These instruments are commer-
cially available (7). A solar averaged reflectance value for a
mirror is usually determined by averaging the spectral hemispher-
ical reflectance data (8), since these data cover the complete
solar spectrum. This value represents the maximum available re-
flected solar energy for a particular mirror; however, depending
on the angular distribution of this radiation, only a portion of
this reflected radiation may be utilized in a solar collector.
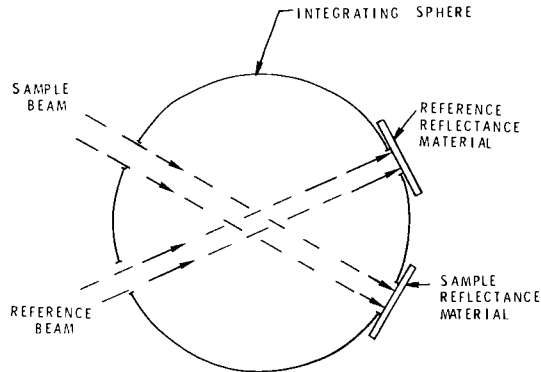
FIGURE 2. Typical double-beam integrating sphere reflec-tometer with wall mounted sample and reference reflectance materials.

   The diffuse reflectance is another quantity that can be meas-ured using an integrating sphere reflectometer. For this measure-ment, the mirror is typically aligned normal to the incident radia-tion in the integrating sphere so that a portion of the normally reflected radiation passes back out the entrance aperture (see Fig. 2) (9). The angular size of this aperture as seen by the sample is usually very large (approximately 5-10°). By subtracting the diffuse reflectance from the hemispherical reflectance, an indi-cation of the specular reflectance properties can be obtained but with very poorly defined incident and collection solid angles.

   The specularity properties of a solar mirror material are measured using a bidirectional reflectometer. Since these instru-ments are not available commercially, several different designs have been built (4,10-13). A schematic of a typical instrument is shown in Fig. 3. The instrument consists of source optics and detection optics. The source optics produce a collimated beam of radiation which is reflected off the mirror and directed into the detection optics. The source beam is typically collimated to a few milliradians (mrad) or to a value that is equal to the angular size of the sun ($\sim$ 10 mrad). The degree of collimation is determined by the size of the source aperture divided by the focal
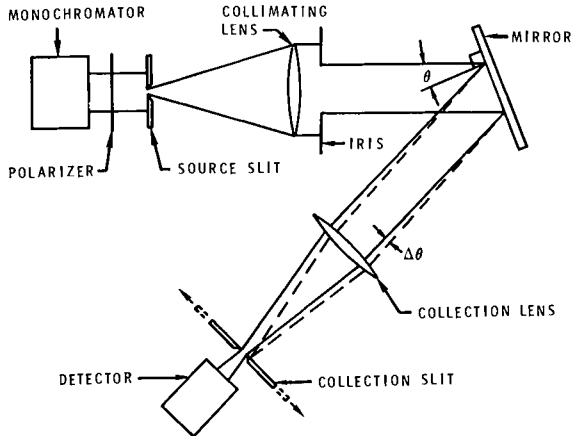
*FIGURE 3. Schematic of a typical bidirectional reflecto-
meter showing the collimation and collection optics.*

length of the collimation lens. The reflected beam is imaged onto
either a circular or slit collection aperture. For a perfectly
specular mirror, all of the reflected radiation is imaged onto the
collection aperture. Reflected radiation that deviates from the
specular direction is imaged adjacent to the collection aperture.
The reflected beam intensity profile is then recorded in one of two
ways: First, the collection aperture size can be increased,
starting at the same size as the source aperture, so that an inte-
gration of the reflected beam profile is recorded. Alternatively,
a fixed collection aperture (whose size is the same as the source
aperture) can be swept through the focused beam so that the re-
flected beam profile is recorded directly. For either technique,
the instrument is usually calibrated by aligning the collection and
source optics to measure a straight-through beam, although standard
mirrors can also be used for calibration. The accuracy of present
instruments is typically $\pm$ 0.01 reflectance units (100% reflectance
= 1.00 reflectance units). The wavelength range covered by the re-
flectometer is determined either by the light source (e.g. laser),
by a monochromator or filters to define a narrow wavelength region,
or by the source optics and detector spectral response characteris-
tics (usually broad band).

Results obtained in this laboratory are shown in Fig. 4 for
silvered float glass (2.7 mm thick), a roll polished aluminum sheet
(Alzak, 0.64 mm thick), and aluminized teflon and acrylic (3M
Scotchcal 5400) films laminated to an aluminum backing sheet.
For these measurements the incident beam was collimated to 1 mrad
and the collection aperture was varied from 1 mrad to 18 mrad.
Note that while the glass and plastic materials reach an approxi-
mately constant reflectance value at an angular aperture of 10 mrad,
the specular reflectance curves for the polished aluminum continue
to increase at the maximum angular aperture of 18 mrad. The hemi-
spherical reflectance values for these materials measured at the
same wavelength of 500 nm are also shown in Fig. 4. Note that at
18 mrad, the specular reflectance values for the silvered glass and
aluminized acrylic mirrors are equal to the hemispherical reflec-
tance values; however the specular reflectance values for the
aluminized teflon and polished aluminum mirrors at 18 mrad are from
0.05 to 0.17 reflectance units below their respective hemispherical
reflectance values even though the reflectance profile for the
aluminized teflon mirror appears to have reached a plateau or con-
stant value. The difference between the specular and hemispherical

MATERIAL	$R_\lambda(2\pi)$	R(18 mrad)	$R_s(2\pi)$
1	SILVERED GLASS	0.92	0.92	0.83
2	ALZAK - PARALLEL	0.89	0.78	0.85
3	ALZAK - PERPENDICULAR	0.89	0.72	
4	SHELDAHL ALUMINIZED TEFLON	0.87	0.82	0.87
5	3 M SCOTCHCAL 5400	0.86	0.85	0.85
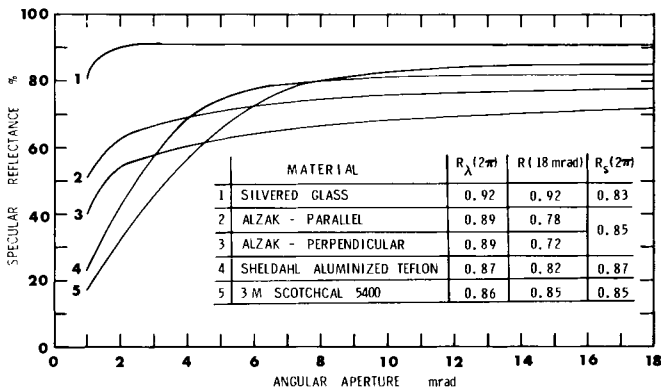
*FIGURE 4. Specular reflectance properties for several solar
mirror materials. The table lists the hemispherical reflectance
$[R_\lambda(2\pi)]$ and the specular reflectance at 18 mrad [R(18 mrad)]
measured at 500 nm. Also listed is the solar averaged hemi-
spherical reflectance $[R_s(2\pi)]$.*

reflectance values is due to large angle scattering at the mirror surface. The reflectance profiles for these materials illustrate the importance of measuring both the specular reflectance and hemispherical reflectance properties at the same wavelengths for all mirror materials.

While the curves shown in Fig. 4 contain all of the information needed to properly compare the different materials, a data analysis procedure has been developed which reduces these curves to a form more easily utilized in collector performance calculations. For this analysis it is assumed that the mirror will scatter the reflected radiation into angles centered aroung the specular direction according to a normal distribution of the form

$$R(\Delta\theta) \ = \ \frac{R_o}{2\pi\sigma^2} \ \exp\left[\frac{-\Delta\theta^2}{2\sigma^2}\right] \tag{1}$$

where $\Delta\theta$ is the deviation of the reflected beam from the specular direction, σ is the dispersion of the distribution, and R_o is the integrated intensity. Since the specular reflectance properties shown in Fig. 4 represent the integration of this distribution as a function of angular aperture, the integration, when carried to large angles, must approach the hemispherical reflectance value. Therefore R_o in Eq. (1) is usually set equal to the hemispherical reflectance value, R_λ (2π), measured at the same wavelength. The specular beam profile measured using a particular bidirectional reflectometer is given by the convolution of the source aperture intensity distribution with the normal distribution of the mirror scattering function. By integrating this profile as a function of the angular collection aperture and comparing the results with the measured curve, a best-fit value for σ (and R_o if it is also varied) can be obtained. Typical results are shown in Fig. 5a for the aluminized acrylic mirror. In this case R_o was set equal to the hemispherical reflectance value of 0.86 measured at 500 nm. Note that although
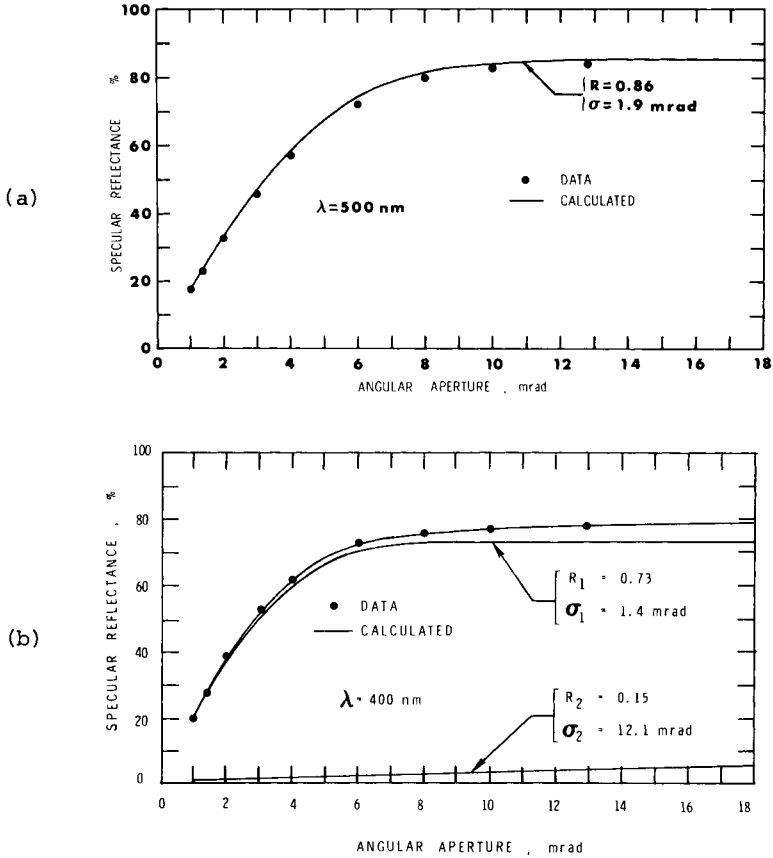
FIGURE 5a. *Comparison between the analytical fit and measured reflectance values for (a) an aluminized acrylic film (3M Scotchcal 5400) at 500 nm using a single normal distribution, and (b) for an aluminized teflon film (Sheldahl, Inc.) at 400 nm using two normal distributions.*

the calculated curve does not reproduce the measured data exactly, it is within the measurement error of $\pm$ 0.01 reflectance units at each angular aperture.

The reflected beam profile for some of the solar mirror materials investigated could not be described by a single normal distribution. For these materials the specular beam appeared to be composed of a sharp central peak together with a broad, diffuse background (see Alzak in Fig. 4). In this case, it was

assumed that the reflected beam is composed of the sum of two
normal distributions. Thus the specular reflectance is given by

$$R(\Delta\theta) = \frac{R_1}{2\pi\sigma_1^2} \exp\left[\frac{-\Delta\theta^2}{2\sigma_1^2}\right] + \frac{R_2}{2\pi\sigma_2^2} \exp\left[\frac{-\Delta\theta^2}{2\sigma_2^2}\right] \tag{2}$$

The division of the reflected beam into distinct components
appears to be a reasonable assumption since areas of the mirror
may be relatively smooth and flat (highly specular component)
while other areas have scratches, bumps, etc. which can cause
large angle scattering (diffuse component). With the assumption
of two normal distributions, four parameters are necessary to
specify the specular reflectance: (R_1, σ_1) and (R_2, σ_2).
The constraint that the sum $(R_1 + R_2)$ should equal the hemi-
spherical reflectance value at the same wavelength is usually
employed, although this constraint can be relaxed so that all
four parameters are varied independently. An example of the
curve fitting results is shown in Fig. 5b for an aluminized
teflon film. The parameters obtained at 400 nm were $R_1 = 0.73$,
$\sigma_1 = 1.4$ mrad and $R_2 = 0.15$, $\sigma_2 = 12.1$ mrad $[(R_1 + R_2) =$
$R_\lambda(2\pi) = 0.88]$.

It should be noted that the agreement found between the
measured curve using the assumption of two normal distributions
for the specular beam does not imply that there are only two
scattering mechanisms associated with these materials. In fact
there are probably more. Therefore without further verification,
the parameters (R_1, σ_1) and (R_2, σ_2) cannot be used to define
the surface structure of these materials, but only the specularly
reflected beam profile over the range covered by the measurements.
If the reflectance measurements are obtained for angular apertures
which range from the incident beam width up to 2π radians
(hemisphere), the assumption of two normal distributions may not
be adequate. However, for measurements obtained in this labora-
tory, the specular beam profile for a wide variety of solar mirror

materials could be characterized by either Eq. (1) or Eq. (2)
over the range covered by the measurements (18 mrad in this case).

It should also be pointed out that for some materials the
specular reflectance values are not very sensitive to small
changes in the calculated parameters, R_1, σ_1 and R_2, σ_2.
This is especially true if one distribution R value is small and
its corresponding σ value is large. Therefore no real signifi-
cance should be attached to the calculated parameters in terms of
the surface characteristics of each material or to small changes
in these parameters with wavelength.

There are many advantages to the data analysis procedure out-
lined above. These include: 1) The results are not dependent on
the measurement characteristics of the bidirectional reflectometer,
2) scattering profiles down to approximately 0.2 mrad can be de-
termined even though the incident beam is collimated to only 1.0
mrad, 3) the results can be easily related to other beam spreading
errors such as tracking errors, slope errors, etc, and 4) the re-
sults are in the proper form for ray-trace computer programs (14).

The reflected beam profile that would be measured by sweeping
a fixed collection aperture through the focused beam is plotted in
Fig. 6 for an aluminized teflon mirror at 400 nm. Note that the
ratio of the reflected beam intensity of the two normal distribu-
tions at $\Delta\theta = 0$ is 320 to 1 while the ratio of the beam inten-
sity at $\Delta\theta = 0$ and $\Delta\theta = 14$ mrad is almost 1000 to 1. These
large ratios illustrate an advantage in measuring the integral of
the specular reflectance curve by increasing the collection aper-
ture as opposed to sweeping the small aperture through the focal
plane and measuring the reflected beam profile directly.

The bidirectional reflectometers used for solar applications
incorporate either a slit aperture system or a circular aperture
system. There are two advantages in a slit aperture system: 1)
Using a slit aperture, asymmetrical distributions can be determined
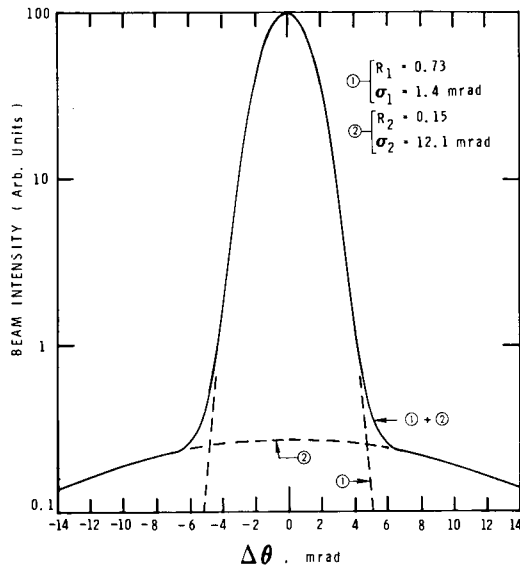
FIGURE 6.   The reflected beam profile for an aluminized teflon film (Sheldahl, Inc.) at 400 nm as a function of angular aperture (compare with Fig. 5b).

(e.g. Alzak). 2) Because the area of a slit can be made much larger than the area of a circular aperture which has the same width, there is more intensity in the slit aperture instrument. The specification of a "standard" measurement technique for specularity determinations is currently being considered by the American Society of Testing Materials (ASTM).

Recently, portable bidirectional reflectometers have been developed for use in the field (15). These instruments are not as versatile as the laboratory instruments, but are designed primarily to determine changes in the specular reflectance due to dust accumulation after outdoor exposure. By comparison with standard samples, the specular reflectance changes for a fixed collection aperture can be determined before and after cleaning.

III. EFFECTIVE SUNSHAPES

A calculation of the amount of solar radiation that is inci-
dent on a receiver surface as a function of the mirror specularity
can be illustrated with a simple example. Consider two mirror ma-
terials which have the following optical properties: Material A
-- R_s = 0.80, σ_A = 1.0 mrad and Material B -- R_s = 0.95, σ_B =
4.0 mrad. Thus Material A has a smaller dispersion (i.e., more
specular) than Material B but it also has a lower solar reflec-
tance value (see Fig. 7a). For simplicity we will assume that the
incident sunshape (i.e., the angular distribution of rays from the
sun) can be approximated by a normal distribution with a dispersion
σ_{SUN} = 3.5 mrad, which is characteristic of a "clear" day [14].
The angular distribution of solar rays after reflection from each
mirror, or the effective sunshape, is given by the convolution of
the incident sunshape with the reflected beam profile of each mir-
ror. In this case, the convolution of the incident sunshape and
the reflected beam profile gives another normal distribution
(effective sunshape) whose dispersion is given by the following
equation

$$\sigma_{A,B}(\text{effective}) = \left[\sigma^2_{SUN} + \sigma^2_{A,B}\right]^{\frac{1}{2}} \tag{3}$$

which gives $\sigma_A(\text{effective})$ = 3.64 mrad and $\sigma_B(\text{effective})$ = 5.32
mrad. The integral of these effective sunshapes together with the
integral of the incident sunshape are shown in Fig. 7b as a func-
tion of the angular acceptance aperture. Note that even for a per-
fect mirror (R_s = 1.0, σ = 0), 95% of the incident solar radiation
is not obtained until the angular size of the receiver is approx-
imately 8.6 mrad. For receiver angular sizes below approximately
10 mrad, Material A reflects more of the sun's energy onto the re-
ceiver; for larger receivers, mirror Material B delivers more re-
flected sunlight onto the receiver. For a complete calculation,
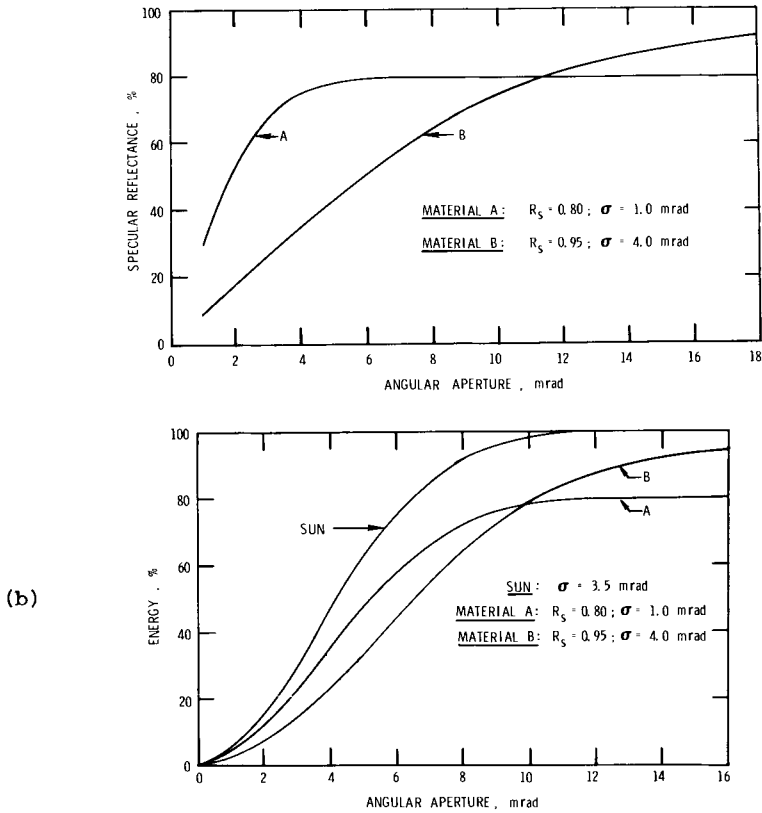
FIGURE 7. (a) Specular reflectance as a function of angular aperture for two hypothetical mirror materials A and B. (b) The integrated energy as a function of angular aperture for the assumed incident sunshape (σ = 3.5 mrad) and the effective sunshape after reflecting from mirrors A and B.

other beam spreading errors must be considered as well as the detailed shape of the incident sunlight.

IV.   REFLECTANCE PROPERTIES OF VARIOUS MATERIALS

Of all of the metals that could be used for solar reflectors, only silver and aluminum have solar reflectance values above 0.90. All other metals, including gold, nickel, chromium, stain-less steel, rhodium, and copper, have lower solar reflectance

values. The spectral reflectance properties of silver and alu-
minum, together with gold, measured for the metal/vacuum inter-
face are shown in Fig. 8. The solar averaged reflectance values
are calculated to be: silver -- 0.98, aluminum -- 0.92 and gold
-- 0.85. These values represent the practical upper limit of
solar reflectance for these materials. The reflectance of alu-
minum is reduced over the solar region primarily due to an inter-
band absorption centered at approximately 800 nm. It has been
suggested that this absorption band may be eliminated by using
amorphous aluminum; this would increase the solar reflectance
several percent (16). In almost all solar applications, the
metal reflecting layer is protected by a transparent coating
such as an oxide (e.g., Al_2O_3), glass, plastic film, etc. The
index of refraction of most coating materials is typically 1.5
through the solar spectral region. With a nonabsorbing dielec-
tric layer applied over the metals, the solar average reflectance
is reduced by 0.01 reflectance units for silver, 0.03 for gold,
and 0.04 for aluminum (see Fig. 8). Thus, in most applications,
silver mirrors will have at most a solar reflectance of 0.97,
while the solar reflectance of aluminum will be closer to 0.88.
Very little effort is currently applied to using gold mirrors,

	VACUUM	DIELECTRIC
Ag	0.98	0.97
Al	0.92	0.88
Au	0.85	0.82

REFLECTANCE
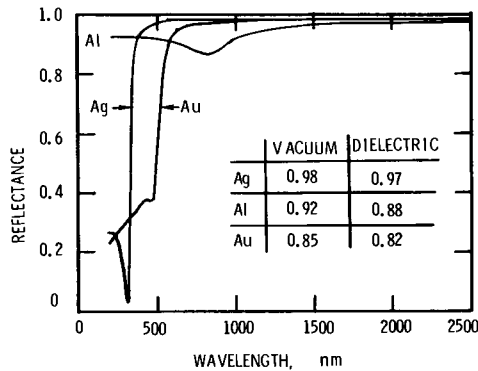
WAVELENGTH,   nm

FIGURE 8. Reflectance properties of silver (Ag), aluminum
(Al), and gold (Au) as a function of wavelength for the metal/
vacuum interface. The table lists the solar averaged reflec-
tance for a metal/vacuum interface and a metal/dielectric
interface with an assumed index of refraction of 1.5.

although it has been suggested that in certain photovoltaic
applications, gold mirrors offer some advantages (17).

    In order to understand the specularity and the reflected
beam intensity of various mirror materials, it is instructive to
consider the construction of a typical reflector. The typical
construction of both a front-surface and second-surface reflector
is shown in Fig. 9. In a front-surface mirror, the reflecting
layer is applied to the substrate and then overcoated with a pro-
tective coating. In a second-surface mirror, the reflecting
layer is applied to a transparent superstrate (e.g. glass, plas-
tic film) which is then bonded to a support structure. Also
shown in Fig. 9 is an adhesive layer and back protection layer
as well as the supporting structure. The entire composite shown
in Fig. 9 is termed a "reflector," while the outer layers which
include the silver or aluminum film are termed the "mirror".

    Both the specularity and the reflected beam intensity can be
affected by all of the components shown in Fig. 9. Depending upon
its optical properties, the outer protective layer can modify the
reflected beam intensity at the metal/dielectric interface as pre-
viously shown. In addition the outer layer can absorb radiation
and thereby reduce the solar reflectance. The specularity can be
affected by scattering within this layer or at the inner or outer
surfaces. If the outer surface is not parallel to the reflecting
surface, multiple reflected images are formed.

    The reflecting surface itself can scatter radiation if it has
a rough surface. In addition, the reflected beam intensity may
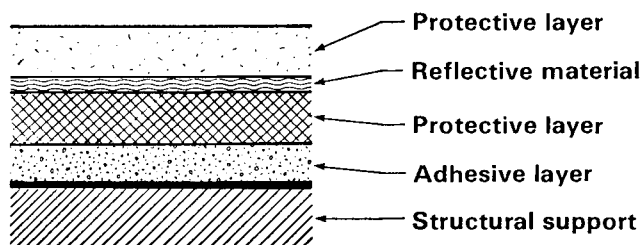
FIGURE 9.   The construction of a typical reflector structure.

depend upon the purity of the metal layer as well as the deposi-
tion process (vacuum evaporation, chemical reaction, ion plating,
etc.). The surface texture of the backing layer, which is typi-
cally a thin metal sheet, can be important in affecting the specu-
larity of the reflector, as well as the lamination or bonding
technique that is used to attach the reflecting surface to the
backing layer. The same is true for the bonding of the backing
layer to the support structure.

The different types of reflector materials can be conveniently
divided into four classes: 1) silvered glass, 2) metallized plas-
tic films, 3) polished aluminum sheet, and 4) protective coatings.
The typical hemispherical and specular reflectance properties and
the environmental characteristics of materials within these groups
are discussed below:

A. *Silvered Glass*

Glass is usually silvered using a commercial chemical process
that has been developed for the mirror industry (18). The solar
reflectance of the silver/glass interface is generally in the
range 0.95 to 0.97, which agrees with the previous calculations.
However, it has been suggested that vacuum evaporated silver may
have a slightly higher (~2%) solar reflectance than chemically
deposited silver. This remains to be demonstrated.

The solar reflectance values obtained for typical silvered
glass mirrors are usually less than the theoretical value of 0.97.
This results primarily from absorption within the glass due to im-
purities, mainly iron. Iron in the Fe^{+2} oxidation state has a
large absorption band centered at approximately 1000 nm (19). For
a typical 3 mm thick float glass with 0.1 weight percent iron con-
tent, the solar reflectance when chemically silvered will be ap-
proximately 0.83. Because of variations in the total amount of
iron within different glasses as well as the amount of this iron
that is in the Fe^{+2} oxidation state, the solar reflectance

properties of silvered glass mirrors from different glass manu-
facturers and for different types of glass (float, sheet, etc.)
must be determined individually.

The solar reflectance properties of silvered glass mirrors
can be improved above the value of 0.83 for 3 mm float glass
in four ways: 1) by reducing the amount of iron in the glass
(low iron glass), 2) by reducing the glass thickness (e.g.,
using microsheet glass which is approximately 0.1 mm thick),
3) by controlling the oxidation state of the iron so that it
is all in the Fe^{+3} state instead of the Fe^{+2} state, or 4) by
addition of chemicals to the glass which form a compound(s)
with the iron and thereby modify the optical absorption. All
of these procedures have been or are currently under study (20).

The specularity of glass mirrors is described by σ values
which are typically less than 0.5 mrad. However, surface slope
errors and thickness variations, which lead to multiple reflected
images, are a function of the glass manufacturing process; typi-
cally the surface slope deviations are less than a 2-3 mrad (21).

Environmentally, glass samples exposed for over 10 years out-
doors exhibit transmittance values that are typically within a 2-3
percent of the original values (21,22). Glass has good abrasion
resistance, which is important for both resistance to blowing dust
particles and mechanical abrasion resulting from cleaning, etc.
Since a meaningful abrasion test for solar mirrors has not been
developed, quantifying this property is not currently possible.

Recently, environmental protection of the chemically depos-
ited silver layer has become an important problem (23). Degrada-
tion of the silver, which appears as black spots or streaks, has
been found after approximately 6 months of outdoor exposure in
some locations for some mirror configurations. Both edge protec-
tion and back surface protection of the silver layer using edge
sealants and paints are currently being investigated. In addi-
tion, the corrosion products and mechanisms are being studied.

Corrosion of the glass surface after extended outdoor expo-
sure may be important, especially in the presence of moisture and
accumulated dust. Although there are some long term samples that
have exhibited little corrosion problems, new glass formulations
for solar applications and the use of glass in non-vertical
orientations may result in corrosion problems. Recent high humi-
dity accelerated testing of different types of glass has shown
significantly different corrosion characteristics, although
interpretation and application of the results to real outdoor en-
vironments remains to be shown (22). A compilation of mechanical,
optical and environmental properties of glasses for solar applica-
tions has recently been published by F. L. Bouquet (23).

B.   Metallized Plastics

There are several metallized plastic mirrors available for
solar applications (4). The reflecting aluminum or silver
layer is usually vacuum deposited. Hemispherical reflectance
values for silver materials are typically near 0.95 while
materials that use aluminum are typically near 0.87-0.85 in
agreement with the previously calculated values for a metal/
dielectric interface. Absorption within the plastic film,
which usually occurs in the near infrared region (greater than
1000 nm), can reduce the solar reflectance below these values.
However, since the films are usually thin (~0.1 mm), this
absorption reduces the reflectance by only a few percent.

The specularity of the reflected beam from the metallized
plastic films is primarily controlled by both the surface rough-
ness of the metallized side of the plastic film and the lamina-
tion procedure used to bond the film to the substrate. The
surface smoothness of a variety of plastic films (including
polyesters, fluorocarbons and polypropylene) have been measured
by Boeing (25). Factors important for the lamination procedure
include the adhesive thickness, adhesive application technique,

substrate roughness, curing temperatures, etc. (26). It is interesting to note that a commercially available aluminized plastic film with a pressure sensitive adhesive has a dispersion less than 1.0 mrad when bonded to a smooth metal substrate. This dispersion is much less than the dispersion of the incident sunlight.

Environmentally, plastics have less abrasion resistance than glass, but again a definitive abrasion test does not exist for solar applications. Unless special UV stabilizers are added, plastics can suffer from ultraviolet degradation which causes increased absorption, crazing or embrittlement. Long term data exist for some plastic materials after outdoor exposure; the results show only a few percent decrease in specular reflectance after two years (27). A recent review of the outdoor aging characteristics of plastic materials indicates that for the most part applicable data are not available (28).

C. Polished Aluminum

Polished aluminum mirror materials are generally protected by the application of an anodized film which is several microns thick. Solar average hemispherical reflectance values of 0.85 to 0.87 for these materials are typical of aluminum reflectors. Most of these materials are mechanically and chemically polished in order to increase their specularity; however, because aluminum is a soft metal, it is very difficult to remove all scratches and pits from the surface during the mechanical polishing. In addition, the anodizing process may introduce small scattering centers which decrease the specularity. Because of these surface defects, the specular reflectance for angular apertures in the range of 15 mrad are usually from 5 to 15 percent below the hemispherical reflectance values. Environmentally, these materials have good abrasion resistance and ultraviolet stability and have maintained their reflectance properties after extended outdoor exposure (27).

D. Protective Coatings

Protective coatings are being developed to improve the abra-
sion resistance of metallized plastic mirrors and offer the ad-
vantages of low cost, light weight, and improved optical perfor-
mance over currently available materials. Protective coatings
that are being considered for front surface mirrors are in an
exploratory stage of development (29). Several existing coatings
are listed in Table I; additional experimental data are needed
in order to determine if any of these materials are suitable for
solar mirrors.

V. INCIDENT ANGLE PROPERTIES

Measurements of the specular and hemispherical reflectance
properties of solar mirror materials as a function of incident
angle have recently been performed (30). In most applications

Table I. Some Commercially Available Protective Coatings

Manufacturer	Coating	Comments
3M Company	(Experimental)	Coating under development for application to FEK-244 acrylic film.
Dow Corning	Vestar	High silica coating; needs high temperature cure (>100°C).
Dupont	Lucite SAR	Abrasion resistant coating applied to acrylic sheet material.
General Electric	Alglas Reflector Finish	High silica coating for sheet aluminum; needs high temperature cure (~100°C).
Optical Coating Lab, Inc.	Type II-R Enhanced High Reflector	Multilayer protective coating for sheet aluminum.
Owens-Illinois	Glass Resin Type 650	Thermoset silicone coating for copper and aluminum.

the incident angle of solar radiation on the mirror will be no
greater than 45 to 50 degrees from normal. However, there are
some applications where the incident angle reaches more than 60°,
especially for non-tracking systems. As the incident angle is
increased, it is reasonable to expect that both the reflected
beam intensity and the reflected beam width may change. Measure-
ments of these properties for silvered glass and metallized
plastic films show that the solar averaged hemispherical reflec-
tance decreases less than 0.04 reflectance units at 65° from
normal (30). The reflectance values as a function of incident
angle for these materials could be accurately calculated using
a multiple beam reflectance model (30). The complex index of
refraction values of the outer protective coating and the metal
reflecting layer are needed for the calculations. For the metal
layer (either silver or aluminum) the optical constants can be
found in handbooks, while the optical constants of the outer
protective layer are easily determined from standard optical
measurements at normal incidence (31).

For a silvered glass sample, the specular beam profile does
not change with incident angle. However, the beam dispersion
for an aluminized acrylic film increased from 1.5 mrad to 1.8
mrad as the incident angle was varied to 65° from normal (30).

VI. CURRENT AND FUTURE RESEARCH AREAS

Optical measurement techniques have been developed so that
meaningful and reliable data on solar materials are currently
being obtained. The National Bureau of Standards is preparing
specular reflectance standards so the calibration of laboratory
instrumentation can be certified (32). There is a need to stan-
dardize the measurement instrumentation and data analysis; an
ASTM committee is presently active in this area.

There are currently a variety of commercial mirror materials, including silvered glass, metallized plastics and polished aluminum, that can be used in solar collectors. Although some new material development in the area of thin glass, low iron float glass and protective coatings is currently being pursued, the major effort in current research on solar mirrors involves the effect of outdoor aging on the optical properties. Testing has generally followed the pattern of exposing materials at various locations throughout the country and periodically returning the samples to the laboratory for measurements. Besides the standard 45° south exposure geometry, samples have been exposed to multi-sun environments through the use of tracking concentrators, in order to accelerate degradation processes. Handling of the sample deserves careful attention since surface scratches and stressing of the samples can adversely affect the optical properties. Samples exposed outdoors will have accumulated dust and pollutants on the outer surface which can strongly influence the specular reflectance properties. Recent studies have been directed toward characterizing the effect of dust accumulation on the specular reflectance properties of various mirrors. Areas of particular interest include determining dust accumulation rates, investigating effective mirror storage strategies (vertical or inverted) and defining cost effective cleaning intervals and procedures. For long term outdoor exposure studies, it can become very difficult to separate the effects of surface abrasion, dust accumulation, ultraviolet aging, surface crazing, or metal degradation since they can have similar effects on the reflectance property. Although limited data exist, some data are subject to misinterpretation due to improper sample handling, measurement technique limitations, or sample cleaning variations.

In addition to outdoor exposure testing, some accelerated laboratory testing has been used to help characterize different materials. These tests have included temperature and humidity cycling through a freeze-thaw cycle, constant temperature at high

relative humidity, weatherometer, ultraviolet lamp exposure at
room temperature or elevated temperatures, salt spray, various
abrasion tests, etc. Depending upon the material being studied,
the type of environment being simulated and the suspected aging
mechanism, these tests must be carefully chosen and correlated
with real time outdoor exposure results. Specific areas of cur-
rent investigation include degradation of the silver/copper
reflecting layer of chemically silvered glass mirrors (24),
improvement of the reflectance of aluminum by alloying with sil-
ver (16), long term effects of dust accumulation, cleaning fre-
quency and cleaning techniques, use of electrostatic coatings
to reduce dust accumulation and the development of accelerated
environmental tests. A detailed discussion of these areas is
contained in the solar reflector materials research and develop-
ment program plan recently published by the Solar Energy Research
Institute (20).

REFERENCES

1. Rabl, A., "Comparison of Solar Concentrators," *Solar Energy 18*,
    93 (1976).
2. Miller, D. W., "A Simulated Hail Test Facility," Sandia
    Labs Report SAND-79 1114 (June, 1979).†
3. Butler, B. L. and Pettit, R. B., "Optical Evaluation Tech-
    niques for Reflecting Solar Concentrators," SPIE Proceedings
    Optics Applied to Solar Energy Conversion 114, 43 (1977).
4. Pettit, R. B., "Characterization of the Reflected Beam Pro-
    file of Solar Mirror Materials," *Solar Energy 19*, 733 (1977).
5. Judd, D. B., "Terms, Definitions, and Symbols in Reflecto-
    metry," *J. Opt. Soc. Am. 57*, 445 (1967).
6. "Thermal Radiative Properties - Metallic Elements and Alloys,"
    Vol. 8, Thermophysical Properties of Matter, (Ed. by Y. S.
    Touloukian and D. P. DeWitt), pp. 32a-37a, Plenum, New York
    (1970).

7.   Commercial instruments are currently available from: (1)
     Beckman Inst., Scientific Inst. Div., 2500 Harbor Blvd., Ful-
     lerton, CA 92634. (2) Gier-Dunkle Inst., 1718 21st Street,
     Santa Monica, Monica, CA 90404. (3) Perkin-Elmer Corp., Inst.
     Div., Box 730, Main Avenue, Norwalk, CT 06856. (4) Varian
     Associates, Inst. Div., 9901 Paramount Blvd., Downey, CA 90240.
     (5) Carl Zeiss, Inc., 444 Fifth Ave., New York, NY 10018.

8.   Lind, M. A., Pettit, R. B., and Masterson, K. D., "The Sensi-
     tivity of Solar Transmittance, Reflectance and Absorptance
     to Selected Averaging Procedures and Solar Irradiance Distri-
     butions," to be published *J. Solar Energy Engineering*.

9.   Alternately, a small port in the sphere wall can be removed
     so that the normally reflected beam exits the sphere.

10. Lind, M. A., Hartman, J. S., and Hampton, H. L., "Specularity
     Measurements for Solar Materials," SPIE Proceedings Optics
     Applied to Solar Energy Conversion 161, 98 (1978).

11. Zentner, R. C., "Performance of Low Cost Solar Reflectors
     for Transmitting Sunlight to a Distant Collector," *Solar
     Energy 19,* 15 (1977).

12. Stickley, R. A., "Solar Power Array for the Concentration
     of Energy (SPACE), Semi-Annual Progress Report," NSF/RANN/
     SE/GI - 41019/PR/74/12, Sheldahl, Inc., Northfield, MN,
     Jan 1-June 30, 1974, pp. 156-159.

13. Sanchez, J., General Electric Co, Valley Forge Space Center,
     P. O. Box 8555, Philadelphia, PA 19101, private communication.

14. Biggs, F. and Vittitoe, C. N., "The Helios Model for the
     Optical Behavior of Reflecting Solar Concentrators," Sandia
     Labs Report SAND 76-0347, (March, 1979).

15. Freese, J. M., "The Development of a Portable Specular Reflec-
     tometer for Field Measurements of Solar Mirror Materials,"
     Sandia Labs Report SAND 78-1918 (Oct., 1978).†

16. Trotter, D. M., et al., "Enhanced Reflectivity Aluminum," in
     Proceedings of Solar Reflective Materials Technology Workshop,
     Battelle PNL Report PNL-2763, (Oct., 1978), p. 75.

17. Saylor, W. and Sanchez, J., "The Effect of Different Reflec-
    tor Surfaces on Photovoltaic Concentrator Performance," Pro-
    ceedings of 1979 Joint Meeting of American Section of
    ISES, May 28-June 1, 1979, Atlanta, GA.

18. Lind, M. A. et al, "Heliostat Survey and Analysis," Battelle
    Pacific Northwest Lab Report - to be published; and Taketani,
    H., and Arden, W. M., "Mirrors for Solar Energy Applications,"
    McDonnell Douglas Report MDC G7213 (Sept., 1977).

19. Vitko, Jr., J., "Optical Studies of Second Surface Mirrors
    Proposed for Use in Solar Heliostats," Sandia Labs Report
    SAND 78-8228-0U0.†

20. "Solar Optical Materials Program Activity Committee -
    Progress Report, July 1, 1978 to Jan. 31, 1979," Solar
    Energy Research Inst. Report SERI/PR-31-137 (July, 1979)
    and "Solar Glass Mirror Program - A Planning Report on
    Near-term Mirror Development Activities," Solar Energy
    Research Inst. Report SERI/PR31-145 (Jan., 1979).

21. Lind, M. A. and Rusin, J. M., "Heliostat Glass Survey
    Analysis," Battelle Pacific Northwest Labs Report PNL
    2868/UC62 (Sept., 1978).

22. Vitko, Jr., J. and Shelby, J. E., "Solarization of Helio-
    stat Glass," Sandia Laboratories Report, to be published.†

23. Bouquet, F. L., "Glass for Solar Concentrator Applications,"
    Jet Propulsion Lab. Report 5102-105 (April, 1979).

24. Burolla, V. P. and Roche, S. L.," Silver Deterioration in
    Second-Surface Solar Mirrors," Sandia Labs Report, to be
    published.†

25. "Solar Central Receiver Prototype Heliostat - Final Techni-
    cal Report," Vol. 1, Boeing Eng. & Construction Co., Report
    SAN/1604-1 (June, 1978), and "One Piece Domb Heliostat
    Studies," Final Report under Sandia Labs Contract 18-7830,
    Sandia Labs Report SAND 78-8184 (July, 1979).

26. Stickley, R. A., Sheldahl Inc., Northfield, MN 55057 –
     private communication.

27. Rausch, R. A. and Gupta, B. P., "Exposure Test Results
     for Reflective Materials," Proceedings of Inst. of Env.
     Science Seminar on Testing Solar Energy Materials, Gaithers-
     burg, MD, May 22–24, 1979, pp. 184–187.

28. Hampton, H. J. and Lind, M. A., "Weathering Characteristics
     of Potential Solar Reflector Materials: A Survey of the
     Literature," Battelle Pacific Northwest Labs Report PNL
     2824/UC62 (Sept., 1978).

29. Bieg, K. W. and Wischmann, K. B., "Plasma-Polmerized Organo-
     silanes as Protective Coatings for Front-Surface Solar Mir-
     rors," Sandia Laboratories Report, to be published.†

30. Glidden, D. N. and Pettit, R. B., "Specular Reflectance
     Properties of Solar Mirrors as a Function of Incident Angle,"
     Proceedings of 1979 Joint Meeting of American Section of
     ISES, May 28–June 1, 1979, Atlanta, GA.

31. Pettit, R. B., "Hemispherical Transmittance Properties of
     Solar Glazings as a Function of Averaging Procedure and
     Incident Angle," *Solar Energy Materials 1*, 125 (1979).

32. Richmond, J. C., "Evaluation of Solar Absorbers, Reflectors
     and Transmitters Physical Reflectance Standards," Proceedings
     of the 25th Annual Technical Meeting of the Inst. of Env.
     Sciences, Seattle, WA, (May, 1979), p. 2.

†Available from: NTIS, U.S. Dept. of Commerce, 5285 Port Royal
                  Rd., Springfield, VA 22161.

CHAPTER 6

THE EFFECT OF SOILING ON SOLAR MIRRORS AND
TECHNIQUES USED TO MAINTAIN HIGH REFLECTIVITY[1]

E.P. Roth
R.B. Pettit

Sandia Laboratories[2]
Albuquerque, New Mexico

I. INTRODUCTION

Solar mirrors are used to concentrate low-level solar radia-
tion to power levels which are practical and efficient for consumption.
Any interference with the collection of that energy not only de-
creases the power level but also increases the cost of the energy
available from a solar power system. Solar mirrors are designed
to initially achieve the maximum possible reflectance. However,
outdoor exposure subjects the mirror materials to environmental
conditions which can quickly degrade their efficiency. One of the
most immediate and drastic effects of outdoor exposure is the re-
flectance loss due to the accumulation of foreign particles on the
mirror surface. Specular reflectance losses as great as 25% have
been observed for mirrors exposed for only a few weeks. The ef-
fect of the deposited particles is to reduce the reflected energy
by both absorbing and scattering light[1,2]. The degree to which
the particles reduce the collection of reflected energy depends
on their composition, number and size distribution[1,2]. An addi-
tional factor is the optics of the collection system. The angular
acceptance aperture of the system, defined as the angle subtended
by the receiver as the concentrator surface, determines the

199

relative importance of the scattering due to dust accumulation.
For flat plate thermal and photovoltaic collectors which have
essentially a 180° angular acceptance aperture, scattering of the
incident light is not critical but absorption can be an important
factor in the loss of energy. For concentrating collection
systems, such as line focus collectors and central receivers,
angular acceptance apertures of a few degrees make scattering at
the concentrator surface much more important and can result in
severe energy losses. Thus, from an economic point of view,
periodic cleaning or reduction of soil accumulation is a practical
necessity.

II. EFFECT OF NATURAL SOILING ON MIRROR REFLECTANCE

Potential methods for controlling the reflectance loss due
to soiling must be based on both measurements of actual particu-
late accumulation in an outdoor environment and an understanding
of the basic physical mechanisms of adhesion and light scattering.
In order to establish a data base for the reflectance loss of
exposed mirrors, a field test study was initiated simulating some
of the operational configurations of solar mirrors.

A. *Long Term Soil Accumulation Study*

Solar mirror materials have been exposed to natural weathering
in Albuquerque, NM for periods exceeding one year.[3] The mirror
materials used were second-surface silvered glass obtained from a
heliostat panel at the 5MW Central Receiver Test Facility (CRTF)
at Kirtland AFB, Albuquerque, NM.[4] These samples are typical
of the type of materials used in many solar thermal power systems.
The specular reflectance of the mirrors was measured with a bidi-
rectional reflectometer over a wavelength range 400-900 nm and
over a 3-15 mrad range of angular acceptance apertures.[5] Figure
1 shows the specular reflectance data for a mirror exposed for
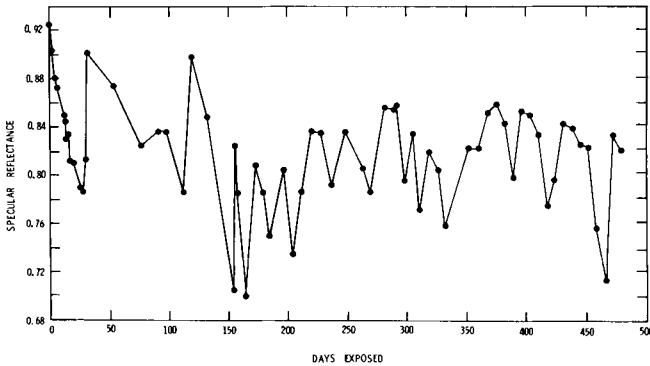
FIGURE 1.   *Specular reflectance of second-surface silvered glass mirrors exposed to natural weathering for 480 days.   Reflectance measured at 500 nm and 15 mrad angular aperture.*

480 days to natural weathering.[6]   The data shown are for a wavelength of 500 nm and a 15 mrad angular aperture.   The data show an initial rapid drop in reflectance of approximately 0.006 reflectance units per day (100% reflectance = 1.00 reflectance units) followed by large fluctuations in reflectance which are induced by variations in weather conditions.   The weather condition at a particular mirror location is one of the critical factors affecting the rate of dust accumulation and the eventual long term reflectance loss of an exposed mirror.   Daily reflectance losses as great as 0.144 reflectance units have been measured under certain conditions (light rain followed by a wind and dust storm) while increases as large as 0.121 reflectance units have been measured at other times (snow-rain weather conditions).[6]   Because of the variation in local weather, it is very difficult to predict long term reflectance losses for a given location and more difficult to apply those results to other locations.   In general, uncleaned mirrors in the Albuquerque area show a long term decrease in specular reflectance of approximately 0.10-0.15 reflectance units with large fluctuations about the average.[3]   Larger reflectance losses can occur in other geographic locations, especially in urban environments where optically absorbing particles from pollutants can lead to additional energy losses.[7]   Additional outdoor

exposure studies at other geographic locations are required to
obtain a more general understanding of mirror soiling.

B.   *Cleaning Cycle Experiment*

When the reflectance of a solar mirror drops sufficiently,
cleaning the mirror surface becomes economical. Increasing the
cleaning frequency should raise the average long-term reflectance
of the mirror, as depicted in Figure 2, although some long-term de-
gradation may result from the cleaning procedures. Figure 3 shows
the results of actual cleaning cycle tests in which three sets of
mirrors were exposed and cleaned on 2-, 6- and 12-day cycles.[3]
The mirrors were measured every two days to show any fluctuations
due to weather conditions. The results show that laboratory
cleaning (three minutes in an ultrasonic bath of distilled water
and wiped dry with a soft tissue) essentially restores the reflec-
tance of each mirror to its initial value. Subsequent exposure
results in a rapid nonlinear drop in reflectance for each set of
mirrors. The average daily reflectance loss for, respectively,
the 2-, 6- and 12-day cycle mirrors was 0.0085, 0.0061 and 0.0051
reflectance units. Thus, the rate of dust accumulation decreases
as the amount of accumulated dust increases. The long term average
reflectance loss for the 2-, 6- and 12-day cycled mirrors is, re-
spectively, 0.0085, 0.018 and 0.031 reflectance units, indicating
that increased frequency of cleaning does raise the average reflec-
tance of the mirrors.

The level of dust accumulation is also seen to affect the re-
sponse of the mirrors to weather conditions.[3] For example, mir-
rors which had an appreciable accumulation of dust were cleaned by
a light rain while newly cleaned mirrors experienced a loss in re-
flectance under the same conditions. These results show that
weather and mirror conditions can significantly affect the reflec-
tance of exposed mirrors and that these conditions must be fully
considered in any method to predict long-term reflectance loss.
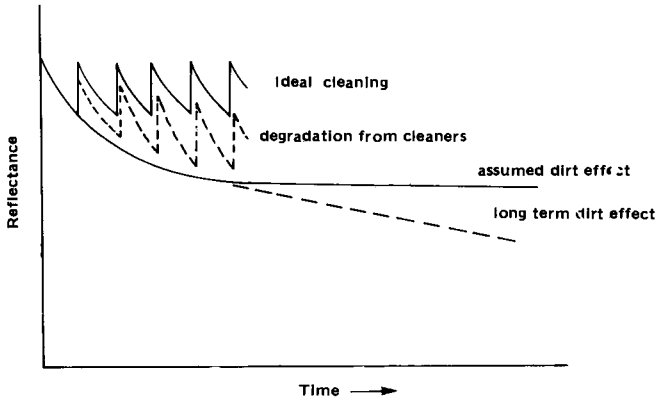
FIGURE 2.   Expected long-term reflectance of an exposed mirror with and without periodic cleaning.
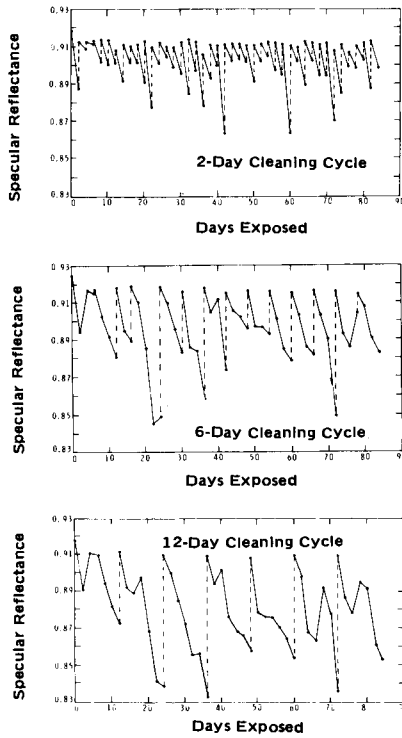
FIGURE 3.   Specular reflectance of mirrors undergoing (a) 2-day, (b) 6-day and (c) 12-day cleaning cycles.   The dashed lines show the reflectance increase due to laboratory cleaning; the solid lines show the reflectance loss due to natural soiling.

C. Orientation Angle Experiment

Several operational parameters can affect the rate of soiling of exposed mirrors. For example, the orientation angle of a mirror during periods of nonoperation can affect the rate of particulate settling on the surface and can maximize the effect of natural cleaning forces such as wind and rain. To investigate the effect of stowage angle on mirror degradation, a set of five mirrors was exposed on a test rack at different angles with respect to the horizontal: 0°, 30°, 45°, 60° and 180° (inverted).[3] These samples were exposed only during daylight hours of good weather, thus representing soiling strictly due to dry deposition. The results of this experiment are shown in Figure 4. Generally, the drop in specular reflectance decreased as the orientation angle increased; however, only the inverted (180°) mirror showed a significant reduction
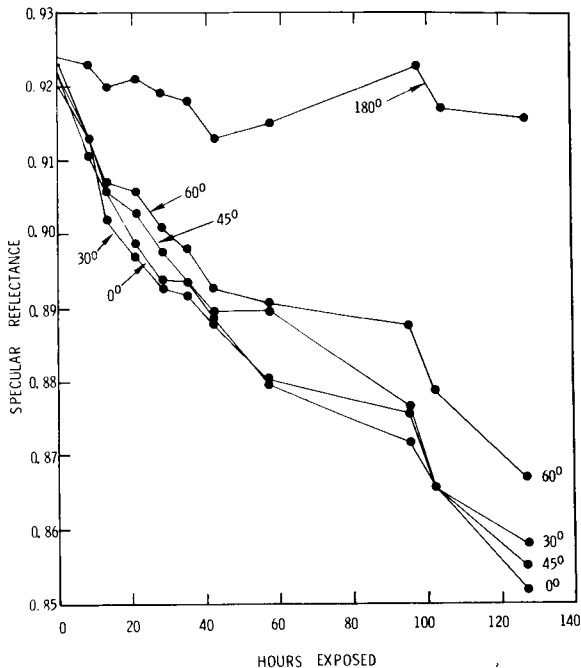
FIGURE 4. Specular reflectance of 5 mirrors as a function of mounting angle (0° = face up; 180° = inverted). The mirrors were exposed for a total of 127 hours (≈5 days) during daylight hours of good weather.

in soiling. In other experiments, a 90° stowage angle has also re-
sulted in a significant decrease in the rate of soiling.[8]   These
experiments show that any method formulated to maintain high re-
flectivity of solar mirrors must involve the optimization of both
the cleaning cycle and the stowage position.

III.   EFFECT OF ACCUMULATED DUST ON SPECULAR REFLECTANCE

The detailed interaction of accumulated dust with the incident
solar radiation is important in understanding and predicting the
loss in collected energy. Measurements were performed on a set of
solar mirrors exposed to natural weathering for a period of five
weeks to determine the wavelength dependent scattering by the par-
ticulates and the effect of the dust on the beam shape of the
scattered light.[9]

A.   Hemispherical Reflectance

Initially, the hemispherical reflectance of a clean mirror was
measured over the wavelength interval 320-2500 nm using an inte-
grating sphere reflectometer.[10]   This device allows collection of
both the specular and diffuse component of the reflected beam over a
solid angle of 2π steradians. Typical data are shown in Figure 5.
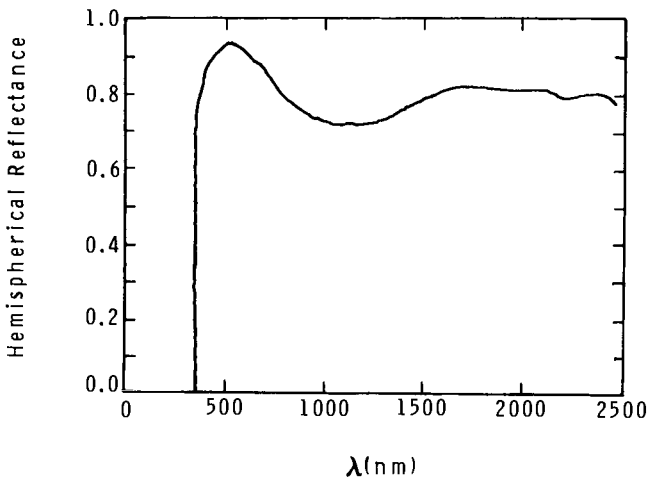
*FIGURE 5.   Hemispherical reflectance for a clean, second-
surface, silvered float glass mirror.*

The large dip in reflectance at 1000 nm is due to absorption in the glass by Fe^{+2} impurities.[11] The cutoff below 400 nm results from from losses in the glass and in the silver reflector layer.[12] Subsequent measurements of hemispherical reflectance after soiling showed no appreciable decrease in reflectance for specular reflectance losses up to ≈ 0.05 reflectance units, indicating that the energy lost from the specular component went into the diffuse scattering background with no measurable loss due to absorption. These results are consistent with the type of losses expected from dielectric (nonconducting) particles which are usually found in a desert environment. However, outdoor exposure to urban environments could lead to contamination by absorbing pollutants which could cause a decrease in the net hemispherical reflectance.[7]

B. Wavelength Dependence

The specular reflectance of mirrors with increasing levels of dirt accumulation is shown in Figure 6 over the wavelength range of 400-900 nm measured at a 15 mrad aperture.[9] The dominant effect of the accumulated dust is the decrease in specular reflectance over the entire wavelength range with increasing level of dust accumulation. At 500 nm the specular reflectance loss varied from 0.065 to 0.24 reflectance units. The wavelength dependence of the specular reflectance loss is shown in more detail in Figure 7. In this figure, the specular reflectance loss, $R_D - R_C$, is normalized by the reflectance value of the clean mirror, R_C, at each wavelength. The wavelength dependence of the reflectance loss is directly proportional to the scattering cross section of the dust particles. The data show that the net scattering by the accumulated particles increases with decreasing wavelength and with increasing level of soiling, with the scattering amplitude still increasing at 400 nm. Since the soil particles accumulated in this experiment do not result in any appreciable absorption, the light lost from the specular beam forms the diffusive reflection background. The wavelength
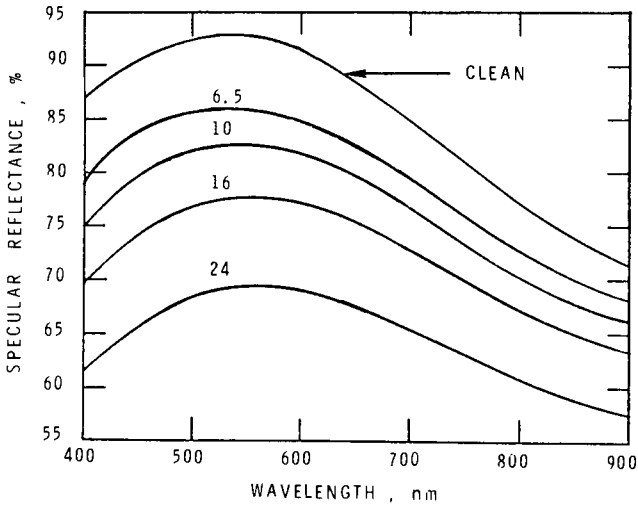
FIGURE 6.   *Specular reflectance as a function of wavelength for an initially clean mirror (upper curve) and after increasing levels of dust accumulation (lower curves). Values listed are the specular reflectance loss measured at 500 nm for a 15 mrad angular aperture due to dust accumulation.*
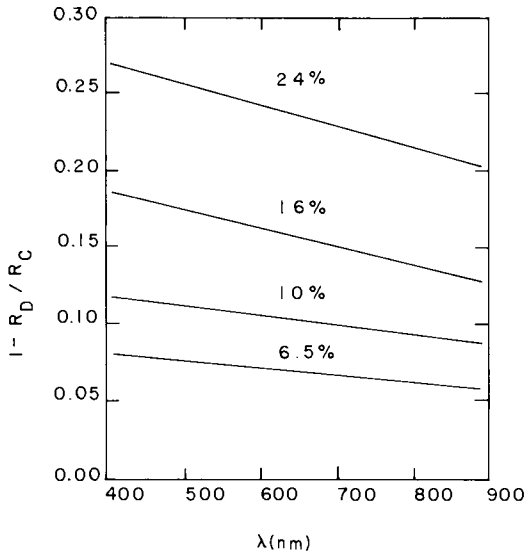
FIGURE 7.   *Specular reflectance loss due to soiling normalized by the specular reflectance of the clean mirror as a function of wavelength.* (R_D = *Dirty mirror,* R_C = *Clean mirror). The functional dependence of the normalized reflectance loss is directly proportional to the scattering strength of the accumulated dust. The data are obtained from the curves in Fig. 6 for the various levels of dust accumulation. The values listed refer to the specular reflectance loss at 500 nm.*

dependence of the diffusive background is shown in Figure 8 for the
levels of soil accumulation shown originally in Figure 6. The
diffusive scattering was measured with the integrating sphere re-
flectometer over the wavelength range 320-2500 nm. Because of dif-
ferences in the beam sizes, collection apertures and measurement
regions, the loss in specular reflectance and the increase in dif-
fuse reflectance are not in exact agreement. However, by norma-
lizing the diffuse reflectance by the value at 500 nm, the wave-
length dependent scattering can be approximately determined,
independent of the degree of soiling. The resulting normalized
curve is shown in Figure 9. The HIGH and LOW curves represent
the maximum and minimum normalized loss values respectively from
all regions measured. This figure shows that within the accuracy
of the data the wavelength dependence of the scattering is inde-
pendent of the concentration of accumulated particles. This
result is useful since it allows a solar-averaged reflectance loss
for this silvered glass mirror to be calculated from a measurement
at a single wavelength. For the type of mirrors used in this ex-
periment, the solar averaged reflectance loss is equal to 0.78
± 0.04 times the specular reflectance loss measured at 500 nm.
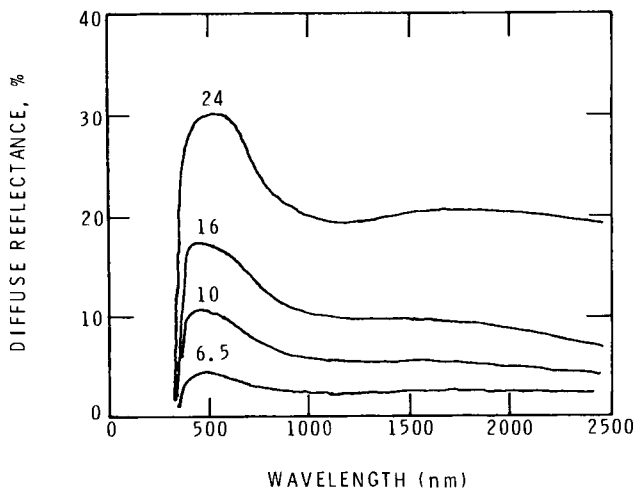
FIGURE 8. Diffuse reflectance as a function of wavelength for
the soiled mirrors shown in Fig. 6. The values listed refer to
the specular reflectance loss at 500 nm.
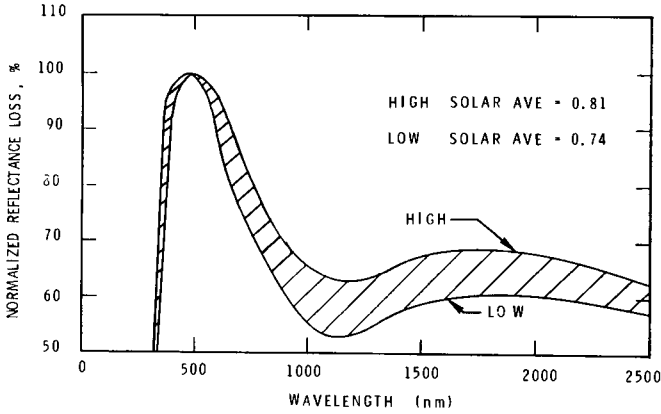
FIGURE 9. *Diffuse reflectance normalized by the diffuse reflec-*
tance at 500 nm as a function of wavelength for all levels of soil
accumulation shown in Fig. 8. The HIGH/LOW curves represent the lim-
its of the normalized curve due to the uncertainty in each measure-
ment.   The HIGH/LOW solar average values refer to the limits of the
solar averaged specular reflectance loss as discussed in the text.
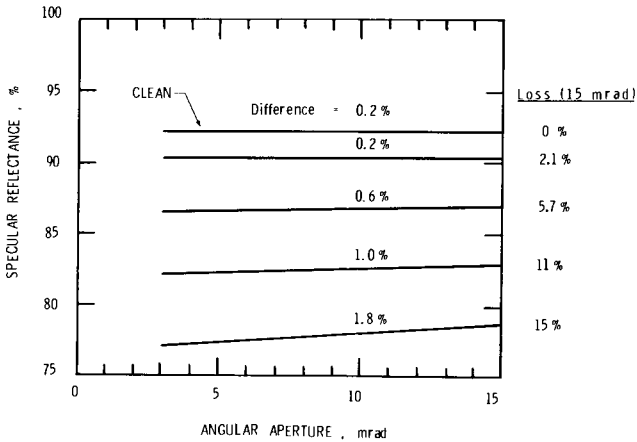
FIGURE 10. *Specular reflectance as a function of angular aper-*
ture for a clean mirror (upper curve) for increasing levels of dust
accumulation.   The difference values listed are the difference in
specular reflectance between 3 mrad and 15 mrad.   The losses listed
at the right are the specular reflectance losses measured at 15
mrad.   All data were measured at 500 nm.

C. Effect of Dust Particles on Beam Shape

Accumulated dust particles can have a significant effect on

the performance of a solar collector with a small angular accep-

tance aperture by affecting the shape of the reflected beam.   The

effect of accumulated particles on beam shape was measured using

the laboratory bidirectional reflectometer over an angular aper-
ture range of 3-15 mrad.[9] The data are shown in Figure 10 at the
standard wavelength of 500 nm for increasing levels of dust accumu-
lation. The values listed in the figure are the differences in
specular reflectance between the 3 and 15 mrad measurement points.
The data show that the main effect of accumulated dust is to de-
crease the overall intensity of the reflected beam and not to sig-
nificantly change the profile. Wide-angle scattering by the accu-
mulated particles (scattering at angles much greater than the
acceptance aperture of the collection optics) can account for this
effect and result in comparable losses for both central receiver
and distributed power systems which both have apertures $\lesssim 2°$.

IV. SCATTERING THEORY

The detailed scattering of light by particles is a complex
function of the optical properties of the particles, the size and
number distribution of the particles, and the wavelength of the
incident light.[1,2] For solar power systems, the incident light
comes from direct radiation by the sun. The wavelength distribu-
tion of the solar radiation may be modeled as a black body spectrum
corresponding to a temperature of ≈ 5800 K, modified by absorp-
tion in both the solar and terrestrial atmospheres.[1,3] The peak
in the atmospheric spectrum occurs at approximately 500 nm, with
a lower cutoff at 300 nm and an upper cut off at 3500 nm.

A. *Extinction Coefficient and Angular Scattering Function*

The scattering of light by a single particle is a function of
the particles' complex index of refraction, the particle shape and
the size of the particle compared to the wavelength of the inci-
dent light.[1,2] The efficiency of a particle in removing energy
from incident light is derived from Mie scattering theory and is
given by its extinction coefficient:

$$K_{EXT} = K_{SCAT} + K_{ABS} \qquad (1)$$

$$= \sigma_{SCAT}/\sigma_A + \sigma_{ABS}/\sigma_A \qquad ,$$

where K_{SCAT} is the ratio of the effective scattering cross section (σ_{SCAT}) of the particle to its actual geometric cross section (σ_A) and K_{ABS} is the ratio of the effective absorption cross section (σ_{ABS}) to the geometric cross section. The extinction coefficient for a spherical dielectric particle (no absorption) is shown in Figure 11 as a function of the particle circumference/wavelength ratio.[1,2] This curve is valid for most particles of interest for which $1 \lesssim |m| \lesssim 2$ where m is the complex index of refraction. The figure shows that the extinction coefficient drops off rapidly for particles small compared to the wavelength of the incident light, peaks at a value where the particle size is comparable to the wavelength and then undergoes oscillations of decreasing amplitude about a value of ≈ 2 with increasing particle circumference/wavelength ratio. For increasing magnitude of the index of refraction, the peak in the extinction coefficient shifts to longer wavelengths.[1,2]
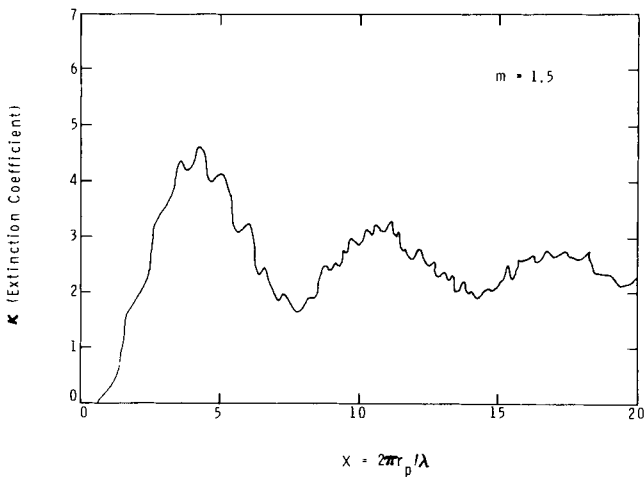
$$x = 2\pi r_p/\lambda$$

FIGURE 11. *Extinction coefficient calculated from Mie scattering theory for a spherical particle with index of refraction $m = 1.5$ as a function of the size parameter $x = 2\pi r_p/\lambda$ where r_p = particle radius and λ = wavelength of incident light.*

The angular distribution of the scattering energy is a compli-
cated function of the relative particle circumference/wavelength
ratio, particle index of refraction and polarization of the inci-
dent light.[2] Figure 12 shows the scattering amplitude as a func-
tion of angle for a particle with 1.55 index of refraction and with
circumference/wavelength ratio $2\pi r_p/\lambda = 3.0$ (r_p = particle radius).
As the size of the particle becomes equal to or larger than the
wavelength of the incident light the scattering amplitude becomes
peaked in the forward direction with weaker lobes occurring at
larger angles. However, for most naturally occurring particles, the
majority of the scattered energy still occurs at angles greater than
the few degree angular acceptance apertures of most concentrated
power systems. These calculations agree with the large-angle scat-
tering which previously accounted for the negligible effect of accu-
mulated dust on the shape of the specularly reflected beam profile.
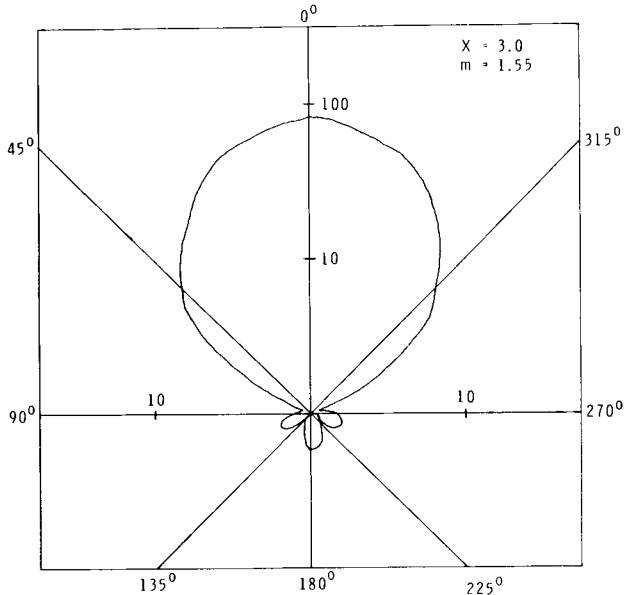
FIGURE 12. Amplitude of scattered light as a function of
angle for a spherical particle with index of refraction m = 1.55
and size parameter x = $2\pi r_p/\lambda$ = 3.0. The angle of the inci-
dent light is 0° and the polarization normal to the plane of
the paper.

B. *Loss in the Specular Reflection Component*

The loss in the specular component of reflected solar energy due to scattering by dust particles can be calculated by convoluting the particle extinction coefficients, particle size distribution and solar spectral distribution over all particle sizes and solar wavelengths.[1] The expression for this loss is given as

$$\Delta I_m / I_o = 2 \int_0^\infty dr \int_0^\infty d\lambda \left\{ \pi r^2 K_{EXT} \left(\frac{2\pi r}{\lambda}, m \right) n(r,m) f(\lambda) \right\}$$

$$= 2 \int_0^\infty dr \left\{ \pi r^2 n(r,m) \int_0^\infty K_{EXT} \left(\frac{2\pi r}{\lambda}, m \right) f(\lambda) d\lambda \right\} , \tag{2}$$

where r = particle radius, $n(r,m)$ = number of particles/unit area-unit radius, m = complex index of refraction, I_o = solar spectral intensity and $f(\lambda)$ = wavelength function of the solar spectrum. In this expression, the incident solar radiation is assumed to have interacted with the surface layer of dust particles twice as shown schematically in Figure 13a. The result of convoluting the wavelength dependent extinction coefficient for a spherical particle with $m = 1.5$ and the solar distribution function is shown in Figure 13b. The net loss in intensity of the specular beam is then obtained by further convoluting the function shown in Figure 13b with the particle area and the particle size distribution function shown in Figure 13c. The particle size distribution function shown in this figure is representative of the distribution function actually measured on exposed mirrors. This function will be discussed in more detail in Section V, B. The resultant energy lost from the specular beam per unit particle diameter; i.e., the integrand in the second line of Eq. (2), is shown in Figure 14, assuming a particle distribution function of the form $n(r,m) \propto r^{-3}$ for ease of calculation. The peak in energy loss occurs near 500 nm, corresponding to the peak in the solar spectrum. This analysis emphasizes the importance of the small particle ($0.05 \ \mu m \lesssim r_p \lesssim 1 \ \mu m$) in

$$\gamma(r) = \int_o^\infty \kappa_{ext}\left(\frac{2\pi r}{\lambda},\ m\right)I_o^f(\lambda)d\lambda$$
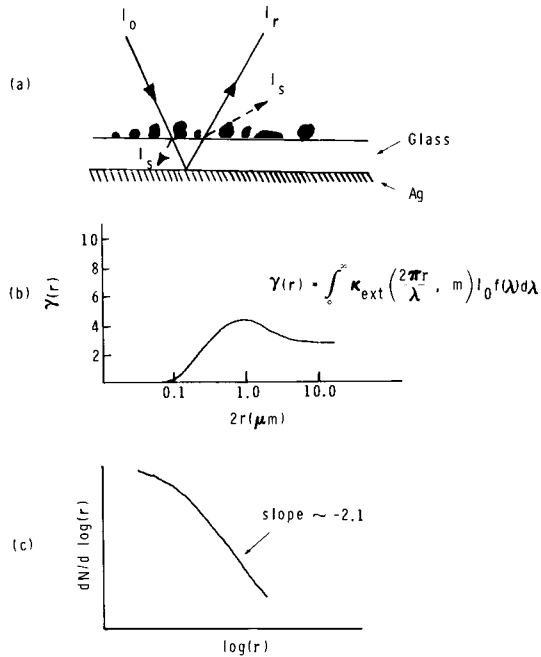
FIGURE 13. (a) Schematic of light scattering by dust particles on a second-surface mirror where I_o = incident light, I_s = scattered light and I_r = reflected light. (b) Convolution of wavelength dependent extinction coefficient and the solar spectral distribution as a function of particle diameter. (c) Particle size distribution function for a naturally soiled mirror.
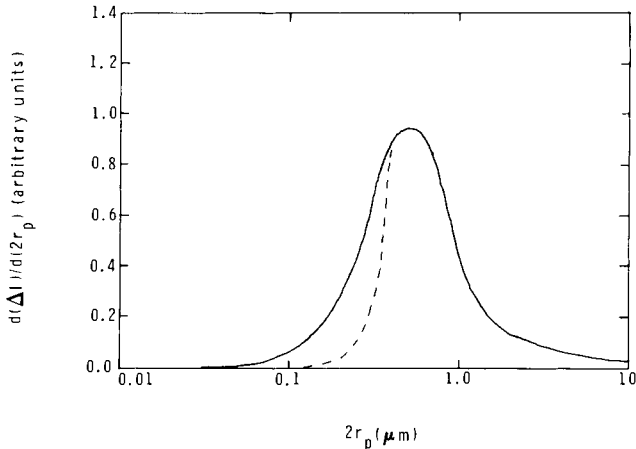
FIGURE 14. Energy loss as a function of particle size assuming a particle size distribution function $n(r) \propto r^{-3}$ (solid curve). Energy loss assuming a drop off in the particulate concentration for $r_p \lesssim 0.2$ μm (dashed curve). The incident radiation is assumed to have the standard solar distribution at sea level.

the scattering loss. A decrease in the number density of small particles ($r_p \lesssim 0.2 \ \mu$m), which has been measured by some investigators, would cause a sharper cutoff in the energy loss function for the small particle diameters, as shown by the dashed curve in Figure 14. However, the major loss of energy still results from particles in the submicron range.

V. DEPOSITION AND ADHESION

The deposition of particles on a mirror surface is controlled by the complex fluid mechanical interaction of the dust-laden airstream with the entire mirror structure.[14] Processes such as convective diffusion, impaction and sedimentation play important roles in the deposition process depending on particle size and wind velocity. In general, particles whose Stokes velocity is less than the ambient wind velocity will be carried to the mirror surface and can be subsequently deposited. Particles with diameters $\lesssim$ 100 microns will be suspended by wind velocities of only a few miles per hour, resulting in a broad size spectrum of deposited particles.

A. Forces of Adhesion

A wide range of forces are responsible for the adhesion of the particles to the surface, as listed in Table I. The magnitude of

Table I. Mechanisms of Dust Adhesion

Mechanism	Affecting Material Property
Gravity	Mass
Electrostatic	Surface (coating) conductivity
Charge Double Layer	Contact potential (difference in work functions)
VanderWalls Force	Particle size; Surface roughness
Surface Energy	Solid surface relaxation
Capillary Force	Fluid surface relaxation
Chemical/Physical Bond	Chemical activity

these forces depends strongly on the nature of both the particles
and the mirror surface, varying from a fraction of the gravitational
force on the particle to several orders of magnitude greater than
the gravitational force.[15] The details of these different mecha-
nisms are not sufficiently well understood to permit accurate esti-
mations of the type and magnitude of forces responsible for particle
adhesion. However, the initial forces of adhesion are probably dom-
inated by electrostatic forces and surface energetics, while after
sufficiently long periods of time stronger chemical and physical
bonds can develop. The few experiments that have been performed show
that the forces of adhesion in general increase with decreasing par-
ticle size and with increasing time of surface contact.[15] The de-
velopment of the stronger chemical bonds will depend strongly on the
amount of moisture present at the particle mirror interface and are
thus affected by such parameters as relative humidity and rainfall.

B. *Particle Distributions*

As discussed in Section IV, B, the small particles ($r_p \lesssim 1$ μm)
are the most important source of scattering for the solar spectrum
and, as stated in the previous section, experience the greatest sur-
face adhesion. Measurements of the actual particle size distribu-
tion on weathered mirrors can yield information on the relative
significance of the various particle sizes and how different en-
vironmental conditions can affect their rates of accumulation.

Particle size distributions have been measured using a Quanti-
met particle sizer.[16] This instrument measures the number of
particles in selected size intervals from direct optical images of
the mirror surface and from high magnification micrographs taken on
a scanning electron microscope. Overlapping particle size measure-
ments are made at different magnifications at several random loca-
tions on the surface to obtain a representative characterization
of the entire mirror surface. An average of 60-70 different loca-
tions are measured using five different magnifications covering

particles with diameters $\gtrsim 0.3$ μm. A typical particle distribu-
tion for a mirror subjected to several months of outdoor exposure
is shown by the open circles in Figure 15. For convenience in
comparing to atmospheric aerosol distributions reported in the
literature, the size distribution is presented as a logarithmic
function,

$$dN/Ad(\log r) \quad (cm^{-2}) \quad , \qquad (3)$$

where N is the number of particles with radii $\leq r$, r is the par-
ticle radius and A is the unit area of mirror surface.[17-19] In
general, the size distribution is described as

$$dN/Ad(\log r) \propto r^{-k} \qquad , \qquad (4)$$
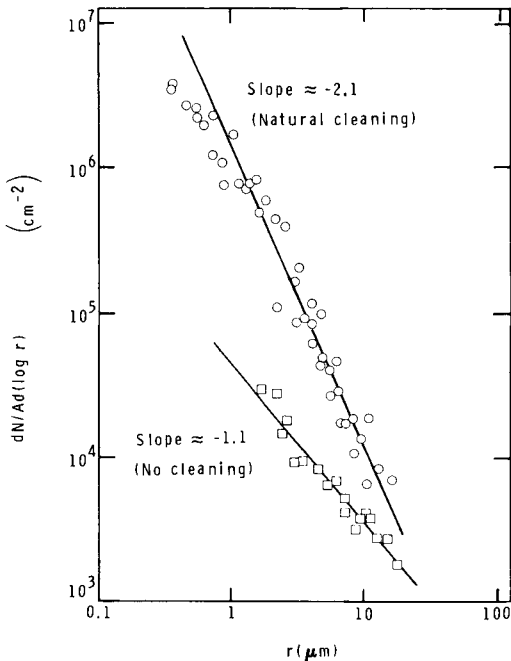
FIGURE 15. *Particle size distribution functions for naturally
soiled mirrors. Open circles: mirror exposed to natural cleaning
(wind and rain) for several months. Open squares: mirror exposed
only to "good" weather conditions for a period of 2 days.*

where $k \approx 2$ for this sample. The particle distribution measured in atmospheric aerosols for particle radii $\gtrsim 1$ μm is usually described by a power law distribution. The actual logarithmic slope can vary significantly depending on location, weather and time of year.[17-19] Below 1 μm the atmospheric particle distribution function usually levels off or actually decreases. The entire distribution is often referred to as a lognormal distribution which is modeled with a logarithmic Gaussian function plus a power law background distribution.[18] The distribution of particles accumulated on the exposed mirror shows some deviation from the power law distribution function below 1 μm but the decrease is smaller than observed in aerosols, indicating some preferential adhesion of the small particles out of the atmospheric distribution. This result is consistent with experiments which have shown increased adhesion for small particles.[15]

If indeed the small particles adhere more strongly to the mirror surface, then the small particles should likewise be more difficult to remove. The result of preferential adhesion of the small particles can be seen by comparing the particle distribution of the weathered mirror to the distribution of a mirror which has undergone only dry deposition. The open squares in Figure 15 show the particle distribution for a mirror which has undergone only two days of exposure during dry weather. The measured slope is ≈ -1.1 compared to ≈ -2.1 for the weathered mirror. The greater magnitude of the slope of the weathered mirror occurs because of "natural" cleaning conditions, such as wind and rain, which preferentially remove the larger particles while the relative number of smaller particles continue to increase. This result has been confirmed by measurements on other mirrors which have undergone varying lengths of outdoor exposure to both "dry" and "wet" environments.

VI.   ACCELERATED DEPOSITION STUDY

Variations in weather conditions cause such large fluctuations
in the reflectance of exposed mirrors that long-term predictions
of reflectance loss are difficult to make. Measurement of reflec-
tance loss and particle accumulation under controlled conditions
can yield a better understanding of the effect of such parameters
as wind velocity, particle flux and humidity on the rate of reflec-
tance loss. In addition, controlled particle deposition allows an
accurate comparison of soiling rates for various mirror materials
and cleaning techniques.

A. Wind Tunnel

Representative mirror materials have been exposed to accele-
rated dust deposition in a low-velocity wind tunnel equipped with
a dust injector/disperser unit and laser optical systems capable
of monitoring the flux rate of the incident particles and the real-
time reflectance loss of the exposed mirrors. The mirrors are
exposed to controlled amounts of a well-defined Arizona Desert
Dust[20] over velocity ranges of ≈10-30 MPH. The samples are
mounted normal to the incident airstream to achieve the maximum
rate of dust accumulation. The dust injector/disperser unit is
capable of injecting particles at densities ≈10^4 times greater
than the particle densities present in normal atmospheric aerosols.
The injector has also been designed to maintain a constant injected
particle size distribution over the period of deposition. Specular
reflectance losses observed after several months of outdoor expo-
sure have been simulated in approximatly 30 minutes in the wind
tunnel. Although this accelerated deposition system is not in-
tended to exactly duplicate outdoor exposure, it does allow a com-
parative measurement of dust accumulation on various materials
under a wide range of exposure conditions.

B.   Laser Optics

The dust-laden airstream is monitored using a laser velocimeter
apparatus and a multichannel analyzer to record the flux of inci-
dent particles during the deposition period, as shown in Figure 16.
The green beam (λ = 0.5145 nm) from an argon laser is split into
two components and recombined in front of the exposed mirror to
form a region of interference fringes. As particles pass through
the sampling volume, they scatter light with an intensity pattern
characterized by the spacing of the interference fringes and the
particle velocity, thus allowing the particle transit to be distin-
guished from background noise in the phototube[21]. Typical flux
levels levels range from 5 x 10^4 - 5 x 10^5 particles/cm^2-sec.

During the deposition, the reflectance of the mirror is moni-
tored using a He-Ne reflectometer. A He-Ne laser beam is expanded
to approximately 1 cm diameter and is split into a sample beam
and a reference beam. The two beams (45° to the mirror surface)
follow identical optical paths through the wind tunnel so that
any loss in intensity due to the dust-laden airstream is equal
for both beams. The ratio of the intensity of the sample beam
to the reference beam yields the normalized specular reflectance
of the mirror independent of fluctuations in the laser beam inten-
sity. The reflectance losses measured with this system have been
compared with specular reflectance losses measured with a labora-
tory bidirectional reflectometer at 633 nm and agreement has been
found to be within 0.013 reflectance units over a loss range of
0.05-0.9 reflectance units. A typical reflectance loss curve as
a function of deposition time is shown in Figure 17 for a second-
surface silvered glass mirror (mirror A). This particular depo-
sition was performed at a wind velocity of 20 MPH and a flux rate
of ≈1.2 x 10^5 particles/cm^2-sec. Note that the reflectance loss
is approximately a linear function of deposition time. An identi-
cal mirror (mirror B) was exposed to the same particle flux but
at a velocity of 25 MPH, also shown in Figure 17. At this higher

REFLECTANCE MONITOR AND RECORDER
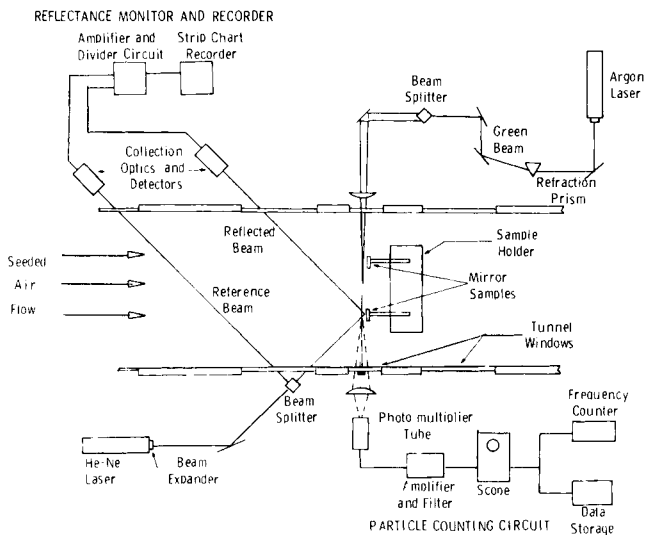
FIGURE 16. *Accelerated deposition wind tunnel with laser op-*
tics for monitoring particle flux and measuring real-time reflec-
tance loss of exposed mirrors.
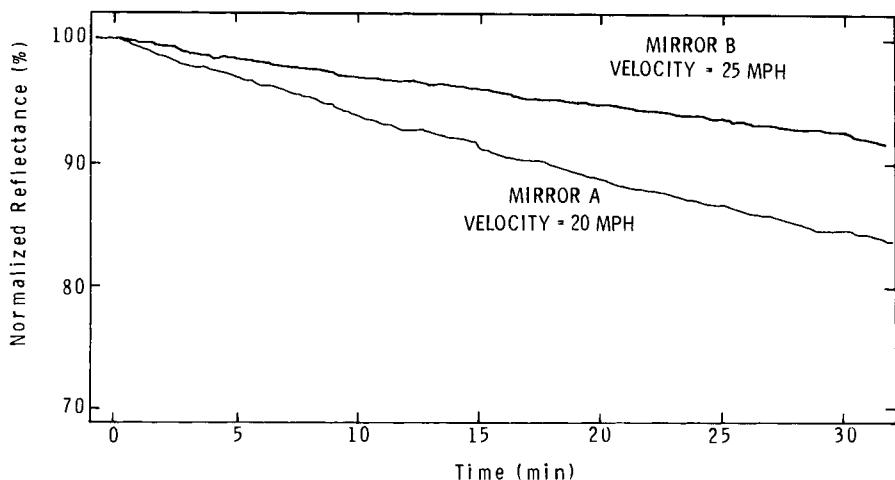
FIGURE 17. *Normalized real-time reflectance loss for mirrors*
exposed to a particle flux of $\approx 1.2 \times 10^5$ *particles/cm^2-sec at*
wind velocities of 20 MPH (Mirror A) and 25 MPH (Mirror B).

velocity, the rate of reflectance loss decreased by a factor of
≈ 1.8. The variation of this single parameter shows that the
reflectance loss rate is a rather strong function of wind velocity

under conditions of dry deposition. This effect results from the
increased kinetic energy of the particles at higher wind velocities
which causes the particles to rebound from the surface rather than
be held by the acting forces of adhesion.[15] A change in velocity
should have the greatest effect on the small particles which under-
go the greatest deacceleration along the stagnation line of the
mirror. Increasing the kinetic energy of these particles raises
their energy above the effective "capture threshold" energy of the
mirror and results in a drop in the effective "sticking coeffi-
cient" of the small particles. The energy of a significant number
of the larger particles at low velocities already would exceed the
"capture threshold" of the mirror so that they would be less af-
fected by a change in velocity. Initial measurements of the par-
ticle distribution on these two mirrors indeed show a significant
increase in the relative numbers of small particles ($r_p \lesssim 5$ μm)
for mirror A (V = 20 MPH) compared to mirror B (V = 25 MPH). The
1 μm particle density ratio of mirror A to mirror B was ≈3.1
while the ratio was ≈1.3 at a radius of 10 μm. These results
again point to the significant role of the small particles in
determining the reflectance loss of exposed mirrors. Experiments
are currently being conducted to extend the scope of these con-
trolled depositions to include other mirror materials, coatings
and exposure conditions.

VII. CLEANING STRATEGIES

An understanding of the mechanisms of dust deposition and ad-
hesion can lead to the development of techniques to maintain high
reflectivity under outdoor exposure conditions. Current cleaning
strategies can be generalized into the following categories:

    (1) Keep dirt from settling and adhering to the surfaces.
    (2) Wash off dirt with water or low surface energy detergent-
         type solutions before strong chemical or mechanical
         bonding can develop.

(3)   Wash off dirt with chemically or mechanically active
cleaning techniques capable of breaking the chemical
and mechanical bonds that have developed.

(4)   Modify the surface so that strong bonding cannot develop.

The above strategies can be divided generally into either
active or passive cleaning methods. Active cleaning methods
(strategies 2 and 3) are labor intensive techniques which can have
serious economic restrictions on the operation of a solar power
system, while passive techniques (strategies 1 and 4) are pri-
marily capital intensive and can possibly result in lower, long-
range cleaning costs. Currently, strategies 1 and 4 are being
investigated as possible approaches to the soiling problems, en-
compasing such techniques as ultrasonic vibration, electrostatic
biasing and antistatic, antisoiling surface coatings.[22,23]

Investigation of strategies 2 and 3 has indicated that glass
mirrors can be cleaned to within 2% and acrylic mirrors to within
8% of their initial reflectance using a high-pressure (1000 psi)
tap water spray. In locations containing hard water, a final rinse
with deionized water or tap water containing a sheeting agent may
be required. Mechanically or chemically active cleaning is re-
quired to restore 100% of the initial mirror reflectance. However
it is not clear if there may be some long-term buildup of nonremov-
able soil or degradation of the mirror surface due to cleaning.[24]

Preliminary tests using conducting oxide coatings, [(SnO_2)
coupled with an electrostatic field] have resulted in the reduction
of dust accumulation during wind tunnel exposures.[14] More exten-
sive experiments are planned using this technique to characterize
the independent effects of the coatings and the applied fields on
the rate of dust accumulation and the particle size distributions.
Eventually this technique will be applied to field test experiments.

VIII.   CONCLUSIONS

    The accumulation of dust and the resulting loss in specular re-
flectance of exposed mirrors is a complex function of mirror ma-
terial, weather conditions, geographical location and operational
methods.   Some general conclusions based on natural and artificial
soiling of solar mirrors are:

    (1)   Specular reflectance of a freshly exposed mirror under-
        goes an initial rapid drop (0.0085 reflectance units/day
        from 2-day cycle exposure) followed by a decreasing loss
        rate as the accumulated dust level increases.

    (2)   The long-term reflectance loss of uncleaned silvered
        glass mirrors in Albuquerque is approximately 0.10-0.15
        reflectance units with large fluctuations about the
        average.   Similar data at other locations and for other
        materials are needed.

    (3)   Increased cleaning frequency raises the average reflec-
        tance of the mirror.

    (4)   Inverted or vertical storage of the mirrors can signi-
        ficantly reduce the rate of dust accumulation.

    (5)   The effect of weather on the specular reflectance of a
        mirror depends on the mirror's level of dust accumulation.

    (6)   Dust accumulated upon exposure in the Albuquerque area
        results in wide-angle scattering of the incident light.
        The effect on the specular reflectance is primarily to
        reduce the intensity of the reflected beam while essen-
        tially maintaining the shape of its intensity profile.

    (7)   Dust accumulated in the Albuquerque area results in little
        absorption.   The specular reflectance loss to hemispheri-
        cal reflectance loss ratio is approximately 5 to 1.

    (8)   Scattering caused by accumulated particles increases with
        decreasing wavelength and increasing level of soiling,
        with the scattering amplitude increasing below 400 nm,

and with the wavelength dependence of dust particle scattering independent of particulate concentration.

(9)   Small particles ($0.3 \ \mu m \lesssim r_p \lesssim 1 \ \mu m$) are the most significant source of scattering for the solar spectrum.

(10)   The concentration of small particles ($r_p \lesssim 5 \ \mu m$) tends to increase more rapidly than the concentration of larger particles for mirrors exposed to natural weathering.

(11)   Decreasing wind velocity increases the relative rate of accumulation of small particles ($r_p \lesssim 5 \ \mu m$).

(12)   Surface coatings and electrostatic biasing can possibly reduce the rate of dust accumulation.

The development of any technique to reduce the rate of soiling of exposed solar mirrors must necessarily involve the optimization of both the operation and design of the mirrors.   Long term field test studies will help determine the eventual technique or combination of techniques used.

REFERENCES

1.   Friedlander, S. K., "Smoke, Dust and Haze: Fundamentals of Aerosol Behavior" (John Wiley and Sons, New York, 1977).

2.   Van de Hulst, H. C., "Light Scattering by Small Particles" (John Wiley and Sons, New York, 1957).

3.   Freese, J. M., Effects of Outdoor Exposure on the Solar Reflectance Properties of Silvered Glass Mirrors, Sandia report SAND 78-1649, Sept. 1978.†

4.   Arvizu, D. E., "The Solar Central Receiver Test Facility Heliostat Development," presented at Solar Energy Research Institute International Symposium on Concentrator Solar Collection Technology (June 14, 1978), Denver, CO.

5.   Pettit, R. B., *Solar Energy 19*, 733 (1977).

6.   Freese, J. M., "Effects of Outdoor Exposure on the Solar Reflectance Properties of Silvered Glass Mirrors,"

presented at the 1979 International Solar Energy Society
Congress (May 28 - June 1, 1979), Atlanta, GA.

7.   Forman, S. E., "Endurance and Soil Accumulation Testing
     of Photovoltaic Modules at Various MIT/LL Test Sites,"
     Report #COO-4094-23 (September, 1978).†

8.   Dave King, Sandia Labs., personal communication.

9.   Pettit, R. B., Freese, J. M. and Arvizu, D. E., "Specular
     Reflectance Loss of Solar Mirrors Due to Dust Accumulation,"
     Proceedings of the Institute of Environmental Sciences
     Solar Seminar on Testing Solar Energy Materials and Systems
     (May 22-24, 1978), at the National Bureau of Standards,
     Gaithersburg, MD, pp. 164-168.

10. Edwards, D. K., et al., *J. Opt. Soc. Am. 51,* 1279 (1961),
     and Beckman Instructions 1220-B (1962).

11. Taketani, H. and Arden, W. M., "Mirrors for Solar Energy
     Applications," Proceedings of the 1977 Annual Meeting
     American Section of ISES (June 6-19, 1977), Orlando, FL,
     Vol. 1, pp. 5-15 to 5-19, and Vitko, J., Optical Studies
     of Second Surface Mirrors Proposed for use in Solar Helio-
     stats, Sandia report SAND 78-8228 OUO, April 1978.

12. Huebner, R. H., Arakana, E. T., MacRae, R. A. and Hamm, R. N.,
     J. Opt. Soc. Am. 54, 1434 (1964).

13. Meinel, A. B. and Meinel, M. P., "Applied Solar Energy: An
     Introduction" (Addison-Wesley Publishing Co., Menlo Park, CA,
     1977).

14. Berg, R. S., Heliostat Dust Buildup and Cleaning Studies,
     Sandia report SAND 78-0510, March 1978.†

15. Zimon, A. D., "Adhesion of Dust and Powder" (Plenum Press, New
     York, 1969).

16. Quantimet 720, Image Analyzing Computers Ltd., Subsidary of
     Metals Research Ltd., 40 Robert Pitt Drive, Monsey, NY 10952.

17. Gillette, D. A. and Blifford, Jr., I. H., *J. Geophys. Res. 79,*
     4068 (1974).

18.   Quenzel, H., *J. Geophys. Res. 75,* 2915 (1970).

19.   Blifford, Jr., I. H. and Ringer, L. D., *J. Atmos. Sci. 26,* 716
      (1969).

20.   Standardized Test Dust obtained from A. C. Spark Plug Div., GMC,
      P. O. Box 1001, Flint, MI   48501.

21.   Lapp, M., Penny, C. M. and Asher, J. A., Application of Light-
      Scattering Techniques for Measurements of Density, Temperature,
      and Velocity in Gasdynamics, Aerospace Research Laboratories
      Report ARL 73-0045 (April, 1973).

22.   Schumaker and Associates, Inc., "Preliminary Design Report on
      New Ideas for Heliostat Reflector Cleaning Systems," Sandia
      Report SAND 79-8181, Aug. 1979.

23.   Electrostatic repulsion of dust using a corona discharge system
      has been investigated by Prof. Stuart A. Hoenig, Dept. of
      Electrical Engineering, Univ. of Arizona, Tucson, AZ   85721

24.   McDonnell Douglass Astronautics Co., Final Report: Cleaning
      Agents and Techniques for Concentrating Solar Collectors,
      Sandia report SAND 79-1979, Sept. 1979.†

†Available from: National Technical Information Service (NTIS), U. S.
Department of Commerce, 5285 Port Royal Road, Springfield, VA   22161.

CHAPTER 7

THE EMISSIVITY OF METALS[1]

A.J. Sievers

Laboratory of Atomic and Solid State Physics
and
Materials Science Center
Cornell University
Ithaca, New York

I. INTRODUCTION

Although radiant heat transfer processes have been studied
for many years, with entire textbooks and journals devoted to the
subject, the high temperature thermal radiative properties of
metals was not described correctly until 1978 (1). It is the
purpose of this chapter firstly to show what is wrong with the
early radiant heat transfer models of metals and secondly to
provide the physical insight behind the new model, which does
correctly describe the temperature dependent thermal radiative
properties of metals.

In 1915, Foote (2) calculated the thermal radiation emitted
normally from a heated metal surface using the Planck radiation
law. By comparing this amount to that expected for a black body,
he obtained an expression for the total normal emissivity of the
metal. Foote's equation, which has been only slightly modified
in the intervening years, is (3):

$$\varepsilon_N = 0.578(\rho T)^{1/2} - 0.178(\rho T) + 0.0584(\rho T)^{3/2} , \tag{1}$$

where ρ is the resistivity of the metal in ohm-cm and T is the absolute temperature.

Somewhat later, Davisson and Weeks (4) compared the amount of thermal radiation emitted at all angles from a heated platinum surface with their calculated values using Planck's law. This thermal radiation expression of Davisson and Weeks, in which the hemispherical emissivity also is written as a power series in the square root of the metal resistivity times the temperature is (3):

$$\varepsilon_H = 0.766(\rho T)^{1/2} - [0.309 - 0.0889 \ln(\rho T)]\rho T$$

$$- 0.0175(\rho T)^{3/2}. \tag{2}$$

The measured hemispherical emissivity of Pt versus temperature is fairly close to the values predicted by the Davisson-Weeks expression (Eq. 2), as demonstrated in Fig. 1. The data measured by Abbott (5) are represented by the dots and the calculated values from Eq. 2 are given by the dashed curve. The measured temperature dependent d.c. resistivity (6) which is used in Eq. 2 is represented by the lowest solid curve in Fig. 1. The other curves are described later in the text.

Both Eqs. 1 and 2 have been used extensively in the literature since they relate the total emissivity to one characteristic property of the metal, namely the d.c. electrical resistivity. The series expansions are described in some detail in the classic text by M. Jakob (7) and in the review by G. Rutgers (8). More recently, they are reviewed in Touloukian's "Thermophysical Properties of Matter", Vol. 7 (3).

In 1965, Parker and Abbott (9) noted that the assumption $\omega\tau << 1$, which had been used in all of the above derivations, was not completely valid throughout the frequency region in which thermal radiation was emitted. They calculated the total normal
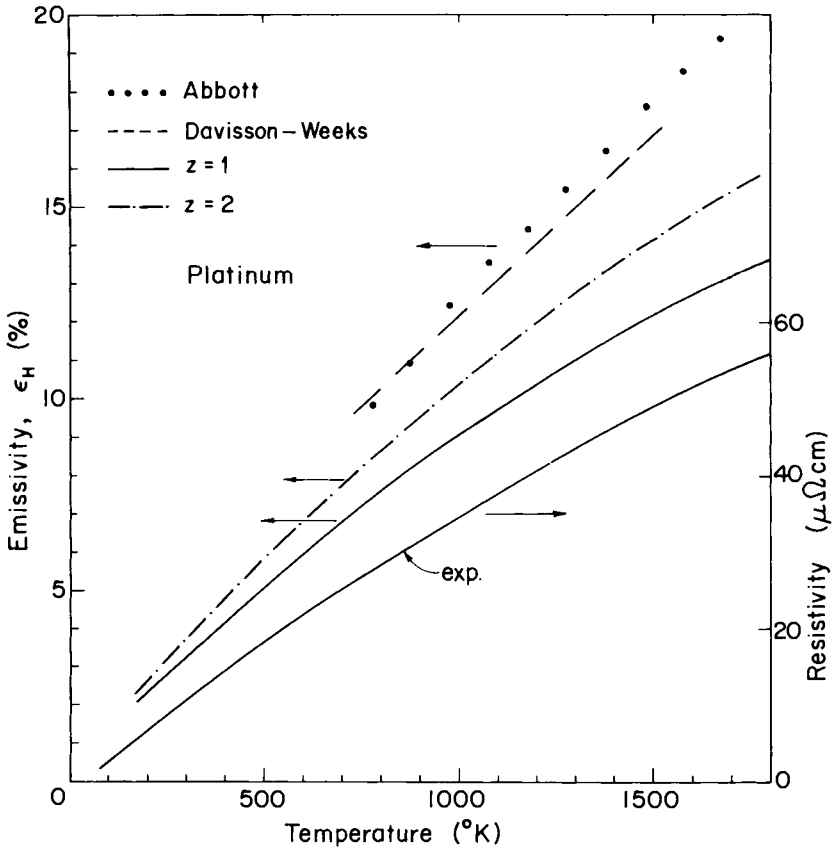
FIGURE 1.   *Temperature dependence of the hemispherical emis-*
sivity of platinum.   The data of Abbott (5) was represented by
the dotted curve and the Davisson-Weeks result by the dashed
curve.   The dot, dashed and solid curves describe the emissivity
within the framework of the Drude model as detailed in the text.
z indicates the number of free electrons per atom, assumed for
each case.   The temperature dependence of the d.c. resistivity,
in $\mu\Omega cm$, is also shown.

and total hemispherical emissivity by simulating the infrared

properties of the metal with a series of exponential functions

and then expanded the result as a power series in $(\rho T)^{1/2}$.   For

the total normal emissivity they found

$$\varepsilon_N = 0.578\, p_1\, (\rho T)^{1/2} - 0.178\, p_2\, (\rho T) + 0.0584\, p_3\, (\rho T)^{3/2} \qquad (3)$$

while for the total hemispherical emissivity they found

$$\varepsilon_H = q_1 (\rho T)^{1/2} - (q_2 - q_3\, \ln\, \rho T)\rho T + q_4 (\rho T)^{3/2} \qquad (4)$$

where p_1, p_2, p_3, q_1, q_2, q_3 and q_4 are nonlinear functions of the electron relaxation time.

Experimental studies of the temperature dependence of the emissivity of good conductors shows that Eqs. 1 and 2 give results which are much larger than experimentally measured values (10,11), while Eqs. 3 and 4 give results which are much smaller (1,10,11). Since the Drude free electron model describes the infrared properties of metals quite closely (12), then Eqs. 1-4 do not correctly reflect this model. One of our tasks is to understand this discrepancy.

Because of the excellent heat trapping ability of metals (small thermal emissivity), they are an essential component of the solar absorber in weakly focused solar thermal systems (13). The high temperature selective absorber materials (5) which have been tried to date are summarized in Table 1. Inspection of this table shows that fairly uniform solar absorptivities can be obtained with a variety of materials but that the hemispherical emissivities range from 0.07 to 0.50 at elevated temperatures. This large variation in the emissive properties of selective surfaces indicates that this physical parameter is not yet under control. Until 1978 one could not even determine a limit to the emissivity of a selective surface at a given temperature since the emissivity of a bare metal surface had not yet been properly characterized. One motivation, then, for obtaining accurate expressions for the emissivity of bare metals is to construct a solid foundation for the future determination of the minimum emissivities of the more intricate and complex surface configurations appropriate for selective radiators.

TABLE I.   High Temperature Selective Surfaces

Coating Material	Fabrication Technique	Solar Absorptivity $(T^{\circ}C)$	Hemispherical Emissivity $(T^{\circ}C)$	Sta-bility	Ref.
GE	Gas evap.	0.91	0.5(350)	-	15
Si(on AG)	CVD+AR coat	0.80	0.07(500)	500	16
PbS	Vac. Deposit.	0.98	0.3(300)	300	15
Al_2O_3+Ni	Evap. Composite	0.94	0.35(500)	600	17
Al_2O_3+Pt	Evap. Composite	0.94	0.3(500)	600	17
CrO_x-Cr	Electrodeposit	0.94	0.2(350)	-	18
Cr_2O_3+Co	Plasma spray	0.90(800)	0.5(800)	800	15
NiS-ZnS	Electrodeposit	0.88	0.16(300)	<220	15
WC+Co	Plasma spray	0.95(600)	0.4(600)	>800	15
Al_2O_3/Mo/ Al_2O_3	Vac. Evap.	0.85-0.95	0.11(500)	>500	19

II.   SPECTRAL EMISSIVITY

The infrared properties of good conductors are determined by intraband transitions. These optical transitions, which are characteristic of a free electron metal, involve the excitation of an electron from one state to another in the same band. Experimentally, it has been found that the free electron model is a good first approximation for most metals in the infrared. Drude (20) was first to treat a metal as a free electron gas and, although the logic behind the model has changed over the years, Drude's name is still associated with it. Here we shall only review the details required to obtain the spectral emissivity. For a more complete discussion, the reader is referred to Reference (21).

The metal is modeled by a uniform distribution of zn electrons/cm^3 where n is the number of atoms per cm^3 and z is the number of free electrons per atom and an equal and opposite

uniform positive charge density of infinite mass. Since the velocity of light is much larger than the electron velocity, only the long wavelength limit need be considered in describing the interaction of the electron polarization with electromagnetic radiation. A shift of zn electrons by a position vector $\vec{r}$ with respect to a positive background produces a polarization $\vec{p}$, where

$$\vec{p} = zne\vec{r}. \tag{5}$$

This polarization can be related to the applied electric field by means of Newton's second law, which for no damping of the electron motion is

$$nm\ddot{\vec{r}} = (zn)e\vec{E} \tag{6}$$

The polarization and E field must also satisfy Maxwell's equations, which can be written in terms of the wave equation:

$$-\nabla^2\vec{E} + \frac{1}{c^2}\frac{\partial^2\vec{E}}{\partial t^2} - \frac{4\pi}{c^2}\frac{\partial^2\vec{p}}{\partial t^2} = 0. \tag{7}$$

To solve this equation we try travelling waves

$$\vec{E} = \vec{E}_o e^{i(\vec{k}\cdot\vec{r} - \omega t)}, \qquad \vec{p} = \vec{p}_o e^{i(\vec{k}\cdot\vec{r} - \omega t)} \tag{8}$$

which give a solution when

$$k^2 = \frac{\omega^2}{c^2}\varepsilon_m \tag{9}$$

where

$$\varepsilon_m = 1 - \frac{\omega_p^2}{\omega^2} \tag{10}$$

with $\omega_p^2 = \frac{4\pi zne^2}{m}$. Although the dielectric function in Eq. 10 is real, the real and imaginary parts of the dielectric function are

not independent but are related by a Kramers-Kronig transform
(22). In general

$$\hat{\varepsilon}_m = \varepsilon_{m1} + i\varepsilon_{m2} \tag{11}$$

and if

$$\varepsilon_{m1} = 1 - \frac{\omega_p^2}{\omega^2} , \tag{12}$$

then for no damping

$$\omega\varepsilon_{m2} = \frac{\pi}{2} \omega_p^2 \; \delta(\omega) . \tag{13}$$

The frequency dependency of ε_{m1} and ε_{m2} are shown in Fig. 2(a).
Both curves are characterized by one parameter of the metal, ω_p,
which is directly related to the electron density.

An electromagnetic wave of frequence ω incident on a metal
responds differently depending on whether $\omega < \omega_p$ or $\omega > \omega_p$. For
$\omega < \omega_p$, k in the metal is imaginary and a propagating wave cannot
exist. Since absorption has been excluded, a wave incident on
the metal must be completely reflected. For $\omega > \omega_p$, k is real
and a wave can propagate in the metal, part of the incident
intensity is transmitted and part is reflected.

In general, scattering of the electrons in the metal cannot
be ignored. This effect is usually included by introducing a
scattering time, τ, between electron collisions. Newton's
second law now becomes

$$nm\ddot{\vec{r}} + \frac{nm\dot{\vec{r}}}{\tau} = zne\vec{E} . \tag{14}$$

The dielectric function which describes the wave in the metal
is
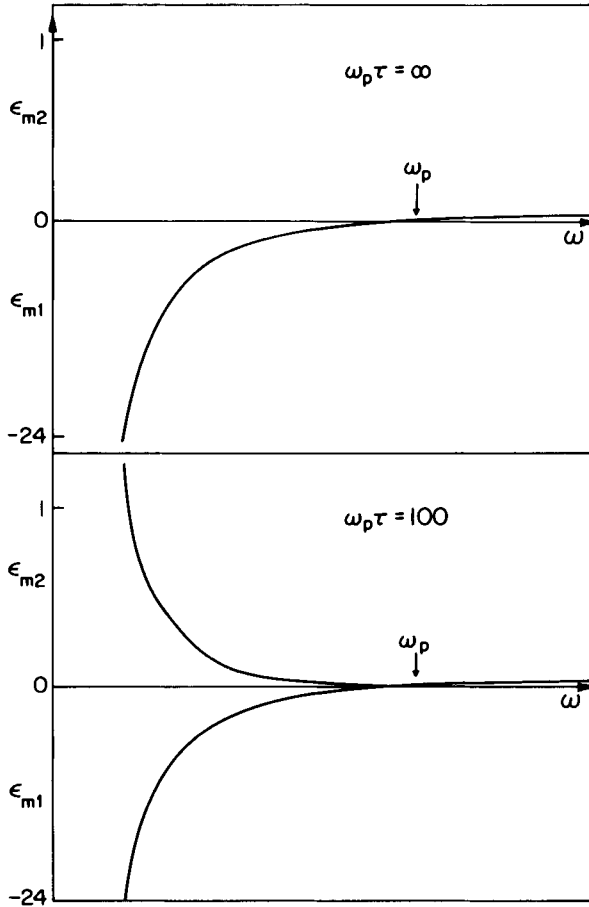
FIGURE 2. Frequency dependence of the dielectric function of a Drude electron model. Both the real and imaginary parts are shown. (a) No damping ($\omega_p\tau = \infty$). (b) Damping ($\omega_p\tau = 100$). This value is appropriate for a good conductor such as copper.

$$\hat{\varepsilon}_m = 1 - \frac{\omega_p^2}{\omega(\omega + \frac{i}{\tau})} \quad , \tag{15}$$

where

$$\varepsilon_{m1} = 1 - \frac{\omega_p^2 \tau^2}{1 + \omega^2\tau^2} \tag{16}$$

and

$$\varepsilon_{m2} = \frac{\omega_p^2 \tau^2}{\omega\tau(1 + \omega^2\tau^2)} \quad . \tag{17}$$

The frequency dependences of ε_{m1} and ε_{m2} are shown for $\omega_p\tau = 100$ in Fig. 2(b). Two parameters, ω_p and τ, completely determine the infrared response of the metal.

Equation (15) is the dielectric function of the Drude model for one kind of an electron. For more than one kind of free carrier the model is readily generalized:

$$\hat{\varepsilon}_m = 1 - \sum_j \frac{\omega_{pj}^2}{\omega(\omega + \frac{i}{\tau_j})} \quad . \tag{18}$$

Once the dielectric function has been found, the reflection coefficient of the electromagnetic wave can be obtained by matching boundary conditions on the $\vec{E}$ and $\vec{H}$ fields at the air-metal interface. This is usually done by writing the dielectric function in terms of the optical constants, n and κ, or in terms of the surface impedance, r and x,

$$\hat{\varepsilon}_m = (n + i\kappa)^2 = \frac{1}{(r - ix)^2} \tag{19}$$

then the boundary conditions give

$$R(\omega) = \frac{(n-1)^2 + \kappa^2}{(n+1)^2 + \kappa^2} = \frac{(1-r)^2 + x^2}{(1+r)^2 + x^2} \tag{20}$$

where both r and x are normalized with respect to the impedance of free space.

In the infrared region for metals thicker than $\sim$ 400 Å, the transmission coefficient of the electromagnetic wave can be set equal to zero. The spectral absorptivity, $A(\omega)$, which is the

fraction of incident energy adsorbed by the metal, then is

$$A(\omega) = \frac{4n}{(n + 1)^2 + \kappa^2} = \frac{4r}{(1 + r)^2 + x^2} \tag{21}$$

also in the infrared n, $\kappa \gg 1$ and r, $x \ll 1$ so

$$A(\omega) \cong \frac{4n}{n^2 + \kappa^2} = 4r \ . \tag{22}$$

By Kirchhoff's law, the spectral absorptivity is equal to the
spectral emissivity, so Eq. (21) also describes the normal spec-
tral emissivity of a Drude metal. Notice that in one represen-
tation both optical constants are required to obtain the spectral
emissivity, while in the second, only the surface resistance need
be calculated. As long as $\omega_p^2 \gg \omega^2$, Eq. (22) gives

$$A(\omega) = \varepsilon(\omega) = (\frac{2}{\omega_p \tau}) \ (2\omega\tau)^{1/2} \left[(1 + \omega^2\tau^2)^{1/2} - \omega\tau \right]^{1/2}. \tag{23}$$

At small frequencies where $\omega\tau \ll 1$, the degree of electron polar-
ization is controlled by τ (see Eq. 14) and the spectral emis-
sivity is

$$\varepsilon(\omega) = (\frac{2}{\omega_p \tau}) \ (2\omega\tau)^{1/2} \tag{24}$$

which is the Hagen–Rubens limit (1). At large frequencies,
$\omega\tau \gg 1$, the accelerating electric field reverses the electron
motion before a scattering event can occur so it is the inertia
of the electrons which limits the electron polarization in this
frequency range. The spectral emissivity approaches

$$\varepsilon(\omega) = \frac{2}{\omega_p \tau} \ , \tag{25}$$

which is the frequency independent Mott–Zener limit. Equation

(23) and its limiting value, Eqs. 24 and 25, all depend on temperature because τ depends on temperature. For temperatures above room temperature, τ is determined by the electron-phonon interaction.   Since the number of phonon scatterers in this temperature regime is proportional to $k_B T$,

$$\frac{1}{\tau} \sim T \ . \tag{26}$$

A more exact expression can be obtained from the d.c. resistivity. Because the electron density, or plasma frequency, is almost temperature independent, the temperature dependence of τ is directly reflected in the temperature dependence of the d.c. resistivity, ρ, where

$$\frac{1}{\tau(T)} = r = \frac{\omega_p^2}{4\pi} \rho(T) \tag{27}$$

where r is the relaxation frequency.

The normal spectral emissivity given by the Drude model with parameters appropriate to copper at 600°K is shown in Fig. 3. At the relaxation frequency, r, the emissivity is over 90% of its final, asymptotic value. Frequencies are given in cm^{-1} where $\omega = 2\pi c\tilde{\nu}$ so $\tilde{\nu} = \frac{1}{\lambda}$, where λ is the electromagnetic wavelength. As the metal temperature is increased, the frequency where $\omega\tau = 1$ moves to large frequencies in direct proportion to the temperature.

III.   TOTAL EMISSIVITY

The radiant spectral power emitted by a surface element of a black body in a given direction per unit frequency interval per unit solid angle is given by Planck's law
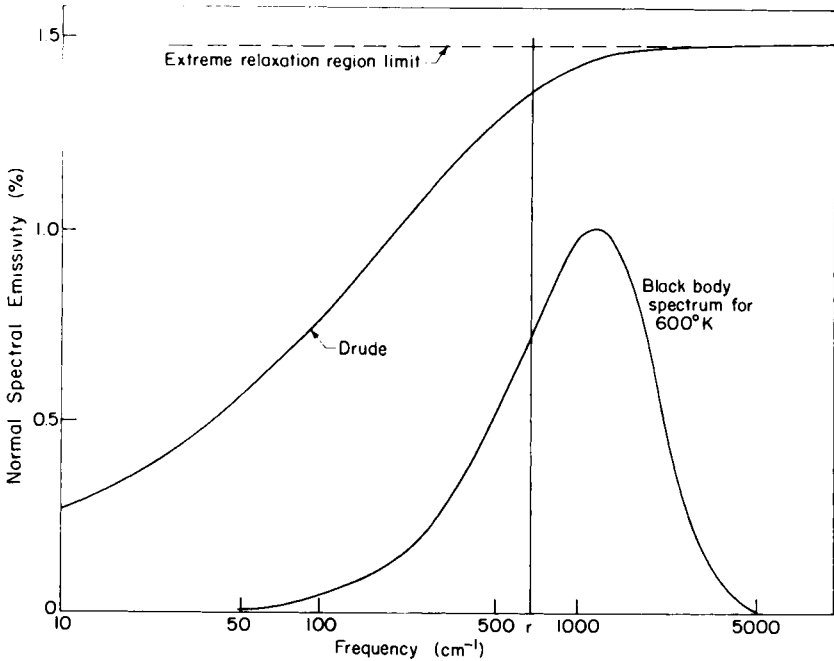
FIGURE 3. The normal spectral emissivity of the Drude free
electron model as a function of frequency. The parameters are
chosen to illustrate the infrared properties of copper at 600°K.
Also shown is the spectral distribution appropriate to a 600°K
black body radiator. The ordinate for this curve is not shown.

$$L_\omega = \frac{1}{\pi} \left(\frac{1}{2\pi c}\right)^2 \frac{\hbar \omega^3}{\left(\exp\left(\frac{\hbar \omega}{k_B T}\right) - 1\right)} \qquad (28)$$

where ω is the angular frequency, c the velocity of light in
vacuum, $\hbar$ is Planck's constant divided by 2π and k_B is Boltz-
mann's constant. The black body spectrum, L_ω, at a temperature
of 600°K, is shown in Fig. 3. The abscissa is the frequency axis
but the ordinate is an arbitrary scale. The area under the black
body spectrum at temperature T is proportional to T^4 and the
centroid frequency of the spectrum, $<\omega>$, is proportional to
temperature.

A.   *Normal*

The total normal emissivity is defined as the spectral emissivity weighted by the black body spectrum divided by the spectral emissivity of a black body weighted by the black body spectrum. By definition, the spectral emissivity of a black body is one, so

$$\varepsilon_N = \int_0^\infty \varepsilon(\omega) L_\omega \, d\omega \bigg/ \int_0^\infty L_\omega \, d\omega \ . \tag{29}$$

In general, the folding of the spectral emissivity together with the black body spectrum can only be carried out numerically; however, there are two limits where the integration can be done analytically. One of these limits is for $\omega\tau << 1$ (Eq. 24). Foote (2) derived Eq. 1 in this limit. The other limit (1) is $\omega\tau >> 1$ (Eq. 25). We must decide if either limit is appropriate for describing the total normal emissivity of good conductors.

Since the spectral emissivity is weighted by the black body spectrum, the appropriate emission frequency is that of the black body centroid:

$$<\tilde{\nu}> \ = \ 2.665 \ T(^\circ K) \ cm^{-1}. \tag{30}$$

In Fig. 3, the centroid frequency is at 1600 cm^{-1}, which is much larger than the relaxation frequency, r, of copper shown in the same figure. At least at 600°K, the $\omega\tau >> 1$ limit should be more appropriate than the $\omega\tau << 1$ limit. What about at higher temperatures? By Eq. 30, the black body centroid is proportional to temperature, but by Eq. 27 so is the relaxation frequency of the metal. Therefore, although both quantities change, they change in such a manner that their ratio remains fixed. If the $<\omega> \tau >> 1$ limit is satisfied at room temperature then it will remain satisfied at still larger temperatures.

The high frequency limit of the spectral emissivity (Eq. 25) is independent of frequency and can be factored out of the integral given in Eq. 29. The remaining integrals cancel so the total normal emissivity becomes

$$\varepsilon_N = \frac{2}{\omega_p \tau} \qquad \text{for} \quad <\omega> \tau > 1 \ . \tag{31}$$

In terms of the d.c. resistivity, this expression becomes

$$\varepsilon_N = \frac{\omega_p}{2\pi} \rho \qquad \text{for} \quad <\omega> \tau > 1 \ . \tag{32}$$

This expression should give an upper limit to the total normal emissivity because the frequency dependent spectral emissivity shown in Fig. 3 has been replaced by its high frequency limit. For good conductors, such as Cu or Al, Eq. 32, not Eq. 1, gives the Drude value for the total normal emissivity.

B.   Hemispherical

The total hemispherical emissivity of a metal is defined as the total power radiated by the metal into a hemisphere compared to the total power radiated by a black body into the same solid angle (3), so

$$\varepsilon_H = \int_0^\infty \int_0^{\pi/2} \varepsilon(\omega,\theta) \cos\theta \cdot \sin\theta \ d\theta \ L_\omega \ d\omega \Bigg/ 1/2 \int_0^\infty L_\omega \ d\omega \tag{33}$$

where θ is the polar angle measured with respect to the metal normal, the cosine θ describes the projected area radiating at that angle and

$$\varepsilon(\omega,\theta) = 1/2[\varepsilon_{TM}(\omega,\theta) + \varepsilon_{TE}(\omega,\theta)] \tag{34}$$

is the frequency and angular dependent emissivity for the two

polarizations of the radiation. The azimuthal integral is the
same in the numerator and denominator of Eq. 33 and cancels.
$\varepsilon_{TE}(\omega,\theta)$ is the spectral emissivity for plane polarized radiation
with the plane of polarization normal to the plane of incidence
(the electric field is parallel to the metal plane, usually called
transverse electric). For metals, $\varepsilon_{TE}(\omega,\theta) = \varepsilon(\omega) \cos\theta$, so by
Eq. 33,

$$\frac{\varepsilon_{H(TE)}}{2} \cong < \cos^2\theta > \varepsilon_N = \frac{1}{3}\varepsilon_N.$$

For the other polarization the electric field is perpendicu-
lar to the metal plane and the emissivity is $\varepsilon_{TM}(\omega,\theta)$. This
polarization has an anomalous angular dependence because at some
angle, Brewsters angle, the emissivity goes from the small value
characteristic of a metal to 1. For good conductors, this angle
occurs near $90°$. In this limit, the emissivity is

$$\varepsilon_{TM}(\omega,\theta) \cong \varepsilon(\omega)(\cos\theta)^{-1}$$

so

$$\frac{\varepsilon_{H(TM)}}{2} \cong <1> \varepsilon_N = \varepsilon_N. \tag{35}$$

Because of the smaller effective area radiating at large angles,
the total radiated power for TM waves at a given angle is inde-
pendent of angle. The total hemispherical emissivity is

$$\varepsilon_H = \frac{\varepsilon_{H(TM)} + \varepsilon_{H(TE)}}{2} \cong \frac{4}{3}\varepsilon_N. \tag{36}$$

Davisson-Weeks (4) derived Eq. 2 in the limit $\omega\tau << 1$. It is
now evident that $<\omega>\tau >> 1$ is more appropriate for good conduc-
tors. From Eqs. 32 and 36, the Drude value for the total hemi-
spherical emissivity is

$$\varepsilon_H \cong \frac{2}{3\pi} \omega_p \rho .$$

(37)

This result should be compared with Eq. 2.

Whereas Eqs. 1 and 2 have only one parameter, the d.c. resistivity, Eqs. 32 and 37 have two, the d.c. resistivity and the plasms frequency or electron density. The second parameter may also be derived from a non-optical measurement by making use of the Hall constant (23):

$$R_H = - \frac{1}{(zn)ec}$$

(38)

so

$$\varepsilon_N \cong \frac{2.49 \times 10^{-8}}{|R_H|^{1/2}} \rho_\mu$$

(39)

and

$$\varepsilon_H = \frac{4}{3} \varepsilon_N$$

(40)

where $|R_H|$ is measured in m^3/coulomb and ρ_μ in $\mu\Omega$cm. For most metals $|R_H|$ and ρ_μ can be looked up in Tables (6).

Equations 39 and 40 have been derived from the same free electron model that was used to obtain Eqs. 1 and 2. For good conductors with $\rho \sim T$, both sets of equations predict a linear temperature dependence of the total normal and hemispherical emissivity. The main difference between the two sets of equations is that the coefficients of Eqs. 1 and 2 are much larger than those of Eqs. 39 and 40 (for copper, Eq. 1 is $\sim$ 2.6 (Eq. 39)). But from our derivation, both Eqs. 39 and 40 represent upper limits to the total emissivities, hence for good conductors Eqs. 1 and 2 should be poor approximations.

C.   Model Corrections

Equations 1 and 2 do give values of the total emissivities which are larger than experimental values (10,11) but Eqs. 39 and 40 give values which are smaller. Since these latter two equations were derived as upper limits to the emissivities of the Drude model, this model as it stands does not provide an accurate description of the emissivity of a good conductor.

To correctly describe the infrared emissivity of metals one must take account of the properties of metal surfaces. Even if the electrons do not scatter in the bulk they do scatter diffusely from the surface (24) (remember, the conduction electron wavelength is a few atomic spacings). For these electrons there is one collision with the surface in the time needed by the electron to cross the electromagnetic skin depth ($\delta = \dfrac{c}{\omega_p}$ for $\omega\tau >> 1$) to the surface and back again. Thus, the surface scattering time, τ_s, is

$$\tau_s \doteq \frac{2c}{\omega_p} \, / \, v_F$$

so

$$\varepsilon_{Ns} = \frac{2}{\omega_p \tau_s} = v_F/c \; .$$

A more accurate calculation of the spectral emissivity associated with diffuse scattering gives (24,25)

$$\varepsilon_{Ns} = 3 \, v_F/4c \; . \tag{41}$$

Next we assume that bulk and surface scattering processes are independent so

$$\tau_e^{-1} = \tau_b^{-1} + \tau_s^{-1} \; .$$

The total normal surface scattering including diffuse surface scattering is then

$$\varepsilon_N = \frac{2}{\omega_p \tau_e} = \frac{2}{\omega_p \tau} + \frac{3v_F}{4c} \; . \tag{42}$$

For the free electron model both the Fermi velocity and the Hall coefficient are related to the electron density, so Eq. 42 can be expressed in terms of ρ_μ and R_H:

$$\varepsilon_N = \frac{2.49 \times 10^{-8}}{|R_H|^{1/2}} \rho_\mu + \frac{3.55 \times 10^{-6}}{|R_H|^{1/3}} \tag{43}$$

where again

$$\varepsilon_H = \frac{4}{3} \varepsilon_N . \tag{44}$$

The values obtained from Eqs. 43 and 44 are in good agreement with recent experimental studies on copper and aluminum (10,11). In Fig. 4 we show the experimental temperature dependence of the hemispherical emissivity of copper. The temperature dependence according to Eqs. 43 and 44 is given by the solid curve. The agreement between theory and experiment is quite satisfactory for free electron-like metals.

For the transition elements such as tungsten $\omega < \tau > \sim 1$ and the total emissivity can only be calculated by a numerical integration (1,26). In addition, one needs to know not only the temperature dependence of the free electron properties, but also the temperature dependence of the infrared properties of the interband transitions. As this process has not been studied in detail, we cannot incorporate it into our emissivity calculation. By ignoring this physical process, the emissivity calculated from Eq. 44 will be smaller than the true emissivity. As an example, we compare the experimentally measured (27) emissivity of tungsten
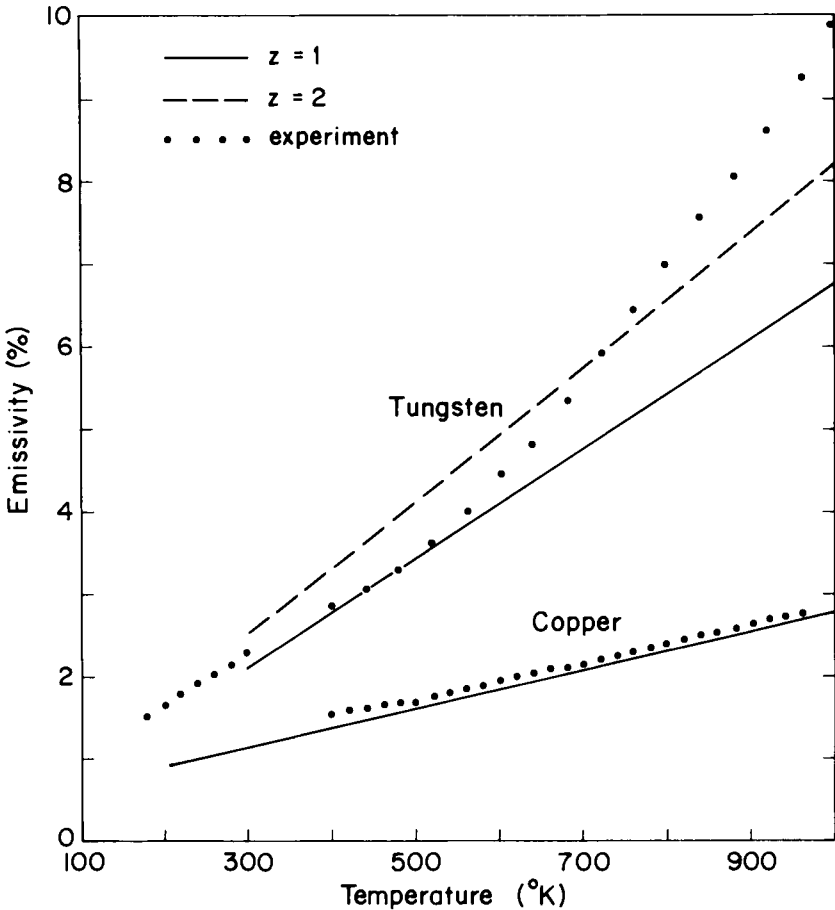
FIGURE 4. Temperature dependence of the hemispherical emis-
sivity of copper and tungsten. The solid circles show the exper-
imental data (10,27). The solid lines show the calculated emis-
sivities for the Drude model with one electron per atom (z = 1)
and the dashed line, the emissivity for two electrons per atom
(z = 2).

with the values calculated from the d.c. conductivity (6). In

Fig. 4 the experimental data for tungsten are represented by the

solid circles. The solid line is calculated from the d.c. resis-

tivity, with an assumed one free electron per atom, while the

dashed curve shows the same calculation for two free electrons

per atom. Both for copper and for tungsten, the one free elec-
tron per atom model provides a better fit to the data. At
temperatures above 600°K, (corresponding to frequencies above
1600 cm^{-1}) interband effects become important for tungsten and
the emissivity becomes larger than that given by the Drude model.

IV. CONCLUSIONS

For metals which are not particularly good conductors, the
derivation of the emissivity must start with Eq. 21 not Eq. 22,
which we have used here and it is no longer possible to obtain a
simple analytic solution for the emissivity. To see how well Eq.
43 describes the emissivity of all metals, we have performed
exact calculations of both the total normal and hemispherical
emissivities and divided these numerical values by the values
obtained from Eq. 43. The comparison is shown in Fig. 5. For
the total normal emissivity the difference between the numerical
calculation and Eq. 43 is less than 1% for ρ_μ < 10 μΩcm and less
than 10% for ρ_μ < 100 μΩcm. Although the error is somewhat
larger for the hemispherical emissivity calculation, it is per-
haps worth a ten or twenty percent error just to avoid the
numerical calculations involved.

For completeness we show in Fig. 6 for a number of elements
the numerically calculated hemispherical emissivity versus the
metal resistivity. The hemispherical emissivity ranges from 1%
for a good conductor to over 20% for the highest resistivity
metals. In every case except aluminum (3) and beryllium (2) the
metal is assumed to have one free electron per atom. The elec-
tron densities were obtained from Mott and Jones (28). This
assumption gives the smallest reasonable emissivity for the metal
and these curves represent lower bounds to the true hemispherical
emissivities.

This chapter has been devoted to the emissivity of pure
metals since the elements themselves provide the lowest thermal

emissivities. Metal alloys which have large d.c. resistivities
due to disorder-induced electron scattering should have large
emissivities. If the scattering is made large enough so that
$<\omega>\tau<<1$ and the centroid of the black body spectrum is at a
frequency much less than the relaxation frequency, then the
Hagen-Rubens relation should provide a reasonable estimate of
the spectral emissivity and the Foote (2) and Davisson-Weeks (4)
equation follows. As the temperature is increased, however, the
black body centroid increases in frequency while the relaxation
time remains temperature-independent, and at some large tempera-
ture the material may still obey $<\omega>\tau>1$ since τ is temperature
independent for disorder scattering.

An important alloy for solar applications is stainless steel
304. Recently, Roger et al. (29) have measured the temperature
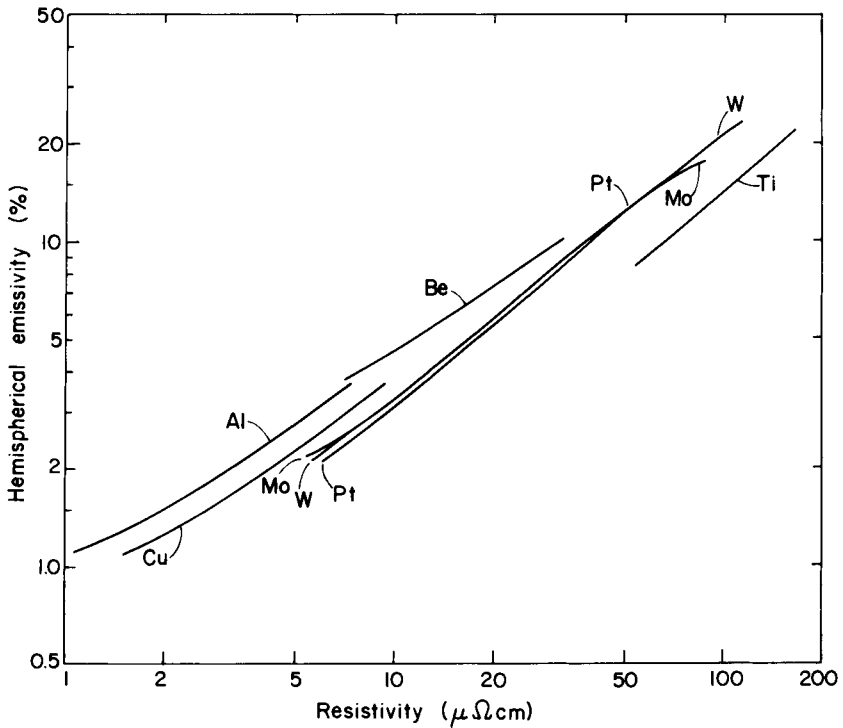
FIGURE 6. The total hemispherical emissivity as a function
of d.c. resistivity for a number of elements. These curves are
obtained from exact numerical calculations of the Drude model
and define lower bounds for real metals. A small error discov-
ered in Fig. 11 of Reference 1 has been corrected here.

dependence of its hemispherical emissivity from 340 to 1100°K.

In Fig. 7 we compare these experimental data with calculated

values obtained from various models. The Davisson-Weeks Equation

(Eq. 2) gives results which are larger than the experimental

values over the entire temperature range indicating that the

Hagen-Rubens relation is not strictly valid in this temperature

regime and indeed as expected at high temperatures the disagree-

ment is larger than at low temperatures. By fitting the Parker-

Abbott Equation (Eq. 4) to the data at 400°K, reasonably good

Stainless Steel 304
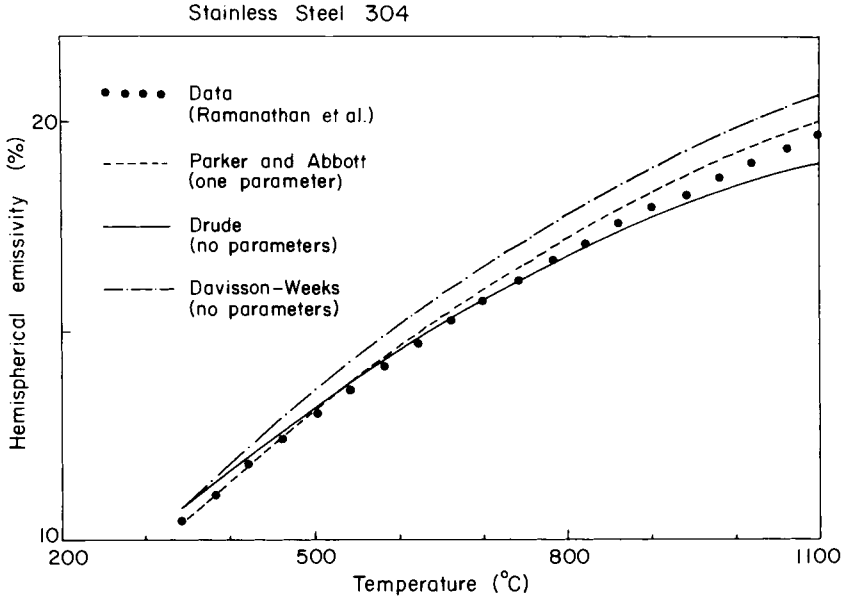
FIGURE 7.   *Temperature dependence of the hemispherical emis-*
sivity of stainless steel 304.   The solid dots show the experi-
mental data points of Ramanathan et al. (29).   The dashed curve
is calculated from Eq. 4 in the text with a one parameter fit to
the data.   The solid curve gives an exact Drude model calculation
as described in Reference 1.   The dot-dash curve is calculated
from Eq. 2 in the text.   All of these models use the same values
of the temperature dependent d.c. resistivity.

agreement is obtained over the entire range.   The solid curve in

Fig. 7 represents the Drude model as described in this paper.

The same temperature dependent d.c. resistivity is used as in

the other models but in addition the average of the electron

densities of the metal components is used here.   No free param-

eters are available and the agreement is quite satisfactory over

the entire temperature range.

To conclude this study of the emissivity of metals, let us

reexamine Fig. 1.   Data shown there on the hemispherical emis-

sivity of platinum was found to be in good agreement with the

Davisson-Weeks expression.   In this same figure, exact

calculations with the Drude model developed in the text for one or two electrons per atom are also shown. As expected, neither of these calculated cruves is large enough to fit the experimental data since the Drude model calculation does not include the emissivity contribution from interband transitions and as such represents a lower bound to the measured emissivity. Of course, this same comment applied to the Davisson-Weeks expression. The apparent agreement of Eq. 2 with the experimental data occurs for two reasons: 1) because an incorrect limit was used to describe the spectral emissivity of the metal, and 2) because the influence of surface scattering was not included. Now that we have obtained correct minimum values for the emissivity of bare metals, it should be possible to extend this analysis to find the minimum emissivity of more complex selective surfaces.

REFERENCES

1.   Sievers, A.J., *J. Opt. Soc. Amer. 68,* 1505 (1978).

2.   Foote, P.D., *Bull. Natl. Bur. Stand. 11,* 607 (1914-15).

3.   "Thermophysical Properties of Matter" (Y.S. Touloukian, ed.), Vol. 7, p. 24a. Plenum Press, New York, (1970).

4.   Davisson, C., and Weeks, J.R., *J. Opt. Soc. Am. 8,* 581 (1924).

5.   Abbott, G.L. in "Measurement of Thermal Radiation Properties of Solids",(J.C. Richmond, ed.), p. 293. NASA SP-31, (1963).

6.   "American Institute of Physics Handbook", 3rd Edition, (D.E. Gray, ed.), p. 4-13, McGraw-Hill Book Co., New York, (1972).

7.   Jakob, M., "Heat Transfer", p. 51. New York, Wiley, (1949).

8.   Rutgers, G.A.W. in "Handbuch der Physik", (S. Flugge, ed.), Vol. 26, p. 154. Berlin, Springer-Verlag, (1958).

9.   Parker, W.J., and Abbott, G.C., in "Symposium on Thermal Radiation of Solids", (S. Katzoff, ed.), p. 11, NASA SP-55, (1965).

10. Ramanathan, K.G., Yen, S.H. and Estalote, E.A., *Appl. Opt.* *16*, 2810 (1977).

11. Smalley, R.,and Sievers, A.J., *J. Opt. Soc. Am. 68*, 1516 (1978).

12. Bennett, H.E., and Bennett, J.M. in "Proceedings of the International Colloquium of Optical Properties", (F. Abeles, ed.), p. 175. North-Holland, Amsterdam, (1966). Bennett, H.E., Bennett, J.M., Ashley, E.J., and Motyka, R.J., *Phys. Rev. 165*, 775 (1968).

13. Seraphin, B.O. in "Solar Energy Conversion--Solid State Physics Aspects", (B.O. Seraphin, ed.), ("Topics in Applied Physics", Vol. 31), Springer-Verlag, Berlin, (1979).

14. Lampert, C.M., *Solar Energy Materials 1*, 319 (1979).

15. Mattox, D.M., et al., Sandia Laboratories, Albuquerque, NM, SAND 75-0361 (July 1975). Also see Mattox, D.M., *J. Vac. Sci. and Technol. 13*, 127 (1976).

16. Seraphin, B.O., "Proc. Symp. on the Materials Science Aspects of Thin Film Systems for Solar Energy Conversion", Tucson, AZ, (July 1974). Also see Ref. 13.

17. Craighead, H.G., Bartynski, R., Buhrman, R.A., Wojcik, L., and Sievers, A.J., *Solar Energy Materials 1*, 105 (1979).

18. McDonald, G.E., and Curtis, H.B., Lewis Research Center, Cleveland, OH, NASA TMX-71731, (May 1975).

19. Peterson, R.E., and Ramsey, J.W., *J. Vac. Sci. Tech. 12*, 471 (1975).

20. Drude, P.K.L., "Theory of Optics", Dover, New York (1959).

21. Wooten, F., "Optical Properties of Solids", Chapter 4. Academic Press, New York (1972).

22. Kittel, C., "Elementary Statistical Physics", p. 207. New York, Wiley (1958).

23. Trotter, D.M., and Sievers, A.J., *Applied Optics*, (to be published 1980).

24. Holstein, T., *Phys. Rev. 88*, 1427 (1952).

25. Dingle, R.B., *Physica 19*, 311 (1953).

26. Sievers, A.J., *Solar Energy Materials 1*, 431 (1979)

27. Verret, D.P., Ramanathan, K.G., *J. Opt. Soc. Am. 68*, 1167 (1978).

28. Mott, N.F., and Jones, H., "The Theory of the Properties of Metals and Alloys", p. 268. Dover, New York, (1936).

29. Roger, C.R., Yen, S.H., and Ramanathan, K.G., *J. Opt. Soc. Amer. 69*, 1384 (1979).

CHAPTER 8

FUNDAMENTAL LIMITS TO THE SPECTRAL
SELECTIVITY OF COMPOSITE MATERIALS [1]

A.J. Sievers

Laboratory of Atomic and Solid State Physics
and
Materials Science Center
Cornell University
Ithaca, New York

I. INTRODUCTION

A variety of selective surfaces have been proposed and fab-
ricated for solar thermal applications (1,2). Most of these
surfaces are constructed as absorber-reflector tandems. Either
the solar radiation is transmitted through a heat mirror to a
nonselective absorber or the solar radiation is absorbed by a
visibly dark mirror which has a small thermal emissivity. For
both proposed systems the end result is the same: the solar
radiation is absorbed and the thermal reradiation is suppressed.
Since the construction of these two types of spectrally selective
surfaces is very different it is important to determine which
approach has more potential. At first glance, this comparison
would appear to be a formidable task. A number of heat mirror
candidates are available (2). Each makes use of smooth or
textured metallic or semiconducting films to obtain the large

transmissivity in the visible and the large reflectivity in the
infrared. A paramount advantage to this selective reflector-
absorber tandem is that the selective surface remains at room
temperature. If the solar transmissivity could be made large
enough, this approach would be preferred since material stability
problems would be greatly reduced.

An even larger number of candidates are available for dark
mirror applications. Composite media, interference films and
semiconducting films have all been proposed (1,2) for the solar
absorbing layer which is in direct contact with the infrared
reflecting mirror. The main advantage of this construction is
that the solar absorptivity can be made very large but the asso-
ciated disadvantage is that the selective surface must run at an
elevated temperature. Because the thermal emissivity is tempera-
ture dependent, the optical properties of this absorber-reflector
tandem measured at room temperature will not provide the correct
information for a realistic assessment of the system's efficiency
at operating temperature.

The approach which is taken in this chapter in order to
assess the potential of each system is to assume in both cases
the best configuration consistent with physical constraints.
Although conducting micromeshes have been proposed to increase
the transmissivity of the heat mirror it is shown in the next
section that the intrinsic absorption produced by the texture and
finite conductivity of the mexh severely limits their usefulness.
For semiconducting meshes, it is shown that a 90% transmissivity
in the solar region is not compatible with a 90% reflectivity in
the thermal reradiation region while for aluminum and magnesium
meshes with submicron wire diameters, some potential improvement
in selectivity can be obtained over that found with metallic
films.

The procedure for obtaining the limits to the spectral selec-
tivity of dark mirrors is somewhat more intricate since the
temperature dependent properties must be included. Starting from

the results of the previous chapter, where we determined the smallest physically allowable emissivity for a given d.c. resistivity we go on to catalogue the different emissivity contributions as a solar absorber is constructed on the metal. By summing all the different contributions, we find the smallest ε_H due to intrinsic physical processes. No matter what composite film-metal substrate combination is assembled, our results provide definite lower limits to the hemispherical emissivity. These limits are determined by the temperature dependent properties of the metal, the influence of the index of refraction associated with the composite film and the effect of thermal broadening on the solar absorptivity profile. In the last section we compare our findings for heat mirrors and dark mirrors and conclude that dark mirrors have the most potential for intermediate temperature weakly focus solar thermal systems.

II. TRANSPARENT HEAT MIRRORS

Tin oxide in the form of a thin film on glass has been used for a number of years as a transparent electrode or a transparent heater (4). Such films can be applied by spraying a mixture of tin chloride with ethanol onto a glass substrate which has been heated to 400°C. The tin chloride is transformed into the semi-conducting tin oxide.

A tin oxide coating reduces the infrared emissivity of window glass because of the large free carrier density in the semiconducting coating: however, the carrier density is still small enough that the plasma frequency occurs below the solar spectrum. Carrier concentrations of $10^{20}/cm^3$ have been achieved by adding some antimony chloride or HF to the tin chloride solution before spraying (6). The infrared emissivity is reduced to about 0.2. An even smaller emissivity, $\varepsilon \sim 0.1$ has been obtained for indium oxide doped with tin (7). Although these coatings may play an important role in increasing the thermal insulation of window

glass (3,5), their usefulness for the intermediate temperature heat mirror configuration is severely limited by the low visible transmissivity. The coatings have a large index of refraction, hence a large reflectivity, due to low lying interband transi- tions in the ultraviolet region of the spectrum. To increase the transmissivity of these heat mirrors, several investigators (7,8) have proposed that the continuous film be replaced by a conduc- ting micromesh. Both metallic and semiconducting meshes have been suggested. Such meshes already have been used successfully as transmission filters in the far infrared and microwave region (10).

An end view of the heat mirror selective configuration for a tubular geometry is shown in Fig. 1. The mesh heat mirror is attached to the inside of a glass housing enclosing a nonselec- tive black absorber. If the black absorber is approximated by a cylinder of radius r_a inside a mesh coated cylinder of radius r_m then the effective emissivity is (11):

$$\varepsilon_{eff} = \left[\frac{1}{\varepsilon_a} + \frac{r_a}{r_m} \left(\frac{1}{\varepsilon_m} - 1 \right) \right]^{-1} \tag{1}$$

where ε_a and ε_m are the emissivities of the absorber and the wire mesh, respectively. For this equation to hold, the radiation is assumed to scatter diffusely from either the absorber, the mesh or both. If the absorber is much smaller than the mesh shell, $r_a/r_m << 1$, ε_{eff} is controlled by ε_a; conversely, if $r_a/r_m \sim 1$, the emissivity is determined by ε_m. Only in the second limit is the heat mirror concept effective. Let us determine ε_m for a mesh.

The three lengths required to define a mesh are given in Figs. 2a and 2b. The mesh spacial period d is assumed to be square. For the infrared, the wavelength of the radiation, λ, is much larger than d so the mesh acts like a reflecting film. The
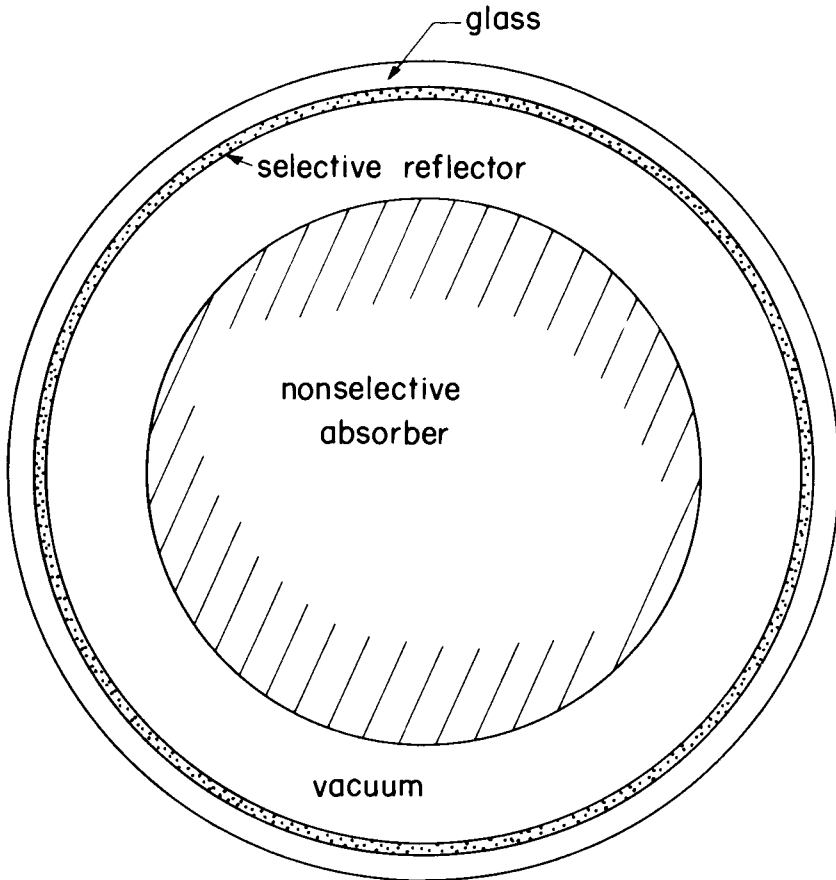
FIGURE 1.   *End view of a heat mirror--non selective absorber*
tandem.   The assembly has cylindrical symmetry.   The conducting
mesh is attached to the inside of the evacuatable glass contain-
er.

large reflectivity of both metal and semiconducting meshes is a

consequence of shielding currents induced in the grid wires

parallel to the incident infrared electric field.

To simplify the estimate of the emissivity of the mesh (12)

in this long wavelength region, consider the problem of the

parallel wire grid (not a mesh), with the infrared wave normally

incident, the wire grids and infrared electric field perpendicular

to the figure and the infrared magnetic field, B_i in the plane
of the figure as shown in Fig. 2b. The grid wires are taken
thick compared with the electromagnetic skin depth, $(t > \delta)$, a
necessary requirement to obatin a reflectivity near unity.
Further, assume that the grid is characterized by transmission
and absorption coefficients, T and A, near zero and a reflection
coefficient, R, near one, since that is the only situation of
interest. The magnetic field near the grid can be characterized
by the amplitude of the incident and reflected fields, $B_i \overset{\sim}{\sim} B_r$,
since T = 0 and R = 1, as shown in Fig. 2b. The shielding
current is distributed within a skin depth of the surface of the
wire and for $d >> a$, the case of interest here, the current is
uniformly distributed around the wire. If we call this sheet
current density K_g, then the energy dissipation in the wire (per
unit length) around the perimeter is proportional to K_g^2 so

$$W_g \propto pK_g^2 \tag{2}$$

where p is the wire perimeter. The induced magnetic field is
proportional to the sheet current density around the perimeter so

$$B_r = B_i \propto pK_g . \tag{3}$$

For the uniform film, the surface current density, K_f, is
uniform and appears only on the incident face as shown in Fig.
2c. The energy dissipated in the surface (per unit length) is
proportional to K_f^2 so

$$W_f \propto dK_f^2 . \tag{4}$$

Again, the induced magnetic field is proportional to K_f itself
so

$$B_r = B_i \propto dK_g . \tag{5}$$
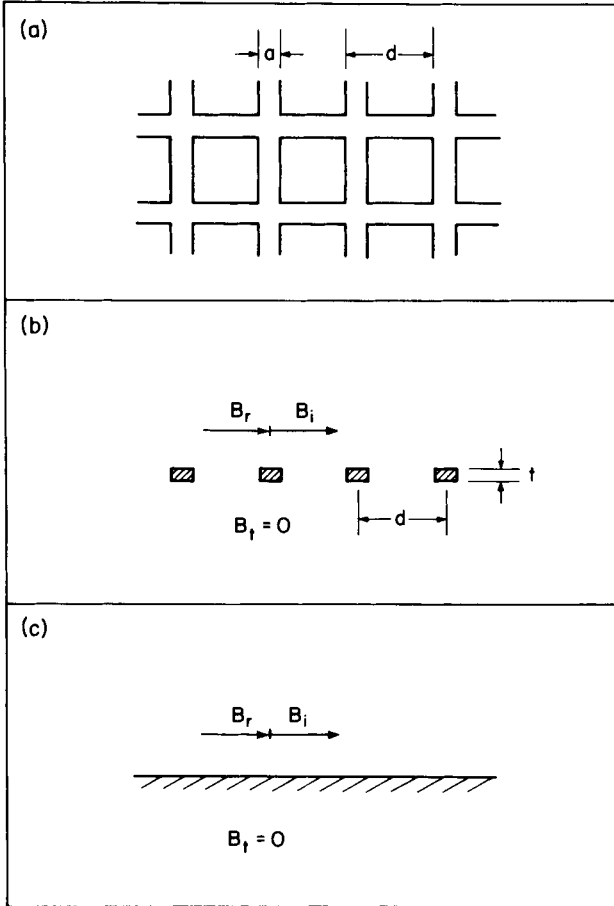
FIGURE 2.   (a) Top view of a conducting mesh.   (b) Geometri-
cal configuration of the parallel wire grid for the long wave-
length absorptivity calculation (end view).   The TM wave is
normally incident, the wire grids and the infrared electric
field are perpendicular to the figure and the infrared magnetic
field, B_i is in the plane of the figure as shown.   (c) Geometri-
cal configuration of the uniform conducting film.   The fields
are the same as for 2(b).

The absorptivity of the grid is conveniently expressed in terms of that of the film, giving

$$\frac{A_g}{A_f} = \frac{W_g}{W_f} \sim (\frac{d}{p}) \; . \tag{6}$$

Taking further for convenience, $t << a$, Eq. (6) becomes

$$\frac{A_g}{A_f} \sim \frac{d}{2a} \tag{7}$$

so the grid absorptivity (or emissivity) is increased over that of the uniform film of the same material by one half of the geometric projection of the parallel wire grid or by roughly the full projection of the corresponding square mesh.

For the indium oxide doped with tin semiconducting film the homogeneous film absorptivity (3) at 10 μm wavelength is 9%. By Eq. (7) the long wavelength absorptivity is increased by a factor ≥ 1.5 when the film is converted to a particular mesh size. Experimentally, Fan (3) has found that the absorptivity of this mesh is increased by a factor of 1.9. It isclear from the theoretical calculations and from the experimental results that semiconducting meshes cannot provide the desired selectivity.

The theoretical spectral characteristics of perfectly conducting opaque meshes have already been treated in some detail (13). Although no transmission occurs for $\lambda >> d$, for $\lambda < d$ the transmission rapidly approaches that expected from geometric objects, i.e., the fraction of mesh width that is open (13). In this limit, the solar transmissivity is approximately $(1 - a/d)^2$. Thus, to obtain a 90% transmissivity through a thin aluminum mesh in the short wavelength limit, the absorptivity in the long wavelength limit (inductive shielding) limit by Eq. (7) must be 10 times the absorptivity of the uniform film. The 98.5% infrared reflectivity of an aluminum film implies only an 85% infrared

reflectivity of a thin mesh with a 90% geometrical aperture; how-
ever, for a square wire (a = t) the infrared reflectivity would
increase to 92%. In principle, the large absorptivity associated
with the mesh can be reduced still more by using wire with large
t/a ratios, although increasing t/a to much beyond unity decreases
the geometrical aperture of the system for light of non-normal
incidence. In any event, the limits are clear.

III. DARK MIRRORS

A. *Dark Metal*

    An end view of the dark mirror selective configuration for a
tubular geometry is shown in Fig. 3. The dark mirror, which con-
sists of a solar absorbing layer in direct contact with an
infrared mirror, must, because of its design, operate at elevated
temperatures. The temperature dependence of the optical proper-
ties plays an important role in determining the system perform-
ance. In this section, we indicate how one can determine the
smallest possible temperature dependent emissivity of these
selective dark mirrors.

    To simulate the temperature dependent optical properties of
an ideal dark mirror, we coat a metal with a hypothetical material
which does not change the infrared emissivity of the metal but
causes the absorptivity of the composite structure to be 1
throughout the solar spectrum. We choose a steplike function
for this additional absorptivity but one which has a width of a
few $k_B T$ where k_B is Boltzmann's constant and T is the temperature
in °K. The high frequency tail of the black body thermal rerad-
iation spectrum will overlap the low frequency end of the blurred
step function absorptivity and produce a contribution to the
emissivity of the composite structure. The total emissivity is
the sum of the total emissivity of the metal plus the total
emissivity of the coating. The temperature dependences of these
two emissivity components are shown in Fig. 4. The open circles
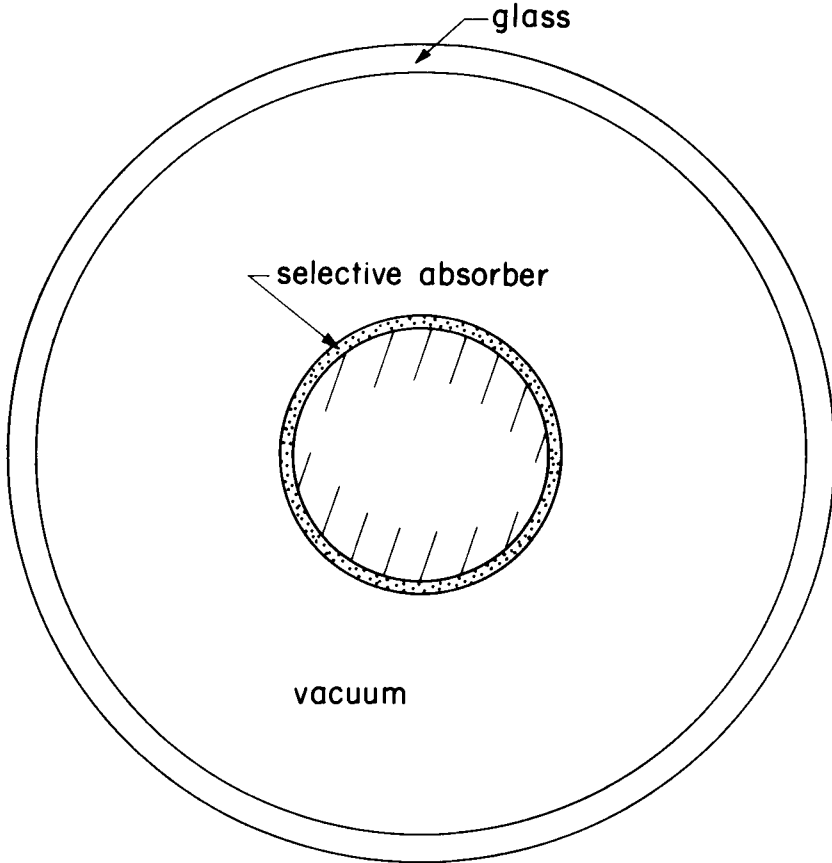
FIGURE 3. End view of a dark mirror absorber--reflector tandem. The assembly has cylindrical symmetry. The selective absorber is attached to the working fluid. The selective absorber diameter can be much smaller than the envelope diameter in contrast with the heat mirror assembly shown in Figure 1.

and the crosses give the experimental values of the total hemi-spherical emissivities of copper and tungsten, respectively. The solid lines show the calculated values for copper, tungsten and platinum, obtained from the previous chapter. The dashed curves in Fig. 4 portray the contribution to the total emissivity from the blurred absorptivity edge of the coating for different cutoff frequencies. To absorb most of the solar spectrum, the cutoff
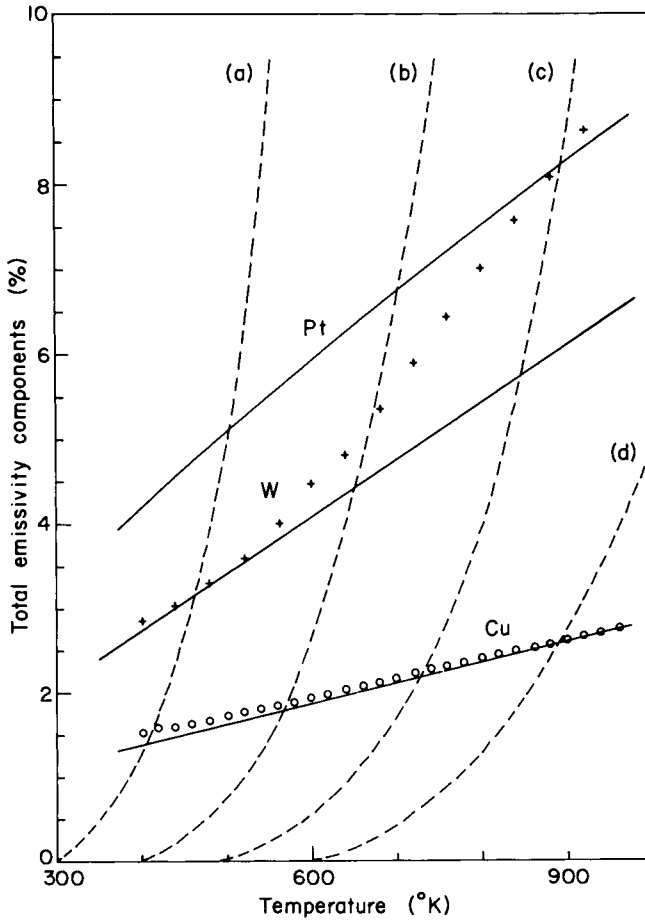
FIGURE 4.   *Total emissivity components for an ideal selective
surface vs. temperature.   The experimentally measured hemispher-
ical emissivities are represented by discrete values: copper,
..., and for tungsten, xxx.   The calculated hemispherical emis-
sivity curves from the previous chapter are represented by solid
lines.   The dashed curves indicate the contribution to the
emissivity from the thermally broadened absorption edge in the
solar spectrum.   The edge frequency is a) 3000 cm⁻¹, b) 4000 cm⁻¹,
c) 5000 cm⁻¹, and d) 6000 cm⁻¹.   The spectral shape of the
assumed solar absorptivity is described in Reference 2.*

should be near 2 microns wavelength (case c). This contribution, when added to the Drude emissivity of the metal substrate produces a new lower bound to the hemispherical emissivity of the selective surface. So far we have ignored the influence of the optical properties of the selective coating on the infrared emissivity. Including the dielectric properties increases the hemispherical emissivity to still larger values.

B. Metal Plus Dielectric Film

A metal is a good reflector in the infrared because its optical constants are very different from those of free space. An electromagnetic wave traversing the boundary between the two media is almost completely reflected, irrespective of whether the wave is incident from the metal or from the free space side. A dielectric has optical constants in between those of the metal and free space, and when inserted at the metal interface, it in general provides a better match between the metal and free space and the reflectivity is decreased. As an example of this matching, we consider first the interface between a half space of dielectric and a half space of metal (14). The total hemispherical emissivity (from the metal to the dielectric) is calculated as a function of the index of the dielectric by using the equations developed in the previous chapter. The results for Drude copper at three different temperatures are shown in Fig. 5. The emissivity of the interface increases almost linearly with the index, showing that ever increasing amounts of radiation are coupled out of the metal into the dielectric as the index is increased. The emissivity for an index = 3 (Si) is twice as large as for an index = 1.4 (MgF_2).

When the dielectric is made into a thin film, two additional optical processes come into play: total internal reflection and interference. Thermal radiation emitted from the metal into the dielectric at angles larger than the dielectric free space critical angle remains trapped in the dielectric. This effect causes
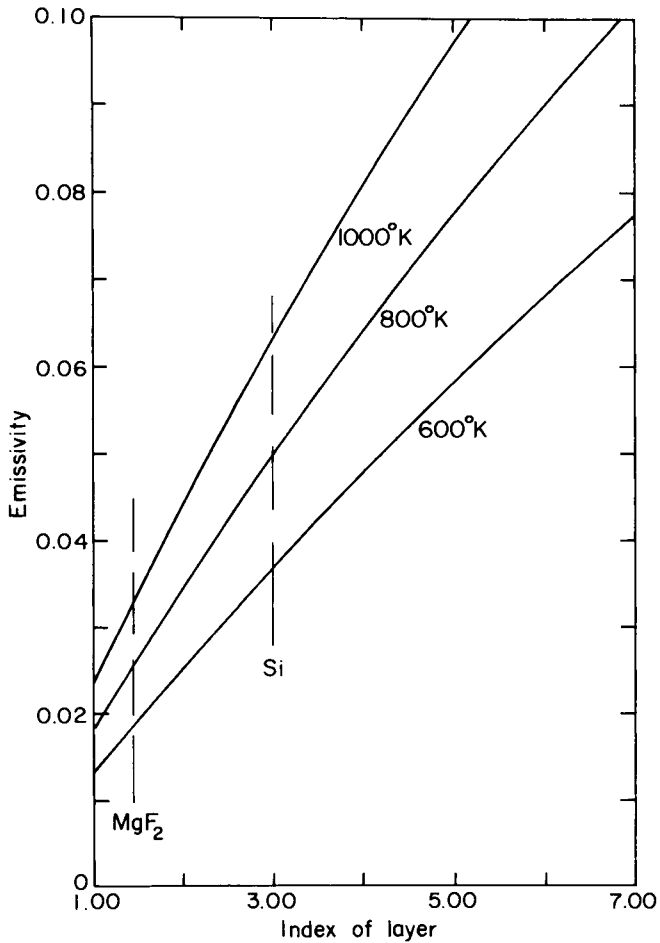
FIGURE 5.   Hemispherical emissivity vs. index of refraction
for the interface between a half space of dielectric and a half
space of Drude copper.   The dielectric is assumed to be non-
absorbing.   (After Reference 14.)   The dashed vertical lines mark
the index of refraction of two dielectrics, MgF_2 and Si.

a decrease in the emissivity.   Thin film interference produces a

good match from the metal to free space for some wavelengths and

a poor match for an equal number of other wavelengths of the black

body spectrum.   Since the reflectivity of the metal is typically
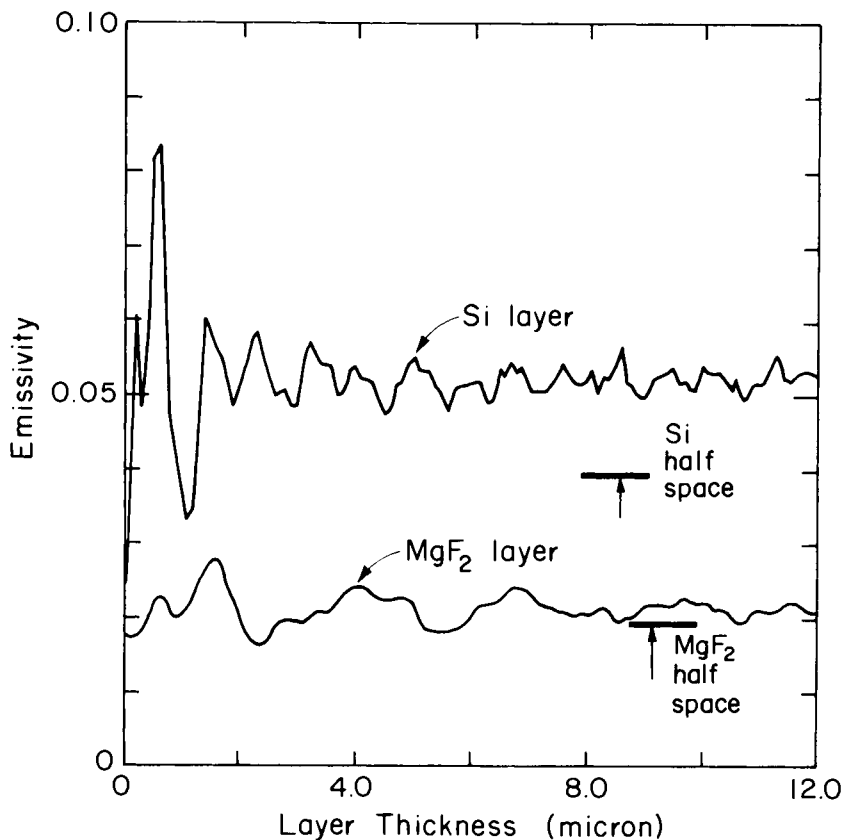
FIGURE 6. Hemispherical emissivity vs. film thickness for a composite composed of a dielectric layer on a Drude metal substrate. Upper curve: silicon on copper. Lower curve: MgF₂ or SiO₂ on copper. (After Reference 14.) The interference patterns go away when the films are made optically absorbing (see Fig. 8).

greater than 0.95 in the infrared, a good match can produce a much larger decrease in the reflectivity than a poor match can an increase. This effect causes the emissivity to increase. The net result of both effects is an increase in total emissivity, as shown in Fig. 6. The emissivity of the system as a function of film thickness is calculated for a variety of temperatures and the results are averaged to simulate operation as the solar flux

varies over the course of the day (14). The interference pattern
is due to the peak of the black body spectrum coinciding with
fractional multiples of the optical thickness of the coating.
Clearly, a dielectric film with a small index of refraction is
most desirable from the standpoint of reducing the emissivity of
the system.

C. *Metal Plus Absorbing Film*

We now consider the emissivity of a metal covered with an
absorbing dielectric film (15). The frequence dependence of the
absorption coefficient is illustrated in the lower part of Fig.
7. The value of α_o is determined by the film thickness d, since
α_o must be large enough so that all the solar energy is absorbed
in passing through the film.

Since the two parts of the complex refractive index of the
film are related by a Kramers-Kronig integral the contribution to
the real part of the film index, $n(\omega)$ is determined by $\alpha(\omega)$. For
$\alpha(\omega)$ given by the solid curve, the Kramers-Kronig relation yields
the $n(\omega)$ given by the top curve in Fig. 7. Note that $n(\omega)$ is
essentially constant throughout the infrared and equal to

$$n(0) \cong 1 + \frac{\alpha_o c}{\pi \omega_L} . \tag{8}$$

Since atomic transitions in the dielectric composite at still
higher frequencies also contribute an amount, say n, to the in-
frared index of refraction, the total index of refraction is

$$n_t \cong n + \frac{\alpha_o c}{\pi \omega_L} . \tag{9}$$

For films thinner than 0.4 microns, $n \sim \alpha_o c/\pi \omega_L$ and the emissivity
is increased by the appreciable increase in n_t. For films thick-
er than 1 micron, a much smaller α_o can be used to absorb almost
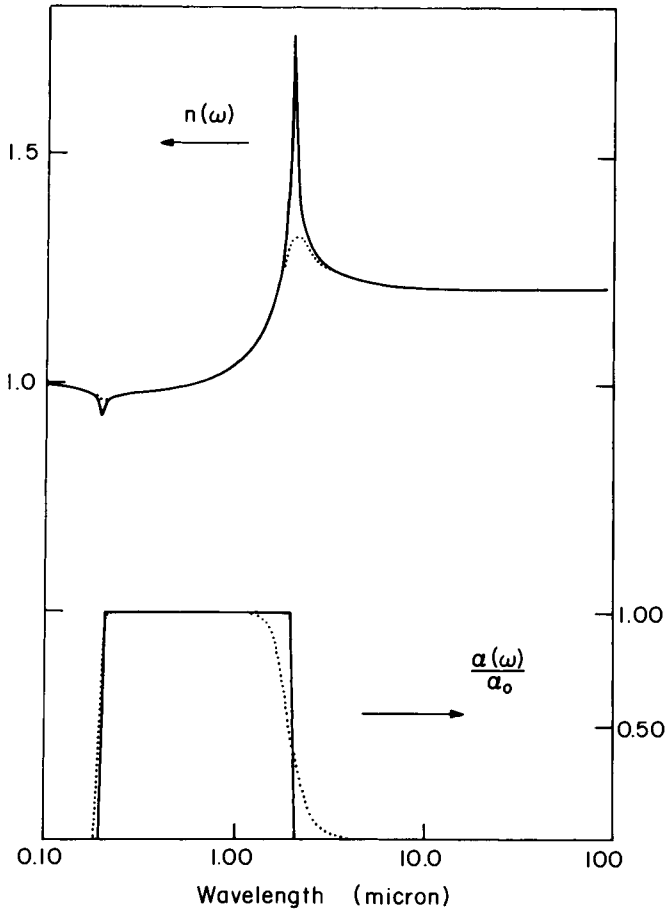
FIGURE 7. Frequency dependence of the optical constants of a selective composite film. Lower curve, solid--the absorption coefficient, $\alpha(\omega)$ for an ideal selective surface. Lower curve, dotted--$\alpha(\omega)$ for a real selective surface showing finite k_BT width of the step in the absorptivity $(T \sim 800°K)$. Upper curves, solid--$n(\omega)$ for the ideal selective surface as calculated from Kramers-Kronig. Upper curve, dotted--$n(\omega)$ for a real selective surface. (After Reference 15.)

all the solar energy and the contribution to the effective index, $\alpha_o c / \pi \omega_L$, no longer plays a significant role in determining the emissivity. In fact, since the complex refractive index of the film is usually graded over a couple of optical wavelengths to

enhance the coupling to the solar spectrum, a film thickness
d $\sim$ 2 microns is to be preferred (16).

Next, we must include the contribution to the emissivity from
the thermal blurring of the absorptivity profile in the dielec-
tric film, which is represented by the dotted curve in Fig. 7.
Simply calculating the overlap between the absorptivity profile
and the black body distribution as we did earlier clearly under-
estimates the contribution of this term to the total hemispheri-
cal emissivity since it ignores the properties of the dielectric.
In fact, since off-thermal rays must pass through a greater
effective thickness of the absorbing dielectric, the hemispheri-
cal emissivity will be much larger than for the dark metal con-
sidered earlier.

Including front surface reflections and interference produces
a more complicated angular dependence for the emissivity, but the
tendency for both ε_{TE} and ε_{TM} to increase with increasing angle
remains.   The importance of thermal blurring can be seen by exam-
ining Fig. 8.   The hemispherical emissivity of platinum at $900^{\circ}K$
is shown for three cases (17).   The lowest curve, a, represents
the hemispherical emissivity of platinum, the next, curve b, for
platinum coated with an optically absorbing dielectric but one
which has a cutoff at 2 micron wavelength, and the last, curve c,
for an optically absorbing dielectric which has a thermally
blurred cutoff at 2 micron wavelength.   This thermally induced
absorption increases the resultant emissivity of the selective
surface by a factor 2 over that of the base metal itself.

By summing these contributions, we find the smallest hemi-
spherical emissivity, ε_{H}, due to intrinsic physical processes.
For example, we can calculate the minimum emissivity of a dark
mirror assembly which contains a 99% optically absorbing film
(not counting front surface reflections) having a thickness of 2
microns, for a variety of metal substrates.   The calculated
results are shown in Fig. 9.   The hatched areas in the figure
identify non-physical regions of the emissivity versus temperature
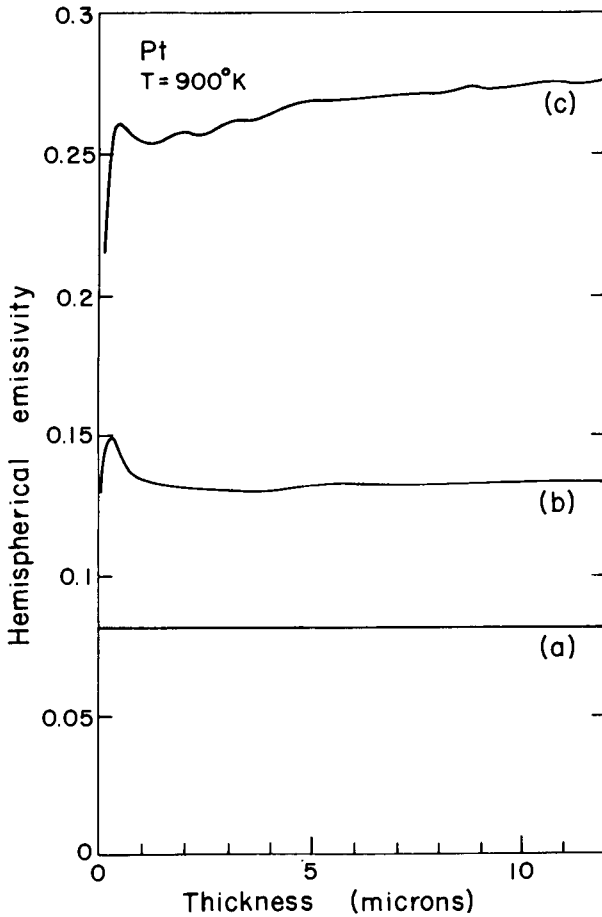
FIGURE 8. Hemispherical emissivity of a metal coated with an
ideal and a real selective surface. Curve (a) represents the ε_H
of a bare metal, platinum. Curve (b) represents the ε_H of plat-
inum coated with a selective absorber which absorbs the solar
spectrum with a sharp cutoff at 2 micron wavelength. Curve (c)
represents the ε_H of platinum coated with a selective absorber
which has the same optical properties as (b) except thermal
blurring of the 2 micron cutoff is assumed. (After Reference 17.)

plot for different elements. The solid lines describe the

smallest attainable hemispherical emissivities for a selective

surface at a given operating temperature on a given substrate.

IV.   CONCLUSIONS

No matter what composite film--metal substrate combination is
assembled, Fig. 9 indicates that the hemispherical emissivity
will be appreciable at high temperatures. Moreover, there are
physical processes which have not been included which would make
the hemispherical emissivity still larger. Neither interband
transitions in the metal nor lattice vibrational absorption in
the composite has been included in these estimates, although both
are intrinsic contributions. In addition, extrinsic processes
such as those associated with surface pits, surface reconstruc-
tion, etc., have been ignored. If the coating does not have the
ideal case of $k_B T$ blurred step function behavior, so the absorp-
tivity changes more slowly with wavelength than the step func-
tion, then the emissivity will be increased accordingly although
the temperature dependence will be less rapid.

In the temperature region below $700^\circ K$ the effective emissivity
is a sensitive function of the optical properties of the compos-
ite structure, both of the absorption edge and the base material.
By $900^\circ K$ the difference between the effectiveness of different
base metals is small. For such high temperature applications,
the base metal should be chosen for its physical stability, not
its hemispherical emittance, since all good conductors, when
used in the selective surface mode, have about the same high
temperature emissivity.

At the present there is not much measured data which can be
compared with the dark mirror emissivity calculation given in
Fig. 9 (see next chapter by Buhrman). The labelled points shown
in the figure are taken from Table I of the previous chapter and
Reference 18. Before comparing emissivity values, it should be
remembered that the minimum emissivity is directly related to the
solar absorptivity and the solar absorptivity used to calculate
Fig. 9 corresponds to $\alpha_s \approx .94$. The appropriate limits for other
values of solar absorptivity are described in Reference 16. Some
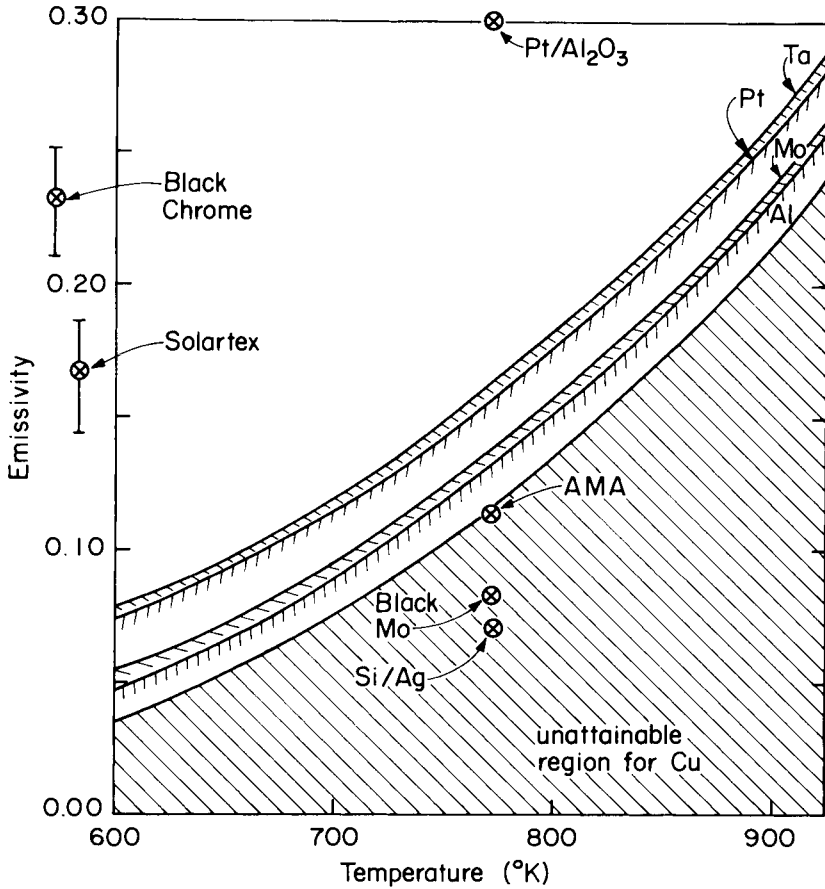
FIGURE 9. Calculated minimum hemispherical emissivities for
selective surfaces on various metal substrates. The solar
absorptivity is assumed to be 0.94. These limits are determined
by the temperature dependent properties of the metal, the influ-
ence of the dielectric index of refraction and the thermal
broadening of the solar absorptivity profile. The hatched region
of the figure identifies emissivity values which are excluded on
physical grounds. The data points are taken from Table 1 in the
previous chapter and also from Reference 18. The three data
points in the hatched region were obtained by using room temp-
erature optical constants to calculate the 500°C hemispherical
emissivities.

of the composites listed in this figure have smaller α_s's, hence could also have smaller ε_H's; however, all three of the data points shown in the hatched region have been obtained by using room temperature optical constants to calculate the hemispherical emissivity at 500°C.

Finally, we should compare the potential of the heat mirror and dark mirror concepts. As long as one maximizes α_s first and is constrained to weakly focused systems, a simple figure of merit of the selectivity is α_s/ε_H. For the heat mirror tandem the maximum figure of merit can be estimated by taking the best aluminum mesh with square wires and a 90% geometric transmissivity. Equation (7) then leads us to an $\alpha_s/\varepsilon_H < 11$. At low temperature, below 700°K, Fig. 9 shows that dark mirrors can have larger values of α_s/ε_H and indeed experimental values of the figure of merit at very low temperatures are already somewhat larger than this metal mesh heat mirror limit (1,18). However, because of the very temperature dependent emissivity shown in Fig. 9, should selective absorber temperatures ever rise above 800°K, the heat mirror may ultimately provide the larger figure of merit. For the immediate future, however, it appears that dark mirrors have the greater potential.

ACKNOWLEDGMENTS

REFERENCES

1.   Seraphin, B.O. in "Solar Energy Conversion--Solid State Physics Aspects", (Topics in Applied Physics, Vol. 31), (B.O. Seraphin, ed.), p. 5. Springer-Verlag, Berlin, (1979).

2.   Sievers, A.J. in "Solar Energy Conversion--Solid State Physics Aspects", (Topics in Applied Physics, Vol. 31),

(B.O. Seraphin, ed.), p. 57. Springer-Verlag, Berlin,(1979).

3. Fan, J.C.C. in "Solid State Chemistry of Energy Conversion
    and Storage", (Advances in Chemistry Series, 163), (J.B.
    Goodenough and M.S. Whittingham, eds.), p. 149. American
    Chemical Society, Washington, D.C.,(1977).

4. Rosebury, F., "Handbook of Electron Tube and Vacuum Tech-
    niques", p. 207. Addison-Wesley, Reading, MA,(1962).

5. Sievers, A.J., in "Materials Research Council Summer Confer-
    ence. Vol. II-Solar Energy", (E.E. Hucke, ed.), p. 85.
    Dept. of Materials and Metallurgical Engineering, Univ.
    Michigan,(1973).

6. Groth, R., and Kauer, E., *Philips Tech. Rev. 26,* 105 (1965).

7. Groth, R., *Phys. Stat. Sol. 14,* 69 (1966).

8. Fan, J.C.C., Bachner, F.J., and Murphy, R.A., *Appl. Phys.
    Lett. 28,* 440 (1976).

9. Horwitz, C.M., *Optics Commun. 11,* 210 (1974).

10. Ulrich, R., *Appl. Opt. 7,* 1987 (1968).

11. Jakob, M., "Heat Transfer", Vol. 2, p. 5. Wiley, New York,
    (1957).

12. Pramanik, D., Sievers, A.J., and Silsbee, R.H., *Solar Energy
    Materials 2,* 81 (1979).

13. McPhedran, R.C., and Maystr, D., *Appl. Phys. 14,* 1 (1977).

14. Trotter, D.M., Craighead, H.G., and Sievers, A.J., *Solar
    Energy Materials 1,* 63 (1979).

15. Trotter, D.M., and Sievers, A.J., *Appl. Phys. Lett. 35,* 374
    (1979).

16. Trotter, D.M., and Sievers, A.J., *Appl. Optics* (to be
    published).

17. Trotter, D.M., private communication.

18. Call, P.J., "National Program Plan for Absorber Surfaces
    R & D", p. 10. Solar Energy Research Institute, Golden, CO.
    TR-31-103, (1979).

CHAPTER 9

COMPOSITE FILM SELECTIVE-ABSORBERS[1]

R. A. Buhrman
H. G. Craighead[2]

School of Applied and Engineering Physics
Cornell University
Ithaca, New York

I.   INTRODUCTION

    The effectiveness of finely divided metal/dielectric com-
posite coatings for the collection of solar radiation is well
established. Dielectric rich composites (cermets) are, in
general, strongly absorbing over much, if not all, of the solar
spectrum. In the infrared spectral range they rapidly become
highly transparent with increasing wavelength. When such a
composite coating is formed on a highly reflecting metal surface
the resulting absorber-mirror tandem can be a strongly absorb-
ing, yet selective, photothermal collector. A schematic repre-
sentation of such a system is shown in Fig. 1.

Composite Selective Surfoce

Metal
Low ε

Graded Metal/Insulator Coating
High α
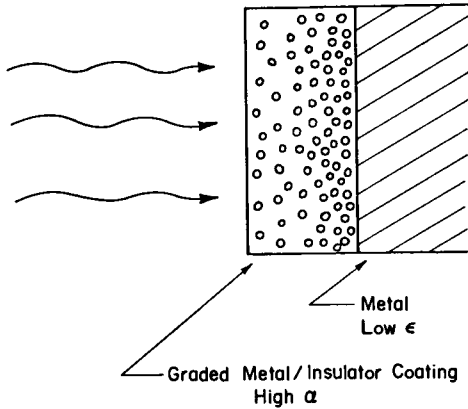
FIGURE 1. *Schematic representation of a composite absorber-
mirror tandem selective-surface.*

The most intensively studied, if not the best understood,
example of such a collector is the black chrome coating (1).
This electroplated coating is basically a mixture of Cr parti-
cles and Cr oxides with particularly useful microstructure
plated onto specially prepared metallic substrates. At present
it is by far the most widely employed low temperature
(T ≲ 300 C) selective absorber.

For demanding high temperature (T > 350 C) applications,
where electro-plated coatings tend to fail, it is again dielec-
tric/metal composites that deliver the best performance. In
this case the coatings are either vacuum or sputter deposited.
Such films, due to their superior integrity, tend to be con-
siderably more stable in hostile high temperature environments.
With such composite films, unexcelled high temperature selec-
tive absorber performance and stability has recently been

achieved (2).

In this chapter we discuss the general physical and optical properties of composite films. This discussion is largely based on the findings of recent experiments with vacuum deposited films but it is also generally relevant to the understanding of electroplated coatings. Following this discussion we present some general guidelines for producing high performance absorber-mirror tandems for particular photo-thermal applications. Finally some recent developments in producing high performance selective absorbers for high temperature applications are reviewed.

II.   PHYSICAL AND OPTICAL PROPERTIES OF COMPOSITE FILMS

A.   *Production of Composites*

Metal/dielectric composite coatings can be produced by a wide variety of techniques. These techniques can be divided into two general types; wet chemical techniques and vacuum deposition techniques. Electroplating is the most common example of the first type. This type also includes impregnation of porous dielectrics by chemical precipitation of metal ions (3) and pyrolysis of organometallic coatings (4). Included in the second type are co-evaporation of a metal and dielectric (2), co-sputtering (5) and reactive sputtering (6).

In general, the wet chemical approaches are relatively inexpensive, while the vacuum deposition approaches tend to be more versatile, and more controllable and tend to yield coatings which are more amendable to systematic micro-structure analysis. The wet chemical approaches usually are restricted to only certain metal-dielectric combinations. Particularly in the case of electroplating this combination is generally that of a metal and its oxide. In the non-reactive vacuum deposition approaches the choice of one constituent can usually

be made independent of the other. Control over such coating
features, as constituent grain size and compositional gradients
within the coatings can readily be achieved with vacuum deposi-
tion techniques. Such control can sometimes be achieved with
electroplating processes by varying the chemical baths and
plating conditions, often with excellent results. The range
of possible variation is however more limited.

B.   Composite Microstructure

     The microstructure of the type of dielectric-rich metal/
dielectric composite coating which is of interest here has
considerable variability. It depends strongly on the particu-
lar method of production employed and upon the choice of con-
stituents. In general the metallic constituent takes the form
of small, often crystalline, grains rather uniformly dispersed
in the dielectric matrix. In some instances the average
metallic grain diameter can be as large as 50 nm, in other
cases, the grains, if they exist at all, are too small, < 1 nm,
to be detectable by conventional electron microscopy. Substrate
conditions during production and, particularly, the level of
reactivity of the metal play major roles in determining this
grain size. The choice of dielectric is also a factor.
     The form of the dielectric is also quite variable. For
vacuum deposited coatings the dielectric typically forms an
amorphous matrix within which the metallic grains are dispersed.
This is the case for composites with, for example, aluminum,
silicon and chromium oxide dielectrics. In less typical instan-
ces, for example with MgO dielectric, the composite consists
of small $\lesssim$ 5 nm, crystallites of dielectric inter-dispersed
with very small metallic grains.
     For electro-plated coatings the available microstructure
data is quite limited owning to the difficulties of doing
electron microscopy on such coatings. The indications are that

in many cases, including that of black chrome, the coating consists of small metallic grains dispersed within an amorphous, often porous, matrix of non-stoichiometric oxide (7).

C. Optical Properties-Theory

The theory that is usually invoked to explain the optical response of finely divided composite material is the so-called Maxwell-Garnett theory published in 1904 (8). This theory is a straightforward mean-field approach to the problem of accounting for the effect of particle-particle interactions in affecting the overall response of metallic particles embedded in a dielectric host. In recent years this theory has received renewed attention. The fundamental assumptions of the theory have put on a sounder theoretical footing and previously neglected structural multipole effects have been included in the theory (9).

In its simplest form the Maxwell-Garnett (M-G) theory considers the composite to consist of electrically-isolated, spherical metal particles uniformly dispersed within an ideal dielectric matrix. Generalization of the theory to non-spherical particle shape is straightforward, but it is done at the expense of introducing additional parameters (depolarization factors) into the theory. While such a generalization may be necessary to make definitive tests between theoretical predictions and the observed response of a particular composite (10) for which the particle shapes are precisely known, it is of limited value in *predicting* the optical response of composite materials.

There is an alternative mean field theory first proposed by Bruggeman (11) which is sometimes used in attempts to explain the optical response of composite materials. The basic difference between the Bruggeman approach and M-G is that the former assumes a quite different composite topology than does

the latter. Bruggeman assumes the composite to consist of
randomly intermixed particles of dielectric and metal. M-G
assumes the metal to be dispersed as particles throughout the
dielectric. While the distinction may appear subtle the result
is that the Bruggeman theory tends to predict broader absorp-
tion curves than does the M-G theory. If encountered experi-
mentally these broader absorption curves would be somewhat
more favorable for solar energy applications.

D.   Optical Properties-Experiment

While composite coatings have been actively studied for
quite some time there is very little data available concerning
the intrinsic optical properties of these materials. Recently
a series of experiments have sought to establish the value of
theory in predicting the optical behavior of composites, and
to determine the suitability of various composite coatings
for selective-surface applications. Thin, semi-transparent
films of uniform composition were produced by co-evaporation
from separate electron beam heated sources. The reflectance
and transmittance of these films, which were deposited on
quartz substrates, were measured over the visible and near
infrared spectral ranges. The complex index of refraction of
the composite was then numerically determined from this data.
The results were then correlated with the topology and micro-
structure of the composite and compared with theoretical pre-
dictions.

A variety of vacuum deposited composites have been examin-
ed, including Ni/Al_2O_3, Au/Al_2O_3, Au/MgO and Pr/Al_2O_3 compo-
sites. The results of these and related studies can be sum-
marized as follows: The optical behavior of a composite is in
general characterized by a broad absorption peak, centered in
the visible spectral region, with significant absorption ex-
tending into the infrared region. In the near infrared region,
this absorption typically decreases only gradually with in-
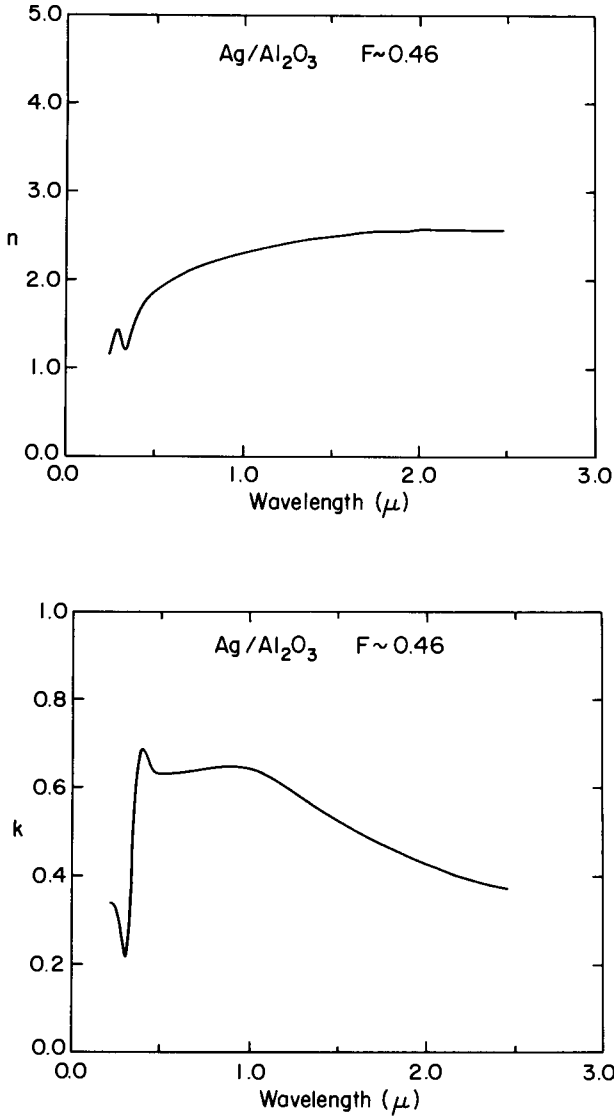
FIGURE 2.   *The index of refraction and extinction coefficient of a typical composite of relatively high (46%) metallic composition.*
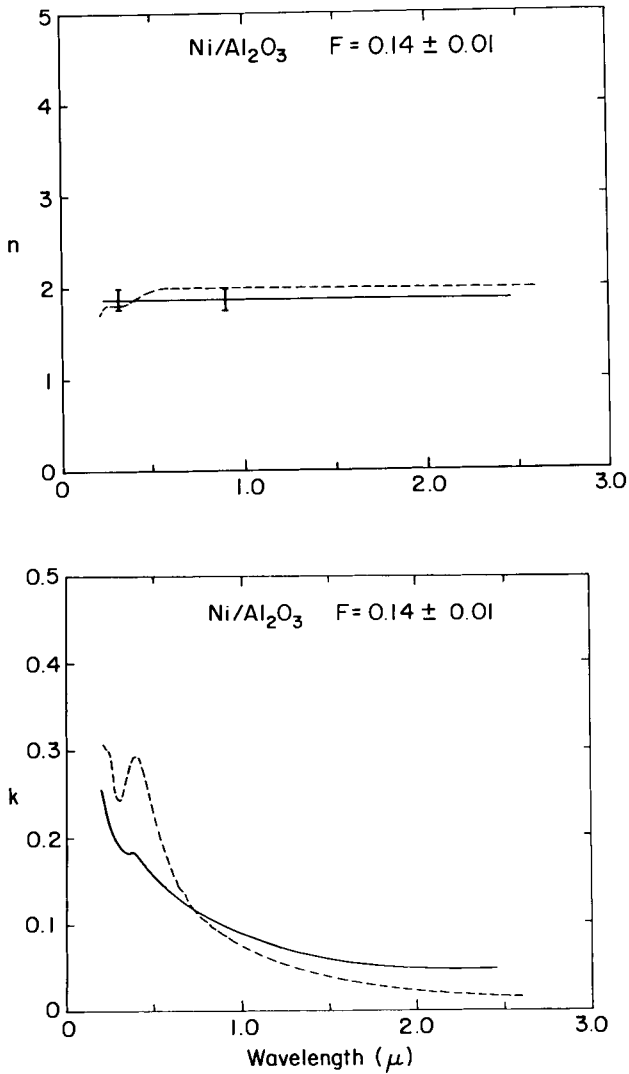
FIGURE 3. *The optical constant of a relatively low metal fraction Ni/Al_2O_3 composite (solid line) compared to the M-G prediction (dotted line).*
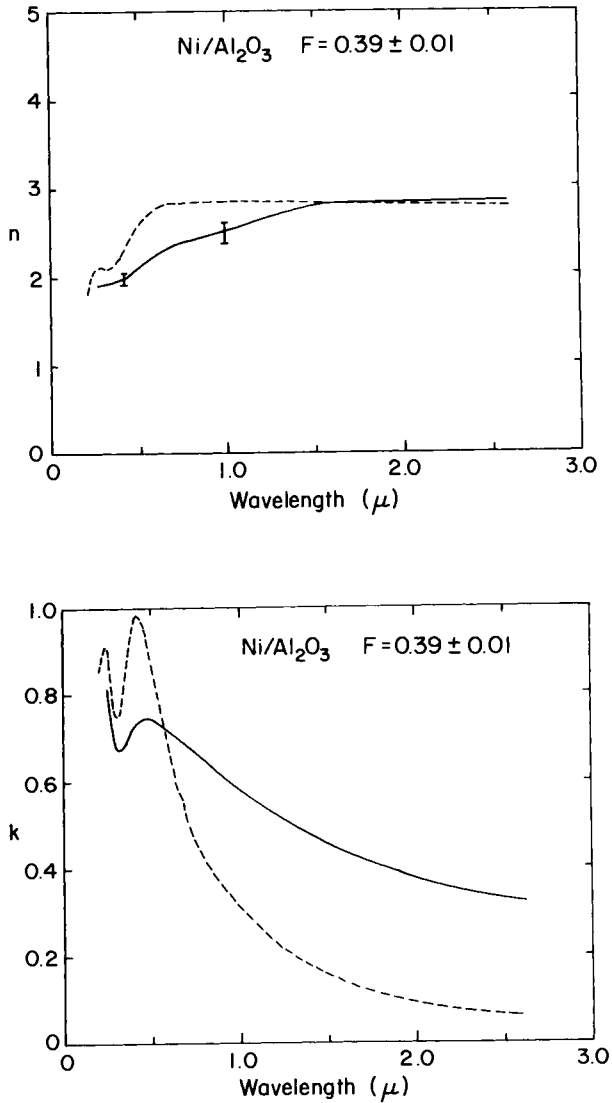
FIGURE 4.   The optical constant of a high metal fraction
Ni/Al₂O₃ composite (solid line) compared to the M-G theory
prediction (dashed lines).
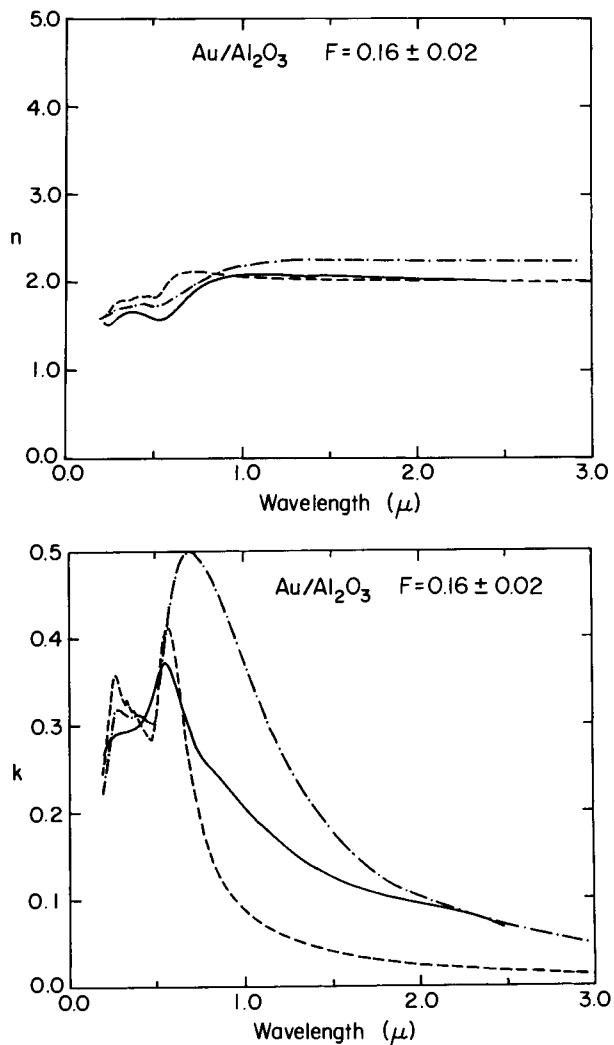
FIGURE 5.   *Optical constants of Au/Al$_2$O$_3$ composites (solid line) compared to the M-G theory (dashed line) and Bruggeman theory (dot-dashed line).   In making the theoretical prediction, corrections were made for short mean free path effects within the Au particles.*
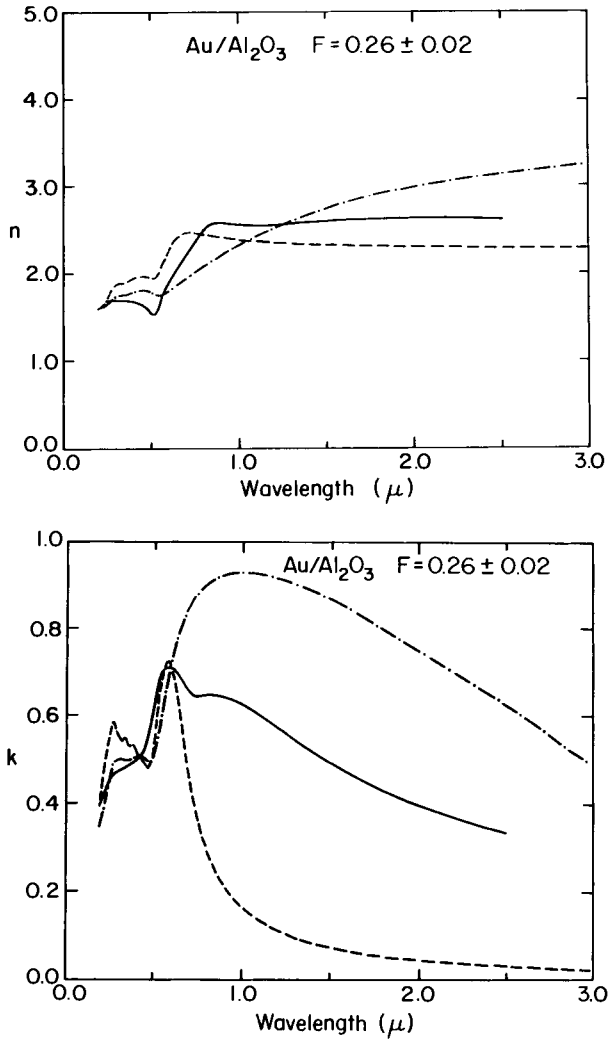
FIGURE 6.   Optical constants of a higher metal fraction
composite.   Again the solid line is the data, the dashed and
dot-dashed lines the M-G and Bruggeman theories, respectively.
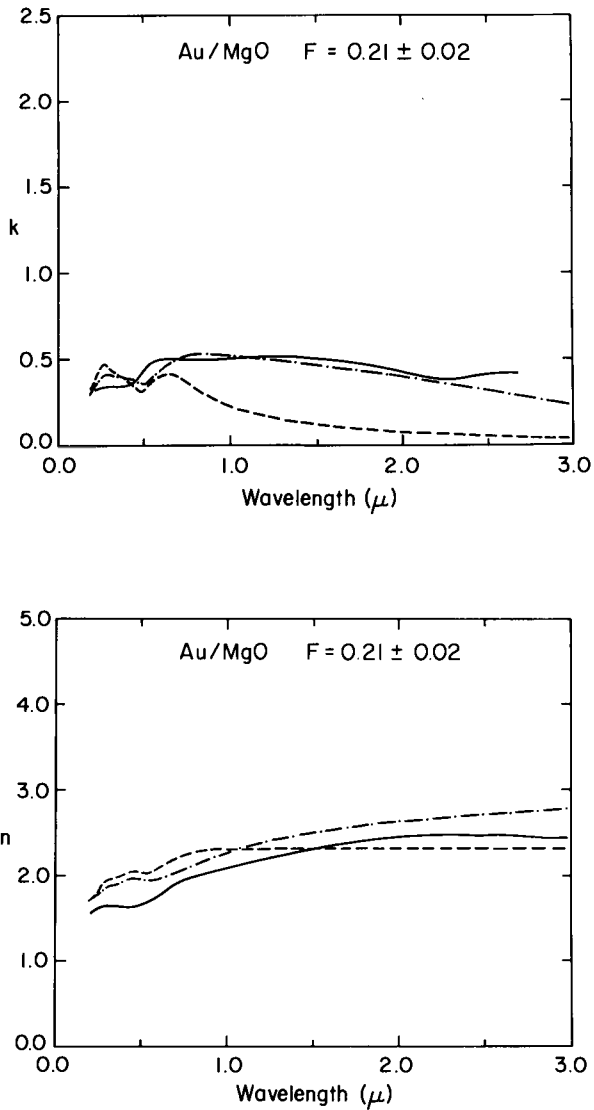
FIGURE 7. *Optical constants of a Au/MgO composite (solid line) compared to the M-G (dashed) and Bruggeman (dot-dashed) theories.*
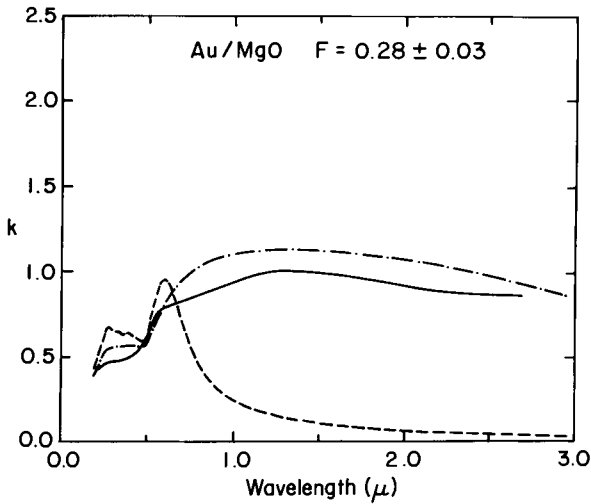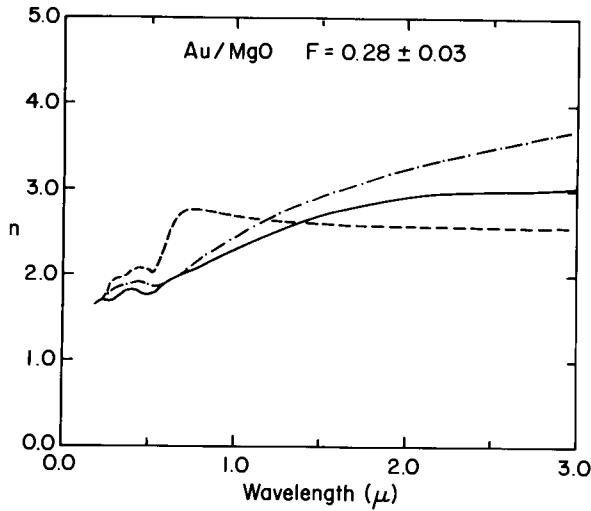
FIGURE 8.   Optical constants of a higher metal fraction
Au/MgO composite.

creasing wavelength. Examples of this behavior are shown in
Fig. 2 where the real and imaginary component of the index of
refraction of a typical dielectric-rich composite Ag/Al_2O_3 is
plotted.

If the details of the composite response is more closely
examined a strong correlation is found between composite micro-
structure and optical behavior. Those composites characterized
as being composed of observable metallic grains randomly dis-
persed in a dielectric matrix, usually amorphous, exhibit be-
havior in qualitative accord with the predictions of the simple
M-G theory. This is illustrated in Figs. 3 and 4 and Figs. 5
and 6 where experimental results for several Ni/Al_2O_3 and
Au/Al_2O_3 composites are compared with the predictions of the
simple M-G theory. In making these comparisons, corrections
were made to account for the shortened electron mean free path
in the metallic microcrystals. This effect acts to extensively
broaden the optical absorption over that predicted from bulk
optical data. The major disagreement between the results for
these composites and the M-G theory is an increased infrared
absorption over the predicted value. This disagreement tends
to grow with increased metal fill fraction. The cause of this
extra absorption is undetermined, although it has been specula-
ted that it is due to electron tunneling between metallic grains.
Other explorations are possible. Regardless of the explanation
the effect can be useful in improving the effectiveness of
composite absorbers.

Composites whose topology consist of randomly distributed
metal and dielectric micro-crystals have optical behavior sig-
nificantly different from that discussed above. This class of
composites includes Au/MgO. The optical absorption of a compo-
site of this type is broader than that of, for example,
Au/Al_2O_3. This is illustrated in Figs. 7 and 8, where the
extinction coefficients of several Au/MgO composites are plot-
ted. The M-G theory does not approximate the behavior of such

composites. This is not surprising since the topology is not
that assumed by the M-G theory. The topology assumed by Brugge-
man is similar to that exhibited by Au/MgO composites and useful
comparisons between theory and experiment can be made. As can
be seen in Figs. 7 and 8 the Bruggeman theory is fairly success-
ful in predicting the optical behavior, although not surprising-
ly, disagreement appears as the metal fill fraction increases.

The third type of composite that is sometimes produced is
the one in which the metal is highly, even atomically dispersed,
with no microstructure detectable by electron microscopy. Such
composites are produced when the metal constituent is relatively
reactive, such as is the case of Fe/Al_2O_3 and V/SiO_2 composites.
Existing composite medium theories are not appropriate for such
materials. Experimentally these materials exhibit broad,
essentially featureless, optical extinction over the visible
and near infrared spectral ranges, as illustrated in Fig. 9.
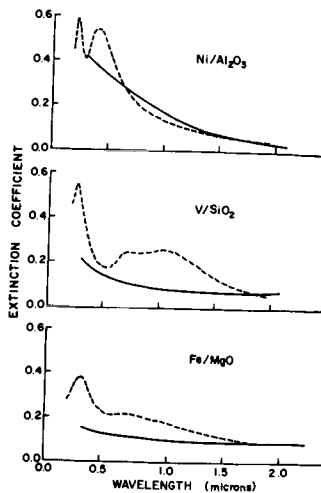
*FIGURE 9. Extinction coefficient of two amorphous and one
crystalline (Ni) composites compared to the M-G prediction
(dashed line).*

We conclude this discussion by reviewing the optical absorption expected from composite coatings. Composites with microstructure consisting of metallic grains dispersed in a dielectric matrix exhibit optical behavior in accord with the M-G theory. Composite coatings of intermixed micro-crystals of metal and dielectric exhibit broad absorption in qualitative accord with the Bruggeman theory. Composites of highly dispersed metal exhibit very broad, or flat, optical absorption through the solar spectrum. In general, if the microstructure of a particular composite system is known, reasonable predictions concerning its optical response can be made. This knowledge can then be effectively employed to engineer selective absorbers.

III. ENGINEERING OF COMPOSITE FILM SELECTIVE ABSORBERS

A.   *Introduction*

The basis of the selective absorber approach to solar energy collection is to develop a surface which is strongly absorbing over the solar spectrum but non-absorbing at longer wavelengths. The "ideal" absorption curve of a selective absorber is illustrated in Fig. 10. By using a solar collector surface with an absorption curve such as that in Fig. 10, the solar radiation is efficiently abosrbed. At the same time the absorptivity, and therefore the emissivity (by Kirchhoff's laws), is low at the longer wavelengths corresponding to the collector's black-body emission wavelengths. The sun's energy is thus efficiently trapped and the heat energy is not lost by reradiation. This spectrally selective absorption is a significant advantage over a flat, non-selective black-body for which the absorptivity (equal to the emissivity) is unity for all wavelengths. The highest attainable solar collector temperature for a black-body is T_o where

$$\sigma \, T_o{}^4 = \text{incident solar flux},\tag{1}$$
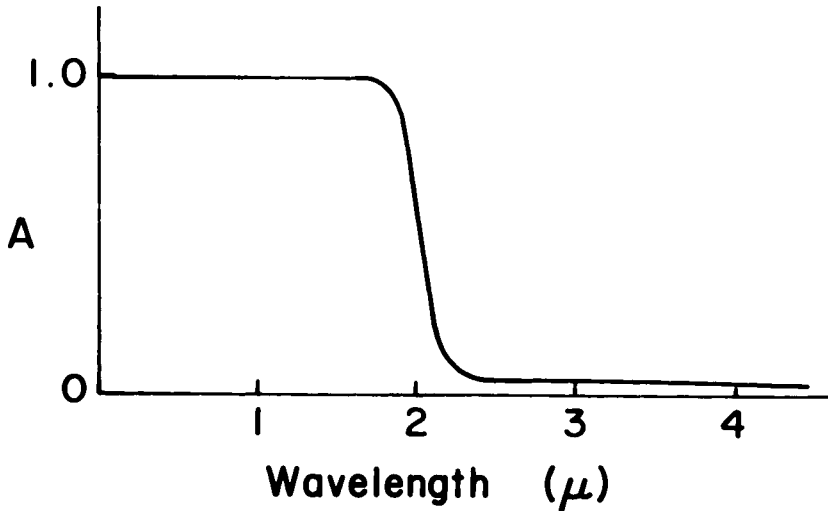
FIGURE 10. Ideal selective surface absorption curve.

and σ is the Stefan-Boltzmann constant. Taking the optimistic
value of 750 Wm^{-2} for the solar flux, T_o = 66°C for a black-
body. To achieve high temperatures and large Carnot and system
efficiencies one must go beyond simple black-body absorbers .

An alternative way around the limit on black-body efficien-
cy is to increase the amount of energy incident on the collector
by focusing the sunlight. However, the use of a highly absorb-
ing solar selective surface yields improved performance at all
degrees of concentration compared to a non-selective surface
with the same solar absorptivity.

Forming composite coatings on low emissivity surfaces, as
shown schematically in Fig. 1, can yield very high performance
selective absorbers. By making proper choice of components
and by careful tuning of coating parameters selective absorbers
can be engineered which give unexcelled performance in practi-
cally all instances. After reviewing the criteria by which
selective absorbers are evaluated, we will discuss the basic
guidelines for producing these composite-mirror selective ab-

sorbers.

B.   *Figures of Merit*

A quantitative measure of the performance of solar selec-
tive surfaces is necessary both for the comparison of different
surfaces and as a means of gauging the efficiency of a system
using a given selective absorber. These relevant parameters
are the solar abosrptivity α, ant the thermal emissivity ε.

The absorptivity α is defined as the fraction of the solar
power absorbed by a film. It is related to the reflectance of
a non-transparent film by:

$$\alpha \approx \frac{\int S(\lambda)[1 - R(\lambda)]d\lambda}{\int S(\lambda)d\lambda} , \qquad (2)$$

where $S(\lambda)$ is the solar power spectrum, $R(\lambda)$ is the wavelength
dependent reflectance and λ the wavelength, integrated over
the range of the solar spectrum. The total hemispherical
emissivity of a film is the total power reradiated into a
hemisphere by the film, divided by the power radiated by a
black-body at the same temperature. By Kirchhoff's laws the
emittance at a given angle θ and wavelength λ, is equal to the
absorptance,

$$\varepsilon(\theta,\lambda) = A(\theta,\lambda) = 1 - R(\theta,\lambda) \qquad (3)$$

for a non-transparent film. By integrating this over all
wavelengths and over the hemisphere we get the total hemispheri-
cal emissivity as

$$\varepsilon(T) = \frac{\int_{0}^{\pi/2} U(\lambda,T)\varepsilon(\theta,\lambda)d\lambda \ d(\sin^2\theta)}{\int U(\lambda,T)d\lambda} , \qquad (4)$$

where U is the Planck distribution function.

These quantities of α and ε are intrinsic properties of
the selective surface. However, of interest also is the total
system performance which involves both the temperature of
operation and the amount of concentration of the solar flux.
The essential quantity of interest in evaluating a selective

absorber system's performance is the fraction of the available
solar energy retained. This is expressed as the collection
efficiency η where

$$\eta = \frac{x \, \alpha \, S \, - \, \varepsilon \, \sigma \, T^4}{xS} \tag{5}$$

or

$$\eta = \alpha \, - \, \varepsilon \, \sigma T^4 / xS. \tag{6}$$

Here σ is the Stefan-Boltzmann constant, T the absolute tempera-
ture, x the solar concentration factor, and S is the total solar
energy flux. The efficiency involves α and ε independently
rather than as the ratio α/ε. The collection efficiency is also
a function of both x and T. For large x, α is relatively more
important than ε. For high concentration applications, where
x is very large, the collection efficiency approaches its upper
limits of $\eta = \alpha$. For an ideal black-body α is equal to unity,
and α can be near unity for actual flat plate type absorbers.
The importance of selectivity is therefore reduced for the large
x concentration applications. It is in this high x range that
thermal stability and large α become most important. The ex-
pression for η also gives the upper limit on T for any system,
which occurs at $\eta = 0$. At this point all the energy is re-
radiated.

C.   *Choice of Composite Absorber Components*

No known metal/dielectric composite has the ideal absorp-
tion properties illustrated in Fig. 10. As indicated previously,
experiments reveal that the optical absorption of composites
is broad, with only a gradual transition observed between the
strongly absorbing short wavelength regime and the weakly absorb-
ing long wavelength regime. Indeed the behavior of most, if
not all composites, can be roughly approximated in the crucial
2 μm wavelength region by a wavelength independence extinction
coefficient k. This yields an absorptivity, $\alpha = 2\pi k / \lambda$, that

decreases only as $1/\lambda$.

Theoretically, neither the M-G nor the Bruggeman theory predicts the possibility of a sharp 2 μm cut-off for any elemental metal composite for which the bulk optical constants are known. The only exception to this statement is that if very non-spherical particles of particular orientation are assumed a sharp absorption edge at 2 μm can be predicted (10). Achieving such control over particle shapes in composites seems highly unlikely. The Bruggeman theory does indicate that composites of the appropriate topology can have a somewhat sharper cut-off than composites with the M-G topology. The differences however are not very strong.

While the ideal composite material is yet to be discovered, the range of choice of constituents for high performance, composite selective absorbers is quite large. Consequently the choice for a particular application can and should be made largely on the basis of cost and stability considerations. For high temperature applications stability is the prime consideration. Thus it is here that vacuum deposition offers the most options, since the choice of the dielectric is basically independent of the choice of the metal. Therefore good candidates for high temperature systems are the relatively non-reactive refractory metals such as Ni, Pt and Mo, and dielectrics such as Al_2O_3, due to its effectiveness as a passivating material, or other stable oxides and nitrides. For lower temperature applications, wet chemical techniques are advantageous due to lower cost even though the dielectric typically must be an oxide or sub-oxide of the metal constituent. The metal choice is made on the basis of its stability and wet chemical deposition characteristics.

The choice of the metal mirror that underlies the composite coating in a dark-mirror selective absorber is also governed by considerations of cost, stability and performance. However since available composite absorbers do not have the ideal ab-

sorption cut-off in the 2 μm region, the near infrared reflecti-
vity of the metal is not as critical as it would be for a more
ideal composite absorber. In currently realizable dark-mirror
systems, the predominant source of emissivity losses at high
temperature (T > 300 C) is the composite film and not the metal
mirror. Consequently nearly any relatively high reflectance
metal mirror will serve, with good quality Mo and Pt films being
particularly good choices due to their high temperature stabili-
ty. For low temperature operations, cost and compatibility with
a particular wet chemical process tends to dictate the mirror
choice.

D. Graded Composition Coatings

Conceptually the simplest approach to the formation of a
dark-mirror tandem is to produce a *uniform* composite coating on
the metal mirror surface. The necessary thickness d of the
coating is determined by the requirement that the absorption
of the composite remain strong out to 1.5 to 2.5 μm wavelengths.
Since the attenuation of radiation upon passing through an ab-
sorbing medium of thickness x and extinction coefficient k is

$$I = I_o \, e^{-2\pi k x/\lambda} \tag{7}$$

the requirement is that kd ~ .1 - .3 μm. Depending upon the
metallic content, the extinction coefficient of most composites
in the 2 μm wavelength region varies from < 1., for low metallic
content, to $\gtrsim$ .5 for fractional metallic content in the .2 to
.5 range. (Typically for metal volume fraction above .5 the
composite becomes electrically conducting which is undesirable
for selective absorption since the extinction coefficient of
the composite then increases with increasing wavelength.)

It is usually advantageous to employ relatively thin
(d $\lesssim$ .5 μm) composite coatings, as this tends to minimize prob-
lems with film adhesion and serves to eliminate undesirable
interference effects in the infrared. Thus a .5 μm composite

coating with metal fill fraction of the order of .3 to .4 is typical, although thicker layers with less metal per unit thickness will also serve.

A detrimental aspect of a composite absorber is that the index of refraction of composites tends to be large, increasing directly with metallic content. The result is significant front surface reflection losses and hence lowered absorber performance. The most effective way to counter this effect is produce the absorber with a compositional gradient (11-14) such that the metallic content is zero at the front surface and maximum at the composite-mirror interface. If properly executed such a compositional gradient can effectively eliminate reflection losses due to the metallic content of the composite, leaving only front surface losses due to the dielectric mismatch between the air and the pure dielectric. Ideally the composite should be graded to a front surface index of refraction of one, to also avoid this loss mechanism. In practice this usually requires the composite to be porous, which is apparently the case for some electroplated black chrome coatings. For vacuum deposited coatings this can only be achieved by additional processing.

The precise nature of the compositional grade is not critical to achieving the desired effect. This is illustrated in Fig. 11 where the results of some model calculations for the reflectivity of composite films deposited on copper surfaces are shown. (The optical constants assumed in these calculations is typical of composite materials.) One of the model films (No. 1) is of uniform composition with a metal content of $F = .25$ and a thickness of 4000 Å. The other three films graded are with the same average metal content and thickness as the uniform film; so the only parameter varied is the shape of the composition grade. The shape of these three composition grades along with the calculated absorptivity α and thermal emissivity

CALCULATED NORMAL REFLECTANCE
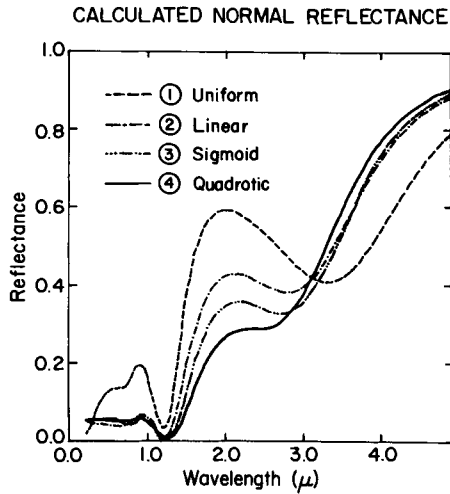
FIGURE 11.   The reflectance curves of a uniform composite film and three graded composition films, all with the same thickness and total metal content.

ε at 300°C are shown in Fig. 12.   All three graded films, al-though graded in quite different ways, have essentially identi-cal α and ε values.   Distinct advantages in both α and ε can be seen for the graded films compared to the uniform film. More subtle changes in the optical response among the graded films can be seen in Fig. 11.   But these   differences are in-significant in terms of practical solar performance.   The reflectance in the 0.2 - 1.0 µ range was reduced to the lowest possible value for all three grades.   At longer wavelengths the quadratic grade formed a slightly sharper absorption edge.

The primary benefit of a graded composition can be seen as the increase of α from 0.84 for the uniform film to 0.94 for the graded films.   A secondary benefit of the graded com-position is a reduction in ε of about 0.03 for the graded films.

Volume Fraction of Metal
vs Depth

①   Uniform
$\alpha = 0.84$
$\epsilon(300°C) = 0.13$

②   Linear
$\alpha = 0.94$
$\epsilon(300°C) = 0.10$

③   Sigmoid
$\alpha = 0.94$
$\epsilon(300°C) = 0.10$

④   Quadratic
$\alpha = 0.94$
$\epsilon(300°C) = 0.09$

Front   Rear
Surface   Surface
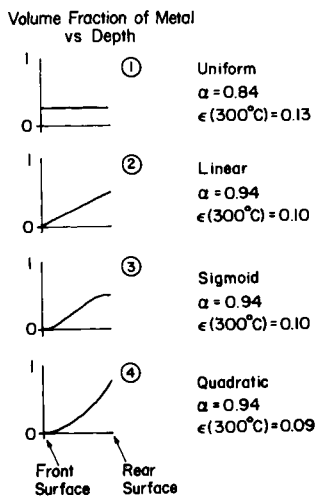
FIGURE 12. The shape of the composition-depth profile used for calculating the reflectance curves of Fig. 12. Also shown are the calculated absorptivity and emissivity at 300°C.

This reduction in ε was explained by Sievers (15) as being due to a decreased optical phase shift for the graded film, yielding a better reflection coating at the long thermal wavelengths. The temperature dependent emissivity for one of these graded films is shown in Fig. 13a. This can be compared with the higher emissivity for the uniform film shown in Fig. 13b.

The solar performance calculated for these typical composite selective absorbers is well within the limits for graded composite absorbers calculated by Trotter and Sievers (16). They have calculated the maximum attainable α/ε value for a graded composite film on Cu to be about 33 at 300°C. For the above calculation for practical graded composite materials, α/εwas 9.4 at 300°C. This indicates the advances which remain to be made by obtaining the ideal selective absorber material, i.e. one with a more abrupt absorption cut-off.
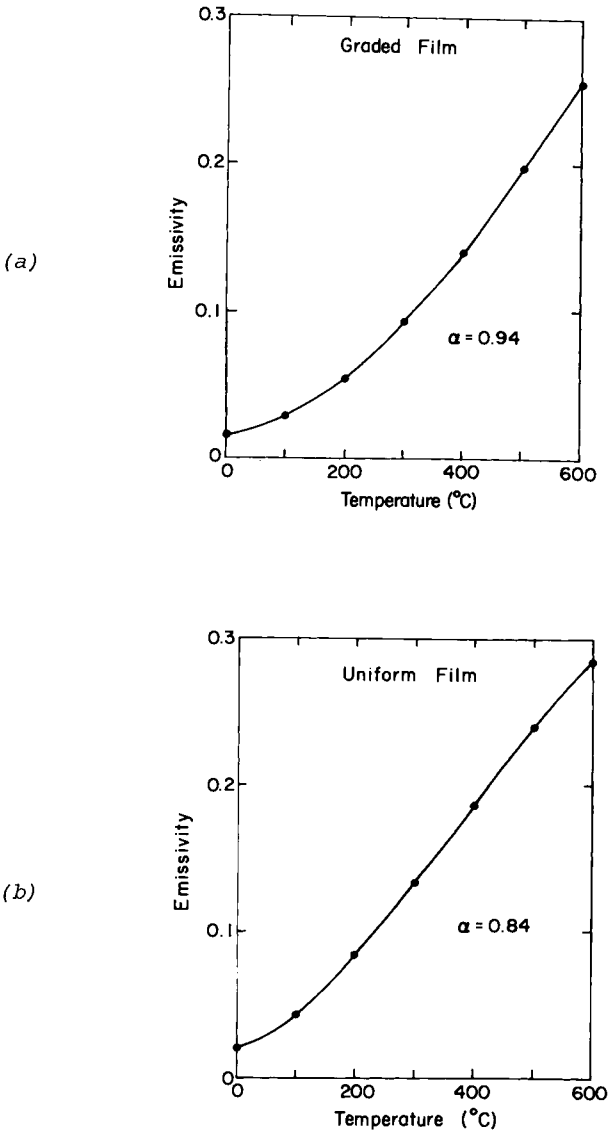
FIGURE 13. Calculated emissivity of a graded and of a uniform composition film.

E.   *Production of High Temperature Selective Absorbers*

   With a knowledge of the optical behavior of composite
materials and with the means available to achieve compositional
gradients, it is a straightforward matter to produce selective-
ly absorbing coatings. Since a composite with ideal optical
constants is as yet not available, the performance of such
coatings is not perfect; it can be quite good. Moreover, by
adjusting the parameters of the coating it is a straightforward
matter to engineer the response of a coating to optimally match
the requirements of nearly any selective absorber application.

   To illustrate this point we describe the behavior of
several Ni/Al_2O_3 and Pt/Al_2O_3 composite coatings. These coat-
ings were produced by electron beam deposition in the course
of a research program designed to develop selective absorbers
for a high temperature applications. The composite materials
were chosen mainly on the basis of physical stability consid-
erations. In this work graded and ungraded composite films
were deposited on metal coated quartz, stainless steel and
copper substrates. The metal coating was either a Ni or Pt
film. Hemispherical reflectivity and emittance calorimetry
measurements were made on these films and from this data the
solar performance of each film was determined. Series of
films, each with different thickness but all with maximum
back surface metal concentration of approximate 40%. In
Fig. 14 we show the reflectance spectrum of one such Ni/Al_2O_3
film deposited on a copper substrate. The extrema in the
curve are the result of thin film interference effects rather
than intrinsic sharp absorption lines of the composite. The
overall absorption edge of this film is approximately at the
desired wavelength of ~ 2 μ. The solar absorptivity for this
film is a fairly high 0.93. The price for this fairly high α
value is a rather high ε value as well which we will discuss
below.
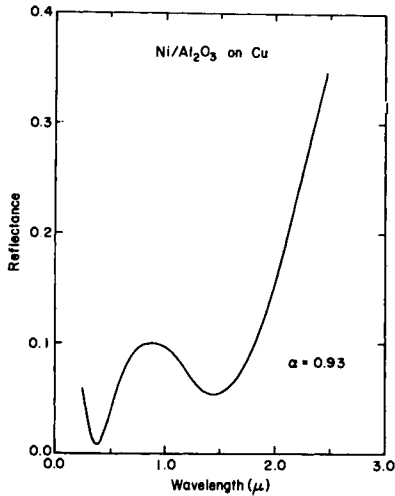
FIGURE 14. *Reflectance curve of a typical graded Ni/Al$_2$O$_3$ film on Cu.*

Reflectance spectra for three members of this family of Ni composite films on Cu are shown in Fig. 15. (This figure includes the spectrum of the film in Fig. 14. - here it is number 5). The numbering of the films is in increasing order of thickness ranging from ~ 1500 Å with film number one the thinnest. The α values for this group of films is listed in Table 1 A. The list of α values in this table shows that the absorptivity clearly increases with film thickness. The whole point of solar selective surfaces, is, of course, to have both high α and low ε. Figure 16 shows the measured ε for this family of surfaces. The emissivity of the surfaces is seen to generally increase with the thickness with α. The rather strong increase in ε, with increasing temperature, is the result of the broad absorption edge of these composites. Table 1 a lists the ε values for the films at selected temperatures for comparison. As the temperature increases and the
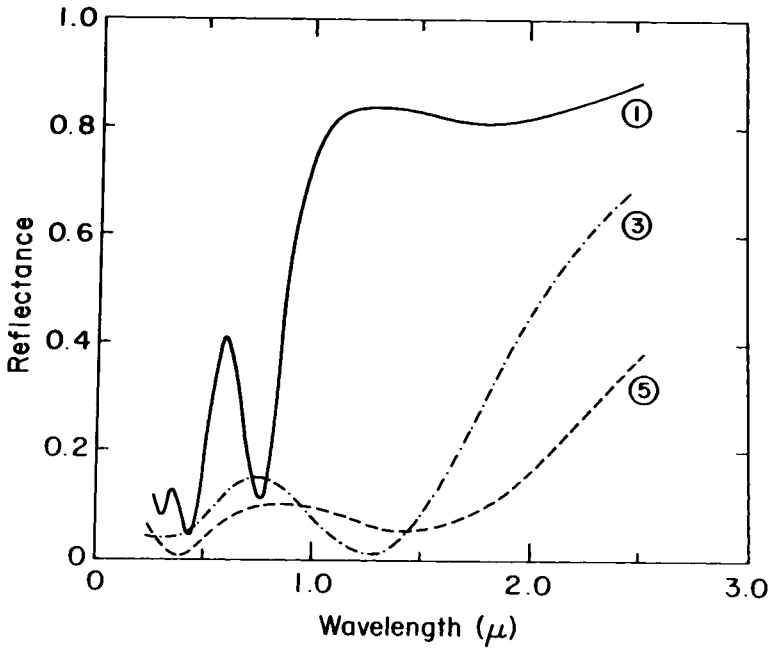
*FIGURE 15. Reflectance curves for a series of Ni/Al$_2$O$_3$
composite coatings on Cu. Films 1, 3 and 5 are of progressively
greater thickness.*
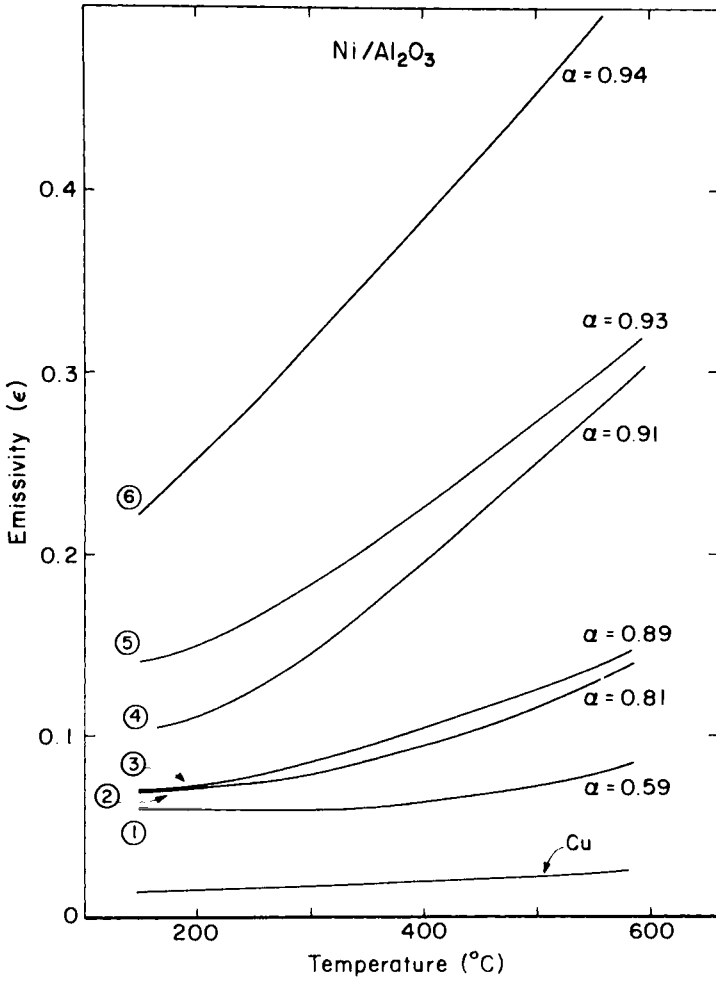
FIGURE 16.   The curves are the measured temperature dependent
emissivity of six Ni/Al₂O₃ films on Cu and the curve for pure Cu.
The curves also are labeled with the solar absorptivity values α,
calculated from the measured reflectance.

TABLE 1 a   Performance Parameters of Ni/Al$_2$O$_3$ Films

Film #	α	ε(150°C)	ε (300°C)	ε (500°C)
1	0.59	0.06	0.06	0.07
2	0.81	0.07	0.08	0.12
3	0.89	0.07	0.09	0.13
4	0.91	0.10	0.15	0.26
5	0.93	0.14	0.19	0.27
6	0.94	0.22	0.32	0.45

TABLE 1 b   Performance Parameters of Pt/Al$_2$O$_3$ Films

Film #	α	ε(150°C)	ε (300°C)	ε (500°C)
1	0.78	0.06	0.07	0.09
2	0.80	0.08	0.10	0.16
3	0.89	0.12	0.16	0.25
4	0.94	0.19	0.24	0.33

   TABLE 1. Performance parameters for the two series of Ni
and Pt composite films. The data are organized in order of
increasing film thickness.

black-body spectrum begins to overlap this absorption edge the
emissivity begins to increase rapidly. An ideal composite with
a much sharper absorption edge would not exhibit this effect
nearly so strongly.

   One important feature should be noted in the family of
curves shown in Fig. 16. In this group of films the only
uniform film, formed without a graded composition, is film
number two. Films two and three have nearly identical emissivi-
ty curves but film number three has a larger α. This shows
experimentally the enhanced performance derived from a composi-
tion and refractive index grade.
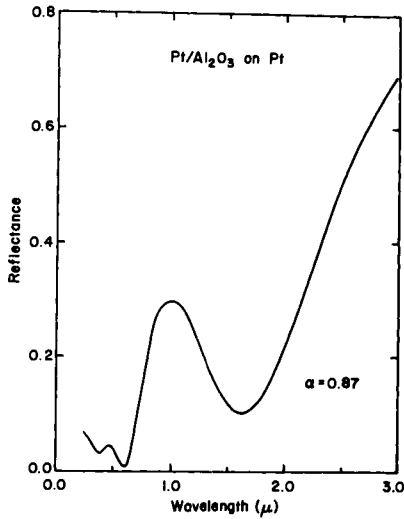
FIGURE 17.   Reflectance of a typical Pt/Al$_2$O$_3$ composite
on Pt.

The second composite system to be discussed here is
Pt/Al$_2$O$_3$.   To compensate for its expensive components the
Pt/Al$_2$O$_3$ composite demonstrates nearly unsurpassed thermal sta-
bility.   A typical reflectance curve for a Pt/Al$_2$O$_3$ film on Pt
is shown in Fig. 17.   The general features are similar to those
seen with the Ni composite films.   The oscillatory nature of
R(λ) again is due basically to thin film interference effects.

In Fig. 18, the total hemispherical reflectance curves
are shown for three members of a family of Pt/Al$_2$O$_3$ films on
polished Cu.   Here again the numbering of the films is in the
order of increasing thickness.   Table 1 b lists the solar ab-
sorptivities for this family of films.   Again the trade-off
between α and ϵ can be seen in Fig. 19, where increases in ϵ
accompany increases in α. ϵ remains low, $\sim$ 0.05 - 0.10 over
the temperature range for the α = 0.78 film but for the highly
absorbing α = 0.94 film ϵ ranges from $\sim$ 0.18 to 0.36 over the
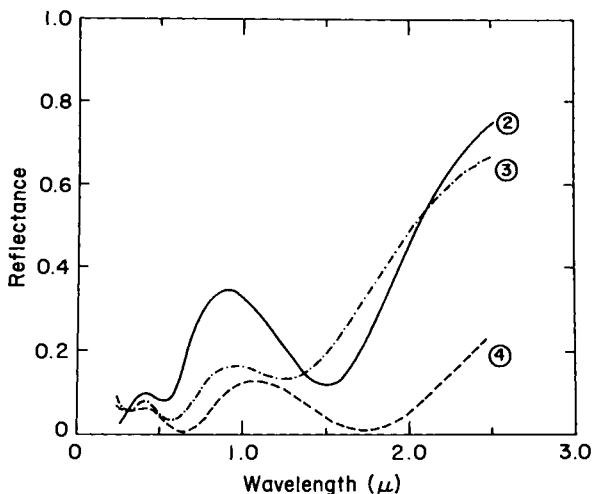
*FIGURE 18. Reflectance curves for three members of a
series of Pt/Al₂O₃ coatings on Cu. The coatings are numbered
in order of progressively greater thickness.*

temperature range. This ε information also is tabulated in
Table 1 b.

An imperfect measure of the value of a selective surface
is the ratio of α/ε. Figures 20 and 21 show the measured α/ε
as a function of temperature for these Ni and Pt composite ab-
sorber films. The quantity of α/ε is often quoted in the lit-
erature as a constant for a film. This is clearly incorrect
since ε is a strong function of T. Figures 20 and 21 give α/ε
over the temperature range of 100°C - 500°C. The ratio α/ε
becomes lower, less favorable, at higher temperatures as the
wavelength range of the emission spectra overlaps more of the
film's absorbing range. The value of α/ε > 13, obtained for
both Ni and Pt composites, is quite large.
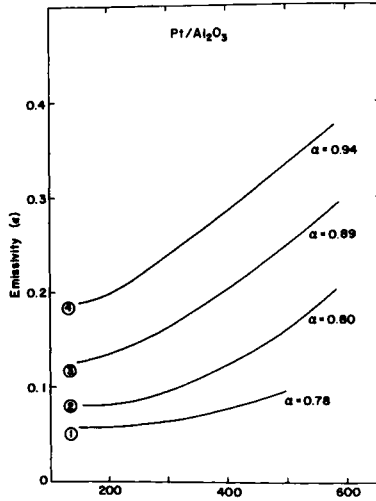
FIGURE 19.   Emissivity as a function of temperature for four
Pt/Al$_2$O$_3$ films on Cu.

However, α/ϵ alone does not fully characterize a selective
surface. Both α and ϵ are independently important in charac-
terizing a film's performance. The collection efficiency de-
fined previously is the proper quantity to consider.

The collection efficiency η as a function of solar concen-
tration x has been calculated for the composite films of Figs.
16 and 19, using the measured values of α and ϵ. For the in-
cident solar radiation the air mass 2 value was taken as given
in reference 16. Figs. 22 and 23 show η vs. x at 150°C for
several of the Ni and Pt composites. Figs. 24 and 25 show
η vs. x for the same films at 500°C. The advantage of selecti-
vity was seen by comparing these curves to the efficiency of a
non-selective black-body ($\alpha = \epsilon = 1$). As pointed out by
Seraphin (17), even at large concentration factors, x > 100,
the lower emissivity of the selective surface leads to effi-
ciencies significantly better than for a black-body. It is
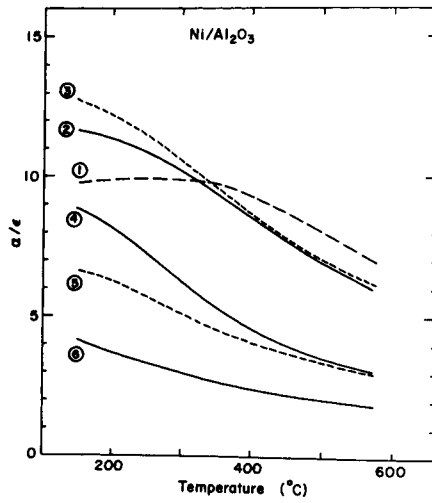
FIGURE 20.   Measured α/ε for Ni/Al₂O₃ selective surfaces.
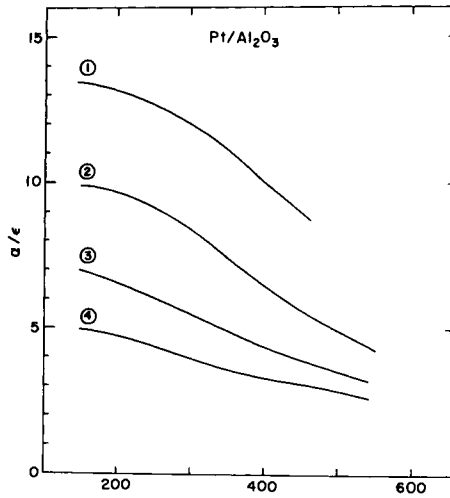
FIGURE 21.   Measured α/ε for Pt/Al₂O₃ selective surfaces.
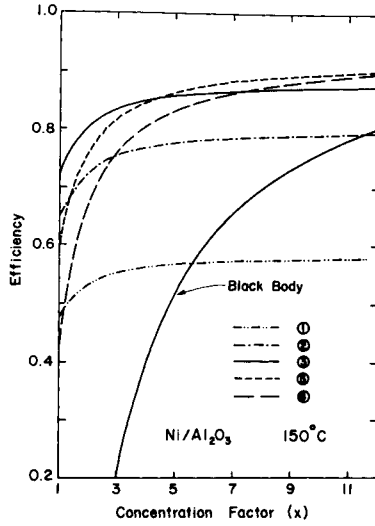
FIGURE 22. *Collection efficiency η as a function of the solar concentration x for Ni/Al*$_2$*O*$_3$ *composite 150°C.*
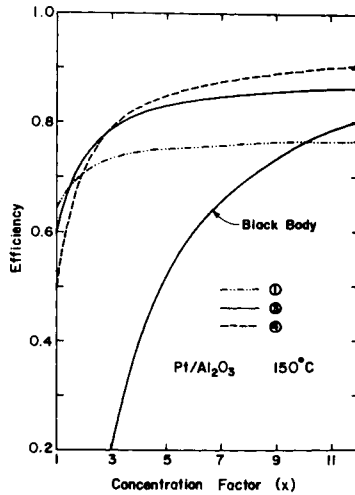
FIGURE 23. *Collection efficiency for Pt/Al*$_2$*O*$_3$ *composites of 150°C.*

readily seen that different films have the largest η at differ-
ent values of x and T. The essential point is that with reason-
able control of composite film parameter one can easily create
a film with the best combination of α and ε for a given applica-
tion within the constraints imposed by the basic optical res-
ponse of these composite materials. For large x the high
α ($\alpha \doteq 0.94$) samples are the best choice. For lower x the best
choice is $\alpha \approx .9$ with ε much lower than that of the $\alpha = .94$
films.

F.   High Temperature Selective Absorber Stability

The ability of a selective absorber to survive in a hostile
high temperature environment is essential if that absorber is to
be of practical value. Fortunately composite absorbers, at
least those produced by vacuum deposition techniques, are dis-
tinguished by their high temperature stability.

For example to test the inherent stability of Ni/Al_2O_3
and Pt/Al_2O_3 selective absorbers, a number of samples were
produced by depositing graded composite layers on fused quartz
substrates. This deposition occurred immediately after the
substrate had been coated with either a Ni or Pt metal film
mirror. Figure 26 shows the specular reflectance spectrum of
a Ni/Al_2O_3 composite on a Ni reflecting layer on quartz before
and after extended tests. There was an initial change of α
from 0.96 to 0.95 in the first 70 hours at 400°C in air.
Within the accuracy of the measurement the absorptivity then
remained at this value for the length of the test. The tri-
angles in Fig. 26 show the reflectance after 260 hours at 400°C
plus 68 hours at 500°C. Problems with film adherence eventually
developed at and above 500°C but the tests reveal the Ni/Al_2O_3
composites to be quite rugged.

Perhaps not too surprisingly, the Pt/Al_2O_3-Pt film selec-
tive absorbers exhibit excellent stability. For example the
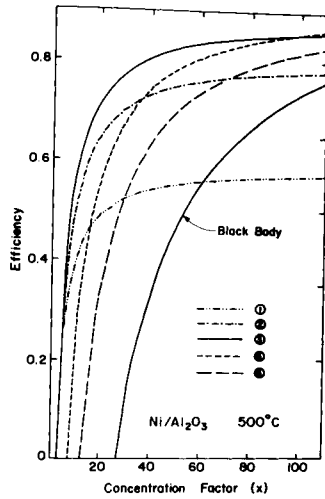
FIGURE 24.   Collection efficiency for the same Ni/Al$_2$O$_3$ composited at 500°C.
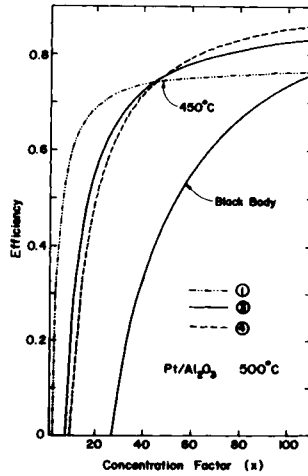
FIGURE 25.   Collection efficiency for the same Pt/Al$_2$O$_3$ composites at 500°C.
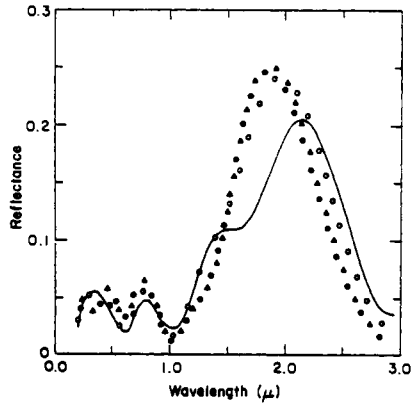
FIGURE 26. Reflectance of a Ni/Al$_2$O$_3$ composite on a Ni layer on quartz: as deposited - solid curve, after 70 hours at 400°C in air - open circles, after 260 hours at 400°C - closed circles, 68 hours at 500°C - triangles.

reflectance of Pt/Al$_2$O$_3$ composite deposited on a Pt layer on fused quartz showed no significant change in reflectance after 50 hours at 500°C or an additional 300 hours at 600°C. The reflectance spectra are shown in Fig. 27. The Pt/Al$_2$O$_3$ composite appears to be very stable, better than any other known metal-insulator composite film, and is at least as stable as any other presently available selective absorber. It is quite promising as a selective absorber material for application in high temperature oxidizing environments.

To show the use of the Pt composite films as a practical surface, coatings have been deposited on bulk pieces of 316 stainless steel. This temperature resistant steel is one of the candidate materials for the high temperature solar central receiver. The total hemispherical reflectance curve for one coating Pt/Al$_2$O$_3$ on stainless steel is shown in Fig. 28. The solid curve in this figure is the reflectance measured immediately after the film deposition. Also plotted with open circles
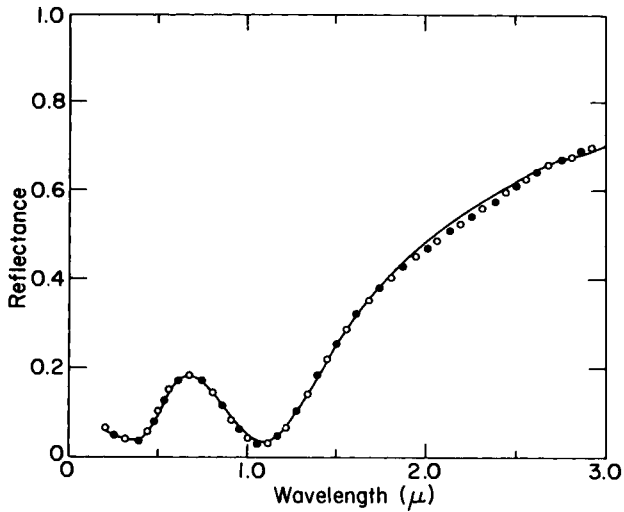
FIGURE 27. Reflectance of a Pt/Al₂O₃ composite on Pt: as deposited - solid curve, after 50 hours at 500°C in air - open circles, after 300 hours at 600°C - solid circles.
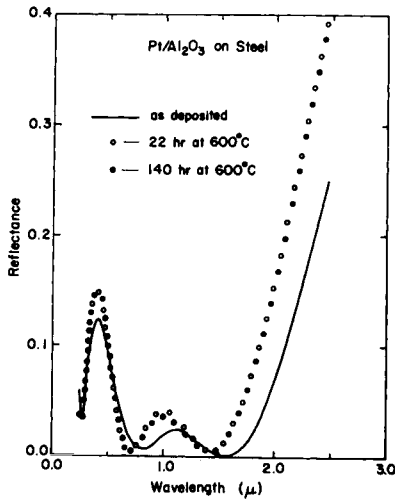
FIGURE 28. Reflectance of Pt/Al₂O₃ composite deposited on 316 stainless steel before and after heating in air.

is the reflectance after heating for 22 hours at 600°C in air. Failure due to detachment of the film from the substrate occurred after heating to 700°C but more sophisticated surface pretreatment could possibly alleviate this problem. Obviously these results are quite encouraging.

IV. SUMMARY

We have descirbed the general nature of the optical properties of metal-insulator composite films and have discussed the engineering of these films into high performance selective absorbers. For demanding high temperature applications vacuum deposited composites, particularly Pt/Al_2O_3, have been shown to have both excellent solar selective properties and the necessary thermal stability.

Theorectically, selective absorber performance superior to that achieved so far is possible. With present composites some improvement can be realized by additional processing, at additional cost, such as, for example, depositing anti-reflection coatings on the composite. A major advance in performance is dependent on the elusive goal of developing an absorber with a more ideal absorption curve. Barring such a breakthrough, in the coming years we can expect the development of a number of alternative composite absorbers with similar optical performances. While all alternative composites should be considered, the eventual development of improved selective absorbers is most dependent on a research program that deals effectively with the problems of coating cost and durability.

REFERENCES

1.   McDonald, G. E., *Solar Energy, 17,* 119 (1975).

2.   Craighead, H. G., Bartynski, R., Buhrman, R. A., Wojcik, L. and Sievers, A. J., *Solar Energy Materials, 1,* 105 (1979).

3. Granqvist, C. G., Anderson, A. and Hunderi, O., *Appl. Phys. Lett., 35,* 268 (1979).

4. Dickson, J., Proceedings DOE/DST Thermal Power Systems Workshop on Selective Absorber Coatings, SERI, Golden, Colo., p. 347 (1977).

5. Gittleman, J. I., Abeles, B., Zanzucchi, P. and Arie, Y., *Thin Solid Films, 45,* 9 (1977).

6. Blickensderfer, R., Deardorff, D. K. and Lincoln, R. L., *Solar Energy, 19,* 429 (1977).

7. Pettit, R. B. and Sowell, R. R., *J. Vac. Sci. Technol., 13,* 596 (1976).

8. Garnett, J. C. M., *Phil. Trans. Roy. Soc. London 203,* 385 (1904).

9. Lamb, W., Wood, D. M. and Ashcroft, N. W., *Phys. Rev. B, 21,* 2248 (1980).

10. Granqvist, C. G. and Hunderi, O., *Phys. Rev. B, 17,* 3513 (1977).

11. Bruggeman, D. A. G., *Ann. Phys. (Leipzig) 24,* 636 (1935).

12. Lord Rayleigh, *Proc. Roy. Soc. London 86,* 207 (1912).

13. Strong, J., *J. de Physique, 11,* 441 (1950).

14. Sievers, A. J., *J. Opt. Soc. Am., 68,* 1505 (1978).

15. Moon, P., *J. Franklin Inst., 230,* 583 (1940).

16. Trotter, D. M. and Sievers, A. J., *Appl. Phys. Lett., 35,* 374 (1979); Trotter, D. M. and Sievers, A. J., *J. Opt. Soc. Am.,* in press.

17. Seraphin, B. O., *Thin Solid Films, 39,* 87 (1976).

CHAPTER 10

CORROSION SCIENCE AND ITS APPLICATION TO
SOLAR THERMAL ENERGY MATERIAL PROBLEMS[1]

Steven L. Pohlman

Solar Energy Research Institute[2]
Golden, Colorado

I. INTRODUCTION

In Chapter One, a basic overview of the role that materials
play in the development of solar energy was presented. The
importance of understanding the limitations imposed upon a system
by the materials employed was emphasized. As with other energy
technologies, it is becoming clear that basic material problems
must be addressed and resolved before the successful advancement
of solar energy can be anticipated. The purpose of this chapter
is to explore the material question once again, but this time
concentrate on problems that may limit the development of solar
thermal systems due to material failure. Failure in this sense
includes chemical, mechanical, or combined modes of degradation.
It is important that, during the early stages of solar thermal
development, basic material problems be identified so that a
proper research and development program can be established to
address the major issues.

The objective of the first section of this chapter is to re-
view each solar thermal technology and discuss the anticipated
material problems, and to present to the reader a ranking of
their currently perceived relative importance. The second section
of this chapter will present the basic theories used in corrosion
and electrochemical research and show their application to labor-
atory studies. Weight loss, direct current (dc), and digital al-
ternating current (ac) methods of studying the kinetics of cor-
rosion will be described and an example of how weight loss data
were employed to determine the corrosion kinetics of a thermal
receiver will be presented.

Solar thermal conversion, like other developing technologies,
has experienced its share of material problems. For example,
shortly after the start-up of the linear concentrator and freon
turbine loop at the Willard, New Mexico solar irrigation site,
the system developed excessive pressure and blew a rupture disc.
An investigation revealed that build-up of corrosion product in
the working fluid created by the corrosion of the steel piping
caused the problem. Also the freon working fluid contained water,
and at operating temperatures, hydrochloric acid was being gener-
ated. Fortunately, the problem was discovered and solved before
excessive material damage had occurred (1).

In another case, a medium temperature concentrating solar
thermal system was forced to shut down shortly after initial test-
ing because corrosion product caused extensive erosion and event-
ual destruction of the high pressure circulation pump. Unfortun-
ately, the corrosion problem was not quickly solved and thousands
of dollars of damage occurred   (2). There are many other examples
of material failures of short-lived solar thermal systems which
show that these problems cannot be ignored and that they are life
limiting.

Material degradation in one form or another appears to be a
common problem facing the development of solar thermal power
(3-5). The corrosion damage anticipated in solar is similar to
that found in other energy technologies and, therefore, knowledge
and experience that has been gained earlier should be incorporated
into any comprehensive research plan. The different forms of
corrosion that will be discussed can be divided into categories
of uniform, local, galvanic and stress assisted attack. Uniform
attack includes all forms of surface degradation that do not ap-
pear to be selective in nature. This type of attack is generally
the easiest to prevent by closely controlling the chemistry of
the working fluid or by the use of corrosion resistant coatings.
Local attack includes pitting, crevice corrosion, erosion, and
selective leaching and is more difficult to control than uniform
attack. By proper system design and proper selection of construc-
tion materials and working fluids, the damage occurring from this
form of attack can be mitigated. Galvanic attack includes corro-
sion caused by surface potential differences arising from thermal
transients, stray currents, cementation of metal ions, and multi-
metal contact. This form of corrosion can be controlled by
proper design that insures the elimination of galvanic cells.
Stress assisted corrosion/cracking includes stress corrosion
cracking, corrosion fatigue, creep/creep-fatigue, and hydrogen
damage. This form of material degradation is the most insidious
of all forms because frequently no overt signs of damage will
appear prior to catastrophic failure. Proper selection of mater-
ial and control of working conditions can help diminish the like-
lihood of this type of attack   (6-8).

A complete list of definitions of the terms used throughout
this chapter is included in Appendix A.

II.   MATERIAL PROBLEMS AND SOLAR THERMAL CONVERSION

     Due to the importance of examining specific material problems
associated with the proposed solar thermal systems, a workshop
was organized to identify and assess anticipated material problems
which could limit their performance or feasibility. Of those
material problems identified, priorities were assigned according
to their potential for limiting solar thermal development. A
lot of the information generated at the workshop will be presented
in this chapter and procedings are available from the Solar Energy
Research Institute information division   (9).
     The highest priority was given to the understanding of creep,
creep-fatigue, thermal and corrosion fatigue, and their inter-
action in high temperature thermal conversion systems. Thermal
energy conversion and transport systems are exposed to high temp-
erature working fluids and experience unique diurnal temperature
cycles that result in severe creep and creep/fatigue interactions.
     The development and/or optimization of materials for unique
solar applications was identified as the second highest priority
issue. The data base of relevant existing information must be
expanded to cover the solar thermal needs. For example, high-
temperature receivers that are inexpensive and can withstand
thermal stresses and diurnal cycles must be developed. Flat-
plate collector systems must not only be inexpensive, but must
employ compatible materials. Optical concentrators must be made
from the materials which resist rapid degradation due to outdoor
exposure. New mirroring processes and mirroring materials must
be developed to provide the solar industry with high quality,
durable mirrors. Other solar energy conversion technologies,
such as thermal storage and ocean thermal energy conversion
(OTEC) also present unique material requirements.

The development of accelerated life tests used to predict
long-term reliability received the next highest priority. It
was also concluded that inexpensive, reliable, easily employed,
and maintained corrosion monitoring devices must be developed.

The development of industrial standards and design rules
especially for solar application was given the next highest
priority. For example, solar thermal conversion differs substan-
tially from nuclear conversion in terms of safety and failure
consequences, yet the container materials of both systems are
subjected to the same pressure vessel code. New design rules and
standards must be developed that are specific for the actual needs
and requirements of solar thermal energy.

Reviewing the major material concerns anticipated for the
various solar thermal systems it should be obvious to the reader
that many of the same material problems occur in the various
solar thermal technologies but differ slightly in degree of
severity due to different operating conditions. The operating
condition for each thermal conversion system that will be discus-
sed is given in Table I. It is the objective of the following
portion of this chapter to discuss the specific material degrad-
ation problems such as creep, fatigue, stress corrosion cracking,
oxidation, etc. for each of the solar energy technologies and
list these in order of importance.

Material problems of thermal concentrating systems that em-
ploy gas, liquid metal, molten salt, water or organic fluids as a
primary heat transfer fluid will be discussed first. Degradation
of the reflective surfaces used to concentrate thermal energy
will be followed by a discussion of material problems associated
with thermal storage. Flat plate collector systems will then be
reviewed and finally the material problems facing ocean thermal
conversion systems will be presented.

TABLE 1. Operating Conditions for Solar Thermal Systems

System[b]	Maximum Operating Temperature	Working Media	Special Working Conditions
High Temperature			
Gas systems	$800°C$ to $1400°C$	air, helium	controlled purity He
Molten salt[b]	$250°C$ to $600°C$	alkali nitrates and nitrities	chlorides, carbonates, sulfates as impurities
H_2O/steam[a]	$500°C$ to $570°C$	H_2O	deionized and treated (NH_3 and hydrazine) water, 100 to 200 kg/cm^2
Liquid metal[b]	$570°C$ to $700°C$	Na, NaK	controlled O_2, C, N
Organic fluid	$250°C$ to $400°C$	petroleum and silicon fluids	
Storage:			
Sensible heat	Ambient to $150°C$	MgO, rocks, Al_2O_3	
Thermo-chemical and latent heat	moderate temperature to $300°C$	CH_4, H_2O, products Ca(OH)$_2$, CaO, H_2O, SO_3, SO_2, O_2	
Medium Temperature			
H_2O	$200°C$ to $350°C$	H_2O	treated water (coordinated phosphate), 200 kg/cm^2
Oil	$150°C$ to $300°C$	synthetic oils, distillate cuts	oxidized in air
Low Temperature			
H_2O	Ambient to $90°C$	H_2O	$200°C$ stagnation temperatures are possible
H_2O/alcohol	Ambient to $90°C$	H_2O/ethanol	freezing conditions
Chemical storage Ammoniated/ methanolated salts reactions		$MgCl_2 \cdot 6\ NH_3$ $CaCl_2 \cdot 4\ NH_3$ $CaCl_2 \cdot X\ MeOH$ $CaCl_2 \cdot H_2O$	
Phase change storage Glaubers salt	$30°C$ to $90°C$	$Na_2SO_4 \cdot 10\ H_2O$	
OTEC	$20°C$ to $40°C$	sea water	periodic cleaning required due to biofouling

[a] Single-pass steam generator receiver tubes experience departure from nucleate boiling (DNB) within the receiver tubes and are therefore subject to high cycle fatigue.

[b] All systems are subject to diurnal cycling plus more rapid thermal cycling from intermittent cloud cover. The liquid metal and molten salt systems will experience thermal stripping (Thermal fatigue induced by fluid flow).

A. Thermal Concentrator Systems

Advanced central receiver concepts being studied by the U. S.
Department of Energy (DOE) are pushing the limit of receiver
material technology. (5). Several types of gas, sodium, salt,
organic, and water cooled prototypes are being investigated.
Materials research is being performed on ceramics, metals, coat-
ings, and their interaction with the various heat transfer fluids.
Although some conditions in solar-thermal power systems are simi-
lar to those in conventional nuclear and fossil fired systems,
the thermal fluctuations caused by diurnal cycling and by inter-
mittent cloud cover represent a thermal and cyclic stress envir-
onment not common to the conventional technologies. The major
material failure problems anticipated for each solar thermal
technology as dictated by the various heat transfer fluids and
operating conditions will be discussed. Chapter one briefly
describes each of these systems and is recommended for readers
who are not familiar with the various solar thermal systems.

   1. Gas-Cooled Systems

   *a. Creep, Fatigue, and Their Combination in Solar Receiver
Material.* Characterization of the behavior of both metallic and
ceramic receiver materials under creep, fatigue, and creep-
fatigue conditions, that result from steady state loads, mechan-
ical vibrations, and thermal cycling conditions is required. The
characterization should include both developing and validating
predictive methods to permit extrapolation of relatively short
time test data to desired design lifetimes. Materials under
current design consideration include nickel and cobalt base alloys
(e.g., Inconel 617, Haynes 188, Incoloy 601) and ceramics, in-
cluding silicon carbide and silicon nitride. Metallic receivers
should be reliable up to about 950°C and ceramic receivers to
about 1400°C.

*b. Oxidation of High-Temperature Alloys and Nonoxide
Refractories.* The long term durability of super alloys and sili-
con carbide as solar receiver materials must be demonstrated in
the total solar receiver environment. The particular problem is
one of structural stability under oxidizing conditions at temp-
eratures in the range of 600 to $1400^{\circ}C$. Breakaway oxidation re-
actions will occur at some point in time. This could result in
failure by an accelerated uniform surface recession or localized
attack and penetration that would weaken the material. Currently
available data on materials have not been obtained under the
complete solar environment and may not accurately represent ac-
tual behavior. More importantly, it is difficult to extrapolate
data with respect to time of exposure due to the nature of oxide
breakaway and, therefore, long-term exposure tests are required.

c. Slow Crack Propagation in Ceramic Receivers. Slow crack
growth can occur as a result of localized creep or by stress
corrosion cracking in the ceramic and metallic components of the
receiver tubes and structural supports. Such crack growth can be
driven by residual stresses and by operating stresses caused by
thermal gradients generated under operating conditions.

d. Fretting and Wear of Ceramic and Alloy Components.
Fretting and wear of metals and ceramics is a potential problem
associated with the joining and sealing of metals and ceramics
particularly when sliding or line contact compression joints are
used to accommodate effects of thermal cycling. Metal-to-metal
interactions at elevated temperatures can lead to welding of the
metals and subsequent mechanical failure. Likewise metal-to-
ceramic and ceramic-to-ceramic contacts can result in unacceptable
wear and/or high stress concentration due to frictional forces.

*e. Alternative Materials for Very High Temperature Solar
Receivers.* Silicon carbide has been selected as the material of
construction for all current receiver designs that will operate

above 900°C. Although results of preliminary efforts promise
success for SiC as a material of construction for this application,
there is no experience that demonstrates suitability for long-
term application. It is possible that work during the next 2-5
years may reveal that SiC is deficient in one or more areas. If
this is the case, no alternate candidate material has been identi-
fied, and programs to develop high temperature solar receivers
will encounter serious delays.

 f. Microstructural Instability in High-Temperature Alloys.
Many candidate alloys for use in high-temperature, gas-cooled
systems undergo significant microstructural change during elevated
temperature service. These changes usually alter the mechanical
properties significantly. For example, thermal aging may reduce
ductility and toughness. Therefore, detailed information on
operating parameters is required to permit creation of reliable
designs for high temperature systems. Candidate materials for
high temperature structures, such as Inconel 617, Incoloy 601,
Haynes 188, etc., must be evaluated. Exposure temperatures should
cover the range of interest and exposure times should be long
enough to permit extrapolation of the predicted lifetime of the
alloy with fair confidence.

 g. Carburization/Decarburization of High-Temperature Alloys.
Certain of the central receiver concepts utilize high-pressure
helium to remove the solar heat from the receiver. Such systems
typically employ a Brayton cycle gas turbine to generate elect-
ricity. Pure helium gas is chemically inert; however, it is
difficult to assure a complete absence of impurity gases. These
impurities can arise from a variety of sources, including leakage
of air or of oil from rotating equipment. The contamination of
the container walls with these impurities can alter the chemical
potential and physical characteristics of the surface sufficiently
to allow the onset of carburization or decarburization. This

problem is particularly important when helium coolant gas is em-
ployed, since the oxygen potential of the gas is generally so
low that protective oxides do not form on metal surfaces.

    *h.   Degradation of Insulation and Changes of Emissivity
Caused by Sintering and/or Devitrification.*   Ceramic insulation
materials are used in high-temperature, gas-cooled heat exchang-
ers primarily to protect structural metals. Fibrous ceramics
are the present candidate materials since low weight and maximum
insulating value are principal requirements and strength require-
ments are minimal. In a cavity receiver, fibrous insulation can
aid in redistributing the radiant thermal energy by acting as a
diffuse reflector. Thus, a fibrous insulator with a very low
absorptivity will function as a good diffuse reflector and,
when exposed to direct radiation, provide increased thermal pro-
tection. By improving thermal distribution within a cavity,
fibrous ceramic insulation aids in reducing thermal gradients in
the heat exchanger tubes within the cavity. Problems with fib-
rous insulation are related to changes in insulating value and,
to a lesser degree, emissivity.

    2.   Liquid Metal and Molten Salt Systems

    *a.   Creep/Fatigue Behavior of Container Materials in Molten
Sodium or Molten Salt.*   Material behavior under creep-fatigue
conditions is extremely important in determining the lifetime
performance of solar receiver tubes. The absorber tubes will
be subjected to daily cyclic loads from shut-down and start-up
operations, with additional cycles imposed upon the system from
intermittent cloud cover and focusing and defocusing cycles.
Thus, the absorber tubes will be expected to undergo hundreds of
thousands of strain cycles over a 30-year service life.

    *b.   Physical and Chemical Data (400-600°C) on Alkali
Nitrate Salt Mixtures.*   Mixtures of molten alkali metal nitrates

and nitrites (i.e., HITEC) have been used extensively as heat
transfer agents. Both these and mixtures of alkali metal ni-
trates (e.g., draw salt) are being considered for use as heat
storage media. For economic reasons, interest is mainly in the
sodium and potassium salts. While the chemical and physical
properties of the above systems are fairly well known at temper-
atures below 400°C, information on their properties at tempera-
tures up to 600°C is scarce.

 c. Sodium Corrosion and Mass Transport Studies. Present
solar system designs specify the use of austenitic steels and
nickel-rich alloys in the receiver, austenitic and ferritic
steels in the piping, ferritic steels in the steam generators,
and carbon steel in the low-temperature storage tanks. Metallic
mass transfer and carbon transfer, which will occur during oper-
ation and be complicated by the presence of the various metals,
may be enhanced by the potentially higher oxygen content of the
sodium employed for solar use. Future high temperature designs
will probably require specifying new receiver materials with
unknown sodium corrosion/carbon transport behavior. Therefore,
corrosion and transport studies under simulated or actual envir-
onments are required.

 d. High-Strength Ferritic Alloy Development. Alternative
structural materials to the 316 and 304 austenitic stainless
steels and Incolloy 800 are needed for use in sodium-heated
steam generators. These materials are prone to chloride and
caustic stress corrosion cracking, and are sensitized at
500-600°C in weld heat affected zones. They have high expansion
coefficients and lower thermal conductivity than ferritic steels,
and in proposed systems require transition weld joints. The
austenitic stainless steels are already ASME code approved,
and it would be advantageous to develop and obtain ASME code
acceptance of high strength ferritic steel that could withstand

temperatures up to 650°C.

     e. Thermal Striping and Thermal Fatigue Damage. Material
evaluation under thermal cycling conditions of the proposed
sodium central receiver system is extremely important. In addi-
tion to diurnal and intermittent thermal cycling, thermal strip-
ing, a phenomenon seen in the nuclear steam generators, will
occur in the receiver and piping. Both of these thermal cycling
phenomena can cause failure due to a thermal fatigue mechanism
and should be investigated.

     f. Forced Convection Loop Studies of Molten Nitrate Salt.
The Martin Marietta Company conceptual design for a central re-
ceiver incorporates molten sodium nitrate as the primary heat
transfer medium in both the receiver and thermal storage sub-
systems. The major concern in the qualification of this salt
for the intended application is the need for quantitive corrosion
information above 400°C.

     *g. Development and/or Qualification of Coolant Containment
Alloys for Receiver Operation to 700°C for Second-Generation
Plant Designs.* Present design strategies for both sodium-cooled
and molten salt-cooled solar thermal conversion systems are based
on present steam generator temperatures and technology. This is
the proper technology base for the short term, but both the
problems and opportunities in the solar thermal technology are
different from those in nuclear technology and, over the long
term, many benefits may result from using higher receiver oper-
ating temperatures.

     h. Caustic Cracking of Steam Generator Tubes. The possibi-
lity of caustic attack or stress corrosion cracking of the water/
steam circuit (steam generator) of a sodium-cooled central re-
ceiver is great. Changes in coolant chemistry may happen as a
result of unplanned intrusion of sodium or sodium hydroxide.

These intrusions result from ineffective control of chemical
constituents in the feed water, as well as from leaks between
the sodium and water/steam circuits. The resistance of container
materials exposed to typical solar environments and to caustic
cracking needs to be explored.

   i. Stress Corrosion Cracking of Alloys by Molten Salts.
Identification of the temperature ranges and stress levels which
cause stress corrosion cracking when molten salts are in contact
with container materials and their weldments is needed. It is
evident that considerable knowledge and expertise are already
available from the nuclear energy industry. However, some inter-
esting and important differences between the two energy-generat-
ing approaches also became apparent. For example, temperature
cycling, resulting from changes in the cloud coverage or the
day-night cycle is likely to lead to unusual high-temperature
creep/fatigue effects, and these will be advanced by the presence
of the chemically active liquid metal/salt environments. Very
little technical data, needed for safe design, is available on
such effects, and this information will have to be generated as
soon as possible. Another difference between solar and nuclear
systems is the absence of radioactive substances. Hopefully,
this will allow use of construction under less-restrictive stand-
ards, hence reducing the cost of the construction, maintenance,
and operation of solar liquid metal and salt loops. Another
difference will be the presence in solar loops of large storage
tanks of molten metal or salt, these being needed to damp out
the temperature oscillations noted above. These will be expen-
sive to construct and maintain, but the number required in any
given loop could be reduced if the maximum operating temperature
in the loop could be increased from 600° up to $700^{\circ}C$. This
seems possible with sodium loops, but will require the qualifica-
tion of alloys not presently in use for these applications. For

salt loops, it will be necessary to obtain more basic chemical
operating data in mixed alkali nitrate salts on the mechanical
reliability of the construction materials in contact with them.

    j. *Secondary Problems.* The following problems are not
considered as significant as those previously discussed but do
warrant consideration: degradation of external containment sur-
faces by oxidation, pitting, sensitization; control of the
chemical constituents in the sodium coolant; control of sodium
fires; improved nondestructive testing of flaws or cracking;
wear and galling of parts due to clean up by sodium and molten
salt; on-line monitoring of the coolant; heat flux and asymmetric
thermal stress effects on corrosion and oxide scale spalling in
the salt coolants; establishment of the mechanics of fracture
mechanics of receiver materials in a sodium or salt environment;
corrosion and degradation of internal (storage tank) insulation
materials in sodium and salt; and development or modification
of material standards and codes.

    3. *Water/Steam Cooled Systems*

    a. *Methodology and Basis for Receiver Design.* The mechan-
ical reliability of the receiver, particularly as a function of
the thermal and environmental variables encountered in this appli-
cation, is of primary importance. These are the two major issues
in this area. First, the applicability of the existing ASME
high-temperature design code (Code Case 1592) needs to be exam-
ined. This code often requires detailed elastic-plastic-creep
analysis, which is both expensive and time consuming to apply,
and may not be appropriate for the solar receiver. For example,
during operation the hot side of a receiver tube is loaded in
axial compression which is not appropriately reflected in the
code. The code would also demand ultraconservative designs which
would economically penalize solar applications. Development and
validation of a simpler design basis compared to that required

of a nuclear system would be a very useful step in advancing solar technology.

Secondly, data are lacking in a number of areas that would facilitate developing reliable, economical receiver designs. High-temperature design data are available on relatively few alloys (i.e., 304 and 316 stainless steel, Incoloy 800, and 2 1/4 Cr-1 Mo). Even with these relatively well known materials, information is lacking on the creep-fatigue interaction, particularly in the multiaxial aspects; on corrosion fatigue in the relevant aqueous and steam environments; on the effects of low-frequency cycling stress superimposed on crack growth rate; about long term creep, particularly with respect to temperature transients; about creep-fatigue and corrosion-fatigue on weldments and bimetallic joints; on the fundamental, time-dependent inelastic, deformation behavior under multiaxial conditions and solar environments; and on the potential importance and role of residual stresses.

   b. Coolant Chemistry. There are five general concerns regarding the maintenance of coolant chemistry and the interaction of the working fluid with container materials. First, the selection of feedtrain and condenser materials with respect to coolant technology and systems design must be considered in order to minimize corrosion product generation during operation and the diurnal lay-up cycle. This selection process will decrease the probability of receiver-tube corrosion or burn-out. Secondly, the frequency and difficulty of cleaning receivers which is required to maintain proper chemical resistance and thermal transfer properties, needs to be determined. Thirdly, the extent of thermally shock-induced spalling of the natural oxides of heat exchanger tubes needs to be determined. Fourthly, the effect of soluble contaminants in superheated steam needs to be measured

for their effect on promoting localized attack based on the
diurnal wet/dry cycle. Finally, the long-term compatibility of
the selective coating on the outside diameter of metallic receiv-
er tubes needs to be studied.

　　4. Aqueous and Oil Systems

　　　a. System Design--Choice of Coolants/Container Materials.
The choice of coolant and the selection of container materials
should be integrated decisions. For example, the choice of an
organic coolant will reduce system operating pressures and make
possible the use of thinner wall sections than necessary for an
aqueous coolant, and may reduce the necessity for corrosion con-
trol. On the other hand, a substantial inventory of organic
coolant may be necessary, and continuous clean-up capability may
need to be installed. The decisions about the coolant and con-
tainer material should be made with joint input and designers
must be advised that changing from one coolant to another will
have ramifications with regard to overall design and material
selection.

　　　*b. Thermal and Thermal-Mechanical Stability of Selective
Coatings.* Selective coatings are essential to the technical
feasibility of mid-temperature (150-350°C) thermal systems. These
coatings must have high absorptivity to solar radiation and low
emissivity at the operating temperature. They must not be de-
graded by either thermal history or environmental interactions.
They must be produced economically and have consistent properties.
While the technology for black chrome seems adequate to meet
current needs, its degradation mechanism is not well understood.
Perhaps, the currently used black chrome process could be im-
proved, or a new coating technology could be developed to further
the design options.

c. Thermal and Corrosion Fatigue of Receiver Tubes. The
primary piping and receiver tubing will be subjected to a non-
uniform load history resulting from thermal cycling of the con-
centrator heat source, to impulse overloads due to wind and
movement of coupled structures, to high-cycle, low-amplitude
loads due to vapor locks in aqueous cooling systems, and to
differential thermal expansion at seals and couplings at the
receiver. These combined loadings are likely to be more variable
and extreme than in process-heat boilers due to the unique therm-
al cycling, longer piping runs, varying degrees of insulation,
and greater use of dissimilar materials. Therefore, thermal and
corrosion fatigue of the receiver tubes and primary heat transfer
systems needs to be investigated.

d. Control of Critical Parameters. Success of solar therm-
al designs depends on awareness of the critical parameters, ex-
perience of existing technology, and careful and continual con-
trol of variables. For example, for a water-cooled carbon steel
system to be reliable, there must be a control of water chemistry
(pH, redox potential, dissolved oxygen and solids) to avoid oper-
ating under corrosive conditions. Similar controls are required
independent of the alloy selection. The nature of solar conver-
sion systems will compound the problems compared with conventional
steam generators operating under the same temperature and pressure
boundaries.

e. Standardized Information on Organic Coolants. Physical
and chemical data on organic heat transfer fluids and systems are
not readily accessible to designers and builders of solar systems.
Lack of uniform service simulation tests has resulted in conflict-
ing and misleading performance data. Potential users of organic
heat transfer fluids often lack bases for evaluating comparative
performances of different fluids and therefore, find it difficult
to determine how different fluids will perform in their systems.

Solar system designers/builders are much less familiar with
organic heat transfer technology than with water/steam technology.
Therefore, they express preference for water/steam systems even
when there are technical advantages favoring organic coolant
working fluids.

   5.   *Solar Concentrators*

      a.   *Development of Industry Standards and Test Procedures.*
At the present time there are few standards or test procedures
that are generally accepted by the industry for many materials
used for solar concentrators. This situation exists with respect
to metals, glasses, and polymers, and is due in part to the rapid
growth of the industry. Accordingly, manufacturers and test
laboratories are often unable to compare data on the properties
and performance of materials. For example, when a mirror vendor
states that his product has a weathering resistance of six years,
a potential user has no idea what this means, since many times
no standard test conditions are specified. Specific tests should
be developed for evaluating weatherability of the mirrors that
can be related to loss of reflectance and estimated life.

      b.   *Degradation of Metallic Reflective Coatings.* Reflective
surfaces normally lose their reflective properties as a result of
chemical degradation of the metallic surface. The chemical de-
gradation is probably caused by corrosion of the reflective sur-
face resulting from the combination of water and at least one
other contaminant. A loss in reflectance results in a decrease
in performance so either more concentrator are required or the
mirrors have to be replaced. In existing systems, the corrosion
of the silvered surface has been the major reason for loss of
reflectance. Extensive degradation has been observed within a
few months of atmospheric exposure, as discussed in more detail
in the chapter by Czanderna.

   c.   Degradation of Reflective Support Materials. Substrate
or superstrate materials support and/or protect the reflective
surface. Degradation or failure of supporting materials may
shorten the useful life of the concentrator.

   d.   Interfacial Adhesion of Materials. Good interfacial
adhesion between materials, i.e., metal/glass, metal/polymer,
and metal/metal, is of primary importance for long term reliabil-
ity of solar concentrator systems. Reflective metals on glass
or polymers must maintain good adhesion to have a cost-effective
lifetime. Weakly bonded silver, for example, will flake or peel
away from the glass resulting not only in a loss in reflectance
but will provide further reactive sites for moisture and other
aggressive contaminants. Protective copper coatings over silver
reflective coatings must adhere to the silver to impede the in-
gress of corrosive species. Protective organic coatings over
metallized surfaces must adhere to them in order to provide pro-
tection from moisture, atmospheric pollutants, etc.   Structural
adhesives used to join the structural back-up panel to the re-
flective surface must adhere in order to maintain the structural
integrity and dimensional stability of the subsystem. Sealants
must adhere intimately to panel edges (glass, plastic, metal,
wood, etc.) to stop moisture or airborne pollutants from inward
migration and eventual attack of the metallized reflective sur-
face. As indicated, good adhesion is essential for all concentra-
tor components and the effect of thermal cycling and long-term
environmental exposure can create bond degradation at an inter-
face even though initial adhesion was good.

   e.   Surface Contamination by Environment. Solar collector
systems inevitably accumulate dust or dirt on surfaces exposed
to the environment. The rate of accumulation depends on a number
of parameters including system design, mode of operation, mater-
ials of construction, weather, and location. Nevertheless,

degradation of system performance can be expected due to both
absorption and scattering of light by the contaminants.

    f. Dimensionally Stable Material and Systems. The long
required lifetimes of solar energy components, specifically con-
centrators, require dimensionally stable materials. This specif-
ic problem deals not only with the need for a long-term stable
structure, but also with the dimensional stability of bulk mater-
ials used in the construction of these concentrator systems.

    g. Development of Improved Reflective Materials. Mirrors
currently available commercially, were not designed for applica-
tion to solar systems. Degradation by erosion and/or corrosion
will significantly reduce system performance. The future of the
solar energy program depends on being able to generate power
reliably or convert its thermal energy to a useful output at
competitive costs. An improved corrosion-resistant mirror assem-
bly is needed to guarantee that both objectives are met.

    6. Thermal Storage

    a. Sensible Heat-Dual Media Systems. The underlying mater-
ials reliability concern of sensible heat storage is compatibility
of the dual media with each other and with the containment vessel.
The primary motivation for designing storage systems to incorpor-
ate a second material other than the working fluid is economic
(i.e., to reduce the amount of the expensive working fluid). A
secondary issue is that a steep thermocline cannot be maintained
in a single medium. Present and anticipated dual-phase storage
concepts include hydrocarbon oils with granite, molten salts with
taconite (iron ore), air or gas with refractories, and air with
rock.

    Inevitably, cyclic-elevated temperatures will degrade both
the solids, and may promote detrimental interactions between the
two. For example, hydrocarbon oils will readily crack at high
temperatures in the presence of oxygen, react with the granite,

and form organic acids which could then corrode the storage
vessel. Also, the liquid or gas may cause fragmentation of the
rock by combined action of chemical attack and thermal stress.
Thermal-stress fracture and corrosion of rock are probably coup-
led phenomena, as they are in most ceramics. It would be useful
to search for ceramics or rocks which are more resistant to one
or the other aspects of this phenonemon. For example, taconite
is more resistant to chemical attack than is granite; hence,
the former is used in molten salt systems. Ability of the rocks
to arrest cracks should be separated from their absolute resist-
ance to fracture. In other words, crack propagation may be quite
tolerable if it ultimately ceases before the rock fractures.
Candidate solid storage media should be ranked on the basis of
appropriate thermophysical properties. Representative tests are
needed to guide the development of economic systems with adequate
thermomechanical and chemical stability for both near-term demon-
strations and long-range application.

Representative tests should be developed, and conducted on
proposed systems. These tests must accurately duplicate operat-
ing conditions, (i.e., be capable of scale-up to full size). The
tests must incorporate mass transport, heat transfer, and cyclic
operation. For example, thermomechanical and chemical stability
of rock and brick in the presence of working fluids and under
cyclic temperature conditions is of specific concern. Contamin-
ation of the liquid by the solid should be addressed because it
may affect the heat transfer characteristics of the fluid, or
induce chemical attack on the containment vessel. Potential
solid media (rocks, bricks, ceramics) should be rank-ordered with
respect to critical thermophysical properties, and then with
respect to chemical stability. Increase in storage vessel diame-
ter by ratchetting may be induced by the cyclic thermal stresses

and, therefore, should be investigated. Analytical predictions
are conflicting, and some well-designed tests to resolve the
issue definitely would be useful. Environmental considerations
including the effects of working fluid vapors on local atmosphere,
potential spillage of nitrate salts, and disposition of the
products of chemical degradation within the storage vessel, should
be addressed.

   b. *Latent Heat Thermal Storage Systems*. The highest prior-
ity problem area is a requirement to establish compatibilities
of the inorganic hydrates, organics (waxes), eutectics, and ni-
trate compounds identified for storage use with containment
materials. Molten salts are currently the leading candidates
for the high-temperature thermal storage in large scale solar
systems. The normally corrosive characteristics of molten salts
are aggravated by the cyclic temperature conditions encountered
in solar systems. Containment is the single most important con-
cern, since large storage components, once in place, will be
difficult and expensive to repair.

   Compatibility tests including both localized and general
corrosion between working fluids and containment materials should
be conducted and the effects of varying the operating parameters
such as flow velocities and fluid chemistry should be studied.
In all tests, cyclic temperature control must be featured to
reflect solar needs. Working fluids should include inorganic
hydrates, organics, urea-based eutectics, and alkali nitrates/
hydroxide systems. Container materials should include stainless,
ferritic, and carbon steels, as well as common building materials.

   A continuing basic research effort to obtain fundamental data
relevant to predicting the stability of candidate container mat-
erials in contact with their proposed high-temperature storage
media is required to increase the cost effectiveness of develop-
ment programs. Research investigation employing redox potentials,

polarization curves, Pourbaix diagrams, and reaction kinetics is
essential.

    c. Thermochemical Energy Storage Systems. Thermochemical
energy storage utilizing reversible chemical reactions have sev-
eral advantages over sensible and latent heat process. Among
these, higher energy density, long-term and ambient temperature
storage capabilities and lower energy capacity cost are the most
important.

    Work to date has identified several promising types of re-
versible reactions such as thermal decomposition reactions (e.g.,
$CaO/Ca(OH)_2$), and solution/dissolution reactions (e.g., SO_3/SO_2).
A system based on sulfuric acid concentration has been tested
successfully in a small pilot-type unit. Cost considerations and
materials selection appear to be the major unresolved issues.

    Important issues affecting reliability of several promising
processes vary according to system type. For example, in the
thermal decomposition reactions, the major outstanding problem
is lack of knowledge and understanding of the long-term dynamic
behavior of reactant/product particles. For thermal decomposi-
tion reactions, such as ammonium hydrogen sulfate decomposition,
the main reliability issue is lack of understanding and knowledge
of the long-term kinetic reversibility of the reaction steps
involved.

    The lack of long-term data on catalyst performance under
temperature cycling conditions is an important unresolved problem
in the catalyzed type of reactions. The corrosion and selection
of construction are issues of lower priority at this stage of
development. Based on the present state of development of pro-
cess conditions in these systems, processes involving sulfur and
oxygen species at elevated temperature are judged as providing
the most severe conditions for material containment. An addit-
ional complication in some of the designs considered is the

presence of thermal cycling of the system components.

  7. *Flat-Plate Collectors*

  The most conventional thermal conversion system is the flat-
plate collector used for space and water heating. Although solar
heating and cooling is technically feasible, it is not yet econom-
ically competitive with conventional heating and cooling methods.
The main barriers to commercialization are the high initial cost
and low reliability associated with liquid-cooled, flat-plate
collectors. The annual costs of solar systems are primarily de-
pendent upon investment recovery and thus, the expected lifetime
of the system is an extremely important factor.

  High costs and corrosion of the absorber plate are the major
problems with flat-plate collectors. The most widely used absorb-
er materials are copper, aluminum, carbon steel, and stainless
steel. Except for its high cost, copper is the most attractive
metal because of its excellent corrosion resistance in aqueous
media and its good thermal properties. Aluminum is less expensive
and lightweight, but is susceptible to severe galvanic and local-
ized attack. Although carbon steel is the least expensive in
dollars per pound, it's general corrosion characteristics makes
the use of thicker absorber plates necessary. Certain stainless
steels exhibit excellent corrosion resistance and look very
promising. Plastics have also been considered, but they generally
cannot withstand stagnation temperatures (150-230°C) or pressures
(about 1.73 mpa) of high-performance flat-plate systems.

  Protection against freezing is necessary for most systems and
this complicates corrosion problems for all the candidate mater-
ials. Presently, ethylene or propylene glycol/water solutions
are most frequently used. Unfortunately, glycols degrade at
temperatures near their boiling point to form corrosive organic
acids. Since stagnation and high temperatures are likely to
occur, inhibition, buffering, monitoring, and periodic replenish-

ing of the solution are necessary to prevent corrosion by such
acids. The use of glycols with proper treatment is effective,
but the complicated water chemistry and maintenance make it a
complicated procedure for typical homeowners. Organic fluids,
such as paraffin oils and silicone oils, are possible alternatives
to aqueous antifreeze solutions. They are noncorrosive, but
their expense, high viscosity, and poor thermal properties make
their use less practical at this time.

Another approach to the freezing problem is the use of water
(an excellent heat transfer fluid) along with automatic drainage
of the collector at low temperatures or at night. Untreated
water could possibly be used with copper or stainless steel ab-
sorber plates, but distilled or deionized water and some inhib-
ition must be used for aluminum or carbon steel collectors. The
main disadvantage of the drainage method is that the corrosivity
of water increases dramatically upon exposure to air, and frequent
drainage would create corrosion problems unless some protective
scheme, such as, vapor phase inhibition, inert gas blankets, or
chemically adsorbed coatings was used.

The reliability of flat-plate collectors must be improved
before space heating and cooling of buildings becomes competitive
with traditional heating and cooling methods. Protection against
freezing and corrosion must be developed that is less complicated,
inexpensive, and more reliable than current methods. The enthu-
siasm with which the public greets the solar energy program will
be strongly influenced by the success of the most visible compon-
ent of solar energy systems, the flat-plate solar collector.

a. *Materials Selection*. Generally materials of construc-
tion have not been chosen on the basis of adequate supporting
data. All too often the choice of materials has been left to
low-technology fabricating organizations with no appreciation of

the potential dangers from corrosion, etc. It is important that
sufficient long-term data be assembled to permit optimization of
material selection for both air- and liquid-type flat-plate solar
collector systems. The following material problems have been
identified and could be mitigated by the proper material select-
ion. Corrosion of metallic materials by interaction with the
working fluid or by weathering of external surfaces; degradation
of non-metallic materials under conditions of stagnation, ultra-
violet exposure and thermal cycling; degradation of coatings
(applied to external surfaces) caused by weathering, thermal
cycling and ultra violet radiation; degradation of the insulation
materials; and degradation of the heat transfer fluids.

    b. Monitoring Performance of Materials. Corrosion damage
which proceeds undetected may lead to unexpected catastrophic
failure of solar collectors. The potential for such failures is
especially pronounced in systems with recirculated liquids.
Localized corrosion (pitting, crevice corrosion) is particularly
insidious since perforations can occur with relatively little
total loss of metal. The corrosiveness of recirculated fluids
may change with time under operating conditions as the result of
breakdown of organic chemicals, exhaustion of inhibitors, etc.
Thus, initially unreactive fluids may become corrosive. A low-
cost, reliable, on-line monitoring system is needed to detect
changes that show fluids have become corrosive. If changes are
detected early enough, timely corrections can be made.

    c. Cleaning and Maintenance. To maintain good thermal
efficiency, surfaces of flat-plate collector systems must be
cleaned without surface degradation. Cleaning is normally per-
formed without disassembly of the apparatus, and thus chemical
cleaners must be compatible not only with the specific part to be
cleaned, but also with all other adjacent parts. This includes
all metallic and nonmetallic collector materials (metals, plastic,

glass, sealants, etc.).

A greater appreciation is needed concerning the importance
of cleaning procedures to the long-term reliability of solar
conversion systems. Corrosion of the solar panels may result
from inadequate cleaning and maintenance, use of improper clean-
ing methods, or the use of corrosive cleaning agents. Procedures
should be developed and cleaning agent identified which may be
used by nontechnical personnel with minimum supervision in the
cleaning of solar apparatus.

8.   *Ocean Thermal Energy Conversion (OTEC)*

Another solar thermal technology that is capable of generat-
ing large outputs of energy is ocean thermal energy conversion.
(10).

The problem of biofouling and corrosion in heat exchanger
tubes exposed to a primary heat transfer fluid seawater is a
major technical obstacle to making OTEC power plants economically
feasible. The most crucial problem is the loss of heat transfer
efficiency associated with biofouling and corrosion of the heat
exchanger surface on the seawater side. Because of the small
temperature differences involved in the heat transfer process
in OTEC systems, heat transfer surfaces must be maintained at
optimum efficiency. Since the cost of the heat exchanger com-
prises nearly 50% of the cost of an OTEC plant, the efficiency of
the heat transfer process is an important economic consideration.
The loss of heat transfer efficiency can be associated with all
types of corrosion and biofouling, but of most importance is the
formation of primary organic films. These films are the results
of adsorption of organic materials and living organixms on the
exposed surfaces. They begin to form almost immediately upon
exposure to marine invironments. A film 0.25 mm thick can reduce
heat transfer efficiency by a minimum of 50%. Corrosion products,

macrofouling (attachment of algae, barnacles, fungus), and scale
(chemical precipitates from seawater) also contribute to and com-
plicate the problem   (11).

Biofouling can also accelerate the corrosion process. Micro-
organisms (bacteria) can directly accelerate anodic dissolution
(corrosion) of the surface or they can create a corrosive environ-
ment by producing localized concentrations of acid. Macroorgan-
isms can ititiate crevice attack and produce organic acids which
create corrosive conditions   (12).

Presently, titanium is the preferred material for heat ex-
changer tubes because it shows good corrosion resistance and is
compatible with ammonia (the preferred working fluid) and aqueous
mixtures of ammonia. Other materials being considered are alumi-
num, 90/10 copper/nickel, high nickel/chromium/molybdenum iron-
base alloys, and plastics. The cupronickel alloy is an excellent
material for marine use because the toxic effect of copper on
marine organisms makes it the least susceptible to fouling. How-
ever, using copper is questionable because of severe stress-corr-
osion compatibility problems with ammonia, the proposed working
fluid. Aluminum is very attractive because of cost advantages,
but its predicted lifetime is much shorter than that of titanium.
The predicted lifetime of a plastic heat exchanger is even
shorter.

Research is required to characterize all candidate materials
with respect to localized attack and the effect of cleaning on
the long-term compatibility of the heat exchanger material   (13).

III. CORROSION SCIENCE

The identification of the critical material issues that are
confronting the expeditious development of solar thermal energy
is only the first step. Once the anticipated material problems

have been identified initiating and completing the research re-
quired to address and solve the problems become the next object-
ives. Since the material problems have been identified it is
appropriate to discuss the various scientific techniques by which
these material problems may be examined. First, a brief discuss-
ion of the basic theories of corrosion science will be presented
and then a description of some of the laboratory techniques which
apply these theories will be given. It is not practical at this
time to discuss all the laboratory techniques available to ex-
amine the interaction of a material with its environment, so an
emphasis will be placed upon describing the electrochemical tech-
niques employed to evaluate nonmechanical electrolytic degrada-
tion.

A.   Corrosion Kinetics

   The investigation of corrosion kinetic processes is normally
pursued by either measuring weight change or monitoring electro-
chemical reactions. The weight change method gives the total
magnitude of the corrosion reaction(s), integrated over both
time and area of the corroding surface. An increased understand-
ing of the processes involved and how they change with time may
be obtained by using electrochemically induced polarization tech-
niques which continuously measure the rate of a reaction(s) as
an electrical current. Polarization curves are therefore a
graphical representation of the current to an electrode surface
as a function of an applied potential. The current is a measure
of the rate of a reaction or reactions on the electrode, and it
is usually dependent on the environment in which the measurements
are carried out. The measurement of polarization curves in dif-
ferent environments thus provides a rapid and sensitive method
for the evaluation of corrosion rates and aids in the selection
of the material or the environment which may give superior
service performance. Such techniques have been employed in the

fields of alloy development, inhibitor research and application, localized corrosion, and industrial corrosion monitoring and control   (14-16).

The direct current electrochemical methods (i.e. linear polarization, and Tafel polarization) may be used to determine corrosion rates and the change in rate with time if the change is slow enough. Alternating current techniques have also been used to monitor corrosion rates but the variation with time is usually very tedious to follow. For determining rates, the ac measurements must be made at several different frequencies, and if the corrosion rate changes before the necessary frequency range can be swept, errors will result   (17). In principle, however, the ac measurement techniques are very powerful and provide more information than dc methods. Both of these methods will be described in greater detail.

B. *Corrosion Thermodynamics*

The useful energy that may be derived from a chemical reaction is the Gibbs free energy (ΔG) of the reaction. The free energy can be obtained as electrical energy in an electrochemical cell and the two are related by the expression $\Delta G = - n F E$, where ΔG is the free energy change per mole of reactant, n is the number of electrons involved in the reaction per mole of reactant, F is Faraday's constant, and E is the cell voltage   (18). The free energy provides the driving force for the reaction to occur, and a larger (more negative) driving force produces a larger cell voltage.

Consider the reaction $Zn(metal) + 2H^+ = Zn^{+2} + H_2(g)$, where the reaction is carried out in an electrochemical cell. In the cell the reaction can be considered as half-reactions, one involving the zinc oxidation, $Zn = Zn^{+2} + 2e^-$ and the other the

hydrogen reduction, $2H^+ + 2e^- = H_2$ (g). The separation of the
two reactions causes electrons to build up at the anodic elect-
rode and to be depleted at the hydrogen electrode. This creates
a cell voltage where the zinc electrode is negative with respect
to the hydrogen electrode. Useful work may then be derived by
allowing current to flow in the external circuit. Different
metals will produce different voltages with respect to the hydro-
gen electrode, allowing the metals to be ranked in the electromo-
tive force series by these voltage differences   (19).

There is a relationship between the free energy change and
the cell potential of an electrochemical reaction. If the free
energy change for a given reaction is negative, the reaction is
thermodynamically possible. If the sign is positive, the reac-
tion will not proceed unless the conditions are altered. There-
fore, a measureable electrochemical variable, the cell potential,
can be related directly to a thermodynamic quantity.

The application of thermodynamics to corrosion processes has
been greatly enhanced by the efforts of Pourbaix who implemented
the use of potential -pH diagrams to predict the direction of
reactions, estimate corrosion products by measuring solution pH
and corrosion potential, and to predict environmental conditions
that would be benign to various materials   (20).

The Pourbaix diagrams are based upon the conditions of the
Nernst equation:

$$E = E^O + \frac{RT}{\eta F} \ln Q$$

where E^O is the standard half cell potential, R is the gas con-
stant, T is the absolute temperature, η is the number of electron
transfered, F is the Faraday constant, and Q is the activity of
the oxidized species divided by the activity of the reduced
species   (21). An example of a Pourbaix diagram is shown in

Figure 1. One must be careful in using the Pourbaix diagrams
because they are subject to the same limitations as any thermo-
dynamic calculation, but they can be extremely valuable if used
properly (22). Once it has been determined that thermodynami-
cally the reaction may occur, it then becomes desirable to use
electrochemical equations to calculate the rate at which the
reaction will take place.
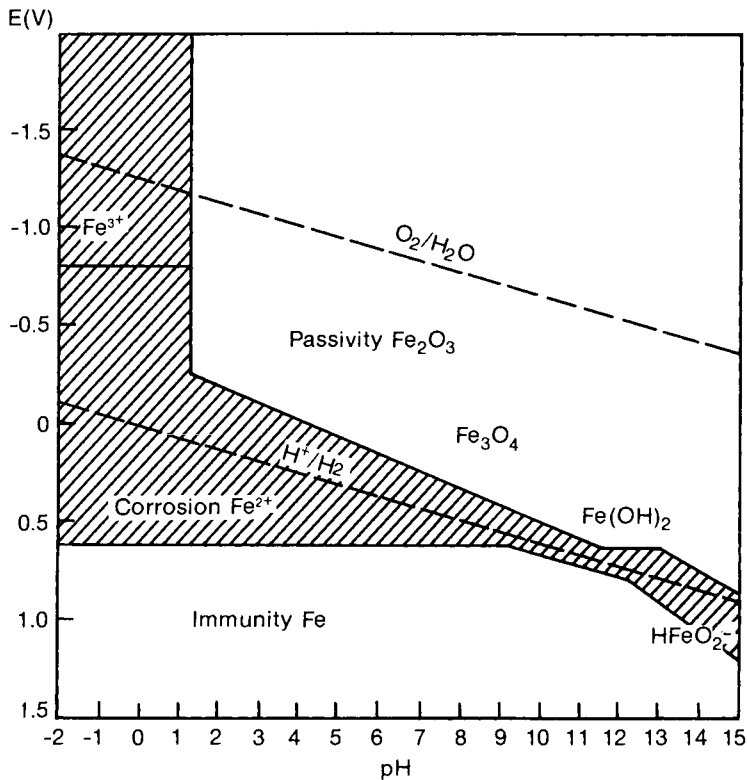
FIGURE 1. Potential Versus pH Diagram for Iron.

C.   Electrochemical Relationships

The rate of an electrochemical reaction is measured by the current flow to the electrode surface. The current is related to the driving force for the reaction by the expression

$$i = i_O \left[\exp \left(\frac{\alpha_a F}{RT} (E - E_O) \right) - \exp \left(-\frac{\alpha_c F}{RT} (E - E_O) \right) \right] \quad (1)$$

where i_O is the exchange current density, α_a and α_c are kinetic parameters, and $(E - E_O)$ is the driving force in volts   (23). The driving force is the actual measured potential of the elect- rode minus its equilibrium potential, and is termed the "over- potential." The overpotential is also denoted by the symbol η in the electrochemical literature. At equilibrium, there is zero net current since the anodic reaction rate is balanced by the reverse cathodic reaction rate. The magnitude of this (balanced) current at equilibrium is i_O, the exchange current density. The exchange current density, i_O, is a function of the concentration of the oxidation and reduction species in solution, and is affected by the physical state and condition of the sur- face such as the roughness of the surface or the presence of films or contaminants on the surface   (24).

For most corroding systems, multiple chemical reactions occur simultaneously on the corroding surface. The simplest way to treat multiple electrode reactions is to take the net current as the sum of the partial currents for each reaction. This prac- tice is useful only if the characteristics of the individual reactions are known. Multiple reactions are encountered, for example, in the corrosion of a zinc electrode in an acid solution. The zinc electrode now has two reactions which occur simultan- eously, the zinc dissolution reaction and the hydrogen discharge reaction. The zinc electrode will adopt a potential which is

intermediate between the reversible zinc potential and the
reversible hydrogen potential. This "mixed" potential is the
potential at which the total zinc anodic dissolution current is
balanced by the total hydrogen ion reduction current. Each
reaction drives the other until the balance is achieved. The
net current density, i_{total} is equal to i_a (the anodic current)
minus i_c (the cathodic current) and is equal to zero at the
mixed or corrosion potential   (25).

D.   Corrosion Rate Calculations

Wagner and Traud's mixed-potential theory, as described above,
forms the basis for two electrochemical methods used to determine
corrosion rate.   These are the Tafel extrapolation and linear-
polarization techniques   (26).

  1.   Tafel Extrapolation Method. The Tafel extrapolation
method uses data obtained from cathodic and anodic polarization
measurements and is based on the current to potential relation-
ship given in equation (1). The exponential behavior of current
density with potential allows the anodic contribution to the
total current density to be ignored if the specimen potential is
50 mV more negative than the open circuit value, while the cath-
odic contribution can be ignored at potentials 50 mV more posi-
tive than the open circuit value. Using this principle of elect-
rode polarization corrosion currents can be calculated   (27).

By polarizing a working electrode at least 50 mV negative of
the open circuit potential and then polarizing the same electrode
at least 50 mV positive of the open circuit electrode and plot-
ting the data on a semilogarithmic plot, the corrosion current
density value can be obtained. This is shown in Figure 2.
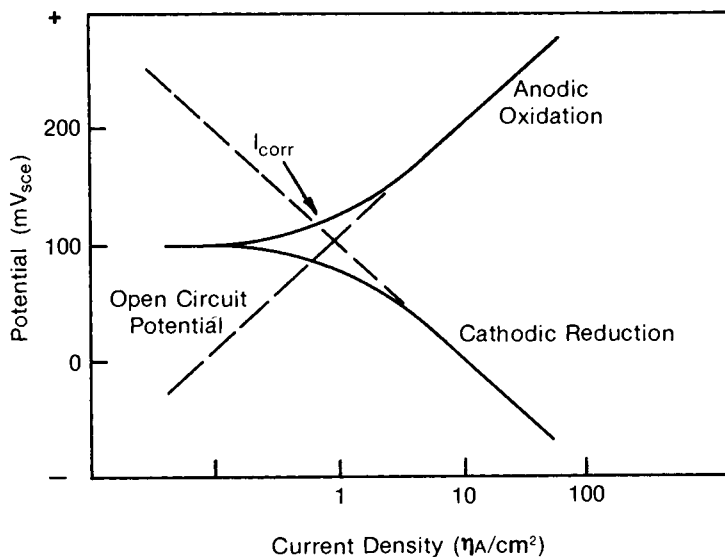
FIGURE 2.   *Tafel Extrapolation Method for Estimating Corrosion Rate.*

Under controlled conditions, the results of the Tafel ex-
tropolation method has correlated well with rates calculated
using conventional weight-change methods. Using this technique
it is possible to measure extremely low corrosion rates, and to
perform the measurements in a short period of time. Although
these measurements can be performed rapidly with high accuracy,
there are numerous restrictions which must be met before this
method can be used successfully. To ensure reasonable accuracy,
the linear region of the semilogarithmic plot (Tafel region)
must extend over a current range of at least one order of magni-
tude. In many systems this cannot be achieved because of the
interference from concentration polarization and other extraneous
effects. Furthermore, the method is difficult to use with sys-
tems containing more than one reduction process, since the Tafel
region is usually distorted and a linear plot cannot be obtained
(28).

   2. Linear Polarization Method. The linear polarization
technique is based on the theory that the current is activation
controlled (i.e., not diffusion controlled) and that the relation-
ship between current and potential is linear when the overpoten-
tial is very small. The mathematical basis of this theory, as
developed by Stern and Geary, extracts the corrosion rate from
the slope of the polarization curve, called the polarization
resistance, as it passes through the corrosion potential.

   Stern and Geary derived the relationship (29) between the
polarization resistance and corrosion rate;

$$R_p = \frac{\Delta E}{\Delta I} = \frac{1}{2.3 I_{corr}} \left(\frac{B_a B_c}{B_a + B_c} \right) \tag{2}$$

where R_p is the polarization resistance, B_a and B_c are the Tafel
constants.

   The polarization resistance can then be measured experiment-
ally as the slope of the linear polarization plot at the corros-
ion potential as shown in Figure 3. The corrosion rate (I_{corr})
can then be calculated by substituting values into equation (2).

   The Tafel constants, B_a and B_c, may be approximated for a
quick, semiquantitative estimate of corrosion rate or they may
be measured experimentally using semilogarithmic Tafel plots.
(30). The latter will give more accurate corrosion rate but re-
quires additional experimental work.

   3. Polarization Characteristics. Besides aiding in the
calculation of corrosion rates, the shape of polarization curves
can be used to determine the relative susceptibility of an alloy
to localized attack   (31). By examining the polarization curves
of a material susceptible to pitting, the pitting and protection
potentials can be determined. The potential at which the anodic
current density begins to dramatically increase as the potential
reaches higher values in the passive region is called the pitting
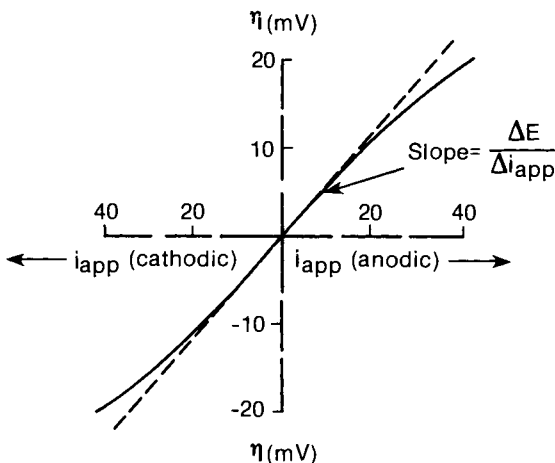
FIGURE 3. *Linear Polarization Method of Estimating Corrosion Rate.*

potential. The potential at which the current returns to a
passive current density upon its return scan is called the pro-
tection potential   (32).

    In very simplified terms, the pitting and protection poten-
tials divide the corrosion characteristics of a metal into three
regions with regard to electrode potential. At potentials below
the protection potential, the metal will not pit or crevice
corrode; between the protection and pitting potentials, the metal
may be susceptible to both pitting and crevice corrosion; and at
potentials above the pitting potential, the alloy or metal will
undergo very rapid failure. Therefore, after the pitting and
protection potentials are determined, the corrosion potential or
natural electrode potential of the material will show whether
the system is residing in a region of general corrosion, possible
pitting and crevice corrosion, or extremely severe localized
corrosion. Figure 4 indicates the position of these various
potentials on an idealized curve. Potential and polarization
measurements can also be effectively employed to predict and
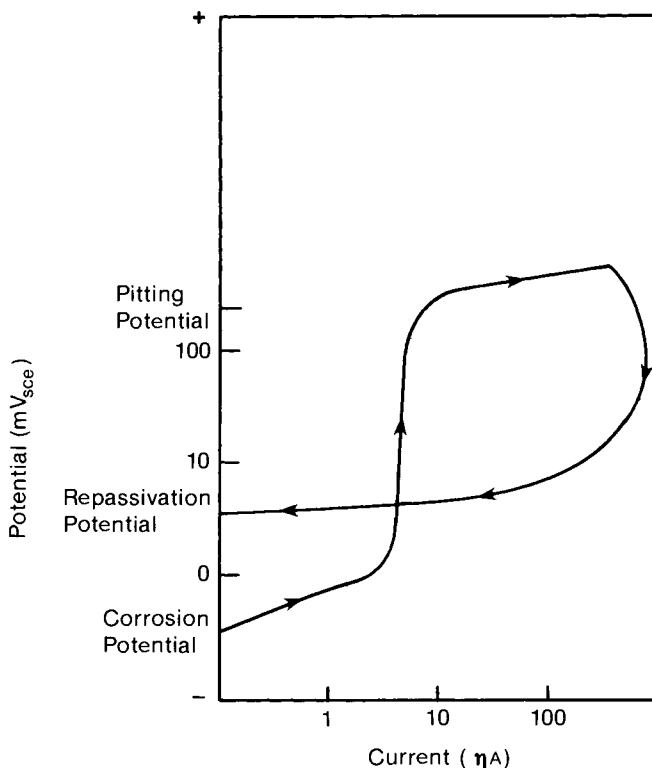
FIGURE 4. *Polarization Curve Showing Corrosion, Pitting and Repassivation Potentials.*

measure galvanic corrosion   (33).

4. *Digital AC Impedance Measurements.* Direct current elect-
rochemical techniques are extremely powerful in analyzing
corrosion processes. The advance of modern digital analysis has
also made it possible to consider digital alternating current
(ac) impedance measurements as a viable technique for corrosion
rate termination   (34). The important characteristic of the
digital system is that of high speed computation, and in partic-
ular, the use of the Fast Fourier Transform (FFT). This permits
the transformation of the data from the time domain into frequen-
cy domain, and as described below, permits the immediate calcu-
lation of the ac impedance as a function of frequency. Thus a

multiple frequency spectrum input which covers the necessary
frequency range can be used to determine the corrosion rate
rapidly and accurately.

In discussing the digital FFT technique, it is convenient to
use the idealized equivalent electrical circuit for the metal-
solution interface   (35). In this approximation, the interface
behaves as a "leaky" capacitor as shown in Figure 5. The elect-
rical double layer capacitance, C_{dl}, is in parallel with the
Faradaic reaction, R_p. The Warburg impedance, W, represents the
effect of diffusion in solution on the electrochemical reaction.
The solution resistance term R_s, which is taken to be in series
with the interfacial terms, is normally considered the magnitude
of the ohmic drop in solution caused by current flow between
the reference electrode and the working electrode.

In systems where the diffusion impedance is not important,
the total impedance of the circuit as a function of the frequency
is written in complex notation as (36).

$$Z(\omega) = Z_r(\omega) - iZ_i(\omega) = R_s + \frac{R_p}{1 + \omega^2 C_{dl}^2 R_p^2} - i\,\frac{C_{dl}\,R_p^2}{1 + \omega^2 C_{dl}^2 R_F^2} \quad (3)$$

where i is the $\sqrt{-1}$, ω is the frequency, R_p is the Faradaic
corrosion resistance, R_F is the solution resistance, and C_{dl} is
the double layer capacitance.

The use of the above relationship to describe a corroding
metal has other limitations in addition to that imposed by ig-
noring the effect of the Warburg diffusion factor. The most im-
portant limitation is that the system be "linear," and for the
Faradaic corrosion reaction to be linear, the ac signal must be
of small amplitude (i.e., 1-2 millivolts). Also, the system must
be in a steady-state over the time period of the measurement.
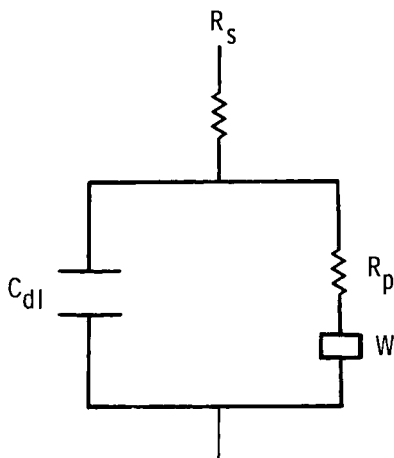
FIGURE 5. Equivalent Circuit of the Impedance of an Electrochemical Cell.

The use of digital data acquisition and signal analysis has made it possible to automate the measurements and to greatly re- duce the time required to obtain the data. The key elements in digital signal analysis are the sampling of a time varying signal to obtain N samples with an interval spacing of t, so that the total sampling period is $N\Delta t$; the transformation of this discrete set of samples to a discrete frequency set, usually performed by some variation of the Fast Fourier Transform computing algorithm; (37-38) and the calculation of the impedance as a function of frequency from the voltage and current spectra.

Once the voltage and current data have been obtained, and the Fourier Transform calculated, the impedance may be calculated. The impedance "transfer function" may be shown to be

$$Z(\omega) = \frac{V\,\omega}{I(\omega)} = \frac{\text{Fourier Transform of Voltage Spectrum}}{\text{Fourier Transform of Current Spectrum}}$$

at each frequency, ω, of the discrete set. Essentially, one applies noise spectra of known frequency content, such as Gaussian

"white noise," and the impedance function is known immediately
at these frequencies. Imposing the multiple frequencies simul-
taneously then avoids both the tedium involved in sweeping the
measurement frequency and the uncertainty involved with variation
of the interfacial processes in time   (39-41). In the treatment
of data, (42-45), the most useful plot is a plot of the imaginary
part of the impedance versus the real part, as a function of
frequency   (46). From the intercept and slope of the
platted linear data the values for C_{dl}, R_p and R_s can be
determined.

   The experimental system to be described here is based on a
Hewlett Packard 9830 Programmable Calculator. This calculator
with 16 K words of memory controls the repeated acquisition of
digital data on a Biomation 1015 Transient Waveform Recorder.
The calculator initiates the data-recording cycle and controls
the readout of data into the calculator memory for further
manipulation. The transient recorded operates as a buffer,
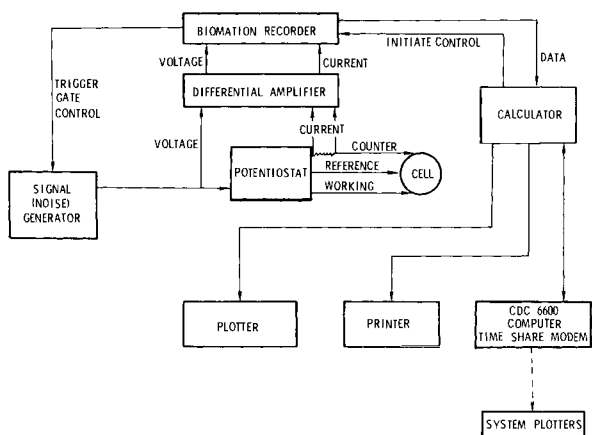
   *FIGURE 6. Block Diagram of the Digital Signal Analysis
System.*

wherein data is stored on its memory (1024) words/channel, with
4 channels) until it is called back into the calculator.

    Data are recorded as the voltage input impedance to a poten-
tiostat, and the current output from the same instrument. The
voltage input signal (Gaussian white noise) is supplied by a
Hewlett Packard 3722A Noise Generator, which provides repeated
sequences of pseudo-random noise. The sequence length is an
integral multiple of the periods of the frequencies of the signal,
which thus minimizes round-off errors. The noise generator is
operated so that 102 frequencies are used in the input spectra.
A summary of the various elements of the digital system are
shown on the block diagram (Figure 6). The data transmission
lines and the logic control line are Hewlett Packard 11202A
Interface Cables.

    The technique is rapid and experimental results show it to be
quite reliable   (47). It may be applied to systems with a wide
range of corrosion parameters, and solution conductivities.

    5. *Corrosion Science Application*. It should be concluded
that both dc and ac electrochemical techniques are extremely
useful and can be employed to investigate corrosion processes
with proper limitations   (48). All of the ac and dc techniques
described have been used to investigate corrosion processes re-
lated to solar thermal energy ranging from the investigation of
the corrosion of mirrored surfaces to the characterization of
aluminum alloys for use as OTEC heat exchangers. Weight-change
measurements, the simplest corrosion rate determination technique,
can also be used to develop the mathematical models that can be
used to predict the life expectancy of a thermal conversion
system. As an example, a recent investigation of a parabolic
dish thermal conversion system will be outlined   (49).

    A solar concentrator purchased for the evaluation of its

thermal and electrical performance used a cavity-type receiver mounted at the focus of a 6 m parabolic reflector. Figure 7 is a schematic diagram showing the receiver and reflector mounted on the tracking base. The manufacturer had recommended that the receiver be operated at temperatures up to 980°C in order to deliver high-pressure steam to an experimental turboelectric generator. The cavity was fabricated from Inconel 600 alloy and the steam coil and receiver walls were constructed of ASI-type 316 stainless steel. In operation, solar radiation is focused into the cavity by the mirrors which heats the aluminum-filled interior of the receiver. The aluminum then conducts heat from the cavity interior to the steam coil. The aluminum melts at temperatures above 660°C, making the energy of fusion thus stored available to generate a continuous supply of steam even if the solar flux is briefly interrupted by occasional cloudiness.

Aluminum is a good heat transfer and storage medium because of its high heat of fusion, high thermal conductivity, relatively low melting point, and availability. However, because iron, Inconel, and ferrous alloys are extremely soluble in aluminum, (50-52), the reliability of the receiver at temperatures above the melting point of aluminum was questioned. Concern was expressed that a dissolution-induced weakening of the receiver wall might cause a failure resulting in the release of molten aluminum or dissolution and failure of the steam coil might cause a failure that would release highly-pressurized wet steam into the interior of the receiver vessel, which is not designed to withstand high pressures. The resultant explosion could scatter molten aluminum over a wide area. Also, momentary confinement of the steam in the receiver vessel could lead to the generation of gaseous hydrogen in amounts sufficient to ignite upon release, (53), greatly increasing the violence of the explosion.

Cavity Receiver
Water/Steam
Tubing

Parabolic
Dish
Reflector

Service
Building
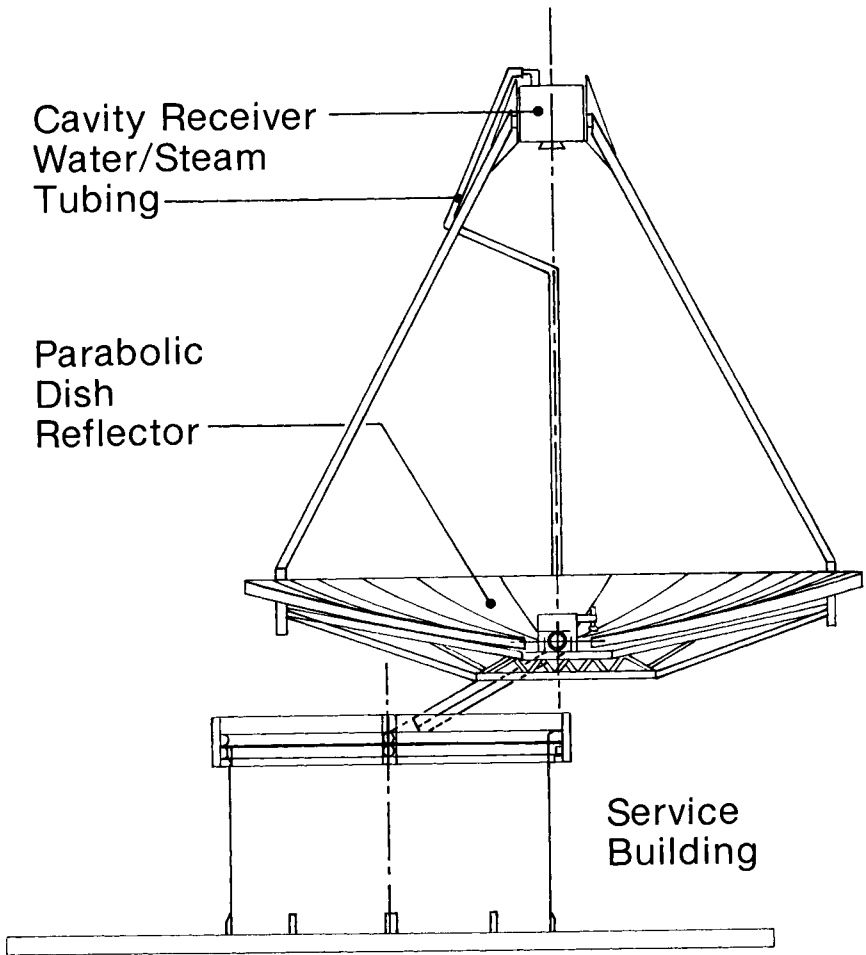
FIGURE 7.   Point-Focus Solar Concentrator.

    With these concerns in mind, a study was performed to deter-
mine the effect of molten aluminum, similar to that employed in
the receiver, on Type 316 stainless steel. The goals of this
effort were to assess the rate of attack of aluminum on 316
stainless steel; to predict a useful lifetime for the steel com-
ponents of the receiver under exposure to molten aluminum through
study of the temperature dependence of the attack rate; and to
compare these predictions to actual data gathered from tested
receivers.

    To accomplish these goals, samples of Type 316 stainless
steel were immersed for varying lengths of time in crucibles
containing molten aluminum. The crucibles were maintained at
several temperatures ranging from 700°C to 930°C in order to span
the range of operating temperatures proposed for the receiver.
After immersion, the steel samples were cleaned and weighed to
determine the amount of steel lost by dissolution. Using these
data, a dissolution rate model was constructed which enabled
lifetime predictions for steel receiver components to be made.
These predictions were then checked against operating data gath-
ered from actual receiver tests. To provide additional informa-
tion, the interior portion of another receiver containing the
aluminum filling was tested in a furnace at 820°C.

    Laboratory tests on samples of stainless steel of the type
used in the receiver were conducted to determine the mechanism
and rate of attack after it was determined that dissolution of
steel components of the receiver was a primary failure mode.
Steel samples immersed in molten aluminum in a laboratory furnace
showed a rapid growth of hemispherical pits accompanied by an
exponential increase in weight loss with time. A simple geomet-
ric model for the pitting process was developed which correlated
well with the weight loss data (See Figure 8).

$$W_T = n(K_2 T)^3$$
$$n = 93$$
$$K_2 = 0.0615$$

Time at 927 °C, Hr
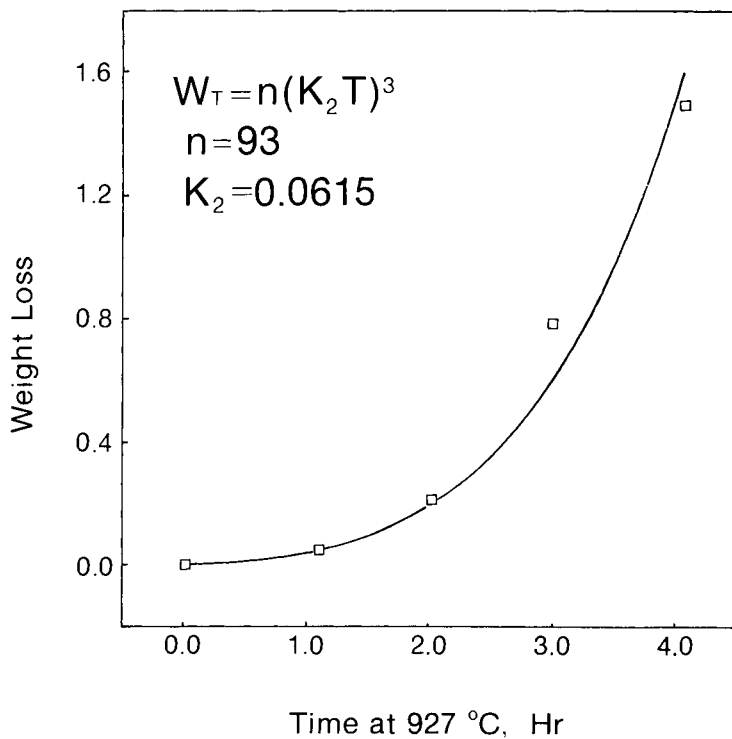
FIGURE 8. Fit of Pitting Rate Model to Steel Coupon
Weight Loss Data. Correlation Coefficient of Linearized
Data = 0.99.

The model equation was

$$W_T^{1/3} = n^{1/3} K_2 t, \qquad (4)$$

where W_T is total sample weight loss, n is number of pit initiation sites, and K_2 is a rate constant. Using this relation, values of K_2 for the dissolution process were determined at $700^\circ C$, $760^\circ C$, $820^\circ C$, $870^\circ C$, and $930^\circ C$, and an activation energy of 17.5 kcal/mole was calculated. Validity of the correlation was established using standard statistical analyses of variance.

The general expression for the rate constant K_2 enabled use of the pitting model to predict failure time envelopes for the receiver steam coil and container walls. The maximum (upper limit) lifetimes of these components were predicted to be 94 and 172 hr at $700^\circ C$, respectively. The lower and upper limits of the envelopes were determined at the 95% level of confidence.

Mean predicted lifetimes and lifetimes predicted at higher temperatures were much shorter. For example, at $820^\circ C$, a mean lifetime of only 17 hr was predicted for receiver steam coils immersed in molten aluminum. A receiver module, consisting of the steel receiver interior, underwent a violent steam coil failure after 12 hr of testing in a diffusion furnace at $820^\circ C$. In conclusion, the materials used in the design were not compatible and results showed that there was a need to involve material scientists at an early stage of the system design. The use of weight changes or electrochemical methods to predict life performance is extremely important and is becoming even more important for solar applications, due to the high capital investment costs of solar installation and long life requirements.

IV.   CONCLUSION

    By the application of thermodynamic data, environmental
observations and electrochemical measurements, chemical and
mathematical models of corrosion processes can be developed and
used to effectively predict corrosion failure and can be employed
to develop accurate and meaningful accelerated testing techniques.
The future of solar energy is not solely dependent upon the
capability of material scientists to determine means to prevent
material failure but the advance of solar energy can be severely
hindered by a lack of preventative procedures to decrease the
frequency of failure. Earlier in this chapter, most of the major
material problems facing the solar thermal industry were identi-
fied, now it is necessary that a sound analytical research
approach be employed to address the problems and increase the
reliability of the materials and subsequent reliability of the
various solar thermal systems.

REFERENCES

1.   Pohlman, S.L., and Dees, D., Sandia Laboratory Internal
     Memo, New Mexico (1977).
2.   Pohlman, S.L., and Dees, D., Sandia Laboratory Internal
     Memo, New Mexico (1977).
3.   Pohlman, S.L., "Corrosion of Solar Energy Systems: An
     Overview", NACE Publication No. 198, (March, 1979).
4.   Pohlman, S.L., "Materials and Corrosion in Solar Energy
     Systems, Materials and Corrosion Problems in Energy
     System", p. 10-1, NACE, New Orleans, (February 1980).
5.   Pohlman, S.L., and Swearengen, J. (eds.), "Containment
     Materials for Solar Thermal Energy Transport Systems: An
     Overview of Research and Development Needs. SERI/MR
     334-347.

6. Uhlig, H.H., "Corrosion and Corrosion Science", John Wiley & Sons, N.Y., (1971).

7. Fontana, M.G., and Breene, N.D., "Corrosion Engineering", McGraw-Hill, N.Y., (1978).

8. Shreir, L.C., "Corrosion", Newnes-Butterworths, London, (1978).

9. Staehle, R., and Pohlman, S.L. (eds.), "Reliability of Materials for Solar Energy". Proceedings Vols. 1 and 2, SERI/TP-31-248, (1978).

10. The National Research Council, "Selected Issues of the Ocean Thermal Energy Conversion Program," CON-EX-76-C-01-2, (1977).

11. Fetkovich, J., et al., "Fouling and Corrosion Studies in OTEC-Related Heat Exchanger Tubes," TD27028, (1976).

12. Gray, R.H. (ed.), "Proceedings of the OTEC Biofouling and Corrosion Symposium," PNL-S-A-7115, (1977).

13. Draley, J. (ed.), "Proceedings of the OTEC Biofouling, Corrosion, and Materials Workshop," ANL/OTEC-BCM-002, (1978).

14. Bockris, J., and Reddy, A., "Modern Electrochemistry", Vol. 1 and 2, Plenum, N.Y. (1977).

15. Smyrl, W., and Pohlman, S.L., "Experimental Application of Design Principles in Corrosion Research," *Corrosion,* (April, 1979).

16. Jones, D.A., "Ind. Eng. Chem. Prod. Res. Develop.,", Vol. II, No. 1, (1972).

17. Pohlman, S.L., "Determination of Corrosion Parameters by Electrochemical Techniques," NACE (October, 1978).

18. Moore, W., "Physical Chemistry," Prentice Hall, (1962).

19. Uhlig, H.H. (ed.), "Corrosion Handbook", Wiley, N.Y. (1948).

20. Pourbaix, M., "Atlas of Electrochemical Equilibrium in Aqueous Solutions," Pergamon Press, London, (1966).

21. Scully, J.C., "Fundamentals of Corrosion," Pergamon, (1975).

22. LaQue, F., "Shortcuts to Prediction of Corrosion Rates,"
     Materials Performance, (June, 1979).

23. Robinson and Stokes, "Electrolyte Solutions," Academic
     Press, N.Y., (1955).

24. Oldham, K.B., and Mansfield, F., *Corrosion Science, 13,*
     No. 70, (1973).

25. Wagner, C., and Traud, W., *Electrochem., 44,* 391 (1938).

26. Tafel, J., *Phys. Chem., 50,* 641 (1905).

27. Mansfield, F., *Corrosion, 29,* 10 (1972).

28. Greene, N.D., *Corrosion, 18,* 136t-42t (1962).

29. Stern, M., and Beary, A.C., *J. Electrochem. Soc., 104,*
     56-63 (1957).

30. Brown, R.H., and Means, R.B., *Trans. Electrochemical Soc.,*
     74 (1938).

31. Pourbaix, M., *Corrosion, 26,* 431 (October 1970).

32. Verink, Jr., E.D., and Pourbaix, M., *Corrosion, 27,* 495
     (December 1971).

33. Pohlman, S.L., "Corrosion and Electrochemical Behavior of
     Boron/Aluminum Composites," NACE No. 30, San Francisco,
     (1977).

34. Smyrl, W.H., and Pohlman, S.L., "Determination of Corrosion
     Parameters by Digital Impedance Analysis," NACE, Pub. No.
     166, (March, 1978).

35. Randles, J.B., *Faraday Soc. Discussions, 1,* 11, (1947).

36. Sluyters, J.H., *Rec. Trav. Chem., 79,* 1092, (1960).

37. Stearns, S.D., "Digital-Signal Analysis," Hayden, Rochelle
     Park, New Jersey, (1976).

38. Smith, D.E., "Electroanalytical Chemistry," A.J. Bard,
     (ed.), M. Dekker, Inc., N.Y., Vol. 1, (1966).

39. Smith, D.E., "Computers in Chemistry and Instrumentation,"
     Vol. 2, M. Dekker, Inc., N.Y., (1966).

40. Smith, D.E., *Anal. Chem., 48,* 221A, (1976).

41. Creason, S.C., and Smith, D.E., *J. Electroanal. Chem., 36,*
     App. 1, (1972).

42.   Rehbach, M., and Sluyters, J.H., *Rec. Trav. Chem., 80,* 469, (1961).

43.   Rehbach, M., and Sluyters, J.H., *Rec. Trav. Chem., 82,* 553, (1963).

44.   Rehbach, M., and Sluyters, J.H., *Rec. Trav. Chem., 82,* 535, (1963).

45.   Rehbach, M., and Sluyters, J.H., *Rec. Trav. Chem., 82,* 525, (1963).

46.   Cole, K.S., and Cole, R.H., *J. Chem. Phys., 9,* 341, (1941).

47.   Smyrl, W., and Pohlman, S.L., NACE No. 166, (March, 1978).

48.   Sheldon, D., "Electrochemical Methods of Corrosion Testing," NACE No. 113, (March, 1976).

49.   Webb, J., and Pohlman, S.L., SERI/TR-31-338, (September, 1979).

50.   Lelby, C.C., and Ryan, T.C., - ARCRL-TR-73-p421, Air Force Cambridge Research Laboratories, (1973).

51.   Ecully, E., *Mem. Sci. Rev. Metall,* Vol. 72 (No. 11), pp. 815-822, (November 1975).

52.   Fegel, O., - Farnholz, et al., *Aluminum,* Vol. 5, pp. 496-498, (August 1969).

53.   Hess, P.D., and Brondyke, K.J., "Met. Prog.," pp. 93-100, (April 1969).

APPENDIX

GLOSSARY OF TERMS   (6, 7, 8)

Breakaway Oxidation - a type of corrosion in which a finely-
    subdivided porous oxide layer forms at the metal-oxide
    interface.

Carburization/Decarburization - the process of providing a metal
    surface with a carbon layer to provide a harder, more wear-
    resistant surface. Consists of heating the surface in an
    atmosphere rich in Co or hydrocarbon gases at a temperature
    of 900-1000°C. Decarburization is the reduction of the
    carbon level by heating in air or other oxidizing or re-
    ducing gases.

Cementation - the process by which one substance is caused to
    penetrate and change the character of another, by interfaci-
    al interactions, at temperatures below their melting points.

Corrosion Fatigue - the reduction of fatigue resistance due to
    the presence of a corrosive medium. Strongly influenced by
    environmental factors. Prevented by reducing stress on the
    component or introducing corrosion inhibitors. Probably a
    special case of stress-corrosion cracking.

Creep - the continous plastic elongation of a metal under an
    applied stress. Increasingly important at high temperatures.
    Creep rate or resistance is usually expressed as percent
    plastic deformation for a given time period at a constant
    applied load.

Creep-Fatigue - stressing caused by repeated cyclic deformations
    in conjunction with long-term continuous deformation.

Crevice Corrosion - pitting corrosion occurring in metal crevices
    or other areas where a corrosive medium becomes stagnant.
    Can be combated by keeping corrosive medium in motion over
    metal surface.

Erosion - the wearing away of a material by friction processes
    of another material or liquid.

Erosion Corrosion - corrosion of metal when subjected to high-
    velocity liquids, characterized by pitting. Also called
    impingement attack. Examples of attacked materials are
    copper and brass condenser tubes.

Fatigue - the tendency of a metal to fracture under repeated
    cyclic stressing;   failures usually occur at stress levels
    below the yield point after many cyclic stress applications.

Fretting - Damage occuring at the interface of two contacting
    surfaces (one or both metal), subject to slight relative
    slip, usually oscillatory or vibrational. Also called wear
    corrosion and friction oxidation. Characterized by dis-
    coloration of metal surface and pitting if oscillatory.

Galvanic Corrosion - if two dissimilar metals are placed in a
    conductive solution and are placed in electrical contact, a
    potential difference will exist which will produce an
    electron flow. This flow will be due to two reactions; an
    oxidation occuring at the anode, and a reduction reaction
    occuring at the cathode.

Intergranular Corrosion - localized attack at and immediately
    adjacent to grain boundaries with relatively no attack on
    the grains themselves.

Inhibition - substance which when added in relatively small
    concentrations to an environment decreases the corrosion
    rate.

Hydrogen Embrittlement - severe loss of ductillity in some
    stressed alloys on metals due to the absorption of atomic
    hydrogen into the metal lattice.

Linear Polarization - a method of electrochemical corrosion-rate
    measurement. Within 10mV more passive or more active than
    a material's corrosion potential, the applied current density
    is a linear function of the electrode potential. The slope
    of this Function, $\dfrac{\Delta E}{\Delta i_{applied}}$, is approximately equal to
    $.026/i_{corr}$ where i_{corr} is the current density for corrosion
    of the material .

Passivity - loss of chemical reactivity of a material due to the
    presence of a self-produced, self-healing film (oxide salt,
    etc.) which seperates the active metal surface from the
    environment.

Pitting - a form of extremely localized attack which results in
    cavities in the metals. By convention the surface diameter
    to depth ratio is less than one.

Polarization - the deviation from equilibrium potential between
    two metal electrodes in a cell, defined as the displacement
    of electrode potential resulting from a net current.
    Frequently measured in terms of over voltage, η.

Polarization curve - the graphic representation of a material's
    potential, taken by plotting the potential of an electrode
    of the material against the logarithm of applied current.
    The curve becomes linear at higher currents on a semi-
    logrithmic plot.

Pourbaix Diagram - a graphic interpretation of thermodynamic
    data relating to the electrochemical and corrosion behavior
    of a metal in water. Using potential vs. pH, the diagram
    indicates specific conditions in which the metal either does
    not react (immunity) or can react to form specific oxides
    on complex ions.

Selective Leaching - the removal of one component on element of
    a solid alloy by corrosion processes.

Sensitization - making an alloyed metal surface susceptible to
    intergranular corrosion by heating. The heating causes
    the alloy to disintegrate (grains of material fall out)
    and/or lose its strength.

Slow Crack Growth - crack extension caused by stress less than
    that of the materials critical stress.

Spallation - the cracking, breaking, or splintering of materials
    due to heat or impact stress.

Stress Corrosion - corrosion caused by the simultaneous presence
    of tensile stress and a specific corrosive medium.
    The metal is basically unattached over most of its surface,
    while fine cracks progress through it.

Stress Corrosion Cracking - if a metal, subject to a *constant*
    tensil stress and exposed simultaneously to a *specific*
    environment, cracks immediately or after a given time,
    that failure is called stress corrosion cracking (SCC).

Tafel Constant - $2.3\dfrac{RT}{\alpha nF}$, where R = gas constant, T = absolute
    temperature, n = number of electrons transferred between
    two electrodes, F = Faraday constant, α = symmetry coeffic-
    ient describing the shape of the rate-controlling energy

barrier. This constant is used in the equation describing
the relationship between reaction rate and overvoltage,
$\eta = B \log \frac{i}{i_0}$, where η = overvoltage, B = Tafel constant,
and i = rate of oxidation or reduction in terms of current
density.

Thermal Striping - thermal fatigue caused by thermally gradiated
fluid flow.

Transpassivity - potential region in which the protective/passive
film is no longer stable causing a rapid increase in re-
activity of the substrate metal.

Uniform Attack - Removal of material by chemical or electriochem-
ical reaction over an entire exposed surface is called
uniform attack.

Ca(OH)$_2$

Na$_2$SO$_4\cdot$10H$_2$O
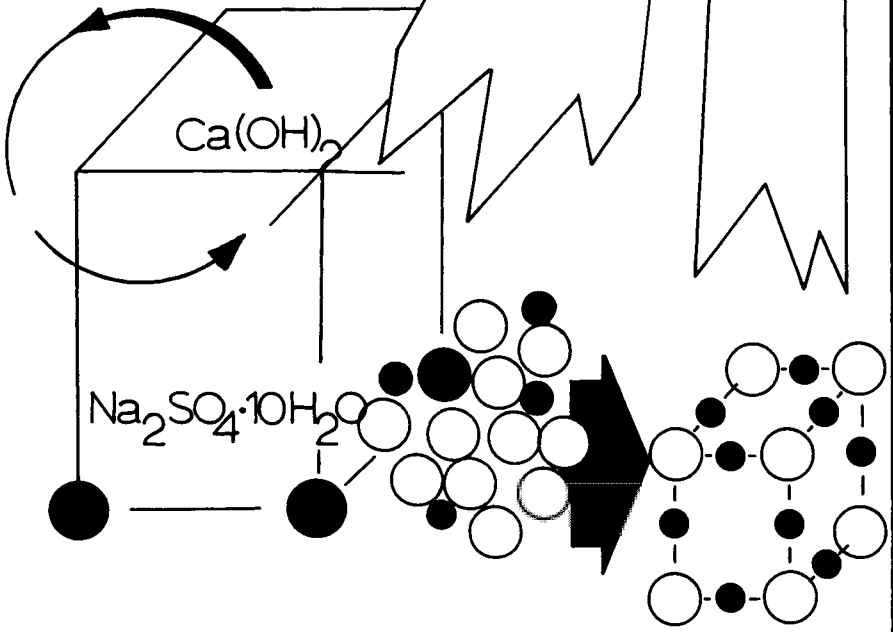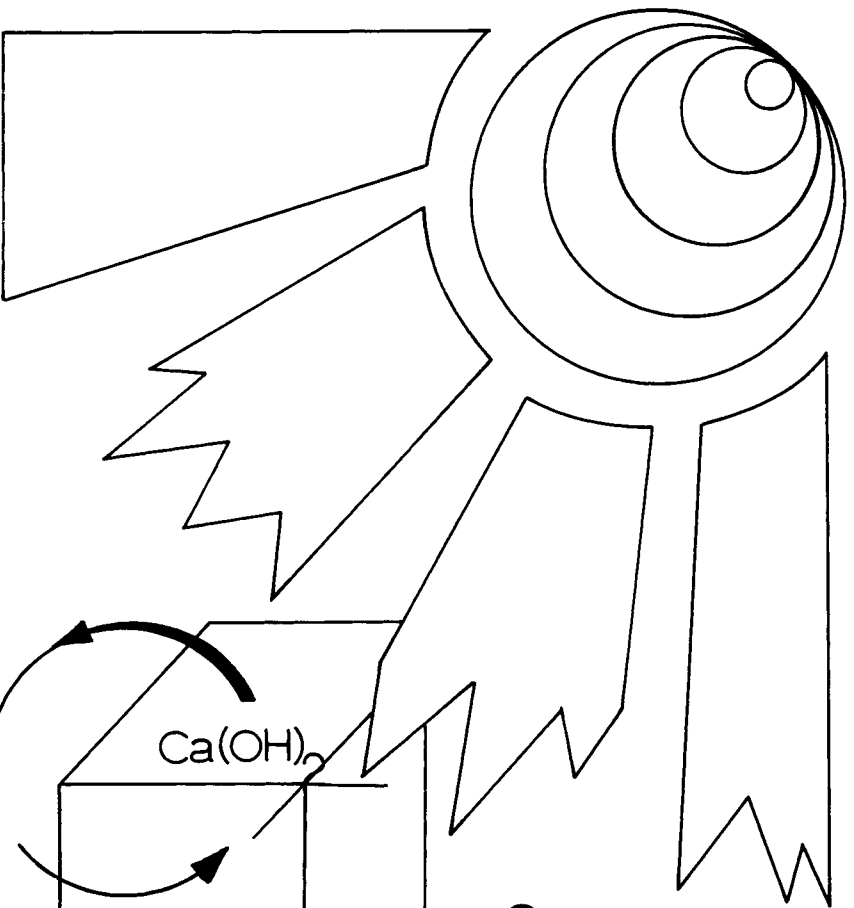
SECTION 2

2. SOLAR STORAGE AND THERMOCHEMICAL MATERIALS

*Many successful solar applications are dependent and will
continue to be dependent upon the ability to store heat energy,
or to be able to utilize collected solar heat energy at some
future time. This can be achieved by a number of means, but the
most economical and practical involve simple thermodynamic prin-
ciples. To a large extent, solar storage systems and system
economics are dictated by storage materials cost and the neces-
sary storage volume. Two storage principles characterizing two
categories of materials are described in this section. These
involve the heat of fusion and the storage of solar heat in salts,
salt hydrates and other materials as the heat of fusion, and re-
versible solar thermal reactions of various kinds in a variety of
materials systems. The so-called heat of fusion materials gener-
ally require 15-18 times smaller volumes than rock storage sys-
tems and 8-10 times less volume than that required for water
storage of solar thermal energy. Such materials are, with the
addition of nucleating and thickening agents, able to undergo un-
limited cycling, and this concept can be utilized in heating as
well as cooling cycles. Heat of fusion salt storage is ideally
suited to home heating and other low volume systems with space
limitations. At higher temperatures and in systems involving
large solar thermal power fluxes, photochemical or more appropri-
ately thermochemical materials and reactions constitute an attrac-
tive and practical scheme for solar energy storage as well as
transport. Thermochemical materials science is concerned not only
with the materials reactions but also materials compatibility and
related system problems involved in both heating and cooling.*
*The first two chapters of this section describe practical
salt-hydrate storage systems, the heat of fusion concept, the
thermodynamic basis for heat storage materials selection; and
provide an overview of related materials problems. The second
two chapters present an overview of thermochemical reaction appli-
cations to solar energy storage and finally an outline of asso-
ciated materials science activities and problem areas, including
effects of thermal cycling, heat transfer, corrosion and struc-
tural degradation, and the like. Examples of reaction control by
product separation, energy transport in distributed systems, and
the chemical heat pump concept are also presented. This section,
together with the presentations in the previous section, should
provide the reader with a practical and fundamental basis for
assessing and understanding the materials science problems re-
lated to contemporary and future solar energy collection and
storage.*

THERMAL STORAGE IN SALT - HYDRATES

Maria Telkes

Solar Thermal Storage Development
AEC Research Institute
Killeen, Texas

I. INTRODUCTION

Salt hydrates may be regarded as "alloys" of anhydrous salts
with a definite number of moles of water forming typical crystal-
line solids. The melting point of salt-hydrates is usually,
(but not necessarily), below $100^{\circ}C$, even if the melting point
of the anhydrous salt is much higher. Water itself has a rather
high entropy of fusion per unit weight, and when combined with
anhydrous salt of high entropy of fusion, a salt hydrate of
conveniently lower melting point may result, usually with the
combined high entropies of fusion of the components.

II. MELTING AND RECRYSTALLIZATION

Salt hydrates of the type $AB.nH_2O$, when heated, usually
change to another salt-hydrate $AB.mH_2O$ containing fewer moles
of water, while some part, or the entire amount of $AB.mH_2O$
dissolves in (n-m) moles of water. Several salt hydrates change
to the anhydrous form when heated, changing from $AB.nH_2O$ to
$AB + nH_2O$, as the anhydrous salt dissolves partly or completely
in mH_2O. The amount of water forming the salt-hydrate is the

"water of crystallization" and the traditional expression:
"melting in its water of crystallization" aptly describes the
process of transition at the melting point.

The solubility of the salt determines the condition above
the melting point. The composition of the salt-hydrate is
usually ex pressed in percent anhydrous salt AB,in the salt-
hydrate (AB/AB.nH$_2$O). In Tables 1A and 1B, this is compared
with the solubility of the anhydrous salt above its melting
point. Congruent melting occurs when the solubility is suf-
ficiently high. Partly incongruent melting occurs when some
salt remains undissolved above the melting point, or even at
some higher temperature. In such melts, the solid residue is
usually of greater density than the melt and it settles to the
bottom of the container.

When the partly incongruently melting salt-hydrate is sub-
sequently cooled, while the mixture is stirred, recrystalli-
zation occurs without difficulty. When cooled in closed con-
tainers, without stirring or mixing, the solid residue at the
bottom of the container is "frozen in", being surrounded by
solid salt-hydrate crystals. Some of the residue, therefore,
cannot re-combine with its water of crystallization and some
saturated solution remains, after the mixture has cooled below
its melting point. In such cases the conditions are not com-
pletely reversible, that is, only part of the heat required
to melt the salt-hydrate can be recovered when the system is
cooled. Several methods have been developed to prevent the
settling of residual solids in partly incongruently melting
salt-hydrates, with the result that the conditions can become
completely reversible.

Table 1A. Properties of Salt-Hydrates

Compound	H₂O Change	Melting Point °C	Observed Heat of Fusion cal/g	Observed Heat of Fusion Btu/lb	Entropy of Fusion Obs	Entropy of Fusion Calc	Calc/Obs
$Ba(OH)_2$	8-0	78	72	130	64.5	53.3	0.83
$CaCl_2$	6-2	29.5	40.7	73	29.4	31.6	1.07
$Ca(NO_3)_2$ α β	4-2	42.6 39.7	33.5	60	25.0	25.5	1.02
$Cd(NO_3)_2$	4-3	59.5	25.3	45	23.5	30.7	1.30
$Co(NO_3)_2$	6-4	57	30.4	55	26.7	36.0	1.34
$CoSO_4$	7-1	96	40.7	73	31.5	40.1	1.27
$Cu(NO_3)_2$	6-4	24	29.4	53	29.5	36.0	1.22
$FeCl_3$	6-0	37	54	97	47.1	46.8	0.99
$LiNO_3$	3-0	30	71	128	28.7	29.0	1.01
$Mg(NO_3)_2$	6-4	90	38.2	68	27.0	36.0	1.33
$MgSO_4$	7-1	48	48.2	87	37.5	40.1	1.07
$MgCl_2$	6-4	117	41.2	74	21.6	21.7	1.01
$MnCl_2$	4-2	58	42.5	76	25.5	21.7	0.85
$Mn(NO_3)_2$	3-2	35.5	28.8	52	21.0	30.7	1.46
$Mn(NO_3)_2$	6-4	26	33.5	60	32.1	36.0	1.12
$NaC_2H_3O_2$	3-0	58	43.0	77	21.0	26.1	1.24
$NaOH$	1-0	64	65	117	11.2	11.4	1.02
Na_2CO_3	10-1	34	60	108	56.6	64.5	1.14
Na_2CrO_4	10-4	20	39	270	46	53.1	1.15
Na_2HPO_4	12-2	36.5	63	114	66	71.3	1.08
Na_3PO_4	12-2	70	52.5	94	58	71.9	1.24
$Na_2S_2O_3$	5-0	49			37	42.3	1.14
Na_2SO_4	10-0	32.4	60	108	63.5	62.3	0.98
$Ni(NO_3)_2$	6-4	57	36.4	65	33.3	36.0	1.08
$Zn(NO_3)_2$	6-4	36.4	31	56	29.7	36.4	1.23
PROP.-136°F		58.0	63	113	25.6	26.1	1.02
PROP.-190°F		94	62	112	77	84.6	1.10

Table 1B. Properties of Salt-Hydrates

Compound	H_2O Change	Density	Anhyd. Salt %	Solub. > mp %	Specific Heat Solid	Liquid
$Ba(OH)_2$	8-0	2.18	54.5	50	0.28	
$CaCl_2$	6-2	1.68	50.5	56	0.345	0.55
$Ca(NO_3)_2$	4-2	1.82	69.5	74	0.35	
$Cd(NO_3)_2$	4-3	2.45	76.5	73	0.26	0.38
$Co(NO_3)_2$	6-4	1,87	63	64	0.37	0.50
$CoSO_4$	7-1	1.95	55	45		
$Cu(NO_3)_2$	6-4	2.07	63.5	62	0.33	0.48
$FeCl_3$	6-0		60	76		
$LiNO_3$	3-0		56	61		
$Mg(NO_3)_2$	6-4	1.46	58	65	0.54	0.88
$MgSO_4$	7-1	1.64	49	39	0.36	
$MgCl_2$	6-4	1.56	47	50	0.38	0.68
$MnCl_2$	4-2	2.01	63.5	52		
$Mn(NO_3)_2$	3-2		77	v.s.	0.34	0.41
$Mn(NO_3)_2$	6-4	1.82	62.5	67		
$NaC_2H_3O_2$	3-0	1.45	60.5	60	0.47	0.80
$NaOH$	1-0		69	75		
Na_2CO_3	10-1	1.44	37	34	0.45	0.80
Na_2CrO_4	10-4	1.48	47	48		
Na_2HPO_4	12-2	1.52	40	44	0.37	0.76
Na_3PO_4	12	1.64	43	44		
$Na_2S_2O_3$	5-0	1.69 s 1.66 l	64	67	0.35	0.57
Na_2SO_4	10-0	1.46	44	34	0.425	0.79
$Ni(NO_3)_2$	6-4	2.05	63	64	0.38	0.74
$Zn(NO_3)_2$	6-4	2.07	64	67	0.32	0.54
PROP.-136°F		1.30	62	62	0.48	0.77
PROP.-190°F		1.64		78	0.36	0.80

III.   SUPERCOOLING

     Salt-hydrates heated in closed containers above their melting
points, when subsequently cooled, may supercool considerably
below their melting points, before they recrystallize. When
melts are cooled below a definite temperature, (the temperature
of labile supersaturation), crystal formation occurs spontane-
ously, but the difference between the real melting point and
the temperature of labile supersaturation may be as high as
30 to 40°C (54 to 72°F). This is usually too large and imprac-
tical for heat storage systems. The typical example of water-
ice is well known, supercooling to 40°C (-40°F) may occur before
supercooled water freezes spontaneously. In supercooled melts,
solidification or crystallization can be induced by nucleation
or "crystal seeding".

IV.   NUCLEATION OR CRYSTAL SEEDING

     The literature of the problems of crystal formation and
nucleation is very extensive, involving crystallography, phase
equilibria, the physical-chemistry of solid-liquid transitions,
and finally the fascinating subject of crystal growth and the
formation of large, hyper-pure crystals. Reviews by Mullin
(1), Van Hook (2), and Tipson (3), summarize most of the his-
tory, theory, and practical applications of these subjects.
     For practical heat storage applications, the basic problem
is the prevention of supercooling when the material is perma-
nently sealed into its container. Supercooling must be pre-
vented and reversible melting and recrystallization must be
attained at the melting point, or within a few degrees of it,
without opening the container. External influences must be
avoided, such as stirring, shaking, or applying other mechanical
or physical means, except the delivery or withdrawal of thermal
energy.

The following methods can be used to attain nucleation of
salt-hydrate melts, when sealed into containers and cooled
slightly below their melting points:

a) Introducing solid crystals of the original salt-hydrate
    forming the melt. (Self-nucleation.)

b) Providing solid crystals which are isomorphous, epi-
    taxial, or partly isomorphous, with the salt-hydrate
    crystals. (Heterogeneous nucleation.) These nucleating
    agents should not appreciably influence the melting
    point, or the heat of fusion of the salt-hydrate.
    Telkes (4) studied epitaxy, that is, nucleation of
    inorganic salt-hydrates by partly isomorphous crystals.
    Heterogeneous, nucleating crystals must be at least
    partly similar in crystal form, lattice spacing and
    atomic arrangement, within a range of 15 percent. This
    was originally found to be the condition of nucleation
    in metallic alloys (Hume-Rothery (5)).

c) Nucleation can occur in melts which are heated only
    slightly above their melting points. Crystals grow
    from the walls of the container, or from the surface
    of heterogeneous materials within the container. Ac-
    cording to Turnbull (6), this observation can be ex-
    plained by assuming that submicroscopic crevices are
    present in solid walls, and that minute crystals of
    salt-hydrate are lodged there. Interfacial tension
    increases the melting point of the salt-hydrate in the
    crevices slightly above the true melting point ("super-
    heating"). The surviving solid crystals act as self-
    nucleating agents.

Additional methods suggested in the past included the use
of nucleating devices in the form of tubular or other external
attachments that are kept cooler than the melt and, in this
way, retain solid crystals for subsequent nucleation. From
the shape of these external devices, the name "cold finger"

describes them rather aptly. The performance of these devices
is best if they are near the top level of the container, but
in good contact with the melt, so that growing crystals can
protrude, break off, and provide numerous additional nuclei.
Crystals grow more slowly if they have to surmount gravity.
This occurs when growth starts from a tube or other small con-
tainer located near the bottom of the melt that should be nu-
cleated.

The patent literature is replete with various methods in-
cluding supersonic devices, or thermal expansion disks, which
have not been successfully used due to high cost or other draw-
backs. Relatively low cost proprietary devices exist which
have been used successfully (7).

V.   RATE OF CRYSTAL GROWTH

Extensive literature covers the subject of nucleus forma-
tion, supercooling and viscosity of the melt, or solution.
The classical work of Tamman (8) (9), proved that in supercooled
melts the rate of nucleus formation is very low near the melting
point, but increases rapidly at lower temperatures, reaching
a maximum and then decreasing again. The velocity of crystal-
lization is usually expressed as the linear velocity of the
movement of the solid-liquid boundary in a tube of small dia-
meter, containing the supercooled melt. The ice-forming velocity
of water, supercooled to $-9^{\circ}C$, is 6 cm/sec. (nearly 12 foot/min-
ute) while in salt solutions, at the same temperature, the
velocity is 1.0 to 4.0 cm/sec. (2 to 8 foot/minute). It is
probable, therefore, that a container of one foot length, filled
with supercooled salt-hydrate and nucleated at one end, should
be filled with a network of growing crystals in a matter of
minutes. During this short time, the temperature of the salt-

hydrate increases abruptly to its melting point. Crystalli-
zation, of course, may continue for a long time, depending upon
heat removal from the container.

The conditions differ considerably with melts that are al-
ready nucleated, or where supercooling has been prevented by
using a nucleating device. In the vicinity of the melting point
T_f and at the temperature of the liquid T_1, the rate of crystal
growth C is related to the heat of fusion H_f, the density D,
and the specific heat conductivity k in the following equation:

$$C = \frac{(T_f - T_1)k}{H_f D}$$

For typical salt-hydrates such as those listed in Tables 1A,
1B, and 2, average values are the following:

$k = 0.002$ to 0.008 cal/$(cm^2 sec\,^\circ C)$

$H_f = 40$ to 65 cal/gram

$D = 1.5$ to 1.7 gram/cm^3

Using these values in eq. 7., the range of the linear velocity
of crystal growth is:

$C = 0.12 (T_f - T_1)$ to $0.48 (T_f - T_1)$ cm/hour

For an acceptable temperature difference of $3\,^\circ C$

C for $3\,^\circ C = 0.36$ to 1.5 cm/hour (about 0.14 to 0.6 inch/hour)

VI. THE RATE OF HEAT REMOVAL

The rate of heat removal from a crystallizing melt, encased
into a container of high heat conductivity, depends upon the
specific heat conductivity of the salt-hydrate.

The corresponding equation is:

$$Q = \frac{(T_f - T_w)k \cdot A}{d} \qquad \text{Btu/hour} \qquad \ldots \text{eq. 5)}$$

A = area of container wall in contact with salt-hydrate, assuming that the container has parallel walls for heat removal, (ft^2).

d = the thickness of the salt-hydrate layer (inch) between parallel wall.

T_f = melting point of salt-hydrate (^oF).

T_w = wall temperature (^oF).

Q = heat removal from A area in Btu/hour.

k = thermal conductivity of the salt hydrate $\dfrac{Btu}{hr.ft.\,^oF}$

The equation can be modified for containers of cylindrical or other shape, or for internally finned containers.

In actual experiments, the value of k was found to be as much as k = 1 to 2 Btu/(hr.ft ^oF). The reason for this increased heat transfer is due to the fact that the interface between solid and liquid is not perpendicular to the distance between plates, but it is more complex following the contours of the growing crystals.

VII.   CALCULATION OF THE HEAT OF FUSION FROM HEATS OF SOLUTION

The heat of solution of salts and salt-hydrates can be used to calculate the heat of fusion (H_f) of the salt-hydrate, provided that the heat of solution is known for the hydrates involved in the phase change.

H_s is the heat of solution (cal/mole) of an anhydrous salt. H'_{sh}, H''_{sh} of its salt-hydrates.

$$H_f = H_s - H_{sh} \qquad \text{or} \qquad H_f = H'_{sh} - H''_{sh}$$

Summary data of heat of solution have been published by Rossini
(10) and Bichowsky and Rossini (11). As an example:

H_s Na_2SO_4 280 cal/mole

H'_{sh} $Na_2SO_4 \cdot 10H_2O$ -18740   "

$H_s - H'_{sh}$ = 280 -(-18740) = 19020 cal/mole = 59.1 cal/gram
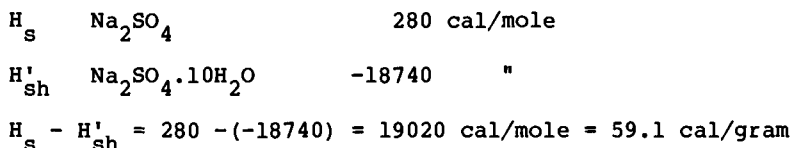
This is in good agreement with the observed value (60.5) and
the value calculated from the entropies of fusion. The impor-
tance of selecting the correct heat of solution, relating to
the number of moles of water involved in the phase change, is
shown in the following example:

$MgCl_2 \cdot 6H_2O \longrightarrow MgCl_2 \cdot 4H_2O + 2H_2O$

H_s $MgCl_2$ 36300 cal/mole

$H'_{sh}MgCl_2 \cdot 4H_2O$ 12000   "

$H''_{sh}MgCl_2 \cdot 6H_2O$ 3400   "

$H'_{sh} - H''_{sh}$ = 12000 - 3400 = 8600 or 42.3 cal/g (observed 41.2)
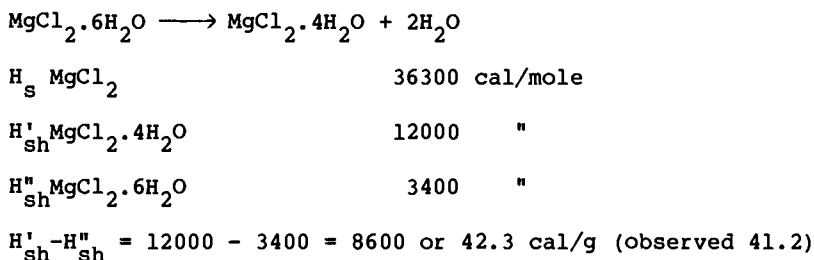
If the difference 36300 - 1200 = 24300 is used, a much higher
value (120 cal/g) is obtained, but this does not agree with
the facts, as the phase change does not involve the formation
of anhydrous $MgCl_2$, but only that of the tetrahydrate.

VIII. CALCULATION OF THE HEAT OF FUSION FROM ENTROPIES OF FUSION

As previously outlined, the entropy of fusion (S_f) of a
salt-hydrate is calculated from the sum of the entropy of
fusion of the anhydrous compound and the entropy of fusion of
water, (S_f = 5.26). In those salt-hydrates which change from
$AB \cdot nH_2O$ to $AB \cdot mH_2O$ the number (n - m) is used for the number
of water moles, as listed in column two of Table 1A. The cal-
culated S_f is then compared with the observed S_f, when this

is known. The method can be used to calculate the unknown heat
of fusion of any salt-hydrate, provided its melting point is
known and also the number of moles of water that are involved
in the phase change.

As an example, using data from Table 1A:

		S_f Calc	S_f Obs	S_f Calc/Obs
$Na_2SO_4 \cdot 10H_2O$ $Na_2SO_4 + 10\ H_2O$				
Na_2SO_4 (transition + fusion)		9.7	8.38	1.16
$Na_2SO_4 \cdot 10H_2O$ 9.7 + 52.6 =		62.3	63.5	0.98

Using S_f Calc and the melting point of $Na_2SO_4 \cdot 10H_2O$ (305.6°K),
we obtain for the heat of fusion:

H_f = 62.3 x 305.6 = 19,100 cal/mole or 61.5 cal/gram

This is an excellent agreement with the observed value. The
same type of calculation can be applied to another example:

		S_f Calc	S_f Obs	S_f Calc/Obs
$MgCl_2 \cdot 6H_2O$ $MgCl_2 \cdot 4H_2O + 2H_2O$				
$MgCl_2$		11.2	9.4	1.07
$MgCl_2 \cdot 6H_2O$ 11.2 + (2 x 5.26) =		21.7	21.6	1.01

The melting (transition) point is 390°K, giving:

H_f = 21.7 x 390 = 8450 cal/mole or 41.5 cal/gram.

This value is in excellent agreement with experimental observa-
tions.

IX.   CALORIMETRIC MEASUREMENTS AND DATA

Several books describe calorimetric methods, based on the
pioneering work of Thomsen (12), and others.   "The Modern Calo-
rimeter" by White (13), and the publications of Kubaschewski
(14) (15) describe most of the methods in use.

The heat of fusion of salt-hydrates can be measured by direct
calorimetry.   A somewhat modified method has been used for salt-
hydrates which can be supercooled below their melting points.
The method consists of placing the supercooled salt-hydrate,
(encased in its container) into the calorimeter.   After tempera-
ture equilibrium is reached, at a temperature below the melting
point, the melt is nucleated with small crystals of the same
salt-hydrate.   The amount of heat evolved during crystallization
is measured in the calorimeter.   This amount of heat must be
corrected for the heat content of the salt, between its melting
point and the temperature of the calorimeter.   The correction
can be obtained by measuring the specific heat of the salt-
hydrate.

This method has been applied by Perreu (16) (17) to a number
of salt-hydrates and to their saturated solutions.   The results
are incorrect when the saturated solution contains excess water.
In such cases, salt remains in solution and, as a result, only
part of the heat of fusion can be measured.   Perreu's measure-
ments were at least 10 percent lower than other data for con-
gruently melting salt-hydrates and up to 60 percent lower for
partly incongruent melts.

Some of the relatively few direct calorimetric measurements
of the 19th century are still quoted in literature summaries,
but could be confirmed by exact measurements.   Person, in 1949
(18), may have been the first to measure the heat of fusion
of di-sodium phosphate dodekahydrate.   Berthelot, in 1878 (19),
and Thomsen, in 1883 (12), quoted most of the earlier results.

Koppel, in 1905 (20), published results on sulfates, Leenhardt,
in 1912 and 1913 (21) (22), on several salt-hydrates, Riesenfeld,
in 1914 (23), on nitrates. Muller used the supercooled nuclea-
tion method on a number of organic chemicals. Lithium salt-
hydrates were measured by Slonim (24), sodium thiosulfate penta-
hydrate and sodium acetate trihydrate by Sturley (25), $MgCl_2.6H_2O$
by Auzhbekovich (26), $CaCl_2.6H_2O$ by Lannung (27).

Special calorimeters for precision measurements have been
described by Johnston (28), Ticknor and Bever (29), Leake (30),
Oelsen (31), Nachtrieb (32), Schottky and Bever (33), and Bever
(34).

Tables 1A, 1B, and 2 contain available data, listing salt-
hydrates, change in the number of moles of water, density, salt
content in weight percent based on total weight of salt-hydrate,
solubility above the melting point expressed as percent anhydrous
salt in 100 gram salt-hydrate, specific heat of solid and liquid.
Tables 1A and 1B list the melting point in $^{\circ}C$ and $^{\circ}F$, the obser-
ved heat of fusion in calories per gram, and Btu/lb, the entropy
of fusion S_f observed (Obs.) and calculated (Calc.), and finally,
the ratio S_f Calc/Obs, serving the purpose of establishing the
validity of calculations.

X.   PROPERTIES OF SELECTED SALT-HYDRATES

A.   *Barium Hydroxide Octahydrate*

This salt-hydrate has many advantages. In addition to its
high heat of fusion, 72 cal/gram = 130 Btu/lb, its density is
high (2.18) and the heat of fusion per unit volume is conse-
quently also high (157 cal/cm^3 = 17,700 Btu/ft^3, based on the
volume of solid salt-hydrate). The heat of fusion calculated
from the heat of solution is 82 cal/g (de Forcrand (35)). The
volume change during melting is small.

The solubility of Ba(OH)$_2$ in water has been determined by
Cabot (36). The salt melts congruently and recrystallizes with
negligible supercooling. One of the disadvantages is due to
the fact that Ba(OH)$_2$ absorbs CO_2 from the air, but this can
be prevented in sealed containers. The major difficulty with
this material is its corrosiveness and toxicity. The melting
point $78^{\circ}C = 172^{\circ}F$ may be decreased to some extent by additives.

Table 2. Properties of Hydrates of Bromides and Iodides

Compound	Mols H_2O	Melting p. $^{\circ}C$	Solid %	Soluble at Mp.%	Heat of Fusion cal/g	Btu/lb	$S_f$calc
LiI	3	73	71	67	41	74	22.2
NaBr	3	51	74	54	36	65	15.5
MgI$_2$	8	41	66	48	38	68	52
CaBr$_2$	3	80	79	95	38	68	27.5
CaBr$_2$	6	38	65	92	43	78	43.3
CaI$_2$	6	42	73	95	34	61	43.6
FeBr$_3$	6	27	73	v.s.	36	65	48.2
FeI$_2$	4	90	81	v.s.	32	58	33
CoBr$_2$	6	47	66	60	43	78	43.4
SrBr$_2$	6	20		v.s.	35	63	43.4
SrI$_2$	6		76	v.s.			43.6
CdBr$_2$	4	36	79	v.s.	30	54	32.8
BaBr$_2$	2	75	90	67	23	41	22.3

v.s. = very soluble

B.   *Sodium Hydroxide - Monohydrate*

The properties of $NaOH.H_2O$ and $LiOH.H_2O$ are listed in Tables
1A and 1B. In addition to the monohydrate, the following hy-
drates are known.

		Melting p. $^\circ C$	$^\circ F$	Heat of fusion cal/gram	Calc Btu/lb
NaOH.	1 H_2O	64.3	148	65	117
NaOH.	2 "	12.3	54	62	112
NaOH.	3.5 "	5.0	41	65	117

The calorimetrically determined heat of fusion of $NaOH.H_2O$
agrees well with the theoretical value of 65 cal/gram, or 113
cal/cm^3.

NaOH.H$_2$O is highly corrosive and hygroscopic, but it has
several advantages. It melts congruently and recrystallizes
with only slight supercooling. Its crystal form is orthorhombic,
group P_{cab}, a = 6.21, b = 11.72, c = 6.05, z = 8. Density is
1.72. The specific heat of the melt is 0.69, of the solid 0.38.
The mono-hydrate contains 62.5 percent anhydrous salt. The
phase diagram and solubility have been determined by Staniford
(37). The thermal conductivity is advantageously high, accor-
ding to measurements by Riedel (38), and Boehm (39). The volume
contracts slightly when the salt solidifies.

NaOH.H$_2$O can be handled in sealed polyethylene or polypro-
pylene containers. For special applications, corrosion resis-
tant silver containers can be used.

C.   *Sodium Acetate Trihydrate*

Sodium acetate trihydrate melts at $58.3^\circ C$, $(137^\circ F)$. The
density of the solid is 1.45. The trihydrate melts partly
incongruently but dissolves entirely in its water of crystal-
lization at $77^\circ C$ $(170^\circ F)$.

The heat of fusion reported in the literature was 39 to 43 cal/gram; Leenhardt (22), Sturley (25). Recent measurements made by the writer with melts of the trihydrate (supersaturated solution) give a higher value of 63 cal/gram = 114 Btu/lb in excellent agreement with calculations based on the entropy of fusion. The heat of fusion per unit volume is 81 cal/cm^3 or 9100 Btu/lb. The heats of solution of anhydrous sodium acetate and its trihydrate have been determined. Their difference is 8490 cal/mole = 63 cal/gram, in perfect agreement with experimental results and calculations.

The solubility of sodium acetate decreases in the presence of acetic acid; Heubel (40).

D. Lithium Acetate

Lithium acetate forms a dihydrate, $LiC_2H_3O_2 \cdot 2H_2O$, which at its reported melting point 58°C (136°F), dissolves congruently. This salt could provide an interesting confirmation of the calculations based on the entropy of fusion. Calculations based on acetic acid give 67 cal/gram, but when based on the sum of entropies of fusion of the elements, the heat of fusion should be 94 cal/gram.

According to Nesterova (41), a ternary eutectic, melting at 73°C (163°F), can be obtained in the anhydrous system: sodium acetate + potassium acetate + urea. Although this material is not a salt-hydrate, it is listed here for comparison.

E. Ammonium Aluminum Sulfate Dodekahydrate

This salt-hydrate has the highest heat of fusion of "alums" that have been studied. Its heat of fusion is 62 cal/gram or 112 Btu/lb. The density is 1.64, with negligible volume change at the melting point. Its heat of fusion per unit volume is 102 cal/gram^3 or 11,500 Btu/ft^3.

Ammonium aluminum sulfate or "ammonium-alum" forms cubic crystals of the T_h^6 group, with unit cell edge of 12.18 A; Z = 4. It is isomorphous with an extensive group of alums, including those of sodium and potassium; Klug (42). It supercools, but when combined with a nucleating device, the effect of super- cooling can be eliminated completely. This salt-hydrate has been used in one of the heat storage containers developed com- mercially. After extensive tests in an ambient of minus 65°F, the salt-hydrate continued to give trouble-free performance.

Based on solubility studies, the system $Li_2SO_4 + Na_2SO_4$ + water shows the formation of a double salt $Li_2SO_4 \cdot 3Na_2SO_4 \cdot 12H_2O$ with transition temperature at 48.5°C (119°F) according to Lepeshkov (43), Bodaleva (44), and Khu (45).

The heat of fusion of the related $AlK(SO_4)_2 12H_2O$ has been measured. It is only 44 cal/gram = 79 Btu/lb. The salt hydrate melts at 91°C = 196°F.

F. Hydrated Sulfates

Tables 1A and 1B list three sulfates, all melting partly incongruently. Their pertinent data are the following:

	Melting p.		Heat of fusion	
	$^{\circ}$C	$^{\circ}$F	cal/g	Btu/lb
$Na_2SO_4 \cdot 10H_2O$	32.4	90	60.5	108
$MgSO_4 \cdot 7H_2O$	48.4	118	48.2	87
$CoSO_4 \cdot 7H_2O$	40.7	105	40.7	74

In this list, $Na_2SO_4 \cdot 10H_2O$ has the highest heat of fusion, measured repeatedly by Cohen (46), Perman (47), Kobe (48), Pitzer (49). The density is 1.46, giving 89 cal/cm^3 or 10,000 Btu/ft^3 as the heat of fusion per unit volume.

The writer has used $Na_2SO_4 \cdot 10H_2O$ for the storage of heat derived from solar energy and has evolved a nucleating mixture, consisting of $Na_2SO_4 \cdot 10H_2O$ with 3 to 5 percent of the isomorphous borax $Na_2B_4O_7 \cdot 10H_2O$; Telkes (50). This mixture melts at $89^\circ F$ and invariably nucleates when the temperature drops to $82^\circ F$. The melting is partly incongruent; the salt-hydrate contains 44 percent anhydrous salt, but only 34 percent is soluble at its melting point. The balance, 15 percent of the original salt-hydrate, settles to the bottom of the container (it "stratifies") and on subsequent cooling it is "frozen in", being unable to recombine with its water of crystallization.

Some experimentors, doubtless unaware of the requirements for nucleation and the possibilities of the prevention of settling, have reported pessimistically about the heat storage capacity of this salt-hydrate; Whillier (51), and Hodgins (52). The writer has conducted a number of alternate heating and cooling cycles with this salt-hydrate, proving definitely that settling can be prevented with thickening agents, Telkes (7) (53) (54). Recent applications of this material have been described (55) (56) (57) (58).

G. *Disodium Phosphate Dodekahydrate*

Disodium phosphate Na_2HPO_4 and water form several salt-hydrates:

		Density	*Crystal form*
$Na_2HPO_4 \cdot 12H_2O$	*dodekahydrate*	*1.52*	*monoclinic*
$Na_2HPO_4 \cdot 7H_2O$	*heptahydrate*	*1.68*	*monoclinic*
$Na_2HPO_4 \cdot 2H_2O$	*dihydrate*	*2.06*	*rhombic*
$Na_2HPO_4 \cdot H_2O$	*monohydrate*		

Transition of hydrates	Temperature °C	°F	Heat of fusion cal/g	Btu/lb
12 to 7	36	97	53	60
7 to 2	48	119	30.0	54
2 to 1	60	140		
1 to 0	95	203		
12 to 2			63	114
12 to 0			67	120

The heat of fusion has been measured by Person (59), Leenhardt (22), and Menzel (60). The 12 to 7 transition has a partly incongruent melting point, that is, the salt with $12H_2O$ does not melt completely if the $7H_2O$ form is present. Partington (61), measured the heats of solution.

The solubility of the salt has been measured by Menzel (62), Ingerson (63), and Hammick (64), indicating that $Na_2HPO_4 \cdot 12H_2O$ dissolves completely in its water of crystallization, if it is heated above 50°C (122°F). According to the writer's observations, it is possible to melt the $12H_2O$ salt completely at its melting point (97°F) if there are no crystal nuclei of the $7H_2O$ salt in a closed container.

The specific heat is 0.37 Btu/(lb.°F) solid

0.65 " " " liquid

A nucleating process has been described by the writer (7).

H. Sodium Thiosulfate Pentahydrate

This salt is extensively used in photographic development, (named "hypo"). It melts slightly incongruently at 49°C = 120°F, but dissolves completely at 52°C = 126°F. It changes to the dihydrate at 48°C and to anhydrous at 52°C. Its heat of fusion has been determined by Leenhardt (22), Muller (61), Sturley (25), and Perreu (16). The most probable value of the heat of fusion is 47.9 cal/gram or 86 Btu/lb., although calculations

based on the entropies of fusion lead to a somewhat higher value of 55 cal/gram = 99 Btu/lb. The density of the solid salt is 1.69, of the liquid 1.66, indicating negligible volume cahnge at the melting point. The heat of fusion per unit volume of the melt is 80 cal/cm^3 or 10,200 Btu/ft^3. The salt-hydrate supercools easily but with a nucleating device, supercooling is completely eliminated.

I. Magnesium Thiosulfate Hexahydrate

Magnesium thiosulfate hexahydrate melts at 100°C, changing to the trihydrate, which in turn transits to the anhydrous state at 120°C; Okabe and Hori (66). The calculated entropy of fusion, involving 3 mole water is S_f = 33.0 and the heat of fusion is 50 cal/gram = 90 Btu/lb.

J. Ferric Chloride Hexahydrate

The rather complex solubility relations and the formation of the hydrates of FeCl$_3$ have been studied by Bakhius Roozeboom (67). The heat of fusion of FeCl$_3$.6H$_2$O is moderately high, 54 cal/gram = 97 Btu/lb., its melting point is 98°F.

K. Magnesium Chloride Hexahydrate

MgCl$_2$.6H$_2$O melts congruently at 117°C (242°F); its boiling point is 159°C (318°F), density is 1.56.

The heat of fusion has been determined by Riesenfeld (23), as 41.2 cal/gram and by Auzhbekovich (26), who found 40.0 cal/gram, or 72 to 74 Btu/lb. At the melting point, the transition is from 6 to 4 H$_2$O and if these values are used, the calculated value agrees perfectly with the experimentally found 41.2 cal/gram. Based on unit volume, the heat of fusion is 64 cal/cm^3 or 7300 Btu/ft^3.

L.   *Other Hydrated Chlorides*

Hydrated chlorides listed in Tables 1A and 1B include the following:

	Melting Point ^{o}C	^{o}F	Heat of Fusion cal/g	Btu/lb
$CaCl_2.6H_2O \longrightarrow 2H_2O$	29.4	85	40.7	73.5
$MnCl_2.4H_2O \longrightarrow 2H_2O$	58	136	42.5	76.5

Data by Leenhardt (22), Lannung (27), and Perreu (16).

Additional melting, or transition temperatures, have been reported for the following chlorides:

	Melting Point ^{o}C	^{o}F	Calculated Heat of Fusion Cal/g	Btu/lb
$Cocl_26H_2O \longrightarrow 2H_2O$ (*)	54.4	130	47	85
$SrCl_2.6H_2O \longrightarrow 2H_2O$ (*)	61.6	143	34.5	62
$BaCl_2.2H_2O \longrightarrow H_2O$ (*)	101.9	213	25	45
$NiCl_2.6H_2O \longrightarrow 2H_2O$ (**)	60	140	50	90
$FeCl_2.4H_2O \longrightarrow 2H_2O$ (**)	37	99	34	61

*   *Borchardt (1957)*

**   *Mellor (1928)*

M.   *Hydrated Nitrates*

The salt-hydrates of nitrates listed in Tables 1A and 1B show rather low heat of fusion values, with the exception of $LiNO_3.3H_2O$ (71 cal/gram = 128 Btu/lb., melting at $30^{o}C = 86^{o}F$). These salts are highly soluble and melt congruently. None of the hydrated nitrates can be expected to show unusually high heat of fusion values, with the exception of $Al(NO_3)_3.9H_2O$, but according to the literature, it decomposes at $70^{o}C = 158^{o}F$.

N.   Other Salt-Hydrates

Compounds formed of light-weight, low atomic number elements
and anions, have potentially higher heat of fusion than compounds
formed of heavier elements. The compounds and their salt-hy-
drates have already been described, forming acetates, hydrox-
ides, carbonates, nitrates, oxides, fluorides, sulfates, chlor-
ides and phosphates. Additional salt-hydrates can be found
in the group of bromides, iodides (Table 2), and others, but
their heats of fusion are rather low, in the range of 34-44
cal/g, (60 to 80 Btu/lb) and they cannot be considered as suit-
able heat storage materials. Additional salt-hydrates exist
in the group of borates, perchlorates, chlorates, fluorides
and fluosilicates, listed in the following table. The melting
points of some of them are not known, but where possible, the
expected heat of fusion has been calculated from the entropy
of fusion of their component elements, assuming that the salt-
hydrate changes to its anhydrous form at the melting point.

Material	*Mp* ^oC	*Calc. Heat of Fusion cal/g*	
Metaborates:			
$NaBO_2 \cdot 4H_2O$	49	56	*Melts incongruently*
$LiBO_2 \cdot 8H_2O$	47	87	*Melts partly incongruently*
Tetraborate:			
$Na_2B_4O_7 \cdot 10H_2O$	60	79	*Melts incongruently*
Perchlorate:			
$LiClO_4 \cdot 3H_2O \ H_2O$	93	69	*Ref. Ropp (68)*

Material	Mp °C	Calc. Heat of Fusion cal/g	Solubility Percent at 20°C
Chlorates:			
$Al(ClO_3)_3 \cdot 6H_2O$ d.	60	68	v.s.
$NaClO_3 \cdot 10H_2O$			v.s.
$Sr(ClO_3)_2 \cdot 8H_2O$			v.s.
$Zn(ClO_3)_2 \cdot H_2O$	60	47	v.s.
Fluorides:			
$BF_3 \cdot 2H_2O$	6	64	
$KF \cdot 4H_2O$	18	34	v.s.
$KF \cdot 4H_2O$	41	52	v.s.
$MnF_2 \cdot 4H_2O$	24	58	v.s.
$CrF_3 \cdot 9H_2O \; 4H_2O$			v.s.
$CoF_2 \cdot 6H_2O$			v.s.
Fluosilicates:			
$Li_2SiF_6 \cdot 2H_2O$	100	70	43
$MgSiF_6 \cdot 6H_2O$	60 ?	75	39
$FeSiF_6 \cdot 6H_2O$	70 ?	73	56
$CuSiF_6 \cdot 6H_2O$	80 ?	65	70

In this group of salt-hydrates, $LiBO_2 \cdot 8H_2O$ has the highest heat of fusion although it melts partly incongruently. Sodium tetraborate (borate) melts incongruently and according to tests already made, it does not crystallize reversibly. Magnesium fluosilicate $\cdot 6H_2O$ and aluminum chlorate $\cdot 6H_2O$ appear to merit further study.

REFERENCES

1. Mullin, J.W., "Crystallization", CRC Press, Cleveland, (1972).

2. Van Hook, A., "Crystallization, Theory and Practice", 325 pp. Reinhold Publishing Co., New York, (1961).

3. Tipson, R.S., "Crystallization and Recrystallization", in "Technic of Organic Chemistry", Vol. 3, (A. Weissberger, ed). Interscience Publishers, New York, (1956).

4. Telkes, M., *Ind. and Eng. Chem. 44,* 1308-10 (1952). Nucleation of supersaturated inorganic salt-solutions.

5. Hume, Rothery W., "Atomic Theory for Students of Metallurgy", Institute of Metals, London, (1946).

6. Turnbull, D., "Solid State Physics", Vol. 3, p. 283, Academic Press, New York, (1956).

7. Telkes, M., Unpublished results.

8. Tamman, G., "Kristallisieren und Schmelzen", Barth, Leipzig, (1903).

9. Tamman, G., "The States of Aggregation", trans. R.F. Mehl, Van Nostrand, New York, (1925).

10. Rossini, F.D., Wagman, D.D., Evans, W.H., Levine, S., and Jaffe, I., National Bureau of Standards (U.S.) Circular 500 (1952).

11. Rossini, F.D., Wagman, D.D., Evans, W.H., Levine, S., and Jaffe, I., "Selected Values of Chemical Thermodynamic Properties", National Bureau of Standards, Washington, Circular 500 (1952).

12. Thomsen, J., "Thermochemische Untersuchungen", Vol. 3, p. 179 (1883). Heats of hydration of numerous salts.

13. White, W.P., "The Modern Calorimeter", New York, (1928).

14. Kubaschewski, O., Catterall, J.A., "Thermochemical Data of Alloys", Pergamon Press, (1956).

15. Kubaschewski, O., Dench, W.A., "Calorimetry", p. 171, in
     "Physico-chemical Measurements at High Temperatures" (J.
     Brockris, ed). Butterworths, London, (1959).

16. Perreu, J., *C.R. 199,* 48-51, 1934. Heat of crystallization
     of several hydrates.

17. Perreu, J., *C.R. 212,* 701-3, 1941. Heats of solution of
     $FeCl_2 \cdot 4H_2O$, $Ni(NO_3)_2 \cdot 6H_2O$.

18. Person, C.C., *C.R. 23,* 162, 1946, and *29,* 300, 1949.
     Heat of fusion of $Na_2HPO_4 \cdot 12H_2O$.

19. Berthelot, *C.R. 87,* 573, 1978, Heat of fusion of Na_2CrO_4
     $\cdot 10H_2O$.

20. Koppel, J., *Z. Anorg. Allgem. Chem. 52,* 385-436 (1905).
     Sollubility and formation of salt hydrates.

21. Leenhardt, C., Boutaric, A., *C.R. 154,* 113-4, 1912,
     $Na_2S_2O_3 \cdot 5H_2O$ crysoscopy.

22. Leenhardt, C., Boutaric, A., *Bull. Soc. Chim. de France 13,*
     651-7 (1913). Heat of fusion by calorimetry.

23. Riesenfeld, E.H., Milchsack, C., *Z. Anorg. Chem. 85,*
     401-21 (1914).

24. Slonim, C., Huttig, G.F., *Z. Anorg. Chem. 181,* 55-64 (1929).
     Heats of hydration of Li-halogen-hydrates.

25. Sturley, L.R., *J. Soc. Chem. Ind. 51,* 271-37 (1932).
     Specific heat and heat of fusion of $Na_2S_2O_3 \cdot 5H_2O$, Na
     acetate $\cdot 3H_2O$, and K-alum.

26. Auzhbekovich, A.E., *J. Appl. Chem. USSR, 9,* 594-598 (1936).
     Heat capacity and hydrates of MgCl.

27. Lannung, A., *Z. Anorg. Chem. 228,* 1-18 (1936). Heat of
     hydration of $CaCl_2$.

28. Johnston, H.L., Kerr, E.C., *J.A.C.S. 72,* 4733-7 (1950).
     Calorimetry (description).

29. Ticknor, L.B., Bever, M.B., *Trans. AIME 194,* 941 (1952).
     Calorimetry using tin as liquid.

30. Leake, L.E., *J. Sci. Instr. 31,* 447-9 (1954). Calorimeter.

31. Oelsen, W., *Arch. Eisen hutten w. Bergakademie, Clausthal, German 26*, 253-66 and 519-22 (1955). New calorimetric method and specific heats and heats of fusion of metals.

32. Nachtrieb, N.H., Clement, N., *J. Phys. Chem. 62*, 876 (1958). Heat of fusion of InSb.

33. Schottky, W.F., Bever, M.B., *Acta Met. 6*, 320 (1958). Heat of fusion of GaSb and InSb.

34. Bever, M.B., Calorimetric Investigations of III-V Compounds in "Compound Semiconductor Series", Vol. I (Willardson and Goering, eds) (1961).

35. de Forcrand, R., *C.R. 147*, 165-168, 1908. Heat of solution of $Ba(OH)_2$.

36. Cabot, G.L., *J. Soc. Chem. Ind. 16*, 417 (1897). Solubility of $Ba(OH)_2$.

37. Staniford, F.C., Badger, W.L., *Ind. Eng. Chem. 46*, 2400-3 (1954). Solubility and phase diagram of $NaOH \cdot H_2O$ system.

38. Riedel, L., *Chem. Engn. Techn. 22*, 54-6 (1950). Thermal conductivity of NaOH solutions.

39. Boehm, J., *Arch. ges. Warmetchen. 1*, 209-14 (1950. Thermal conductivity of NaOH solutions.

40. Heubel, J., Coup, D., *C.R. 250*, 1058-60, 1960, *C.A. 54*, 14876h, 1960. The system Na acetate – acetic acid – H_2O.

41. Nesterova, A.K., Bergman, A.G., *Zhur. Obschei Khim 30*, 317-20 (1960), *C.A. 54*, 19138f, 1960. The system sodium acetate – potas sium acetate-urea.

42. Klug, J., Alexander, L., *J.A.C.S. 62*, 2992-5 (1940). Crystal-chemical studies of alums.

43. Lepeshkov, I.N., Romashova, N.N., *Zhur. Neorg. Khim. 4*, 2812-5 (1959), *C.A. 54*, 23690g, 1960. Double salt $LiSO_4 \cdot 3Na_2SO_4 \cdot 12H_2O$.

44. Bodaleva, N.V, Khu, K.Y., *Zhur. Niorg. Khim. 4*, 2816-9 (1959). Solubility in the system Li_2SO_4-Na_2SO_4-H_2O.

45. Khu, K.Y., *Zhur. Neorg. Khim. 4*, 1910-18 (1959), *C.A. 54*, 11677e, 1960. The system Na_2SO_4-Li_2SO_4-H_2O.

46.   Cohen, E., *Z. Phys. Chem. 14,* 86 (1894). Heat of fusion of
      $Na_2SO_4 \cdot 10H_2O$.

47.   Perman, E.P., Urry, W.D., *Trans. Far. Soc. 24,* 337 (1928).
      Heat of hydration of $Na_2SO_4 \cdot 10H_2O$.

48.   Kobe, K.A., Anderson, C.H., *J. Phys. Chem. 40,* 429-33 (1936).
      Heat capacity of sa. Na_2SO_4 solutions.

49.   Pitzer, K.S., Coulter, L.V., *J.A.C.S. 60,* 1310-3 (1938).
      Heat capacity, entropy and heat of solution of Na_2SO_4.

50.   Telkes, M., "Solar Heat Storage", in "Solar Energy Research",
      (F. Daniels and J.A. Duffie, eds). University of Wisconsin
      Press (1955).

51.   Whillier, A., *Sun at Work 2,* 2 June 1957 (letter to the
      editor), Stored heat of $Na_2SO_4 \cdot 10H_2O$.

52.   Hodgins, J.W., Hoffman, T.V., *Canadian J. Techn. 33,* 293,
      July (1955). Glauber's salt as a heat storage material.

53.   Telkes, M., U.S. Patent No. 3,986,969, "Thiotropic Mixture
      and Method of Making Same", issued October 19, 1976.

54.   Telkes, M., U.S. Patent No. 4,187,189, "Heat Exchange Bodies
      Utilizing Heat of Fusion Effects and Method of Making Same",
      to issue February 5, 1980.

55.   Telkes, M., "Heat of Fusion Systems for Solar Heating and
      Cooling", Solar Engineering Magazine, September (1977).

56.   Telkes, M., "Trombe Wall with Phase Change Storage Material",
      Second National Passive Solar Conference, Philadelphia,
      Pennsylvania, pp. 283-287, March (1978).

57.   Telkes, M., "Latent Heat Storage Techniques", Institute of
      Gas Technology Symposium on ENERGY FROM THE SUN, April 3-7,
      1978, Chicago, Illinois.

58.   Telkes, M., "Thermal Storage in Salt-Hydrate Eutectics",
      1978 Annual AS/ISES Solar Conference: SOLAR DIVERSIFICA-
      TION", August 28-31, 1978, Denver, Colorado.

59.   Person, C.C., *Ann. de. Chim. Phys. 27,* 250 (1849). Heat of
      fusion of $Na_2HPO_4 \cdot 12H_2O$.

60. Menzel, H., Sieg, L., *Z. f. Elektrochem.* *38,* 283, 1932.
    Solubilities of phosphates.

61. Partington, J.R., Winterton, R.J., *J. Chem. Soc. (London),*
    635-43. Heat of hydration of Na_2HPO_4.

62. Menzel, H., von Sahr, *Z. f. Elektrochem.* *43,* 104-19 (1937).
    Alkali phosphates and Na_3PO_3.

63. Ingerson, E., *Amer. Mineral 28,* 448 (1943). Solubility of
    Na_2HPO_4.

64. Hammick, D.L., *J. Chem. Soc. 117,* 1589 (1920). Solubility
    of Na_2HPO_4.

65. Muller, A.H.R., *Z. Phys. Chem. 86,* 177-242 (1914). Heat of
    fusion of $Na_2S_2O_3$, also many organic chemicals.

66. Okabe, T., Hori, S., *Technol. Repts. Tohoku Univ. 23,* No. 2,
    85-9 (1959). *C.A. 54,* 20449g, 1960. Entropy of fusion of
    $MgSO_3 \cdot 6H_2O$ and $MgS_2O_3 \cdot 6H_2O$.

67. Bakhuis, Roozeboom, H.W., *Z. Phys. Chem. 10,* 479 (1912).
    Solubility of $FeCl_3$.

68. Ropp, C.D.L., *J.A.C.S. 50,* 1650-3 (1928). Hydrates of
    $LiClO_4$.

THERMODYNAMIC BASIS FOR
SELECTING HEAT STORAGE MATERIALS

Maria Telkes

Solar Thermal Storage Development
AEC Research Institute
Killeen, Texas

I. INTRODUCTION

A. *Theoretical Basis of Estimating Heat of Fusion Values*

Search for materials with high heat of fusion values in
any designated temperature range, can follow two paths. The
empirical way is to examine all compounds which melt in the
selected ranges of temperatures and to search for heat of fusion
data in the literature. Such work could involve thousands of
materials and although many could be bypassed by analogy, the
necessary work could involve many man-years (1).

The other approach is to consider the theoretical basis
of heat of fusion and its correlation with other known physical
properties, with the aim of evolving a selection-method, pre-
ferably corroborated with data obtained for wider temperature
ranges.

The effect of heat on materials is one of the primary fac-
tors in our consummate knowledge. The melting point T_f is used
for the identification of chemical compounds; therefore, it
is a determining factor.

Materials in the solid state contain atoms arranged in lattices with three vibrational degrees of freedom. Theory predicts that the *specific heat* per unit volume C_v = 3R = 6 cal/degree per gram atom. The specific heat at constant pressure C_p is higher in most solids and increases with temperature in a well known manner. *Kopp's rule* postulates that the specific heat of any compound is equal to the sum of specific heats of the elements forming the compound. This rule has been confirmed for a large number of materials. The usual value of C_p is between 7 to 7.25 cal/degree per gram atom. It is well known that the specific heat of some solids of very high melting points follow this rule only at higher temperatures. The specific heat of any compound is obtained by adding the specific heats of all atoms forming the compound.

The *heat of evaporation* of a liquid Q_e, according to *Trouton's rule* may be calculated from the entropy of evaporation (S_e) and the boiling point (T_e in K^o).

$$S_e = Q_e/T_e = 22 \text{ cal}/^oK \text{ per mole. (e.u.)}$$

The fact that the molar entropy of evaporation is approximately 22 (e.u.) has been confirmed for many compounds. It does not apply to low boiling point materials, or to substances which change in chemical composition during evaporation.

Hildebrand, (2) modified Trouton's rule, using the heats of evaporation at equal vapor pressures (Q_e') and the corresponding temperature (T_e'). This modified entropy of evaporation (S_e') is around 27 entropy units (e.u.) for most normal liquids and around 32 e.u. for polar liquids (including water).

The change from liquid to vapor phase involves the larger change in bonding energy between atoms and the corresponding entropy of evaporation is nearly ten times greater than the entropy of fusion.

Conditions are less easily understood during phase changes
between two solid crystal forms of the same substance, giving
rise to the *heat of transition* (Q_{tr}) at the transition tempera-
ture (T_{tr}). The entropy of transition is correlated with the
crystal structure and the co-ordination number, but no definite
method has been proposed for its evaluation.

The entropy of fusion can be expected to be definitely lower
than the entropy of evaporation, because the change in bonding
energy during fusion is smaller. Tamman (3) (4), found that
for some metals the entropy of fusion was 2.2 e.u., others mea-
sured the heat of fusion of several metallic elements and their
intermetallic compounds and compared the observed entropy of
fusion of the compounds with the entropy of fusion calculated
additively from those of the elements. The observed values
were usually 20 to 30 percent higher than those calculated
additively. The assumption was offered that this was due to
"disassociation" of bonding energy in the alloys during melting.

Kubaschewsky, (5) (6) examined an extensive series of metal-
lic phases and found that if the molten alloy is completely
disordered, its entropy of fusion could be obtained by adding
the entropies of fusion of the component elements. In ordered
alloys the observed entropies of fusion were invariably higher
than the calculated values, while in partly ordered alloys this
difference was smaller. According to Kubaschewsky this differ-
ence (Diff) can be calculated from the positional entropy part
of the heat of mixing of alloys. In a binary alloy containing
n_A and n_B atomic fraction of element A and B the difference
was:

$$\text{Diff} = -R(n_A \ln. n_A + n_B \ln. n_B).$$

(R is the constant, 1.986 cal/deg and ln - natural logarithm)
For alloys of the composition AB the difference was 1.38, while
for alloys AB_2 it was 1.23. Kubaschewsky, (7) recommended an
approximate value of 3.5 cal/deg per gram-atom for ordered alloys
and 2.2 cal/deg per atom for disordered alloys, for calculating
the entropy of fusion of metallic alloys.

   Kubaschewsky attempted to apply the above rule to inorganic
compounds, mostly chlorides, fluorides, bromides and oxides.
He stated that the entropy of fusion can be calculated by using
3.0 to 3.5 e.u. for ionic compounds with co-ordination numbers
of 6. Less than 3.0 e.u. had to be used with compounds of
higher co-ordination numbers. In molecular crystals an even
lower value, usually less than 2.0 e.u. was recommended. Layer-
type lattices and covalent compounds had intermediate values
around 2.6 e.u.

   Blanc, Darmois, and Petit published a series of articles,
(8) - (13) on measurements of heat of fusion of inorganic com-
pounds and the theory of fusion. They derived an equation:

$$S_f = Q_f/T_f = 3Rn \cdot L_n \ V_s/V_1 = 3n/2$$

(V_s is the molar volume of the solid material, V_1 of the melt,
while R=2.) Most materials expand in volume when melting, there-
fore V_s is smaller than V_1.

   If $V_s = V_1$ the above equation changes to $S_f/3 = n$.

Tabulation of values by Blanc, reported results with metallic
chlorides, fluorides and bromides giving n-values ranging from
1.0 to 2.5.

Schinke and Sauerwald, (14) (15), measured the V_1-V_s molar-
volume change during melting and compared it with the entropy
of fusion per molar volume (S_f/V_s) and the effect of the applied
pressure (P) on the melting point. They used a modified Clausius-
Clapeyron equation:

$$\frac{V_s-V_1}{V_s} = \frac{dT_m}{dP}\frac{S_f}{V_s}$$

Vogel, Schinke and Sauerwald, (16), found that the volume change,
expressed as per cent of the solid volume, was proportional
to the lattice energy and increased with the entropy of fusion.
It was not possible, however, to calculate heats or entropies
of fusion from their data.

Ubbelohde, (17) (18) (19) (20), studied the entropy of fusion
in relation to volume changes during melting and changes in
lattice parameters, viscosity of melt and electrical conduc-
tivity.

The physical aspects of "Changes of State" have been treated
by Temperley, (21) (22) who has summarized various theories
of the melting process.

The relationship of the heat of fusion, melting point,
lattice energy and other physical properties have been studied
by Vorob'ev, (23) (24).

Rather extensive work is being carried out on phase equilib-
ria in binary, ternary and even more complex systems, including
measurements of heats of fusion.

This intentionally brief survey of the theoretical approach
indicates a deficiency in our present knowledge in using known
physical constants for the purpose of calculating the entropy
or heat of fusion of elements.

The conclusion can be reached that Kubaschewsky's rule can
be applied to calculate the heat of fusion of inorganic com-
pounds, by using definite values for the entropy of fusion per
gram atom. These values are approximately 3.0 to 3.5 e.u. for
ionic compounds, 2.6 e.u. for layer-type lattices and less than
2.0 e.u. for molecular crystals of inorganic compounds.

B. Heat of Fusion and Entropy of Fusion of Elements

Most of the theoretical work of the past has been hampered
by lack of data on the heats of fusion of elements. Using
recently published results a nearly complete table has been
prepared, listing melting points, transition points, heats of
fusion and transition, also entropies of fusion and transition.
Table 1 shows these data arranged according to the atomic num-
bers of the elements. Combined data of entropies of transition
and fusion in relation to atomic numbers are shown in Figure 1.

There is an obvious correlation with the periodic table
of the elements as this is demonstrated by Figure 1. High
entropy of fusion values are shown in the following tabulation
with values in excess of 3.3 e.u. being outlined heavily.

III A	IV A	V A	VI A	VII A
B	C	N	O	F
2.48	(6.1)	2.13	3.47	3.37
Al	Si	P	S	Cl
2.76	7.2	0.47	1.12	4.45
Ga	Ge	As	Se	Br
4.42	6.7	(1.17)	2.65	4.76
In	Sn	Sb	Te	I
1.82	3.4	5.25	5.77	4.85
Tl	Pb	Bi	Po	At
1.86	1.86	4.77	(1.76)	(5.0)

Table 1. Heat of Fusion and Entropy of Fusion of Elements

Atomic No. Element			Melting Point °K	Heat of Fusion cal/mole	cal/8	Entropy of Fusion
1	H		14	14	14	1.00
2	He		3.5	5	1.2	1.4
3	Li		454	717	104	1.58
4	Be		1556	3520	390	2.26
5	B		2310	5720	525	2.48
6	C		(4100)	(25000)	(2100)	(6.1)
7	N	tr	36	27	2.0	0.77 ⎤
		f	63	86	6.1	1.36 ⎦ —2.13
8	O	tr	23.7	11.2	0.7	0.47 ⎤
		tr	43.8	88.8	5.5	2.02 ⎬— 3.47
		f	54.4	53.1	3.3	0.98 ⎦
9	F		54	186	10	3.37
10	Ne		25	80	4	3.26
11	Na		371	622	27	1.68
12	Mg		923	2127	88	2.30
13	Al		933	2570	95	2.76
14	Si		1683	12100	432	7.20
15	P		317	150	5	0.47
16	S	tr	369	85	2.7	0.27 ⎤ —1.12
		f	392	336	10.5	0.85 ⎦
17	Cl		172	766	21.5	4.45
18	A		84	281	7	3.35
19	K		337	570	15	1.69
20	Ca	tr	713	220	7	0.38 ⎤ —2.23
		f	1123	2070	52	1.85 ⎦
21	Sc		1845	3700	84	2.05
22	Ti	tr	1155	950	20	0.82 ⎤ —2.72
		f	1950	3700	77	1.90 ⎦
23	V		2120	(3830)	(75)	(1.76)
24	Cr		2120	3470	67	1.62

Table 1. Heat of Fusion and Entropy of Fusion of Elements
         (cont'd.)

Atomic No. Element			Melting Point °K	Heat of Fusion $\frac{cal}{mole}$	$\frac{cal}{8}$	Entropy of Fusion
25	Mn	tr	1000	535	10	0.53 ⎤
		tr	1374	545	10	0.40 ⎥ 3.53
		tr	1410	430	8	0.30 ⎥
		f	1517	3500	64	2.30 ⎦
26	Fe	tr	1183	215	4	0.18 ⎤
		tr	1673	165	3	0.10 ⎥ 2.30
		f	1812	3670	66	2.02 ⎦
27	Co		1766	3700	69	2.10
28	Ni		1728	4220	72	2.44
29	Cu		1356	3120	49	2.3
30	Zn		693	1765	27	2.55
31	Ga		303	1335	19	4.42
32	Ge		1210	8100	112	6.70
33	As		1087	(6600)	(83)	(6.1)
34	Se		490	1300	16	2.65
35	Br		266	1263	8	4.76
36	Kr		116	391	5	3.47
37	Rb		312	560	7	1.8
38	Sr		1043	2400	28	2.3
39	Y		1820	2730	30	
		tr	1135	1040	0.91	
40	Zr		2130	5000	53	2.36 3.27
41	Cb		2770	(4800)	(52)	1.76
42	Mo		2890	6650	69	2.3
				6100		
43	Tc		(2400)	(5500)	(56)	(2.3)
44	Ru		2700	(6200)	(61)	(2.3)
45	Rh		2239	5200	50	2.3
46	Pd		1823	4200	40	2.3
47	Ag		1234	2780	26	2.25

Table 1.   Heat of Fusion and Entropy of Fusion of Elements
(cont'd.)

Atomic No. Element		Melting Point °K	Heat of Fusion cal mole	cal 8	Entropy of Fusion
48	Cd	594	1450	13	2.44
49	In	429	780	7	1.82
50	Sn	505	1720	15	3.4
51	Sb	903	4740	40	5.25
52	Te	723	4180	33	5.77
53	I	387	1885	7	4.85
54	Xe	161	549	4	3.42
55	Cs	302	510	4	1.69
56	Ba tr f	643 983	150 1830	1 13	0.23 ⎤ 1.86 ⎦ 2.09
57	La	1193	(2750)	(20)	(2.3)
58	Ce	1077	3100	22	2.32
59	Pr	1208	3800	27	3.15
60	Nd	1297	2990	21	2.3
61	Pm	(1300)	(3000)	(21)	(2.3)
62	Sm	1325	3050	20	2.3
63	Eu	(1100)	(2500)	(17)	(2.3)
64	Gd	(1600)	(3700)	(24)	(2.3)
65	Tb	(1700)	(4100)	(25)	(2.3)
66	Dy	1773	(4100)	25	2.3
67	Ho	1733	(4600)	25	2.3
68	Er	1800	(4100)	(26)	(2.3)
69	Tm	(1900)	(4400)	(26)	(2.3)
70	Yb	1097	(2200)	(13)	(2.3)
71	Lu	(2000)	(4600)	(26)	(2.3)
72	Hf	2495	5790	32	2.3
73	Ta	3250	(7500)	(41)	(2.3)
74	W	3650	(8400)	(46)	(2.3)

Table 1. Heat of Fusion and Entropy of Fusion of Elements
(cont'd.)

Atomic No. Element			Melting Point ^{O}K	Heat of Fusion $\frac{cal}{mole}$	$\frac{cal}{8}$	Entropy of Fusion
75	Re		3400	8000	43	2.3
76	Os		3000	(6900)	(36)	(2.3)
77	Ir		2730	(6300)	(33)	(2.3)
78	Pt		2043	4700	24	2.3
79	Au		1336	2955	15	2.2
80	Hg		234	549	3	2.3
81	Tl		577	1020	5	1.86
82	Pb		601	1140	6	1.86
83	Bi		545	2600	12	4.77
84	Po		527	(3000)	(14)	(5.7)
85	At		(575)	(2850)	(14)	(5.0)
86	Rn		202	693	3	3.43
87	Fr		(300)	(495)	(2)	(1.65)
88	Ra		973	(2250)	(10)	(2.3)
89	Ac		(1470)	(3420)	(15)	(2.3)
90	Th	tr	1650	860	19	2.3
		f	1980	3300		
91	Pa		(1500)	(3500)	(15)	(2.3)
92	U		1406	4750	20	3.38
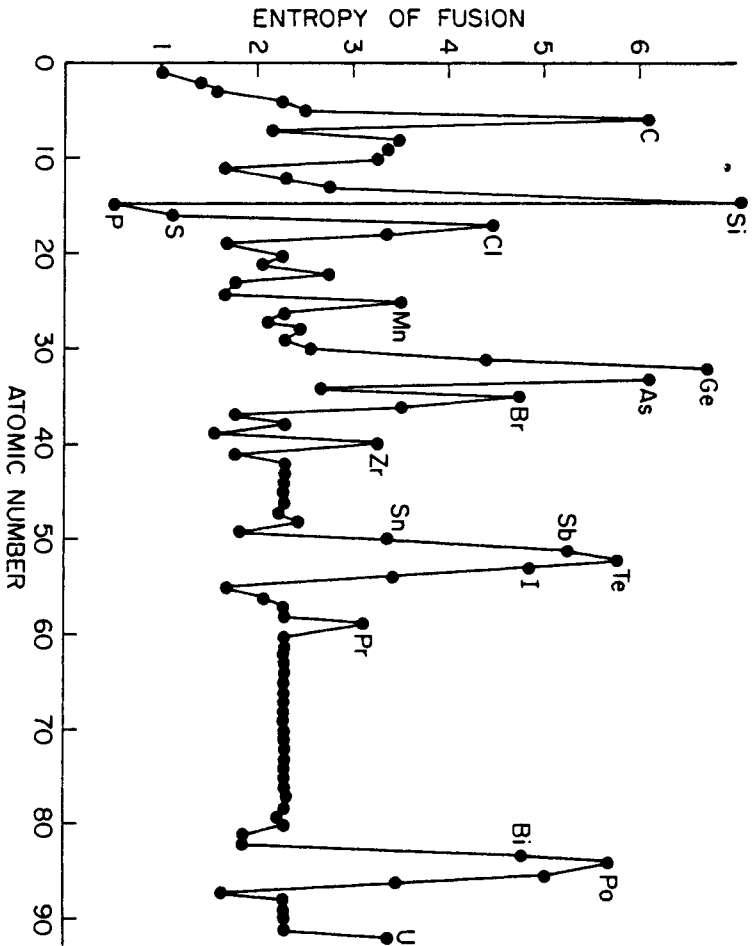
FIGURE 1.

The highest heat of fusion values in cal/gram are listed in decreasing order as follows:

Atomic No.	Element	Melting Point		Heat of fusion cal/gram
		^{o}K	^{o}C	
6	C	(4100)	(3800)	(2100)
5	B	2310	2040	525
14	Si	1683	1410	432
4	Be	1556	1283	390
32	He	1210	940	112
3	Li	454	181	104
13	Al	933	660	95
12	Mg	923	650	88

It is of interest to note that high heat of fusion values (cal/g) are found only in elements of low atomic numbers. Values higher than 50 cal/gram cannot be found in elements with atomic numbers in excess of 47.

The purpose of preparing an exact list was to test the applicability of a proposed method of calculating heat of fusion, which is now outlined.

C. Proposed Method of Calculating the Heat of Fusion

The proposed method consists of calculating the heat of fusion of compounds, from their entropies of fusion, obtained by adding the entropies of fusion of their component elements. We designate the entropy of fusion of elements A and B as S_{fA} and S_{fB}. The elements form a compound of the type A_2B_3 (other numbers may be applicable). The proposed method of calculation is:

$$S_f \text{ of } A_2B_3 = 2yS_{fA} + 3zS_{fB}$$

y and z are to be evaluated later.

For compound A_2B_3: $S_f \cdot T_f = Q_f$ cal/mole

II. THERMOPHYSICAL PROPERTIES

To test the validity of the proposed method of calculating the heat of fusion of any compound, a survey has been made of the most extensive data that can be found for groups of compounds. The most prevalent data occurs in the groups of chlorides, fluorides and oxides and for this reason the calculations have been applied to these groups.

CHLORIDES. Data is listed in Table 2 in the order of the atomic number of the atom forming the chloride. The table lists 72 chlorides with known compositions and melting points, values of heats of fusion, and entropy of fusion have been reported in the literature for more than 50 chlorides, (S_f Obs.). The entropy of fusion of all listed chlorides has been calculated from equation 3, (S_fCalc.). The ratio of S_f Calc/Obs is shown in the last column of Table 2. Agreement for calc/Obs = 1.00 cannot be expected in view of the obvious difficulties in measuring heats of fusion, especially at higher temperatures. Ratios between 0.7 to 1.3 were therefore accepted as "reasonable agreement", of 1.0±0.3. The following table summarizes results of Table 2. Similar categories are shown for 1.65 + 0.35 or 1.31 to 2.0 and for higher deviations.

Elements forming chlorides	*Number of Compounds*	*S_f Cal/Obs.*
H Li F Na Mg Al K		
Mn Fe Co Ni Zn Ga Rb Zr Pd Cd	*21*	*0.7 to 1.0*
Cs Ta Tl Th		
B C Ca Cr Cu Sr Cb Mo Ag I		
Ba La Ce Pr Nd Gd Hg Pb Bi	*19*	*1.31 to 2.0*
Be Si P Ti As Sn Sb Te Ho Er W	*11*	*2.01 to 4.0*

Maria Telkes

Table 2. Heat of Fusion and Entropy of Fusion of Chlorides

Compound			Melting Point °C	Heat of Fusion cal g	Btu lb	Entropy of Fusion Obs	Calc	Calc Obs
1	HCl	tr	-175	8	14	5.9	5.45	0.93
		f	-115	13	23			
3	LiCl		607	112	202	5.43	6.03	1.11
4	$BeCl_2$		440	25	45	2.8	10.7	3.8
5	B_2Cl_4		-93	16	29	14.31	19.96	1.39
6	CCl_4	tr	-48	7	13	7.27	13.35	1.83
		f	-23	-9	7			
7	NCl_3		-43	(30	54)	-	15.48	-
	NH_4Cl		185	18	32	2.05		
8	Cl_2O_7		-92	(33	59)	-	33.2	-
9	F_3Cl		-76	24	43	11.14	14.56	1.40
11	NaCl		800	114	205	6.20	6.13	0.99
12	$MgCl_2$		714	108	194	10.44	11.2	1.07
13	$AlCl_3$		193	65	117	18.4	16.11	0.88
14	$SiCl_4$		-70	11	20	9.0	25.0	2.8
15	PCl_3		-87	8	14	6.0	13.82	2.3
	$POCl_3$		1	20	36	11.4		
16	S_2Cl_2		-76	(16	29)	-	11.1	
17	Cl_2		-101	22	40	8.9	8.9	1.00
19	KCl		770	86	155	6.10	6.14	1.00
20	Cl_2		772	61	110	6.44	11.13	1.73
21	$ScCl_3$		939	(127	229)	-	15.85	-
22	$TiCl_4$		-25	12	22	9.04	19.6	2.17
23	VCl_4		-26	(26	47)	-	20.1	-
24	$CrCl_2$		815	62	112	7.1	11.2	1.57
25	$MnCl_2$		650	71	128	9.8	11.2	1.14
26	$FeCl_2$		677	81	146	11.9	11.2	0.94
	$FeCl_3$		304 307	55	99	15.4	15.35	1.00

Table 2.   Heat of Fusion and Entropy of Fusion of Chlorides (cont'd.)

Compound		Melting Point °C	Heat of Fusion cal g	Heat of Fusion Btu lb	Entropy of Fusion Obs	Entropy of Fusion Calc	Calc Obs
27 $CoCl_2$		724	79	142	10.1	11.2	1.10
28 $NiCl_2$		1030	142	256	14.15	11.34	0.80
29 $CuCl$		430	26	47	3.72	6.75	1.81
$CuCl_2$		498	(64	115)	-	11.2	-
30 $ZnCl_2$		275	40	72	10.0	11.45	1.14
31 $GaCl_3$		78	37	67	17.8	17.8	1.00
32 $GeCl_4$		-49	(38	68)	-	24.5	-
33 $AsCl_3$		-16	13	23	9.35	19.08	2.0
34 $SeCl_4$		305			-	20.5	-
35 $BrCl$		-23			-	9.2	-
37 $RbCl$		722	47	85	5.70	6.25	1.09
38 $SrCl_2$	tr	730	25	45	3.38	6.75	1.3
	f	873	10	18	1.65		
39 YCl_3		677	(77	139)	-	15.77	-
40 $ZrCl_4$		437	61	110	17.0	20.1	1.18
41 $CbCl_5$		205	26	47	14.4	24.45	1.7
42 $MoCl_5$		188	29	52	17.2	24.5	1.4
44 $RuCl_3$		d.					
45 $RhCl_3$		d.					
46 $PdCl_2$		678	55	99	10.2	11.2	1.1
47 $AgCl$		455	21	38	4.25	6.76	1.6
48 $CdCl_2$		568	41	74	9.0	11.34	1.25
49 $InCl_3$		586	(41	74)	-	10.7	-
50 $SnCl_2$		247	23	41	6.3	12.3	1.5
$SnCl_4$		-33	8	14	9.1	21.2	2.3
51 $SbCl_3$		73	13	23	8.82	18.6	2.1
52 $TeCl_4$		224	17	31	9.05	23.5	2.6
53 ICl		27	11	20	6.1	9.3	1.5

Table 2. Heat of Fusion and Entropy of Fusion of Chlorides
          (cont'd.)

Compound	Melting Point °C	Heat of Fusion cal/g	Btu/lb	Entropy of Fusion Obs	Calc	Calc/Obs
55 CsCl	645	30	54	5.27	6.14	1.16
56 BaCl$_2$	920 / 960	38	68	6.6	11.0	1.65
57 LaCl$_3$	857	53	95	13.0	15.6	1.20
58 CeCl$_3$	822	52	94	11.8	16.23	1.3
59 PrCl$_3$	827	49	85	12.1	16.5	1.35
60 NdCl$_3$	784	48	86	12.0	15.6	1.3
62 SmCl$_3$	678	(57	103)	–	15.6	–
63 EuCl$_3$	627	(54	97)	–	15.6	–
64 GdCl$_3$	632	36	65	10.6	15.6	1.48
65 TbCl$_3$	588	(50	90)	–	15.6	–
66 DyCl$_3$	657	(54	97)	–	15.6	–
67 HoCl$_3$	718	26	47	7.0	15.6	2.2
68 ErCl$_3$	773	29	52	7.4	15.6	2.1
69 TmCl$_3$	845	(63	113)	–	15.6	–
80 HgCl$_2$	277	15	27	7.6	11.2	1.5
Hg$_2$Cl$_2$	539	2.5	4.5	1.5	6.8	4.5
81 TlCl	429	16	29	5.4	6.1	1.13
82 PbCl$_2$	495	20	36	7.53	10.8	1.5
83 BiCl$_3$	234	18	32	11.2	18.0	1.6

The table indicates that agreement between calculated and obser-
ved values was found in about half of the compounds. Largest
deviations were found in groups IV A, and V A of the periodic
table of elements.

   FLOURIDES. Table 3, shows data for fluorides; containing
data for 41 compounds, with observed heat of fusion values
listed for 31 compounds, with the following results:

Elements forming fluorides	*Number of Compounds*	S_f *Calc/Obs.*
H Li Be Na Mg P Cl K Rb *Sr Zr Cs Ce Re*	*14*	*0.7 to 1.3*
B N Al Si Ca As Br Cb *Mo Cd I U*	*12*	*1.31 to 2.0*
C Br Ba Pb Bi	*5*	*2.01 to 3.1*

   The deviation factor is 1.0 in half of the compounds. Some
of the data may be in error due to difficulties in determining
the heat of fusion of fluorides, which melt at higher tempera-
tures than the corresponding chlorides. Repeated measurements
have been made with LiF, MgF_2 and NaF - which show rather high
heat of fusion values. Here the ratio of S_f Calc./Obs. is near
1.0.

   OXIDES offer an excellent opportunity for testing the appli-
cability of the proposed calculation. They are mostly stable
compounds and usually do not disassociate or decompose during
melting. Most of the measurements have been performed with
precision calorimetry. (Table 4)

   During calculation of S_f the recently determined combined
entropy of transition and fusion of oxygen has been used
(S_f=3.47), while the previously available value for fusion alone
(1.0) was not suitable for calculating the entropy of fusion
of water. The first two lines of Table 4 show excellent agree-
ment (within 4 percent) between the calculated and observed

Table 3. Heat of Fusion and Entropy of Fusion of Fluorides

Compound Mol. W.		Melting Point °C	Heat of Fusion cal/g	Heat of Fusion Btu/lb	Entropy of Fusion Obs	Entropy of Fusion Calc	Calc/Obs
	F				3.37		
1	HF	-83	47	85	4.93	4.	0.90
3	LiF	848	249	448	5.77	5.0	0.87
4	BeF$_2$	543	139	250	8.0	8.5	1.06
5	BF$_3$	-128	16	29	7.6	12.4	1.6
6	CF$_4$ tr f	-197 -184	6	11	6.52	17.0	2.6
7	NF$_3$ tr f	-216 -207	6	11	7.78	12.2	1.6
11	NaF	995	192	346	6.20	5.1	0.8
12	MgF$_2$	1263	224	403	9.15	9.1	1.0
13	AlF$_3$	1040	96	173	6.25	12.9	2.06
14	SiF$_4$	-87	22	40	12.0	20.7	1.7
15	PF$_5$	6	22	40	10.0	10.0	1.0
17	ClF$_3$ tr f	-82 -76	23	41	11.1	14.5	1.3
19	KF	856	106	191	6.0	5.1	0.85
20	CaF$_2$ tr f	1151 1418	14 92	25 166	0.79 ⎤ 4.2 ⎦	8.9	1.8
24	CrF$_2$	1097	(111	200)	-	9.0	-
25	MnF$_2$	856	(113	203)	-	10.2	-
27	CoF$_2$	1127	(111	200)	-	12.4	-
28	NiF$_2$	1450			-	9.2	-
29	CuF	908	(82	148)	-	5.7	-
30	ZnF$_2$	872	(77	139)	-	9.2	-
31	GaF$_3$	1027	(150	270)	-	14.5	-
32	GeF$_4$				-	20.2	-
33	AsF$_3$	-6	19	34	9.3	15.8	1.7
35	BrF$_3$	9	21	38	10.2	14.9	1.45
35	BrF$_5$	-60	9	16	7.05	21.61	3.1

Table 3. Heat of Fusion and Entropy of Fusion of Fluorides
(cont'd.)

Compound Mol. W.		Melting Point °C	Heat of Fusion cal/g	Btu/lb	Entropy of Fusion Obs	Calc	Calc/Obs
37	RbF		795	59	106	5.76	5.17	0.9
38	SrF_2		1397	94	169	8.1	9.0	1.1
39	YF_3		1367	98	176	8.7	12.5	1.45
40	ZrF_4		932	92	166	12.7	15.8	1.2
41	CbF_3		77	20	36	8.3	12.4	1.5
42	MoF_6	tr	-10	9	16	7.5 ⎤ 22.5		2.0
		f	18	5	9	3.6 ⎦		
48	CdF_2		1047	55	99	6.2	9.2	1.50
53	IF_5		9	18	32	13.9	21.70	1.56
55	CsF		713	34	61	5.32	5.06	0.95
56	BaF_2		1277	29	52	3.2	8.83	2.8
58	CeF_6		1459	67	121	7.62	9.6	1.26
75	ReF_6		19	17	31	17.1	22.5	1.32
82	PbF_2		818	18	32	3.81	8.6	2.25
83	BiF_3		649	20	36	5.6	14.9	2.65
92	UF_6		64	13	23	13.6	22.4	1.7
94	PuF_3		1425	51	92	9.0	11.4	1.27

Table 4. Heat of Fusion and Entropy of Fusion of Oxides

Compound	Melting Point °C	Heat of Fusion cal mole	cal g	Btu lb	Entropy of Fusion Obs	Calc	Calc Obs
O					3.47		
H_2O	0	1437	80	144	5.26	5.47	1.04
H_2O_2	2	2560	76	137	9.35	8.94	0.96
Li_2O	1700	(13000	440	790)	–	6.63	–
BeO	1500	17000	680	1220	6.10	5.27	0.9
B_2O_3	450	5500	79	142	7.6	15.0	2
CO tr+f	-200	351	13	23	5.4	7.0	1.3
CO_2	-56	1990	46	83	9.15	10.44	1.14
NO	-163	550	18	32	5.1	5.6	1.09
N_2O_5	57	8300	77	140	27.5	21.6	0.78
N_2O	-93	1563	36	65	8.6	7.7	0.89
O_2	-219	153	10	18	6.94	6.94	1.00
Na_2O	920	11200	180	320	9.35	6.83	0.73
MgO	2800	18500	462	830	6.0	5.77	1.0
Al_2O_3	2000	26000	258	460	11.4	15.9	1.4
SiO_2	1610	3600	34	62	1.91	14.1	7.4
P_2O_5	572	5750	40	72	6.8	18.3	2.7
SO_2	-75	1769	28	50	8.95	7.06	0.78
$(SO_3)_2$	62	6090	38	68	18.95	23.0	1.21
CaO	2600	17000	305	550	5.9	5.7	0.97
TiO	2020	14000	219	395	6.1	6.19	1.01
TiO_2	1940	15500	194	350	7.3	9.66	1.3
VO_2	1545	14000	168	303	7.7	9.24	1.2
V_2O_5	670	15500	86	155	16.4	20.9	1.25
MnO	1750	13000	183	330	6.5	7.0	1.08
FeO	1380	8000	111	200	4.8	5.77	1.20
Fe_3O_4	1600	33000	143	260	17.6	20.8	1.17
CoO	1800	(12000	160	290)	–	5.81	–

Table 4.   Heat of Fusion and Entropy of Fusion of Oxides (cont'd.)

Compound	Melting Point °C	Heat of Fusion			Entropy of Fusion		
		cal/mole	cal/g	Btu/lb	Obs	Calc	Calc/Obs
NiO	1950	(13100	164	295)	–	5.9	–
Cu$_2$O	1230	13400	94	170	8.95	8.1	0.91
ZnO	1800	(12600	155	280)	–	6.0	–
GeO$_2$ tr	1030	5050 tr	48	86	3.9 ⎤	13.6	2.0
f	1115	4100 f	39	70	2.95 ⎦		
ZrO$_2$	2680	20800	169	305	7.17	9.24	1.28
Cb$_2$O$_5$	1510	24590	93	188	13.8	21.9	1.6
MoO$_3$	795	12500	87	156	11.6	12.7	1.09
BaO	1920	14700	90	164	6.7	6.86	1.03
PbO	875	6100	28	50	5.3	5.33	1.00
Bi$_2$O$_3$	820	7400	16	29	6.8	8.24	1.21
UO$_2$	2840	25300	94	170	8.1	10.3	1.28

entropy of fusion for water and hydrogen peroxide. Confirmation
of the calculations as applied to water indicate that these
could be extended to salt-hydrates, as this will be shown later,
reaching rather excellent agreement with known measurements.

   HYDROXIDES are listed in Table 5, containing the data for
9 anhydrous compounds; and 4 hydrates. Deviations occur only
with the hydroxides of Ca, Sr, and Ba.

   BROMIDES AND IODIDES, listed in Table 6 and 7, contain most
of the observed values of heats of transition, fusion and en-
tropy of fusion. An analysis of Bromides and Iodides follows:

$$S_f \text{ Calc/Obs} = 1+0.3 \qquad S_f \text{ Calc/Obs} = \quad 1.3$$

BROMIDES

Li Na Mg K Fe   C N Al Ca Ti Cu Zn As Sr Ag
RB CD Cs Ta Tl   Sn Sb Ba La Pr Nd Gd Hg Pb U

IODIDES

Li Na K Ca Fe   N Al Ti Cu Sr Cd Sn Ba Ce Pr Pb
Rb Ag Cs Nd Hg

   OTHER COMPOUNDS are listed in Table 8.

   NITRATES. In the group of nitrates, those of NH_4, Na, K,
and Ag have average deviation factors of 1.8, Nitric acid, its
hydrates and $LiNO_3$ do not deviate from the additive rule.

   SULFATES. In the group of sulfates, sulfuric acid shows
a deviation factor of 2. With this correction the entropies
of fusion of the sulfates of Li Na K Ba and Pb, as well as the
acid sulfates of NH_4 Na and K follow the additive rule. The
sulfates of Ca and Tl show higher ratios. It is, of course,
possible that some of the data is inaccurate, or that decompo-
sition occurs during melting. Later data may provide better
proof of the additive rule, which has been reasonably accurate
in giving heat of fusion values for more than half of the stud-
ied compounds.

Table 5.   Heat of Fusion and Entropy of Fusion of Hydroxides

Compound	Melting Point °C	Heat of Fusion cal mole	Heat of Fusion cal g	Heat of Fusion Btu lb	Entropy of Fusion Obs	Entropy of Fusion Calc	Calc Obs
(OH)					4.45	4.45	1.0
H_2O	0	1437	80	144	5.26	5.43	1.03
LiOH	471	5290	220	395	7.1	6.03	0.85
$B(OH)_3$	d 185	(7250	118	212)	–	15.8	–
NH_4OH	-179	1568	45	81	8.1	10.5	1.10
NaOH tr	300	1720	43	77	3.00 ⎤ 6.15		1.10
f	320	1520	38	69	2.56 ⎦		
$NaOH.H_2O$	64	3850	66	119	11.41	11.41	1.00
$NaOH.2H_2O$	13.5	3859	51	92	13.5	15.7	1.16
$NaOH.3.5H_2O$	15.5	5380	52	94	18.5	21.0	1.13
KOH tr	249	1520	27	49	2.93 ⎤ 6.14		1.00
f	400	2050	37	67	3.20 ⎦		
NaOH.KOH	177	(5100	53	95)	–	12.29	–
$Ca(OH)_2$	835	6900	93	165	6.25	11.1	1.8
$Sr(OH)_2$	510	5230	43	77	6.7	11.2	1.67
$Ba(OH)_2$	417	4590	27	49	6.65	10.7	1.60
$Ba(OH)_2 8H_2O$	78	22700	72	130	64.6	53.1	0.82
RbOH tr	225	1290	13	23	2.58 ⎤ 5.25		0.90
f	385	2120	21	37	3.22 ⎦		
CsOH tr	220	1450	10	18	2.95 ⎤ 5.05		1.05
f	315	1090	7	13	1.85 ⎦		

Table 6. Bromides

Atom No.			Melting Point °C	Heat of Fusion cal/g	Btu/lb	Entropy of Fusion Obs	Calc	Calc/Obs
3	LiBr		550	51	92	5.1	6.3	1.2
6	CBr₄	tr	47	4	7	4.4 ⎤		
		f	93	3	5	2.6 ⎦ 22.5		3.1
7	NH₄Br		542	51	92	6.1	10.9	1.8
11	NaBr		750	61	110	6.1	6.4	1.05
12	MgBr₂		711	48	86	9.0	11.8	1.3
13	AlBr₃		98	25	45	7.3	17.0	2.3
19	KBr		735	51	92	6.1	6.4	1.05
20	CaBr₂		743	35	63	6.9	11.8	1.7
22	TiBr₄		39	9	16	9.9	21.7	2.2
29	CuBr	tr	382	10	18	2.1 ⎤		
		f	487	16	29	3.0 ⎦ 7.0		1.4
30	ZnBr₂		394	17	31	5.6	12.1	2.15
33	AsBr₃		31	9	16	9.2	20.4	2.2
37	RbBr		692	34	61	5.8	6.6	1.15
38	SrBr	tr	645	12	22	2.7 ⎤		
		f	657	10	18	3.2 ⎦ 11.8		2.0
47	AgBr		430	12	22	3.1	7.0	2.3
48	CdBr₂		568	29	52	9.5	11.9	1.25
50	SnBr₂		232	6	11	3.4	12.9	3.8
51	SbBr₃		97	10	18	9.5	19.5	2.0
55	CsBr		636	27	49	6.2	6.4	1.0
56	BaBr₂		850	26	47	6.7	11.6	1.7
57	LaBr₃		788	53	95	11.6	16.6	1.4
59	PrBr₃		699	30	54	11.7	17.4	1.5
60	NdBr₃		682	28	50	11.4	16.5	1.45
64	GdBr₃		785	28	50	8.3	16.5	2.0
73	TaBr₅		267	19	34	19.8	26.1	1.3
80	HgBr₂		238	12	22	8.4	11.8	1.40

Table 7.   Iodides

Atom No.			Melting Point °C	Heat of Fusion		Entropy of Fusion		
				cal / *g*	*Btu* / *lb*	*Obs*	*Calc*	*Calc* / *Obs*
3	LiI		469	26	47	4.7	6.4	1.36
7	NH_4I		551	35	63	6.1	11.0	1.8
11	NaI		660	38	68	6.04	6.5	1.08
13	AlI_3		191	10	18	8.6	12.5	1.45
19	KI		681	35	63	6.0	6.4	1.09
20	CaI_2		779	34	61	9.5	9.9	1.04
22	TiI_4		150	8	14	9.9	22.1	2.23
26	FeI_2		594	46	83	16.1	12.0	0.86
29	CuI		590	10	18	2.2	7.15	3.2
37	RbI		647	25	45	5.7	6.65	1.16
38	SrI_2		538	17	25	5.8	12.0	2.06
47	AgI	tr	150	6	11	3.5	7.15	1.16
		f	558	10	18	2.7		
48	CdI_2		387	14	25	7.6	12.1	1.6
50	SnI_4		145	7	13	11	22.8	2.1
55	CsI		626	22	40	6.27	6.5	1.04
56	BaI_2		711	16	29	6.4	11.7	1.84
58	CeI_3		760	24	43	12.0	17.4	1.45
59	PrI_3		738	24	43	12.6	17.7	1.40
60	NdI_3	tr	574	6	11	4.0	12.0	0.90
		f	787	19	34	9.2		
80	HgI_2	tr	129	1	1	1.6	12.0	0.90
		f	254	10	18	8.60		
82	PbI_2		412	13	23	8.8	11.5	1.3

The conclusion can be reached that the proposed rule can definitely establish the maximum possible value of the heat of fusion of any compound.

A. *Entropy of Fusion Per Gram Weight*

In Tables 1 and 2 the entropy of fusion is shown in calories/mole^{O}K. It would be desirable to compare the entropy of fusion of elements and anions forming the compounds on the basis of equal weights.

In Table 9, the cationic elements are arranged according to atomic numbers and the anions Cl F O Br I NO$_3$, according to their atomic numbers, showing deviation factors. The second column lists the combined heats of transition S$_{tr}$ and fusion S$_f$, while the rest of the columns give the deviations from the additive rule. For the anions the following S$_{tr}$ and S$_f$ values were used: Cl = 4.45, F = 3.37, 0 = 3.47, Br = 4.76, I = 4.85, NO$_3$ = 11.6. The elements and anions with the lowest atomic weight(atomic No) show the highest entropy of fusion.

B. *Entropy of Fusion and the Periodic System*

It is advantageous to correlate the ratios S$_f$Calc/Obs and the deviation factors from the additive rule, with the periodic system of the elements by listing them according to atomic numbers. This is shown in Table 8, where the entropy of fusion of elements in included for comparison. There are striking similarities between the peaks of the curve for the elements and the deviations of chlorides, fluorides and oxides. In many groups the ratios are close to unity (within the 0.7 to 1.3 range). This group includes the compounds of H Li Ma K Rb Mg Mn Fe Al, where data was available for at least two compounds. It is probable that several other elements belong to this group but data was not available to prove this.

Table 8.   Heat of Fusion and Entropy of Fusion of Compounds

Nitrates		Melting Point °C	Heat of Fusion			Entropy of Fusion		
			cal mole	cal g	Btu lb	Obs	Calc	Calc Obs
(NO$_3$)							11.6	
HNO$_3$		-42	2503	40	72	10.81	12.6	1.15
HNO$_3$.H$_2$O		-37	4184	52	93	17.76	17.9	1.0
HNO$_3$.3H$_2$O		-18	6954	54	107	27.30	28.4	1.0
LiNO$_3$		251	6390	93	167	12.1	13.2	1.1
NH$_4$NO$_3$	tr	32	1710	21	38	4.66		
	tr	125					16.6	2.2
	f	170	2900	16	29	2.94		
NaNO$_3$	tr	276	944	11	20	1.26		
	f	310	3800	45	82	6.50	13.3	1.7
KNO$_3$	tr	128	1400	14	25	3.5		
	f	337	2800	28	51	4.6	13.3	3.3
	tr	160	930	9	16	2.15		
Ca(NO$_3$)$_2$		561	5700	35	63	6.8	15.2	2.25
Cd(NO$_3$)$_2$		300	4350	14	25	7.6	14.0	1.85
AgNO$_3$	tr	159	560	3	6	1.30		
	f	208	3020	18	32	6.25	13.9	1.85
LiNO$_3$2KNO$_3$		129	(16000	59	107)	-	39.8	
			(11200	42	75)	-	27.9	
LiNO$_3$NaNO$_3$		204	(12700	82	148)	-	26.5	
Sr(NO$_3$)$_2$		645	10650	50	90	11.6	25.3	2.2
Ba(NO$_3$)$_2$		592	9950	38	69	11.5	25.3	2.2
RbNO$_3$		308+u	2480	17	31	6.0	13.3	2.2
CsNO$_3$		406	3370	17	31	5.0	13.3	1.85
KNO$_3$NaNO$_3$		222	(7900	42	76)	-	15.9	-
LiNO$_3$.2NH$_4$NO$_3$		97	(10000	43	78)	-	26.9	-
LiNO$_3$.4KNO$_3$		112	(17500	37	67)	-	45.6	-

Table 8. Heat of Fusion and Entropy of Fusion of Compounds
          (cont'd.)

Sulfates		Melting Point °C	Heat of Fusion $\frac{cal}{mole}$	$\frac{cal}{g}$	$\frac{Btu}{lb}$	Entropy of Fusion Obs	Calc	$\frac{Calc}{Obs}$
SO_2		-75	1769	28	50	8.95	8.06	0.90
H_2SO_4		10	2360	24	44	8.32	17.00	2.0
$H_2SO_4 \cdot H_2O$		9	4630	40	72	16.44	22.26	1.3
SO_4 (basis)						6.32	15.00	2.35
Li_2SO_4	tr	575	7000	64	115	8.25	9.48	0.85
	f	859	3350	30	54	2.95		
Na_2SO_4	tr	241	2068	15	27	3.48	9.7	1.5
	f	884	5800	41	74	4.90		
$Na_2SO_4 \cdot 10H_2O$		32	19400	60	108	63.5	62.3	1.0
$NaHSO_4$		182	2480	21	38	5.45	5.84	1.5
NH_4HSO_4		144	4300	43	77	8.18	10.29	1.5
K_2SO_4	tr	583	2570	43	27	3.0	9.7	1.0
	f	1070	9060	52	93	6.75		
$KHSO_4$	tr	164	590	4	7	1.33	5.85	1.0
	f	219	2220	16	29	4.52		
$CaSO_4$	f	1300	6700	49	88	4.26	8.55	2.0
$BaSO_4$	tr	1149	9700	42	76	6.00	8.41	1.4
	f	1350						
Ti_2SO_4		632	5500	11	20	6.1	10.0	1.5
$PbSO_4$	tr	866	4060	13	23	3.56	8.18	0.8
	f	1087	9600	32	58	7.1		
$Na_2S_2O_7$	tr		1620	7	13			
	f	403	9760	44	80	14.4	29.1	2.0
$MgSO_4$		1130	3500	29	52	2.5	8.6	3.45

The majority of elements of higher valence form compounds
where the ratio S_fCalc/Obs is greater that 1 + 0.3. At least
two observations of this type are available for B C Si P As
Cb Mo, forming deviations. With elements of lower valence higher
deviations occur in Ca Sr Ba Cd Sn Pb.

According to Table 9 the ratios for the chlorides, fluorides
and oxides of the same element deviate from 1 + 0.3 to the same
extent. We can, therefore, assign a factory to each element
as a multiplier to change its ratio to unity.

$$y(S_f\text{Calc/Obs}) = 1 + 0.3$$

With this simplification the previous equation is changed
to:

$$S_f\text{Calc/Obs for } A_2B_3 = y(2S_{fA} + 3S_{fB}) = 1 + 0.3$$

The factory y is shown in the following Table:

Element	Valence	Average deviation	1/y		y
Al	3	1.5	3/2	=	1.5
C	4	2.0	4/2	=	2.0
B	3	1.7	7/4	=	1.75
Si	4	2.0 (except SiO$_2$)	4/2	=	2.
P	5	2.5	5/2	=	2.5
Ca	2	1.8 (except CaO)	4/2	=	2
As	3	1.7	3.2	=	1.5
Cd	2	2	4.2	=	2
Ba	2	2	4/2	=	2
Pb	2	2	4/2	=	2

This comparison shows that the y factors are common fractions where the denominator corresponds to the valence of the element forming the compounds. In monovalent elements the factor should be y=1 and this explains the fact that the entropies of fusion of such compounds can be obtained directly by adding the s_f values of the elements. This rule is applicable to the bromides and iodides of Na and K.

According to Table 9 the y factor is within the 1+0.3 range for the compounds of several bivalent and tribalent elements, including Mg, Mn, Fe and possible several others. This could be explained only by introducing an integer multiplier for these elements, equal to their valence.

Until further data will be available, we may conclude, therefore, that it is possible to calculate the entropy of fusion by adding those of the elements and using the correction factors y as shown in the table.

C. *Materials of High Heat of Fusion*

The highest heat of fusion is shown by LiH, a compound of the lowest molecular weight, (7.95), storing 1120 cal/gram. The material melts at 1267^OF, but it decomposes near its melting point. It has been tested for space applications (25). The next highest heat of fusion values are shown by lithium compounds, by fluorides, the refractory carbides, nitrides, borides, silicides and some oxides. Some of these have heat of fusion values up to 700 cal/gram, 1260 BTU/lb as shown in Table 8.

The high melting point materials are of interest because some of them can be used in binary or ternary systems, forming compounds or eutectics with considerably lower melting points. The most extensive change in melting point can be achieved in salt-hydrates. some of the high melting point materials with high heats of fusion form salt-hydrates which melt below 100^OC.

III.   CONCLUSIONS

Collection of extensive data are presented, giving heats
of transition and fusion of elements and their compounds.
Analysis of data, based on theoretical considerations, reveal
that it is possible to calculate heat of fusion values of com-
pounds by using the entropies of fusion of elements, forming
the compounds, correcting these data with correlation factors
to compensate for deviations from the simple additive rule.
In this way entropy of fusion and heat of fusion data can be
obtained for eutectics, or compounds, provided their melting
point is known, in addition to molar composition. Calculated
values agree with observed values within ±30% and often within
± 10%, which can be considered satisfactory, in view of experi-
mental difficulties in determining heat of fusion values, espe-
cially at high temperatures and with materials that may decom-
pose near their melting points.

The search for the "highest" heat of fusion material in
a selected melting point range can be simplified greatly, by
calculating the probable entropy and heat of fusion before em-
barking on highly time consuming experiments, because such ex-
periments can be restricted to those compounds, or eutectics,
that have been found to be "promising", by calculations.

Tables and Figures indicate that only those compounds have
higher heat of fusion values, based on unit weights, that are
formed of elements of low atomic weights. These consideration
eliminates from the group of candidates a large group of mater-
ials of higher atomic weights.

Materials formed of low cost and low atomic weight compounds
include H, B, C, N, O, Na, Mg, Al, Si, P, S, Cl, K, Ca, Ti and
Fe. Some of these elements can combine to form groups, such
as borates, carbonates, nitrates, phosphates, including the
addition of water in the form of hydrates.

Other compounds that include Li and fluorides of some of
the groups listed above are available only at a higher cost
level.

REFERENCES

1. Lane, George A., et al., "Solar Energy Subsystems Employing
   Isothermal Heat Storage Materials", ERDA-117, UC-94a, May,
   (1975).

2. Hilderbrand, *J. Anal. Chem. 24,* 720 (1952).
   Hilderbrand, *J. Chem. Phys. 20,* 1520 (1957).

3. Tamman, G., "Kristallisieren und Schmelzen", 1903, Barth,
   Leipzig.

4. Tamman, G., "The States of Aggregation", trans. R.F. Mehl,
   1925, Van Nostranc, New York.

5. Kubaschewski, O., Dench, W.A., "Calorimetry", p. 171, in
   "Physico-chemical Measurements at High Temperatures" (J.
   Brockris, ed), Butterworths, London, (1959).

6. Kubaschewski, O., et al., "Metallurgical Thermochemistry",
   Pergamon Press, 1967 edition.

7. Kubaschewski, O., *Trans. Faraday Soc. 45,* 931 (1949).

8. Blanc, M., *C.R. 246,* 570-1, 1958. Heat of fusion of Li, Na,
   K bromides.

9. Blanc, M., *C.R. 249,* 2012-3, 1959. Heat of fusion of KF
   + K_2SO_4 and LiCl + $SrCl_2$.

10. Blanc, Mme M., *C.R. 247,* 273, 1958. Heat of fusion
    (Calculated) of A, Cl, AgBr.

11. Blanc, M., *Compt. Rend. Acad. Sci. Paris 247,* 273 (1958).

12. Blanc, M., and Petit, G., *Compt. Rend. Acad. Sci. Paris
    248,* 1305 (1959).

13. Blanc, Mme M., *C.R. 248,* 1305, 1959. Heat of fusion of Pb
    salts.

14. Schinke, H., Sauerwald, F., *Z. Anorg. Chem. 287,* 313-24
    (1956). Volume change during melting.

15.   Schinke, H., Sauerwald, F., *Z. Anorg. Chem. 304*, 25-36
      (1960).   Volume change during melting.

16.   Vogel, E., Schinke, H., Sauerwald, F., *Z. Anorg. Chem. 284*,
      131-41 (1956).   Volume change during melting.

17.   Ubbelohde, A.R., *Quart. Rev. Chem. Soc. 4*, 356 (1950).
      Entropy of fusion of inert gases.

18.   Ubbelohde, A.R., *Quart. Rev. (London) XI*, 246 (1957).
      Thermal transformations in soldis.

19.   Ubbelohde, A.R., Heat of fusion calculations.

20.   Ubbelohde, A.R., Melting and Crystal Structure, Clarendon
      Press, Oxford, (1965).

21.   Temperly, H.M.V.,"Changes of State", (1956).

22.   Temperly, H.M.V., "Changes of State, A Mathematical-
      Physical Assessment". Interscience Publishers, New York,
      (1956).

23.   Vorob'ev, A.A., *Izvest. Vysshikh Ucheb. Zavedenii Fiz No. 1*,
      160-2 (1958), *C.A. 54*, 9418d (1960).   Properties of ionic
      crystals and lattice energy, heat of fusion theory.

24.   Vorob'ev, A.A., et al., *Izvest. Vysshikh Ucheb. Zavedenii
      Fiz No. 6*, 162-5 (1959), *C.A. 54*, 9416f (1960).   Heat of
      fusion theory.

25.   Caldwell, R.T., McDonald, J.W., and Pietsch, A., "A Solar
      Energy Receiver with Lithium-Hydride Heat Storage", *Solar
      Energy J. 9(1)*, 48-60 (1965).

CHAPTER 13

THE APPLICATION OF REVERSIBLE CHEMICAL REACTIONS
TO SOLAR THERMAL ENERGY SYSTEMS

Raymond Mar

Sandia Laboratories
Livermore, California

I. INTRODUCTION

   Numerous investigators have proposed reversible thermochemical
reactions as a means for storing thermal energy in solar energy
systems. In this application, thermal energy is stored in the
form of chemicals created by endothermic reactions. The thermal
energy is recovered by recombining the chemicals, which releases
a quantity of energy equivalent to the heat of reaction. In addi-
tion to the storage applications, there is interest in applying
reversible reactions to solar thermal energy transport and solar
thermal heat pumping for space heating and cooling systems.

   This paper reviews all three of these applications in order to
introduce the reader to the use of reversible chemical reactions
in solar energy systems. The characteristic features of reversi-
ble chemical reaction systems are described and compared to
sensible and latent heat systems. The different uses of reversi-
ble chemical reactions in solar energy applications are reviewed
and their potential impact (i.e., economic viability) is
appraised. The following chapter discusses materials science
issues relevant to the development of thermochemical schemes.

   Only those reversible chemical reactions which are thermal in
nature are discussed; electrochemical, photochemical, and

radiochemical reactions are specifically excluded. The term "thermochemical" is used based on the fact that thermal energy is stored and released as a consequence of net changes in chemical bonding.

II. GENERAL CHARACTERISTICS OF THERMOCHEMICAL SYSTEMS

Solar thermal energy can be stored in three forms: 1) as sensible heat, 2) as latent heat of transitions, and 3) as chemical bond energy, i.e., the use of thermochemical reactions. Because enthalpies of reaction are generally much greater than either enthalpies of transition or sensible heat changes over reasonable temperature intervals, storage densities (based on either mass or volume) are greater for thermochemical storage systems than for sensible or latent heat systems. Typical energy density differences are illustrated on Figure 1, where the
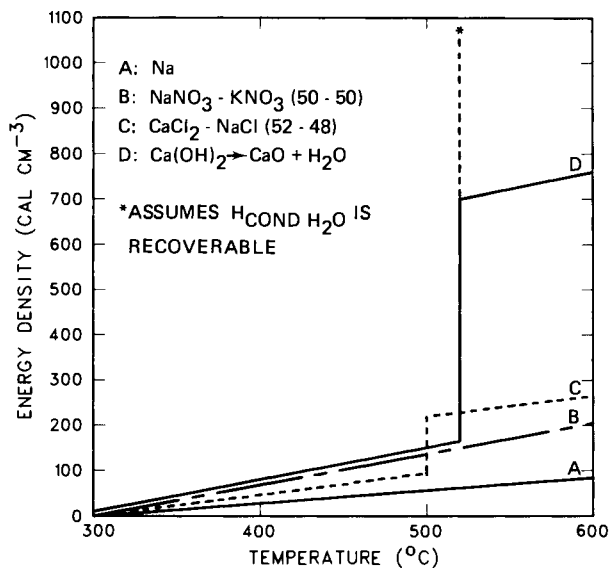
FIGURE 1. *A comparison of energy storage densities for sensible heat (curves A and B), latent heat of fusion (curve C) and reversible chemical reaction (curve D) storage media. Energy densities are based on chemical properties only.*

requirements of thermal energy storage systems in solar central receiver systems (i.e., a nominal temperature swing of 300°C – 600°C) are met by four different systems: 1) a sensible heat liquid sodium system, which is the baseline approach adopted for systems designed by General Electric(1) and Rockwell International(2); 2) a sensible heat nitrate draw salt system, adopted by the Martin Marietta design(3); 3) a heat of fusion system based on the $NaCl-CaCl_2$ eutectic; and 4) the use of the $Ca(OH)_2 = CaO + H_2O$ reaction. The energy densities were calculated based on the chemical properties and are not totally reflective of the density in actual practice. For example, a dual tank approach to sensible heat storage would require the storage volume to double, thereby decreasing the effective storage density by a half. Nevertheless, the implications drawn by Figure 1 are reasonably accurate: storage densities associated with thermochemical systems are typically greater than sensible and latent heat systems by a factor ranging from two to more than an order of magnitude.

One important criterion for selecting thermochemical reactions is that one must be able to prevent the products of the endothermic reaction from reversing. This is typically accomplished by selecting reactions whose products are easily separated physically, or reactions which do not proceed in the absence of a suitable catalyst. Control over the reaction enables one to store energy at ambient temperatures by cooling and storing the products of the endothermic reaction. The ability to store energy at ambient temperatures has associated attributes. First, the potential for corrosion is reduced because large quantities of material are not kept at elevated temperatures. Second, one is not faced with potential heat losses and insulation needs. However, it should be noted that storing energy at ambient temperatures requires careful process design and engineering to use the sensible heat associated with cooling to ambient. If these sensible heat losses are not

utilized in the operational cycle, the overall system efficiency
suffers. The ability to store at ambient temperatures provides
operational design flexibility in that long-term storage options
may be considered.

Because chemicals at ambient temperature can be easily trans-
ported over long distances, thermochemical reactions can be used
to transport thermal energy. Chemical reactions involving
liquids or gases are the most amenable to energy transport
applications, since pipeline transport is simple and straight-
forward. However, the transport of solids has also been
proposed (4,5).

The cost of an energy storage system is divided into power
related costs and energy related costs (6). The former are costs
associated with transferring heat to and from the storage unit,
and includes costs for heat exchangers, chemical reactors, and
pumps. Energy related costs are associated with the quantity of
energy stored, and include costs for the storage media, storage
tanks and insulation. Thermochemical systems are characterized
by the ability to physically separate and power and energy
components; therefore, the sizes of these components can be
varied independently. Since the energy related costs are
generally low for thermochemical systems, scenarios calling for
added storage capacity (e.g. long-term storage) at fixed power
delivery can be explored. This situation can be contrasted with
latent heat systems where the heat exchanger is an integral part
of the storage tank. Any increase in storage tank volume must
necessarily be accompanied by a corresponding increase in the
heat exchanger surface area.

Thermochemical systems have several drawbacks. Round trip
efficiencies, defined as the ratio of amount of energy out of
storage to that entering, are low because of the numerous energy
loss steps (such as heat exchanging and gas compression) required
for a complete operational cycle. Also, the operational and
maintenance requirements may be more demanding and costly due to

the complexity of thermochemical systems.

III.   THERMAL ENERGY STORAGE

   The intermittant nature of solar energy requires that there
be a means to store thermal energy to cover short term transients
such as daily cloud coverage, and longer term transients, such as
diurnal cycling and days of poor insolation. A simplified flow
schematic for the reaction $Ca(OH)_2 = CaO + H_2O$ is used to illus-
trate the basic features of a thermochemical energy storage
scheme (Figure 2). To store thermal energy, $Ca(OH)_2$ is trans-
ported to the endothermic chemical reactor and decomposed into
CaO and H_2O. H_2O is condensed and the products of reaction, CaO
and H_2O, are stored until there is a need for the energy. The
system is discharged by first vaporizing the water and then
running the exothermic reaction between steam and CaO in the
exothermic reactor. $Ca(OH)_2$ exiting from the exothermic reactor
is cooled and stored until used in the charging cycle.
   It is possible to design the system whereby only one heat
exchanger is used for both the exothermic and endothermic
reaction. Further, the chemical reactor may be used for chemical
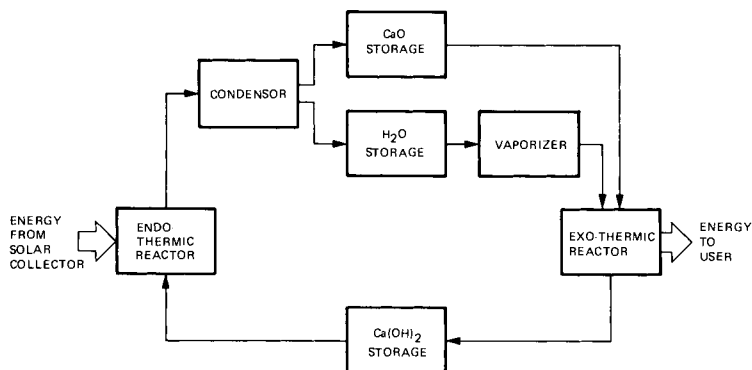
FIGURE 2.   The use of the reaction $Ca(OH)_2 = CaO + H_2O$ for
thermal energy storage in a two reactor/heat exchanger system.

storage; such a system is schematically represented in Figure 3. In this approach, the energy and power related components are no longer decoupled. While the overall system is less complex than the moving solids approach of Figure 2, the fixed bed concept suffers from heat transfer and mass transport concerns.

Figure 4 gives an example of a reaction which is catalytically controlled, as opposed to being controlled by physically separating the products. In this case, SO_3 is decomposed into SO_2, which is condensed and stored as a liquid, and O_2, which is compressed and stored as a gas. Energy is recovered by catalytically recombining SO_2 and O_2 in the exothermic reactor; the product of this exothermic reaction is then condensed and stored.

The schematics in Figures 2 through 4 are very simplistic and do not show all of the heat recovery steps necessary for developing an efficient process. More realistic process schemes have been developed and analyzed (7-9) but their discussion is outside of the scope of this paper.
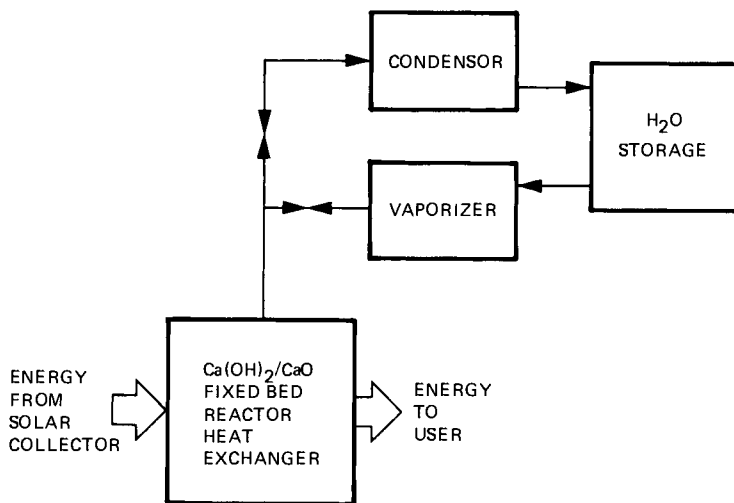
FIGURE 3. The use of the reaction $Ca(OH)_2 = CaO + H_2O$ for thermal energy storage in a one reactor/heat exchanger system.

```
                          ┌────────────┐   ┌────────────┐
                          │ COMPRESSOR │──▶│     O₂     │
                          └────────────┘   │  STORAGE   │
          ┌────────────┐                   └────────────┘
          │ CONDENSER  │                   ┌────────────┐   ┌────────────┐
          └────────────┘                   │    SO₂     │──▶│ VAPORIZER  │
                                           │  STORAGE   │   └────────────┘
                                           └────────────┘
  ENERGY    ┌────────────┐                          ┌────────────┐   ENERGY
  FROM      │ ENDO-      │                          │ EXO-THERMIC│   TO
  SOLAR  ▷  │ THERMIC    │              ▷           │ CATALYTIC  │▷  USER
  COLLECTOR │ CATALYTIC  │                          │ REACTOR    │
            │ REACTOR    │                          └────────────┘
            └────────────┘
          ┌────────────┐   ┌────────────┐   ┌────────────┐
          │ VAPORIZER  │◀──│    SO₃     │◀──│ CONDENSOR  │
          └────────────┘   │  STORAGE   │   └────────────┘
                           └────────────┘
```
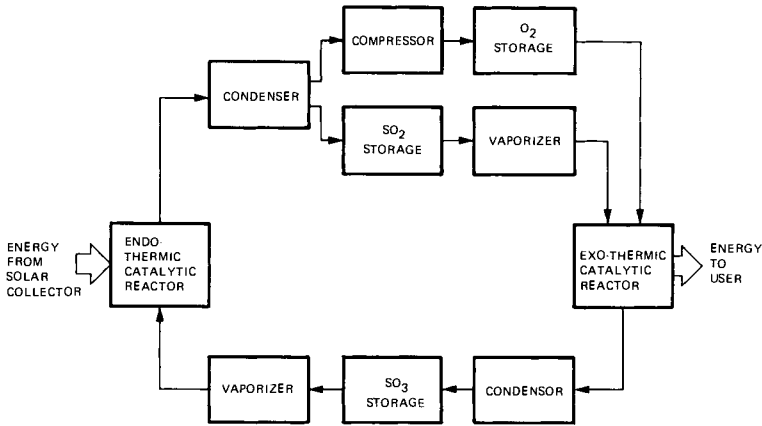
FIGURE 4.   A simplified schematic for a thermal energy storage system based on the reaction $2SO_3 = 2SO_2 + O_2$.

IV.   TRANSPORT OF THERMAL ENERGY

Thermochemical reactions can be used in distributed solar power systems, where solar energy is collected by numerous collectors and transmitted to an energy storage and central power generating facility. Figure 5 shows a specific example, the Solchem process proposed by Chubb (10), which uses the reaction $2SO_3 = 2SO_2 + O_2$ to transmit thermal energy from a field of high concentration parabolic collectors to a molten salt heat of fusion energy storage system. The ammonia dissociation reaction has also been proposed for this application by Carden (11). In principle, thermochemical reactions can also be used as the primary heat transfer fluid in central receiver thermal electric large power systems of the type discussed in Reference 12.

High concentration solar central receiver systems have been proposed where the end product is thermal energy rather than electricity (13,14). In this application, thermochemical re-actions are used to transport the thermal energy from the solar collection site to the user. An example of this application is
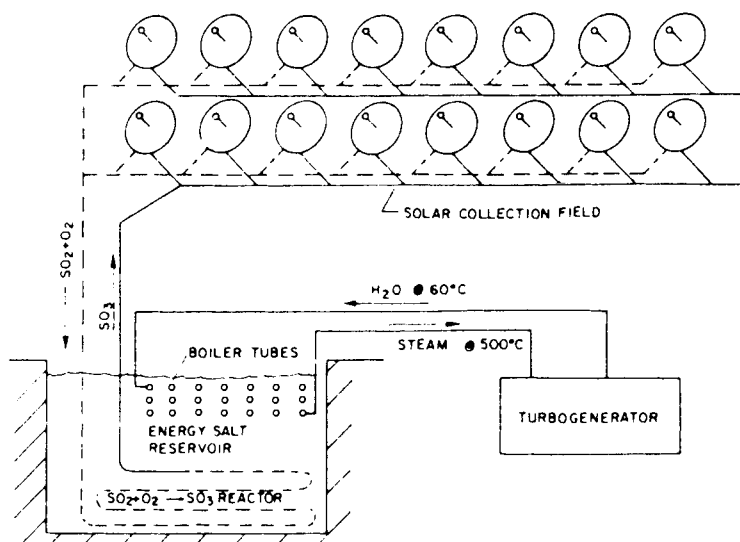
FIGURE 5. The use of the reaction $2SO_3 = 2SO_2 + O_2$ to trans-port thermal energy in a distributed solar power plant (Reference 10).

given in Figure 6, where the reforming/methanation reaction

$CH_4 + H_2O = CO + 3H_2$ is used to transport energy from a solar

collection device to an end user, e.g. industrial process heat.

A slight variation of this process has been studied by Baker,

et al., (12) in which the thermochemical reaction is not used in a

reversible manner, but rather as a step in the generation and

transmission of synthetic natural gas. The concept shown in

Figure 7 is identical to the system studied in detail by Baker,

et al., (15) only the ash agglomerating gasifier plant is replaced

by a solar powered coal gasifier. Pulverized coal and steam are

heated to generate a mixture of H_2 and CO, which is then piped

over long distances to a methanator where the methanation

reaction is catalytically carried out. The end result is the

production of substitute natural gas, with the added feature that

the heat of methanation is now generated at a site selected such

that the heat can be put to good use (e.g. industrial process
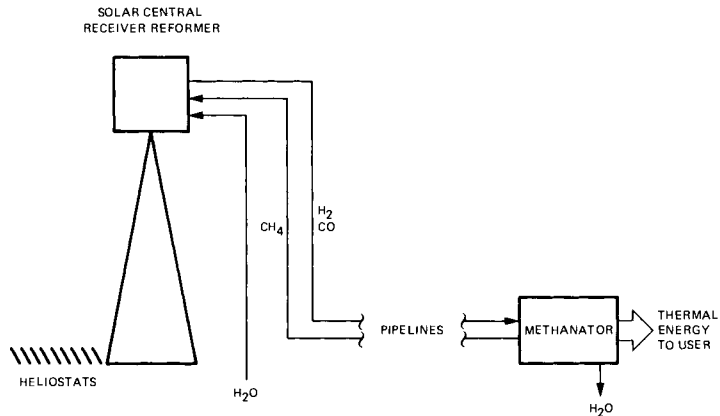
heat).

FIGURE 6.   The transport of thermal energy from a solar
central receiver facility, using the reaction $CH_4 + H_2 = CO + 3H_2$.
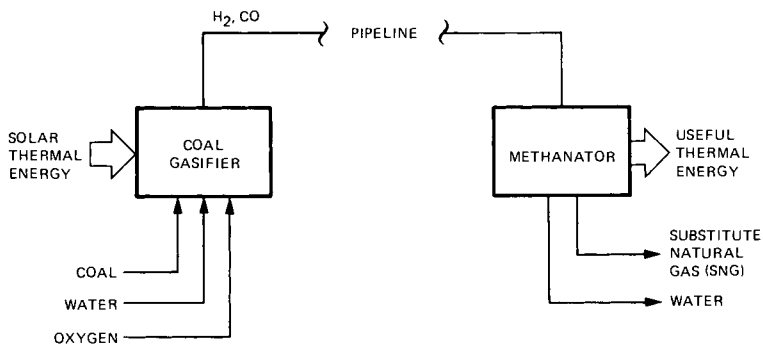
FIGURE 7.   The use of the methanation reaction in an open
loop energy transmission system.

V. SPACE HEATING AND COOLING

Solar chemical heat pump systems capable of space heating and
cooling have been proposed by many different investigators (16-18).
The essential elements of the chemical heat pump system are
illustrated in Figure 8. Two thermochemical reactions which have
a common vapor species are needed. In the example, $NH_{3(g)}$ is the
transferring gas species, and the two reactions used are:

$$MgCl_2 \cdot 6NH_3 = MgCl_2 \cdot 2NH_3 + 4NH_3 \qquad\qquad (1)$$

$$CaCl_2 \cdot 8NH_3 = CaCl_2 \cdot 4NH_3 + 4NH_3 \ . \qquad\qquad (2)$$
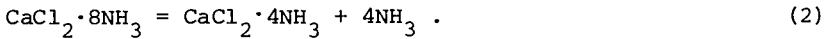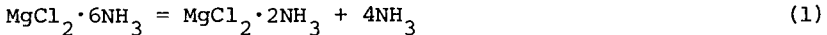
These two reactions are selected such that Reaction (1) takes
place at a higher temperature than Reaction (2). During the
charging cycle, solar energy is used to decompose the salt in the
high temperature reactor (HTR); this may be done by direct
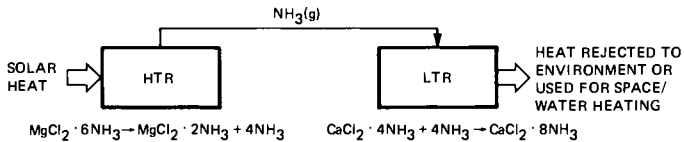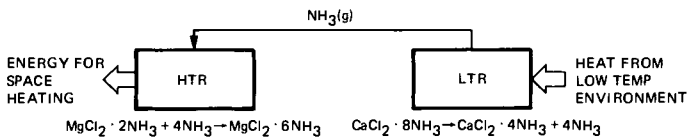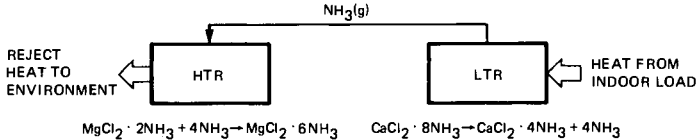
*FIGURE 8. The operation of a chemical heat pump system based
on carrying out the reaction $CaCl_2 \cdot 8NH_3 = CaCl_2 \cdot 4NH_3 + 4NH_3$ in
the low temperature reactor (LTR) and $MgCl_2 \cdot 6NH_3 = MgCl_2 \cdot NH_3 + 4NH_3$
in the high temperature reactor (HTR).*

absorption (18), or indirectly by means of a heat transfer
fluid (17). The ammonia generated is transferred to the low-
temperature reactor (LTR) where an exothermic reaction forms
$CaCl_2 \cdot 8NH_3$. This heat of reaction may be used for space or
water heating, stored, or simply rejected to the environment.
When the heat pump system is discharged for space heating, energy
is absorbed by the low-temperature unit at outdoor ambient tem-
peratures; the $CaCl_2 \cdot 8NH_3$ salt in the low-temperature reactor is
decomposed, and the ammonia transfers to and reacts with the
$MgCl_2 \cdot 2NH_3$ in the high-temperature unit. The resulting heat of
reaction is used for space heating. Space cooling is achieved by
using the low-temperature reactor to absorb heat from the indoor
environment, and the exothermic heat of reaction generated in the
high-temperature reactor is rejected outdoors. The two reactions
must be selected such that their pressure-temperature curves are
consistent with temperature and pressure differential require-
ments for spontaneous gas transfer.

The example given in Figure 8 is for two solid dissociation
reactions. If the vapor species were easily condensible (such as
in the case of hydrated salts and methanolated salts), one could
replace the low-temperature reactor with a condenser unit (16,18).
One further modification is worth mentioning; the high-tempera-
ture reaction may be a liquid phase solution/dissolution reaction
such as that found for sulfuric acid systems (19).

VI.   ASSESSMENT OF POTENTIAL

Before discussing the materials science issues associated
with each of the thermochemical concepts, it is important to
place the applications in the proper perspective. Therefore,
their economic viabilities as determined by cost/benefit studies
are discussed in this section. It should be noted that
definitive conclusions cannot be drawn in many cases because the

solar and thermochemical technologies have not yet been developed
to a stage where reliable data are available. In addition,
systems studies generally tend to be system specific, and unique
characteristics of different systems are often neglected. There-
fore, one is cautioned against universally applying the results
of one study. However, preliminary assessments have been made
and their implications must be seriously considered.

A. *Thermal Energy Storage*

The capital cost of an energy storage system can, as a first
approximation, be divided into two components: a power related
component and an energy capacity term. Therefore,

$$C = C_p + C_E \cdot t \tag{3}$$

where C is the cost of the storage system ($/kW), C_p is the power
related cost ($/kW), C_E is the energy capacity related cost
($/kW-hr), and t is the time of storage (hr). In general, C_p for
thermochemical systems are large relative to sensible and latent
heat systems, and C_E is small. Therefore, it is not cost
effective to use thermochemical systems in lieu of sensible and
latent heat systems for short storage times. However, at long
storage times, the costs of thermochemical systems become low
relative to sensible and latent heat systems, which is simply a
manifestation of the relatively small energy capacity related
costs for thermochemical systems. This suggests that extended
storage scenarios which take advantage of the low energy
capacity costs associated with thermochemical storage systems may
be attractive. However, it is the cost of energy to the consumer
and not the cost of the energy storage system that is of interest.
Therefore, the impact of thermochemical systems must be deter-
mined by considering the total solar energy system and deriving
a delivered energy cost.

Detailed cost/performance analyses have recently been
completed at Sandia (20-23) and Rocket Research (23-24). In these
studies, computer simulations of solar thermal electric

conversion facilities were carried out in which the solar energy
system facility was parametrically modeled as a collection of
subsystems (collector field, receiver, turbogenerator, and energy
storage) which process energy with various efficiencies and
capacities. Using real time insolation data and assuming a
constant baseload output, the minimum energy cost configuration
was identified. The results of these studies, summarized recent-
ly by Iannucci, Fish, and Bramlette (25), show that long duration
storage scenarios which take advantage of the low energy capacity
costs for thermochemical systems will probably be unattractive.
The basic problem is the low thermal efficiencies characteristic
of thermochemical systems. These low efficiencies are levered
back through the most expensive component of the solar facility,
the heliostat, and the end result is a greatly increased total
system cost. When very long duration storage scenarios are
considered (where the majority of storage capacity is used for
infrequent periods when isolation is poor), the use of this addi-
tional storage capacity and associated collector area is too low
to justify the initial capital investment. Therefore, sensible
heat storage systems (perhaps hybridized with a small quantity
of fossil fuel (24-25)) and not thermochemical systems seem to be
best suited for use in solar thermal electric power generating
systems.

B.   *Transport of Thermal Energy*

Cost/benefit studies of reversible chemical reactions used to
transport thermal energy from a point of collection to a central
point (for storage, power generation, or thermal use) are just
now evolving. Turner (26) and Williams (27) have calculated energy
transport costs using reversible chemical reactions, and they
show significant improvements over those projected for sensible
heat systems. However, Iannucci (28) has pointed out that the
cost of energy transport is itself not the most meaningful figure

of merit. Rather, the total system cost (or cost of energy delivered to the consumer) must be calculated. As such, the costs associated with the required chemical reactors and process inefficiencies must be factored in. On the other hand, it may be that for some high-temperature applications, thermochemical techniques are the only option available due to the thermal instability of sensible heat transfer fluids. To date, the potential role of thermochemical reactions in distributed solar systems is as yet undetermined.

The use of the reforming/methanation reaction $CH_4 + H_2O = CO + 3 H_2$ to transport solar generated energy for industrial process heat has been the subject of several studies (13-15). Vakil et al. (14) concluded they could not unambiguously determine the economic viability because of cost and performance uncertainties associated with the solar energy collection system. Assuming all technical/materials problems can be overcome, their study concludes that a solar based industrial process heat distribution system can provide energy at an incremental cost of $2-4/MBTU above that of the solar energy collection system. For comparison, current costs for process heat generated from synthetic natural gas boilers are approximately $5/MBTU.

In another study, Richardson and Wendlandt developed and analyzed a process cycle called SOLTHERM (13). The estimated cost of process steam delivered 100 miles from a solar energy collection facility was $3.5/MBTU; this cost is incremental to the solar collection plant. Comparative costs for process steam generated by other energy sources were $3.75/MBTU, $6.00/MBTU, and $6.50/MBTU for natural gas, synthetic natural gas, and electrically generated steam respectively. Given projected escalation rates of fossil fuels, Richardson and Wendlandt concluded their SOLTHERM process would be competitive by the early 1990's. It should be noted that Richardson and Wendlandt's conclusions, like Vakil's, are subject to uncertainties associated with the cost of the solar collection system.

Baker et al. (15) have carried out cost/performance analyses
for several thermal energy transport concepts. They concluded
the production of process steam and substitute natural gas with
a concept consisting of a coal gasification plant to produce
hydrogen and carbon monoxide was economically promising. A 100-
mile long pipeline that would transmit the reformed gas to a
methanator which would produce heat for process steam and
substitute natural gas may be currently competitive and would
almost certainly be attractive in the immediate future (15).
Solar-powered coal gasifiers are a possibility, but are in a
very early stage of conceptualization and evaluation; therefore,
the potential impact of a solar-powered, open-loop energy trans-
port system reamins undetermined.

C. *Solar Heating and Cooling*

A recent study (29) has suggested chemical heat pump systems
for space heating cannot possibly compete with the more conven-
tional solar heating systems. However, several critical over-
sights were made in this study. The fact that chemical heat
pumps can operate with a coefficient of performance greater than
unity was not duly accounted for; the direct effect of a greater
than unity COP could be a sizeable reduction in the collector
area. Since collectors are a major cost item in the system, a
significant reduction in the overall system cost can potentially
be realized. Although the heat pump system itself is expensive,
the total system cost may be lower since reduced collector costs
may compensate for the heat system costs.

The same chemical heat pump device can be used for both
heating and cooling, which is not possible with conventional
solar heating devices. When the cooling capability is included
in cost/benefit analyses, chemical heat pumps become even more
attractive. Preliminary cost/benefit studies have been carried
out by several investigators (30-33), and all results show the
chemical heat pump device has potential merit.

In summary, of the three applications discussed, preliminary
cost/benefit studies have shown solar chemical heat pump systems
for space heating and cooling applications to be the most attrac-
tive. Several innovative schemes have been proposed for the use
of reactions for transporting thermal energy for industrial
process heat, but a definitive evaluation of the economic
potential has not yet been made. Furthermore, solar collection
technologies must be advanced before reliable data are generated
for use in systems studies. The use of thermochemical reactions
strictly for thermal energy storage in solar thermal electric
power plants does not appear to be attractive; high efficiency,
less costly sensible heat systems are difficult to displace for
this application.

VII. SUMMARY

Reversible thermochemical reactions can be used for various
solar energy applications. Based upon studies to date, their
use in chemical heat pump systems for space heating and cooling
appears to be very promising. Several innovative schemes to use
thermochemical reactions to transport industrial process heat
from a solar energy source have been proposed; preliminary cost/
benefit studies have concluded the application has potential.
The most obvious use of thermochemical reactions is thermal
energy storage; however, detailed cost/benefit analysis have
shown this application to be of marginal interest. It is
doubtful that thermal energy storage by thermochemical reactions
will ever be competitive with less complex, less expensive,
higher efficiency sensible heat systems.

REFERENCES

1. Brower, A.S., Doyle, J.F., Gerels, E.E., Ku, A.C., Pomeroy,
    B.D., Roberts, J.M., and Salemme, R.M., "Conceptual Design

of Advanced Central Receiver Power Systems", General Electric Corporate Research and Development report No. SED-79-035 (DOE Report No. SAN/20500-1), June, 1979.

2.   "Conceptual Design of Advanced Central Receiver Power Systems Sodium-Cooled Receiver Concept", Rockwell International report ESG-79-2 (DOE report No. SAN/1483-1/1), June, 1979.

3.   Tracey, T.R., "Conceptual Design of Advanced Central Receiver Power System, Phase I", Martin Marietta Corporation, final report for contract EG77-C-03-1724, September, 1978.

4.   Taube, M., Furrer, M., Frick, E., and Chevalley, B., "Thermochemical System for the Management of Heat from LWR's, "American Nuclear Society 1978 Annual Meeting, San Diego, CA, June 18-23, 1978.

5.   Taube, M., *Nuclear Technology,* April, 1978.

6.   Kalhammer, F.R., "Energy Storage: Applications, Benefits and Candidate Technologies", in Proc. Symposium on Energy Storage, Berkowitz, J.B. and Silverman, H.P. (eds), The Electrochemical Society, Inc., 1976.

7.   Bhaktar, M.L., "Chemical Storage of Thermal Energy Using the SO_3-SO_2O_2 System", M.S. Thesis, University of California, Berkeley, 1976.

8.   Dayan, J., Foss, A.S., and Lynn, S., "Evaluation of a Chemical Heat Storage System for a Solar Steam Power Plant", Proc. 12th IECEC Conf., Washington, D.C., 1977.

9.   Springer, T., "Solar Energy Storage by Reversible Chemical Processes Final Report", Rockwell International report under contract FAO-92-7671, 1979.

10.   Chubb, T.A., *Solar Energy, 17,* 129 (1975).

11.   Carden, P.O., *Solar Energy, 19,* 365 (1977).

12.   Tallerico, L.N., "A Description and Assessment of Large Solar Power Systems Technology", Sandia Laboratories Report SAND79-8015, August, 1979.

13.   Richardson, J.T., and Wendlandt, W.W., "Cyclic Catalytic Storage Systems", University of Houston final report for

DOE Contract #EG-77-C-04-3974, May, 1979.

14. Vakil, H.B., and Flock, J.W., "Closed Loop Chemical Systems for Energy Storage and Transmission", General Electric Company, Power Systems Laboratory Report COO-2676-1, 1978.

15. Baker, N., "Transmission of Energy by Open-Loop Chemical Energy Lines", Institute of Gas Technology, final report for Sandia Contract #87-9181, February, 1978.

16. Offenhartz, P. O'D, Turner, M.J., Brown, F.C., Warren, R.B., Pemsler, J.P., and Brummer, S.B., "Methanol-Based Heat Pumps for Storage of Solar Thermal Energy, Phase I", issued as Sandia report SAND79-8188, September, 1979.

17. Jaeger, F.A., Howerton, M.T., Podlaseck, S.E., Myers, J.E., Beshore, D.G., and Haas, W.R., "Development of Ammoniated Salts Thermochemical Energy Storage Systems", Martin Marietta Corporation report SAN/12294, May, 1978.

18. Greiner, L., "The Chemical Heat Pump: A Simple Means to Conserve Energy", Chemical Energy Specialists, final report for DOE Contract #EY-76-C-03-1332, February, 1977.

19. Hiller, C.C., and Clark, E.C., "Development and Testing of the Sulfuric Acid-Water Chemical Heat Pump/Chemical Energy Storage System", Sandia Laboratories report SAND78-8824, July, 1979.

20. Iannucci, J.J., "The Value of Seasonal Storage of Solar Energy", Jet Propulsion Laboratory Thermal Storage Applications Workshop, Volume II, p. 213, February 14-15, 1978.

21. Iannucci, J.J., and Eicker, P.J., "Central Solar/Fossil Hybrid Electrical Generation: Storage Impacts", Proceedings of the 1978 Annual Meeting, Americal Section of International Solar Energy Society, Inc., Denver, Colorado, p. 904, August 28-31, 1978.

22. Iannucci, J.J., "Goals of Chemical Energy Storage", Focus on Solar Technology: A Review of Advanced Solar Thermal Power Systems, Report DOE/JPL-1060-78/5, Department of Energy, p. 145, November 15-17, 1978.

23.   Iannucci, J.J., Smith, R.D., and Swet, C.J., "Energy Storage
      Requirements for Autonomous and Hybrid Solar Thermal Elec-
      tric Power Plants", proceedings, International Solar Energy
      Congress, New Delhi, India, January, 1978.

24.   Smith, R.D., Poole, D.R., Li, C.H., Carlson, D.K., and
      Peterson, D.R., "Chemical Energy Storage for Solar Thermal
      Conversion", Rocket Research Company, final report for
      Sandia Contract #18-2563, April, 1979.

25.   Iannucci, J.J., Fish, J.D., and Bramlette, T.B., "Review and
      Assessment of Thermal Energy Storage Systems Based Upon Re-
      versible Chemical Reactions", Sandia Laboratories report
      SAND79-8239, August, 1979.

26.   Turner, R.H., "Economic Optimization of the Energy Transport
      Component of a Large Distributed Collector Solar Power
      Plant", Proceedings 11th Intersociety Energy Conversion
      Engineering Conference, Volume II, p. 1239, September, 1976.

27.   Williams, O.M., *Solar Energy*, *20*, 333 (1978).

28.   Iannucci, J.J., Sandia Laboratories, Livermore, CA, private
      communication.

29.   Lawrence, T., "Economic Assessment of Thermal Energy Storage
      Technologies", Little, A.D., Inc. final report under con-
      tract #31-109-38-3944, 1979.

30.   Offenhartz, P. O'D, EIC Corporation, Newton, Massachusetts,
      private communication.

31.   Clark, C., Rocket Research Company, Redmond, Washington,
      private communication.

32.   Hiller, C.C., Sandia Laboratories Livermore, Livermore,
      CA, private communication.

33.   Gorman, R., and Moritz, P.S., "Metal Hydride Solar Heat Pump
      and Power System (HYCSOS)", Argonne National Laboratory
      report CONF-781133-5, 1978.

CHAPTER 14

MATERIALS SCIENCE ISSUES ENCOUNTERED
DURING THE DEVELOPMENT OF THERMOCHEMICAL CONCEPTS

Raymond Mar

Sandia Laboratories
Livermore, California

I. INTRODUCTION

This chapter introduces the reader to materials problems
that have been encountered during development of thermochemical
concepts and schemes. Because space does not allow an in-depth,
detailed discussion of all problems, an overview approach is
used with a few selected topics treated in greater detail. The
thermodynamics of reactions is discussed first, emphasizing
those aspects which directly affect the selection of candidate
reactions. Materials problems are then discussed in generic
fashion; this discussion is broken down with the class of
reaction as a common element. Then, a more detailed discussion
of corrosion and catalyst development activities follows.

II. THERMODYNAMICS OF REACTIONS

Thermodynamic considerations are useful for preliminary
screening of reactions for solar energy applications; reactions
which do not meet thermodynamic requirements are dismissed from
further consideration. Reactions which meet the thermodynamic

requirements must be evaluated further with regard to parameters such as rate of reaction, kinetic reversibility, long term cyclability, cost, and toxicity.

Any reaction that occurs with increasing temperature on an equilibrium temperature-composition diagram will necessarily occur with the absorption of heat ($\Delta H > 0$) and a positive entropy change ($\Delta S > 0$). In other words, any reaction of potential interest for solar energy applications will necessarily have $\Delta H > 0$ and $\Delta S > 0$ when written in the energy charge direction. Also, the exothermic discharge reaction will take place at a temperature less than the endothermic reaction, unless one adds energy to the system, for example as pressure/volume work. These statements are various corallaries to the "principle of successive entropy states" (1), which is derived directly from the First and Second Laws of Thermodynamics.

A. *Reaction Temperature*

For any reaction the free energy change can be written:

$$\Delta F_T = \Delta F_T^o + RT\ln K \tag{1}$$

where ΔF_T is the free energy change at temperature T, ΔF_T^o is the free energy change for the reaction when all reactants and products are in their standard states, and K is the equilibrium constant. Free energies are generally calculated from enthalpy, entropy, and heat capacity data; the useful relationships are:

$$\Delta F_T^o = \Delta H_T^o - T\Delta S_T^o \tag{2}$$

$$\Delta H_T^o = \Delta H_{298}^o + \int_{298}^{T} \Delta C_p \, dT \tag{3}$$

$$\Delta S_T^o = \Delta S_{298}^o + \int_{298}^{T} \frac{\Delta C_p}{T} \, dT. \tag{4}$$

Also, the equilibrium constant can be written as

$$K = \frac{a_Q^q \, a_R^r \cdots}{a_L^l \, a_M^m \cdots} \tag{5}$$

for the general reaction

$$lL + mM + \cdots = qQ + rR + \cdots , \tag{6}$$

where a_I is the activity of species I. Substituting Equations (2) through (5) into (1) gives

$$\Delta F_T = \Delta H^\circ_{298} + \int_{298}^{T} \Delta C_p \, dT - T\Delta S^\circ_{298} - \int_{298}^{T} \frac{\Delta C_p}{T} \, dT$$

$$+ RT\ln \frac{a_Q^q \, a_R^r \cdots}{a_L^l \, a_M^m \cdots} . \tag{7}$$

When considering reactions for solar applications, one is interested in reversible conditions. Under such conditions, Equation (7) can be set equal to zero and then solved for the temperature T*. The significance of this T* is that at T > T* the endothermic reaction proceeds; at T < T*, the exothermic reaction takes place. This T* serves as the critical thermo-dynamic parameter which is compared to the requirements of the application. The application requires energy to be supplied and extracted at a certain temperature(s), and these applica-tion needs must be consistent with T*.

Several problems exist with regard to solving Equation (7) for T*: 1) enthalpy, entropy, and heat capacity data are not always available; 2) the solution is often tedious and time consuming, and therefore is not amenable to quick screening uses; and 3) a unique solution for T* does not always exist (an example is given below when the reaction $2SO_3 = 2SO_2 + O_2$ is discussed). A useful simplification has been proposed and used by Wentworth and Chen (2), in which all reactants and products are assumed to be in their standard states and ΔC_p is taken as 0. In this special case, Equation (7) becomes

$$\Delta F_T = \Delta H^\circ_{298} - T\Delta S^\circ_{298} \tag{8}$$

and at equilibrium,

$$T^* = \Delta H^\circ_{298} / \Delta S^\circ_{298}. \tag{9}$$

The standard state equilibrium temperatures calculated by Equation (9) are compared with realistic endothermic and exothermic reaction temperatures on Table I. These latter temperatures were determined by preliminary design studies of thermochemical plants based on the reaction in question (3,4). It is seen that the standard state equilibrium temperature is, in general, a useful screening tool; however, the actual temperatures of operation (endothermic and exothermic) can vary significantly from T*.

Simple thermal decomposition reactions can be treated more precisely by a simple extension of Equation (9). Consider the general reaction

$$\text{Solid I = Solid II} + \sum_i^i \nu_i G_i \tag{10}$$

where G_i is the gas species formed upon reaction and ν_i is a numerical coefficient. In this case,

$$\Delta F_T = \Delta F^\circ_T + RT \sum \ln P_{G_i}^{\nu_i} \tag{11}$$

where P_{G_i} is the partial pressure of species G_i. Assuming equilibrium conditions and $\Delta C_p = 0$,

$$0 = \Delta H^\circ_{298} - T\Delta S^\circ_{298} + RT \sum \ln P_{G_i}^{\nu_i}. \tag{12}$$

Solving for T gives

$$T^* = \frac{\Delta H^\circ_{298}}{\Delta S^\circ_{298} - R \sum \ln P_{G_i}^{\nu_i}} \tag{13}$$

If P_T represents the total pressure, the reaction stoichiometry requires that

Reaction	ΔH°_{298} (KCAL)	ΔS°_{298} (CAL/DEG)	$T^* = \dfrac{\Delta H^\circ_{298}}{\Delta S^\circ_{298}}$ (K)	T_{endo} (K)	T_{exo} (K)
$C_2H_6(g) = C_2H_4(g) + H_2(g)$	32.7	28.8	1136	1200	1000
$CaCO_3(s) = CaO(s) + CO_2(g)$	42.6	38.4	1110	1125	1000
$2SO_3(g) = 2SO_2(g) = O_2(g)$	47.0	45.4	1037	1100	800
$CH_4(g) + H_2O(g) = CO(g) + 3H_2(g)$	49.0	51	960	1100	700
$Ca(OH)_2(s) = CaO(s) + H_2O(g)$	26.1	34.7	752	800	675
$NH_4HSO_4(l) = NH_3(g) + H_2O(g) + SO_3(g)$	80.4	108.9	740	1200	700
$MgCO_3(s) = MgO(s) + CO_2(g)$	28.0	41.8	620	700	600
$C_6H_{12}(g) = C_6H_6(g) + 3H_2(g)$	49.2	86.7	568	590	670
$Mg(OH)_2(s) = MgO(s) + H_2O(g)$	19.4	36.5	531	550	450

a - Taken from preliminary design studies in Reference (3).

$$P_{G_i} = \frac{\upsilon_i}{\sum_i \upsilon_i} P_T . \tag{14}$$

Finally, from Equations (13) and (14), one can derive the expression

$$T^* = \frac{\Delta H^{\circ}_{298}}{\Delta S^{\circ}_{298} - R \sum_i \left[\upsilon_i \ln P_T - \upsilon_i \ln \frac{\upsilon_i}{\sum_i \upsilon_i} \right]} . \tag{15}$$

In most cases of interest (see Table I), only one gas species is produced upon reaction, in which case, Equation (15) reduces to

$$T^* = \frac{\Delta H^{\circ}_{298}}{\Delta S^{\circ}_{298} - R \ln P_T} \tag{16}$$

when the reaction is written for one mole of gas generated.

The most complex situation to analyze is one whereby gaseous species are present both as reactants and products. In this case, there is not a single unique temperature above which the endothermic reaction proceeds and below which the exothermic reaction is favored. Rather, the reaction reverses itself over a range of temperatures. To illustrate the point, consider the reaction $2SO_3 = 2SO_2 + O_2$. If one initially has n moles of SO_3, from which x moles of O_2 form, the amounts of SO_3 and SO_2 present are $(n - 2x)$ and $2x$ moles respectively, as determined by the reaction stoichiometry. If the total system pressure is P_T, the partial pressures of each chemical constituent in the reactor are

$$P_{SO_3} = \frac{(n - 2x)}{(n + x)} P_T \tag{17}$$

$$P_{SO_2} = \frac{(2x)}{(n + x)} P_t \tag{18}$$

$$P_{O_2} = \frac{(x)}{(n + x)} P_T . \tag{19}$$

The free energy change for the reaction is given as

$$\Delta F_T = \Delta F_T^\circ + RT\ln \frac{P_{SO_2}^2 P_{O_2}}{P_{SO_3}^2} . \tag{20}$$

Under reversible conditions, one sets Equation (20) equal to zero; then substituting the pressure expressions given in Equations (17), (18), and (19), one has a relationship established between temperature, pressure, and the relative amounts of SO_2, SO_3, and O_2:

$$\Delta F_T^\circ = -RT\ln P_T + RT\ln \frac{(n+x)(n-2X)^2}{4x^3} . \tag{21}$$

Equation (21) can be solved to give the amount of SO_3 as a function of temperature and pressure; the solution is plotted in Figure 1 for several different values of P_T. It is clear from Figure 1 that there is not a singular temperature below which the exothermic reaction proceeds to completion (i.e., the SO_3 is the only stable chemical species) and above which the endothermic reaction is complete (i.e., complete conversion of SO_3 to SO_2 and O_2). Rather, the reaction reverses itself over a range of temperatures, and a design decision must be made with regard to the degree of reaction completion to be achieved during both the endothermic and exothermic process.

   Williams and Carden [5] have developed a singular analytical expression for a T* applicable to the type of reaction just discussed. For a generalized gaseous dissociation reaction,

$$\sum_i \upsilon_{ri} G_{ri} \rightarrow \sum_j \upsilon_{rj} G_{rj}$$

they have shown that T* as defined by

$$T^* = \frac{\Delta H_{298}^\circ}{\Delta S_{298}^\circ - (m-1) R \ln P_T + \Delta S_{mix}} \tag{23}$$

where
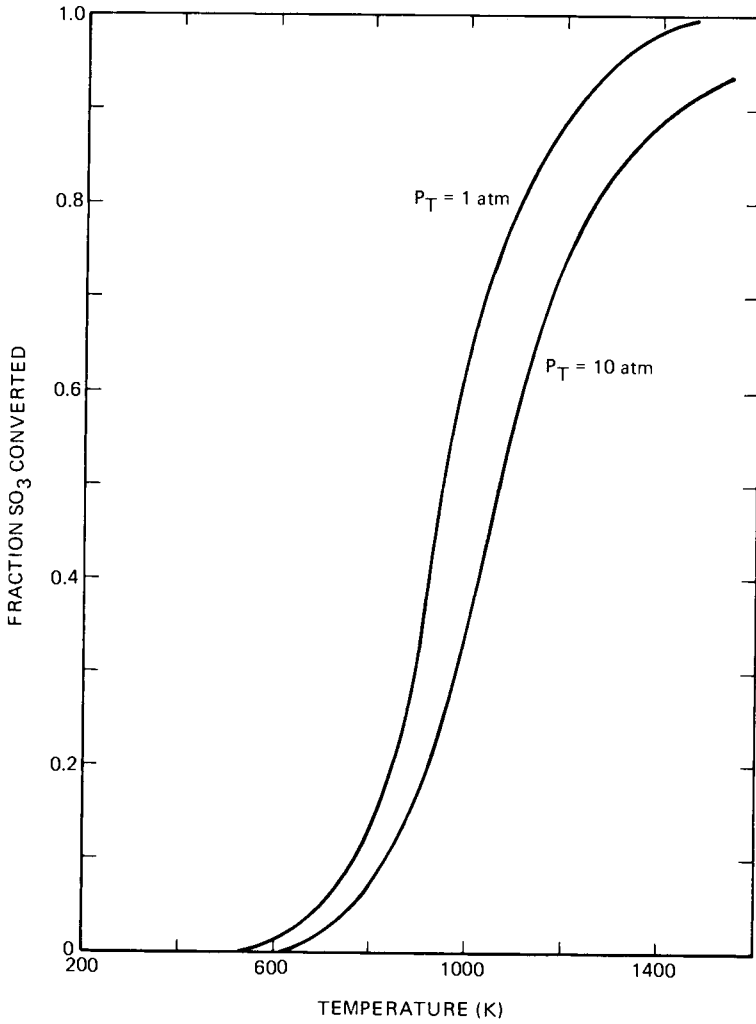
FIGURE 1.   The equilibrium conversion of SO_3 to SO_2 and O_2 as a function of temperature at two different pressures.

$$\Delta S_{mix} = -R \left[\sum \upsilon_{pj} \ln \frac{\upsilon_{pj}}{m} - \sum \upsilon_{ri} \ln \upsilon_{ri} \right] \tag{24}$$

$$m = \sum_{j} \upsilon_{rj} / \sum_{i} \upsilon_{ri} \tag{25}$$

is a useful approximation for screening these types of reactions.

B.   *Coupled Reaction Considerations*

The discussions above pertain to the use of one thermo-chemical reaction. Additional constraints are introduced when two reactions must work in concert, as in the chemical heat pump concept. For example, consider a system based upon the two reactions:

$$MgCl_2 \cdot 6NH_3 = MgCl_2 \cdot 2NH_3 + 4NH_3 \tag{26}$$

$$CaCl_2 \cdot 8NH_3 = CaCl_2 \cdot 4NH_3 + 4NH_3. \tag{27}$$
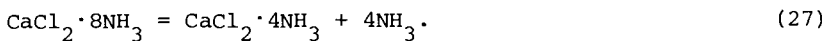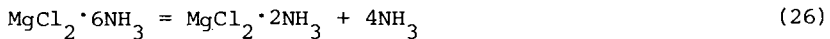
The charge and discharge reactions of the chemical heat pump cycle are illustrated in Figure 8 of the preceding chapter. The charge and discharge reaction can also be shown on a ln P vs 1/T plot (see Figure 2). Three key temperatures are shown: 1) T_H - the solar charging temperature, 2) T_M - the outlet temperature of pumped heat, and 3) T_L - the temperature from which heat is pumped. During the charge cycle, reaction 26 occurs at T_H, and the reverse of reaction 27 at T_M. The free energy changes for each reaction are given by

$$\Delta F_{26} = \Delta H_{26} - T_H \Delta S_{26} \tag{28}$$

$$\Delta F_{27} = \Delta H_{27} - T_M \Delta S_{27} \tag{29}$$

where the subscripts 26 and 27 refer to reactions 26 and 27. Assuming equilibrium conditions, $\Delta F_i = 0$ and therefore

$$\Delta H_{26} = T_H \Delta S_{26} \tag{30}$$

$$\Delta H_{27} = T_M \Delta S_{27}. \tag{31}$$

It is assumed that entropies for similar reactions are equal
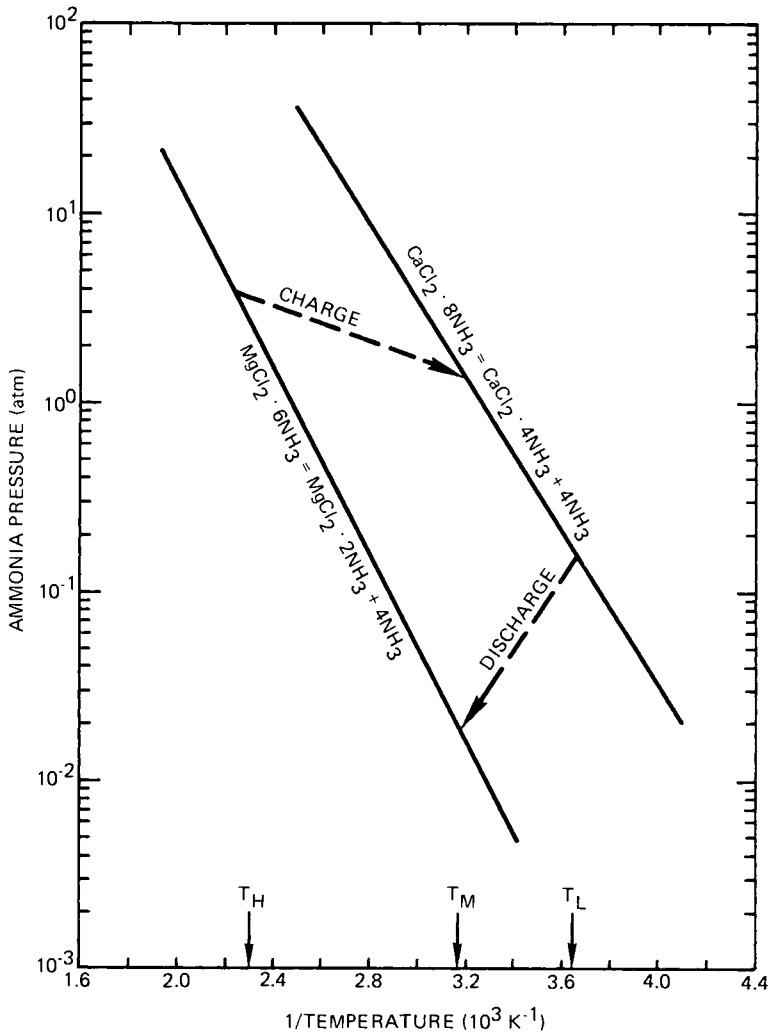
FIGURE 2. Chemical heat pump operation depicted on a pressure-temperature plot of the dissociation of $MgCl_2 \cdot 6NH_3$ and $CaCl_2 \cdot 8NH_3$. The solar collector is at temperature T_{H1} heat is pumped from T_2 to T_M.

(discussed in the next section); therefore

$$\Delta S_{26} = \Delta S_{27} \tag{32}$$

and from Equations 30 and 31

$$\frac{\Delta H_{26}}{\Delta H_{27}} = \frac{T_H}{T_M}. \tag{33}$$

Similarly, for the discharge reaction where the reverse of reaction 26 takes place at T_M and reaction 27 at T_L, one can show that

$$\frac{\Delta H_{26}}{\Delta H_{27}} = \frac{T_M}{T_L}. \tag{34}$$

Chemical heat pump reactions must be selected with these relationships (Equations 33 and 34) in mind. Studies of factors influencing the enthalpies of formation of chemical compounds are useful for "tailoring" compounds for heat pump applications. For example, it is well known that the dissociation pressures of AB_5 hydrides can be altered by the substitution of elements for B (6,7,8). Gruen et al. have studied the $LaNi_{5-x}AL_x$ system (9) with the objective of optimizing the hydrides used in the HYCSOS chemical heat pump and conversion system (10,11). The enthalpy dependence on the amount of Al is illustrated in Figure 3.

C.   Entropy Considerations

Positive entropy changes are associated with net increases in the following: number of molecules, number of gaseous species, molecular complexity, and number of liquid species. The magnitude of entropy changes of reactions are predictable, and "rules of thumb" have been developed and are often used for estimation purposes. Familar examples are Troutons rules (the entropy of vaporization of metals is circa 92 J/K/mole) and Richards rule (the entropy of fusion of metals is circa 9.2 J/K/mole). Reactions involving the net generation of one or more gas species are generally of interest for solar applications for several
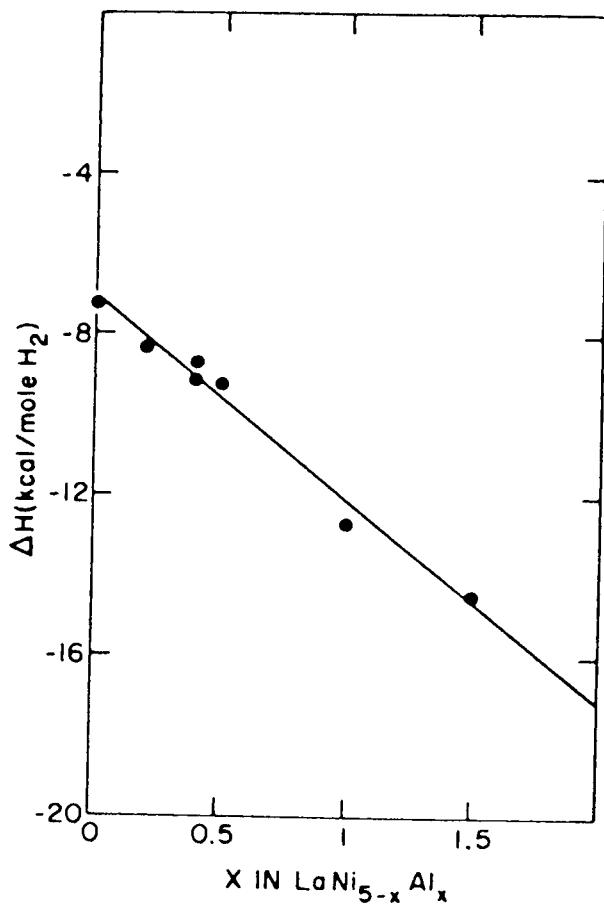
FIGURE 3. The enthalpy of hydrating $LaNi_{5-x}Al_x$ as a function of χ (Reference 9).

reasons: 1) back reactions can be guarded against by simply
separating the products of reaction, and 2) the large entropy
changes are associated with high energy densities. Entropies
of reactions typical of various classes of reaction are given in
Table II. As shown, the generation of one mole of polyatomic
gas is associated with an entropy change of approximately 40 cal/
mole deg. To maximize the energy density, one must select re-
actions with large values of ΔH; based on Equation (9), this means
selecting reactions with large entropy changes. A corollary is
that if a system is designed to use a class of reaction (for
example the decomposition of carbonates), a limit to the energy
density is established once the application temperature is set,
since both T and ΔS will have been established.   Further, it is

TABLE II. Entropies of Thermal Decomposition Reactions

Reaction	$S^{\circ}_{298}{}^{a}$ (cal/deg)
$M(OH)_2(s)$ $= MO(s)$ $+ H_2O(g)$	35.6
$MCO_3(s)$ $= MO(s)$ $+ CO_2(g)$	40.5
$M_2CO_3(s)$ $= M_2O(s)$ $+ CO_2(g)$	36.7
$MSO_4(s)$ $= MO(s)$ $+ SO_3(g)$	45.5
$M_2SO_4(s)$ $= M_2O(s)$ $+ SO_3(g)$	42.7
$2/n\ M_mN_n(s)$ $= 2m/n\ M + N_2(g)$	45.2
$2/n\ M_mO_n(s)$ $= 2m/n\ M + O_2(g)$	44.4
$2/n\ M_nS_n(s)$ $= 2m/n\ M + S_2(g)$	43.0
$2/n\ MF_n(s)$ $= 2/n\ M$ $+ F_2(g)$	39.3
$2/n\ MCl_n(s)$ $= 2/n\ M$ $+ Cl_2(g)$	36.5
$2/n\ MBr_n(s)$ $= 2/n\ M$ $+ Br_2(g)$	35.5
$2/n\ MI_n(s)$ $= 2/n\ M$ $+ I_2(g)$	37.3

a - Taken from References (1) and (2)

clear from Equation (9) that for analogous reactions (i.e.,
constant ΔS), higher energy densities are achieved for higher
temperature systems.

III. MATERIALS SCIENCE ACTIVITIES

A. *Generic Materials Problems*

In this section an overview of the materials science issues
faced during the development of thermochemical systems for solar
applications is presented. It is convenient to organize the
discussion into three areas according to the three classes of
thermochemical reactions which are of interest: catalyzed
reactions, thermal decomposition reactions, and dissolution/
solution reactions.

   1. Catalyzed Reactions. Catalyzed reactions which have
stimulated the greatest interest in the thermal energy storage
and transport community are

$$2SO_3 = 2SO_2 + O_2 \tag{35}$$

$$CH_4 + H_2O = CO + 3H_2 \tag{36}$$

$$C_6H_{12} = C_6H_6 + 3H_2. \tag{37}$$
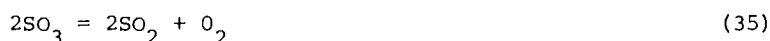
Major materials concerns arise from the fact that catalytic
reactor technologies, which are generally well established, must
now be interfaced with solar energy, an energy source which is
intermittant in nature. Chemical reactor technologies have been
developed for constant isothermal heat loads, and very little
emphasis has been placed on thermally cyclic conditions. There-
fore the major unresolved issues are the effects of thermal
cycling on reactor performance, catalyst performance, and struc-
tural materials. Catalyst pellets typically used in chemical
reactors will be subject to break-up and crushing on repeated
thermal cycling. The response of structural metals to the cycl-
ing thermal environment are also of concern. These metals
behavior problems are of particular concern for the high tempera-

ture reactions such as the reforming/methanation reaction. The metals problems are by no means unique to thermochemical systems; the same concerns exist for any high temperature solar energy system. The unique element added by thermochemical reactions is the specific chemical environment.

The nature of catalyst availability problems varies depending upon the specific reaction. The endothermic and exothermic reactions of the SO_3/SO_2 system are effectively catalyzed by platinum based catalysts; however they are prohibitively expensive. Low-cost V_2O_5-based catalysts have been developed for the catalysis of the low-temperature exothermic reaction. However, the endothermic reaction takes place at temperatures where V_2O_5 is not stable; therefore, alternate catalyst compositions are needed. Transition metal oxides that melt at high temperature should be studied with regard to the catalytic effectiveness in decomposing SO_3.

Hydrogenation/dehydrogenation reactions have been shown to be potentially attractive for energy transport applications (12) but here again current catalyst technologies fall short. Selective catalysts have been developed in the petroleum industry for these reactions, but with the emphasis on once-through reactors where 99% efficiency is more than adequate. However, in cyclic closed loop operation, the generation of small amounts of non-reversibles on each cycle is unacceptable.

Suitable catalysts are available for the reforming/methanation reaction, where Ni catalysts are well developed.

A concern with all catalyzed reactions is that one must develop a thorough understanding of poisoning and degradation mechanisms. Solar energy systems are generally designed to meet 20-30 year lifetimes, and our understanding of long-term catalyst performance must be consistent with these lifetime requirements.

2.   *Thermal Decomposition Reactions*. Thermal decomposition reactions can be used over a large temperature range; for example, the decomposition of carbonates, sulfates, and oxides

requires high temperatures, hydroxides require intermediate
temperatures, and lower temperature processes involve coordina-
tion compounds such as hydrates and ammoniates. Despite the wide
range of decomposition temperatures, the materials problems
encountered tend to be generic.

Very little data exists on reaction kinetics. Previous
studies have tended to concentrate on the endothermic decomposi-
tion reaction; very few studies of the exothermic recombination
reaction have been carried out, and even fewer studies of the
effects of reaction cycling have been reported. Evidence to date
suggests potential cycling problems. For example, selected
results from Barker's study (13,14) of the reaction $CaCO_3$ = CaO +
CO_2 are shown in Figure 4. It is seen that there is a continual
decrease of reaction rate upon cycling. Barker was able to find
a sample which showed a constant reaction rate; he concluded the
particle size distribution was the key parameter to achieving
constant rates. Bowry and Jutsen(15) in their studies observed
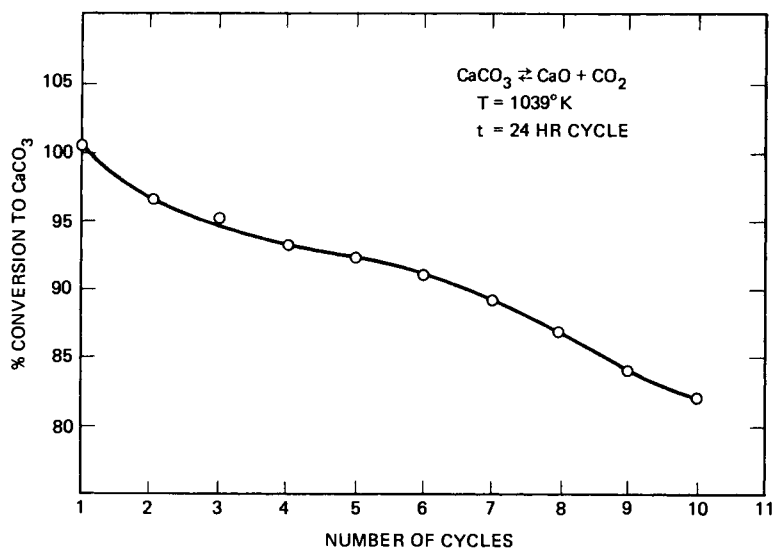
FIGURE 4. *The effect of reaction cycling on the reversibil-
ity of the $CaCO_3$ = CaO + O_2 reaction (Reference 13).*

variations in rates for the reaction $2BaO_2 = 2BaO + O_2$ which was attributed to crusting of the powders; they concluded that crusting was caused by high heating rates and high temperatures. These studies have identified several parameters which correlate with reaction rates, but indepth experimentation has not been carried out to convincingly prove causation.

An important consideration when studying reaction kinetics and designing component hardware is the volume change occurring during reaction. Volume changes for several reactions are given in Table III, where it is seen that changes of 100-200% are not uncommon. These large volume changes can have grave consequences on the design and operation of energy systems. If expansion takes place in a restricted volume, densification and sintering can occur that result in the formation of a dense, sintered mass of material. This mass may be an impermeable barrier to reactants, and hence render the entire chemical bed inactive. Volume expansion upon reaction has also been observed to cause large stresses on structural members, and structural metal failures have resulted (16,17). One approach to solving these problems is to use fluidized or moving beds. Dynamic systems also offer

---

TABLE III.

Volume Changes for Some Thermal Decomposition Reactions

Reaction	*Volume Expansion (Percent)*
$CaO + CO_2 = CaCO_3$	*101*
$CaCl_2 + 8NH_3 = CaCl_2 \cdot 8NH_3$	*195*
$CaO + H_2O = Ca(OH)_2$	*95*
$MgCl_2 + 6H_2O = MgCl_2 \cdot 6H_2O$	*230*
$ZnO + SO_3 = ZnSO_4$	*214*

for the possibility of improving the poor heat transfer associ-
ated with fixed-bed systems. However, the behavior of materials
and chemicals in a dynamic environment would have to be thorough-
ly researched if long life systems are to be designed.

While dynamic bed systems are attractive for several reasons,
they are generally not applicable to small, low-power applica-
tions such as residential heating and cooling devices. Here,
fixed-bed approaches seem to make the most sense. The mass
transport of reactants (gases) through the fixed bed has been
found to be a critical problem (16). The use of pelletized
chemicals eliminates the mass transport problem, but introduces
other potential concerns such as the performance and integrity
of the pellets during reaction and temperature cycling.

Thermal decomposition reactions generate gaseous species that
must be stored. The cost for the compression and high-pressure
storage of gases is extremely high and is the one major cause for
poor storage system efficiency and economics. Many candidate
reactions involve the generation of O_2 and CO_2; there is a clear
need for new materials which are capable of solid-state storage
of these gases in the same manner in which hydrogen can be stored
in AB_5 compounds at densities greater than liquid hydrogen (18).

3. *Solution-Dissolution Reactions*. Numerous solution/disso-
lution reactions exist with high heats of solution. Perhaps the
most promising reaction, and certainly the one that has been most
thoroughly studied, is the sulfuric acid reaction (19-21):

H_2SO_4(dilute) = H_2SO_4(conc.) + H_2O(g).
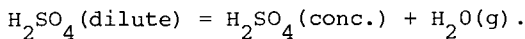
This reaction is very well understood, and its use in thermo-
chemical schemes lends itself to high-confidence designing since
the heat exchanger/reactors will be liquid phase systems. The
primary concerns are material corrosion/compatibility issues.
Sulfuric acid can be handled and contained in glass lined tanks
and glass piping. However, the development of a sulfuric acid
compatible metal alloy has obvious merit as a heat exchanger
material and as a non-breakable material of construction.

B.   *Materials Corrosion and Compatibility*

Corrosion is a problem common to all thermochemical systems. The nature of the problem tends to be specific to the reaction and application; but the impetus is the same, namely the desire to predict and guarantee long-term performance without failure due to materials corrosion.

The operating conditions (e.g. temperature) and operational lifetimes of energy systems are generally limited by corrosion and compatibility phenomena. General corrosion, stress corrosion, pitting corrosion, and fatigue cracking are concerns which must be addressed for every system. Compounding the problem in solar energy systems is the cyclic nature of solar thermal energy which cause cyclic stress states. These concerns are of course not unique to thermochemical systems, but apply to all solar energy systems.

Of particular concern to the operation of thermochemical systems is the generation of noncondensable gases as a result of corrosion reactions. The thermochemical system's performance will degrade with time since the transport of gaseous chemical species from one portion of the system to another will be impeded (vapor flow blockage). The corrosion necessary to cause vapor blockage is generally much less than that required to compromise the structural integrity of containment and component alloys.

Experiments have shown that if water vapor is present, as found in systems using hydroxides and hydrated salts, the potential for a serious problem exists. The reaction between water vapor and metals to form the metal oxide and hydrogen is highly favored thermodynamically. Normally, oxidation resistant alloys rely upon the formation of protective oxides on the surface. However, in closed systems the formation of protective oxides may still generate an unacceptable amount of hydrogen. Furthermore, it is uncertain that the oxide layers formed in an operating thermochemical system will indeed be protective against continued

oxidation and hence continued hydrogen generation, since the
protective qualities of oxide layers are strongly dependent upon
the conditions of formation.

     Pittinato (22) has studied the effect of hydrogen generation
on the performance of water heat pipes. His results can be
directly related to materials problems anticipated in thermo-
chemical energy storage and transport systems. In fact, one may
argue that evaporation/condensation heat pipes are a special case
of thermochemical system. Pittinato's data have been re-cast in
terms of the number of moles of hydrogen present in the heat pipe
as a function of time on Figure 5. The hydrogen concentration
was measured indirectly by monitoring the performance of the heat
pipe; the temperature difference between the hot and cold ends of
the pipe was directly related to the concentration of hydrogen in
the pipe. The general behavior is identical for all alloys.
There is a rapid initial increase in the hydrogen concentration,
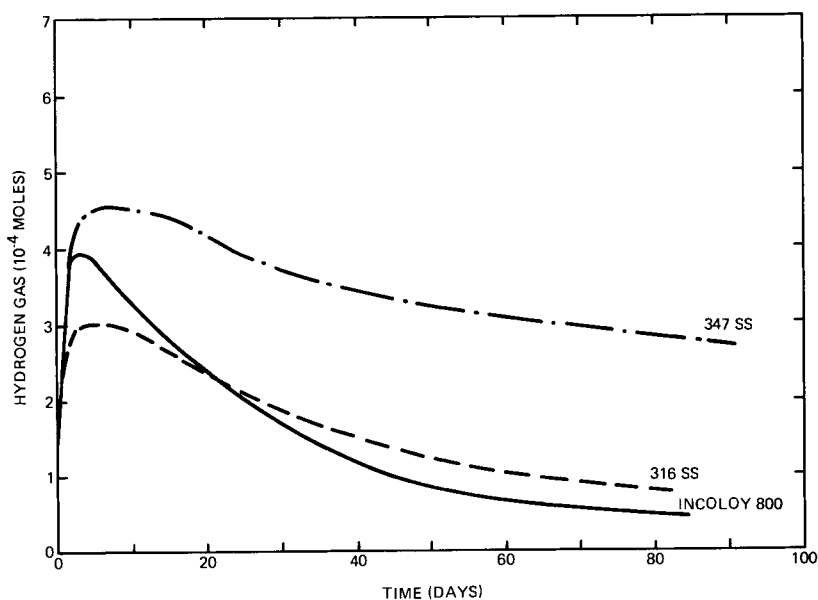
     FIGURE 5. The generation of hydrogen in water heat pipes as
a function of time. The heat pipes were operated at 110°C
(Reference 22).

followed by a slow but steady decrease. The hydrogen generation
portions of the curves on Figure 5 undoubtedly result from the
oxidation of the metal by H_2O, with metal oxide and hydrogen as
the products of reaction. The decrease in hydrogen concentration
has been attributed primarily to the loss of hydrogen by permea-
tion through the oxide and metal wall.

The generation of non-condensables in an operating thermo-
chemical system would most probably be fatal to the operation of
a commercial thermochemical system. It may not be practical to
remove the non-condensables by periodic maintenance. However,
surface pre-treatment techniques might be all that is required
to eliminate the problem (22).

C. *Catalyst Development Activities*

Considerable interest has been expressed in the reaction
$2SO_2 = 2SO_2 + O_2$ for solar energy applications (23,24), and
catalyst development activities have been encourage in support
of these interests. The requirement of continuous operation at
temperatures of $\sim$ 1100 K places severe requirements on the per-
formance of the catalyst support material. Support materials,
marketed under various trade names, are typically composed of
stable ceramics such as alumina, silicate, and aluminosilicate.
Studies have shown these support materials are not inert to
changes in surface area upon heating.

The surface areas of several commercial catalyst carriers,
as determined by N_2 adsorption BET, are shown in Figure 6 to
vary with time when held at 1155 K. In general, there is an
immediate drop in surface area, followed by a slower decrease
with time. Scanning electron photomicrographs of $\gamma-Al_2O_3$
carrier supplied by Reynolds are shown in Figure 7, where it is
seen that the reduction in surface area appears to be correlated
with the reduction in fines and the enhanced definition of
crystallites. The consequences of the decrease in surface area
seen on Figure 6 are not yet known, since the ideal surface areas
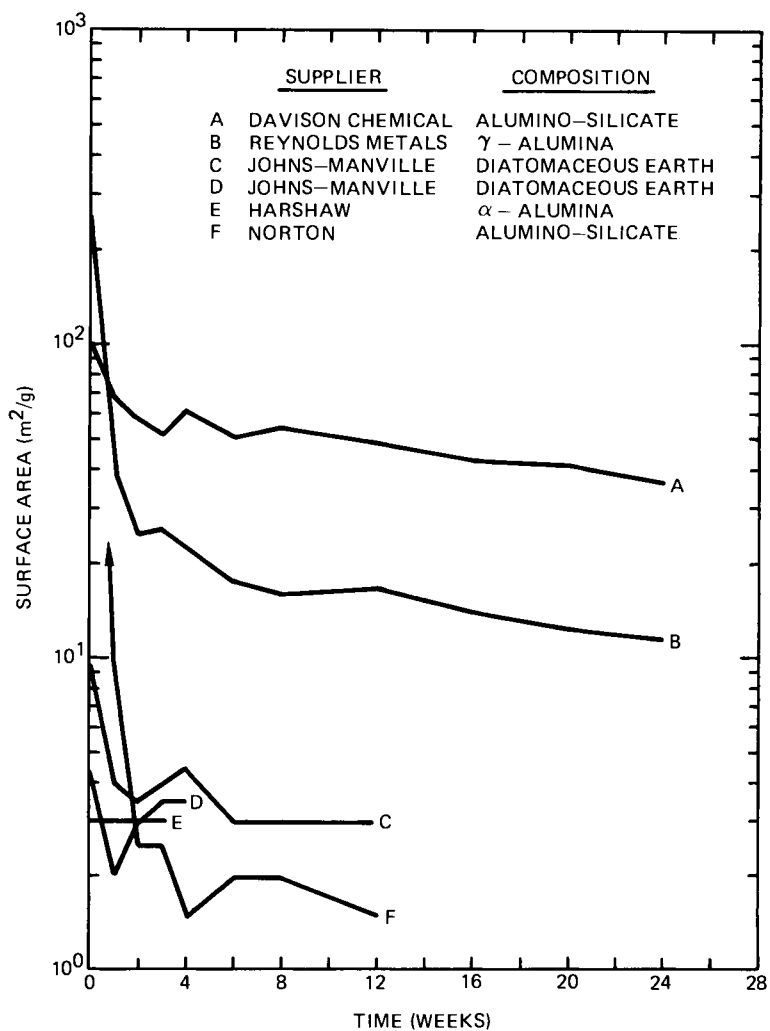
FIGURE 6. The loss of effective surface area of commercially available catalyst support structures when held at 1155 K (data courtesy of E. Schmidt, The Rocket Research Company, Division of Rockcor, Inc.).

(a)   (b)
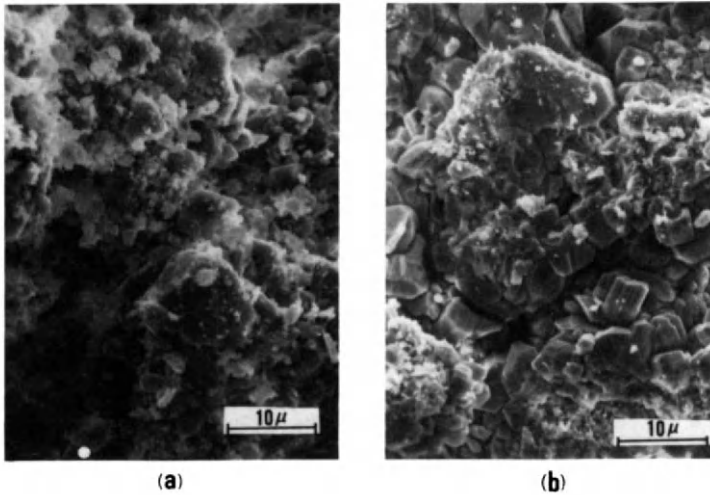
FIGURE 7.   Scanning electron photomicrographs at $\gamma-Al_2O_3$ catalyst support materials before (a) and after (b) exposure to 1155 K for 20 weeks.

have not yet been established.

In general, one looks to the transition metals and rare earths for catalytic activity.   In the SO_3/SO_2 application, the environment is highly oxidizing and, except for the noble elements, the active catalyst element will be in the form of an oxide.   In addition to being catalytically active, the ability to achieve the chemical conversions at high space velocities is highly desirable in order that smaller, more compact reactors can be designed.

An extensive screening study to identify active catalysts has been conducted by Schmidt [15]; selected results are summarized on Figure 7.   A differential catalytic reactor was used for these studies, and the effectiveness of the catalyst in catalyzing the dissociation of SO_3 at 1100 K was measured by observing the extent of SO_3 conversion in and out of the reactor.   The experiments were carried out at space velocities ranging from 10,000 to 90,000 hr^{-1}.   The catalysts shown in Figure 8 were all loaded to 10% on $\gamma-Al_2O_3$ support materials.
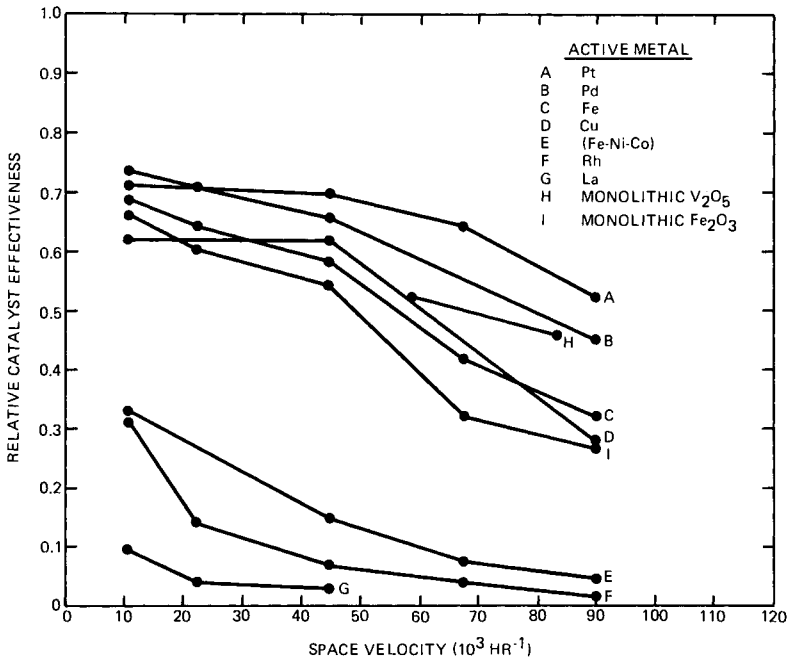
FIGURE 8.   The relative effectiveness of various active elements in catalyzing the dissociation of SO$_3$ to SO$_2$ and O$_2$ at 1100 K (data courtesy of E. Schmidt, The Rocket Research Company, Division of Rockcor, Inc.).

The results in Figure 8 show that the top performing supported catalyst elements are Pd and Pt; of the lower cost alternatives, Fe and Cu look promising. Monolithic V$_2$O$_5$ and Fe$_2$O$_3$ are seen to be reasonably effective. Evidence for significant mass transfer, due evidently to vaporization and condensation processes, has been observed experimentally for V$_2$O$_5$ and CuO (25,26). Therefore, Fe$_2$O$_3$ emerges as the leading low-cost alternative to the noble metal catalysts. This conclusion is consistent with the results by Norman (27), but counters the experience reported by Farbman (26). Long-term performance and de-activiation studies are required before one can comment further on the potential of Fe$_2$O$_3$ catalysts.

IV.   SUMMARY

Materials science plays an obvious role in energy systems
which have long intended lifetimes; long-term materials perform-
ance and degradation issues must be well understood. For ther-
mochemical systems, materials science issues are also at the
immediate focal point; that is, problems must be solved in order
to prove a thermochemical system is technically feasible.
Concerns with catalyzed reaction systems include effects of
thermal cycling on reactor materials, catalyst availability and
lifetime, and undesirable side reactions. Problems have arisen
in thermal decomposition systems due to poor or variable
kinetics and volume expansion effects. Reactions which make use
of the heat of solution suffer least from materials problems;
the major concerns are with the corrosive nature of the chemicals
involved (e.g., sulfuric acid, sodium hydroxide).

REFERENCES

1.   Searcy, A.W., "High-Temperature Reactions" in Survey of
     Progress in Chemistry, Vol. 1 (Academic Press, Inc., New
     York) 1963.

2. Wentworth, W.E., and Chen, E., *Solar Energy, 18,* 205 (1976).

3. "Reversible Chemical Reactions for Electric Utility Energy Applications", Rocket Research Company report RRC-77-R-559, April, 1977.

4. Smith, R.D., Poole, D.R., Li, C.H., Carlson, D.K., and Peterson, D.R., "Chemical Energy Storage for Solar Thermal Conversion", Rocket Research Company, final report for Sandia contract 18-2563, April, 1979.

5. Williams, O.M., and Carden, P.O., *Solar Energy, 22,* 191 (1979).

6. Lundin, C.E., Lynch, F.E., and Magee, C.B., *J. Less Common Metals, 56,* 19 (1977).

7. Mendelsohn, M.H., Gruen, D.M., and Dwight, A.E., *Nature, 269,* 45 (1977).

8. Takeshita, T., Malik, S.K., and Wallace, W.E., *J. Solid State Chem., 23,* 271 (1978).

9. Mendelsohn, M.H., Gruen, D.M., and Dwight, A.E., *J. Less Common Metals, 63,* 193 (1979).

10. Gruen, D.M., Schreiner, F., and Sheft, I., Proc. 1st World Hydrogen Energy Conference, Vol. II, 8B-73-77, Miami Beach, FL, March 1-3, 1977.

11. Gruen, D.M., Sheft, I., Lamich, G., and Mendelsohn, M., "HYCSOS: a Chemical Heat Pump and Energy Conversion System based on Metal Hydrides", Argonne National Laboratory report ANL-77-39, June, 1977.

12. Vakil, H.B., and Flock, J.W., "Closed Loop Chemical Systems for Energy Storage and Transmission", General Electric Corporate Research and Development final report for DOE contract #EY-76-C-02-26-76, February, 1978.

13. Barker, R., *J. Appl. Chem. Biotechnol., 23,* 733 (1973).

14. Barker, R., *J. Appl. Chem. Biotechnol., 24,* 221 (1974).

15. Bowrey, R.G., and Jutsen, J., *Solar Energy, 21,* 503 (1978).

16. Jaeger, F.A., Howerton, M.T., Podlaseck, S.E., Myers, J.E., Beshore, D.G., and Haas, W.P., "Development of Ammoniated

Salts Thermochemical Energy Storage Systems", Martin
Marietta Corporation report SAN/12294, May, 1978.

17. "Solar Energy Storage by Reversible Chemical Processes",
Rockwell International final report for contract FAO-92-7671,
January, 1979.

18. Juipers, F.A., and von Mal, H.H., *J. Less Common Metals, 23*,
395 (1971).

19. "Sulfuric Acid-Water Energy Storage System", Rocket Research
Corp. report RRC-76-R-530, August, 1976.

20. Huxtable, D.D., and Poole, D.R., "Thermal Energy Storage by
the Sulfuric Acid-Water System", Internat. Solar Energy
Society Meeting, Winnepeg, Canada, Vol. 8, p. 178 (1976).

21. Hiller, C.C., and Clark, E.C., "Development and Testing of
the Sulfuric Acid-Water Chemical Heat Pump/Chemical Energy
Storage System", Sandia Laboratories report SAND78-8824,
July, 1979.

22. Pittinato, G.F., *J. Engr. Materials and Technology, 100*,
313 (1978).

23. Gintz, J.R., "Technical and Economic Assessment of Phase
Change and Thermochemical Advanced Thermal Energy Storage
Systems", Boling Engineering and Construction Company report
EPRI EM-256, December, 1976.

24. Chubb, T.A., *Solar Energy, 17*, 129 (1975).

25. Schmidt, E., Rocket Research Company, Redmond, Washington,
private communication.

26. Farbman, G.H., "The Westinghouse Sulfer Cycle Hydrogen
Production Process", in Proc. Hydrogen for Energy Distribu-
tion Symposium, p. 317, Chicago, IL, July 24-28, 1978.

27. Norman, J., General Atomics, La Jolla, CA, private communi-
cation.

SECTION 3
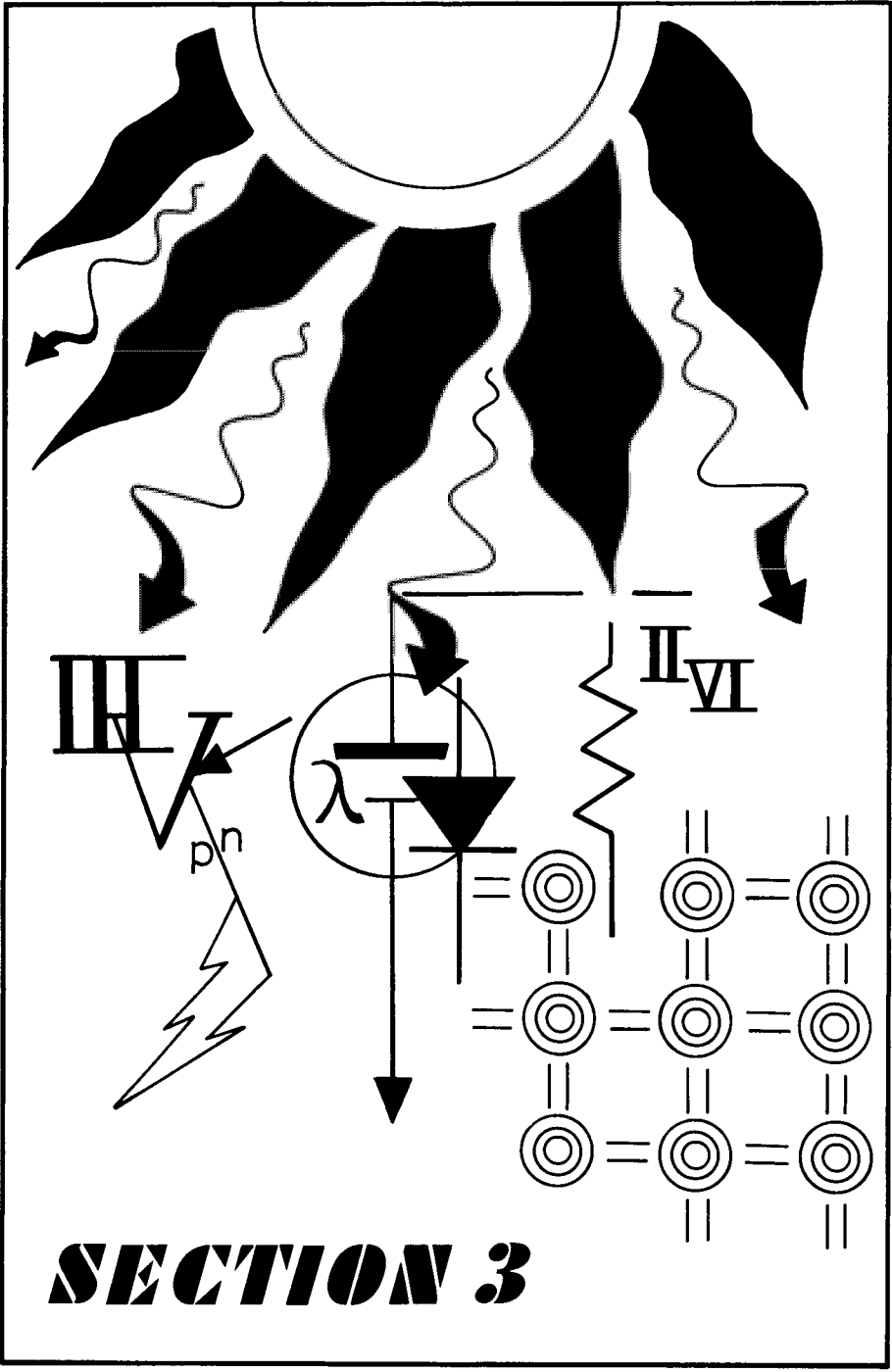
3. SOLAR CONVERSION (PHOTOVOLTAIC) MATERIALS

*Solar cells or semiconductor junction devices can produce
electricity in the form of a DC voltage and current directly from
the sun's radiation by the photovoltaic effect. Silicon solar
cells have already proven their utility in the powering os satel-
lites and the like, but for large-scale power production, their
efficiency and cost of production are currently major obstacles
to their use in modules, arrays, and system design and fabrica-
tion. To a large extent, photovoltaic materials represent per-
haps the broadest ranges of solar materials science and materials
and design problems because there are uncertainties involved in
materials preparation, materials performance, and materials util-
ization. The approaches and techniques involved in photovoltaic
materials preparation are discussed in this section along with
basic junction physics, the role of crystal defects, interfacial
phenomena, and the combined role of these features upon device
efficience, array and system design, and specific materials or
system utilization. Many of these features involving the physics,
materials aspects, and technology of photovoltaics along with
analytical methods for junction characterization (applying con-
cepts originally described in Chapter 3) are described in a
broad introductory fashion in the first two chapters in this
section, while the third and fourth chapters elucidate some of
the fundamentals associated with junction thin-film devices, in-
cluding electronic properties of junctions, the role of energy
gaps, direct and indirect gap semiconductors, Schottky barrier
concepts, buried junction behavior, and other related phenomena.
In the fourth chapter of this section, several photochemical
devices are described and the role of grain boundaries and re-
lated grain boundary effects and other device performance are
described. The enhancement of solar cell efficiencies seems to
be a consequence of passivation while the nature of passivation
of grain boundaries is not completely understood. Passivation
is, however, discussed in the context of contemporary materials
science. In the last chapter in this section amorphous semicon-
ductor photovoltaics are described. The challenges presented in
this section focus on the manipulation of materials properties
and fabrication technologies to achieve efficient photoconversion
at a reasonable cost. To a large extent, these features are the
ultimate goal of all solar programs underlined by a basic under-
standing utilizing principles of materials science. This section
also emphasizes the role of modern analytical techniques in the
elucidation of surface and interfacial phenomena involved in
solar energy conversion and at the same time provides for a link-
ing of the initial or introductory section of this book with the
very last chapters. It is to a large extent this emphasis of the
application of basic materials science principles and techniques
to the elucidation of solar materials-related problems which
forms one of the principal thrusts of this book.*

CHAPTER 15

INTRODUCTION TO PHOTOVOLTAICS:
PHYSICS, MATERIALS AND TECHNOLOGY

Lawrence Kazmerski

Photovoltaics Branch
Solar Energy Research Institute
Golden, Colorado

I. INTRODUCTION

Before 1978, the word "photovoltaics" would have scarcely been recognized outside the scientific community. With the onset of the energy crisis and the subsequent interest in obtaining independent and inexhaustible sources of energy, the term has become increasingly common in the vocabularies of legislators, media representatives, voters, and even school children. The term "photovoltaics" is now commonly applied to those devices that provide energy from sunlight. The *solar cell* or *photovoltaic device* (or solar battery, which it was descriptively called in its early stages of development) is usually a solid-state (semiconductor) device that produces useful electricity in the form of a DC voltage and current *directly* from the sun's radiation via the photovoltaic effect. The *photovoltaic effect,* discovered over 100 years ago, involves the creation of an electromotive force (voltage) by the absorption of light (or any ionizing radiation) in an inhomogeneous solid or materials system. Three processes are necessary for the photovoltaic effect:

489

- Negative (electrons) and positive (holes) carrier pairs (in excess of thermal equilibrium conditions) must be generated by the radiation.
- The excess charges of opposite charge sign must be separated at some electrostatic inhomogeneity (e.g., pn-junction, metal-semiconductor contact, etc.)
- The carriers generated must be mobile and must continue in their separated state for a time that is long compared with the time they require to travel to the localized charge-separating inhomogeneity.

Therefore, the first and third of these requirements are associated with the *current generation* aspect of the photovoltaic effect. The second is necessary for producing the *voltage*.

A. *Device Makeup and Hierarchy of Terms*

The generic solar cell is illustrated in Fig. 1. The major elements of the junction-type device presented here include: (a) the top contact, which must either be transparent (e.g., a conducting glass) or partially open (e.g., a metal grid or finger pattern) in order to allow the light to reach (b) the top semiconductor layer or emitter, here shown as n-type. The junction is made to the (c) base semiconductor, having the opposite carrier type of (b). An ohmic contact is made to the base, and the top and bottom contacts are connected to the external load. Usually, an antireflection coating (abbreviated ARC) is deposited on the top semiconductor to minimize loss of radiation by reflection. In its basic form, the solar cell is composed of these five layers.

For even the most complex and largest photovoltaic energy-generation installation, the single-component *solar cell* is the basic building block. These individual devices are connected into series (to provide increased voltage) and parallel (to provide increased current) combinations in a *module* that encapsulates the cells, protecting them from the environment. The connection of
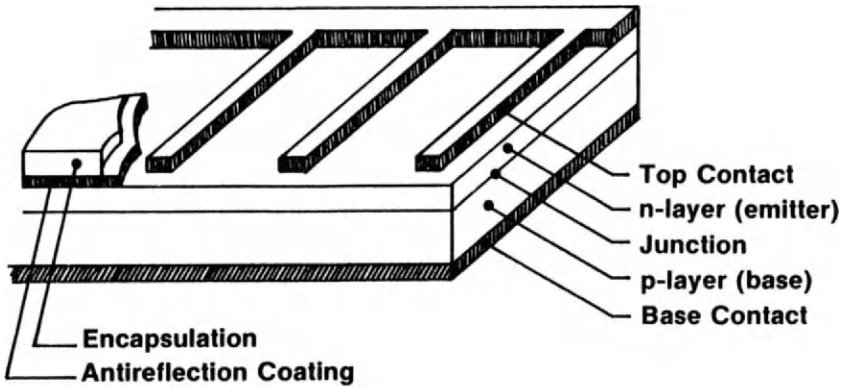
FIGURE 1. The generic solar cell.

modules into a single structure is called an *array*. An *array field* is the grouping of such arrays with support structures to provide the needed electricity. This hierarchy of photovoltaic components is presented in Fig. 2. The full *photovoltaic system* is composed of the array field, any necessary power conditioning (inverters to provide AC, voltage regulators, etc.) and any needed storage components (e.g., batteries).

The history of photovoltaics is not as recent as most people presume, although most of the more significant advances have occurred since the mid-1950's. The first report of the photovoltaic effect was that of Becquerel in 1839 (1). He studied metal electrodes emersed in a liquid electrolyte and noticed two phenomena: (1) the current between two electrodes changed significantly when exposed to light; and, (2) the measured photocurrent depended upon the spectral content of the light source. Working on selenium with platinum contacts, Adams and Day provided in 1877 the first report of the photovoltaic effect (although they did not identify it with that term) in an all-solid materials system (2). From that time through the early 1950's, a variety of devices

Solar Cell

Module

Array

Array Field
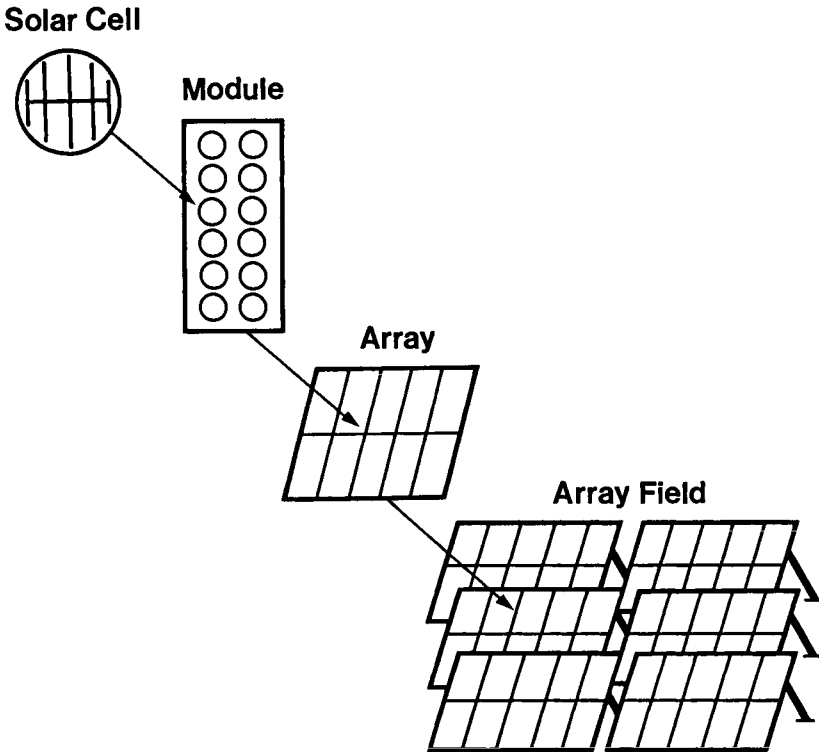
FIGURE 2. *Hierarchy of photovoltaic terms.*

and material systems were studied, with the best efficiencies
(converting sunlight into electricity) usually less than 4%. Re-
search progressed on a variety of materials. Notably, in 1954
Reynolds *et al.* observed the photovoltaic effect at metal (in-
cluding Cu)/single crystal CdS junctions (3). This work led to
the development of the Cu_2S/CdS thin-film solar cell during the
early 1960's (4-6). However, in 1954 a significant step was the
fabrication of a ~6% efficient, p-n junction device on single-
crystal Si by Chapin, Fuller, and Pearson (7). This work led to
the commercialization the next year (8) of the device that still
remains the only type available in the present market - the

single-crystal silicon solar cell.

B. *Device Categories*

There are several systems used to classify photovoltaic de-
vices. Two of these are employed in this chapter.

The *first* classification system focuses on the macro- and
microstructure or degree-of-perfection of the materials used to
make the solar cell. In this classification scheme, cells are:

(1) *Single crystal:* primarily bulk (e.g., silicon) materials, al-
though some single-crystal film devices (9) are included.
These types are the highest efficiency solar cells due to
the crystal perfection (low-loss situation) of the materials.
These are also the most expensive, primarily due to the time
and energy-intensive methods needed to provide such quality
material. Single-crystal solar cells are presently used in
both non-concentrator (flat-plate) and concentrator (using
focusing devices such as lenses, parabolic troughs, etc.)
applications.

(2) *Polycrystalline:* primarily thin-film devices, but some bulk
types also. It is less energy intensive and time-consuming
to produce polycrystalline materials. Bulk materials can be
cast (10), sintered (11), directionally-solidified (12),
screen-printed (13), and grown by simple melting (14). Thin
films can be evaporated (15), sputtered (16), ion-beam de-
posited (17), and sprayed (18). These and other fabrication
techniques are discussed in detail elsewhere (19). Although
less-expensive to produce, these polycrystalline device
types sacrifice efficiency and possibly stability (20) due
to inherent imperfections, primarily the grain boundaries.
The complexity is illustrated for the case of a Cu_2S/CdS
thin-film device in Fig. 3.

(3) *Amorphous:* thin-film almost exclusively. This material has
no short-range order, and electronically and optically

TYPICAL

SiO   0.07μm
Au   12x2μm
Cu₂S 0.1-0.3μm

CdS   8-30μm

Zinc   0.5μm
Copper 20-30μm

GENERIC

Encapsulant/AR
Grid
Cu₂S 0.1→0.3μm

CdS 8→20μm

Ohmic Contact
Substrate
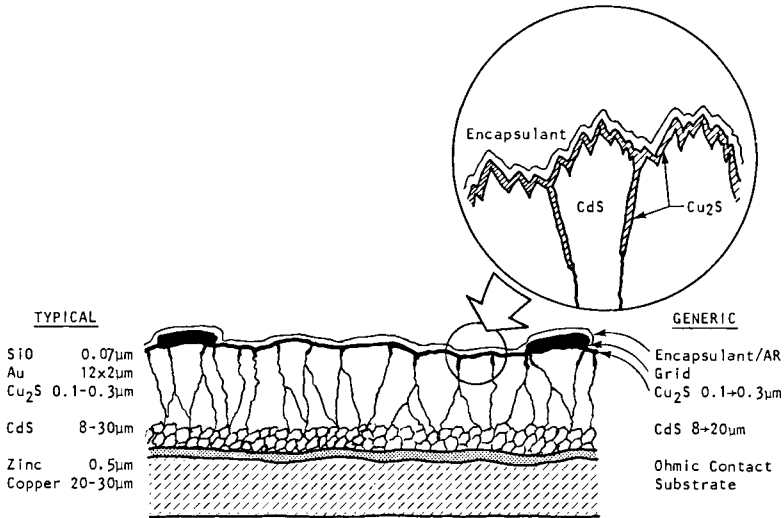
*FIGURE 3. Thin-film solar cell, illustrating complexity
due to microstructure and non-uniformities (from Rothwarf,
et al, (55).*

different in behavior from either the polycrystalline or
single-crystal material. Research on these devices is still
quite new, and much more work on basic material properties
remains to be done before efficient, stable devices appear
on the commercial market. However, amorphous materials pres-
ently hold the greatest promise for an inexpensive solar
cell - *if* certain performance and materials problems can be
overcome.

The *second* classification is according to the method of junc-
tion formation. The major methods are illustrated in the energy-
band diagrams shown in Fig. 4. The *homojunction* is formed by
metallurgically joining two semiconductors of the same species
(e.g., Si) but doped (e.g., with B and P) differently to provide
different majority carrier types (p- and n-type). If the junction
is formed between p-type and n-type semiconductors of different
species (e.g., Cu_2S and CdS) a *heterojunction* is formed. In each

(a) Homojunction
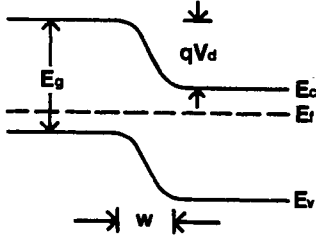
(b) Heterojunction
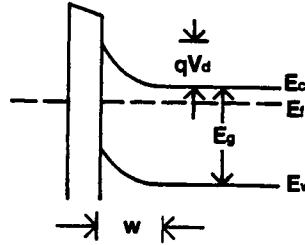
(c) Metal-Semiconductor
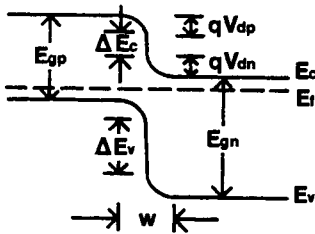
(d) Metal-Insulator-Semiconductor
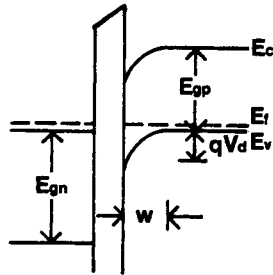
(e) Semiconductor-Insulator-Semiconductor
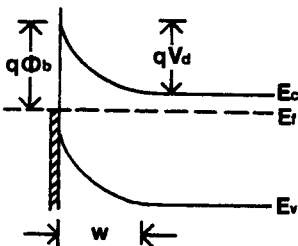
(f) Electrolyte-Semiconductor
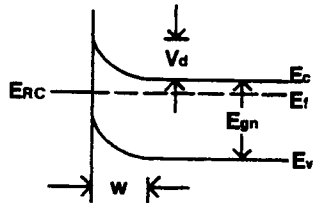
FIGURE 4. Energy-band diagrams for (a) homojunction, (b) heterojunction, (c) Schottky barrier, (d) MIS, (e) SIS and (f) electrochemical cells.

of these cases, an ohmic contact must be made to each side of the
junction for connection to an external circuit. A rectifying con-
tact may also be made between a metal and semiconductor, as shown
in Fig. 4c, forming a *metal-semiconductor* or *Schottky barrier*
solar cell. A thin insulating layer can also be used to separate
the metal from the semiconductor, forming a *metal-insulator-semi-
conductor,* or MIS, structure. The purpose of the insulator (usu-
ally an oxide form of the semiconductor) is to increase the volt-
age output of the device. It must be thin (usually 10-30Å), how-
ever, in order to keep reasonable current levels. The metal in
the MIS structure can be replaced by a degenerate semiconductor
(e.g., indium-tin-oxide, or ITO) to form the *semiconductor-
insulator-semiconductor,* or SIS, device. Finally, a liquid elec-
trolyte can be used to contact the semiconductor and provide the
necessary inhomogeneity. This *electrolyte-semiconductor,* or *elec-
trochemical cell,* is shown in Fig. 4f. The structures and devices
4b-f are discussed in detail in later chapters of this volume.
For the purpose of emphasizing the major materials properties
necessary to fabricate an efficient device, the homojunction will
be used as an example in the following sections. The devices and
the materials used in these devices are varied and numerous. A
summary and status of the major types are included in Appendix I
attached to this chapter.

II. AN ARGUMENT FOR MATERIALS/DEVICE RESEARCH

Currently, the only commercially-available solar cell is the
single-crystal Si solar cell. This device owes its development
status to two sources. First, Si forms the basis of the electron-
ics industry and more is known about Si than any other element.
The data base is extensive. Second, during the space efforts in
the 1960's, the silicon solar cell was developed and used almost
exclusively, primarily due to its reliability as a power source
for that application. The argument for Si can continue. It is an

abundant element (21) and could only suffer shortages if *produc-
tion* could not meet the demand for pure, single-crystal material
(22). It can be processed in several device types and configura-
tions. It has provided reliable, efficient, terrestrial solar
cells. With these attributes, why is more R&D needed, let alone
research on the development of alternative materials for photo-
voltaic applications? The major reason is cost: unless several
breakthroughs or major developments are realized in materials
production, device processing, contacting, interconnection, and
encapsulation, the Si solar cell *may* remain too expensive for all
but special remote, rural, and federal/military applications (23).

Future research directions and the status of photovoltaic
commercialization efforts can be assessed using Fig. 5. This anal-
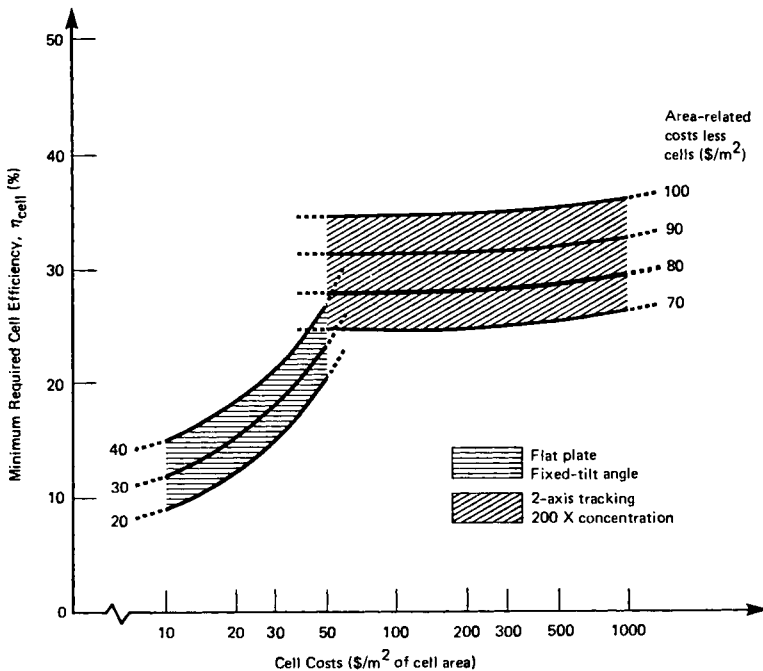
*FIGURE 5.   Necessary cell efficiency as a function of cell
cost   (in 1975 dollars) for (a) flat-plate and (b) concentrator
array types. Range of area-related costs are indicated (from
DeMeo (24)).*

ysis was provided by DeMeo (24). The minimum required cell effi-
ciency is shown as a function of cell cost per unit area (in 1975
$/m^2), for various area-related (land, structure, wiring) costs.
The shaded regions represent cost-effectiveness for two technolo-
gies. The shaded area on the left of Fig. 5 represents the analy-
sis for a flat-plate array. For even a very inexpensive solar
cell - a thin-film device, for example - with a $10-12/m^2 cell
cost, a greater than 10% AM1 conversion efficiency would be re-
quired for reasonable area-related costs of $25-30/m^2. In the
case of a concentrator system (indicated in the Fig. 5 analysis
by the shaded region on the right of the diagram), a much higher
cell cost can be tolerated, since even the more expensive single-
crystal cell costs can be minimal with respect to concentrator-
system (lenses, or focusing mechanisms, tracking, support, etc.)
costs. However, for reasonable area-related costs ($80-90/m^2) for
a concentrator), a greater than 30% efficient concentrator solar
cell would be required. Neither the 10% efficient thin-film nor
the 30% single-crystal concentrator photovoltaic device has been
demonstrated - not even a laboratory or research version. The
present costs of silicon solar cells are about $1000/m^2, with
best efficiencies of selected devices nearing 20% (25). Even pro-
jecting costs to $80-100/m^2 for these devices would require an
efficiency near the theoretical limit of the device (26). Clearly,
much R&D remains to be done both on materials and device develop-
ment if the solar cell is to become cost-competitive and viable
as an alternative energy source.

III. DEVICE PHYSICS

For the purpose of discussion, the photovoltaic homojunction
(see Fig. 4a) is used as an example in this chapter. The results
for other device types (Fig. 4b-f) are similarly obtainable, and
are discussed in other chapters of this book. In this section,
the current-voltage (or J-V, where J is the current density)

characteristics are derived in a form that highlights the major
materials properties and requirements necessary for a photovol-
taic device. Finally, efficiency and equivalent circuits are dis-
cussed.

A. Homojunction Solar Cell

The solar cell is basically a diode that is configured and
designed to provide a voltage and current when exposed to light.
From basic pn junction theory, the dark, current-voltage charac-
teristic for a diode (shown in Fig. 6) is (27):

$$J = J_s \left[\exp \left(qV/AkT\right) - 1\right], \tag{1}$$

where J_s is the reverse saturation current; q, electronic charge;
V, the voltage; A is the diode ideality factor, usually > 1 (28);
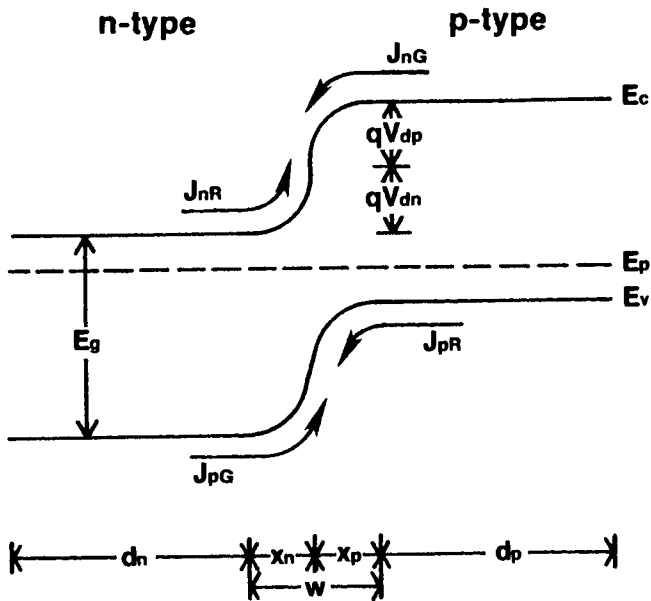
FIGURE 6. Basic energy-band diagram for homojunction.

k, Boltzmann's constant; and, T is temperature. The reverse satu-
ration current can be expressed in basic materials parameters
(27),

$$J_o = q \left[(D_n/L_n)/n_{po} + (D_p/L_p) \, p_{no} \right], \tag{2}$$

where $D_{n,p}$ is the diffusion coefficient of electrons or holes;
$L_{n,p}$, the diffusion length of electrons or holes; and n_{po} and p_{no}
are the equilibrium minority carrier concentrators (i.e., n_p
refers to the density of electrons in the p-type material). The
simple diode equation given by Eq. 1 must be modified for the
case of the solar cell to account for (1) absorption of radiation,
inherent to device operation, and (2) width of the p and n re-
gions, which can be quite thin.

For the present discussion, two assumptions are made:

- $h\nu \geq E_g$ (i.e., the incident photon energy exceeds the
energy bandgap value),

- $d_p < L_n$; $d_n < L_p$ (i.e., the widths of the p and n layers
are small with respect to the minority carrier diffusion
lengths).

The first assumption ensures that carriers gain sufficient energy
to be excited from valence to conduction bands or vice-versa.
The second one enables the minority carriers to diffuse across the
n or p layer to reach the junction.

The starting point in deriving the J-V characteristics is to
find the time rate of change of minority carriers in terms of the
fields (thermal, electric, radiation) to which the carriers are
exposed. This is known as the *continuity equation*, and for holes
(on the n-side) it is given by:

$$\frac{dp_n}{dt} \; = \; \underbrace{G(T) - R}_{(i)} + \underbrace{G(X)}_{(ii)} + \underbrace{D_p \, \frac{d^2 p_n}{dx^2}}_{(iii)} \tag{3}$$

where term (i) is the net recombination rate; (ii) the carrier
generation rate due to photon energy $h\nu$ at a distance X from the

surface; and (iii) is the diffusion term. In equilibrium, Eq. 3 becomes

$$(p_{no} - p_n)/\tau_p + G(x) + D_p(d^2p_n/dx^2) = 0, \tag{4}$$

where $p_{no}-p_n$ represents the excess carrier density, and τ_p the effective minority carrier lifetime. A similar expression can be written for electrons on the p-side. Since

$$J = J_p + J_n \tag{5}$$

and

$$J_{p(or\ n)} = qD_{p(or\ n)}(dp(or\ n)/dx)\Big|_{edge\ of\ SCL} \tag{6}$$

one must solve the differential Eq. 4 and its complement for dp/dx (and dn/dx), substitute this result into Eq. 6, and sum the electron and hole currents via Eq. 5. However, the generation rate G(x) remains to be expressed in more basic materials parameters.

In general, the generation term can be written

$$G(x) = \int_{E_g}^{\infty} \phi(E)\ \alpha(E)\ exp\left[-\alpha(E)\ x\right]\ dE, \tag{7}$$

where $E=h\nu$, the incident photon energy; $\phi(E)$, the incident light flux; and $\alpha(E)$, the absorption coefficient of the semiconductor. The incident light flux depends upon the solar spectrum to which the device is exposed. Fig. 7 presents three such spectra for air mass zero (AM0), or extraterrestrial conditions; air mass one (AM1), terrestrial condition with one atmosphere between the device and sun (this is essentially at high noon); and air mass two (AM2) conditions (29).

The expression for the absorption coefficient, OC, depends upon the material and the wavelength of the incident radiation. For *direct bandgap* semiconductors (e.g., GaAs or InP),

$$\alpha(E) \propto (h\nu-E_g)^{1/2} \tag{8}$$

For *indirect bandgap* materials (e.g., Si), the need to conserve momentum in the transition requires the participation of a phonon
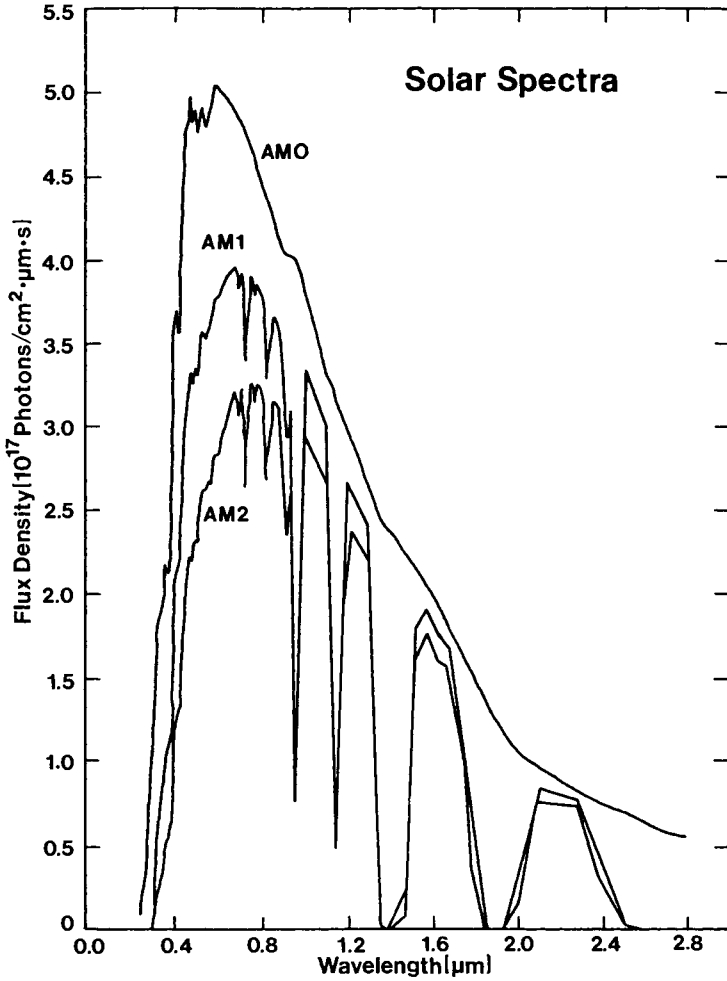
FIGURE 7.   Solar spectra for Golden, Colorado, under air-mass-one (AM1) and air-mass-two (AM2) conditions. Air-mass-zero (AM0) spectrum is included for reference (from Ireland, et al (29)).

or a scattering center. In a pure material, the phonon mechanism dominates (30), and

$$\alpha(E) \propto (h\nu - E_g)^2. \tag{9}$$

This general functional dependence also holds for a material that has a large concentration of defects. Comparing Eqs. 8 and 9, it can be observed that the rise in α with photon energy for a direct bandgap material is more abrupt.

For this solution, assume that $\alpha(E)$ is a *constant*, representative of the energy range of interest. For this less exact situation,

$$G(x) = g(\alpha, \Phi_0), \tag{10}$$

where

$$\Phi_0 = \int_{Eg}^{\infty} \phi(E)\ dE,$$

the total flux density.

Substituting $g(\alpha, \Phi_0)$ into Eq. 4 and solving that differential equation (27) yields the expression for dp_n/dx (or dn_p/dx). Using Eqs. 6 and 5, the current density can be expressed:

$$J = \left[q\, g\, (\alpha, \Phi_0)\, \tau_p (D_p/L_p)\ \tanh\ (d_n/L_p) \right] +$$
$$\left[q\, p_{no}\ (D_p/L_p)\tanh(d_n/L_p) + q n_{po} (D_n/L_n)\tanh(d_p/L_n) \right].$$
$$\left[\exp(qV/AkT) - 1 \right] \tag{11}$$

or,

$$J = J_L + J_s \left[\exp(qV/AkT) - 1 \right], \tag{12}$$

where J_L is the current due to the incident radiation. The total current expressed in Eqs. 11 and 12 is seen to be a combination of the normal diode (dark) term and the light-generated term. The important light-generated current is a function of both external factors (i.e., the light flux) and many materials-determining parameters (e.g., absorption coefficient, minority carrier lifetime, diffusion coefficient, diffusion length).

B. Equivalent Circuit

From Eq. 12, the solar cell can be represented electrically as
a light-dependent current generator in parallel with a diode. Ad-
ditional resistance arises from the bulk n- and p-layers and the
contacts giving rise to a series resistance, R_s. Losses occur
from junction leakage and alternate current paths providing a
parallel or shunt resistance across the diode. The resulting equiv-
alent circuit is presented in Fig. 8a. R_L represents the load re-
sistance. The effects of changing R_s and R_{sh} on the light J-V
characteristic are shown in Fig. 8b. The best case is with $R_s=0$
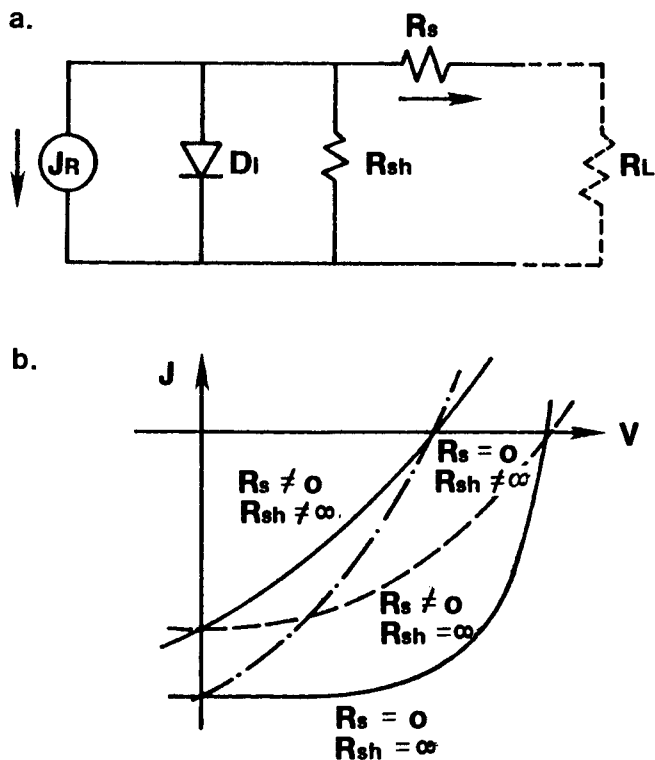
FIGURE 8.   (a) Equivalent electrical circuit for solar cells,
connected to load resistance, R_L; (b) J-V characteristic of
solar cell under illumination indicating effects of changing
series and shunt resistances.

and $R_{sh} = \infty$. Changing either of these resistances leads to the lowering of useful voltages and currents, and the limiting of the overall device performance.

C. Efficiency

Fig. 9 shows the generic dark and light characteristics for a solar cell. Under illumination, the characteristics shift downwards, and the intersection of the curve with the current and voltage axes are the short-circuit and open-circuit voltage, respectively. The maximum of the current-voltage product along this
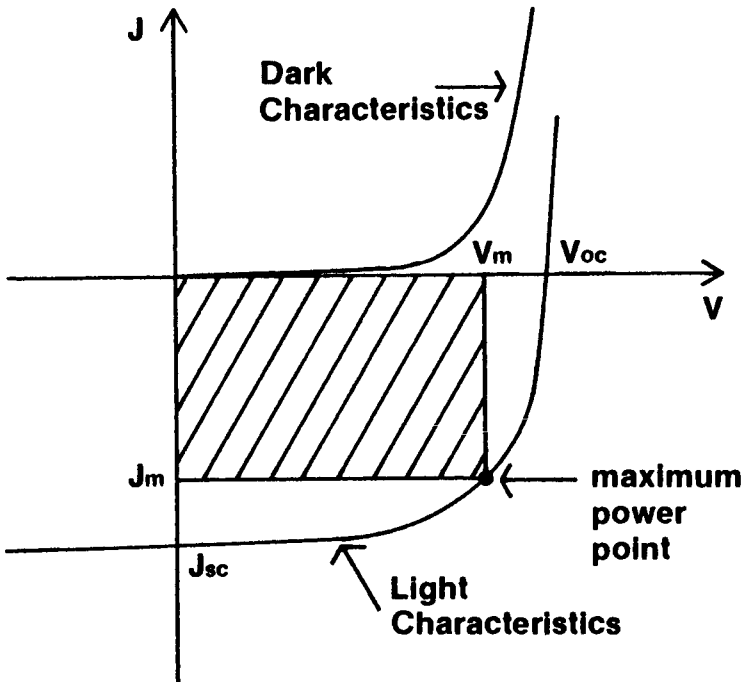
FIGURE 9. *Typical and light J-V characteristics for solar cell, defining open-circuit voltage (V_{oc}), short-circuit current density (J_{sc}), and maximum power point (J_m, V_m). Shaded region is maximum power rectangle.*

curve gives the maximum power point J_m, V_m. The maximum area rectangle inscribed within this characteristic is shown in Fig. 9 and represents the maximum power output from the device.

The efficiency is defined

$$\eta = p_{out}/p_{in}, \tag{13}$$

where $p_{out} = J_m V_m$, the maximum power output density, and p_{in}, the input power density, usually expressed in mW/cm^2. The output power density is

$$p_{out} = J_m V_m$$

$$= J_{sc} V_{oc} \cdot FF, \tag{14}$$

where FF ($=J_m V_m/J_{sc} V_{oc}$) is called the fill-factor. For a perfect device, FF = 1 (i.e., the maximum power rectangle would coincide with the light characteristic). This is never attained in real devices. For good devices, 0.7<FF<0.9. Thus, the device efficiency can be determined using the J-V characteristics from

$$\eta = J_{sc} V_{oc} FF/p_{in} . \tag{15}$$

The parameters (temperature, load, air mass conditions, etc.) are critical in the determination of device efficiency. Standards have been established (31) and should be adhered to when reporting device performance. In this way, a uniformity in measurement provides a basis for comparison both among and between device types.

IV. PHOTOVOLTAIC MATERIALS: PROPERTIES AND REQUIREMENTS

Many different materials and materials' interfaces are encountered in fabricating the photovoltaic array. Support structures, encapsulation materials, contacts and interconnections, and antireflection coatings are major and important components of such a system. However, this section will emphasize the

basic requirements for the photovoltaic materials - i.e., those
that provide the essential ingredients for the photovoltaic ef-
fect discussed in Section I. Seven such properties, some of which
are interrelated, are presented herein.

A. *Energy Gap*

The energy gap of the absorbing layer is considered the first
indication of performance potential for a photovoltaic material.
An examination of these layers in Fig. 4 indicates that photons
with energies less than E_g cannot contribute to the light-gener-
ated current (Eq. 11) by creating electron-hole pairs. Absorbed
photons with energies exceeding E_g can provide the desired elec-
tron-hole pairs, but will also provide excess energy (losses) in
terms of lattice heating. If the solar spectrum were constant at
all wavelengths, the choice of potential absorbing materials would
be broad indeed. However, the spectrum under any air mass condi-
tion has some maximum region and a great deal of structure (see
Fig. 7) due to various atmosphere absorption bands (29). The
matching of the energy gap to the solar spectra has led to a num-
ber of calculations of the optimum energy gap for a photovoltaic
material (26, 32-34). These calculations involve modeling the
basic solar cell performance, such as the approach used in Sec-
tion III-*A*. All involve some assumptions but lead to basically
the same results. Fig. 10 presents one set of results for a homo-
junction device, under AM0 conditions. Curve (a) represents the
solar cell with ideal behavior (i.e., A=1 in Eq. 13), and curve
(b), A=2, the case in which generation-recombination mechanisms
dominate (28). Curve (a) is usually cited to predict an optimum
energy gap of 1.5-1.6 eV for a semiconductor. However, three fac-
tors are usually not considered in these references:
  (1) Curve (a) is for AM0, not terrestrial conditions. A slightly
      lower optimum E_g would be expected for AM1 or AM2, primarily
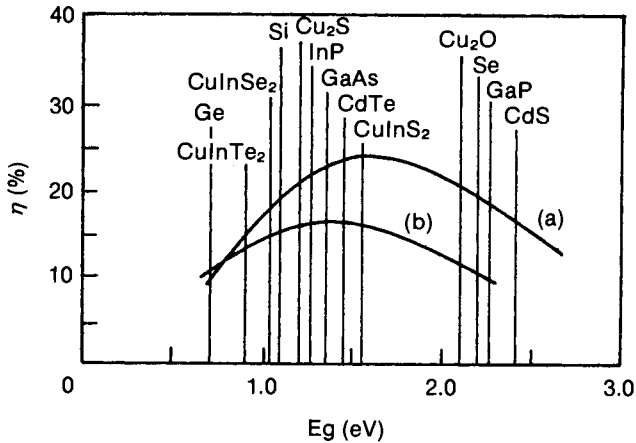
FIGURE 10. Theoretical efficiencies of homojunction solar cells as a function of energy gap for (a) ideal diode with A=1 in Eq. 12, and (b) non-ideal diode with A=2 under AMO conditions. (From Loferski (26)).

    due to the presence of the absorption bands observable in Fig. 7 (29).

(2) Many of the solar cells reported in the literature have non-ideal (A>1) dark characteristics. Therefore, curve (b) is more proper to use. In this case, the peak is not as pro-nounced, with the maximum near 1.3-1.4 eV.

(3) These curves are for homojunctions.

Recently, corresponding calculations for heterojunctions have been reported (32). These are shown in Fig. 11, with the maximum efficiency as a function of absorber energy gap for various window layers. The window is a large bandgap semiconductor that provides the junction with the active absorber but does not absorb any significant quantity of photons itself. These curves are shown for AM1 conditions. The calculations do not account for refinements such as grain size (33-35) or lattice matching between the absorber and window (36-37), which can further affect performance. It should be stressed that calculations, such as those presented in Figs. 10 and 11, should be considered as guides for selecting ranges of optimum bandgaps in solar cell materials.
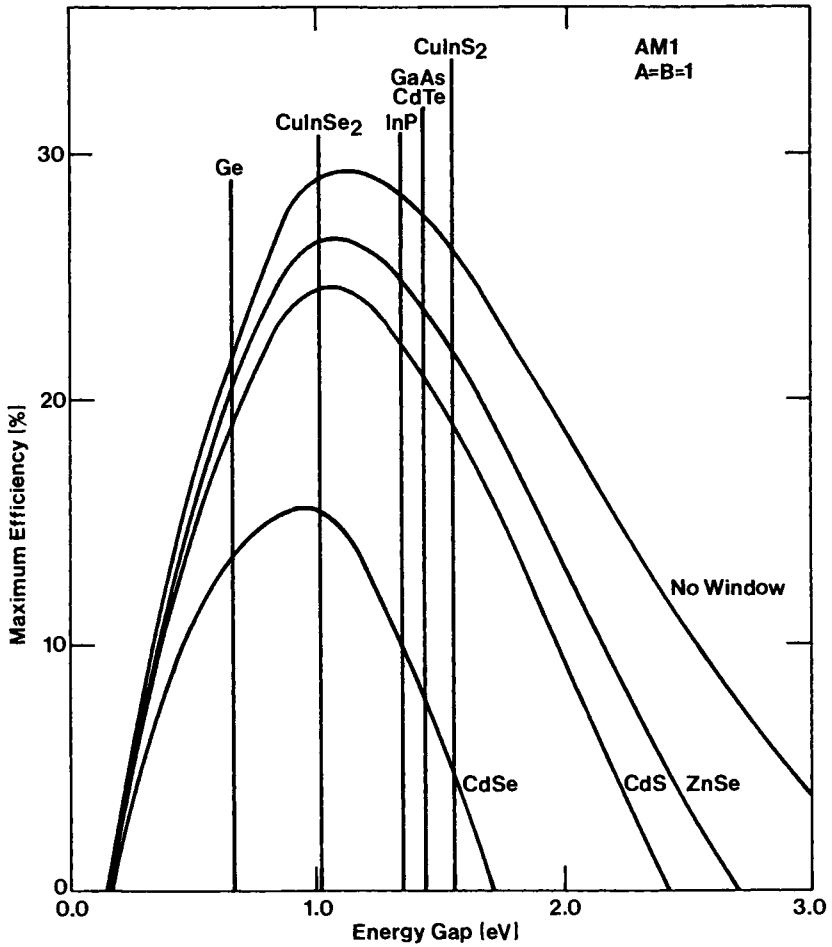
FIGURE 11.   Theoretical efficiencies of heterojunction solar
cells as a function of energy gap. Results are calculated for
various absorber levels and window materials.

Optimum bandgap is a necessary condition, but not sufficient since
many other requirements must be met.

B. Absorption Coefficient

    Photon absorption is a very important property for a photo-
voltaic material for two reasons: (1) for satisfying the device
performance criteria discussed in Section III-*A* and specifically
in Eqs. 7-10, and (2) for device economics. In general, absorber
materials should have large absorption coefficients, which result
from interband transitions (38). Since the necessary absorber
thickness equals $1/\alpha$, large absorption coefficients permit the
absorber layer to be thin (i.e., photons are absorbed nearer the
surface). As a result, less material is necessary for solar cell
fabrication, which has positive implications for device cost.

    Fig. 12 presents the absorption coefficient as a function of
photon energy for various photovoltaic candidate materials. In
general, α increases with energy greater than E_g. Two types of
materials are evident: *direct bandgap* (e.g., GaAs), in which in-
crease to high α (10^4/cm) is abrupt; and *indirect bandgap* (e.g.,
Si), in which the rise is more gradual. A direct bandgap material
would be more desirable, since the absorption takes place within
a smaller depth, requiring less material. As an example, all
photons would be absorbed within ~2 μm of GaAs, but about 100 μm
is required for Si. Fig. 13 compares the effect of absorption co-
efficient in determining the generated photocurrents for the
direct (GaAs) and indirect (Si) bandgap materials. It can be seen
that under the three air mass conditions, the photocurrents for
the GaAs device reach their saturation values at lower thicknesses
than the corresponding Si cases. In addition, the GaAs photocur-
rents are higher than those for Si until the saturation region is
reached.

C. Diffusion Length

    The photogenerated carriers in the absorber semiconductor
must be able to move across that region to the junction, space
charge, or depletion layer of the solar cell. Carriers that
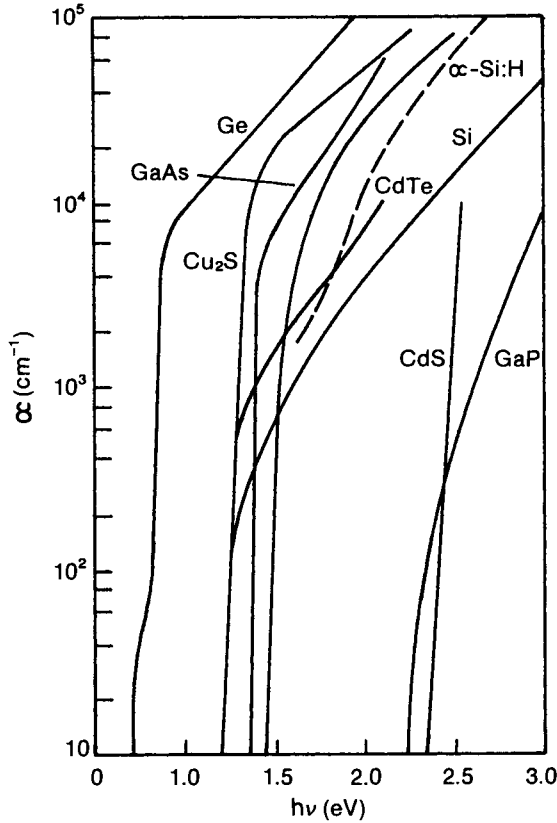
FIGURE 12. Optical absorption coefficients as a function of photon energy for several solar cell materials.

recombine before arriving at the junction are lost to the photo-voltaic effect and cannot take part in the generation of J_L (Eq. 12). Diffusion is the mechanism with which the minority carriers move to the depletion region. Therefore, minority carrier diffu-sion length is a most important material parameter. Electrons and holes have characteristic diffusion lengths (L_n and L_p, respec-tively) that are material dependent. In general, the diffusion length should be of the order of $1/\alpha$, as discussed in the pre-vious section.
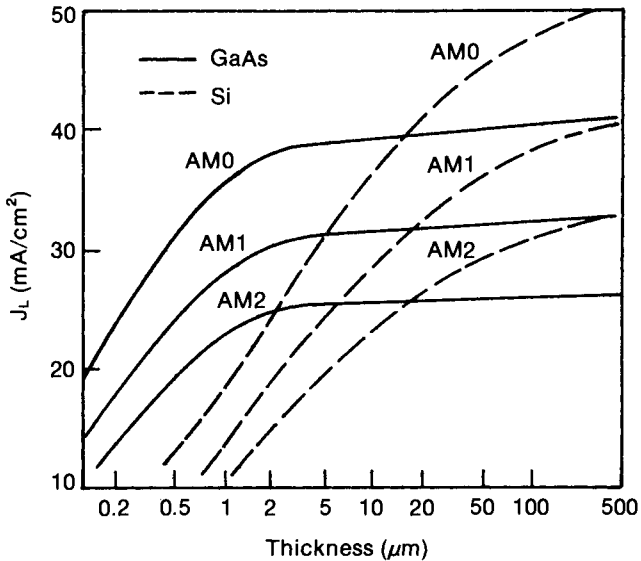
FIGURE 13. Short-circuit current densities (ideal) as a function of solar cell thickness, comparing Si (indirect bandgap) and GaAs (direct bandgap) for various air mass conditions (from Hovel (67)).

The diffusion length can be expressed in terms of basic material parameters (39):

$$L_{n,p} = \left[(kT/q)\mu_{n,p}\tau_{n,p} \right]^{1/2} . \tag{16}$$

Thus, the diffusion length should be expected to depend, as the dependent variables in Eq. 16 do, on

- impurity concentration (40,41)
- crystallinity (single, poly, amorphous) (42)
- crystal orientation (43)
- defect concentrations (39,44)
- stoichiometry (45)

An example of the effect of impurity concentration on the hole and electron diffusion lengths is presented in the GaAs data of Fig. 14. In general, diffusion lengths are very limited at high
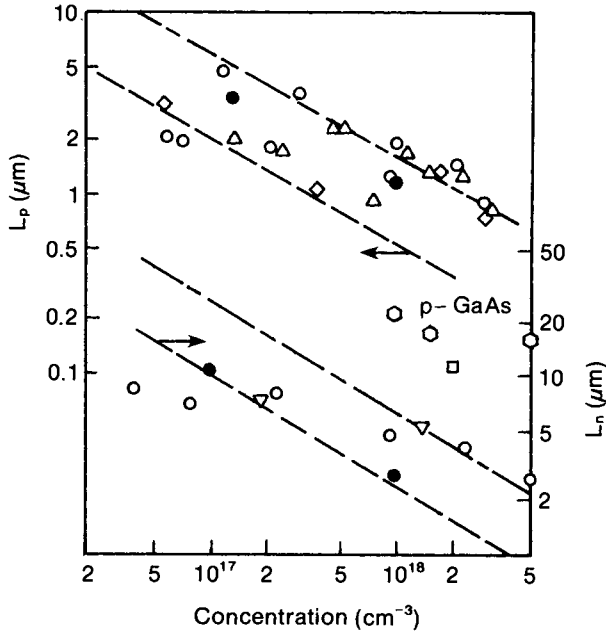
FIGURE 14. Effect of impurity concentration on hole (L_p) and electron (L_n) diffusion lengths in GaAs. (From Marfaing (40)).

doping levels. An important factor in the fabrication of thin polycrystalline solar cells is the effect of the grain boundaries on minority carrier diffusion length. These boundaries are con- sidered regions of high recombination and sinks for minority carriers (33). One obvious solution is to make grain sizes much larger than the minority carrier diffusion lengths, minimizing the recombination problem. Calculations and data illustrating the effect of grain size on open cell performance have been re- ported in the literature for GaAs (46), Si (47-48), Cu_2S (49), and $CuInSe_2$ (50,51).

D. Minority Carrier Lifetime

The minority carrier lifetime is a major material property that is fundamental in determining the effectiveness of a semi-

conductor as a photovoltaic candidate. A number of fundamental
processes exist that determine the recombination minority car-
rier lifetime:

- Radiative recombination
- Auger band-to-band recombination
- Electron/hole recombination centers
- Auger recombination through recombination centers
- Defect recombination

The exact identification of the dominant-mechanism is difficult,
but electron/hole recombination and Auger recombination are
probably the most likely. The development of reliable measure-
ment techniques for minority carrier lifetime determination in
solar cells remains a research problem. Although the determina-
tion of lifetimes in single-crystal Si that are in the micro-
second range has been accomplished (52-53), the accurate measure-
ment of τ in direct bandgap, small grain polycrystalline and
amorphous semiconductors, which can have lifetime 10^{-9} sec or
less, is much more difficult. An estimation of τ_n in p-type
$CuInSe_2$ as a function of grain size is shown in Fig. 15 (50). Its
effect on the open-circuit voltage of the $CdS/CuInSe_2$ thin-film
polycrystalline solar cell (2 μm grain size) is shown in Fig. 16
(51).

E. Doping

Impurity concentration levels have profound effects on ab-
sorption, diffusion length, energy bandgap (54), and minority
carrier lifetimes discussed previously. One must be able to dope
(either extrinsically or stoichiometrically) absorber and window
layers to acceptable levels in order to reduce series resistance
and to control whether the photovoltaic activity takes place on
the n- or p-side of the junction (55). For example, the Cu_2S lay-
er in the conventional CdS/Cu_2S solar cell is degenerate
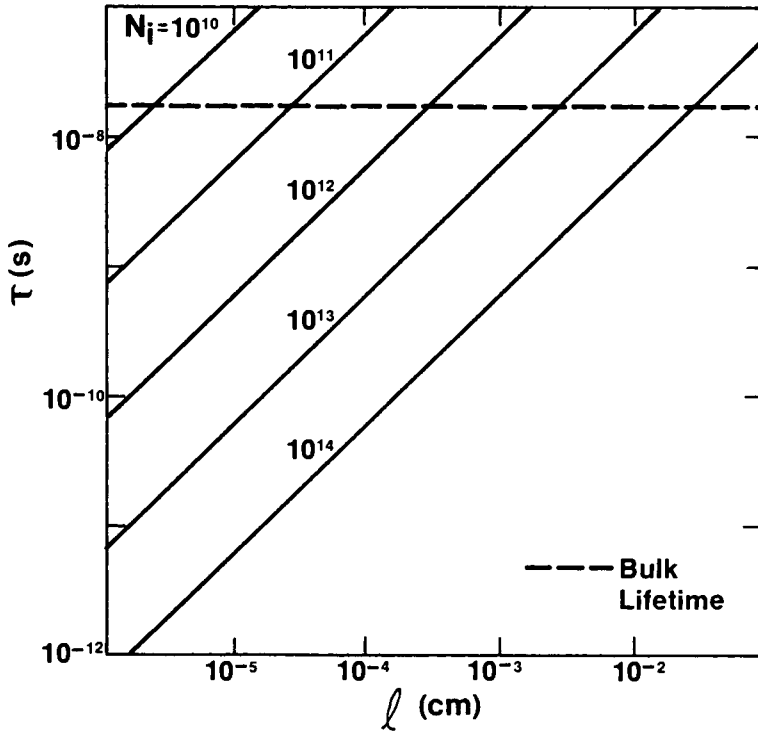
FIGURE 15. The dependence of minority carrier lifetime on grain size in p-type CuInSe$_2$ (from Kazmerski (50)).

($\sim 10^{20}$/cm^3), while the CdS is of moderate concentration (10^{16}/cm^3). This means that the photovoltaic action takes place almost entirely on the CdS - side of the junction. Lowering the concentration would move the active region into the Cu$_2$S (55).

A more subtle consequence of doping is the ability to fabricate homojunctions. This has been a major problem with some materials. Zn$_2$P$_3$, for example, possesses an excellent E$_g$ (1.6 eV), a direct bandgap, high absorption coefficient, and a high minority carrier diffusion length (56); it has, however, been produced only p-type to-date. Thus, it is presently restricted to Schottky
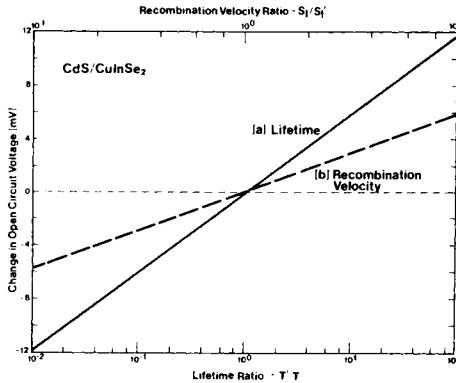
*FIGURE 16. Change in open-circuit voltage upon the (a) minor-
ity carrier lifetime, and (b) recombination velocity ratios in
the CdS/CuInSe₂ heterojunction (AMl conditions) (from Kazmerski
(51)).*

barrier and heterojunction applications.

F. Surface Recombination

In photovoltaic devices, surfaces with high recombination veloci-
ties are in competition with the junction (depletion) regions for
the collection of photogenerated carriers. This high surface re-
combination velocity is due to the presence of *surface states*
that result from dangling bonds, native oxides, metal/organic
precipitates, chemical residues, and similar effects. In an illu-
minated solar cell, the number of photogenerated carriers is
highest at the surface and decreases exponentially into the mate-
rial (see Eq. 7). Thus the surface recombination velocity is a
critical parameter, especially in direct bandgap materials like
GaAs in which most carriers are generated close to the surface.
The surface recombination velocity for Si and GaAs lies in the
10^5-10^6 cm/s range. Etching has been used to lower this to 10^2cm/s
in Si. It is desirable to passivate photovoltaic materials sur-
faces in order to keep the surface recombination velocity low.
The effect of surface recombination velocity on the photogener-
ated current is shown for Cu_2S in Fig. 17 (57) and the open-
circuit voltage in Fig. 16 (51). The composite effect of
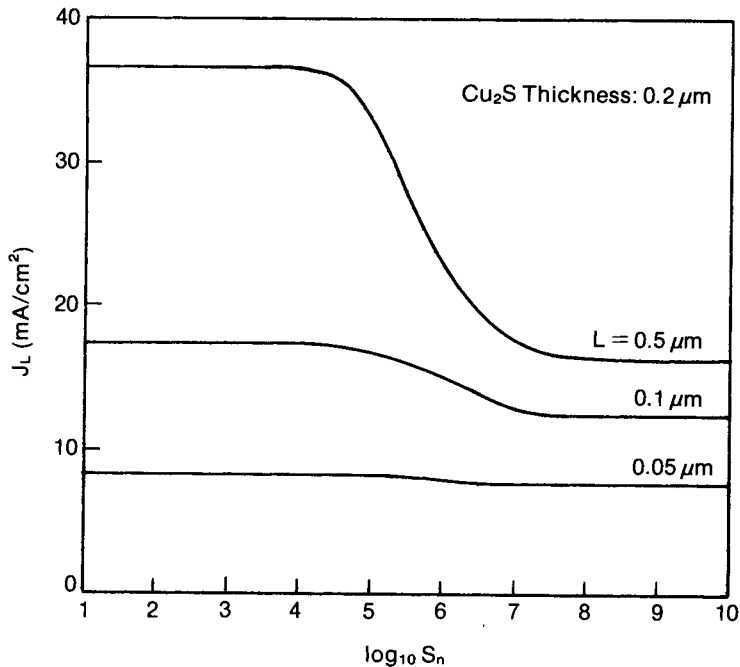
FIGURE 17.   *Dependence of the photogenerated current on sur-*
face recombination velocity for a 0.2 μm thick Cu$_2$S/CdS solar
cell. Effect of various diffusion lengths are indicated (from
Coutts (57)).

diffusion length is also in evidence.

G. Density of States in Gap

High density of states within the bandgap result in extremely
poor diffusion lengths. It is also difficult to dope such mate-
rials effectively, form necessary barriers,and obtain reasonable
minority carrier lifetimes. Density of state problems are es-
pecially critical for *amorphous materials*. Such densities have
been reduced by alloying and complexing (58, 59). Fabricating
amorphous Si in a hydrogen discharge greatly reduced the density
of localized gap states (60). Recently, a glow discharge Si:H:F
alloy has been shown to reduce such gap states even higher and
therefore holds some promise as a photovoltaic material (61).

V.   DEVICE REFINEMENTS

To conclude this discussion of photovoltaics, some examples
of device and materials engineering will be cited to illustrate
the advancement of solar cell technology, and the single-crystal
silicon cell in particular. From the 5-6% devices of the 1950's
to the near-20% (25,62) devices of today, several major develop-
ments have been made. In 1972, the *violet cell* was reported by
Comsat Laboratories (63). This silicon cell incorporated a
heavily-doped shallow junction that provided enhanced blue res-
ponse and less material utilization. The higher resistance emit-
ter necessitated the development of a more sophisticated top
grid. The cell also had an improved ARC and an advanced encapsu-
lation. Some 10-15% improvement in cell output resulted. At this
same time, NASA Lewis Research Center developed the *back-surface-
field (BSF) cell* (64). This design prevented photogenerated mi-
nority carriers from recombining at the back ohmic contact sur-
face by placing a low-high junction adjacent to the back contact.
This p-p$^+$ blocking back contact shielded the carriers from the
recombination surface with its electric field. The *black cell,*
reported in 1974, was a refinement of the violet cell (65). The
Si surface was textured to trap more incident radiation. Finally,
a thin metal reflector was used at the back contact to provide
the *back-surface-reflector cell* (66). This thin layer reflected
photons back through the cell, providing multiple passes of the
radiation and improved collection efficiency.

VI. SUMMARY

The purpose of this chapter is to present a *brief* introduc-
tion to photovoltaics and to provide a *basis* for understanding
the major properties and requirements of those materials which
are used in fabricating solar cells. Readers are directed toward
several *in-depth* treatments of this subject area given in

references 15, 19, 20, 27, 40, 60, 67-70. The meeting records of the IEEE Photovltaic Specialist Conferences (e.g., ref. 62) provide excellent technical records of all solar cell technologies.

ACKNOWLEDGMENTS

REFERENCES

1. Bequerel, E., *Compt. Rend. 9,* 561 (1839).

2. Adams, W.G., and Day, R.E., *Phil. Mag. 1,* 295 (1877).

3. Reynolds, D.C., Leies, G., Antes, L.L., and Marburger, R.E., *Phys. Rev. 96,* 533 (1954).

4. Shirland, F.A., A.R.L. Tech. Report 60-293 (Harshaw Chemical Co.; 1960).

5. Shirland, F.A. and Heitonen, J.R., Proc. 5th IEEE Photovoltaics Spec. Conf. Sect. IIC-3. IEEE, New York 1965; Also, Shirland, F.A., and Augustine, F., ibid, IIC-4.

6. Shiozawa, L.R., Sullivan, G.A., Augustine, F., Proc. 7th IEEE Photovoltaics Spec. Conf., pp. 39-46. IEEE, New York (1968)

7. Chapin, D.M., Fullerand, C.S., and Pearson, G.L., *J. Appl. Phys. 25,* 676 (1954).

8. See, for example, Wolf, M., Proc. 25th Power Sources, Symp. pp. 120-124, (1972).

9. See, for example, Hovel, H.J., "Solar Cells", pp. 191-203. Academic Press, New York, 1975.

10. Lindmayer, J., Proc. 12th IEEE Photovoltaics Spec. Conf.
    pp. 82-85. IEEE, New York, 1976.

11. Ciszek, T.F., Schwuttke, G.H., Yang, K.H., *J. Cryst. Growth*
    46, 527 (1979).

12. Vojdani, S., Sharifnai, A., and Doroudian, M., *Electron*
    Lett. 9, 128 (1973)

13. See, for example, Kaldis, E., (Ed.), "Current Topics in
    Materials Science, Vol. 1", North-Holland, Amsterdam, 1978.

14. Shirland, F.A., "*Adv. Energy Conv. 6,* 201 (1966).

15. See, for example, Hill, R., in "Active and Passive Thin
    Film Devices" (Coutts, T.J., Ed.) pp. 526-587. Academic
    Press, New York, 1979. Also, Harrison, R., Jenkins, G.,
    and Hill, R. Solar Cells *1,* 55 (1979)

16. Bachmann, K.J., Sinclair, W.R., Thiel, F.A., Schreiber, H.,
    Schmidt, P.H., Spencer, E.G., Buehler, E., and Feldman, W.L.,
    Proc. 13th IEEE Photovoltaics Spec. Conf. pp. 524-527, IEEE,
    New York, 1978.

17. Chamberlain, R.R., and Skarman, J.S., *J. Electrochem. Soc.*
    113, 86 (1966), *Solid-State Electron. 9,* 819, (1966).

18. J.L. Vossen and W. Kern, "Thin Film Processes" Academic
    Press, New York, 1979.

19. Backus, C.E. (Ed.), "Solar Cells". IEEE, New York, 1976.

20. Neville, R.C., "Solar Energy Conversion: The Solar Cell",
    Elsevier Scientific, Amsterdam, 1978.

21. Brobst, D.A., and Pratt, W.P., "United States Mineral
    Resources", Paper 820. United States Geological Publ.
    Office, Washington, D.C., 1973.

22. Costogue, E.N., "Silicon Material Supply Outlook Study",
    Proc. DOE Semiannual Review of Photovoltaics, Pinehurst,
    N.C., Novl. 7, 1979.

23. Maycock, P.D., Proc. 13th IEEE Photovoltaics Spec. Conf.,
    pp. 5-8. IEEE, New York, 1978. Also, Costello, D., and

Posner, D., Solar Cells *1*, 37 (1979).

24. DeMeo, E.A., Bos, P.B., "Perspectives on Utility Central Station Applications", EPRI Rep. ER-589-SR, 1978.

25. Frank, R.I., and Kaplow, R., *Appl. Phys. Lett. 34*, 65 (1979).

26. Loferski, J.J., *Proc. IEEE 51*, 677 (1963).

27. Sze, S.M., "Physics of Semicondutor Devices", pp. 640-653. Wiley, New York, 1969.

28. Sah, C.T., *IEEE Trans. Electron Dev. ED-9,* 94(1962).

29. Ireland, P.J., Wagner, S., Kazmerski, L.L., and Hulstrom, R.L., *Science, 204,* 611 (1978).

30. Pankove, J.I., "Optical Processes in Semiconductors", pp. 36-38. Prentice-Hall, New Jersey, 1971.

31. Brandhorst, H.W., "Interim Solar Cell Testing Procedures for Terrestrial Applications". NASA TID-26871, July, 1975.

32. Kazmerski, L.L., and Ireland, P.J., Proc. DOE Adv. Mat. Rev. Mtg. -CdS Based Solar Cells, Dept. of Energy, Washington, 1978.

33. Card, H.C. and Yang, E.S., IEEE Trans. Electron Dev. *ED-24,* 397 (1977).

34. Kazmerski, L.L., Solid-State Electron. *21,* 1545 (1978).

35. Rothwarf, A., Proc. 12th IEEE Photovoltaics Spec. Conf., p. 488, IEEE, New York, 1977.

36. Kazmerski, L.L., in "Ternary Compounds 1977", (Holah, G., Ed.), pp. 217-228. Instit. of Physics, Great Britain, 1977.

37. Loferski, J.J., Shewchun, J., Roessler, B., Beaulieu, R., Piekoszewski, J., Gorska, M. and Chapman, G., Proc. 13th IEEE Photovoltaics Spec. Conf. pp. 190-194. IEEE, New York, 1978.

38. Bube, R.H., "Photoconductivity in Solids", pp. 197-254. John Wiley, New York, 1960.

39. Moll, J.L., "Physics of Semiconductors", pp. 110-121. McGraw-Hill, New York, 1964.

40. Marfaing, Y., "Solar Energy Conversion and Applications" p. 671. C.N.R.S., Paris, 1978.

41. Iles, P.A., and Soclof, S.I., Proc. 10th IEEE Photovoltaic
    Spec. Conf., p. 19. IEEE, New York (1973).

42. Matare, "Defect Electronics in Semiconductors", Wiley-Inter-
    science, New York, 1971.

43. Wang, S., "Solid-State Electronics" pp. 275-308. McGraw-
    Hill, New York, 1966.

44. Fraas, L.M., *J. Appl. Phys. 49,* 871 (1979). Also, in
    "Polycrystalline and Amorphous Thin Films and Devices"
    (L.L. Kazmerski, Ed.) Chapter 5. Academic Press, New York,
    1980.

45. Armantrout, G.A., Yee, J.H., Fischer-Colbrie, E., Leong, J.,
    Miller, D.E., Hsieh, E.J., Vindelov, K.E., and Brown, T.G.,
    Proc. 13th IEEE Photovoltaics Spec. Conf. pp. 383-392.
    IEEE, New York, 1978.

46. Soclof, S., and Iles, P.A., Extended Abst., Electrochem.
    Soc. Fall Meeting, New York, p. 618 (1974). Also, Blakeslee,
    A.E., and Vernon, S.M., Solar Cells *1*, 81 (1979).

47. Hovel, H.J., "Solar Cells", pp. 103-109. Academic Press,
    New York, 1975.

48. Ghosh, A., SERI/DOE Quarterly Reports 1 and 2 (EXXON),
    January-June, 1979.

49. Rothwarf, A., and Barnett, A.M., *IEEE Trans. Electron Dev.*
    24, 381 (1977).

50. Kazmerski, L.L., Sheldon, P., and Ireland, P.J., *Thin Solid*
    Films 58, 95 (1979).

51. Kazmerski, L.L., Annual AVS Symposium, San Francisco (1978).

52. Wolf, M., Energy Conv. *11,* 63 (1971).

53. Ross, B., and Madiagan, J.R., *Phys. Rev.* 108, 1428 (1957).

54. Hovel, H.J., "Solar Cells" pp. 8-110. Academic Press, New
    York, 1975.

55. Rothwarf, A., and Boer, K.W., *Prog. in Solid-State Chem. 10,*
    71 (1975).

56. Catalano, A., Dalal, V., Devaney, W.E., Gagen, E.A., Hall,
    R.B., Masi, J.V., Meakin, J.D., Warfield, G., Wyeth, N.C.,

and Barnett, A.M., Proc. 13th IEEE Photovoltaics Spec. Conf.
p. 228. IEEE, New York, 1978.

57. Hill, R., "Active and Passive Thin Film Devices" (Coutts,
    T.M., Ed.) p. 561. Academic Press, London, 1979.

58. Spear, W.E., and LeComber, P.G., *Solid-State Comm. 17,*
    1193 (1975).

59. Spear, W.E., and LeComber, P.G., Phil. Mag. *33,* 935 (1976).

60. See, for example, Carlson, D.E., in "Polycrystalline and
    Amorphous Thin Films and Devices", (L.L. Kazmerski, Ed.),
    Chapter 7, Academic Press, New York, 1980.

61. Ovshinsky, S. *New Scientist,* p. 674, November (1978).

62. See, for example, "Proc. 14th IEEE Photovoltaics Conf.,
    San Diego", IEEE, New York, 1980.

63. Lindmayer, J., and Allison, J.F., Proc. 9th IEEE Photovol-
    taics Spec. Conf., p. 83. IEEE, New York, 1977.

64. Mandelkorn, J., and Lamneck, J., Proc. 9th IEEE Photovol-
    taics Spec. Conf. p. 66. IEEE, New York, 1972.

65. Hyenas, J.G., Allison, J.F., Arndt, R.A., and Meulenberg,
    A., Proc. Int. Conf. on Photovoltaic Power Generation,
    p. 487 (1974).

66. Scott-Monck, J., Gay, C., Stella, P., and Uno, F., "High
    Efficiency Solar Panel (HESP)", p. 487. AFAPL-TR-77-36,
    July, 1977.

67. Hovel, H.J., "Solar Cells" p. 94. Academic Press, New York,
    1975.

68. Pulfrey, L., "Photovoltaic Power Generation". Van Nostrand-
    Reinhold, New York, 1978.

69. Fonash, S., "Solid-State Energy Conversion". Academic Press,
    New York, 1980.

70. Fahrenbruch, A., and Bube, R.H., "Photovoltaic Solar Energy
    Conversion". Academic Press, New York, 1980.

APPENDIX

PHOTOVOLTAIC MATERIALS, DEVICES AND PARAMETERS

Photovoltaic research has expanded rapidly over the past dec-
ade. This activity has been directed both toward the development
of new materials and various device types. This appendix provides
a listing of solar cells according to device configuration (i.e.,
homojunction, heterojunction, Schottky barrier, metal-oxide-semi-
conductor and semiconductor-insulator-semiconductor). Parameters
including crystallinity (S=single crystal, P=polycrystalline, R=
ribbon and A=amorphous); energy gap, E_g; open-circuit voltage,
V_{oc}; short-circuit current, J_{sc}; fill-factor, FF; conversion ef-
ficiency, η; illumination conditions (either in air mass, AM; or
in mW/cm^2); and, antireflective coating, ARC. Although this list-
ing is extensive, it is not all-inclusive. It is hoped that it
does provide a flavor of the diversity and amount of R&D activity
that has existed in this semiconductor device area.

Lawrence Kazmerski

Device	Type	E_g (eV)	V_{oc} (V)	J_{sc} ($\frac{mA}{cm^2}$)	FF	η(%)	ARC	Illumination	Ref.	Comments
Homojunctions										
Si (n/p)	S	1.11	0.59	46.0	0.76	15.5	Ta_2O_5	AMO	1,2	CNR cell (Comsat)
Si (n/p)	S	1.11				~18	Ta_2O_5	100	3,2	Violet cell
Si (n/p)	S	1.11	0.61	42.9		15.2	Ta_2O_5	AMO	4	(100)Si; $n^+/p/p^+$
Si (p/n)	P	1.11	0.636	24.5	0.79	12.6	Al_2O_3	97.5	5	(111)Si; $p^+/p/n/n^+$ (epi)
Si (n/p)	S	1.11	0.53	29.7	0.68	10.7	none	AM1	6,7	Inversion layer
Si (n/p)	S	1.11	0.58	25.0	0.69	10	$SiO_2;Si_3N_4$	AM1	8	$n^+/p/n^+$ (two junction)
Si (p/n)	S	1.11	0.60	37.1	0.775	17.2	$TiO_2;SiO_2;$ ZrO_2	100.3	9	$n^+/n/p^+$
Si (p/n)	S	1.11	0.52	22.4	0.72	8.2	none	81	10	Corona cell
Si (n/p)	S	1.11				8	none	33	11	Series array device
Si (n/p)	R	1.11	0.572	27.4	0.754	11.8	none	AM1	12,13	EFG ribbon
Si (n/p)	R	1.11	0.560	26.0	0.69	10.0	SiO_2	99	14	$n^+/n/p$(graded)/p-ribbon
Si (n/p)	R	1.11				>7		AM1	15	RTR
Si (n/p)	R	1.11	0.51	16.2	0.66	5.8	none	93.8	16	Twinned Si
Si (n/p)	R	1.11	0.55	35	0.753	10.7		AMO	17,18	Web-dendrite
Si (n/p)	C	1.11	0.551	37.8	0.755	11.6	TiO_x	AMO	19-21	(100) p-Silso;10^3µm grain
Si (n/p)	C	1.11	0.57	25.1		10		AM1	22	2-3 mm grain size
Si (n/p)	P	1.11				7-8	SiO_2	AM1	23-26	Epi on metallurgical-grade
Si (n/p)	P	1.11	0.51	21	0.70	7.5		100	27,28	Si on ceramic
Si (p/n)	P	1.11	0.4	12	0.66	3.1	none	AM1	10	Corona discharge
Si (n/p)	P	1.11	0.32	16.7	0.06	3.2	SiO	100	29	$n^+/p/p^+$,CVD on Al_2O_3
Si (p/n)	P	1.11	0.22	10	0.6	1.9	none	75	30	Vacuum evaporation
Si (p/n)	S	1.11	0.77		0.77	19.0		300 suns	31	EMJV (Concentrator)
Si (n/p)	C	1.11	0.6	38.7		16.0		100	32	Semicrystalline
Si (n/p)	R	1.11	0.525	24	0.54	6.9		AM1	33	n^+/p RAD
Si (p/n)	P	1.11	0.56	27	0.746	9.75	SnO_2	AM1	34	Metallurgical grade Si sub.
Si (n/p)	P	1.11			0.6	2.1		AM1	35	Evaporated
Si (n/p)	P	1.11	0.44			1.9		AMO	36	6.5 cm^2 area
Si (p/n)	R	1.11	0.56	26	0.69	10	SiO_2	99	37	Polysilicon EFG substrate
Si (n/p)	P	1.11	0.56	14	0.73	4.3		AMO	38	Highly doped p-region
Si (n/p)	P	1.11	0.52	19.2	0.75	7.5		AM1	39	30 cm^2 area
Si (n/p)	P	1.11	0.25	15.0	0.56	2.15		AM1	40	Evaporated
Si (n/p)	S	1.11	0.60	26.5	0.792	12.6		AM1	41	15 µm epitaxial n
	P	1.11	0.57	24.8	0.734	10.3		AM1	41	15 µm epitaxial n on poly

Device	Type	E_g (eV)	V_{oc} (V)	J_{sc} ($\frac{mA}{cm^2}$)	FF	η(%)	ARC	Illumination	Ref.	Comments
Si (n/p)	S	1.11	0.76			19.1		732 suns	42	Vertical junction
Si (p/n)	S	1.11	0.59	31.1	0.807	15.9	Si_3N_4	AM1	43	BSF; p^+-n-n^+
GaAs (n/p)	S	1.4	0.97	25.6	0.81	20.5	SiO/MgF_2	98	44	CVD; $n^+/p^+/p/n^+$
GaAs (p/n)	S	1.4				13-14		AM1	45	
GaAs (n/p)	S	1.4	1.00	21.0	0.82	16.7	Anodic oxide	AM0	46	Radiation resistant
GaAs (n/p)	S	1.4	0.79	20.4	0.73	12.0	Anodic oxide	AM1	47	Laser Annealed; $n^+/p/p^+$
GaAs (n/p)	S	1.4	0.92	23	0.76	16.0	Anodic oxide	100	48	MBE; $n^+/p/p^+$
GaP (n/p)	S	2.25	1.15	3.9		3	none	100	49	
$Ga_{1-x}Al_xSb$ (p/n)	S		0.44	16.4	0.43	3.1	none	AM1	50	x=0.36 (best result)
InP (p/n)	S	1.34	0.74	10	0.63	6.7		70	51	
InP (p/n)	S	1.34	0.85	20	0.747	17.2		AM2	52	LPE
$CuInS_2$ (n/p)	P	1.54	0.41	18.2	0.49	3.6	none	100	53,54	1.5 µm grain size
$CuInSe_2$ (n/p)	P	1.02	0.32	19.4	0.5	3.0	none	100	53	2.0 µm grain size
$CdGeP_2$ (n/p)	S	1.72	0.6						55,56	77K; (112)-crystal
$CdSiAs_2$ (n/p)	S	1.55	0.6				none		57	Incandescent lamp
$CdSnP_2$ (p/n)	S	1.17	0.4						58	(112)-crystal
$ZnSiAs_2$ (p/n)	S	1.75	0.6						59	
CdTe (p/n)	S	1.44	0.75	9.8	0.63	6.0	none	77.2	60,61	
CdTe (n/p)	P	1.44	0.33	9	0.25	1.1	none	AM1	62	Electrodeposited

Heterojunctions

Device	Type	E_g (eV)	V_{oc} (V)	J_{sc} ($\frac{mA}{cm^2}$)	FF	η(%)	ARC	Illumination	Ref.	Comments
$Cu_xS(p)/CdS(n)$	S	1.2/2.41				8			63-66	Dry process
	P					5.5				
$Cu_xS(p)/CdS(n)$	P	1.2/2.41	0.51	25	0.71	8.6	SiO	100	67-72	Wet process(Clevite proc.)
$Cu_xS(p)/CdS(n)$	P	1.2/2.41	0.42	19.6		4.92	SnO_x	107.3	73	Spray pyrolysis
$Cu_2S(p)/CdS(n)$	P	1.2/2.41	0.52	21.8	0.71	9.15	SiO_x	87.9	74	1 cm^2 area; textured
$Cu_2S(p)/CdS(n)$	P	1.2/2.41	0.48	20.0	0.63	6.0			75	4 cm^2 area; textured cell
$Cu_2S(p)/(Cd,Zn)S(n)$	P	1.2/2.5	0.64	12.7	0.623	6.29	none	80.9	76	Planar cell
$Cu_2S(p)/(Cd,Zn)S(n)$	P	1.2/2.5	0.58	21		8.7		AM1	77-78	Textured cell

Device	Type	E_g (eV)	V_{oc}(V)	J_{sc}($\frac{mA}{cm^2}$)	FF	η(%)	ARC	Illumi-nation	Ref.	Comments
InP(p)/CdS(n)	S	1.34/2.41	0.62	15	0.71	12.5	SiO	53	79	0.23cm² area
InP(p)/CdS(n)	S	1.34/2.41	0.79	18.7	0.75	15.0	SiO$_x$	AM2	80,83	(111)-InP
InP(p)/CdS(n)	S	1.34/2.41	0.807	18.6	0.74	14.4	SiO$_x$	77	84	13.4mm² area
InP(p)/CdS(n)	P	1.34/2.41	0.46	13.5	0.68	5.7	SiO$_x$	AM2	80,81,85	CVD growth
InP(p)/CdS(n)	P	1.34/2.41	0.51	8.0	0.51	2.1	none	100	86	Two-source evaporation
InP(p)/CdS(n)	P	1.34/2.41	0.4	21.0	0.31	2.8	SiO	93	87	Carbon substrate
InP(p)/CdS(n)	P	1.34/2.41	0.37	18.0	0.30	2.0	SiO	AM1	88	0.41cm² area
Cu$_{1.85}$Se(p)/ InP(n)	P	1.2/1.34	0.33	5.2		0.7	none	140	89	
Cu$_x$Se(p)/ InP(n)	P	1.2/1.34	0.34	11	0.47	1.7	SiO	AM1	88	
CdSe(n)/ CdS(n)	S	1.74/2.41	0.3						90	CdSe vacuum evaporated
CdSe(n)/ ZnTe(p)	S	1.74/2.26	0.68			~1		87	91-92	(111)-ZnTe
CdSe(n)/ ZnTe(p)	S	1.74/2.26	0.80			7		AM2	93	(110)-ZnTe
CdSe(n)/ ZnTe(p)	P	1.74/2.26	0.61			~1		87	92	
Cd(S,Se)(n)/ ZnTe(p)	S	2.3/2.26	0.9						94	
CdS(n)/CdTe (n)/CdTe(p)	S	2.41/1.44/ 1.44	0.67	20.4	0.60	10.5	none	68	95,96	
CdS(n)/CdTe (n)/CdTe(p)	P	2.41/1.44/ 1.44	0.69	31.1		8.1	In$_2$O$_3$	140	97	OnIn$_2$O$_3$; 0.36cm² area
Cu$_x$Te(p)/CdTe (i)/CdTe(n)	S P					5 ~1			98-100	
CdS(n)/CdTe(p)	S	2.41/1.44	0.63	16.1	0.658	7.9	ITO and Glycerol	85	101	Evaporated CdS
CdS(n)/CdTe(p)	S	2.41/1.44	0.53	17.2		6.6	ITO	85	91,102	Sprayed CdS
CdS(n)/CdTe(p)	P	2.41/1.44	0.52	15	0.45	6	none	50	103	CVD CdTe
CdS(n)/CdTe(p)	S	2.41/1.44	0.53	16.4	0.63	6.5		85	102	
CdS(n)/CdTe(p)	S	2.41/1.44	0.67	17.9	0.60	10.5		68	95	0.57cm² area
CdSe(n)/CdTe(p)	S	1.74/1.44	0.63	1.43	0.32	0.3	ITO	87	104	
(Cd,Zn)S(n)/ CdTe(p)	S	2.5/1.44	0.79	12.7	0.64	7.8	ITO	99	105	

Device	Type	E_g (eV)	V_{oc}(V)	$J_{sc}(\frac{mA}{cm^2})$	FF	η(%)	ARC	Illumi- nation	Ref.	Comments
CdTe(n)/(Cd,Hg) Te(p)	S		0.235	40	0.44	4.0	none	100	106	
ZnO(n)/CdTe(p)	S	3.3/1.44	0.37	18	0.53	4.2	none	85	105	
ZnSe(n)/CdTe(p)	P	2.67/1.44	0.48	1.55	0.36	0.3	ITO	87	104,105	
ZnTe(p)/CdTe(n)	S	2.26/1.44	0.60	0.32	0.37		none	87	104	
ZnSe(n)/ZnTe(p)	P	2.67/2.26	0.69	0.06	0.52		none	87	104	
ZnTe(p)/(Zn,Hg) Te(n)	S	2.26	0.28	38		2.3	none	140	106	
$Cu_xSe(p)/CdSe$ (n)	P	1.2/1.74	0.36	7.5	0.40	2		56	107,108	
$Cu_xTe(p)/CdTe$ (n)	S	1.08/1.44	0.75			7.5	none	AM1	109,110	
$Cu_xTe(p)/CdTe$ (n)	P	1.08/1.44	0.56	12.2		6	none	70	110	η=5% in sun
$Cu_xTe(p)/CdTe$ (n)	P	1.08/1.44	0.59	15.9		6.55	yes	100	99,111- 113	Flash evaporated Cu_xTe
$Cu_xSe(p)/ZnSe$ (n)	S	1.2/2.67	1.1				none		114	Sunlight
CdS(n)/CuInSe₂ (p)	S	2.41/1.02	0.49	38	0.60	12	SiO	92	115-118	(112)-CuInSe₂
CdS/(n)/CuInSe₂ (p)	P	2.41/1.02	0.49	25.1	0.54	6.6		100	53,119	Dual source evaporation
CuInSe₂(p)/ CdS(n)	P/S	1.02/2.41	0.26	31.1	0.61	5.6	none	88	120	Dual source evaporation
CuInSe₂(p)/ CdS(n)	P	1.02/2.41	0.32	25.2	0.54	3.63	none	100	53	Frontwall cell
CdS(n)/CuInSe₂ (p)	P	2.41/1.02	0.34	31	0.54	5.7	none	100	122	3-source deposition
	P	2.41/1.02	0.39	33	0.58	7.5	none	100	123	Annealed
CuInSe₂(p)/ CdS(n)	S	1.02/2.41	0.34	31	0.44	4.7	none	100	124	MBE growth of CuInSe₂
CdS(n)/CuInS₂ (p)	S	2.41/1.54	0.42			0.8			121	
CdS(n)/CuInS₂ (p)	P	2.41/1.54	0.51	12.5	0.51	3.25	none	100	53,86	1.5 µm grain size
CdS(n)/CuInTe₂ (p)	P	2.41/0.96				0			53	

Device	Type	E_g (eV)	V_{oc} (V)	$J_{sc}(\frac{mA}{cm^2})$	FF	$\eta(\%)$	ARC	Illumi- nation	Ref.	Comments
CdS (n)/CuGaIn Te(p)	P		0.65	29	0.69	13.0	none	100	125	0.2cm^2; sintered
CdS(n)/CuInSe Te$_2$(p)	P		0.53	28	0.68	10.1	none	100	125	0.2cm^2; sintered
Cu$_2$Se(p)/AgIn Te$_2$(n)	S	1.24	0.12						126	
CdS/(n)/CuGa Se$_2$(p)	S	1.68	0.5	13.1	0.55	5	none	71	127	
AlAs(n)GaAs(p)	S	2.15/1.43	0.78	28	0.82	18.5	AlAs-oxide	AM1.3	128	(110)-GaAs
AlAs(n)/GaAs(p)	P	2.15/1.43	0.65					AM1	128	Graphite substrate
AlAs(p)/GaAs(p)/ GaAs(n)	S	2.15/1.43	1.0	23	0.8	13.5	SiO_x	AMO	129	
Ga$_{0.5}$Al$_{0.5}$As(n)/ GaAs(p)	S	1.8/1.43	0.88	16.9	0.77	13.5		AM2	130	
GaAlAs(n)/ GaAs(p)	S	1.43	0.88	27.7	0.76	13.6	Si_3N_4	AMO	131	
GaAlAs(p)/ GaAs(p)/GaAs(n)	S	1.43	1.015	33.1	0.745	18.5	TiO_2	AMO	132,133	
GaAlAs(p)/ GaAs(p)/GaAs(n)	S	1.43	0.976	27.8	0.76	21.9	TiO_2	93.9	133	(100)-GaAs
GaP(n)/GaAs(p)	S	2.25/1.43	0.49			7			134	(100)-GaAs
GaP(p)/GaAs(n)	S	2.25/1.43	0.5			8			134	
CdS(n)/GaAs(n)	S	2.41/1.43	0.43	1.7					135	
Cu$_{1.8}$Se(p)/GaAs (n)	P	1.2/1.43	0.54	15	0.52	4.26	Krylon	100	136	
ZnSe(n)/GaAs(p)	S	2.67/1.43	0.9	30		8-9	none		137	(111) and (110)-GaAs
AlGaAs/GaAs	S		3.96	4.5	0.625	13.85	none	81.95	138	Monolithic Series Array
InGaP(p)/GaAs(n)	S		0.96	17.3	0.82	14.0		97	139	Abrupt
Al$_{0.92}$Ga$_{0.08}$As (p)/Al$_{0.14}$Ga$_{0.86}$ As(n)	S		1.32		0.84	21.7		1000 suns	140	Concentrator cell
AlGaAs(p)/GaAs (n)	S		1.14		0.757	19.0	Si_3N_4	700 suns	141	AM1:V_{oc}=1.01V
AlGaAs(p)/GaAs (n)	S		1.07		0.822	24.7		178 suns	142	50°C

Device	Type	E_g (eV)	V_{oc}(V)	$J_{sc}(\frac{mA}{cm^2})$	FF	η(%)	ARC	Illumi-nation	Ref.	Comments
Schottky Barriers										
Al/Si(n)	S	1.11	0.38	30		8.0		AM1	143	Only V_{oc},J_{sc}
Au/Si(p)	s	1.11	0.29	25	0.67	4.8	none	100	144,147	(111)Si
Au/Si(p)	S	1.11	0.37	32	0.59	12	none	52	148,144	(100)Si
Cu/Cr/Si(p)	S	1.11	0.54	25.4	0.62	10.6	SiO	80-100	149	(100)Si
Cu/Cr/Si(p)	R	1.11	0.54	20.1	0.67	7.3	SiO	100	150	
Cr/Cu/Cr/Si(p)	P	1.11	0.43	22.8	0.61	6.4	SiO	92	151	Silso cast
Pt/Si(n)	S	1.11	0.28	19.5	0.58	3.9	In_2O_3	82	152	(111)Si
			0.41	29.2	0.60	8.8	In_2O_3	82		
Ti/Si(p)	S	1.11	0.55	33	0.65	11.7	TiO_2	AM1	153	(110)Si
Ti/Si(p)	S	1.11	0.50	32	0.5	8	TiO_x	AM1	154,155	(111)Si
Ti/Si(p)	P	1.11	0.38	24	0.48	3.9	TiO_2	AM1	156	
Y/Si(p)	P	1.11	0.49	15.7	0.64	5.4	SiO	92	151	Silso cast
Cr/Cu/Cr/Si(p)	S	1.11	0.425	23.5	0.60	6.5	SiO	92	151	(111)Si
Y/Si(p)	S	1.11	0.484	17.8	0.64	6.0	SiO	92	151	
Ag/GaAs(n)	S	1.43	0.765	13.7			none	AM1	157	
Al/GaAs(n)	S	1.43	0.42	14			none	AM1	157	
Au/GaAs(n)	S	1.43	0.452	27.1		8.5	none	100	158,159	(100)-GaAs
Au/GaAs(n)	S	1.43	0.67(0.83)		0.72(0.83)	13-17	Yes	100	158-160	(100)-GaAs
Au/GaAs(n)	S	1.43	0.741	16	0.761		none	100	160,161	(111)-GaAs
Au/GaAs(n)	P	1.43	0.705	25.3	0.785	14	Yes	100	162,157	500μm grain size
Au/GaAs(n)	P	1.43	0.79	26.1	0.78	16.2	Yes	100	157	mm grains
Au/GaAsP/(n)	S					20	Ta_2O_5	100	158	(100)-GaAsP
Au/GaAsP(n)	S	1.92	1.0	18		10	none	AM0	163	
Au/GaAsP(n)	S	1.92			0.796	22	none	125	163	
Au/GaAsP(n)	S	1.69				12	Ta_2O_5	93.7	164	
Cu/GaAs(n)	S	1.43	0.70	15			none	100	157	
Pt/GaAs(n)	P	1.43	0.65	13.3	0.59	5.1	SiO	100	136	
Au/GaAs(n)	P	1.43	0.49	20.6	0.54	5.45	none	100	165	3.2mm diameter cell; pas-sivated grain boundaries
Ag/CdS(n)	S	2.41	0.45	0.5			none	AM2	166	
Cu/CdS(n)	S	2.41	0.63	8.5			none	AM2	166	Possible pn junction
Ni/CdS(n)	S	2.41	0.33	0.4				AM2	166	
Au/CdSe(n)	P	1.74	0.55	5		1.5	none	80	167	
Au/CdTe(n)	S	1.44	0.56	5.8				AM0	168,169	

Device	Type	E_g (eV)	V_{oc} (V)	$J_{sc}(\frac{mA}{cm^2})$	FF	η(%)	ARC	Illumi-nation	Ref.	Comments
Au/CdTe(n)	P	1.44				1	none	50	170	
Pt/CdTe(n)	S	1.44	0.62				none	100	169	
Cu/Cu$_2$O(p)	S	1.96	0.35	5	0.32	0.56	none	AM1	171	
Cu/Cu$_2$O(p)	S	1.96	0.30	7.5	0.39	0.8	Epoxy	AM1	171	
Pb/Cu$_2$O(p)	S	1.96	0.23	0.6				AM1	171	
Al/Cu$_2$O(p)	S	1.96	0.35	4.0				AM1	171	
Ag/Cu$_2$O(p)	S	1.96	0.04	1.3				AM1	171	
Sn/Cu$_2$O(p)	S	1.96	0.45	1.5				AM1	171	
Zn/Cu$_2$O(p)	S	1.96	0.13	0.6				AM1	171	
Cd/GaSe(p)	S	2.0	0.45	0.9			none		172	
In/GaSe(p)	S	2.0				>1	none		173	Natural sunlight
Au/Ge$_x$Se$_{1-x}$	A	2.2	0.065	0.1		0.017		10	174	(111)-Ge substrate
Au/InSe	S	1.2	0.28	7.5	0.37	1.4	none	36	175	
Bi/InSe	S	1.17				1.5	none	AM2	173	
Au/MoSe$_2$(n)	S	1.1	0.50	0.6			Ta$_2$O$_5$	51	176	
Al/NSe$_2$(p)	S	1.35	0.504	9.7	0.62	5.3	Ta$_2$O$_5$	57	175	
Mg/Zn$_3$P$_2$(p)	S	1.35	0.5			6.08	SiO	AM1	177	L_n=6µm
Cu/CdGeP$_2$(n)	S	1.72	0.6						178	
Cu/CdSiP$_2$(n)	S	2.1	0.3						179	(112)-CdSiP$_2$
Cu/CdSnP$_2$(n)	S	1.17	0.4						58	
In/ZnGeP$_2$(p)	S	2.0	0.05						180	
Cu/ZnSiAs$_2$(n)	S	1.75	0.35						59	
Pt/ZnSiAs$_2$(n)	S	1.75	0.60						59	
Cu/ZnSiP$_2$(n)	S	2.1	0.3						181	(112)-ZnSiP$_2$
Au/CdInTe$_4$(n)	S	0.9	0.2						182	

MIS

Device	Type	E_g (eV)	V_{oc} (V)	$J_{sc}(\frac{mA}{cm^2})$	FF	η(%)	ARC	Illumi-nation	Ref.	Comments
Al/SiO$_2$/Si(p)	S	1.11	0.47	26.5		8	SiO$_2$	AM1	183	20-40Å SiO$_2$
Al/SiO$_2$/Si(p)	S	1.11	0.52	33.3	0.75	13	SiO$_2$	AM1	184	(111)-Si, Inversion
Al/SiO$_x$/Si(p)	S	1.11	0.618	32	0.60				186-188	
Al/SiO$_x$/Si(p)	S	1.11				~10			185	MISIM
Al/TiO$_x$/Si(p)	P	1.11	0.53						184	Inversion
Al/SiO$_x$/Si(p)	P	1.11	0.51	15					185	Silso-cast
Au/SiO$_x$/Si(n)	S	1.11	0.55		0.72	9	none	100	189	(111)-Si
Al/Si$_3$N$_4$/Si(p)	S	1.11	0.48	~30	0.70	10.2		AM1	190	
Al/SiO$_x$/Si(p)	S	1.11	0.523	17.7	0.76	8.6	ZnS	AM1	191	0.83cm^2 area

Device	Type	E_g (eV)	V_{oc} (V)	$J_{sc}(\frac{mA}{cm^2})$	FF	η(%)	ARC	Illumination	Ref.	Comments
$Cr/SiO_2/Si\cdot(p)$	S	1.11	0.58	29	0.72	12	SiO	AM1	192	$1.5cm^2$ area
$Cr/SiO_2/Si(p)$	S	1.11	0.60	26	0.75	11.7	SiO	AM1	192	$1.6cm^2$ area
$Ti/SiO_2/Si(p)$	S	1.11	0.54	25	0.72	9.8	SiO	AM1	192	$1.5cm^2$ area
$Al,Mg/SiO_x/Si(p)$	S	1.11	0.642	35.6	0.77	17.6	SiO	AM1	193	Active area parameter; grating type cell
$Cr/SiO_x/Si(p)$	S	1.11	0.610	30.0	0.73	13.4	SiO	AM1	194	$2.0cm^2$ active area
$Ti/SiO_x/Si(p)$	S	1.11	0.55	33.0	0.65	11.7	TiO_x	AM1	195	$2.6cm^2$ active area
$Al/SiO_x/Si(p)$	S	1.11	0.583	30.0	0.6-0.7			AM1	196	BSF
$Be/SiO_x/Si(p)$	S	1.11	0.54	24.6	0.61	9.5	none	85	197	
$Al/SiO_x/Si(n)$	S	1.11	0.62					AM1	198	Oxide-charge-induced BSF

SIS

Device	Type	E_g (eV)	V_{oc} (V)	$J_{sc}(\frac{mA}{cm^2})$	FF	η(%)	ARC	Illumination	Ref.	Comments
$In_2O_3(n)-Si(p)$	P-S	3.6-1.11	0.16	0.73			none		199,200	(111)-Si
$In_2O_3(n)-Si(n)$	P-S	3.6-1.11	0.23	0.68	0.53		none		201,200	(100)-Si
$ITO(n)-Si(p)$	S	3.6-1.11	0.51	32	0.70	12	none	92	202,203	η vs Sn content
$ITO(n)-Si(n)$	S	3.6-1.11	0.50	32	0.65	11		100	204,205	Spray pyrolysis ITO
$ITO(n)-Si(p)$	P	3.6-1.11	0.28	25	0.23	1.6	none	100	156	
$SnO_2(n)-Si(n)$	S	3.5-1.11				1.5	none	AM1	206,207	
$SnO_2(n)-Si(n)$	S	3.5-1.11	0.521	29	0.64	9.9	none	AM1	207-210	
$SnO_2(n)-Si(n)$	P	3.5-1.11	0.463	26	0.60	7.2	none	AM1	206	
$ITO(n)-Si(p)$	P	3.6-1.11	0.48	29	0.65	9	none		211	Ion-beam ITO
$SnO_2(n)-Si(n)$	S	3.5-1.11	0.55	27.5	0.69	10.5	none	AM1	212	Sprayed ITO; $1cm^2$ area
$SnO_2(n)-Si(n)$	S	3.5-1.11	0.47	28.9	0.66	9.1	none	AM1	212	E-beam ITO; $4cm^2$ area
$SnO_2(n)-Si(n)$	S	3.5-1.11	0.49	28	0.71	9.8	none	AM1	212	E-beam; $1cm^2$ area
$ITO(n)-Si(p)$	S	3.6-1.11	0.46	37	0.76	13	none	AM1	213	
$ITO(n)-Si(n)$	P	3.6-1.11	0.50	36	0.46	9.1	none	AM1	214	Silso substrate; active
$SnO_2(n)-Si(n)$	S	3.5-1.11	0.615	29.1	0.685	12.26		100	215	$3.8cm^2$ area; sprayed SnO_2
	P		0.56	26.6	0.68	10.1		100	215	$1cm^2$ area
$ITO(n)-CuInSe_2(p)$	S	3.6-1.02		30		8.9	none	100	216	ITO: E-beam deposited
	P	3.6-1.02				3.0-4.5	none	100		
$ITO(n)-GaAs(p)$	S	1.4				5	none	AM2	217	Sputtered ITO
$In_2O_3(n)-GaAs(p)$	S	3.6-1.4	0.084	6.2	0.40		none	AM0	200	
$SnO_2(n)-GaAs(n)$	S	3.5-1.4	0.33	11.4	0.43	1.2		AM0	218	
$In_2O_3(n)-InP(n)$	S	3.6-1.43	0.18	0.6	0.35		none	AM0	200	
$ITO(n)-InP(p)$	S	3.6-1.43	0.76	21.55	0.65	14.4	MgF_2	AM2	219	
$SnO_2(n)-Ge_{1-x}Se_x(p)$	A	3.5				3×10^{-5}	SnO_2	7.8	220	

Device	Type	E_g (eV)	V_{oc}(V)	$J_{sc}(\frac{mA}{cm^2})$	FF	η(%)	ARC	Illumination	Ref.	Comments
$SnO_2(n)-In_{1-x}Se_x(p)$	A	3.5-1.74	0.1	10^{-2}		0.03	SnO_2	7:8	221	
$ITO(n)-CdTe(n)$	S	3.6-1.44	0.82	14.5	0.55	8.0	none	85	222	
$ITO(n)-CuInGaSeTe(p)$	P		0.72		0.55	12.3	none	100	125	Sintered
$ITO(n)-CuInSeTe$	P		0.51	30	0.54	8.3		100	125	Sintered

Amorphous Devices

Device	Type	E_g (eV)	V_{oc}(V)	$J_{sc}(\frac{mA}{cm^2})$	FF	η(%)	ARC	Illumination	Ref.	Comments
$Si(p)/Si(i)/Si(n)$	A	1.55	0.58	10.5	0.40	2.4	ITO	AM1	223,224	Glass covered
$Si(n)/Si(p)$	A/S	1.55/1.11	0.40					15	225	On single crystal Si
Al/Si	A	1.55	0.036	1.43		0.03	none	100	226	Sputtered Si
$ITO/Si(n)$	A	3.6/1.55	0.43	10	0.28	1.2			227	Glow discharge a-Si
ITO/Si	A					0.02	none	100	226	Sputtered Si
Mo/Si	A	1.55				$3x10^{-4}$	none	100	226	Sputtered Si
$Pt/Si(i)/Si(n)$	A	1.55	0.8	7.8	0.38	5.5	ZrO_2,	65	223	
			0.803	12		5.5	Si_3N_4	100	223	$0.02cm^2$ area
$Pt/SiO_2/Si(p)/Si(i)/Si(n)$	A		0.77	7		3.3	none	100	228	$1.6cm^2$ area
$ITO/Si(p^+)/Si(i)/Si(n^+)$	A		0.560	12		4.5	Yes	80	229	Stainless steel substrate
$Pt/Si(i)/Si(n^+)$	A		0.50	15		4.3	none	100	230	
$Si(n^+)/Si(i)/Si(p^+)$	A		0.67	9.3		3.4	none	100	231	Stainless steel substrate
$Ni/TiO_x/Si(i)/Si(n^+)$	A		0.63	7.5		4.8	Yes	60	232	Stainless steel substrate

REFERENCES

(1)   Arndt, R.A., Allison, J.F., Haynos, J.G., and Muelenberg,
      A., Proc. 11th IEEE Photovoltaic Spec. Conf., pp. 40-43.
      IEEE, New York, 1975.

(2)   Brandhorst, H.W., Japan. *J. Appl. Phys. 16*, 399 (1977).

(3)   Lindmayer, J., and Allison, J.F. *COMSAT Tech. Rev. 3,* 1
      (1973).

(4)   Payne, P.A., and Oliver, R.L., Proc. 12th IEEE Photovoltaic
      Spec. Conf., pp. 595-599. IEEE, New York, 1976.

(5)   D'Aiello, R.V., Robinson, P.H., and Kressel, H., *Appl.
      Phys. Lett 28*, 231 (1976).

(6)   Norman, C.E., and Thomas, R.E., Proc. 12th IEEE Photovolt-
      aic Spec. Conf., pp. 993-996. IEEE, New York, 1976.

(7)   Salter, G.C., and Thomas, R.E., *Solid-State Electron 20*,
      95 (1977).

(8)   Chiang, S.Y., Carbajal, B.G., and Wakefield, G.F., Proc.
      Intern. Photovoltaic Solar Energy Conf., Luxembourg,
      pp. 104-112. D. Riedel, Holland, 1977.

(9)   Bae, M.S., and D'Aiello, R.V., *Appl. Phys. Lett. 31*, 285
      (1977).

(10) Wiehner, R., and Charlson, E.J., *J. Electron Mat. 5*, 513
      (1976).

(11) Warner, R.M., Murray, E.M., and Smith, W.K., *Appl. Phys.
      Lett. 31,* 838 (1977)

(12) Ravi, K.V., *J. Cryst. Growth 39*, 1 (1977).

(13) Serreze, H.B., Swartz, J.C., Entine, G., and Ravi, K.V.,
      Mat. Sci. Bull. 9, 1421 (1974).

(14) Kressel, H., D'Aiello, R.V., Levin, E.R., Robinson, P.H.,
      and McFarlane, S.H., *J. Cryst. Growth 39,* 23 (1977).

(15) Lesk, I.A., Baghadi, A., Gurtler, R.W., Ellis, R.J.,
      Wise, J.A., and Coleman, M.G., Proc. 12th IEEE Photovolt-
      aic Spec. Conf., pp. 173-181. IEEE, New York, 1976.

(16) Schwuttke, G.H., *Phys. Stat. Sol. (a) 43*, 43 (1977).

(17) Seidensticker, R.G., *J. Cryst. Growth 39*, 17 (1977).

(18) Davis, J.R., Rai-Choudhary, P., Blais, P.D., Hopkins, R.H., and McCormick, J.R., Proc. 12th IEEE Photovoltaic Spec. Conf., pp. 106-111. IEEE, New York, 1976.

(19) Fischer, H., and Pschunder, W., Proc. 12th IEEE Photo-voltaic Spec. Conf., pp. 86-92, IEEE, New York, 1976.

(20) Fischer, H., and Pschunder, W., *IEEE Trans. Electron Dev. ED-24*, 438 (1977).

(21) Fischer, H., in "Photovoltaic Solar Energy" (Strub, A., Ed.) pp. 52-75. D. Reidel, Holland, 1977.

(22) Lindmayer, J., Proc. 12th IEEE Photovoltaic Spec. Conf., pp. 82-85. IEEE New York, 1976.

(23) Chu, T.L., *J. Cryst. Growth 39*, 45 (1977).

(24) Chu, T.L., Chu, S.S., Duh, K.Y. and Mollenkopf, *J. Appl. Phys. 48*, 3576 (1977).

(25) Chu, T.L., *Appl. Phys. Lett. 29*, 675 (1976).

(26) Chu, T.L., and Singh, K.N., *Solid-State Electron. 19*, 837 (1976).

(27) Zook, J.D., Heaps, J.D., and Maciolek, R.B., Proc. Intern. Electron Dev. Mtg., Washington, IEDM, New York, 1977.

(28) Heaps, J.D., Maciolek, R.B., Zook, J.D., and Scott, M.W., Proc. 12th IEEE Photovoltaic Spec. Conf., pp. 147-150. IEEE, New York, 1976.

(29) Saitoh, T., Warabisako, T., Itoh, H., Nakamura, N., Tamura, H., Minegana, S., and Tokuyama, T., *Japan. J. Appl. Phys. 16*, 413 (1977). Also, IEEE Trans. Electron Dev. *ED-24*, 446 (1977).

(30) Feldman, C., Blum, N.A., Charles, H.K., and Satkiewicz, F.G., *J. Electron. Mat. 7*, 309 (1978).

(31) Frank, R.I., and Kaplow, R., *Appl. Phys. Lett. 34*, 65 (1979).

(32) Lindmayer, J., Proc. 13th IEEE Photovoltaic Spec. Conf., pp. 1096-1100. IEEE, New York, 1978.

(33) Fabre, E., Baudet, Y., and Ebeid, S.M., Proc. 13th IEEE Photovoltaic Spec. Conf., pp. 1101-1105. IEEE, New York, 1978.

(34) Chu, T.L., Chu, S.S., Pauleau, M.Y., and Stokes, E.D., Proc. Photovoltaics Adv. R&D Annual Rev. Mtg., Denver, CO., pp. 423-440. SERI, Golden, CO., 1979.

(35) Feldman, C., Blum, N.A., and Satkiewicz, F.G., Proc. Polycrystalline Silicon Contractors Rev. Mtg., Pasadena, pp. 59-82. SERI, Golden, CO., 1979.

(36) Chu, T.L., *J. Vac. Sci. Technol. 12,* 912 (1975).

(37) D'Aiello, R.V., Kressel, H., and Robinson, P.H., *Appl. Phys. Lett. 28,* (1976).

(38) Chu, T.L., Chu, S.S., Duh, K.Y., and Yoo, H.I., Proc. 12th IEEE Photovoltaic Spec. Conf. IEEE, New York, 1976.

(39) Chu, T.L., "Thin Films of Silicon on Low-Cost Substrates". ERDA, Washington, DC; September, 1977.

(40) Feldman, C., Blum, N.A., and Satkiewicz, F.G., Proc. Polycrystalline Silicon Contractors Rev. Mtg., Pasadena, pp. 59-82. SERI, Golden, CO., 1979.

(41) D'Aiello, R.V., Proc. Polycrystalline Silicon Contractors Rev. Mtg., Pasadena, pp. 233-242. SERI, Golden, CO., 1979.

(42) Ekstedt, T.W., Mahan, J.E., Frank, R.I., and Kaplow, R., *Appl. Phys. Lett. 33,* 422 (1978).

(43) Fossum, J.G., and Burgess, E.L., *Appl. Phys. Lett. 33,* 228 (1978).

(44) Fan, J.C.C., Bozler, C.O., and Chapman, R.L., *Appl. Phys. Lett. 32,* 390 (1978).

(45) Hovel, H.J., and Woodall, J.M., Proc. 12th IEEE Photovoltaic Spec. Conf., pp. 945-947. IEEE, New York; 1976.

(46) Fan, J.C.C., Chapman, R.L., Bozler, C.O., and Drevinsky, P.J., *Appl. Phys. Lett. 36,* 53 (1980).

(47) Fan, J.C.C., Chapman, R.L., Donnelly, J.P., Turner, G.W., and Bozler, C.O., *Appl. Phys. Lett. 34,* 780 (1979).

(48) Fan, J.C.C., Calawa, A.R., Chapman, R.L., and Turner, G.W., *Appl. Phys. Lett. 35,* 804 (1979).

(49) Grimmeiss, H.G., Kischio, W., and Koelmans, H., *Solid-State Electron. 5,* 155 (1962).

(50)   Nguyen van Mau, A., Bougnot, G., Muoy, H.Y., and
       Moussalli, G.M., in "Photovoltaic Solar Energy" (Strub, A.,
       Ed.), pp. 405-414. D. Riedel, Holland, 1977.

(51)   Galavanov, V.V., Kundukhov, R.M., and Nasledov, D.N.,
       Sov. Phys.-Solid State 8, 2723 (1967).

(52)   Shay, J.L., Wagner, S., Bettini, M., Bachmann, K.J.,
       Buehler, E., and Kasper, H.M., Proc. 11th IEEE Photovoltaic
       Spec. Conf., pp. 507-507. IEEE, New York, 1975.

(53)   Kazmerski, L.L., in "Ternary Compounds 1977"(Holah,G.D.,
       Ed.), pp. 217-228. Institute of Phys. Conf. Series 35.
       Instit. of Phys., London, 1977.

(54)   Kazmerski, L.L., and Sanborn, G.A., *J. Appl. Phys. 48,*
       3178 (1977).

(55)   Borshchevskii, A.S., Lebedov, A.A., Mal'tseva, I.A.,
       Ovezov, K., Rud, Y.V., and Undalov, Y.K., *Sov. Phys.-
       Semicond. 9,* 1278 (1975).

(56)   Borchevskii, A.S., Dagina, N.E., Lebedev, A.A., Ovezov,
       K., Polushina, I.K., and Rud, Y.V., *Sov. Phys.-Semicond.
       10,* 934 (1976).

(57)   Dovletmuradov, C., Ovezov, K., Prochukhan, V.D., Rud, Y.V.,
       and Serginov, M., *Sov. Phys.-Techn. Phys. Lett. 1,* 382
       (1975).

(58)   Medvekin, G.A., Ovezov, K., Rud, Y.V., and Sokolova, V.I.,
       Sov. Phys.-Semicond. 10, 1239 (1976).

(59)   Rud, Y.V., and Ovezov, K., *Sov. Phys.-Semicond. 10,* 561
       (1976).

(60)   Naumov, G.P., and Nikolaelva, O.V., *Sov. Phys.-Solid State
       3,* 2718 (1961).

(61)   Vodakov, Y.A., Lomakina, G.A., Naumov, G.P., and
       Maslakovets, Y.P., *Sov. Phys.-Solid State 2,* 1 and 11
       (1960).

(62)   Rod, R., "Improved Semiconductor for Photovoltaic Solar
       Cells", Final Report (49-18)-2457. ERDA, Washington, DC,
       Nov. 1977.

(63) teVelde, T.S., *Energy Conv. 14*, 111 (1975).

(64) teVelde, T.S., and Dieleman, J., *Philips Res. Rep.*
      28, 573 (1973).

(65) Reynolds, D.C., Seies, G., Antes, L.L., Marburger, R.E.,
      Phys. Rev. 96, 533 (1954).

(66) Das, S.R., Nath, P., Banerjee, A., and Chopra, K.L.,
      Solid-State Comm. 21, 49 (1977).

(67) Barnett, A.M., Meakin, J.D., and Rothwarf, A., Proc. 12th
      IEEE Photovoltaic Spec. Conf., pp. 544-546. IEEE, New
      York, 1976.

(68) Boer, K.W., *Phys. Stat. Sol. (a) 40*, 355,(1977).

(69) Boer, K.W., Proc. 11th IEEE Photovoltaic Spec. Conf.,
      pp. 514-515. IEEE, New York, 1975.

(70) Palz, W., Besson, J., Duy, T.N., and Vedel, J., Proc.
      10th IEEE Photovoltaic Spec. Conf., pp. 69-76. IEEE, New
      York, 1973.

(71) Bogus, K., and Mattes, S., Proc. 9th IEEE Photovoltaic Spec.
      Conf., pp. 106-110. IEEE, New York, 1972.

(72) Burton, L.C., Hench, T., Storti, G., and Haacke, G.,
      J. Electrochem. Soc. 123, 1741 (1976).

(73) Jordan, J.F., Proc. 11th IEEE Photovoltaic Spec. Conf.
      pp. 508-513. IEEE New York, 1975.

(74) Barnett, A.M., Bragagnolo, J.A., Hall, R.B., Phillips,
      J.E., and Meakin, J.D., Proc. 13th IEEE Photovoltaic Spec.
      Conf., pp. 419-420. IEEE, New York, 1978.

(75) Rothwarf, A., Meakin, J.D., and Barnett, A.M., "Polycryst.
      and Amorphous Thin Films and Devices". Academic Press, 1980

(76) J.D. Meakin, in "Photovoltaics Adv. R&D Annual Rev. Mtg",
      Denver (Deb, S., Ed.) pp. 167-194. SERI, Golden, CO, 1979.

(77) Meakin, J.D., Proc. CdS/Cu_2S and CdS/Cu-Ternary Compound
      Rev. Mtg., Denver, pp. 79-110. SERI, Golden, CO, 1979.

(78) Hall, R.B., Birkmire, R.W., Eser, E., Hench, T.L., and
      Meakin, J.D., Proc. 14th IEEE Photovoltaic Spec. Conf.

IEEE, New York, 1980.

(79) Wagner, S., Shay, J.L., Bachmann, K.J., and Buehler, E.,
      Appl. Phys. Lett. 26, 229 (1975).

(80) Wagner, S., Shay, J.L., Bachmann, K.J., Buehler, E., and
      Bettini, M., *J. Cryst. Growth. 39,* 128 (1977).

(81) Shay, J.L., Bettini, M., Wagner, S., Bachmann, K.J., and
      Buehler, E., Proc. 12th IEEE Photovoltaic Spec. Conf.
      pp. 540-543. IEEE, New York, 1976.

(82) Shay, J.L., Wagner, S., Bettini, M., Bachmann, K.J., and
      Buehler, E., *IEEE Trans. Electron Dev. ED-24,* 483 (1977).

(83) Ito, K., and Ohsawa, T., *Japan. J. Appl. Phys. 14,* 1259
      (1975).

(84) Yoshikawa, A., and Sakai, Y., *Solid-State Electron. 20,*
      133 (1977).

(85) Bettini, M., Bachmann, K.J., Buehler, E., Shay, J.L., and
      Wagner, S., *J. Appl. Phys. 48*, 1603 (1977).

(86) Kazmerski, L.L., White, F.R., Ayyagari, M.S., Juang, Y.J.,
      and Patterson, R.P., *J. Vac. Sci. Technol. 14*, 65 (1977).

(87) Bachmann, K.J., Buehler, E., Shay, J.L., Wagner, S., and
      Bettini, M., *J. Electrochem. Soc. 123,* 1509 (1976).

(88) Saitoh, T., Matsubara, S., and Minagawa, S., *Japan. J.
      Appl. Phys. 16,* 133 (1977). Also, *Japan. J. Appl. Phys.
      16,* 807 (1977).

(89) Fischer, H., Thesis, Tech. Univ. Braunschweig (1970).

(90) Kandilarov, B., and Andreytchin, R., *Phys. Stat. Sol. 8,*
      897 (1965).

(91) Fahrenbruch, A.L., Buch, F., Mitchell, K.W., and Bube, R.H.
      Proc. 12th IEEE Photovoltaic Spec. Conf., pp. 529-533.
      IEEE, New York, 1976.

(92) Buch, F., Fahrenbruch, A.L., and Bube, R.H., *Appl. Phys.
      Lett. 28,* 593 (1976).

(93) Gashin, P.A., and Simashkevich, A.V., *Phys. Stat. Sol. (a)
      19,* 615 (1973).

(93) Gashin, P.A., and Simashkevich, A.V., *Phys. Stat. Sol. (a) 19*, 615 (1973).

(94) Fedotov, Y.A., Supalov, V.A., Manuilova, T.P., Vanyukov, A.V., and Kondaurov, N.M., *Sov. Phys.-Semicond. 5*, 1396 (1972).

(95) Yamaguchi, K., Matsumoto, H., Nakayama, N., and Ikegami, S., *Japan. J. Appl. Phys. 15*, 1575 (1976).

(96) Yamaguchi, K., Nakayama, N., Matsumoto, H., and Ikegami, S., *Japan. J. Appl. Phys. 16*, 1203 (1977).

(97) Nakayama, N., Matsumoto, H., Yamaguchi, Y., Ikegami, S., and Hioki, Y., *Japan. J. Appl. Phys. 15*, 2281 (1976).

(98) Bernard, J., Lancon, R., Paparoditis, C., and Rodot, M., *Rev. Phys. Appl. 1*, 211 (1966).

(99) Lebrun, J., *Rev. Phys. Appl. 1*, 204 (1966).

(100) Rodot, M., *Rev. Phys. Appl. 12*, 411 (1977).

(101) Mitchell, K.W., Fahrenbruch, A.L., and Bube, R.H., *Solid-State Electron. 20*, 559 (1977). Also, *J. Appl. Phys. 48*, 4365 (1977).

(102) Ma, Y.Y., Fahrenbruch, A.L., and Bube, R.H., *Appl. Phys. Lett. 30*, 423 (1977).

(103) Bonnet, D., and Rabenhorst, H., Proc. 9th IEEE Photovoltaic Spec. Conf., pp. 129-132. IEEE, New York, 1972.

(104) Buch, F., Fahrenbruch, A.L., and Bube, R.H., *Appl. Phys. Lett. 28*, 593 (1976).

(105) Mitchell, K.W., Fahrenbruch, A.L., and Bube, R.H., *J. Appl. Phys. 48*, 4365 (1977).

(106) Cohen-Solal, G., Svob, L., Marfaing, Y., Janik, E., and Castro, E., Proc. 9th IEEE Photovoltaic Spec. Conf., pp. 28-36. IEEE, New York, 1972.

(107) Komashchenko, V.N., and Fedorus, G.A., *Ukr. Fiz. Zh. 13*, 688 (1968).

(108) Komashchenko, V.N., Kinev, S., Marchenko, A.I., and Fedorus, G.A., *Ukr. Fiz. Zh. 13*, 2086 (1968).

(109)   Cusano, D.A., *Solid-State Electron.* 6, 217 (1963).

(110)   Cusano, D.A., *Rev. Phys. Appl. 1*, 195 (1966).

(111)   Justi, E.W., Schneider, G., and Seredynski, J., *Energy Conv. 13*, 53 (1973).

(112)   Guillien, M., Leitz, P., Marshal, G., and Palz, W., in "Solar Cells", pp. 207-214. Gordon and Breach, London, 1971.

(113)   Lebrun, J., and Bessoneau, G., in "Solar Cells", pp. 201-206. Gordon and Breach, London, 1971.

(114)   Lozykowski, H., *Czech. J. Phys. B13*, 164 (1963).

(115)   Shay, J.L., Wagner, S., and Kasper, H.M., *Appl. Phys. Lett. 27*, 89 (1975).

(116)   Wagner, S., Shay, J.L., and Kasper, H.M., *J. Phys.-Coll. 36*, 101 (1975).

(117)   Wagner, S., Shay, J.L., Migliorato, P., and Kasper, H.M., *Appl. Phys. Lett. 25*, 434 (1974).

(118)   Shay, J.L., Wagner, S., Bachmann, K.J., Buehler, E., and Kasper, H.M., Proc. 11th IEEE Photovoltaic Spec. Conf., pp. 503-507. IEEE, New York, 1975.

(119)   Kazmerski, L.L., White, F.R., and Morgan, G.K., *Appl. Phys. Lett. 29*, 268 (1976).

(120)   Kokubun, Y., and Wada, M., *Japan. J. Appl. Phys. 16*, 879 (1977).

(121)   Wagner, S., *J. Cryst. Growth 39*, 151 (1977).

(122)   Mickelsen, R.A., and Chen, W.S., *Appl. Phys. Lett. 36*, 371 (1980).

(123)   Mickelsen, R.A., Personal Communication.

(124)   Grindle, S.P., Clark, A.H., Rezaie-Serej, S., Falconer, E., McNeily, J., and Kazmerski, L.L., *J. Appl. Phys. 51*, 1980.

(125)   Loferski, J.J., and Shewchun, J., in Proc. Photovoltaics Adv. R&D Annual Mtg., Sept. 1979, pp. 182-183. SERI, Golden, CO., 1979.

(126) Tell, B., and Bridenbaugh, P., *J. Appl. Phys. 48*, 2477 (1977).

(127) Tell, B., Bridenbaugh, P.M., and Kasper, H., *J. Appl. Phys. 47*, 619 (1977).

(128) Johnston, W.D., and Callahan, W.M., *Appl. Phys. Lett. 28*, 150 (1976); Also, *J. Cryst. Growth 39*, 117 (1977).

(129) Huber, D., and Bogus, K., Proc. 10th IEEE Photovoltaic Spec. Conf., pp. 100-102. IEEE, New York, 1974.

(130) Konagai, M., and Takahashi, K., Proc. Electrochem. Soc. Spring Mtg., Washington, pp. 554-555. Electrochem. Soc., New Jersey, 1976.

(131) Hutchby, J.A., Sahai, R., and Harris, J.S., Proc. Intern. Electron. Dev. Mtg., Washington, pp. 91-94. IEDM, New York, 1975.

(132) Hovel, H.J., and Woodall, J.M., Proc. 12th IEEE Photovoltaic Spec. Conf., pp. 945-947. IEEE, New York, 1976.

(133) Woodall, J.M., and Hovel, H.J., *Appl. Phys. Lett. 30*, 492 (1977).

(134) Purohit, R.K., *Phys. Stat. Sol. 24*, K57 (1967).

(135) Yoshikawa, A., and Sakai, Y., *Japan. J. Appl. Phys. 14*, 1547 (1975).

(136) Vohl, P., Perkins, D.M., Ellis, S.G., Addiss, R.R., Hui, W., and Noel, G., *IEEE Trans. Electron Dev. ED-24*, 26 (1967).

(137) Balch, J.W., and Anderson, W.W., *Phys. Stat. Sol. (a) 9*, 567 (1972).

(138) Borden, P.G., *Appl. Phys. Lett. 35*, 553 (1979).

(139) Olsen, G.H., Ettenberg, M., and D'Aiello, R.V., *Appl. Phys. Lett. 33*, 606 (1978).

(140) Moon, R.L., James, L.W., VanderPlas, H.A., and Nelson, N.J., *Appl. Phys. Lett. 33*, 196 (1978).

(141) Nelson, N.J., Johnson, K.K., Moon, R.L., VanderPlas, H.A., and James, L.W., *Appl. Phys. Lett. 33*, 26 (1978).

(142) Sahai, R., Edwall, D.D., and Harris, J.S., *Appl. Phys.
       Lett. 34,* 147 (1979).

(143) Card, H.C., Yang, E.S., and Panayotatos, P., *Appl. Phys.
       Lett. 30,* 643 (1977).

(144) Ponpon, J.P., and Siffert, P., *J. Appl. Phys. 47,* 3248
       (1976).

(145) Ponpon, J.P., Stuck, R., and Siffert, P., Proc. 12th IEEE
       Photovoltaic Spec. Conf., pp. 900-903. IEEE, New York,
       1976.

(146) Lillington, D.R., and Townsend, W.G., *Appl. Phys. Lett.
       28,* 97 (1976).

(147) Childs, R., Fortuna, J., Geneczko, J., and Fonash, S.J.,
       Proc. 12th IEEE Photovoltaic Spec. Conf., pp. 862-867.
       IEEE, New York, 1976.

(148) Kipperman, A.H.M., and Omar, M.H., *Appl. Phys. Lett. 28,*
       620 (1976).

(149) Vernon, S.M., and Anderson, W.A., *Appl. Phys. Lett. 26,*
       707 (1975).

(150) Delahoy, A.E., Anderson, W.A., and Kim, J.K., in "Photo-
       voltaic Solar Energy" (Strub, A., Ed.), pp. 308-318.
       D. Reidel, Holland, 1977.

(151) Munz, P., and Bucher, E., Proc. 13th IEEE Photovoltaic
       Spec. Conf., pp. 761-766. IEEE, New York, 1978.

(152) Matsunami, H., Matsumoto, S., and Tanaka, T., Proc. 12th
       IEEE Photovoltaic Spec. Conf., pp. 917-919. IEEE, New
       York, 1976. Also, *Japan. J. Appl. Phys. 16,* 1491 (1977).

(153) Fabre, E., Michel, J., and Baudet, Y., Proc. 12th IEEE
       Photovoltaic Spec. Conf., pp. 904-906. IEEE, New York,
       1976.

(154) Fabre, E., *Appl. Phys. Lett. 29,* 607 (1976).

(155) Peckerar, M., Lin, H.C., and Kocher, Proc. Intern. Electron
       Dev. Mtg., Washington, pp. 213-216. IEEE, New York, 1975.

(156) Fabre, E., and Baudet, Y., in "Photovoltaic Solar Energy" (Strub, A., Ed.), pp. 178-186. D. Reidel, Holland, 1977.

(157) Stirn, R.J., (unpublished).

(158) Stirm, R.J., and Yeh, Y.C.M., *Appl. Phys. Lett. 27,* 95 (1975).

(159) Stirn, R.J., and Yeh, Y.C.M., Proc. 11th IEEE Photovoltaic Spec. Conf., pp. 437-438. IEEE, New York, 1975.

(160) Stirn, R.J., and Yeh, Y.C.M., IEEE Trans. Electron Dev. *ED-24,* 476 (1977).

(161) Stirn, R.J., and Yeh, Y.C.M., Proc. 12th IEEE Photovoltaic Spec. Conf., pp. 883-892. IEEE, New York, 1976.

(162) Dupuis, R.D., Dapkus, R.D., Yingling, R.D., Moudy, L.A., Johnson, R.E., and Campbell, A.G., Proc. 19th Electronic Mat. Conf., Cornell Univ. IEEE, New York, 1977.

(163) Stirn, R.J., and Yeh, Y.C.M., Proc. 10th IEEE Photovoltaic Spec. Conf., pp. 15-24. IEEE, New York, 1974.

(164) Yeh, Y.C.M., and Stirn, R.J., Ref. 259, pp. 391-397.

(165) Ghandhi, S.K., Borrego, J.M., Reep. D., Hsu, Y.S., and Pando, K.P., *Appl. Phys. Lett. 34,* 699 (1979).

(166) Grinmeiss, H.G., and Memming, R., *J. Appl. Phys. 33,* 217 (1962).

(167) Bonnet, D., in "Photovoltaic Solar Energy" (Strub, A., Ed.), pp. 630-637. R. Reidel, Holland, 1977.

(168) Bell, R.O., Serreze, H.B., and Wald, F.V., Proc. 11th Photovoltaic Spec. Conf., pp. 497-502. IEEE, New York, 1975.

(169) Ponpon, J.P., and Siffert, P., *Rev. Phys. Appl. 12,* 427 (1977).

(170) Lebrun, J., *Rev. Phys. Appl. 1,* 204 (1966).

(171) Trivich, D., Wang, E.Y., Komp, R.J., and Ho, F., Proc. 12th IEEE Photovoltaic Spec. Conf., pp. 875-878. IEEE New York, 1976.

(172) Abdullaev, G.B., Akhundov, M.R., and Akundov, G.A., *Phys. Stat. Sol. 16,* 209 (1966).

(173) Segura, A., Besson, J.M., Chevy, A., and Martin, M.S.,
Il Nuovo Cim. 38B, 345 (1977).

(174) Matsushita, T., Suzuki, A., Okuda, M., and Nang, T.T.,
Japan. J. Appl. Phys. 15, 2461 (1976).

(175) Clemen, C., Saldana, X.I., Munz, P., and Bucher, E.,
Phys. Stat. Sol. (a) 55, (1979).

(176) Clemen, C., Moller, A., Munz, P., Honigschmid, J., and
Bucher, E., in "Photovoltaic Solar Energy" (Strub, A., Ed.)
pp. 638-643. D. Reidel, Holland, 1977.

(177) Catalano, A., Dalal, V., Fagen, E.A., Hall, R.B., Masi,
J.V., Meakin, J.D., Warfield, G., Convers Wyeth, N.,
and Barnett, A.M., Proc. 13th IEEE Photovoltaic Spec.
Conf., pp. 288-293. IEEE, New York, 1978.

(178) Borschevskii, A.S., Lebedev, A.A., Maltseva, I.A.,
Ovezov, K., Rud, Y.V., and Undalov, Y.K., *Sov. Phys.-
Semicond. 10,* 934 (1976).

(179) Lebedev, A.A., Ovezov, K., and Rud, Y.V., *Sov. Phys.-
Semicond. 10,* 78 (1976).

(180) Grigoreva, V.S., Lebedev, A.A., Ovezov, K., Prochukhan,
V.D., Rud, Y.V., and Yakovenko, A.A., *Sov. Phys.-Semicond.
9,* 1058 (1975).

(181) Lebedev, A.A., Ovezov, K., Prochukhan, V.D., and Rud,
Y.V., *Sov. Phys.-Techn. Phys. Lett. 1,* 93 (1975).

(182) Bulyarskii, S.V., Koval, L.S., and Radautsan, S.I.,
Proc. All Union Conf. Ternary Semicond. and Appl.,
pp. 165-168. Izd. Shtiintza, Kishinev, 1976.

(183) Charlson, E.J., and Lien, J.C., *J. Appl. Phys. 46,* 3982
(1975).

(184) VanHalen, P., Mertens, R., Van Overstraeten, R., Thomas,
R.E., and VanMeerbergen, in "Photovoltaic Solar Energy"
(Strub, A., Ed.) pp. 280-288. D. Reidel, Holland, 1977.
Also, Proc. 12th IEEE Photovoltaic Spec. Conf., pp. 907-
912. IEEE, New York, 1976.

(185)   Green, M.A., and Godfrey, R.B., in "Photovoltaic Solar
        Energy" (Strub, A., Ed.), pp. 299-307. D. Reidel, Holland,
        1977.

(186)   Green, M.A., and Godfrey, R.B., *Appl. Phys. Lett. 29*, 610
        (1976).

(187)   Pulfrey, D.L., *Solid-State Electron. 20,* 455 (1977).

(188)   St. Pierre, J.A., Singh, R., Shenchun, J., and Loferski,
        J.J., Proc. 12th IEEE Photovoltaic Spec. Conf., pp. 847-
        853. IEEE, New York, 1976.

(189)   Ponpon, J.P., and Siffert, P., *J. Appl. Phys. 47*, 3248
        (1976).

(190)   Charlson, E.J., and Richardson, W.F., Proc. 13th IEEE
        Photovoltaic Spec. Conf., pp. 656-660. IEEE, New York,
        1978.

(191)   Lillington, D.R., and Townsend, W.G., *Appl. Phys. Lett. 31,*
        471 (1977).

(192)   Anderson, W.A., "Silicon Photovoltaic Devices for Solar
        Energy Conversion" Final Rep., June 1976-May, 1978.
        ERDA, Washington, 1978.

(193)   Godfrey, R.B., and Green, M.A., *Appl. Phys. Lett. 34,* 790
        (1979).

(194)   Anderson, W.A., Delahoy, A.E., Kim, J.S., Hyland, S.H.,
        and Dey, S.K., *Appl. Phys. Lett. 33,* 588 (1978).

(195)   Fabre, E., Michel, J., and Baudet, Y., Proc. 12th IEEE
        Photovoltaic Spec. Conf., pp. 904-907. IEEE, New York,
        1976.

(196)   Tarr, N.G., Pulfrey, D.L., and Iles, P.A., *Appl. Phys.
        Lett. 35,* 258 (1979).

(197)   Maeda, Y., *Appl. Phys. Lett. 33,* 301 (1978).

(198)   Neugroschel, A., *IEEE Trans. Electron. Dev. ED-27*, 287
        (1980).

(199)   Matsunami, H., Oo, K., Ito, H., and Tanaka, T., *Japan. J.
        Appl. Phys. 14,* 915 (1975).

(200) Hsu, L., and Wang, E.Y., in "Photovoltaic Solar Energy"
       (Strub, A., Ed.) pp. 1100-1108. D. Reidel, Holland, 1977.

(201) Nagatomo, T., and Omoto, O., *Japan. J. Appl. Phys. 15,*
       199 (1976).

(202) DuBow, J.B., Burk, D.E., and Sites, J.R., *Appl. Phys.*
       Lett. 29, 494 (1976).

(203) Burk, D.E., DuBow, J.B., and Sites, J.R., Proc. 12th IEEE
       Photovoltaic Spec. Conf., pp. 971-974. IEEE, New York,
       1976.

(204) Manifacier, J.C., Szepessy, L., and Savelli, M., in
       "Photovoltaic Solar Energy", pp. 289-298. D. Reidel,
       Holland, 1977.

(205) Manifacier, J.C., and Szepessy, L., *Appl. Phys. Lett. 31,*
       459 (1977).

(206) Franz, S., Kent, G., and Anderson, R.L., *J. Electron.*
       Mat. 6, 107 (1977).

(207) Perotin, M., Szepessy, L., Manifacier, J.C., Parot, P.,
       Fillard, J.P., and Savelli, M., in "Solar Electricity",
       pp. 481-492. Maison des Congres, Toulouse, 1976.

(208) Kato, H., Yoshida, A., and Arizumi, *Japan. J. Appl. Phys.*
       15, 1819 (1976).

(209) Nash, T.R., and Anderson, R.L., Proc. 12th IEEE Photo-
       voltaic Spec. Conf., pp. 975-977. IEEE, New York, 1976.

(210) Kato, H., Fujimoto, J., Kanda, T., Yoshida, A., and
       Arizumi, T., *Phys. Stat. Sol. (a) 32,* 255 (1975).

(211) Cheek, G., Ellsworth, D., Genis, A., and DuBow, J.B.,
       J. Electron. Mat. 8, (1979).

(212) Ghosh, A., (Ed.), "Heterojunction Single Crystal Silicon
       Photovoltaic Cell", Quarterly Reports, Sept. 1976-
       Nov. 1977. ERDA, Washington, 1977.

(213) DuBow, J.B., (Ed.) "Characteristics of OSCS Solar Cells",
       Quarterly Rept., March 1977. ERDA, Washington, 1977.

(214) Schunck, J.P., and Coche, A., *Appl. Phys. Lett. 35*, 863 (1979).

(215) Feng, T., Ghosh, A.K., and Fishman, C., *Appl. Phys. Lett. 35*, 266 (1979).

(216) Kazmerski, L.L., and Sheldon, P., Proc. 13th IEEE Photovoltaic Spec. Conf., pp. 541-544. IEEE, New York, 1978.

(217) Bachmann, K.J., Sinclair, W.R., Thiel, F.A., Schreiber, H., Schmidt, P.H., Spencer, E.G., Buehler, E., and SreeHarsha, K., Proc. 13th IEEE Photovoltaic Spec. Conf., pp. 524-527. IEEE, New York, 1978.

(218) Wang, E.Y., and Legge, R.N., Proc. 12th IEEE Photovoltaic Spec. Conf., pp. 967-970. IEEE, New York, 1976.

(219) SreeHarsha, K., Bachmann, K.J., Schmidt, P.H., Spencer, E.G., and Thiel, F.A., *Appl. Phys. Lett. 30,* 645 (1977).

(220) Okuda, M., Nang, T.T., Matsushita, T., and Yokota, S., *Japan. J. Appl. Phys. 14,* 1597 (1975).

(221) Nang, T.T., Matsushita, T., Okunda, M., and Suzuki, A., *Japan. J. Appl. Phys. 16,* 253 (1977).

(222) Fahrenbruch, A.L., Aranovich, J., Courrages, F., Yin, S.Y., and Bube, R.H., in "Photovoltaic Solar Energy" (Strub, A., Ed.), pp. 608-617. D. Reidel, Holland, 1977.

(223) Carlson, D.E., and Wronski, C.R., *Appl. Phys. Lett. 28*, 671 (1976).

(224) Carlson, D.E., and Wronski, C.R., *J. Electron. Mat. 6,* 95 (1977).

(225) Busmundrud, O., and Jayadeviah, T.S., *Phys. Stat. Sol. (a) 11*, K47 (1972).

(226) Mizrah, T., and Adler, D., *IEEE Trans. Electron. Dev. 24,* 458 (1977).

(227) Carlson, D.E., *IEEE Trans. Electron. Dev. ED-24,* 449 (1977).

(228) Carlson, D.E., Proc. DOE/SERI Photovoltaics Adv. R&D Annual Rev. Mtg., Denver, pp 113-120. SERI, Golden, Co.

(229) Hamakawa, Y., Okamota, H., and Nitta, Y., *Appl. Phys. Lett. 35*, 187 (1979).

(230) See, for example, Stone, J., in Ref. 228, pp. 69-112.

(231) Spear, W.E., and LeConber, P.G., *Solid-State Comm. 17*, 1193 (1975).

(232) Wilson, J.I.B., McGill, J., Kinmond, S., *Nature 272*, 153 (1978).

CHAPTER 16

RESEARCH AND DEVICE PROBLEMS IN PHOTOVOLTAICS

Lawrence Kazmerski

Photovoltaics Branch
Solar Energy Research Institute
Golden, Colorado

I. INTRODUCTION

The state-of-the-art in photovoltaics has been advancing quite
rapidly, especially with the increased emphasis put on this tech-
nology by the U.S. government (1,2). Because of this, it is ex-
pected that some of the problems underscored in this chapter will
be resolved before publication of this book. It is the intent of
this chapter to focus on *some* current photovoltaic research prob-
lems, relating technical barriers and probable areas of future
work. Some effort has been made to present those that are consid-
ered most critical to the development of photovoltaics into a
viable energy alternative. Therefore, attention is directed toward
the status and problems of a pair of technologies that have the
predicted application potential discussed in the previous chapter
(3): intermediate-efficiency, *thin-film* solar cells (including
amorphous and polycrystalline Si, GaAs, CdS-based devices, and
some emerging materials) and high-efficiency, *concentrator* devices
of both multijunction and multidevice types. Throughout this over-
view, the problems associated with the major defect in the polycrys-
talline device--the *grain boundary*--are emphasized, both in terms
of the effects of these regions upon device performance and also

551

in terms of research into circumventing the limits they place on efficient photovoltaic conversion. In addition, the importance of research into the detection of device/materials degradation mechanisms is stressed, since *reliability* and *device lifetime* are of an importance equal to *efficiency* in the eventual deployment of solar cells.

II. OVERVIEW OF RESEARCH PROBLEMS AND TECHNOLOGIES

A. Thin Films

Research on thin-film solar cells has centered in two important areas: (i) the *improvement of materials and device properties* in order to optimize solar cell performance; and, (ii) the *identification of new photovoltaic materials* and the demonstration of device feasibility for these candidate materials. This section examines these R&D activities, emphasizing the areas of needed work.

1. Amorphous Silicon. Research on this material really began in the late 1960s with the published work of Sterling on dis-

TABLE 1. *Status of Several Major Amorphous Si Solar Cells*

Type/Structure[d]	$V_{oc}(V)$	J_{sc} (mA/cm^2)	ARC	$\eta(\%)$	Area (cm^2)	Source
Pt-i-n⁺	0.803	12	yes	5.5[a]	0.02	Ref. 14
Pt-SiO₂-p-i-n	0.770	7	no	3.3[a]	1.6	Ref. 17
ITO-p⁺-i-n⁺	0.560	12	yes	4.5[b]		Ref. 96
Pt-i-n⁺	0.500	15	no	4.3[a]		Ref. 19
n⁺-i-P⁺-Cr	0.670	9.3	no	3.4[a]		Ref. 13
Ni-TiO_x-i-n⁺	0.630	7.5	yes	4.8[c]	0.02	Ref. 95

a. 100 mW/cm²   c. 60 mW/cm²

b. 80 mW/cm²   d. stainless steel substrates

charge-produced amorphous silicon (a-Si) (4,5). It was determined
that the density of energy gap states was several orders of mag-
nitude lower in discharge-produced A-Si than in its evaporated
counterpart (6). The first photovoltaic devices were actually
fabricated from a-Si in 1974 (7). However, in 1975 this discharge-
produced material was shown to actually be an a-Si/hydrogen alloy
(a-Si:H) (8), and the hydrogen (5-50 atomic-%) accounted for the
reduction in gap state density (9). Recent research on discharge-
produced a-Si alloys has included the use of oxygen (10) - a
bridging atom that heals defects, carbon (11), and fluorine (12) -
a highly electronegative element that eliminates unfavorable bond-
ing, to further reduce unwanted gap states.

From the first report of the doping (n- or p-type) of a-Si:H
(13), a variety of device types have been investigated (see Table
1). The theoretical efficiency limit has been calculated to be
~15% for this material (14), but the best device produced to-date
remains the MIS structure reported by Carlson in 1975 (15) for a
small area cell. (Large area devices have been typically <4%.)
A more rapid advancement of the a-Si photovoltaic technology has
been largely impeded by a lack of knowledge of many of the basic
physical, structural, electrical, and optical properties of this
relatively new material, and some seemingly severe materials limi-
tations that must be overcome to provide efficient and reliable
devices.

Foremost among these *materials problems* is that of rather poor min-
ority-carrier transport. Although the hole diffusion length has
recently been *estimated* to be ~ 400Å in *undoped* a-Si:H (16) and
the hole lifetime *appears* to be of the order of 1 ns, little has
been accomplished in either measuring these parameters precisely
or controlling them. Since the hole diffusion length is limited,
the resulting efficiencies of cells are likewise constrained by
small depletion widths of the order of 0.2 μm under AM1 conditions.
The necessity and value of increasing the depletion width by fur-
ther lowering the space-charge density has recently been demon-

strated in p-i-n a-Si:H cells (17). Thus, the undoped a-Si need
not have a very large hole diffusion length *if* a significant frac-
tion of the incident radiation can be made to be absorbed in the
depletion layer.

A large number of the materials problems associated with a-Si:H
relate to the preparation of the material. For example, a-Si:H can
be prepared by glow discharge (RF or DC), reactive sputtering,
electrodeposition, ion-plating, CVD, evaporation with either
in-situ or post-deposition hydrogenation and ion-implantation.
However, it is difficult to control the Si-H bonding types (18),
and little is known about either the gas-solid interactions during
a-Si:H formation or the growth kinetics of the material. In gener-
al, there are a large number of growth parameters that affect in
varying degree the quality of the material produced. In this
relation, control of defects and impurities is difficult (e.g.,
the built-in potential of p-i-n devices is limited to ~1.1V by
the poor quality of the doped material (17), providing V_{oc} <0.85V).
In fact, the roles of both impurities and modifiers (i.e., H, O,
F, etc.) are not well understood. A good deal of work remains to
be done in optimizing the experimental parameters (19).

In order to solve many of the problems with a-Si based solar
cells, the *materials/device characterization* base must be expanded.
In most cases, conventional semiconductor measurement technologies
(e.g., single-crystal Si related) are not sufficient. For example,
no *reliable* methods exist for determining either the density of
gap states or the *exact* hydrogen content of films[1]. At best, it is
difficult to measure the minority-carrier lifetimes and diffusion
lengths, a procedure very necessary to solving some of the trans-
port problems. Theoretical understanding of any of these phenomena
is limited or nonexistent. Finally, for this technology especial-
ly, there is a need to establish relationships between the materi-

---

[1]*Presently, secondary ion mass spectroscopy (SIMS) is the
most dependable, straightforward technique.*

als parameters and the resulting photovoltaic properties. Almost
no work exists in this area, and most results await the develop-
ment of special measurement techniques specifically designed for
this material.

To date, a-Si solar cells have attained respectable open-cir-
cuit voltages (20). However, fill-factors have been low, partly
due to the high series resistance (contact and material caused)
of the devices. However, even if the fill-factor were limited to
0.6, a 10% efficient device can be expected if the small drift
component of current can be improved (e.g., by increasing the
width of the depletion region under illumination).

Amorphous solar cells, like all thin-film devices, are con-
trolled in many cases by the numerous interfaces that are inher-
ent to the complex device structures (21). However, little re-
search has been done on detecting impurities and contaminants at
these interfaces (e.g., using surface analysis techniques (22))
and determining their role on interface state densities and de-
vice performance. The performance of a-Si:H devices could be im-
proved significantly *if* a wide bandgap, conductive p^+-layer could
be developed (17). Thus, high built-in voltages (open-circuit
voltages) and reasonably light transmission (higher short-circuit
currents) could result.

Finally, and equally important, there is a need to determine
the stability and reliability of these devices. No in-depth
studies have been performed to-date, primarily due to the obvious
and justifiable emphasis on developing and demonstrating working
devices. However, as the performance of a-Si devices improve, the
mechanisms of degradation must be uncovered in order to ascertain
15-20 year lifetimes for commercial devices.

In summary, the important areas for future research include:

- Improvement of minority carrier lifetimes and diffusion
  lengths;
- Better understanding of transport phenomena;
- Development and understanding of the density of states;

- Determination of the nature of chemical bonding;
- Understanding of impurities (incorporation, effects);
- Studies of surface states at interfaces;
- Control of deposition parameters, reactions at gas-solid interfaces;
- Development of theoretical base;
- Development of special measurement techniques; and
- Determination of degradation mechanisms/device reliability.

2. *Polycrystalline Silicon.* In the development of an *inexpensive* solar cell for *terrestrial applications,* the use of thin-film Si seems a logical choice due to the large amount of information available on the well-developed single-crystal device, and to the abundance of the element itself. Early work centered on the fabrication of films and devices on inexpensive, non-silicon substrates. Fang *et al.* produced films on aluminum by electron beam evaporation (23). Above 577°C an Si-Al eutectic is formed, and the growth of large-grained films (with columnar grain characteristics under some conditions) has been demonstrated. However, device efficiencies have been insufficient. Chu *et al.* have investigated the fabrication of homojunction devices using CVD on several low-cost substrates including steel (24,25), graphite (25-28), and metallurgical grade polycrystalline silicon (25,28-30). To date, the best thin-film device produced is represented by the J-V characteristics shown in Fig. 1. This polycrystalline solar cell has a respectable area (9 cm^2) and a 9.75% AM1 efficiency. The device configuration is also presented in this figure. However, the potential of the *thin-film polycrystalline Si* device remains high (31-33). Silicon maintains its premier position substantially because of its great abundance. Compared to the amorphous Si cell, thin-film polycrystalline Si promises about a 50% better performance, using a two-pass light analysis for a 5 μm layer (34).

Two questions often arise for the thin-film polycrystalline Si solar cell:

- What is *thin-film?*
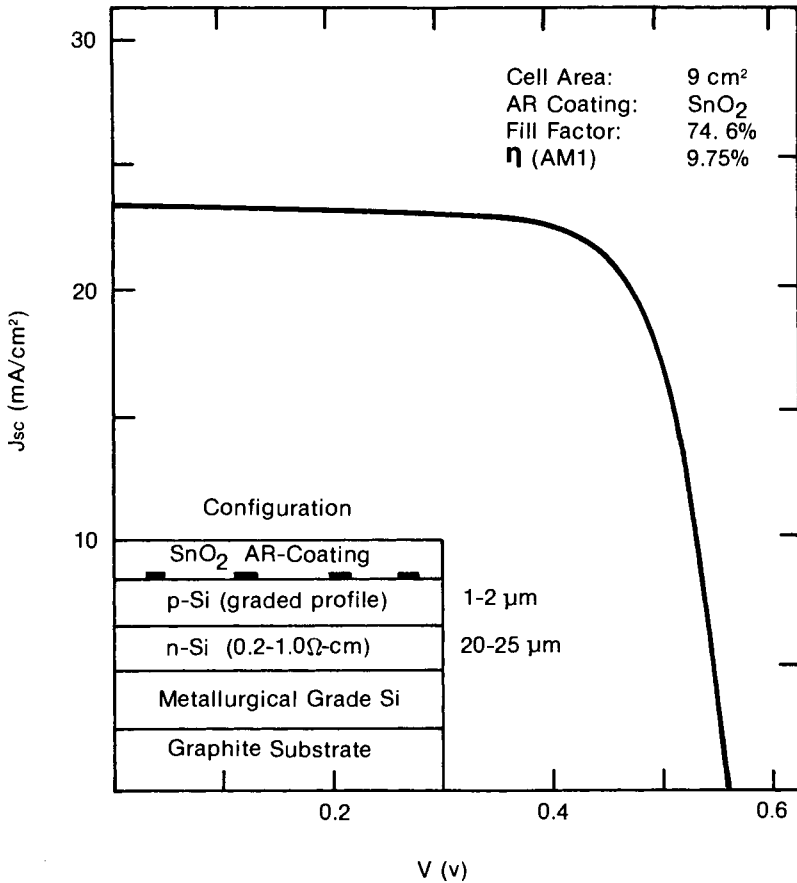
FIGURE 1.   9.75% AM1 polycrystalline Si thin-film solar cell from Chu, et al., ref. 97).

• What is the effect of *grain size?*

The first is difficult to answer either unequivocably or authori-
tatively. A good portion of advanced Si device R&D is being per-
formed on heterojunction, MIS and SIS structures fabricated on
thick (bulk) polycrystalline material (35,36). An example of this
is the work of Shewchun *et al.*, who have produced >9.6% (total
area, AM1) ITO (thin-film)/Si (polycrystalline) devices using
cast material provided by Wacker in Germany (36,37). The sub-
strates in these investigations are typically ~10^3 μm in thickness,

with grain sizes in the 2-10 mm range. The technique used to pro-
duce this material (casting followed by wafer slicing) is a *bulk*
rather than a *thin-film* scheme.

The effect of layer *thickness* upon solar cell performance is
twofold: (i) for thinner layers, especially for indirect bandgap
materials such as Si, there is an increasing loss through nonab-
sorption of the incoming radiation; and, (ii) the back contact
becomes critical. If the minority-carrier diffusion length is
comparable or greater than the device thickness, the collection
efficiency is reduced and the dark current increases due to the
excess recombination of both the photogenerated and dark injected
carriers at the back contact. The thickness influence on Si de-
vice performance is illustrated in Fig. 2 (38). The short-circuit
current density is shown as a function of thickness for an n/p
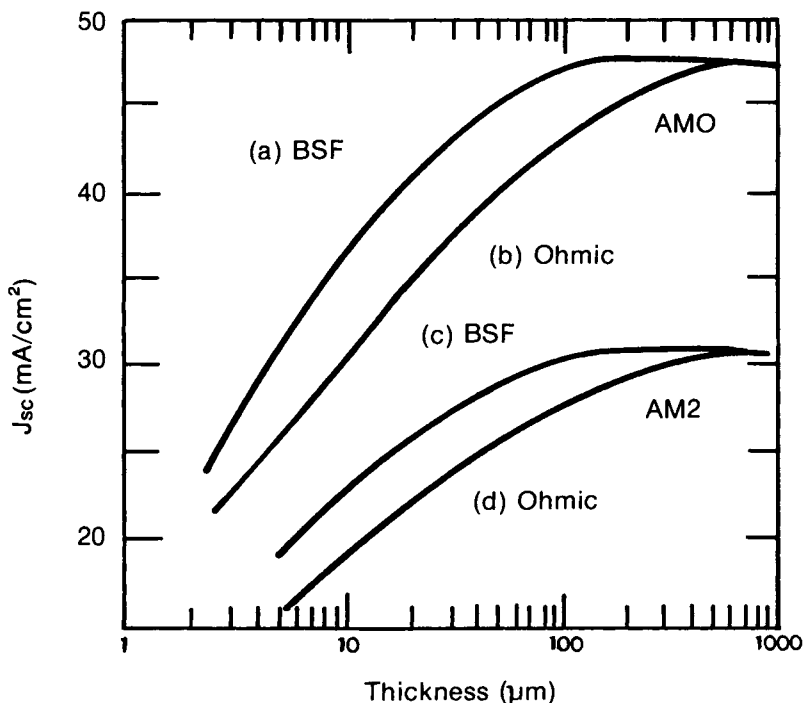
FIGURE 2. *Short-circuit density dependence upon thickness
for an n/p homojunction under AM0 and AM1 conditions (from Hovel,
ref. 38).*

homojunction under AMO and AM2 conditions. For an ohmic back con-
tact, the short-circuit current density is observed to drop for a
thickness less than 500 μm under AM2 conditions. By improving the
back contact, incorporating a back-surface-field (BSF), the thick-
ness influence onset can be seen to begin at ~100 μm. It should be
stressed, however, that the calculations used to generate Fig. 2
consider a *constant* minority-carrier diffusion length. Some recent
work by D'Aiello and Robinson (39) has shown that the actual dif-
fusion length can be much less than expected in their epitaxial
films. As a result, *thinner* layers (15 μm *vs.* 50 μm) actually lead
to somewhat better devices (primarily reflected in higher V_{oc}) for
their material. Defining a thickness-range for "*thin-film* Si solar
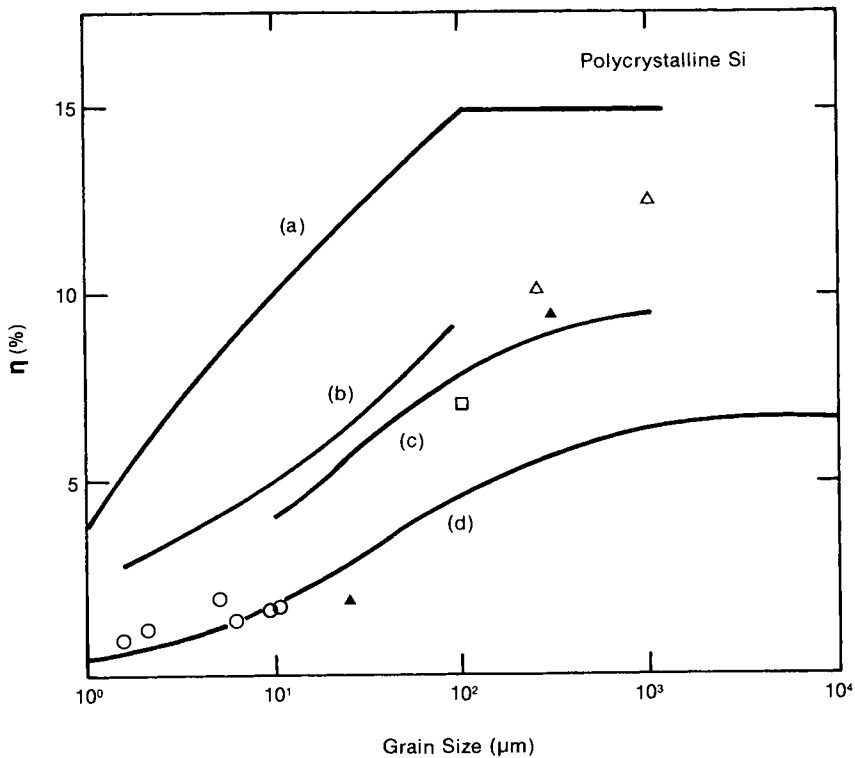
FIGURE 3. *Grain size dependence of efficiency for polycrys-
talline Si (a) ref. 43; (b) ref. 42; (c) ref. 41; and, (d) ref.
40.*
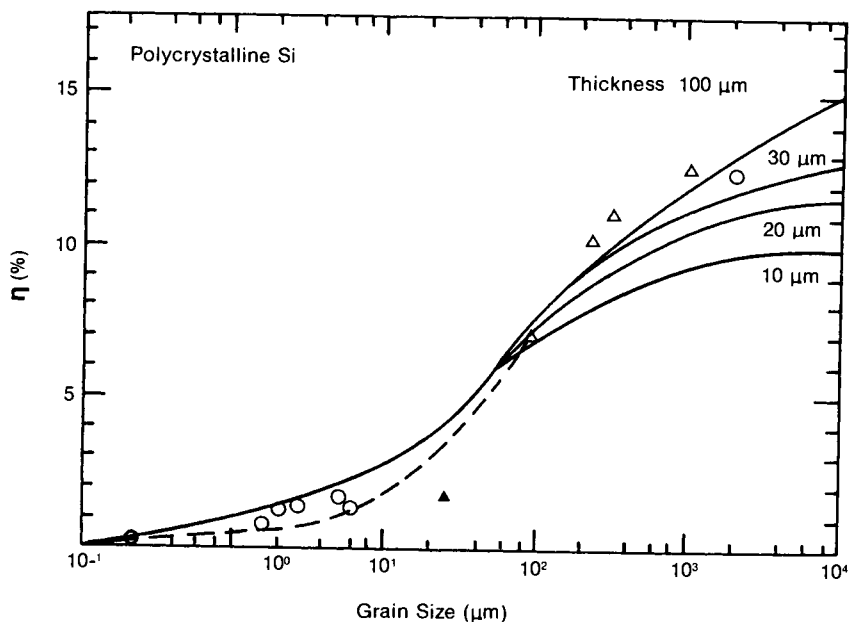
FIGURE 4.   Polycrystalline Si solar cell efficiency depend-
ence on grain size, after calculations of Ghosh, et al.,ref. 44.

cells" is difficult and somewhat arbitrary. But for the purpose of
this chapter, cells less than 100 μm in thickness will satisfy the
criterion for silicon.

The limiting effects of *grain size* on polycrystalline Si solar
cell performance have been studied (40-44). Fig. 3 presents the
results of several investigations for a variety of device types.
Recently, Ghosh *et al.* (44) presented a unified theory of grain
size effects. Their calculations of the dependence of efficiency
on grain size are shown in Fig. 4, with some representative data
points included. The calculations for 100-, 30-, 20-, and 10-μm
thick layers are presented. From Fig. 4, it is predicted that *at
least* 150 μm grain sizes are needed for >10% efficient devices.
Using the data of Fig. 4, one can generate a dependence of thick-
ness on grain size for a 10% efficient polycrystalline device.
These data, presented in Fig. 5, indicate that in the case of
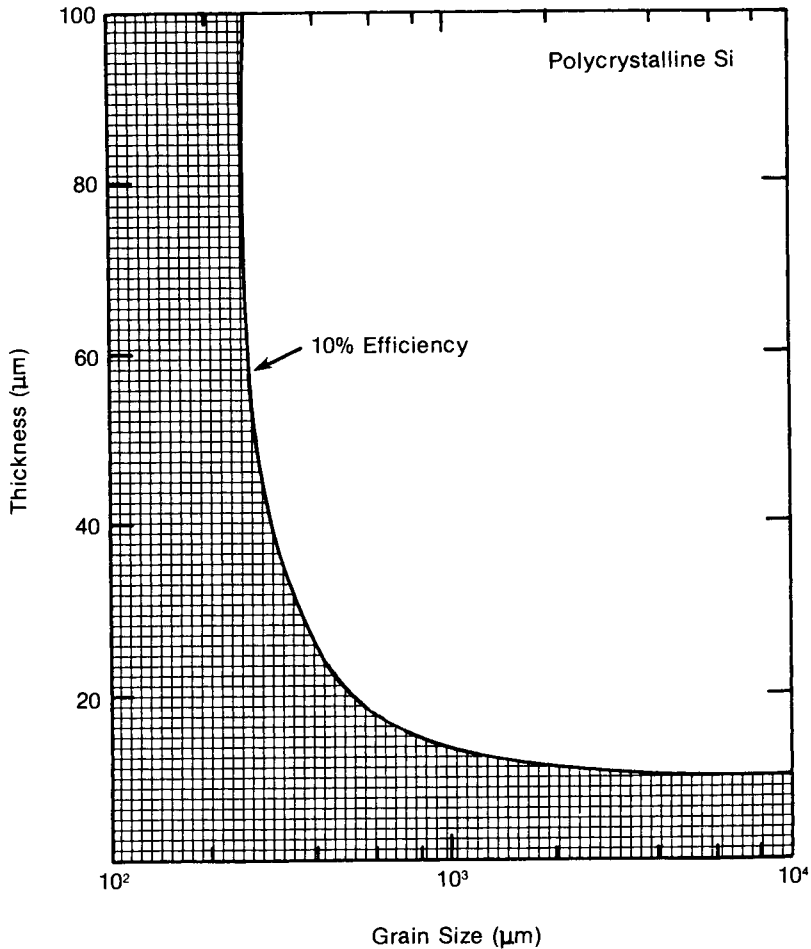
FIGURE 5. Relationship between thickness and grain size for
a 10% (AM1) efficient solar cell.

smaller grain sizes, *recombination at the grain boundaries* must be
reduced if the polycrystalline devices are to realize the 10% ef-
ficiency goal. Methods and the status of such attempts at reducing
grain boundary recombination (i.e., passivation schemes) are dis-
cussed later in this book by D. Ginley (45).

Research in the polycrystalline Si solar cell area presently
has three major thrusts:

• materials development,

- device development, and
- basic studies.

The performance of the polycrystalline Si solar cell depends upon
the *quality* of the material used in its fabrication. The *first
quality factor* is that of impurity content of the starting materi-
al. Chu *et al.* build their devices (see Fig. 1) on a deposited met-
allurgical grade Si layer that has been subjected to a *potentially*
inexpensive acid-leaching purification procedure (30). Although
the procedure has been shown to be effective from a device fabrica-
tion viewpoint, more remains to be learned about the chemistry,
cost, and control of the process. Other research programs are con-
cerned with the purification of metallurgical grade Si into a low-
cost *solar grade* that can serve as a source for either film or
substrate growth (46). The *second quality factor* is that of materi-
al crystallinity and reducing losses at grain boundaries. A major
portion of present polycrystalline Si research is dictated by find-
ing, evaluating, and characterizing various thin-film growth tech-
niques for producing large grain size films on low-cost substrates.
The methods vary from epitaxy (39) (i.e., controlling and maximiz-
ing grain size *during* growth) to annealing (30,46) (i.e., post-
deposition treatments). For those cases in which grain size limi-
tations seem inevitable, passivation schemes are of interest (45,
47-49). Foremost among the present developments are those that
make use of the enhanced diffusion that occurs along the grain
boundaries to selectively chemically modify these regions using
hydrogen or other chemical species (47-49).

Actually, very little current research is concerned with *thin-
film* polycrystalline Si. As previously indicated, most non-single-
crystal silicon research is being performed on *bulk* polycrystal-
line-produced material. Several reasons can be cited. *First*, de-
vice quality thin-film Si is difficult to produce on foreign (i.e.,
non-Si) substrates - especially if low-cost materials are used.
(It should be added that the search for *low-cost* substrates for
these thin-film devices forms a research area in itself.) *Second*,

there has been more emphasis by research groups in this area on developing and optimizing the solar cell structures (MIS, SIS, heterojunction, homojunction) that are compatible with polycrystalline material in order to provide reasonable efficiencies. It is easier to do this in a controllable and reproducible manner on the bulk polycrystalline (e.g., cast) material, rather than fighting the inconsistencies of smaller grain size thin-film Si. This approach is advantageous for optimizing the chemical, structural, and electrical properties of the insulating layers in the MIS and SIS devices. Some better indications of the limitations to polycrystalline solar cell performance are also obtainable. However, these devices are *not* thin-film solar cells and investigators are aware that grain boundaries, oxide growths, diffusion mechanisms, material quality, *etc.,* in *bulk* polycrystalline semiconductors differ from those encountered in *thin* polycrystalline films (50).

Because the polycrystalline state presents a multitude of unknowns and differences from the crystalline state, a good portion of present research on solar cells is dedicated to more *basic research*. Most of this basic work is directed toward understanding the mechanisms that are influenced or controlled by the grain boundaries. There is an obvious need to develop new measurement techniques to characterize the structural, compositional, electrical, and optical properties of polycrystalline Si in terms of cell performance. The electrical transport processes have received much attention in the recent past (51). However, much remains to be accomplished in modeling grain boundary effects and correlating these "models" with direct and comprehensive measurements. It is possible that such activity can lead to the development of theoretical predictions of the fundamental photovoltaic mechanisms that control and limit the polycrystalline Si solar cell conversion efficiency.

   3. Thin-Film GaAs. The cost-practicability of using thin-film (polycrystalline) GaAs in a nonconcentrating solar cell array is

still somewhat doubtful. This is primarily due to the availability
of the constituent elements (52), especially the gallium. However,
there is a reasonable R&D ongoing, dealing with both single-crys-
tal and polycrystalline thin films (53).

Basically, two fabrication approaches are being pursued in the
fabrication of thin-film GaAs solar cells. The *first* involves the
nonepitaxial growth of GaAs on foreign substrates. These films typ-
ically have small grain sizes, with grain diameters approximately
the size of the film thickness. Although the current collection
and resulting short-circuit currents in such devices are reason-
able, the overall device performance is limited by low open-cir-
cuit voltages and relatively high series resistances (poor fill-
factors). Therefore, there is a need to develop reliable grain
boundary passivation schemes for these films and devices. The
second approach involves the *epitaxial* growth of GaAs on suitable
substrates. This fosters the production of either single-crystal
or large grain size films, in order to minimize or avoid the com-
plicating effects imposed by the boundary regions. In some cases,
this second approach involves the recrystallization of thin layers
(e.g., Ge) deposited on metal substrates to provide the suitable
surface on which the epitaxial growth of the GaAs is initiated
(54). In other cases, the recrystallization of the GaAs layer it-
self is accomplished using laser techniques (54-56).

The trend in poly-GaAs research is toward the production of
thinner, device-quality films. This direction dictates that pro-
gress in materials technology must be emphasized. There is some
evidence that the quality of the material within the grain is at
least as important as the grain boundary in limiting device per-
formance (53). Thus, techniques must be developed not only to
minimize grain boundary effects but also to ensure the growth of
defect-free, low-impurity GaAs grains. Research on the nucleation
and growth of GaAs films is needed to provide insight into these
problems. This can lead to the development of processing techni-
ques that promote grain growth and provide grain sizes with later-

al dimensions exceeding the film thickness.

Although progress has been made at grain boundary passivation, this area still needs attention. Ghandhi et al. have reported success with the selective anodization of boundary regions (57,58). This method leaves an oxide "cap" over the grain boundary, and reductions in dark reverse-current densities by six orders of magnitude have been observed shown in Fig. 6 (58). This passivation has resulted in significant improvements in open-circuit voltages ($\Delta V_{oc} \sim 0.3$ V) in these thin-film devices by eliminating grain boundary shorting effects.

Beyond the materials problems, increased research on device processing of these thin polycrystalline cells is needed. Techniques for reliably and reproducibly fabricating p-n junctions remain problem areas - for these as well as other thin-film layers. High-temperature processing must be avoided to minimize material degradation and enhanced grain boundary diffusion (59). MIS structures appear promising, but control of the oxide properties are critical (60). As for any of these thin devices, degradation mechanisms must be identified in order to eventually ensure operating stability (61).
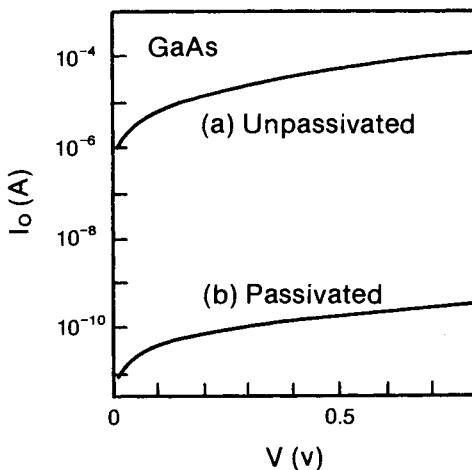
FIGURE 6.   Dark reverse saturation current in polycrystalline GaAs solar cells (from Pande, et al., ref. 58).

   4. CdS-Based Devices. Of the thin-film technologies, the Cu_2S/
CdS technology is the most advanced. From the discovery of the
photovoltaic effect in CdS by Reynolds (62) in 1954, the device
has advanced to exhibit efficiencies in excess of 9% (63). Recent
efforts in the CdS area have been investigating the use of Cu-
ternaries (64-67) and ternary alloys (67-68) in place of the CdS
in order to improve lattice match and material control. These mate-
rials are really in the initial development stages and will not
be emphasized herein. The substitution of Cd(Zn)S for the CdS has
also been instituted, since it provides a better lattice match
with the Cu_2S and a larger bandgap window material (69). Readers
are referred to several reviews of the CdS technologies for in-
depth analyses (63,70,71).

   For these CdS-based solar cells, two device geometries are
used:

- *Frontwall configuration,* in which the sunlight impinges on
  the lower bandgap semiconductor (e.g., Cu_2S, $CuInSe_2$,
  $Cu_xIn_yGa_{1-y}Se_zTe_{1-z}$)
- *Backwall configuration,* in which the illumination is through
  the wide bandgap material (i.e., the CdS or Cd(Zn)S).

These device types are represented in cross section in Fig. 7. The
benefits and limitations of each of these structures have been
thoroughly evaluated (71,72), but the major application of each is
tied to economics (for the Cu_2S cell (63)) or junction formation

A. Frontwall Configuration   **B. Backwall Configuration**
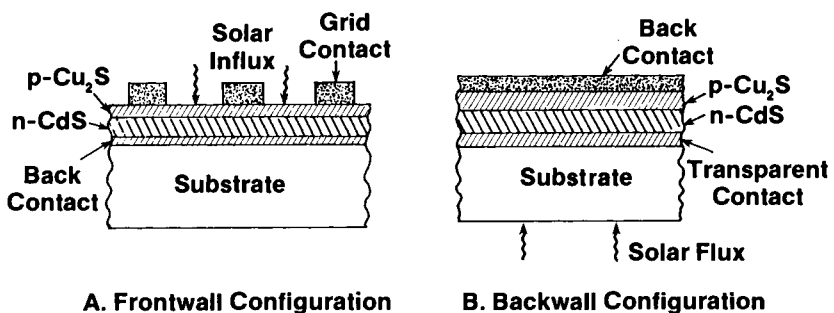
*FIGURE 7. Backwall and Frontwall solar cell configurations
(courtesy of S.K. Deb).*

and degradation (for the Cu-ternary devices (66,74)).

For the Cu_2S/CdS (or $Cd(Zn)S$) thin-film solar cell, two device types have been developed. Their categorization results from the qualitative description of the junction geometry:

• textured cells, and

• planar cells.

The *textured cell* is formed conventionally by etching the CdS layer and subsequently dipping it in a Cu_2Cl_2 solution to form the Cu_2S (71). The resultant junction is highly structured and involves deep intrusions of the Cu_2S into the CdS grain boundaries.
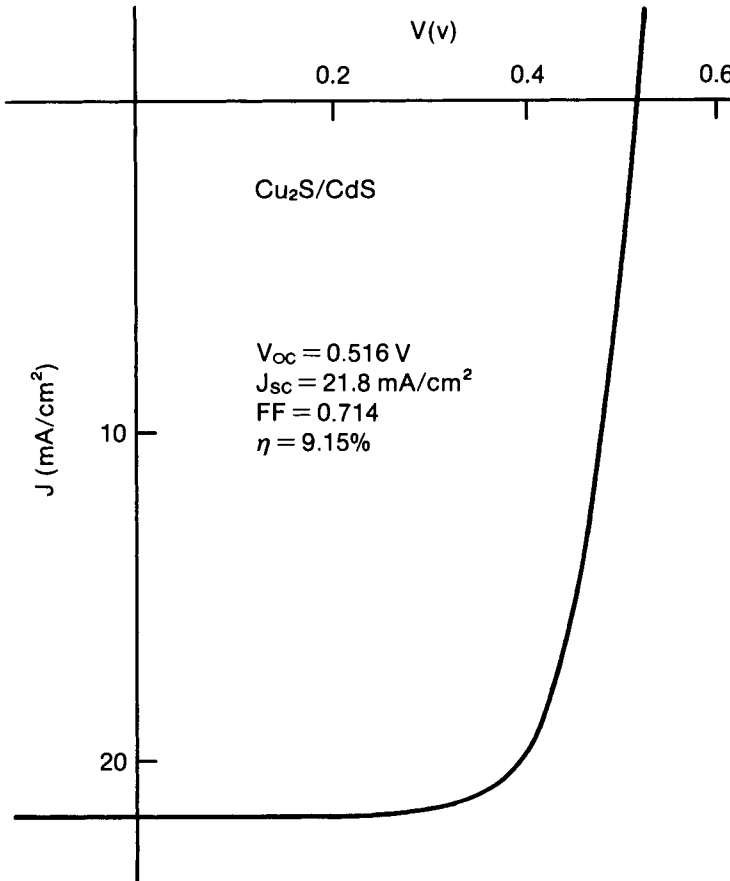
FIGURE 8.   Light J-V characteristics of 9.15% efficient
Cu_2S/CdS solar cell (from Barnett, et al., ref. 63).

Thus, the junction is *textured*. The best device of this type has
a 9.15% AM1 efficiency, and its light J-V characteristics are
shown in Fig. 8. Following an extensive loss detection and mini-
mization scheme, it has been concluded that the near 10% effi-
ciency range is about maximum for this device type, primarily due to
losses of nonuniform carrier generation/collection and shading at
the grain boundary intrusions. Therefore, the *planar configuration*
has evolved. In this, the junction is formed by a solid-state reac-
tion between CdS and a deposited Cu_2Cl_2 film (71). Thus, the grain
boundary penetration problems are minimized. Planar $Cu_2S/Cd(Zn)S$
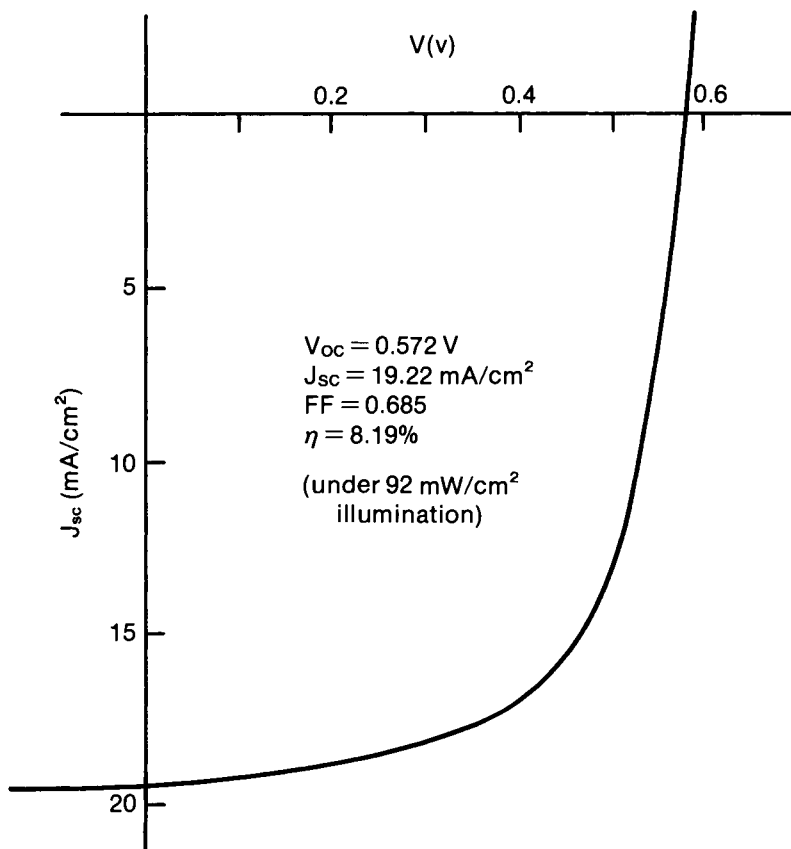
FIGURE 9. Light J-V characteristics of $Cu_2S/Cd(Zn)S$ solar
cell (from Meakin, ref. 71).

cells have reached the mid-8% (AM1) range and a typical character-
istic is shown in Fig. 9. Although these cells have shown good
open-circuit voltages (~0.55V), the major problem has been due to
ineffective light trapping. In order to overcome this, two ap-
proaches are being studied. The *first* involves texturing of the
front surface or the substrate surface in order to minimize re-
flections. The *second* approach is concerned with the development of
more effective antireflection coatings. Primary among these is
the development of two-layer ARCs, of which TiO_x/SiO_2 is present-
ly used, and ZnS (600Å)/MgF (1000Å) is a potential candidate. The
planar $Cu_2S/Cd(Zn)S$ solar cell is expected to reach efficiencies
in excess of 11%.

   Major among the problems of the CdS-based solar cells is de-
vice stability and reliability. Many of the degradation mechanisms
have been identified and solutions have either been implemented
or proposed (33,94). More basic research is needed, however.
Table 2 summarizes some of the leading problems, their effects
and the solutions. However, more R&D activity is needed in this
area. Degradation must be minimized if these devices are to realize
greater than 15-year lifetimes. Some systematic and reliable (!)
accelerated life-testing procedures must be developed. It is ob-
vious that *encapsulation* is critical for these thin-film solar
cells. The extent and cost acceptability of this encapsulation
must be evaluated. The encapsulation scheme might be ameliorated
by the discovery that the initial cell efficiency of the $Cu_2S/$
Cd(Zn)S device can nearly be restored by a suitable heat-treat-
ment (71,94).

   Finally, work is needed on scaling-up the processes that pro-
duce these devices. Large-area devices, with comparable efficien-
cies to research devices of smaller area are necessary. Obviously,
if the technology is to be viable, cost, reliability, and perform-
ance limits must be adhered to.

   In summary, the major R&D areas that need emphasis for these
devices are:

- identification and solution of degradation mechanisms;
- development of reliable lifetime test procedures;
- development of suitable encapsulants;
- improvement in device performance, reproducibility;
- development of low-cost, large-scale production procedures;
- improvement of device geometries, ARCs, film structures; and
- more basic research, and more research activities in this area

Table 2. Examples of Degradation Problems in Cu_2S/CdS Solar Cells.

Cause of Degradation	Parameter(s) Affected	Solution(s)
1. Exposure to high humidity	J_{sc}, η_{coll}	Recovery: Heat *in-vacuo* at 180°C, Hermetic Encapsulation
2. Oxidation (e.g., exposure to air above 60°C	J_{sc}, R_{series}	Hermetic Encapsulation
3. Photo-induced phase change of Cu_2S (e.g., heating above 60°C under illumination	J_{sc}, (V_{oc}), R_{series}	Provide Cu by evaporation (e.g., 100Å on Cu_2S layer)
4. Delamination by temperature cycling (e.g.,-150 to +60°C)	J_{sc}, R_{series}	Minimum effect on performance, Temperature control

5. Other Materials. A number of other materials and materials systems are being investigated for solar cell application. These materials, sometimes called *emerging materials,* possess many of the requirements for a photovoltaic component but are still in their infancies from the device development viewpoint. These include InP (73-75), CdTe (76-78), Cu_2O (79,80), Zn_3P_2 (81), Cu_2Se (82), $ZnSiAs_2$ (83), $CdSiAs_2$ (84), BAs (85), and polyacetylene-

CH_x (86). Research tasks with these devices include:

(1) Theoretical modeling and calculations in order to evaluate the potential (both ideal and attainable) conversion efficiency of the pertinent material and the mechanisms that *limit* the realization of the optimum performance.

(2) The growth and characterization of thin-polycrystalline films (device quality) of these materials, emphasizing the utilization of low-cost substrates.

(3) Understanding of the relationships between the polycrystalline and single-crystal properties of the candidates.

(4) The preparation of devices: pn junctions, MIS, Schottky barriers, heterojunctions. Device performance must be demonstrated.

(5) The understanding and control of material doping.

(6) Development or implementation of experimental procedures to evaluate the basic material and device parameters, most of which have not been measured or reported in the literature.

(7) Investigation of the stability of the device and material parameters under typical environmental and operating conditions.

B. Concentrator Devices

The need and economic outlook for photovoltaic concentrators are discussed in the previous chapter. Overall, the concentrator can reduce the impact of cell cost on the system cost, thus providing a viable means of meeting critical cost goals. The cells also exhibit improved solar conversion efficiency with concentration. At constant temperature, the cell efficiency (neglecting series resistance effects) increases with illumination level. Concentrators reduce the requirements for semiconductor materials, so that elements that are apparently less abundant can be utilized. The concentrator system also has application in hybrid photovoltaic/thermal (or cogeneration) systems, since there is a significant demand for *thermal energy* in the 60-100°C range.

Conventional, single-junction solar cells are limited to even *theoretical* efficiencies in the 26-28% range (87). The best concentrator cell of this type has been a GaAs device with a 24.7% efficiency under 178 suns (88). If such devices are to exceed efficiencies of 30% under very high (>1000 suns) concentration, alternate - *unconventional* - device configurations must be developed. Three such approaches have the potential to satisfy the very high efficiency constraint and are currently receiving a good deal of attention in the research community. These are:

- *Multidevice, beam-splitting photovoltaic convertors*. In this technique, more than one cell is used in a complex spectrum splitting optical system. In this case, the total solar aperture is the same for all the devices, but each device responds to a different part of the solar spectrum. The different portions of the spectrum are provided by *beam splitting* the incident radiation using dichroic filters. Efficiencies (subtracting losses in the optical system) to 28.5% have been demonstrated using a GaAs and Si solar cell (89).

- *Monolithic multijunction or cascade solar cells*. This technique uses a complex planar technology - similar to integrated circuit procedures but with more layers and more critical technological constraints for fabrication. This device can provide energy conversion efficiencies in excess of 30%, even for a two junction device (69). Higher efficiencies are predicted for even more complex structures,utilizing three or more junctions. Such a prediction is shown in Fig. 10 (69). To date, some progress has been made in the demonstration of two junction devices with high open-circuit voltages (90), but technical problems still limit device performance.

Schematic representations of these two concepts are shown in Fig. 11. A third approach is the:

- *Edge multiple vertical junction device*. This technology

utilizes a vertical groove (presently in an Si wafer) that
is doped to provide the vertical junction. The groove is
approximately 10^{-3} cm across, and 10^{-2} cm deep. Grooves
are separated by ~10^{-2} cm. Efficiencies above 20% have
been demonstrated (91). Major problems with this device
are concerned with the electrical and thermal connections
to the cells. Some modeling problems and performance am-
biguities exist, and calculated attainable efficiencies
are somewhat in doubt.

The *beam-splitting approach* has several advantages over other
high-efficiency approaches. Since individual cells are used, ex-
isting technologies are sufficient to fabricate them. No complex
junction coupling is needed, and the cells can be operated inde-
pendently - at *different temperatures*. Thus, different cells (i.e.,
different materials) can be incorporated into such a system by
proper temperature control for each, optimizing the performance
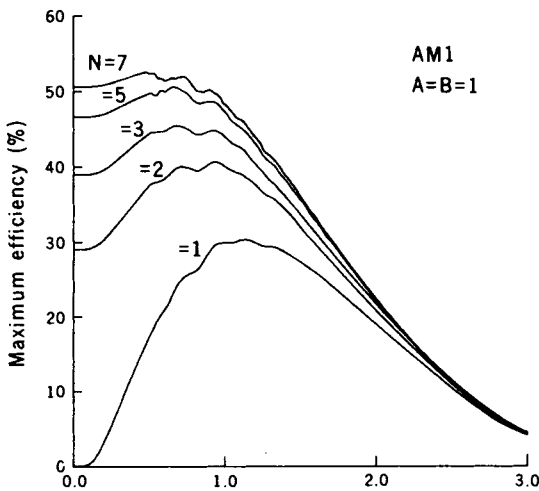
*FIGURE 10.   Multilayer cell efficiency for one to seven
absorber layers (from Ireland, et al., ref. 69).*

Sunlight

Sunlight

Cell II
(low-energy)

Dichroic
Filter

Cell I (high energy)
Low resistance connect
Cell II (low energy)

Cell I
(high energy)

(a) Spectral Splitting

(b) Cascade
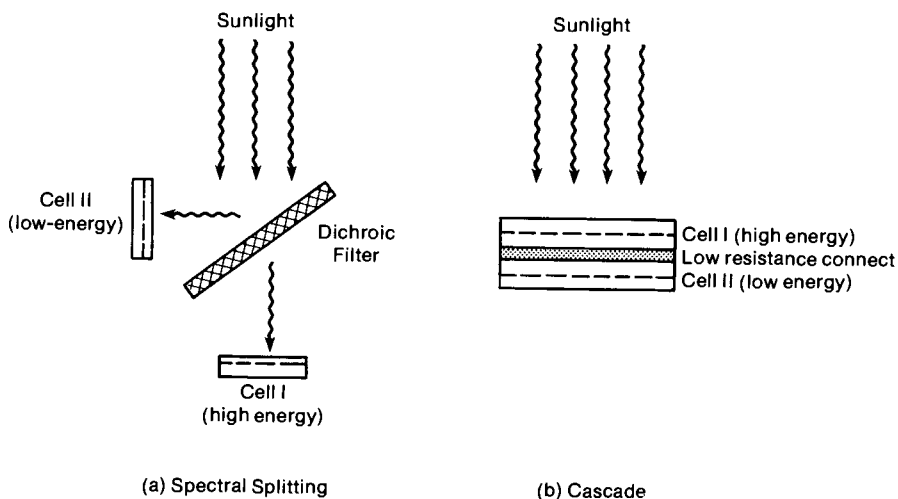
FIGURE 11.   Beam-splitting and multijunction cell concepts.

independently. However, the multidevice approach also has some
severe disadvantages, primarily due to the increased component
population: the more cells, the more cost, the more independent
reliability problems, etc. There is the high cost of using ad-
ditional substrates. More research remains on optimizing indivi-
dual cells to different spectral portions, and demonstrating a
greater than two-cell system. Major problems, however, are as-
sociated with the optical system, which presently contains a high
loss factor. This is especially true for the optical losses due
to the nonideal dichroic filter.

The multijunction or cascade concentrator cell has some con-
trasting advantages compared to the beam-splitting concept. It is
fabricated on a single substrate, and it is a two-terminal de-
vice - no matter how many junctions are stacked. This eliminates
both materials and connection costs, as well as the reliability
problems associated with such interconnections. Obviously, the
dichroic filter loss problem is avoided. However, the cell - even
for a two-junction device - is quite complex. From a fabrication
view, many layers (minimum of seven) are required, and stringent
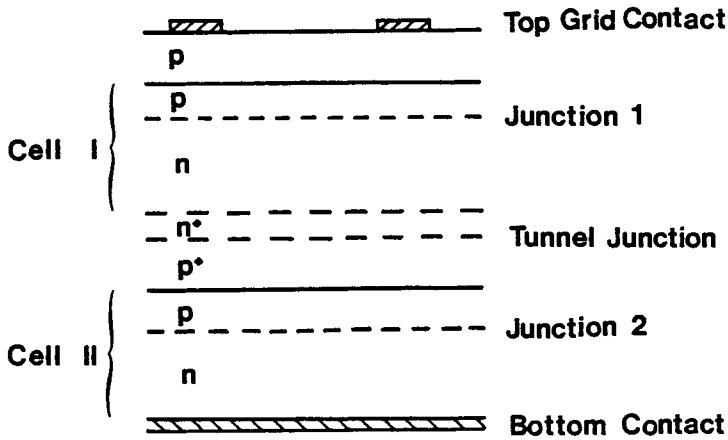
FIGURE 12.   Two-junction cascade solar cells.

material and growth parameters are needed in order to optimize
the device performance. For example, the semiconductors used in
the makeup of such a device - a two-junction version of which is
shown in Fig. 12 - must be nearly lattice matched to maintain
crystal integrity and avoid interface losses. The means to such
lattice matching is to control the composition of III-V binary
alloys. However, as shown in Fig. 13, this not only changes the
lattice parameter, but also the bandgap of the material. The
bandgaps must be precisely adjusted to match effectively the en-
tire solar spectrum. Thus, critical material and composition
choices must be made in the device design, and these must
be strictly adhered to and controlled during device fabrica-
tion.   In addition, the layer thicknesses must be precisely
controlled to provide current continuity (i.e., avoid
current losses) in the structure.   Since many thin layers
are used in such a device, growth temperatures should
be as low as possible to minimize interdiffusion prob-
lems.
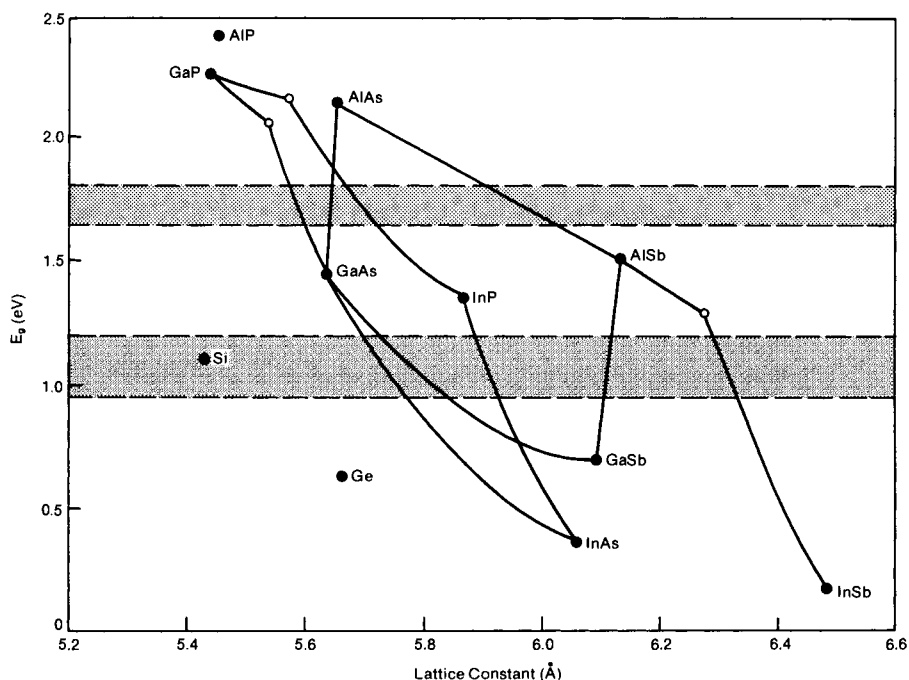
FIGURE 13. Energy gaps of various semiconductors, indicating lattice matches.

A critical requirement for the device shown in Fig. 12 is the low series resistance connection needed between the junctions to avoid unacceptahle voltage losses. One approach is to provide a tunnel junction. However, very high diping levels are needed to accomplish this, and it is quite difficult to achieve such concentrations in the AlGaAs system (92). Other methods presently under consideration involve bonding two cells together to form the stack (93). However, only preliminary concepts and few results have been reported with such techniques.

The technological and research problems associated with these very high efficiency concentrator approaches are both varied and shared among the techniques. Major among these are:

- The *assessment and demonstration* of various III-V
  semiconductor systems for efficient concentrator
  solar cells. Methods include LEP, CVD, MBE,
  VPE, or combinations of such growth techniques.
- Development of the essential *interconnect techno-
  logies* - especially the tunnel junction approach.
- Since AlGaAs cells can degrade, *encapsulants*
  must be developed. *Antireflection coatings* are
  needed to minimize reflection losses.
- *Contacting* the materials is critical. This is
  especially true for the high bandgap semiconductors
  proposed for these devices.
- The *GaAs* (or other *substrates)* must be high
  quality. However, low-cost methods for providing
  such substrates are needed.
- As with all solar cell technologies, the *degrada-
  tion mechanisms* that limit cell reliability must
  be identified and minimized. Sunlight concentra-
  tion conditions are an added factor for these
  devices.
- *Systems-wise,* the necessary concentrator optics
  (low-loss), tracking, control, thermal cooling,
  power conditioning, wiring, *etc.,* remain to be
  developed.

The concentrator solar converter has great potential
as a long-range alternative in the photovoltaic area.
However, it also represents an area that is in need
of a good deal of R&D activity if it is to
succeed.

REFERENCES

1. *National Photovoltaic Program Plan,* U.S. Department of Energy (DOE/ET-0035 (78)), Division of Solar Technology, March, 1978.

2. *Solar Photovoltaic Energy Research, Development and Demonstration Act of 1978,* U.S. Public Law 95-590.

3. Kazmerski, L.L., *Introduction to Photovoltaics: Physics, Materials and Technology* (previous chapter).

4. Sterling, H.F., and Swann, R.C.G., *Solid-State Electron. 8.* 653 (1965)

5. Chittick, R.C., Alexander, J.H., and Sterling, H.F., *J. Electrochem. Soc. 116,* 77 (1969).

6. Spear, W.E., and LeComber, P.G., *J. Non-Crystal Solids 8,* 727 (1972).

7. Carlson, D.E., U.S. Patent 4,065,521 (1977).

8. Triska, A., Dennison, D., and Fritzche, H., *Bull.* APS *20,* 392 (1975).

9. Connell,G.A.N., and Pawlik, J.R., *Phys. Rev. B. 13,*787 (1976).

10. Knights, J.C., Street, R.A., and Lucovsky, G., 8th Int. Conf. on Amorphous and Liquid Semicond., in press (1979).

11. Anderson, D.A., and Spear, W.E., Phil. Mag. *35,* 1 (1977).

12. Ovshinsky, S.R., and Madan, A., Nature *276,* 482 (1978).

13. Spear, W.E. and LeComber, P.G., *Solid-State Comm. 17,* 1193 (1975).

14. Carlson, D.E., and Wronski, C.R., *Appl. Phys. Lett. 28,*671 (1976).

15. Carlson, D.E., in "Polycrystalline and Amorphous Thin Films and Devices", (Kazmerski, L.L., Ed.), Chapter 6. Academic Press, New York, 1980.

16. Staebler, D.L., 8th Int. Conf. on Amorphous and Liquid Semicond., in-press (1979).

17. Carlson, D.E., Proc. DOE/SERI Photovoltaics Adv. R&D Annual Rev. Meeting, Denver, pp. 113-120. SERI (TP-311-428),

Golden, CO, 1979.

18. See, for example, Bosnell, J.R., in "Active and Passive Thin Film Devices" (Coutts, T.J., Ed.) pp 245-320. Academic Press, London, 1978.

19. See, for example, Stone, J., Proc. DOE/SERI Photovoltaic Adv. R&D Annual Rev. Meeting, Denver, pp 69-112. SERI (TP-311-428), Golden, CO 1979.

20. Carlson, D.E., in "Polycrystalline and Amorphous Thin Films and Devices". (Kazmerski, L.L., Ed.). Academic Press, New York, 1980.

21. Kazmerski, L.L., in Proc. DOE/NBS Workshop on Stability of (Thin Film) Solar Cells and Materials, pp 128-143. NBS Spec. Publ. 400-58, Dept. of Commerce, Washington, DC 1979.

22. Kazmerski, L.L., *Interface 2,* 6 (1979).

23. Fang, P.H., Ephrath, L., and Nowak, W.B., *Appl. Phys. Lett. 25,* 283 (1974).

24. Chu, T.L., Mollenkopf, H.C., and Chu, S.S., *J. Electrochem. Soc. 12,* 1681 (1975).

25. Chu, T.L., Lien, J.C., Mollenkopf, H.C., Chu, S.S., and Heizer, K.W., *Solar Energy 17,* 229 (1975).

26. Chu, T.L., Mollenkopf, H.C., and Chu, S.S., *J. Electrochem. Soc. 123,* 106 (1976).

27. Chu, T.L., *J. Cryst. Growth 39,* 45 (1977).

28. Chu, T.L., Chy, S.S., Kelm, R.W., and Wakefield, G.W., *J. Electrochem. Soc. 125,* 595 (1978).

29. Chu, T.L., and Singh, K.N., *Solid-State Electron. 19,* 837 (1976).

30. Chu, T.L., van der Leeden, G.A., and Yoo, H.I., *J. Electro-chem. Soc. 125,* 661 (1978).

31. Barnett, A.M., and Rothwarf, A., *IEEE Trans. Electron. Dev. ED-27,* in-press (1980).

32. Barnett, A.M., 2nd European Comm. Photovoltaic Solar Energy Conf., Berlin, pp 328-343. D. Reidel Publ. Co., Berlin, 1979.

33. Barnett, A.M., Proc. 14th IEEE Photovoltaics Spec. Conf.,

IEEE, New York, 1980.

34. Kazmerski, L.L., Proc. 14th IEEE Photovoltaic Spec. Conf., IEEE, New York, 1980.

35. Surek, T., Cheek, G.C., and Ariotedjo, A., in Proc. SERI/DOE Advanced R&D Annual Review Meeting, Denver, pp 239-256. SERI TP-311-428, Golden, CO, 1979.

36. Shewchun, J., Proc. Polycrystalline Si Contractors Meeting, Pasadena. SERI, Golden, CO, Dec. 1979.

37. Burke, D., Shewchun, J., Spitzer, M., Loferski, J.J., Scholz, F., Singh, R., and Kukulka, J., Proc. 14th IEEE Photovoltaics Spec. Conf., San Diego (IEEE, New York; 1980).

38. Hovel, H., "Solar Cells", pg 95. Academic Press, New York, 1975.

39. D'Aiello, R.V., in Proc. Polycrystalline Si Contractors Rev. Meeting, Pasadena, pp 233-242. SERI, Golden, CO, Dec. 1979.

40. Card, H.C., and Yang, E.S., *IEEE Trans. Electron Dev. ED-24*, 397,(1977).

41. Soclof, S., and Iles, P.A., Electrochem. Soc. Fall Meeting, New York, p 618 (1974). Also, Proc. 11th IEEE Photovoltaic Spec. Conf. p 56. IEEE, New York, 1975.

42. Lanza, C., and Hovel, H.J., *IEEE Trans. Electron Dev. ED-24*, 392 (1977).

43. Hilborn, R.B., and Lin, T., Proc. Nat. Workshop on Low-Cost Polycrystalline Silicon Solar Cells, pp 246-254. ERDA, Washington, DC, 1976.

44. Ghosh, A.K., Fishman, C., and Fang, T., *J. Appl. Phys. 50*, (1979).

45. Ginley, D., this book.

46. Fogarassy, E., Stuck, R., Muller, J.C., Grob, A., Siffert, P., Salles, Y., and Diguet, D., *Solar Cells, 1*, 23 (1979).

47. Seager, C.H., and Ginley, D., *App. Phys. Lett. 34*, 337 (1979).

48. Seager, C.H., and Pike, G.E., *App. Phys. Lett. 35,* 709 (1979).

49. Matare, H.F., "Defect Electronics in Semiconductors". Wiky-Interscience, New York, 1971.

50. Kazmerski, L.L., *Thin Solid Films* 57, 99 (1979).

51. Kazmerski, L.L., in "Polycrystalline and Amorphous Thin Films and Devices", (Kazmerski, L.L., Ed.), Chapter 3. Academic Press, New York, 1980.

52. Brobst, D.A., and Pratt, W.P., "United States Mineral Resources", Paper 820. United States Geological Publ. Office, Washington, DC, 1973.

53. See, for example, Proc. Photovoltaics Adv. R&D Review Meeting, Denver, SERI, Golden, CO, 1979. Also, Proc. 14th IEEE Photovoltaics Spec. Conf.,San Diego. IEEE, New York, 1980.

54. Fan, J.C.C., Proc. Photovoltaics Adv. R&D Review Meeting, Denver, pp 317-323. SERI, Golden, CO,1979.

55. Fan, J.C.C., Calawa, A.R., Chapman, R.L., and Turner, G.W., *Appl. Phys. Lett.* 35, 804 (1979).

56. Fan, J.C.C., Bozler, C.O., and Chapman, R.L., *Appl. Phys. Lett.* 32, 390 (1978).

57. Ghandhi, S.K., Borrego, J.M.,Reep, D., Hsu, Y.S., and Pande, K.P., *Appl. Phys. Lett.* 34, 669 (1979).

58. Pande, K.P., Hsu, Y.S., Borrego, J.M., and Ghandhi, S.K., *Appl. Phys. Lett.* 33, 717 (1978).

59. Kazmerski, L.L., and Ireland, P.J., *J. Vac. Sci. Technol.* 17, in-press, (1980).

60. Kazmerski, L.L., Ireland, P.J., Chu, S.S., and Lee, Y.T., *J. Vac. Sci. Technol.* 17, (in press) (1980).

61. See, for example, Proc. NBS/DOE Workshop on Stability of (Thin Film) Solar Cells and Materials, NBS Spec. Publ. 400-58. U.S. Dept. of Commerce, Washington, 1979.

62. Reynolds, D.C., Leies, G., Antes, L.L., and Marburger, R.E., *Phys. Rev.* 96. 533 (1954).

63. Barnett, A.M., Bragagnolo, J.A., Hall, R.B., Phillips, J.E., and Meakin, J.D., Proc. 13th IEEE Photovoltaic Spec. Conf. pp 419-420. IEEE, New York, 1978.

64. Wagner, S., Shay, J.L., Migliorato, P., and Kasper, H.M., *Appl. Phys. Lett.* 25, 434 (1974).

65. Kazmerski, L.L., White, F.R., and Morgan, G.K., *Appl. Phys. Lett. 29,* 268 (1976).

66. Kazmerski, L.L., in "Ternary Compounds 1977" (G. Holah, Ed.) pp 217-225. Instit. of Phys., London, 1977.

67. Loferski, J.J., Shewchun, J., Roessler, B., Beaulieu, R., Piekoszewski, J., Gorska, M., and Chapman, G., Proc. 13th IEEE Photovoltaic Spec. Conf. pp 190-193. IEEE, New York, 1978.

68. Shewchun, J., Garside, B.K., Polk, D., Loferski, J.J., Burke, D., and Beaulieu, R., Proc. 14th IEEE Photovoltaic Spec. Conf., San Diego. IEEE, New York, 1980.

69. Ireland, P.J., Wagner, S., Kazmerski, L.L., and Hulstrom, R.L., *Science 204,* 611 (1979).

70. Stanley, A.G., "Cadmium Sulphide" (Vol. 1 and 2). JPL Doc. 78-77. Jet Propulsion Laboratory, Pasadena, CA, 1978.

71. Meakin, J.D., Proc. CdS/Cu$_2$S and CdS/Cu-Ternary Compound Program, Denver, pp 79-110. SERI, Golden, CO 1979.

72. Kazmerski, L.L., Ireland, P.J., White, F.R., and Cooper, R., Proc. 13th IEEE Photovoltaic Spec. Conf., pp 184-189. IEEE, New York, 1978.

73. Chu, T.L., Chu, S.S., Lin, C.L., Tzeng, Y.C., Kuper, A.B., and Chang, C.T., Proc. 14th Photovoltaic Spec. Conf San Diego. IEEE, New York, 1980.

74. Bachmann, K.J., Sinclair, W.R., Thiel, F.A., Schreiber, H., Schmidt, P.H. Spencer, E.G., Buehler, E., and Feldman, W.L., Proc. 13th IEEE Photovoltaics Spec. Conf., pp 524-527. IEEE, New York, 1978.

75. Shay, J.L., Bettini, M., Wagner, S., Bachmann, K.J., and Buehler, E., Proc. 12th IEEE Photovoltaics Spec. Conf. IEEE New York, 1976.

76. Lincot, D., Mimilya-Arroyo, J., Triboulet, R., Marfaing, Y., Cohen-Solal, G., and Barbe, M., Proc. 2nd E.C. Photovoltaic Solar Energy Conf. pp 424-431. D. Reidel Publ. Co., Holland, 1979.

77. Bube, R.H., Buch, F., Fahrenbruch, A.L., Ma, Y.Y., and Mitchell, K.W., *IEEE Trans. Electron Dev.* ED-24, 487 (1977).

78. Nakayama, N. Matsumoto, H., Yamaguchi, K., Ikegami, S. and Hioki, Y., *Jap. J. Appl. Phys.* 15, 2281 (1976).

79. Olsen, L.C., Bohara, R.C., and Urie, M.W., *Appl. Phys.Lett.* 34, 47 (1979).

80. Wang, E.Y., Trivich, D., Komp, R.J., Huang, T., and Brinker, D., Proc. 14th IEEE Photovoltaic Spec. Conf. San Diego, CA. IEEE, New York, 1980.

81. Catalano, A., Bhushan, M., and Convers-Wyeth, N., Proc. 14th IEEE Photovoltaics Spec. Conf. San Diego. IEEE, New York. 1980.

82. Lozykowski, H., Czech, *J. Phys.* B13, 164 (1963). Also, see ref. 91, pp 387-416.

83. Rud, Y.V., and Ovezov, K., *Sov. Phys. Semicond.* 10, 561 (1976).

84. Dovletmuradov, C., Ovezov, K., Prochukhan, V.D., Rud, Y.V., and Serginov, M., *Sov. Phys. Tech. Phys. Lett.* 1, 382 (1975).

85. See ref. 91, pp 387-416.

86. Heeger, A.J., and MacDiarmid, A.G., Proc. DOE/SERI Photovoltaics Adv. R&D Annual Rev. Meeting, pp 417-422. SERI, Golden, CO, 1979.

87. See discussion in previous chapter. Also, Loferski, J.J., *Proc. IEEE 51*, 677 (1958).

88. Sahai, R., Edwall, D.D., and Harris, J.S., *Appl. Phys. Lett.* 34, 147 (1979).

89. Moon, R.L., James, L.W., Vanderplas, H., Yep, T.O., Chai, Y.G., and Antypas, T.A., Proc. 13th IEEE Photovoltaics Spec. Conf. pp 859-867. IEEE, New York, 1978.

90. Bedair, S.M., Phatak, S.B., and Hauser, J.R., Proc. 14th IEEE Photovoltaics Spec. Conf., San Diego, CA. IEEE, New York, 1980. Also, Appl. Phys. Lett. 34, 38 (1979).

91. See, for example, Mitchell, K.W., Proc. DOE/SERI Photovoltaics Adv. R&D Annual Meeting, pp 329-352. SERI,Denver,CO, 1979.

92. See ref. 89, p 861.

93. See, for example, Mitchell, K.W., Proc. DOE/SERI Advanced R&D Annual Meeting, Denver, pp 329-352. SERI, Golden, CO, 1979.

94. See, for example, Proc. NBS/DOE Workshop on Stability of (Thin Film) Solar Cells and Materials, NBS Spec. Publ. 400-58, (Sawyer, D.E., and Schafft, A.A., Eds.). U.S. Dept. of Commerce, Washington, DC, 1979.

95. Wilson, J.I.B., McGill, J., and Kinmond, S., *Nature 272*, 153 (1978).

96. Hamakawa, Y., Okamota, H., and Nitta, Y., *App. Phys. Lett.* *35*, 187 (1979).

CHAPTER 17

HETEROJUNCTIONS FOR THIN FILM SOLAR CELLS[1]

Richard H. Bube

Department of Materials Science and Engineering
Stanford University
Stanford, California

I. INTRODUCTION

There are five basic types of semiconductor junction
systems that may be used for the photovoltaic conversion of
solar energy.

Homojunctions consist of p-n junctions of a single semi-
conductor material. The best known example is the standard
p-n junction silicon solar cell. In general homojunctions
exhibit a high junction efficiency, but particularly in direct
bandgap materials with a high absorption coefficient, there
are appreciable losses due to front surface recombination,
which reduce the overall solar efficiency of the device by
decreasing the collected current.

Heterojunctions consist of p-n junctions of two different
semiconductors: a small bandgap semiconductor in which optical

absorption takes place, and a large bandgap semiconductor that
acts as a window for the junction. The active portion of the
solar spectrum is that lying between the bandgaps of the two
materials. In the special case that the two semiconductors have
a good lattice constant match so that the density of interface
states is a minimum, heterojunctions may exhibit the optimum
properties of a homojunction constructed from the small bandgap
material without the problems of front surface recombination loss.
If the interface cannot be effectively ignored, however, the
properties of the junction may be deleteriously affected; normally
this takes the form of a reduction in open-circuit voltage
without any necessary large decrease in short-circuit current.

   Buried homojunctions consist of p-n homojunctions with an
additional heteroface junction with a large bandgap semiconductor
that acts as a window material for the p-n junction. The high
recombination loss front surface of the p-n homojunction is
replaced by the interface with the large bandgap semiconductor
which may provide improved properties. Buried homojunctions
combine several positive aspects of the corresponding homo-
junctions and heterojunctions.

   Schottky barriers consist of metal-semiconductor junctions
in which a blocking contact is formed. Performance is usually
limited by large thermionic emission currents that reduce the
open-circuit voltage.

   *Metal-insulator-semiconductor (MIS) and semiconductor-
insulator-semiconductor (SIS) junctions* are equivalent to the
corresponding Schottky barrier and heterojunction systems,
respectively, with the addition of a thin layer of insulator,
usually an oxide, at the interface to reduce the forward currents
that reduce the open-circuit voltage.

   In this chapter we consider the basic properties of
heterojunctions and heteroface junctions, and provide examples of

heterojunctions with good lattice match (CdS/InP), heterojunctions
with poor lattice match (CdS/CdTe, ZnO/CdTe), and buried
homojunctions (ITO/CdTe, ITO/InP).

II.   CHARACTERIZING A HETEROJUNCTION SOLAR CELL

In order to obtain an overview of the various properties
that are significant for determining the performance of a typical
heterojunction solar cell, it is useful to consider the types of
measurements and considerations that enter the characterization
of an experimental heterojunction cell.

Bulk properties of the component materials. General
information is needed on the basic electronic properties of the
materials involved: purity, carrier type and density, carrier
mobility, absorption constant as a function of photon energy,
minority carrier lifetime, minority carrier diffusion length.
This information can be obtained by analysis using the electron
microprobe or mass spectrography, and by measurements of Hall
effect, thermoelectric power, optical transmission, electron
beam induced currents (EBIC), Schottky barrier capacitance.
The optically absorbing semiconductor is usually chosen to be a
p-type material because of the longer diffusion lengths for
electrons, and to have a bandgap of the order of 1.4 eV, the
optimum for match with the solar spectrum.

In order to construct an Anderson abrupt junction model
of the heterojunction (1), it is useful also to know the
electron affinities of the materials to be used in forming the
heterojunction. This knowledge allows a choice of materials that
will not have an obvious spike in the carrier transport band that
would limit collection of photogenerated current, and a calcula-
tion of the diffusion potential of the junction (2). Since this
junction model assumes no interface states, its predictions must

be considered to have only heuristic purpose.

Crystallographic structure and orientation of component materials. This information is of particular significance for thin film solar cells made from polycrystalline materials. Techniques of X-ray diffraction, scanning electron microscopy (SEM), and transmission electron microscopy (TEM) can be used to obtain data on grain size and film morphology.

Effects of surface treatment on material properties. Knowledge of the bulk properties and the surface properties of the isolated component materials is not sufficient to determine what will happen when a junction is formed. Indeed, the very process used to form the junction may have a major effect on the properties of the junction. As preliminary background for this kind of effect, it is important to know the effect of various kinds of surface treatments on the materials to be used in junction formation. Such surface treatments would include heat treatment in an oxidizing atmosphere, a neutral atmosphere, vacuum, and a reducing atmosphere. Questions to be answered include: Is a surface layer formed? What is it? How will it affect junction properties if such a layer is formed during junction formation? Structural information can be obtained from X-ray diffraction and SEM, chemical information from Auger spectroscopy, and electronic information from measurements of surface conductivity, Hall effect, thermoelectric power, photovoltage, and luminescence. The formation of Schottky barriers on various surfaces can be a valuable diagnostic approach.

Contact resistivities. The contact resistivities of all contacts should be measured in both dark and light. If the expected total series resistance of the cell is estimated by adding all contact and bulk resistances, measurements should be in agreement if the cell is understood.

Dark current vs voltage measurements. Basic information

about the electrical properties of the junction can be obtained
by comparing measured values of current vs voltage with standard
forms for idealized situations:

$$J = J_O \{\exp(qV/AkT) - 1\} \tag{1}$$

$$J = J_O \{\exp(\alpha V) - 1\} \tag{2}$$

A relation such as that given in Eq. (1) corresponds to the
ideal junction behavior in which the diode current is controlled
by diffusion (A = 1) or recombination (A = 2), while Eq. (2) is
the junction behavior if tunneling currents dominate. These
measurements result in the evaluation of A or α, J_o, and the
series resistance R_s, and the shunt resistance R_p. These
measurements should then be repeated as a function of temperature
and the approximate model for junction transport can be developed.

   Light current vs voltage measurements. These standard
measurements enable one to obtain values for the principal
parameters defining solar cell performance: short-circuit current
J_{sc}, open-circuit voltage, V_{oc}, fill factor, and solar efficiency.
These measurements should be repeated as a function of tempera-
ture. From the extrapolated value of a V_{oc} vs T plot, one obtains
a measure of the diffusion potential from the value of V_{oc}
corresponding to $T = 0^{\circ}$K.

   Light diode parameters. At a particular temperature, a
comparison of the dark J vs V data with the variation of J_{sc} vs
V_{oc} obtained by varying the light intensity, indicates whether
or not the junction transport phenomena are light dependent.
This measurement allows the determination of light values for
A or α, J_o, R_s or R_p, if these are different from the values in
the dark.

   Spectral dependence of quantum efficiency. The quantum
efficiency is measured as a function of photon energy. In

addition to the direct data obtained in this way, the variation
of quantum efficiency can often be a simple diagnostic for the
type of junction involved. In an ideal heterojunction the
quantum efficiency will simply be high and constant between the
bandgaps of the two materials. If the minority carrier diffusion
length is small in the absorbing material, the quantum
efficiency decreases toward lower photon energies for which the
absorption coefficient is also lower. If there is appreciable
carrier loss through recombination at interface states, the
quantum efficiency increases under applied reverse bias in a way
that is independent of photon energy. If, instead of a
heterojunction, a particular device is actually a buried
homojunction, the quantum efficiency will decrease toward
higher photon energies due to front interface recombination
on the homojunction. We give examples of these phenomena later
in this chapter.

   Reverse breakdown voltage. The junction voltage for
reverse breakdown is measured in dark and light, and as a func-
tion of temperature, for comparison with diode models.

   Light intensity dependence of cell parameters. Values of
J_{sc}, V_{oc}, fill factor, and solar efficiency are measured over a
wide range (many orders of magnitude) of light intensity. Non-
linear variation of J_{sc} with light intensity indicates a light-
sensitive collection process. Non-linear variation of V_{oc}
with $\ln(I_L/I_o)$ indicates changes in A or α with light intensity.
Comparison of the variation of the fill factor with light
intensity with that of an ideal cell indicates series resistance,
shunt resistance, and voltage-dependent collection phenomena (3).

   Junction capacitance measurements. The junction properties
are explored in dark and light by measuring the junction
capacitance as a function of applied voltage. If a simple
junction is approximated, three important pieces of information

are obtained from a $1/C^2$ vs V plot: the carrier density from the
slope in reverse bias, the zero-bias depletion layer width from
the capacitance for zero bias, and a measure of the diffusion
potential from the intercept on the voltage axis.

Electron beam induced current (EBIC).   These measurements
perform at least two significant functions.   By measuring the
EBIC signal as a function of distance away from the junction,
the minority carrier diffusion length can be measured.   By
comparing the location of the maximum EBIC signal with the
location of the metallurgical junction, it is possible to
distinguish between heterojunction and buried homojunction
systems.

Photoluminescence and electroluminescence.   As indicated
above, photoluminescence can be used to indicate the nature of
semiconductor surfaces and changes with processing.   A particular
use is to measure photoluminescence of the p-type material in
a junction before and after deposition of the large bandgap
n-type material.   Changes in luminescence emission may indicate
the type of surface effects produced by the deposition method
used.   Similarly forward bias may be applied and electrolumi-
nescence measured, if present, as an indication of the type of
defects important for recombination under forward bias conditions.

Chemical composition across the junction.   A variety of
surface techniques may be used to determine the variation of
chemical composition of the material across the metallurgical
junction, thus revealing diffusion effects, new compound
formation etc.

Physical and structural information on the interface.   De-
tailed information of a physical and structural type can be
obtained by applying techniques of TEM to junction interfaces.
This is often a rather difficult enterprise since the preparation
of suitable samples may be a long and involved task.

III. TYPICAL HETEROJUNCTION BAND DIAGRAMS

Two extreme cases for typical heterojunctions exist: a highly conducting p-type optical absorbing material with a less conducting n-type window material, or a highly conducting n-type window material on a less conducting p-type absorber. In the former case, the depletion layer is essentially all in the window material, no appreciable drift field exists in the p-type material to aid in collection of carriers, and modulation of localized charge near the interface in the window material can modulate the barrier properties. In the latter case, the depletion layer is essentially all in the p-type absorber, the depletion field aids in the collection of carriers, and the n-type window material acts primarily as a unaffected contact and junction former.

Examples of these two types of junctions are given in FIGURES 1 and 2, which give approximate band diagrams in the abrupt junction model. FIGURE 1 shows the Cu_2S/CdS system in which degenerate p-type Cu_2S is formed, either by displacement of Cd by Cu in solution or by chemical reaction of CuCl on the surface of CdS, on n-type single crystal or thin film CdS with a lower electron density. Cu_2S has a bandgap of about 1.2 eV, while CdS has a bandgap of 2.4 eV. Lattice mismatch causes the existence of interface states. Diffusion of Cu into the CdS causes a broadened depletion layer region in the CdS. If positive charge is captured in localized states in the CdS near the junction as the result of photoexcitation, the potential profile at the junction can be appreciably altered. The condition labeled *enhanced* in FIGURE 1 corresponds to the situation where positive charge is localized in the CdS near the interface and the depletion layer is narrowed; the condition labeled *quenched* corresponds to the situation where no positive charge is
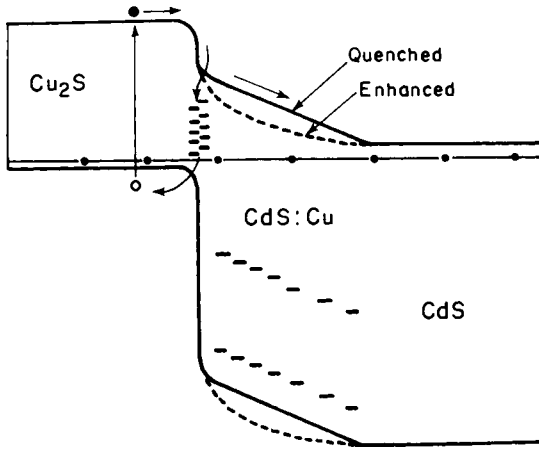
FIGURE 1.   Energy band diagram for Cu₂S/CdS heterojunction.
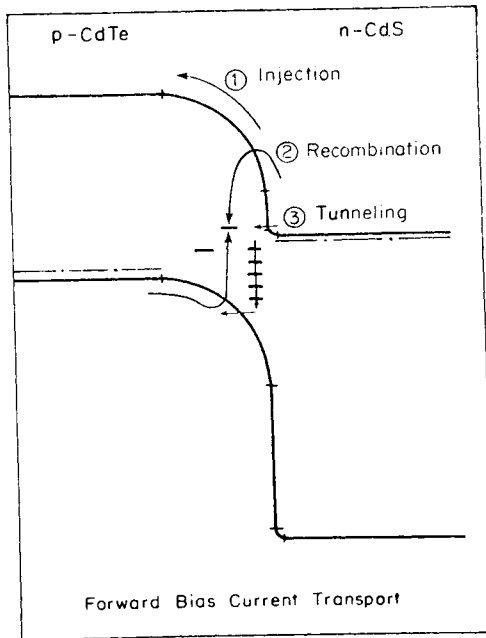
FIGURE 2.   Energy band diagram for CdS/CdTe heterojunction.

localized and the depletion layer is widened (4,5).

FIGURE 2 shows the band diagram for an ideal CdS/CdTe
heterojunction, for which the electron density in the CdS is
normally larger than the hole density in the CdTe. The bandgap
of CdTe is 1.4 eV. This diagram also illustrates the three
principal modes of forward bias transport: (1) injection or
diffusion, (2) recombination through imperfections or interface
states, and (3) tunneling through imperfections or interface
states. CdS and CdTe have about 9% lattice mismatch and a
relatively high density of interface states is predicted. A
tunneling mode of diode transport seems to occur in many hetero-
junction systems, with the result that the value of J_o is larger
than would be predicted from either diffusion or recombination
models.

IV.   CdS/CdTe HETEROJUNCTIONS

Solar cells made from the component materials n-type CdS
and p-type CdTe have been made by a variety of processes,
involving the deposition on single crystal CdTe of thin film
CdS by vacuum evaporation, spray pyrolysis, or chemical vapor
deposition. Solar efficiencies up to 12% have been reported
for such cells.

CdS/CdTe prepared by vacuum evaporation of CdS have been
reported with a V_{oc} = 0.63 V, J_{sc} = 16.1 mA/cm^2 and solar
efficiency of 8% (6). The spectral response of the quantum
efficiency for this cell is shown in FIGURE 3. It is evident
that the cell is a genuine heterojunction. The quantum
efficiency decreases toward lower energies because of a small
electron diffusion length of 0.4 µm in the CdTe, and reverse
bias enhancement of the quantum efficiency is consistent with
interface recombination loss of photoexcited carriers.

Spectral response of n CdS/pCdTe cell E II
3MB (corrected for 12% reflection loss)

FIGURE 4. Spectral dependence of the
quantum efficiency for several CdS/CdTe cells
prepared by spray pyrolysis deposition of CdS
on single crystal CdTe (7).

FIGURE 3. Spectral dependence of the
quantum efficiency for a CdS/CdTe cell
prepared by vacuum evaporation of CdS on
single crystal CdTe (6).

Other CdS/CdTe cells were prepared by deposition of CdS
by spray pyrolysis onto similar CdTe single crystal substrates.
Variables were the temperature of the substrate during deposition
and the temperature of the heat treatment after deposition (7).
The spectral response for the quantum efficiency of three of the
cells are given in FIGURE 4. The cell with the highest
efficiency has an essentially heterojunction spectral response,
with V_{oc} = 0.53 V, J_{sc} = 16.4 mA/cm^2 and a solar efficiency of
6.5% without correction for reflection losses. Cells with
reduced quantum efficiency are also obtained with values of
open-circuit voltage as high as 0.74 V; these cells show a
spectral response more like that expected for a buried homo-
junction. Survey of a variety of cells prepared with different
values of the temperature variables indicates a more or less
monotonic decrease in short-circuit current if the cells are
ordered according to an increase in open-circuit voltage. The
increase in open-circuit voltage with a decrease in short-circuit
current is also evidence for the development of a buried homo-
junction.

CdS/CdTe heterojunctions prepared by epitaxial vapor growth
of CdS on CdTe in H$_2$ show V_{oc} = 0.67 V, J_{sc} = 18.4 mA/cm^2, and
a solar efficiency of 12% (8). These junctions, however, are
reported to be buried homojunctions, presumably because of the
diffusion of indium donors from the CdS into the CdTe in the
process of preparation. There is some evidence that simple
heat treatment of p-type CdTe in H$_2$ is sufficient to convert the
surface to n-type (9). Similar results are indicated for a
CdS/CdTe junction prepared by screen printing techniques with
V_{oc} = 0.69 V, J_{sc} = 31.1 mA/cm^2 (for 140 mW/cm^2 radiation), and
solar efficiency of 8.1%; EBIC measurements indicate that the
method of preparation has produced a buried CdTe homojunction
with the electrical junction about 1 μm inside the CdTe away from

the metallurgical junction.

V.   CdS/InP HETEROJUNCTIONS

     Some of the difficulties with the CdS/CdTe system may be
attributed to the lack of lattice constant match between these
two materials; still it should be noted that this did not pre-
vent the realization of high quantum efficiencies, although it
did reduce the open-circuit voltage in the heterojunction con-
figurations. A major improvement should be expected in the
CdS/InP system, for there exists an excellent lattice match
between CdS and InP. The lattice constant of zincblende InP
is 5.869A, and the corresponding parameter ($2^{\frac{1}{2}}a$) of wurtzite CdS
is 5.850A, yielding only 0.32% lattice mismatch between the (111)
plane of InP and the basal plane of hexagonal CdS. In addition,
the tetrahedral atomic distance in InP is 2.533A and in CdS is
2.532A, indicating that the orientation of the InP is not
critical.
     The first cells were prepared by vacuum evaporation of CdS
on single crystal InP and showed an efficiency of 12.5%, thus
apparently vindicating the above reasoning (10). Heat treat-
ment of this type of cell increased the open-circuit voltage
and gave a solar efficiency of 14%. Further improvement was made
by going to a chemical vapor deposition of CdS on InP using an
open-tube H_2S/H_2 flow system (11-13). Values were obtained as
follows: V_{oc} = 0.79 V, J_{sc} = 18.7 mA/cm^2 and solar efficiency of
15.0%. Although there was no doubt that these were indeed
heterojunctions, capacitance data indicated an abrupt junction
with a diffusion voltage close to the value of 1.25 V character-
istic of an InP homojunction. Thus near-to-optimum heterojunction
performance was being achieved; calculation of the solar
efficiency assuming properties of an InP homojunction indicates

an efficiency of 17.2%, only slightly larger than that realized.

Some of the effect of additional states at the interface is
seen by attempts to prepare CdS/InP junctions on polycrystalline
InP films. The striking result is that almost the same short-
circuit current can be obtained, but the open-circuit voltage
is reduced due to increased forward leakage currents. Cells
were obtained by chemical vapor deposition of CdS onto poly-
crystalline InP (on p^+-GaAs on carbon) with V_{oc} = 0.46 V,
J_{sc} = 13.5 mA/cm^2 and a solar efficiency of 5.7%. FIGURE 5
compares CdS/InP cell properties for cells prepared on single
crystal InP to those prepared on polycrytalline InP (14,15).
Only a relatively small increase in quantum efficiency results
from use of single crystal InP, indicating that recombination loss
at the interface is small even for these randomly oriented
InP grains. FIGURE 5 also shows some response for wavelengths
longer than the absorption edge of InP, which might be inter-
preted as indicating band tails in the polycrystalline InP grains;
the open-circuit voltage increases as the degree of band-tailing
decreases. FIGURE 6 shows the reason that the open-circuit
voltage is so much lower in the single crystal InP cells;
the diode current is about 100 times larger for the polycrystal-
line InP.

CdS/InP junction cells have also been prepared by the
vacuum evaporation of CdS onto single crystal p-type InP
homoepitaxial layers grown by a metalorganic chemical vapor
deposition method on p^+ single crystal InP substrates (16).
The best cell had an efficiency of 11.9% without an antireflection
coating, a typical heterojunction spectral response as shown in
FIGURE 7, and photovoltaic parameters summarized in Table I.
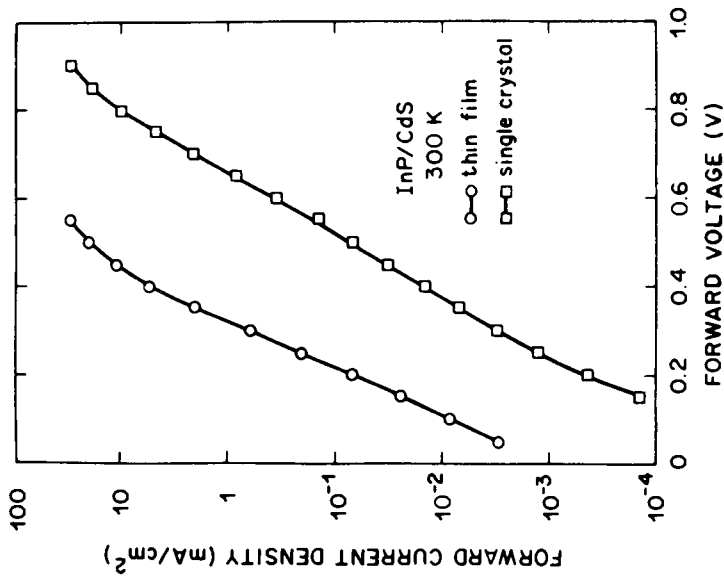
FIGURE 6. Forward bias current-voltage curves for CdS/InP junctions using single crystal InP and using polycrystalline thin film InP (15).
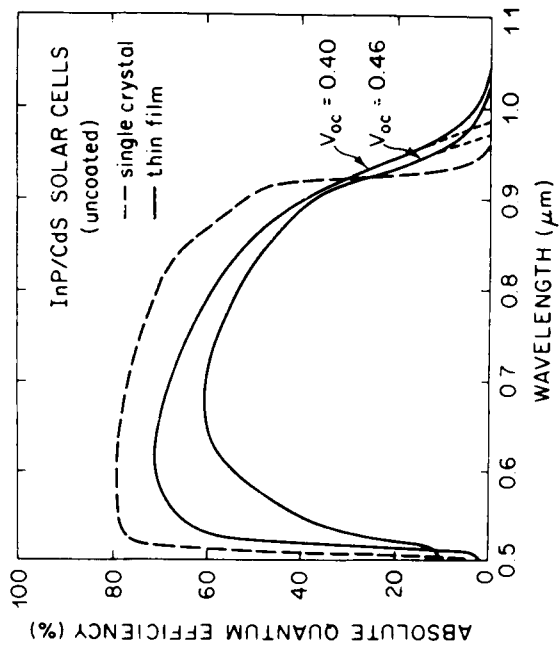
FIGURE 5. Spectral response of the quantum efficiency for CdS/InP cells on single crystal InP and on polycrystalline thin film InP (15).

Richard H. Bube

TABLE I.   Photovoltaic Parameters for CdS/InP and
           ITO/InP Heterojunctions (16)

Parameter[a]	CdS/InP	ITO/InP
V_{oc}, V	0.68	0.69
J_{sc}, mA/cm^2	25.5	23.4
Fill factor	0.62	0.65
Solar efficiency, %	12.4	12.4
Diode factor A	2.99	2.35
J_o, A/cm^2	1.3×10^{-6}	1.6×10^{-7}

[a] Illumination by solar simulator at 85 mW/cm^2.
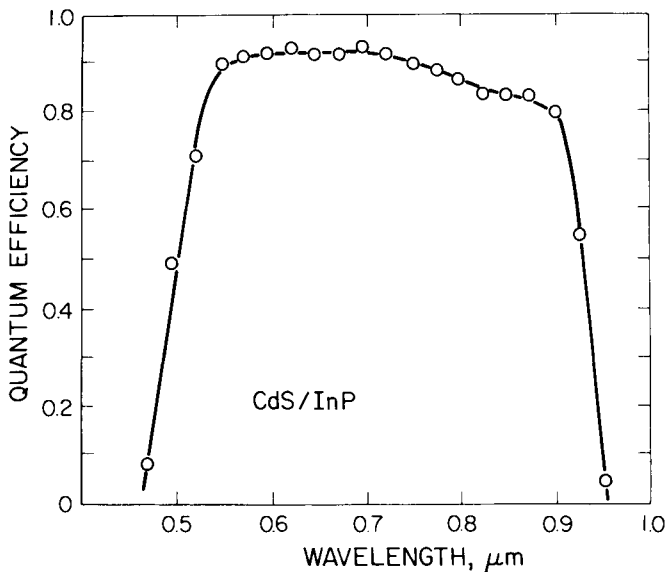
FIGURE 7.   Spectral response of the quantum efficiency
for a CdS/InP junction prepared by vacuum evaporation of CdS
on single crystal homoepitaxial InP layer deposited by chemical
vapor deposition on p^+-InP substrate (16).

VI.   OXIDE/SEMICONDUCTOR PHOTOVOLTAIC JUNCTIONS

Several different oxides exist that are high conductivity, large bandgap n-type materials, which therefore appear to be ideal candidates for the window material on a heterojunction. Other oxides, as mentioned in Section I, play an important role in MIS and SIS devices.

Compared to the CdS/CdTe heterojunction, for example, a degenerate indium-tin oxide (ITO)/CdTe heterojunction would have a bandgap window 55% larger because of the larger bandgap of the ITO (2.98 eV when non-degenerate but effectively up to over 3.4 eV when strongly degenerate) (17), and a diffusion potential 40% larger as estimated from electron affinities. Almost exactly the same kind of expectation would hold also for a ZnO/CdTe heterojunction.

VII.   ZnO/CdTe HETEROJUNCTIONS

ZnO/CdTe heterojunction solar cells may be prepared by deposition of ZnO by spray pyrolysis on single crystal CdTe substrates (18). Once again, as in the case of the deposition of CdS/CdTe junctions by this process, the critical variables are the temperature of the substrate during deposition and during post-deposition heat treatment in hydrogen.

FIGURE 8 shows the development of the photovoltaic proper-ties of the ZnO/CdTe junction with variations in the substrate temperature during deposition(19). The parameters are clearly very sensitive to the substrate temperature, reaching a maximum solar efficiency of 9.2% for a substrate temperature of 460°C, but being less than half of this at 430°C and showing definite decrease at 470°C. Examination of FIGURE 8 shows that the critical photovoltaic parameter is, as usual, the open-circuit
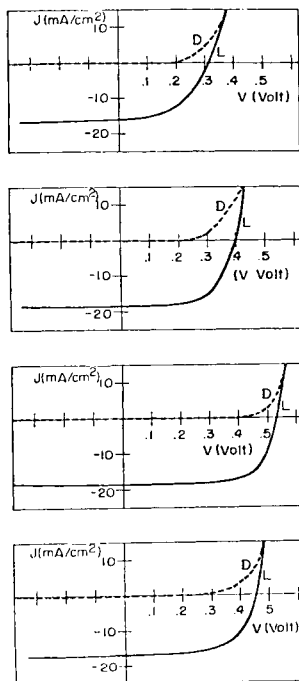
FIGURE 8. Light current-voltage curves at different deposition substrate temperatures for ZnO/CdTe heterojunctions prepared by spray pyrolysis deposition of ZnO. Substrate temperatures from top to bottom are 430°, 445°, 460°, 470°C.
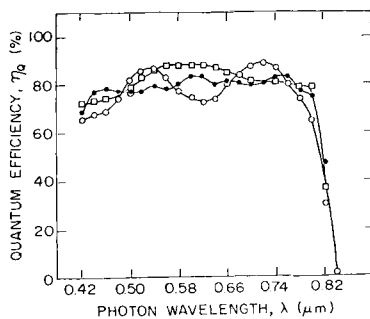
FIGURE 9. Spectral response of quantum efficiency for ZnO/CdTe heterojunctions prepared by spray pyrolysis of ZnO.

voltage, which varies rapidly with substrate temperature. The
short-circuit current, on the other hand, varies very little with
changing substrate temperature. ZnO/CdTe heterojunctions have
a lattice mismatch of some 27%, but it is evident from these
results and from the spectral response of quantum efficiency data
given in FIGURE 9 that high quantum efficiencies are realizable
even with very non-ideal heterojunctions. The specific inter-
face conditions that allow high open-circuit voltage, however,
are strongly dependent on the preparation conditions.

VIII.   MIS AND SIS DEVICES

     In a variety of Schottky barrier and heterojunction con-
figurations, at least a potential gain can be achieved by
inserting a suitable high bandgap insulator film, frequently
an oxide, between the components of the junction. Such an
insulating film often serves to increase the open-circuit
voltage of the device by means of one of three possible
mechanisms: an increase in the effective barrier at the semi-
conductor surface, an increase in the junction diode factor, or
a decrease in J_o without reducing the short-circuit current.
Both Si and GaAs form oxides simply by being exposed to air at
room temperature; in the case of Si, the formation of SiO_x is a
well-integrated aspect of Si technology.
     Examples of three MIS devices prepared with Si and three
different metals are given in Table II. Cells prepared to date
have an efficiency between 8 and 9%, as compared to an estimated
efficiency of 13 to 16% maximum for such devices. The effects
of an interface oxide layer have also been found critical in
improving Schottky barrier performance on GaAs (20,21). FIGURE
10 shows the dramatic effect on the open-circuit voltage of
various stages of oxidation of an n-GaAs surface before applica-

TABLE II. MIS Devices on Silicon

Silicon	SiO_2 Thickness, A	Metal	J_{SC}, mA/cm^2	V_{OC}, volts	Solar Eff., %	Ref.
2 ohm-cm p-type	15	Cr	26	0.50	8.1	(22)
3-15 ohm-cm p-type	20-40	Al	26.5	0.45	8	(23)
1-10 ohm-cm n-type	10-40	Au	22	0.55	9	(24)
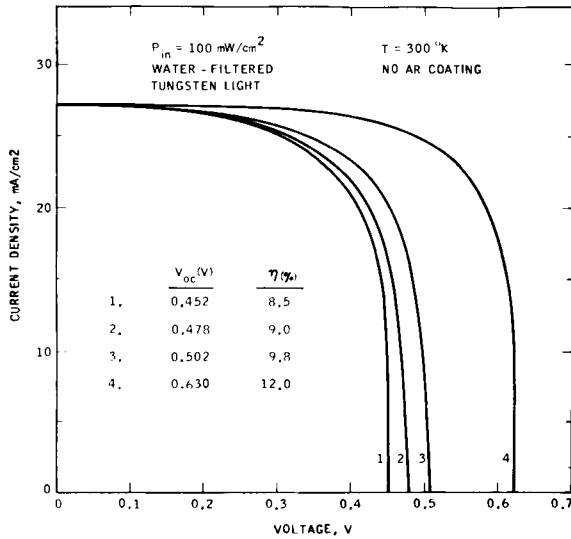
FIGURE 10. Light current vs voltage curves for Au/GaAs Schottky barriers for various treatments of the GaAs surface before application of the metal barrier contact. (1) "Clean" interface, (2) exposed to air at $300°K$ for 4 hr, (3) exposed to air at $300°K$ for 94 hr, and (4) exposed to air at $403°K$ for 70 hr (20).

tion of a Au barrier metal contact. In this case, the magnitude
of J_O was found to actually increase with oxide thickness, but
the increase in the diode factor caused by the oxide layer more
than compensated for this effect and yielded a net increase in
open-circuit voltage. Solar efficiencies up to 15% have been
reported. In this system, the use of a suitable antiflection
coating is essential because of the average 45% reflectivity
of the Au/GaAs surface.

Energy band diagrams for MIS and SIS devices are shown in
FIGURES 11 and 12 respectively. Increases in barrier height
and diode factor appear adequate to explain many of the observed
effects to date, but there is evidence that control of the
transport currents may also be an important factor, particularly
in ITO/Si junctions (25-28). The argument for this behavior goes
as follows. If the thickness of the oxide layer is greater than
30A, tunneling currents through the oxide (minority electron flow
from the p-type Si in a typical ITO/p-Si junction) is very small,
and the ITO and Si are essentially in thermal equilibrium, cor-
responding to a capacitor with an oxide dielectric. If the oxide
layer is less than 10A thick, then the oxide plays little role and
a standard Schottky barrier results. If, however, the oxide layer
thickness is between 10A and 30A, the tunneling current is large
enough to cause the semiconductors to depart from thermal equi-
librium and tunnel SIS diodes are formed. Over a certain range of
bias voltage, such non-equilibrium SIS devices have a diode
current that is controlled by the generation-recombination mech-
anism in the bulk, and the tunnel current simply provides an Ohmic
contact, thus giving a decrease in the magnitude of the J_O of the
device. Such an SIS model predicts a possible efficiency of 20%
for ITO/Si junctions, and possibly even higher efficiencies for
other semiconductor systems with more nearly optimum bandgap.
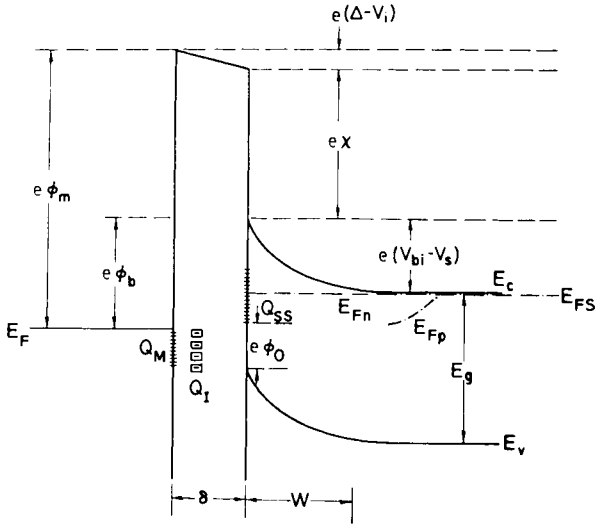
FIGURE 11.   Energy band diagram for an MIS junction.
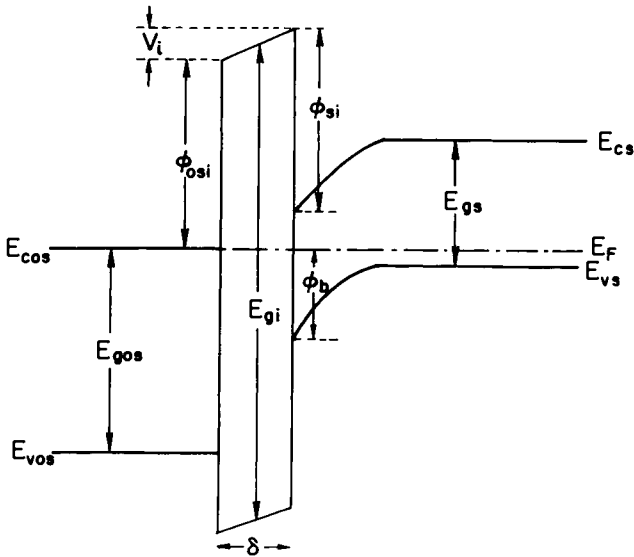
FIGURE 12.   Energy band diagram for an SIS junction.

IX.   SPUTTERED ITO/CdTe JUNCTIONS

    Junctions prepared by sputtering indium-tin oxide (ITO) onto
single crystals of CdTe and InP are considered in the final two
sections of this paper. As we shall see, both represent some
unexpected results with opportunities for detective work using
the methods of characterization summarized in Section II. It is
found that the method of deposition, in this case rf sputtering
at 2.5 KV, 180W, determines the characteristics of the resulting
junction, as well as the properties of the two constituent
materials.

    Typical of the best ITO/CdTe junctions made by this process,
without heat treatment, are the photovoltaic parameters:
V_{oc} = 0.82 - 0.85 V, J_{sc} = 12 - 15 mA/cm^2, and solar efficiencies
of about 8% (29). The large open-circuit voltage is surprising,
since values as large as 0.8 V are more normally characteristic
of a CdTe homojunction.

    The spectral response of two ITO/CdTe cells with quite
different electrical junction properties is given in FIGURE 13.
A gradual decrease in quantum efficiency is observed with in-
creasing photon energy from a maximum at approximately the bandgap
of CdTe. That this decrease cannot be attributed to optical
transmission through the ITO film is illustrated by the ITO
transmission curve included in FIGURE 13. The shape of the
response is, however, consistent with the hypothesis that a buried
homojunction has been formed in the CdTe as a result of the
sputtering process.

    A variety of diagnostic techniques were used in order to
evaluate this hypothesis beyond the circumstantial evidence of
large open-circuit voltage and shape of the spectral response.

    Upon room temperature aging or moderate heat treatment, it
was observed that the open-circuit voltage rapidly decreased,

and that the spectral response changed to a form more consistent
with a heterojunction. It thus appears that annealing removes the
buried homojunction and causes the formation of an actual
heterojunction structure, with decreased cell performance.

In order to simulate the effect of sputtering deposition of
ITO on CdTe without actually depositing ITO, sputter etching of
CdTe surfaces was investigated. Surface photovoltage measurements
showed that the band bending at the surface of the CdTe changed
from a downward bending characteristic of a depletion layer on
a p-type surface for the unsputtered surface to an upward bending
characteristic of a depletion layer on an n-type surface with
sputter etching. Changes in the photoluminescence emission of a
CdTe surface of the same type were observed both as the result
of sputter etching and thermal annealing.

An especially useful technique was the preparation of
In/CdTe junctions on CdTe surfaces given various pre-deposition
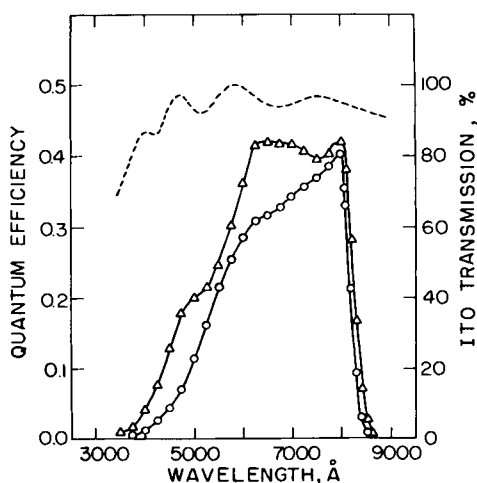
*FIGURE 13. Spectral response of the quantum efficiency for
ITO/CdTe junctions prepared by rf sputtering of ITO onto single
crystal CdTe. Dashed curve shows transmission of ITO film.*

treatments. FIGURE 14 compares the spectral response of the

quantum efficiency for an In/CdTe junction prepared by vacuum

evaporation of In onto chemically etched CdTe (a "normal"

Schottky barrier) with In/CdTe junctions prepared by vacuum

evaporation of In onto sputter etched CdTe surfaces. The latter

all show a sharp decrease in quantum efficiency with increasing

photon energy, becoming more pronounced with higher sputter

etching voltages. The same type of behavior was found for a

In/CdTe junction prepared by sputter deposition of In onto

chemically etched CdTe, as was found for vacuum evaporation of

In onto sputter etched CdTe. The open-circuit voltage for the

In/CdTe cell made on a sputter-etched surface (In contact to
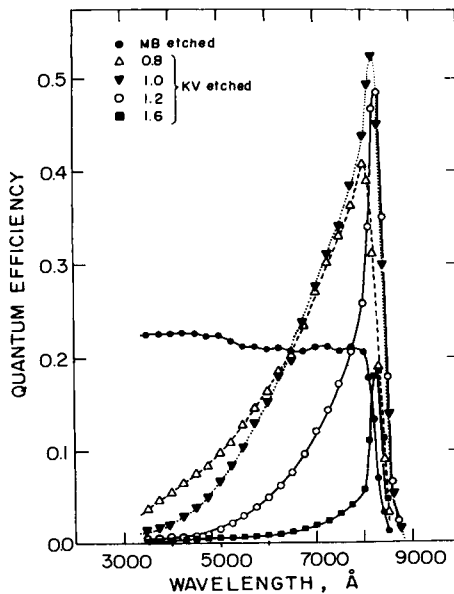
FIGURE 14. Spectral response of an In/CdTe Schottky barrier produced by vacuum evaporation of In onto methanol-bromine etched p-type CdTe. Also spectral response curves for In/CdTe junctions produced by vacuum evaporation of In onto sputter etched CdTe surfaces using the indicated sputtering voltages.

buried CdTe homojunction) was much larger than that for a cell
made by vacuum evaporation of In onto a chemically etched surface;
the 0°K extrapolated value of open-circuit voltage was 1.25 eV
for the sputter-etched surface, compared to 0.85 eV for the
chemically etched surface.

    EBIC measurements were also carried out on non-heated
ITO/CdTe junctions. These showed that the maximum current was
observed inside the CdTe, about 1 μm away from the metallurgical
interface.

    All of these evidences lead to the conclusion that when an
ITO/CdTe junction is formed by rf sputtering of the ITO, a surface
layer of the p-type CdTe is converted to n-type as a consequence
of thermally induced changes in the defect structure. The result
is a buried homojunction with the band diagram given in FIGURE 15.
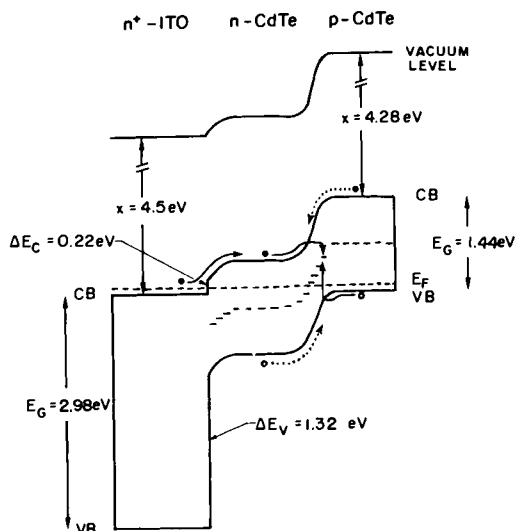
*FIGURE 15. Proposed energy band diagram for an ITO/CdTe
buried homojunction produced by rf sputtering of ITO onto the
surface of a p-type CdTe crystal, showing the n-type layer formed
by thermal effects during sputtering. The diagram is drawn in
the simple form of an abrupt junction.*

X.   SPUTTERED ITO/InP JUNCTIONS

Table I compares photovoltaic cell parameters for cells of
CdS/InP and ITO/InP, both made on the same homoepitaxial single
crystal layers of InP and both exhibiting almost identical
properties.   The high performance of the CdS/InP cells was
attributed to the good lattice match between CdS and InP.   What
was the reason for the good performance of the ITO/InP cells
prepared by sputter deposition of ITO, in view of the fact that
ITO and InP have very poor lattice match?   Actually even better
performance has been reported for similar cells of ITO/InP
with solar efficiency of 14.4% (30).   A direct clue is obtained
by comparing the spectral response of quantum efficiency for the
ITO/InP cells of Table I, as given in FIGURE 16, with the spectral
response for the CdS/InP cells given in FIGURE 7.   It immediately
appears that the ITO/InP cells are not heterojunctions, but
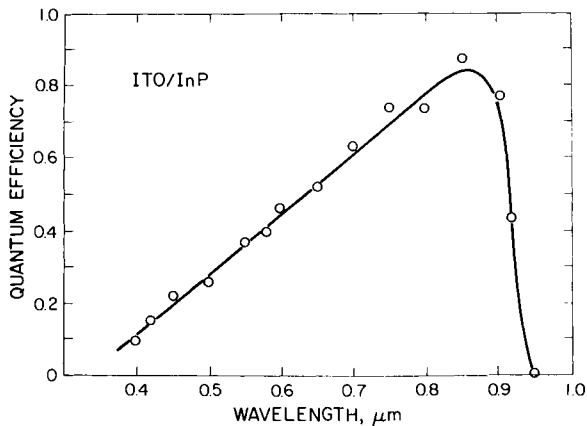
FIGURE 16.   Spectral response of the quantum efficiency for
the ITO/InP cell of Table I, prepared by rf sputtering of ITO
onto homoepitaxial single crystal layer of p-type InP (16).

buried homojunctions, and that the effects described in the
previous section for ITO/CdTe junctions also hold for ITO/InP
junctions.

There are other ways, however, by which a buried homojunction
might be formed. Ion probe analysis has been used to investigate
the diffusion of tin impurity from the ITO into the InP during
sputtering (31,32). Appreciable Sn diffusion occurs, which would
dope the InP n-type, if the InP temperature during sputtering is
$250^{\circ}C$, but little or none if the InP temperature is $25^{\circ}C$.
Experiments indicate that thermal damage to the InP during
sputter deposition of ITO is sufficient to cause conversion of
the InP surface to n-type even under situations where diffusion
of a donor impurity is not possible (33).

FIGURE 17 shows the spectral response of quantum efficiency
for a sputtered ITO/InP cell before and after various degrees of
heat treatment. Before heat treatment the spectral response has
a maximum near the bandedge of InP and a decrease in quantum
efficiency with increasing photon energy, such as is characteristic
of a homojunction. With heat treatment there is a change in the
spectral response to a heterojunction-like form, moderate heating
causing a relatively large increase in quantum efficiency and
then further heating causing a decrease.

EBIC measurements on ITO/InP cells made by sputtering showed
that the maximum EBIC signal occurred about 1 μm away from the
metallurgical junction, inside the InP. After heat treatment,
however, the EBIC maximum shifted to about the position of the
metallurgical junction.

If sputter deposition of ITO on InP produces a buried homo-
junction, then similar results should be obtained for a variety
of oxides if they are all deposited on InP by the same sputtering
process. It has been shown that sputtered In_2O_3, SnO_2, ZnO and
CdO all give substantially the same type of junction with InP as
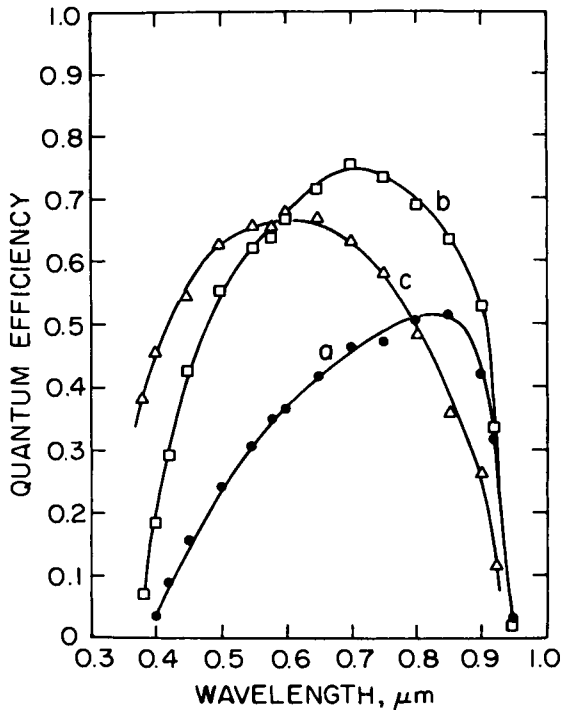
FIGURE 17. Spectral response of an ITO/InP cell produced by rf sputtering of ITO onto single crystal p-type InP. (a) Initial, (b) after heat treatment to reach optimum performance, (c) after excessive heat treatment.

does ITO. All have a spectral response of quantum efficiency

that decreases rapidly for higher energy photons, all have an

open-circuit voltage between 0.53 and 0.67 V, and all (except

the SnO_2 cell which had series resistance problems) have a

short-circuit current between 18 and 24 mA/cm^2, yielding an

efficiency between 7 and 11%. The fact that such similar results

are obtained for ITO and ZnO or CdO, in view of the fact that

Zn and Cd are acceptors if incorporated in InP, indicates that

the conductivity conversion is due to thermal effects of

sputtering and not to impurity diffusion.

To further investigate surface properties of InP important for junction formation, Au/InP junctions were prepared in three different ways: (a) vacuum evaporation of Au onto chemically-etched InP, (b) vacuum evaporation of Au onto sputter-etched InP, and (c) sputtering of Au onto chemically-etched InP. Once again sputter etching was used to simulate the sputtering damage in-volved in oxide deposition. Au/InP junctions prepared by process (a) exhibited the characteristics of a genuine Schottky barrier with a diffusion potential (measured from the 0^OK extrapolated value of open-circuit voltage) of 0.80 V. Au/InP junctions prepared by either process (b) or (c) were quite similar to one another, and quite different from the Schottky barriers produced by process (a); they exhibited a diffusion potential of 1.2 $\pm$ 0.1 V and a spectral response of quantum efficiency that was homo-junction-like. Heat treatment caused the characteristics of cells produced by processes (b) and (c) to change in the direction of becoming actual Schottky barriers.

The n-type electronic character of the sputter-etched InP surface was confirmed by direct surface Hall effect measurements. Similarly the effect on the photoluminescence of the InP surface of sputter etching was the same as that caused by sputter deposition of ITO.

An abrupt junction diagram of the n^+-ITO/n-InP/p-InP buried homojunction produced by rf sputtering of ITO onto InP, as suggested by the above evidence, is given in FIGURE 18. The ITO is degenerate, with the Fermi level lying about 0.2 eV above the bottom of the conduction band. The n-type InP layer has an electron density of 10^{16} cm^{-3}, assumed to be constant over the whole n-type layer. This damaged n-type layer plays a dominant role in both oxide/InP and Au/InP sputtered junctions, causing them to exhibit properties that depart from those of a simple
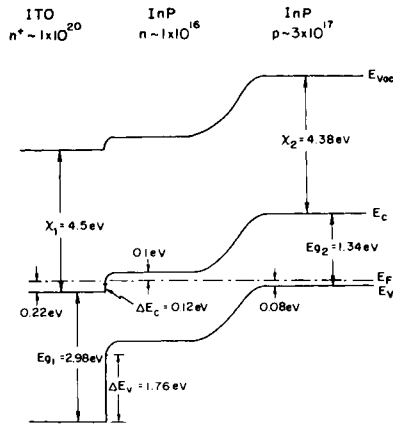
*FIGURE 18.   Energy band diagram for an n^+-ITO/n-InP/p-InP
buried homojunction produced by rf sputtering of the ITO.*

heterojunction or a Schottky barrier, respectively, and approx-
imate those of a buried homojunction structure in both types of
junction.

ACKNOWLEDGMENTS

sity, and Dolores Golmayo of IFM in Madrid.

REFERENCES

1.   Anderson, R. L., *IBM J. Res. Dev. 4,* 283 (1960).

2.   See, for example, Fahrenbruch, A. L., and Aranovich, J.,
     in "Topics in Applied Physics. Vol. 31: Solar Energy
     Conversion. Solid-State Physics Aspects" (B. O. Seraphin,
     ed.), p. 257. Springer-Verlag, Berlin, (1979).

3.   Mitchell, K. W., Fahrenbruch, A. L., and Bube, R. H.,
     Solid-State Electronics 20, 559 (1977).

4.   Gill, W. D., and Bube, R. H., *J. Appl. Phys. 41,* 3731 (1970).

5.   Fahrenbruch, A. L., and Bube, R. H., *J. Appl. Phys. 45,* 1264
     (1974).

6.   Mitchell, K. W., Fahrenbruch, A. L., and Bube, R. H., *J.
     Appl. Phys. 48,* 4365 (1977).

7.   Ma, Y. Y., Fahrenbruch, A. L., and Bube, R. H., *Appl. Phys.
     Lett. 30,* 423 (1977).

8.   Yamaguchi, K., Matsumoto, H., Nakayama, N., and Ikegami, S.,
     Japan. J. Appl. Phys. 15, 1575 (1976); *16,* 1203 (1977).

9.   Werthen, J., unpublished result.

10. Wagner, S., Shay, J. L., Bachmann, K. J., and Buehler, E.,
     Appl. Phys. Lett. 26, 229 (1975).

11. Shay, J. L., Wagner, S., Bettini, M., Bachmann, K. J., and
     Buehler, E., *IEEE Trans. Electron Dev. ED-24,* 483 (1977).

12. Bettini, M., Bachmann, K. J., Buehler, E., Shay, J. L.,
     and Wagner, S., *J. Appl. Phys. 48,* 1603 (1977).

13. Bettini, M., Bachmann, K. J., and Shay, J. L., *J. Appl. Phys.
     49,* 865 (1978).

14. Bachmann, K. J., Buehler, E., Shay, J. L. and Wagner, S.,
     Appl. Phys. Lett. 29, 121 (1976).

15. Shay, J. L., Wagner, S., Bettini, M., Bachmann, K. J., and
     Buehler, E., *IEEE Trans. Electron Dev. ED-24,* 483 (1977).

16. Manasevit, H. M., Hess, K. L., Dapkus, P. D., Ruth, R. P.,
     Yang, J. J., Campbell, A. G., Johnson, R. E., Moudy, L. A.,
     Bube, R. H., Fabick, L. B., Fahrenbruch, A. L., and Tsai,
     M. J., *13th IEEE Photovoltaic Spec. Conf.,* p. 165 (1978).

17. Haines, W. G., and Bube, R. H., *J. Appl. Phys. 49,* 304
     (1978).

18. Aranovich, J., Ortiz, A. and Bube, R. H., *J. Vac. Sci.
     Technol. 16,* 994 (1979).

19. Aranovich, J., Golmayo, D., Fahrenbruch, A. L., and Bube,
     R. H., to be published.

20. Stirn, R. J., and Yeh, Y. C. M., *Appl. Phys. Lett. 27,* 95
     (1975).

21. Stirn, R. J., and Yeh, Y. C. M., *IEEE Trans. Electron Dev.
     ED-24,* 476 (1977).

22. Anderson, W. A., Delahoy, A. E., and Milano, R. A., *J. Appl.
     Phys. 45,* 3913 (1974).

23. Charlson, E. J., and Lien, J. C., *J. Appl. Phys. 46,* 3982
     (1975).

24. Pompon, J. P., and Siffert, P., *J. Appl. Phys. 47,* 3248
     (1976).

25. Shewchun, J., Dubow, J., Myszkowski, A., and Singh, R.,
     J. Appl. Phys. 49, 855 (1978).

26. Shewchun, J., Dubow, J., Wilmsen, C. W., Singh, R., Burk,
     D., and Wager, J. F., *J. Appl. Phys. 50,* 2832 (1979).

27. Shewchun, J., Burk, D., Singh, R., Spitzer, M., and Dubow,
     J., *J. Appl. Phys. 50,* 6524 (1979).

28. Ghosh, A. K., Fishman, C., and Feng, T., *J. Appl. Phys. 49,*
     3490 (1978).

29. Courreges, F. G., Fahrenbruch, A. L., and Bube, R. H.,
     J. Appl. Phys. , to be published (1980).

30. Sree Harsha, K. S., Bachmann, K. J., Schmidt, P. H.,
    Spencer, E. G., and Thiel, F. A., *Appl. Phys. Lett. 30,* 645
    (1977).

31. Bachmann, K. J., Bitner, T., Thiel, F. A., Sinclair, W. R.,
    Schreiber, Jr., H., and Schmidt, P. H., *Solar Energy
    Materials,* in press.

32. Bachmann, K. J., Schreiber, Jr., H., Sinclair, W. R.,
    Schmidt, P. H., Thiel, F. A., Spencer, E. G., Pasteur, G.,
    Feldmann, W. L., and Sree Harsha, K., *J. Appl. Phys. 50,*
    3441 (1979).

33. Tsai, M. J., Fahrenbruch, A. L., and Bube, R. H.,
    to be published.

CHAPTER 18

THE OPTIMIZATION OF SOLAR CONVERSION DEVICES[*]

D.S. *Ginley*
M.A. *Butler*
C.H. *Seager*

Sandia Laboratories[†]
Albuquerque, New Mexico

I. INTRODUCTION

    For the materials scientist, the potential of solar energy con-
version offers an array of opportunities and challenges. The
optimization of materials to achieve optimum device efficiencies
comes into play in almost any conceivable device. The use of
many simple chemical concepts can have considerable utility when
applied to many of these problems. In context, this paper will
discuss the direct and indirect application of simple chemical
potential and electronegativity arguments to two diverse systems
that have considerable potential for solar energy conversion.

    First, photoelectrochemical cells (PEC) have shown potential
for the direct conversion of solar energy into useful chemical
products and/or electricity. It will be shown how the key criteria of
these cells can be delineated. Particular attention will be direc-
ted toward understanding the biasing requirements of these cells,
and to this end an electronegativity model will be presented that can
be used to quantitatively predict biasing requirements. In this
context, the importance of chemisorbed ions from the electrolyte
on the Helmholtz layer will be discussed. We will also demon-
strate how the electromigration of ions in the electrode near-
surface region can substantially affect biasing requirements and
long-term stability of such photoelectrodes.

Second, thin-film polycrystalline semiconductors, especially silicon, show tremendous potential as photovoltaic materials in flatplate solar collectors. The economics for their deposition are generally favorable; however, conversion efficiencies are at present well below the level needed to make the devices economic.

One of the main causes of the reduced efficiencies, compared to single-crystal materials, is the deleterious effects of the grain boundaries. Grain boundaries act as recombination centers for minority carriers as well as shunts across the p-n junction. We will present our current picture of the energy levels in silicon grain boundaries, and a brief discussion of the double-depletion layer, thermal-emission model of conduction over the potential barrier in the boundary. We will also discuss our recent results demonstrating that various chemical agents, when appropriately introduced into silicon grain boundaries, are capable of modifying grain boundary potential barriers. The prospects for increasing polycrystalline silicon solar cell performance by these treatments will be reviewed.

II. PHOTOELECTROCHEMICAL CELLS (PEC)

Introduction

The energy crisis of the seventies has stimulated research in energy-related areas, particularly those useful for utilization of solar energy. One of the many research fields which show promise for solar energy conversion is photoelectrochemistry. A photoelectrochemical device is one in which a semiconducting electrode is illuminated in a liquid cell and drives electrochemical reactions at both electrodes. These cells may be of two types; one directed primarily toward the production of electricity (wet photovoltaic cell) and one making chemical products through a chemical change at the electrode or electrolyte. One of the more attractive chemical reactions is the decomposition of water to form H_2 and O_2 (photoelectrolysis).

An important aspect of applying photoelectrochemical devices
to solar energy conversion is defining the materials properties
of the light-sensitive electrode necessary to optimize its per-
formance. In order to do this, we must delve into the details
of the mechanisms involved in the photoelectrochemical process.
As will be seen, we have not reached the point where the key
criteria for selecting an optimum electrode can be delineated,
though the problem of finding the material has not been solved.

Although photoeffects at electrodes in electrochemical cells
were first observed by Becquerel(1), it wasn't until Fujishima,
Honda and Kikuchi demonstrated(2) the decomposition of water
at a TiO_2 electrode (in 1969) that this field really commenced
to grow. Since then a number of reviews in the field have been
published (3-5).

The typical photoelectrochemical cell appears as shown in
Fig. 1. Here we illustrate a photoelectrolysis cell for decom-
posing water into hydrogen and oxygen. Oxidation occurs at the
photoanode and reduction at the metallic or graphite cathode.

PHOTOELECTROLYSIS CELL
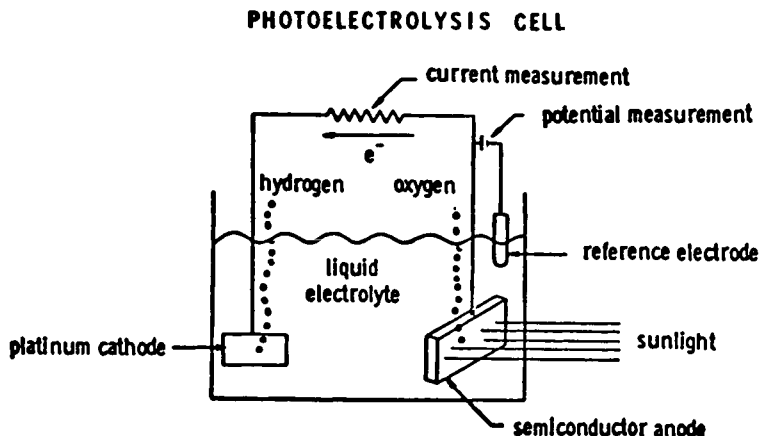
FIGURE 1.   A photoelectrochemical cell for the decomposition
of water into hydrogen and oxygen. The cell consists of a basic
aqueous electrolyte, a photoactive semiconducting anode and a
platinum or graphite cathode. Experimentally, potential is
measured between the anode and a reference electrode and current
between the anode and the cathode.

The easiest way to describe the operation of a photoelectro-
chemical cell is to examine its energy level diagram. The
simplest device consists of a semiconducting electrode, a metal-
lic electrode and a "simple" electrolyte as shown in Fig. 2.

The energy in the electrolyte at which electrons must be pro-
vided to drive the electrochemical reaction is known as the redox
potential and is usually referenced to the normal hydrogen or
energy position at which the conduction and valence bands for
n- and p-type semiconductors, respectively, intercept the solid/
electrolyte interface is known as the flatband potential V_{fb}.
This is because V_{fb} is determined from the changing properties of
the interface (capacitance, photocurrent, etc.) as the bands are
made flat.
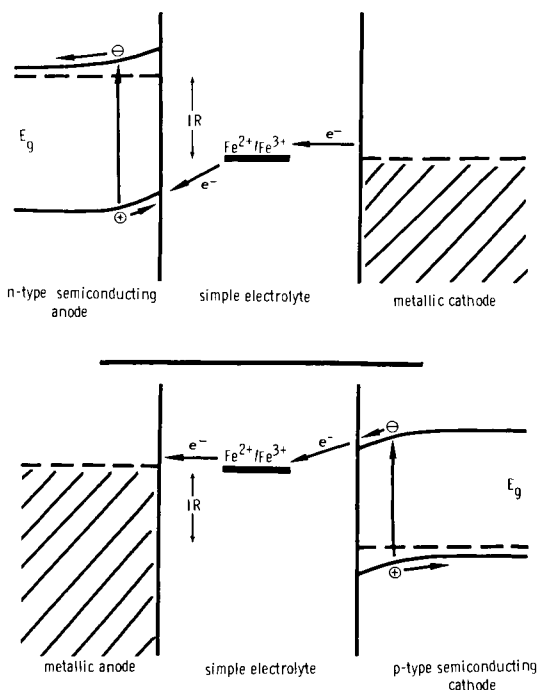
FIGURE 2. *Energy level diagram for simple electrochemical
devices which produce electricity but no chemical products. The
use of both n- and p-type semiconducting electrodes is illus-
trated. A simple electrolyte is one in which only a single
electrochemical reaction can take place.*

The semiconductor can be used as a light sensitive anode
or cathode depending on whether it is n- or p-type, respectively.
This is determined by the need for a region depleted of majority
carriers at the semiconductor surface. In the depletion region
there exists an electric field which is necessary to separate
spatially the optically-excited electron in the conduction band
from the hole in the valence band. Thus, when illuminated with
photons of energy greater than the band gap of the semiconductor
an electron is excited into the conduction band and the electron
and hole are separated by the electric field in the depletion
region before they can recombine. The majority carrier then
flows through the electrical load to the metallic electrode and
drives an electrochemical reaction. The minority carriers flow
to the semiconductor surface driving another electrochemical
reaction.

In Fig. 2, we represent the single electrochemical reaction
by the reversible ferric-ferrous couple ($Fe^{3+}_{aq} + e \rightleftarrows Fe^{2+}_{aq}$). In
such an electrolyte the reaction is driven one way at the anode
($Fe^{2+}_{aq} \rightleftarrows Fe^{3+}_{aq} + e^-$) and the opposite direction at the cathode
($Fe^{3+}_{aq} + e^- \rightleftarrows Fe^{2+}_{aq}$). Thus, in such a system there is no net
chemical change and the power produced must be extracted via the
electrical load. Such cells are commonly called wet photovoltaic
cells in analogy with the corresponding solid state devices.

Another type of PEC results in the production of a chemical
product. Its energy level diagram is illustrated in Fig. 3. The
operation of the device is the same as we have just discussed,
except that two irreversible electrochemical couples are driven,
with one taking place at the anode and the other at the cathode.
This results in a net chemical change in the electrolyte. In
the figure we illustrate this by the reactions for the decomposi-
tion of water to hydrogen and oxygen. At the cathode, the reac-
tion is essentially ($2H^+ + 2e^- \rightleftarrows H_2$) and at the anode the
reaction is ($2OH^- \rightleftarrows 2H^+ + O_2 + 4e^-$). Note that the net amount
of energy stored is the difference between the two couples.
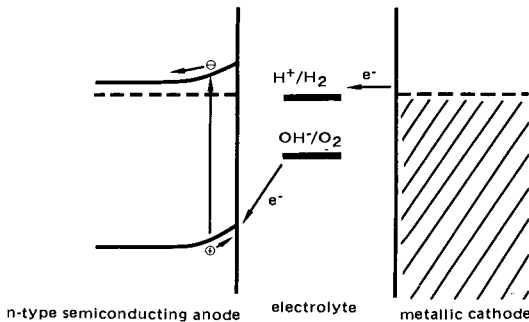
FIGURE 3. *Energy level diagram for electrochemical device*
which produces a chemical product. The electrolyte is illustra-
ted for the decomposition of water in H_2 and O_2. Only an n-type
semiconductor is shown, although a p-type semiconductor could be
used as illustrated in Fig. 2. Normally, chemical producing
cells are operated under short-circuit conditions to maximize
the amount of the chemical product.

Other types of energy storing reactions exist as well. For

example, the production of methanol from CO_2 (6) and of ammonia

from H_2O and N_2 (7) are attracting considerable interest.

From examining these energy level diagrams, it is possible

to discern the basic criteria that a useful semiconducting elec-

trode must satisfy. The first important aspect is efficient

conversion of photons to excited electrons and their efficient

utilization in the electrochemical processes. In general, in

these cells the generation and separation of carriers in the

semiconductor is the rate-limiting step rather than the chemical

kinetics at the interface (8A). Thus, the problem becomes the

same basic one as is faced in solid-state photovoltaic devices

and the same factors are important. In fact, the Schottky

barrier formalism has been applied successfully to the semicon-

ductor/electrolyte interface (8). Since only photons of energy

larger than the band gap of the semiconductor can be used, the

band gap must be chosen to optimize the conversion efficiency.

Another factor is the optical absorption depth compared to the

depletion layer thickness. Since we need the electric field in

the depletion layer to separate the electron-hole pairs and since
most semiconductors have short diffusion lengths, it is important
to absorb most of the light in the depletion layer region. The
optical absorption depth will be significantly different if the
gap is direct rather than indirect. The depletion layer thick-
ness depends on doping level and dielectric constant of the
semiconductor.

   The second most important property of the semiconducting
electrode is the location of the energy bands. Aside from deter-
mining the band gap, the energy band positions relative to the
energy levels in the electrolyte also determine the maximum open-
circuit voltage for the wet photovoltaic cells and the biasing
requirements if any, for the chemical producing cells. This can
be seen by examining Figs. 2 and 3. For the wet photovoltaic
cells shown in Fig. 2, under open-circuit conditions the Fermi
level in the metal electrode will equal the redox potential in
the electrolyte. Under maximum illumination, the bands in the
semiconductor will approach flatband condition. Thus, the maxi-
mum open-circuit voltage for the cell will be the difference
between the redox potential in the electrolyte and the intercept
of the conduction band with the interface (the electron affinity
of the semiconductor). While the redox potential is known for
most couples, the same cannot be said of semiconductor electron
affinities. This means that either this information must be
determined experimentally in each case or a model must be con-
structed to predict semiconductor electron affinities.

   Similar arguments apply to the chemical producing cell shown
in Fig. 3. Since we would like to operate the cell under short-
circuit conditions and maximize the production of chemical
products, the conduction band must intercept the interface so
that a depletion region exists at short-circuit conditions.
Thus, for an n-type semiconductor the electron affinity must be
smaller than the cathodic redox potential in the electrolyte as
measured from the vacuum level. Conversely, for a p-type

semiconductor the valence band should intercept the interface
below the anodic redox potential in the electrolyte.

The third and perhaps most crucial condition that the semi-
conducting electrodes must satisfy is stability under the rather
rigorous conditions in which they are operated. They must not
only be stable against chemical dissolution in the electrolyte
but also against electrochemical corrosion and photocorrosion.
Most of these effects are not well understood so that choosing
stable materials or modifying their properties or the electro-
lyte to induce stability is more art than science. Some
progress has recently been made in defining the conditions for
stability of semiconductors in contact with electrolytes (9,10).
The decomposition reactions are merely additional redox couples
in the electrolyte. Thus, the relative postions of these couples
with respect to the semiconductor band edges will determine the
thermodynamic stability of the semiconductor in that particular
electrolyte. However, some semiconductors which are thermodynam-
ically unstable may be effectively stabilized if the kinetics of
the decomposition reaction are slow enough. There is also the
problem of competition between the decomposition reaction and
other possible reactions both beneficial and detrimental.
Stability is a complex question which is quite difficult to
answer even on an individual basis.

These three criteria: (1) Quantum Efficiency, (2) Potential
Behavior, and (3) Stability, define the characteristics desirable
in a semiconducting photoelectrode. The rest of this discussion
will deal with a model we have developed to describe potential
behavior in detail. We will show that the electron affinity of
a semiconductor can be calculated from the atomic electronega-
tivities of its constituent atoms. It will be demonstrated that
the effects of chemisorbed ions are large and can be measured and
taken into account. Finally, it will be demonstrated that the
electromigration of ions into and out of the electrode surface
can affect the flatband potential of the electrode signficantly.

Potential Behavior

Similar to the case of the solid state device, the overall
conversion efficiency in a photoelectrochemical cell is a function
primarily of the short-circuit current, open-circuit voltage and
the fill factor. The short-circuit current and fill factor are
determined by the number of photons absorbed minus the losses in
the system. These are primarily a function of the intrinsic
properties of the semiconductor, band gap, doping level, carrier
lifetimes and number of traps and recombination centers. The
open-circuit voltage for a wet photovoltaic cell or effective
biasing potential for chemical producing cells, however, depends
on the relative positions of the energy levels in both the semi-
conductor and the electrolyte as shown in Fig. 4.

The energy levels in the electrolyte (redox potential) are
generally known as a function of electrolyte composition (11) or
can easily be determined. However, the energy levels in the
semiconductor are more difficult to obtain. For semiconducting
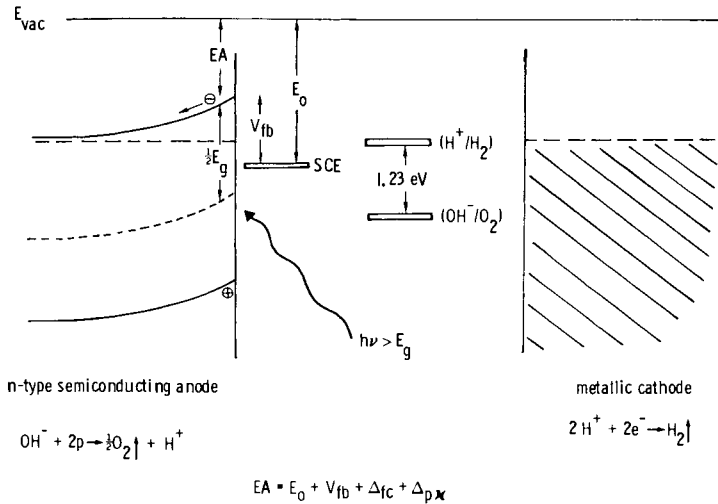
*FIGURE 4. Energy level diagram for a photoelectrolysis cell
illustrating the relationship between the electron affinity (EA)
and the flatband potential (V_{fb}). Energy levels are shown for
zero external bias.*

electrodes, the usual procedure is to measure some property
which depends on applied potential and extrapolate to the flat-
band condition.

The semiconductor/electrolyte interface can be represented
as two capacitances in series; one in the electrolyte near the
surface (Helmholtz layer) C_H and the other capacitor formed in
the semiconductor by the depletion layer C_{sc} (12). Since these
two capacitors are in series and $C_{sc} << C_H$, the net capacitance
is $\sim C_{sc}$. The width of the depletion layer depends on the
applied potential as in a normal Schottky barrier. Since the
depletion layer width goes to zero at the flatband potential, the
capacitance of the junction goes to infinity. The analysis of
this type of behavior for solid-state devices has shown that C^{-2}
is linear in applied potential (Mott-Schottky plot). This
approach can be applied to the semiconductor/electrolyte junc-
tion.[3] The flatband potential V_{fb} is the position of the Fermi
level in the semiconductor when the depletion layer goes to zero
width (no band bending) measured relative to whatever reference
electrode is being employed.

With no depletion layer and therefore no electric field to
separate the photogenerated electron-hole pair, the photocurrent
should also go to zero at this potential. Differences between
the onset of photocurrents and flatband potential determined from
capacitance data indicates the existence of recombination centers
or surface states in the semiconductor gap (13). In many cases
these are absent and the photocurrent onset can be used to deter-
mine the flatband potential.

Determination of the flatband potential is of crucial impor-
tance since it determines the maximum open-circuit voltage of a
wet photovoltaic cell and the bias requirements of a chemical
producing PEC. The potential difference between the semiconduc-
tor band edge and the redox potential at the counter electrode is
the maximum obtainable band bending.

It is particularly useful to be able to predict V_{fb} for a potential semiconductor to evaluate its promise as a photoelectrode. To do this effectively, V_{fb} must be related back to some fundamental property of the semiconductor. This can be done fairly easily, as we have previously demonstrated (14,17) by virtue of the fact that the electron affinity (EA) of the semiconductor is directly related to the flatband potential. This can be seen by referring to Fig. 4 for a typical photoelectrolysis cell. Here we can see that (14)

$$EA = E_o + V_{fb} + \Delta_{fc} + \Delta_{px} \qquad (1)$$

where E_o is a constant relating the reference electrode, normally the standard calomel electrode (SCE), to the vacuum level, Δ_{fc} corrects for the difference between the doped Fermi level and the bottom of the conduction band and Δ_{px} is the potential drop across the Helmholtz layer due to ions adsorbed on the semiconductor surface.

The problem then is to evaluate each of these factors so as to be able to predict V_{fb} for any semiconductor/electrolyte combination. While there is some uncertainty, E_o is taken to be 4.75 eV for the SCE at 23°C (15). Δ_{fc} can be evaluated from Seebeck coefficient measurements (16) and for the highly-doped semiconductors commonly employed in PECs is typically 0.1 eV, a small correction. In our future discussions, we will ignore this term. The most important factors are EA and Δ_{px}.

A detailed understanding of adsorption of ions at the semiconductor/electrolyte interface is not possible at the present time. However, a number of things are known. If the flatband potential of the semiconductor shifts with concentration of ions in the electrolyte, then some species related to the ions in solution is specifically adsorbing on the semiconductor surface. For metal oxides in simple acids and bases, the flatband potential shifts by 59 mV/pH unit due to specific adsorption of H^+ and OH^-. These ideas have also been applied to non-oxides such as CdS (17A)

and GaP (17B). The net surface charge depends on the relative electrochemical potentials for the two adsorbing species in the adsorbed state and in the solution. Since changing concentration in the solution changes the electrochemical potentials, it is possible to vary the relative coverages of the two adsorbing species and thus the net surface charge. Some concentration of ions in the solution exists at which the coverages by the two oppositely charged species are the same and thus the net surface charge is zero (point of zero zeta potential, PZZP). At this point, the potential drop due to adsorbed species is zero ($\Delta_{px} = 0$). Fortunately, techniques exist for determining this concentration of ions for any semiconductor/electrolyte combination (14,17). Thus, for metal oxides we may write:

$$\Delta pH = (59 \text{ mV})(pH_{PZZP} - pH) \tag{2}$$

In general, it is possible to determine the PZZP of a semiconductor having only its undoped powder, and thus, it is not required to actually fabricate electrodes with all the ensuing difficulties.

The final factor we need to know in order to determine the flatband potential is the semiconductor electron affinity. This quantity is difficult to determine experimentally and impossible to calculate from first principles. However, some electron affinities have been calculated using atomic electronegativities (14,17-19). Mulliken defines the electronegativity X of an atom as the arithmetic average of the energy to add and subtract a single electron. Thus, for neutral atoms, we have:

$$X_{atomic} = \frac{1}{2} (A + I_1) \tag{3}$$

where A is the atomic electron affinity and I_1 the first ionization potential. Both the electron affinities (30) and ionization potentials (21) are available for most atoms. For an intrinsic semiconducting solid, the corresponding energies are the bulk electron affinity EA and the energy at the valence band $EA + E_g$. Thus, in the bulk we have:

$$\chi_{bulk} = EA \frac{1}{2} E_g \tag{4}$$

The problem then is to relate the bulk electronegativity to the atom electronegativities of the constituent atoms. Nethercot has postulated (18) that the bulk electronegativity is the geometric mean of the atom electronegativities of the constituent atoms. This hypothesis seems to work for a large number of compounds. For example, for TiO_2 the electron affinity is:

$$EA(TiO_2) = \chi(TiO_2) - \frac{1}{2} E_g(TiO_2) \tag{5}$$

$$= [\chi(Ti) \; \chi^2(O)]^{1/3} - \frac{1}{2} E_g(TiO_2)$$

$$EA(TiO_2) = 4.33 \text{ eV} \tag{6}$$

If we evaluate the correction term Δ_{px}, V_{fb} can be predicted by using Eq. 1. As we have discussed, depending on the concentration of the potential determining ions in the electrolyte and the intrinsic pK_a of the semiconductor of interest with respect to those ions, differing numbers of anions and cations will be absorbed on the surface. There will be a unique concentration of ions in solution at which equal numbers of anions and cations are absorbed on the surface and Δ_{px} is equal to zero, the PZZP. For TiO_2 at this point

$$V_{fb} = EA - E_o$$

$$= 4.33 - 4.75 = -.42 \text{ V vs SCE} \tag{7}$$

The PZZP can be measured by a variety of different techniques (14, 17) one of which is shown in Fig. 5. The dashed curves are a series of differential potentiometric titrations of TiO_2 with NaOH solution where the small peaks are at the PZZP and scale inversely with the amount of TiO_2 added. The solid lines are theoretical curves for the titration of pure H_2O and two buffered H_2O solutions. The peaks in the data points occur because at the the PZZP oxide powder no longer acts as a buffer and Δ_{px}/Δ_{ml}
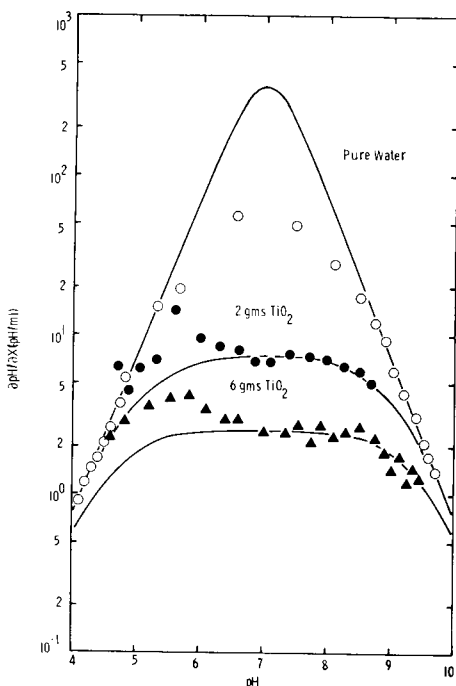
FIGURE 5. Differential potentiometric titrations plotted as $\partial pH/\partial\chi(\Delta pH/\Delta ml)$ vs pH for 3 solutions: ○○○ *600 ml distilled-deionized water, initial pH adjusted with 0.1 M KOH,* ●●● *600 ml distilled-deionized water 0.001 M in KNO_3 with 2 gm of suspended TiO_2 (99.995%) initial pH adjusted with 0.1 M KOH,* ▲▲▲ *600 ml distilled-deionized water 0.001 M in KNO_3 with 6 gm of suspended TiO_2 (99.995%). The solid lines represent theoretical fits for solutions with various concentrations of buffer. All solutions were stirred under a constant purge of argon and all titrations were performed with 0.1 M HNO_3.*

increases correspondingly. The PZZP can also be determined by adding TiO_2 powder to an aqueous solution of known pH. The pH of the solution will drift upon addition of the powder toward the PZZP. At the PZZP, the pH of the solution is independent of the amount of added TiO_2. The PZZP of TiO_2 occurs at a pH of 5.8. Thus, by using Eqs. 2 and 5 and the PZZP, we can calculate V_{fb} for any pH.

The technique illustrated for TiO_2 works well for the rest of the transition metal oxides, and it can be applied to non-oxides, both n- and p-type. The model works quite well for n-CdS

as is normally employed in wet photovoltaic cells such as n-CdS/
1 M Na$_2$S, 1 M NaOH/C. Here though, the potential   determining
ions are not OH$^-$ and H$^+$ as in the metal oxides but are HS$^-$ and
H$^+$. Thus, the PZZP must be determined with respect to these
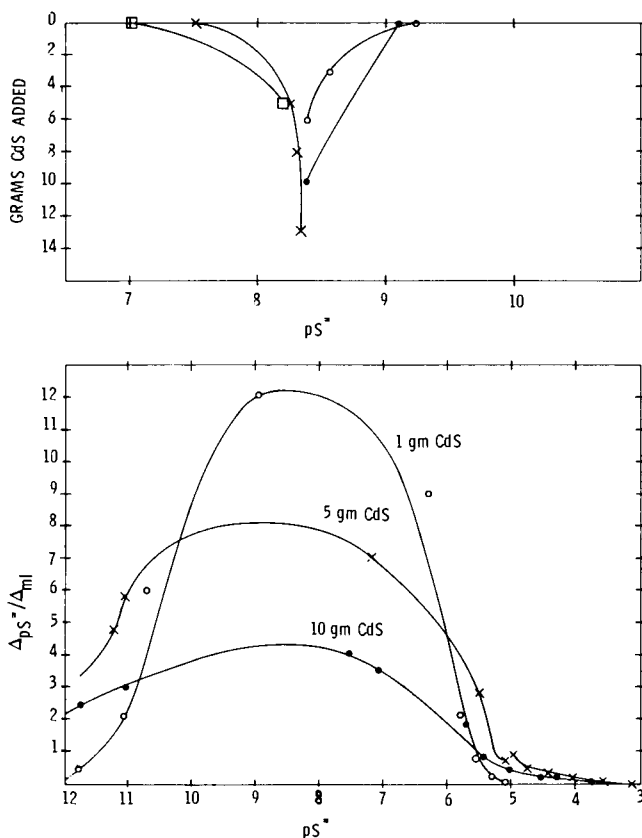
FIGURE 6. Determination of the S$^=$ concentration at the PZZP
of the CdS anode. The top half of the figure represents data
taken by the pX drift technique. In particular, we plot grams of
CdS added to a 600 ml sulfide solution of known initial pS$^=$ and
0.1 M KOH vs. measured pS$^=$. Points on continuous lines repre-
sent successive additions to the same solution. The lower half
of the figure consists of three differential potentiometric
titrations of a suspended amount of CdS, 1, 5, 10 gm in 600 ml
0.1M KOH with Na$_2$S solution. The rate of change of pS$^=$ with
added titrant $\partial pS^=/\partial S$ is plotted vs. pS$^=$. It is of note
that the same peak for the PZZP is observed in both curves and
that $\partial pS^=/\partial x$ scale inversely with the amount of added CdS.

ions as shown for both the drift and differential potentiometric techniques in Fig. 6. Once this is done, the predicted flatband potential can be compared to the experimental value obtained by extrapolating the known dependence of V_{fb} on the concentrations of the potential determining ions as shown in Fig. 7. As can be seen, the agreement is quite good.

The method is also applicable to p-type semiconductors but here Eq. 1 must be rewritten as:

$$EA = V_{fb} + E_o + \Delta_{fc} \Delta_{px} - E_g \qquad (8)$$

where the factor of the band gap takes into account the position of the Fermi level in p-type semiconductors.

The use of Eq. 8 can be illustrated for p-GaP, a promising photocathode in photoelectrolysis cells. We can rewrite Eq. 8 to solve for V_{fb} as:
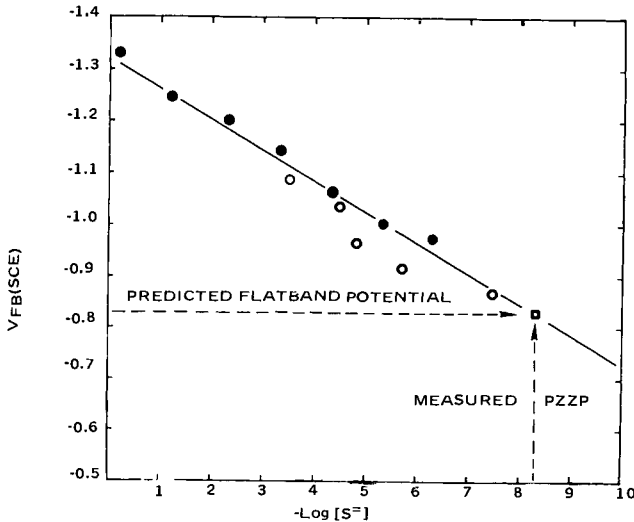
FIGURE 7. Predicted vs. experiment   ial
for n-Cds. The experimentally measured flatband (V_{fb}) for a
number of different sulfide solutions is plotted vs. the measured
sulfide ion concentration as $-log[S^=]$. The solid line has a
slope of 59 mV per $S^=$ unit. The open circle is the calculated
V_{fb} at the measured PZZP.

$$V_{fb} = EA + E_g - E_o - \Delta_{fc} - \Delta_{px}$$ (9)

calculating EA

$$EA = X_{GaP} - \frac{1}{2} E_g$$

$$EA = (X_{Ga} X_P)^{1/2} - \frac{1}{2} E_g$$

$$= 4.20 - \frac{1}{2}(2.22)$$

$$= 3.09$$ (10)

At the PZZP $\Delta_{px} = 0$ and neglecting Δ_{fc}

$$V_{fb} = EA + E_g - E_o$$

$$= 3.09 + 2.22 - 4.75$$

$$= .56$$ (11)
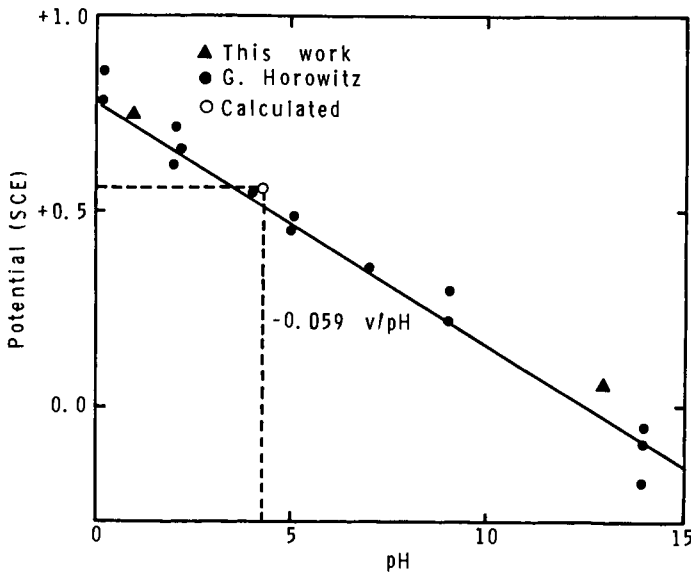
FIGURE 8.   Predicted vs. experimental flatband potential
for p-GaP. Plotted is the variation of the experimentally
measured flatband potential with pH. The solid line has a
slope of 59 mV per pH unit. The open circle is the calculated
V_{fb} at the measured PZZP. [G. Horowitz, J. Appl. Phys. *49*,
3571 (1978)]

In photoelectrolysis cells the experimentally determined PZZP
occurs at a pH 4.25.

Fig. 8 shows the dependence of V_{fb} on pH with the position
of the predicted V_{fb} shown by the dashed lines. As can be seen,
the point falls on the experimental line as expected.

By using the methods discussed to calculate the electron
affinity, it is now possible to predict the flatband potential
for any semiconductor/electrolyte combination. Correcting all
the measurements to the respective PZZPs allows a direct compari-
son of the calculated electron affinity with the measured flatband
potentials. In Fig. 9, we show such a comparison for a number of
different semiconductors. As can be seen, the agreement is quite
good.

This knowledge and the knowledge of the energy level struc-
ture in the electrolyte enables us to predict the maximum
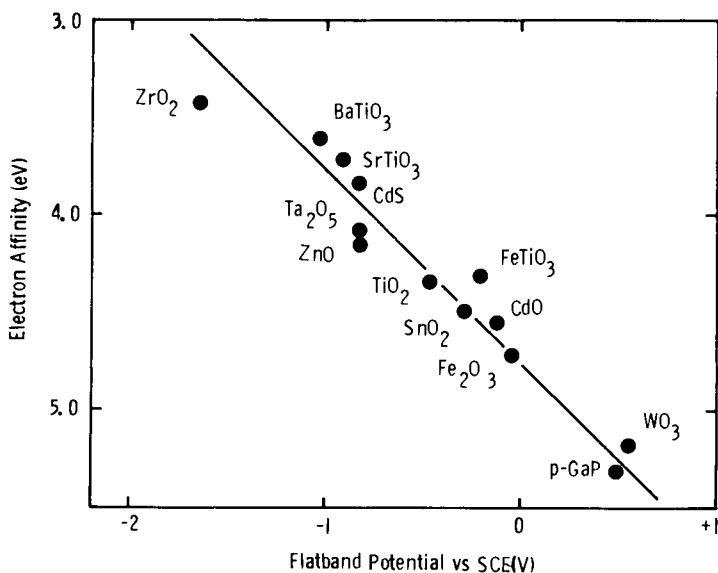
FIGURE 9. The electron affinity calculated from atomic
electronegativities vs. the measured flatband potentials of
several semiconductors corrected to their respective PZZPs. The
solid line is that expected from Eq. 1. The data are from Refs.
13, 14 and 17. The p-GaP data point refers to $EA + E_g$ rather
than the electron affinity.

open-circuit voltage for a wet photovoltaic cell or the bias
requirements for a chemical producing cell.

Another important aspect of the electronegativity model is
that it provides an understanding of the role atomic properties
play in determining the behavior of a semiconducting electrode.
For semiconducting anodes an important requirement is as small
an electron affinity as possible (22) to maximize the open-circuit
voltage or minimize the applied bias. Since oxygen is a very
electronegative atom, the model suggests that metal oxides with
small oxygen content would be the most useful in this respect.

Another quantity which appears to correlate with electron
affinity for metal oxides is band gap. The argument has been
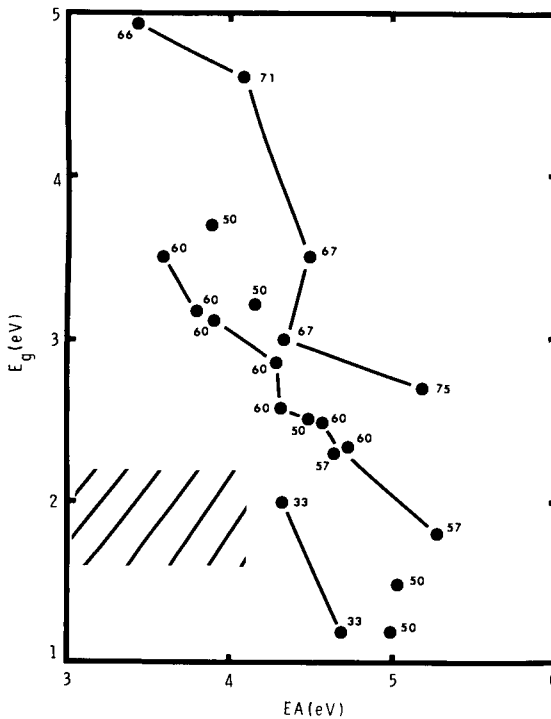
FIGURE 10. Measured band gap versus the electron affinity
calculated using the atomic electronegativity model. The numbers
are the atomic percent oxygen. The cross-hatched area is the
optimum region for photoelectrolysis.

made that since the valence band is formed by O(2p) levels, which
will be approximately the same for all oxides, decreasing electron
affinity corresponds to increasing band gap and vice versa (23).
Both of these arguments are illustrated in Fig. 10. One observes
that there is indeed a correlation between band gap and electron
affinity, if the data are restricted to compounds with about the
same atomic percent oxygen. The figure suggests that compounds
with small metal valences and therefore low oxygen content such
as Cu_2O would be the most fruitful to explore. However, there is
some question as to the stability of this class of compounds.
The atomic electronegativity model has been used to explain the
difference between Fe_2O_3 and $YFeO_3$ where the electron affinity
is lowered by replacing Fe by Y (24).

Electromigration of Ions

Stability in semiconductors for electrodes in photoelectro-
chemical cells is perhaps the crucial criterion these materials
must satisfy. Generally, stability is thought of primarily in
the thermodynamic sense, comparing the redox couples of interest
to the decomposition potentials; and a number of recent models
have been published discussing this in detail (9,10). Kinetics
can sometimes dominate and stabilize a thermodynamically unstable
electrode. While these factors are anticipated to be the most
important, recently a number of other mechanisms (25-28) have
been delineated that appear to be quite important with respect
to determining the photoresponse and flatband. Foremost among
these is ion migration in the surface and near-surface region of
many semiconductors. The high electric fields (kV/cm) at the
electrode surface caused by the potential drop across the very
narrow depletion region are sufficient to cause the electromigra-
tion of ions in this region (25). We will discuss our observa-
tions for the transition metal oxides though analogous arguments
apply to main group semiconductors.

In general, there are two main types of ion migration. If
an electrode is aged at an anodic bias then positive intersti-
tial atoms tend to be removed from the surface region (25). Since
these ions are generally thought to be responsible for the doping
in the transition metal oxides, their removal alters substan-
tially the doping profile in the surface region of the semicon-
ductor. At cathodic bias the reverse process occurs and small
positive ions are injected into the surface region (26). By far
the most important of these is hydrogen, and we feel that the
amount of hydrogen in the near-surface and surface region is
important not only in determining the photoresponse of the
electrode and flatband potential but even its catalytic ability
(29,30). We will illustrate these results for TiO_2 and $SrTiO_3$
and show how the electronegativity model can be applied here to
gain valuable information about the electrodes.

To evaluate the importance of the incorporated hydrogen on
photoelectrochemical properties of TiO_2 anodes in a photoelec-
trolysis cell, a number of electrochemical experiments have been
carried out on illuminated anodes. In general, these experiments
entail aging lightly-doped TiO_2 anodes in 1 M NaOH in various
potential and current regimes. Fig. 11 and Table 1 enumerate
the results of such an experiment on one rutile anode. Scan 1
is that for the virgin, lightly-hydrogen reduced anode and its
photoresponse is that expected giving an effective gap of
approximately 3.0 eV. Its measured flatband of -0.865 V vs. SCE
is also that normally found (14).

As the sample begins to age cathodically, one sees the
gradual hydrogenation of the surface layer of the electrode and
the formation of a deep blue spot in the region exposed to the
electrolyte. Current controlled aging was employed so as to
to avoid the incorporation of too much hydrogen and subsequent
shattering of the sample (Fig. 12) which occurs at current den-
sities between 1 - 10 mA in 1 to 3 days. As the hydrogen doping
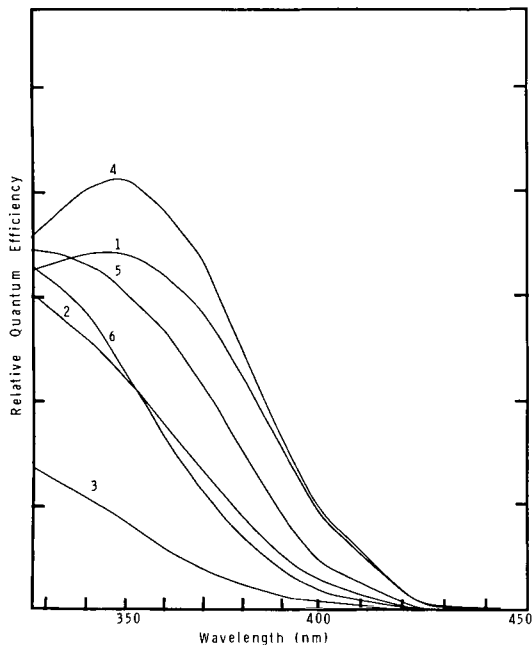
FIGURE 11. Successive agings of a lightly-hydrogen reduced rutile anode in 1 M NaOH: 1) virgin sample, 2) 100 μA 14 hr. cathodic, 3) 100 μA 20 hr. cathodic, 4) 0.0 V vs. SCE 20 hr., 5) +1.0 V vs. SCE 23 hr., and 6) +5.0 V vs. SCE 4 days.

TABLE 1. Dependence of V_{fb} on Aging Conditions for TIO_2

Experiment	Conditions	V_{fb} (vs SCE)
1	Virgin	−0.865
2	Aged Cathodically 100 μA 14 hrs.	−0.735
3	Aged Cathodically 100 μA add. 20 hrs	−0.750
4	Aged 0.0 V vs SCE 20 hrs.	−0.817
5	Aged Anodically +1.0 V vs SCE 23 hrs.	−0.765
6	Aged Anodically +5.0 V vs SCE 4 days	−0.70
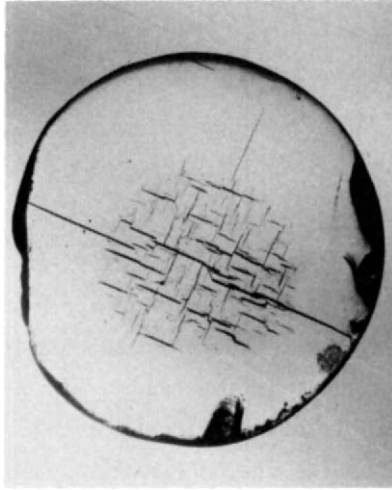
*FIGURE 12. Photograph 5x magnification of an electrochemi-
cally deuterium-doped rutile wafer. Doping was accomplished
by current controlled cathodic aging an undoped TiO$_2$ wafer in
LiOD, D$_2$O for 3 days at 10 mA. This resulted in a shattering
of the sample in the region exposed to the electrolyte.*

proceeds, the flatband starts moving to positive values vs SCE
and then levels off. This shift is generated by three effects.
The introduction of hydrogen into the lattice increases the bulk
electronegativity of the oxide so as to move V_{fb} to more positive
values. We can understand this by looking at the electronega-
tivity model. From Eq. 6 we know that EA for TiO$_2$ is 4.33 eV.
If we return to Eq. 1 and solve for the the electron affinity
change needed to account for the shift in V_{fb} for treatment two,
we find a required EA of 4.46 eV. If this is assumed to be due
exclusively to incorporated hydrogen, which is born out by depth
profiling experiments, then we can solve for the percent hydrogen.
This can be done by returning to our hypothesis that the bulk
electronegativity of a compound is equal to the goemetric mean of
the electronegativities of the constituent atoms. So for a same
unknown amount of hydrogen in the surface region we can write:

$$X_{TiO_2H_x} = [X_{Ti}X_O^2 X_H^x]^{1/3+x} \tag{12}$$

Since we know the apparent electron affinity of 4.46 eV, we can solve for x.

$$EA_{observed} = [X_{Ti}X_O^2 X_H^x]^{1/3+x} - 1/2 \; E_{g_{TiO_2}} \tag{13}$$

If this is done we find that if one out of five TiO_2 moities in the near surface were hydrogenated, the appropriate shift in V_{fb} would result. However, two other factors must be evaluated: the change in the band gap of the oxide, which is small based upon photoresponse measurements and the change in the point of zero zeta potential of the surface which may be significant if the relative pK_a of the surface is substantially altered.

The relative lack of change in V_{fb} from scan two to scan three most likely results from the near saturation of the available surface sites with hydrogen. The substantial loss of quantum efficiency for the cathodically aged sample seems to indicate that the hydrogenated surface region acts as if it has many recombination centers.

Treatment four is the reverse aging of the sample under illumination at 0.0 V vs SCE. Most of the hydrogen is removed from the surface layer in this process, but V_{fb} shows that perhaps 20-30% of the hydrogen remains. This is further substantiated by the continued presence of the blue spot. However, as the photoresponse curve number four shows, the quantum efficiency is totally restored. This indicates that the remaining hydrogen is located on a lattice site that is normally not photoactive in the photoelectrolysis process.

Continued aging in the anodic direction at +1.0 and +5.0 V vs SCE, scans five and six respectively, result in the gradual diffusion of Ti^{3+} interstitials out of the surface layer as has recently been discussed by Butler [25]. The removal of the electropositive Ti^{3+} and concentration of cathodically incorporated

hydrogen at the surface results in a more positive V_{fb} and the reduced number of donors results in the observed decrease in Φ, (the quantum efficiency) and the observed red shift of the photoresponse due to increased depletion layer width. The blue spot remains indicating the continued presence of hydrogen in the surface.

Similar results are obtained for $SrTiO_3$. These are illustrated in Table 2 and Fig. 13. Here the cathodic and anodic aging experiments were done on two separate nearly identical samples. For cathodic aging the partial reversible incorporation of hydrogen, approximately 1 per 3 titaniums, is observed substantially altering V_{fb} and the magnitude (Φ) but not the shape of the photoresponse curve. Anodically, there appear to be mobile interstitials similar to TiO_2 which when removed from the surface layer result in a diminished and red-shifted photoresponse. Here we can clearly see that V_{fb} has not been shifted by the removal of the interstitials. This is the anticipated result because while the ions removed substantially affect the doping profile the number is well below an atomic percent and would not be

TABLE 2.   *Dependence of V_{fb} on Aging Conditions for $SrTiO_3$*

Sample	Light	Conditions	V_{fb} vs SCE
1		Virgin	-1.11
	on	+5 V vs SCE - PC 21 hrs.	-1.15
	on	+1.0 V vs SCE - PC 4 days	-1.15
	off	-1.0 V vs SCE - PC 2 days	-1.16
	off	300°C in air - 16 hrs.	-1.09
2		Virgin	-1.17
	on	.2 mA - cc 25 hrs.	- .95
	on	.2 mA - cc 21 hrs.	- .96
	on	0.0 V vs SCE - PC 27 hrs.	-1.06
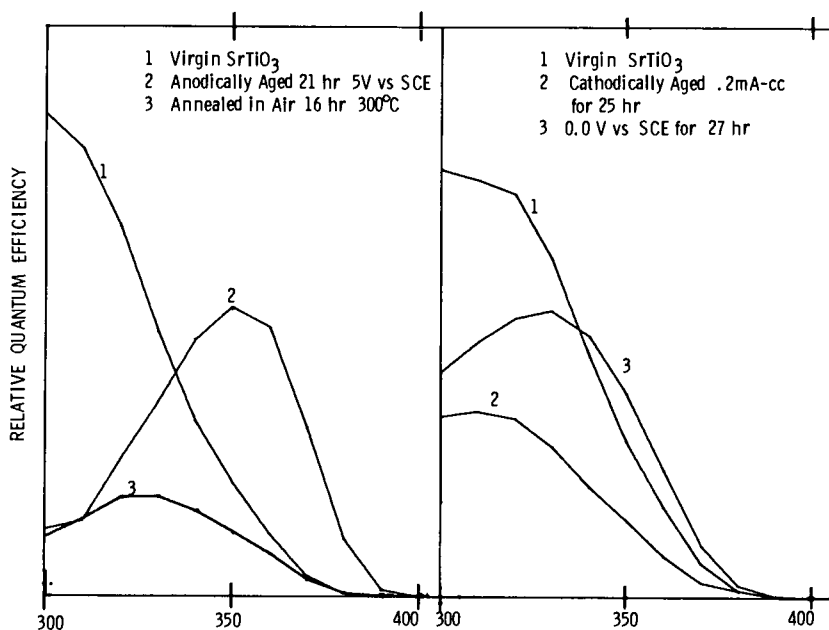
FIGURE 13. Electrochemical aging experiments on two lightly reduced SrTiO₃ wafers. The left-hand portion is for anodic aging, the right for cathodic aging. All experiments were performed in 1 M NaOH.

expected to change the electron affinity. When the samples are allowed to sit at room temperature, the new ion profiles are stable but at temperatures around 250°C donors are redistributed homogeneously.

Thus, large changes in V_{fb} and Φ in these electrodes under both anodic and cathodic bias indicate that the electromigration and the electrochemical doping of the surface layers in oxide photoanodes may be crucial in evaluating electrode stability and performance. The use of an appropriate electrochemical dopant may result in the advantageous modification of the properties of an electrode.

In conclusion, we have demonstrated how a single concept, electronegativity, can give us quantitative information about the biasing requirements of photoelectrodes and how the same concept

can be employed to give us valuable information about aged electrodes.

III.   GRAIN BOUNDARY EFFECTS IN POLYSILICON

Introduction

    The application of solid state photovoltaic devices to con-
vert solar energy to electrical power progressed rapidly in the
early 60's primarily because of the need for space power systems.
Interest in this field has grown dramatically in the last few
years as attention has been turned towards terrestrial applica-
tions. The pressing need to find alternatives to conventional
power sources ensures continued importance to solar cells as
possible large-scale electrical energy sources.

    In the race to find practical devices, one of the attractive
candidates has always been silicon solar cells. The element is
abundant and the device technology for single-crystal material
well established. However, while single-crystal silicon solar
cells are reasonably efficient, they are expensive to fabricate
and their feasibility has yet to be demonstrated. On the other
hand, solar cells constructed from thin films of polycrystalline
silicon (polysilicon) are economically feasible to produce but
suffer from considerably reduced efficiencies (3). The United
States Department of Energy has estimated that at 10% efficiency
and current thin-film fabrication techniques, polysilicon solar
cells would become a viable energy alternative.

    The major reason for the low efficiencies in thin-film poly-
silicon devices is the effects of grain boundaries. Due to the
growth conditions most current thin-film devices have relatively
small grain sizes, on the order of 2 to 20 microns. It is well
known that in efficient single-crystal silicon solar cells minor-
ity carriers collected from distances much greater than 100
microns contribute significantly to device currents. Thus for

polysilicon devices to be adequately efficient, carriers will
have to traverse many grain boundaries. It is known that grain
boundaries possess an attractive potential for photogenerated
minority carriers; more importantly, there exists a high density
of recombination centers that the carriers are exposed to once
they are trapped at the "core" of the boundary. An equally
important effect is the apparent shunting action of grain bounda-
ries which intersect the p-n junction, this causes poor fill
factors and open-circuit voltages (32). These two effects serve
to substantially reduce device efficiencies. Grain boundaries
affect minority carrier lifetimes in semiconductors other than
silicon as well. In any polycrystalline solar cell, especially
thin-film devices, grain boundaries must be seriously considered
as one of the major sources of efficiency loss.

There are two main approaches to alleviating grain boundary
problems. The first is to regrow the material in an attempt to
increase grain size and concurrently reduce the number of bounda-
ries. This may be accomplished by a variety of techniques such
as: laser regrowth, float zone refining, melting and controlled
solidification. Most of these processes are very energy inten-
sive and do not eliminate but merely reduce grain boundary
problems. The second method is to treat the grain boundaries
directly, usually with some variety of chemical agent to render
them electrically inactive (passivated). Historically, the
former method has been the one most often employed because passi-
vating techniques have been unknown until lately. Recently, we
have demonstrated (38) how monatomic hydrogen can indeed passivate
grain boundaries in polycrystalline silicon, and it is this work
which will be discussed here. We will consider the ramifications
of these and other recent results with respect to the improvement
of solar cell performance.

Electrical Nature of the Boundary

   To understand the nature of the passivation process it is
necessary to examine closely the electrical nature of the grain
boundary. Grain-boundary potential barriers are formed in semi-
conductors when the grain boundary region has a lower chemical
potential for majority carriers than the grains. The resultant
influx of electrons or holes into the barrier region creates a
space charge which repels the further flow of majority carriers.

   In silicon it has been demonstrated (32) that the Fermi level
in the grain boundary region lies close to the middle of the for-
bidden gap in both n- and p-type material. Since the chemical
potential of the doped grains is not at midgap, significant bar-
riers are observed in most samples of n- and p-type silicon. One
can picture the formation of the potential barriers as is illus-
trated in Fig. 14. Part A illustrates the neutral grain boundary
region before it is joined to the adjacent (neutral) n-type grains.
This picture is, of course, difficult to duplicate physically
but it serves to illuminate the nature of the charge transfer
process. The boundary width, w, is assumed to be of the order
of ~50 Å, a number which is known to be representative of
the disordered region near the grain boundaries of a material-
like silicon (33). The location of the Fermi level in the
boundary E_{FB} is a function of the nature of the defect states
present in the boundary. These are thought to be primarily due
to unsaturated silicon-silicon bonds, "dangling bonds," and to
trapped impurity atoms, such as oxygen (34). While many bent
bond situations exist, they do not appear to be electrically
active as is born out by the electrical inactivity of twinned
boundaries in germanium and silicon (34).

   Fig. 14(b) illustrates the two grains and the grain boundary
region after they have been joined and equilibrium has been estab-
lished. The accumulated negative charge near x = 0 causes the
energy bands to be bent upwards by an amount ϕ_B and the Fermi
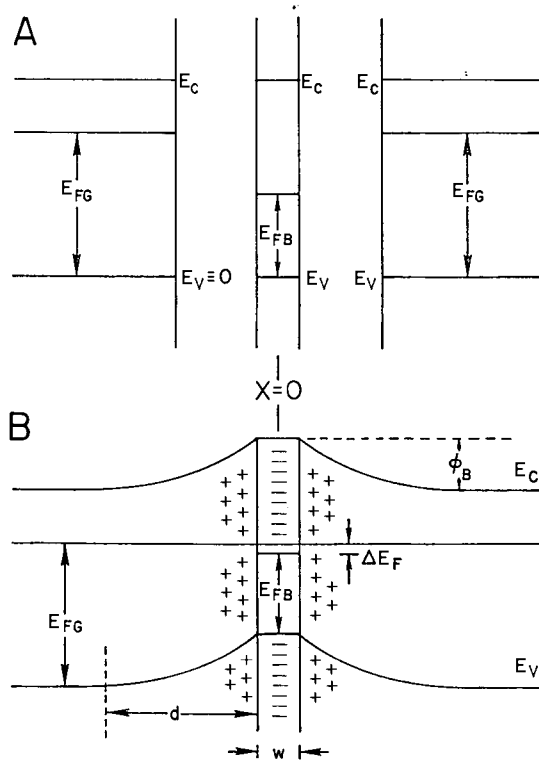
FIGURE 14. Energy band diagram for two semiconductor grains and their boundary region. (a) This part shows the two grains and the region of their boundary schematically as they would be if they were three isolated materials. (b) This part shows the band bending in the grains and the increased Fermi level in the boundary which occurs when the materials in (a) are joined at zero applied bias voltage.

level in the grain boundary region to shift by an amount ΔE_F. Although the width of the depletion region d, has been drawn here as comparable to the GB region width, in general W << d. The width d varies with the doping level in the grains similar to the dependence found for Schottky barriers.

   For wide depletion layers thermionic emission of majority carriers over the potential barrier is expected to be the dominant conduction mechanism (35,36). Pike and Seager (6) have

recently shown that the grain-boundary resistance in silicon can
indeed be modeled by assuming that conduction is dominated by the
thermal excitation of carriers over the barrier. Utilizing this
model they have developed a deconvolution scheme whereby the
energy density of grain boundary states may be obtained from
current-voltage measurements. These densities of states have
been confirmed recently by the first direct measurements of
charge emission from silicon grain boundary defect states (37).
This has been accomplished by monitoring the recovery of the
nonequilibrium grain-boundary barrier capacitance. The use of
the deconvolution scheme for the I-V data and of the capacitance
data allows a direct determination of the density of states in
an individual grain boundary. The measurement of the density of
states serves as a specific probe of the effectiveness of any
passivation procedure. The qualitative effectiveness of grain
boundary passivation can thus be obtained by a simple four probe
determination of the grain boundary conductance. A simple appa-
ratus for these determinations is illustrated in Fig. 15. Current
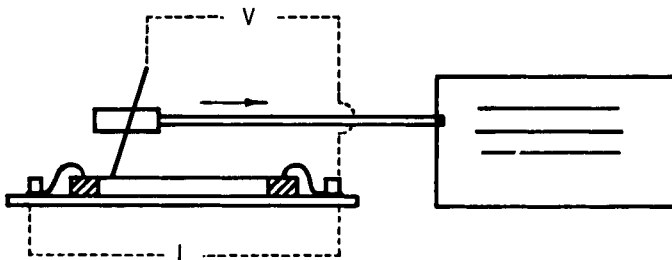
Grain Boundary Conductance Apparatus

FIGURE 15. The four-probe grain boundary conductance appa-
ratus is illustrated diagramatically. A constant current is
applied to the sample (2 mm x 2 mm x 2 cm) through ohmic contacts
(the crosshatched areas). A potential-versus-distance plot is
obtained by having a movable potential probe traverse the sur-
face at a fixed rate and monitoring the potential referenced to
the low-current contact.

is passed through a polysilicon sample, 2 mm x 2 mm x 20 mm, that has been contacted at both ends. The surface potential is measured with a traveling point contact. The potential drop for the largest barrier is kept to less than kT. If one plots potential versus distance, the vertical potential drops correspond directly to grain boundary impedances as is shown in Fig. 16.

Grain Boundary Passivation

Since "dangling bonds" or impurities are responsible for the grain boundary defect states, it should be possible to introduce
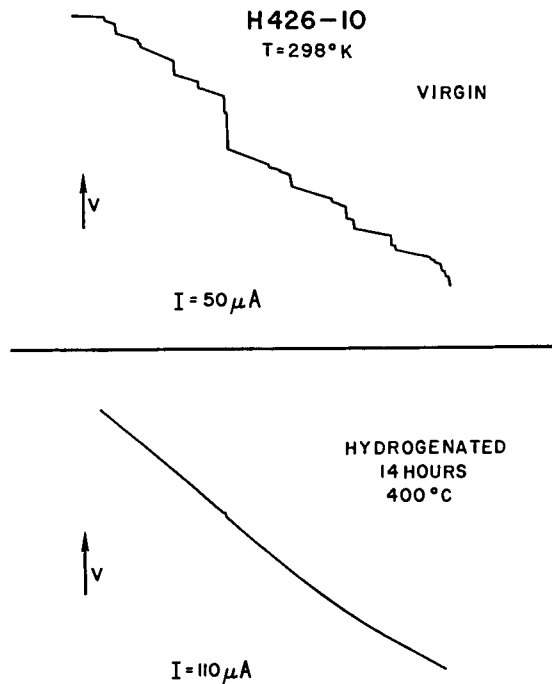
FIGURE 16. *A typical potential vs. distance plot for a virgin (top) and hydrogen plasma-treated (bottom) p-type Honeywell silicon on ceramic polysilicon sample. The voltage scales are the same, and approximately 60 mV is dropped across the sample in each case. Treatment conditions were 14 hrs at 400°C in a 500 millitorr hydrogen plasma.*

a foreign chemical species into the grain boundary to remove or
neutralize them. In effect by reacting the defects with a reagent
of the appropriate electronegativity, their electronic trapping
levels can be displaced to well below the Fermi level. Similarly,
it might be anticipated that other reagents of appropriate electro-
negativities could increase the density of states above the Fermi
level. In fact, monatomic hydrogen plasmas have been demon-
strated (38,39) to be highly effective at removing grain-boundary
in-gap sites in silicon. Heller and Miller (40) have also recently
demonstrated that Ru serves a similar function in thin-film GaAs.

   A typical apparatus is illustrated in Fig. 17. Here all gas
treatments are conducted inside an evacuated quartz vessel, inser-
ted in a horizontal tube furnace. Temperature is monitored with
a platinum/platinum-rhodium thermocouple located near the sample
wafers which are on a tantalum platform. Plasmas were excited by
means of a circumferential metal band which was connected to a
tesla coil (voltage typically 1-5 kV). Plasma composition could
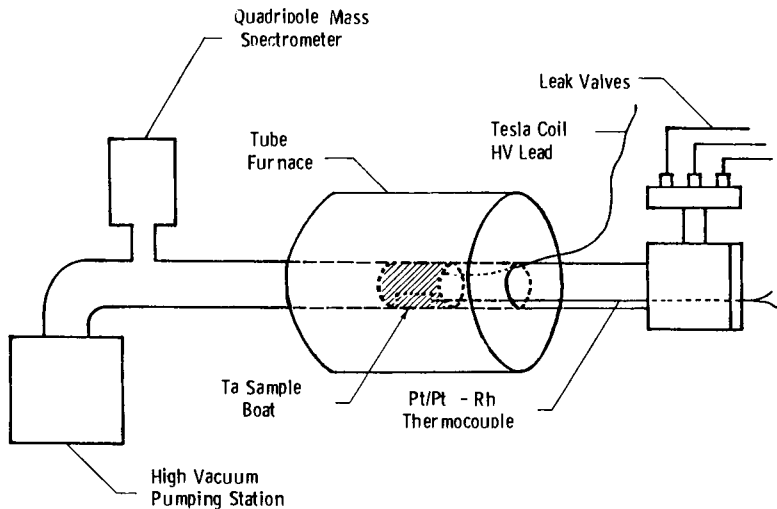
   *FIGURE 17. Diagramatic illustration of the hydrogen passi-
vation apparatus. The sample resides in the Ta boat in the cross-
hatched region, which is the region of highest plasma density.*

be monitored with the attached quadrupole mass spectrometer.
Fig. 16 illustrates two potential vs distance traces for a slice
of Honeywell p-type silicon on ceramic with approximately 100
micron grains. The upper portion of the figure is for the virgin
slice, the vertical steps are across individual grain boundaries.
The lower curve is for the same sample, exposed to a 500 milli-
torr hydrogen plasma for 14 hours at 400°C (note the increased
current). Significant increases in grain-boundary conductance
are seen and the overall sample conductance approaches that of
the bulk. Having established that the passivation process is
quite effective at altering grain boundary conductances, we have
begun to perform experiments to understand and optimize the
process. The rest of the discussion will deal with some of the
observations we have obtained to date.

Fig. 18 illustrates the effect of a series of treatments on
the zero-bias conductance, G_o, of an individual grain boundary in
a sample of neutron transmutation doped polysilicon. Treatments
a, c, f, i and k are hydrogen plasma treatments of various dura-
tions at temperatures between 330 and 400°C and pressures of 60-
100 millitorr. In each case substantial increases in G_o are
observed. Treatments b, d and g are vacuum anneals carried out
at 1×10^{-6} torr or less at 620°C. At this temperature a com-
plete return to virgin conductance levels is observed. Treatment
e was performed under identical conditions to the hydrogen plasma
treatments except for the absence of the electrical discharge.
The conductance actually decreases somewhat which may indicate
the absorption of impurities in the grain boundary. From this
observation, it is clear that the atomic hydrogen generated in
the plasma is essential to the process effectiveness. Treatment
h is at very low hydrogen pressure (10^{-2} torr); this is appar-
ently below the optimum pressure range for passivation (~100-
500 millitorr). Treatment j is an anneal in a low-partial
pressure of oxygen 5×10^{-4} torr at 625°C. This illustrates
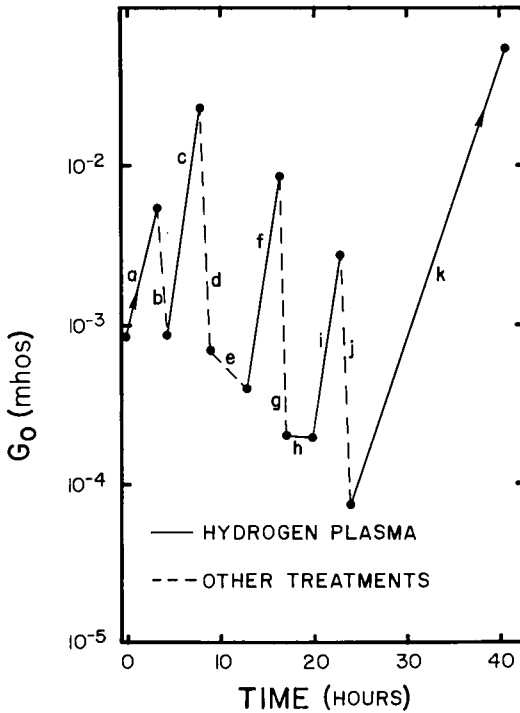
FIGURE 18. The zero-bias conductance at 300°K of one grain boundary potential barrier in a 10^{16}-P/cm^3 neutron transmutation (NTD) doped polycrystaline silicon sample after a series of gas treatments.

that the incorporation of impurity atoms can reduce the grain boundary conductance to values significantly below virgin levels. This effect can be enhanced by higher pressures and has been observed for O_2, SF_6 and N_2.

The zero-bias conductance of two different grain-boundary potential barriers in neutron-transmutation doped polycrystalline silicon are illustrated in Fig. 19. The solid curves show the virgin conductance values, the dashed curves the results after hydrogenation at 400°C for ≈5 hrs. In addition to marked increases in barrier conductance, hydrogenation weakens the temperature variation of the barrier conductance; in the case of the
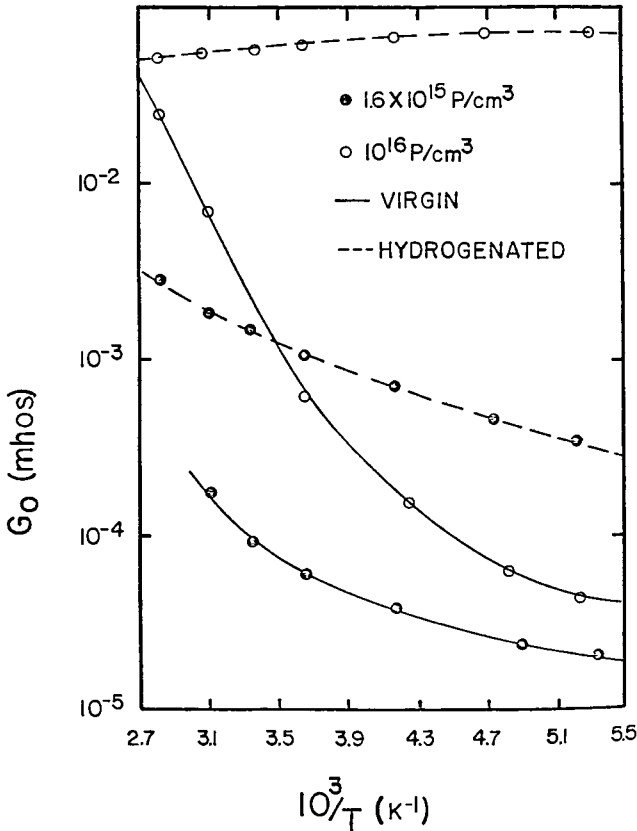
FIGURE 19. *The zero-bias conductance of two different grain boundary potential barriers in neutron transmutation doped poly-crystalline silicon. The solid curves show the virgin conductance values, the dashed curves the results after hydrogenation at ~400°C, 500 microns H_2, for 5 hr.*

10^{16} P/cm^3 sample the observed temperature dependence loses its activated character and takes on an opposite, but weak, variation, characteristic of the conversion of the grain boundary to a simple scattering center for majority carriers. A closer examination of the temperature dependence of the conductance of a virgin and treated sample is illustrated in Fig. 20. The activation energy for conductance in the virgin state is approximately 0.62 eV while that in the hydrogenated sample is 0.035 eV.
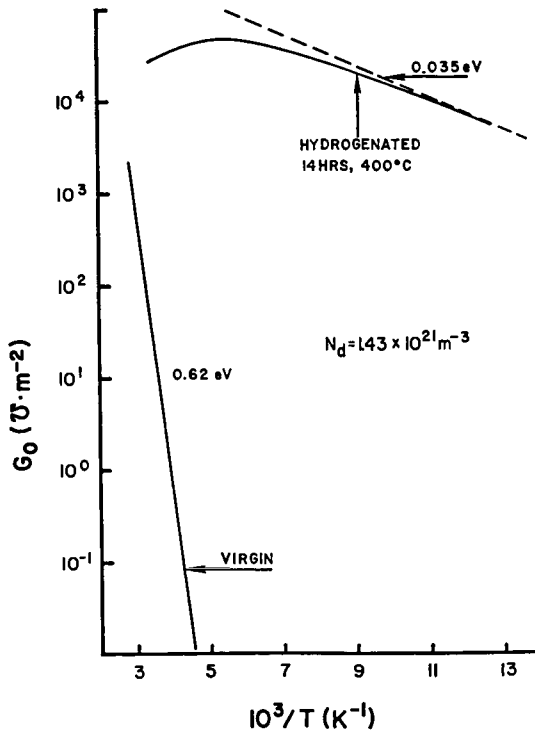
FIGURE 20. Activation energy determinations for a barrier before and after hydrogen plasma treatment in a sample of neutron transmutation doped (10^{16}P/cm^3) polysilicon.

This is indicative of a substantial reduction in the number of trap states in the boundary and consequent reduction of barrier height and ease of emission over the barriers. This is further illustrated in Fig. 21, where for the same sample we plot directly the effective density of grain boundary states $N_t{}^*$ versus energy (in eV) with the zero of energy being the valence band maximum.

The data are obtained by deconvoluting the current-voltage data according to the Pike-Seager deconvolution scheme (36). A substantial reduction in the density of states is observed as expected from the temperature dependence of G_o. Thus, the hydrogen plasma treatment seems to drastically reduce the density of

DENSITY OF G.B. STATES

$$N_d = 1.43 \times 10^{21} m^{-3}$$

[figure: Plot with vertical axis $N_T (m^{-2} eV^{-1})$ showing values 1, 2, 3, 4, 5×10^{16}; horizontal axis E(eV) with values .6, .7, .8, .9, 1.0. Curves labeled VIRGIN and HYDROGENATED 14 HRS, 400°C]

$$E(eV)$$
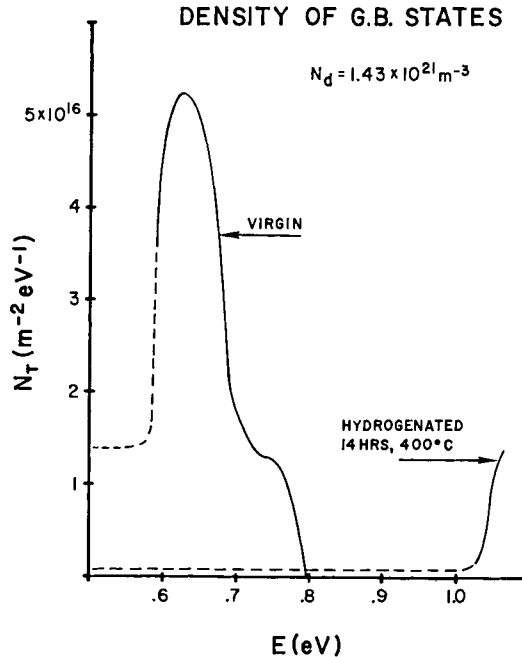
FIGURE 21. The effective density of grain boundary states
(N*$_t$) for a virgin and hydrogen plasma treated boundary vs.
energy (in eV with zero being the valence band maximum (same
sample as in Fig. 20). The data are obtained by deconvoluting
the current-voltage data according to the Pike-Seager deconvolu-
tion scheme.[36]

states in the grain boundary region, giving rise to significant
reductions in the double depletion layers and consequent increases
in the conductance.

In the course of optimizing the treatment it has been ob-
served that the condition of the surface is crucial for optimum
hydrogen penetration. This is illustrated in Fig. 22. Here we
show a 9 Ωcm float-zone refined n-type polysilicon sample before
(top) and after (bottom) hydrogen plasma treatment at 500 microns,
400°C for four hours. The middle portion of the sample had 25
microns etched off with an $HF/CrO_3/H_2O$ etch, and both ends were
left as they were after diamond-wheel cutting. The middle section
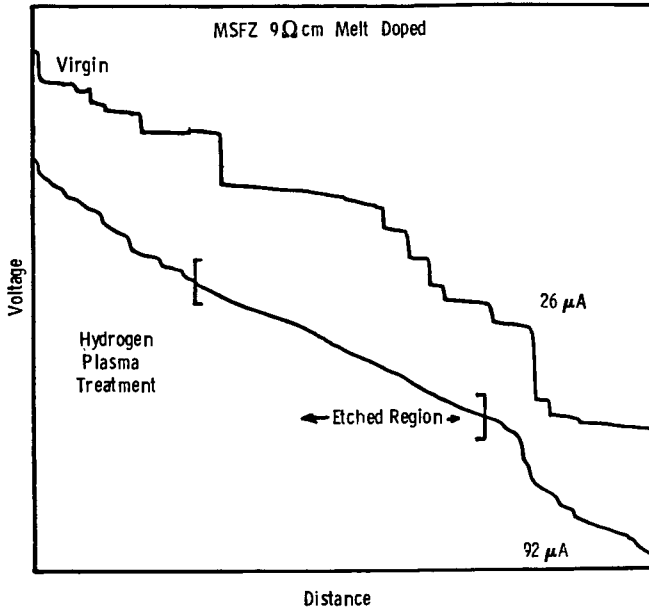
*FIGURE 22.   The potential vs. distance plots for a virgin
and hydrogen plasma treated sample of 9 ohm-cm float-zone refined
n-type polysilicon.   The middle portion of the sample (brackets
had 25 microns etched off with an $HF/CrO_3/H_2O$ etch.*

is extensively passivated but both of the saw damaged ends are
only lightly passivated.   The definition between etched and
unetched areas after treatment is sharp.   This may indicate that
grain boundary diffusion and not bulk diffusion is the main
mechanism for hydrogen introduction into the boundaries.

Fig. 23 also illustrates that the passivation process in the
melt-doped polysilicon is as effective as in the neutron trans-
mutation-doped polysilicon.   This is an indication that any
grain boundary dopant segregation present is not important in
determining the electronic properties of the barriers in the
melt-doped materials.   This is further borne out by the I-V
properties of single melt-doped boundaries which can be modeled
quite well by thermal emission theory.
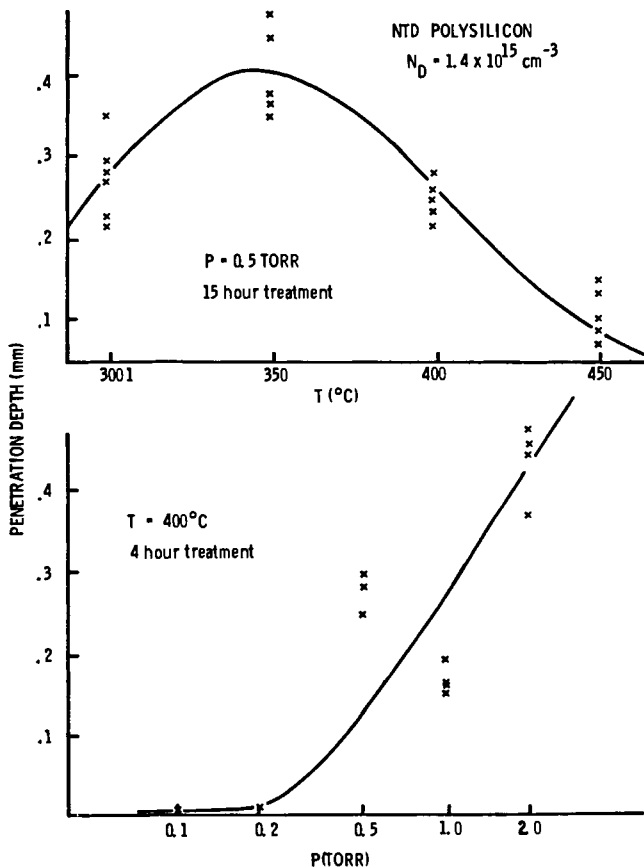
FIGURE 23. The top portion illustrates the effective pene-
tration depth (mm) of the passivation process vs. temperature
at a fixed pressure of 500 microns H_2. The x's represent an
accumulation of data from different boundaries. The bottom
portion illustrates the effective penetration depth (mm) vs. H_2
pressure at a fixed temperature of 400°C. Above 2 torr it
becomes difficult to sustain a plasma.

In order to optimize the process a means to evaluate the
effective penetration depth of the treatment has been developed.
A series of etches are performed with the HF/CrO_3 etch while moni-
toring the grain-boundary conductance. The current flow in the
grain boundary is modeled as a sum of flow through two regions,
the passivated region and the essententially untreated region.

By ratioing the slope of the grain boundary conductance to that
of the bulk, one can calculate the thickness of the conductive
region. Fig. 23 illustrates a plot of depth of penetration of
passivation (in millimeters) versus temperature on the top and
pressure on the bottom. Optimum temperature is around 350°C and
optimum pressure is betwen 1 and 2 torr. Above 2 torr it is
difficult to sustain a plasma.

It is clear that under relatively mild conditions, passiva-
tion can be observed to considerable depths. Thus penetration is
very much in excess of the anticipated thickness of useful thin-
film (10 to 100 microns) devices. In thin films treatment times
of 10-15 minutes might well be sufficient. As Fig. 16 demonstra-
tes, grain boundary impedances can be virtually eliminated (on
a relatively thick, 400 microns, sample). Having established the
viability of the passivation process for bulk and thin-film poly-
crystalline silicon, we turned our attention to some exploratory
experiments on prototype solar cells. The utlization of solar
cells allows a direct probing of minority carrier lifetimes and a
tentative evaluation of the ability of the process to increase
efficiencies. Fig. 24 illustrates typical I-V curves for two
cells before and after treatment. Overall efficiencies are low
because the neutron transmutation doped (NTD) polysilicon employed
suffers from a very low bulk lifetime. The upper set of curves
are for a boron diffused solar cell fabricated from NTD (phospho-
rous) doped polysilicon (200 micron grains). The dashed curves
represent the light and dark traces for the virgin cell; the
solid lines are the curves for the plasma treated cell. The
efficiency increase (AM1) of a factor of   26 is due to two dis-
tinct factors. One is an increase in the short-circuit current
ostensibly due to improved transport of minority carriers across
grain boundaries. The other is a substantial improvement in the
open-circuit voltage due to an elimination of the shunting nature
of the grain boundaries. The lower half of Fig. 24 shows three
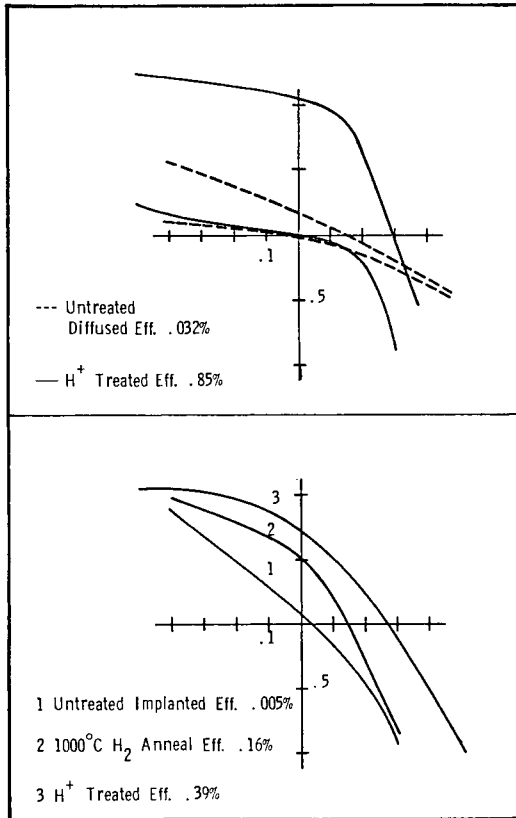
FIGURE 24. The upper portion of the figure is the light and dark I-V curves for a prototype solar cell at n-type neutron transmutation doped polysilicon with a boron diffused p-layer before (dashed curves) and after (solid curve) hydrogen plasma treatment. The efficiencies are AM1. The current is plotted vertically in mA and potential horizontally in volts. The lower portion is a similar cell with a boron ion implanted surface layer. The curves illustrated are the illuminated I-V curves only for the virgin cell, the cell after a 1000°C thermal anneal in hydrogen and after hydrogen plasma treatment. The efficiencies are AM1.

illuminated I-V curves for a boron ion implanted bulk NTD phosphorous doped polysilicon solar cell. The 1000°C H_2 anneal is an attempt to remove some of the ion implantation defects. Curve 3 again shows that the hydrogen plasma treated cell

increases in efficiency as a consequence of improvements in both the short-circuit current and open-circuit voltage in the cell.

The lifetime of the minority carriers and the spectral response of some of the ion implanted cells has been probed more directly as shown in Fig. 25. The lower curve and number refer to the virgin sample, the upper set are after hydrogen plasma treatment. The lifetimes were determined by monitoring the short-circuit current decay after a 5 nsec x-ray pulse. The data indicate that there is substantial increase in bulk minority carrier lifetime after plasma treatment. This is substantiated by an examination of the spectral response curves for the cell.
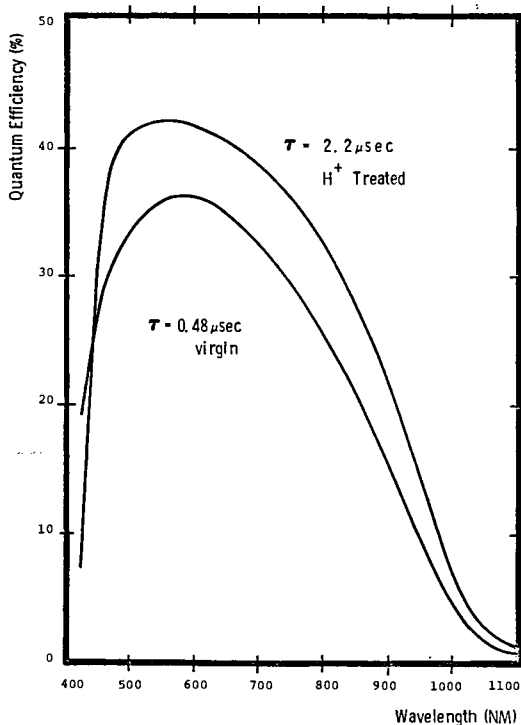
FIGURE 25. *Spectral response curves (quantum efficiency vs. wavelength) for an n-type neutron transmutation doped polysilicon with a boron p-type ion implanted junction before and after hydrogen plasma treatment. The lifetimes are from current vs. time data after the cell receives a 5 nanosecond x-ray pulse.*

There is a large increase in the quantum efficiency of the long
wavelength tail where the photons are adsorbed well below the
junction.

In conclusion, we have demonstrated that by modifying the
chemical potential of the grain boundary defective regions we can
substantially alter their electronic properties in the polycrys-
talline material. It has been demonstrated that boundaries can
be passivated by relatively mild treatments in hydrogen plasma
and that grain boundary potential barriers can be increased by
treatment with O, N and F. The hydrogen passivation process is
very effective on thin films and experiments on prototype solar
cells indicate that the process has considerable potential for
increasing efficiencies in thin-film solar cells.

ACKNOWLEDGMENTS

REFERENCES

1.   Becquerel, E., *C.R. Acad. Sci. 9*, 561 (1839).
2.   Fujishima, A., Honda, K., and Kikuchi, S., *J. Chem. Soc.
     Japan 72*, 108 (1969).
3.   Gerisher, H., in "Physical Chemistry: An Advanced Treatise"
     (H. Eyring, D. Henderson, W. Jost, eds.), Vol. 9A. Academic
     Press, New York, (1970).
4.   Nozik, A.*J.*, *Ann. Rev. Phys. Chem. 29*, 189 (1978).
5.   Butler, M.A., and Ginley, D.S., *J. Mat. Science,* in press.
6.   Inoue, T., Fujishima, A., Konishi, S., and Honda, K., *Nature
     277*, 637 (1979).

7.   Nozik, A.J., 2nd International Conference on Photochemical
     Conversion and Storage of Solar Energy, Cambridge, England,
     Aug. 10, 1978.

8.   (A)   Butler, M.A., *J. App. Phys. 48,* 1914 (1977); (B)
     Kennedy, J.H., and Frese, K.W., *J. Electrochem. Soc. 125,*
     709 (1978); (C) Wilson, R.H., *J. Appl. Phys. 48,* 4292 (1977).

9.   Gerischer, H., *J. Electroanal. Chem. 82,* 133 (1977).

10. Bard, A.J., and Wrighton, M.S., *J. Electrochem. Soc. 124,*
     1706 (1977).

11. Dobos, D., "Electrochemical Data", Elsevier, New York, (1975).

12. Vijh, A.K., "Electrochemistry of Metals and Semiconductors",
     Dekker, New York, (1973).

13. Ginley, D.S., and Butler, M.A., Electrochem. Soc. Mtg.,
     Boston, MA, May 6-11, 1979.

14. Butler, M.A., and Ginley, D.S., *J. Electrochem. Soc. 125,*
     228 (1978).

15. Lohmann, F., *Z. Naturforsch. Tiel A. 22,* 843 (1967).

16. Hannay, N.B., "Semiconductors", Reinhold, New York, (1959).

17. (A) Ginley, D.S., and Butler, M.A., *J. Electrochem. Soc. 125,*
     1968 (1978); (B) Butler, M.A., and Ginley, D.S., *J. Electro-*
     chem. Soc., submitted.

18. Nethercot, A.H., *Phys. Rev. Lett. 33,* 1088 (1974).

19. Poole, R.T., Williams, D.R., Riley, J.D., Jenkins, J.G.,
     Liesegang, J., and Leckey, R.C.G., *Chem. Phys. Lett. 36,*
     401 (1975).

20. Hotop, H., and Lineberger, W.C., *J. Phys. Chem. Ref. Data 4,*
     539 (1975).

21. White, F.A., "Mass Spectrometry in Science and Technology",
     Wiley, New York, (1968).

22. Mavroides, J.G., Tchernev, D.I., Kafalas, J.A., and Kolesar,
     D.F., *Mat. Res. Bull. 10,* 1023 (1976).

23. Kung, H.H., Jarrett, H.S., Sleight, A.W., and Ferretti, A.,
     J. Appl. Phys. 48, 2463 (1977).

24. Butler, M.A., Ginley, D.S., and Eibschultz, M., *J. Appl. Phys. 48,* 3070 (1977).

25. Butler, M.A., *J. Electrochem. Soc. 126,* 338 (1979).

26. Ginley, D.S., and Knotek, M.L., *J. Electrochem. Soc.,* Dec. 1979.

27. Heller, A., Schwartz, A.P., Vadimsky, R.G., Menezes, S., and Miller, B., *J. Electrochem. Soc. 125,* 1156 (1978).

28. Gerischer, H., and Gobrecht, J., *Ber. Bensenges Phys. Chem. 82,* 520 (1978).

29. Knotek, M.L., Proceedings of the 151st Electrochem. Soc. Meeting, 77-6, 234 (1977).

30. Wilson, R.H., 153rd Electrochem. Soc. Meeting, Seattle, WA, Abs. 415 (1978).

31. Chu, T.L., Liu, J.C., Mollenkopf, H.C., Chu, S.C., and Heizer, K.W., *Solar Energy 17,* 229 (1975).

32. Seager, C.H., and Castner, T.G., *J. Appl. Phys. 49,* 3879 (1978).

33. Matare, H.F., "Defect Electronics in Semiconductors", Wiley-Interscience, New York, (1971).

34. Koper, A.B., Proceedings of the 13th IEEE Photovoltaic Specialists Conference, 1978, IEEE, New York,(1979).

35. Taylor, W.E., Odell, N.H., and Fan, H.Y., *Phys. Rev. 88,* 867 (1952).

36. Pike, G.E., and Seager, C.H., *J. Appl. Phys. 50,* 3414 (1979).

37. Seager, C.H., Pike, G.E., and Ginley, D.S., *Phys. Rev. Lett. 43,* 532 (1979).

38. Seager, C.H., and Ginley, D.S., *Appl. Phys. Lett. 34,* 337 (1979).

39. Campbell, D.R., et al., *Bull. Am. Phys. Soc. 24,* Abstract TK, 435 (1979).

40. Heller, A., private communication.

CHAPTER 19

INTRODUCTION TO BASIC ASPECTS OF PLASMA-DEPOSITED AMORPHOUS
SEMICONDUCTOR ALLOYS IN PHOTOVOLTAIC CONVERSION

Richard W. Griffith[1]

Department of Energy and Environment
Brookhaven National Laboratory
Upton, New York

I. INTRODUCTION

   The genre of amorphous semiconductor materials currently en-
joys a renaissance owing to recent technological applications in
areas that span photovoltaic conversion, microelectronics, and a
variety of photoelectronic semiconductor devices. An especially
promising class of such materials is that of the hydrogenated
amorphous silicon alloys (a-Si:H). The role of $\sim$ 5-20% alloyed
hydrogen in a-Si:H films is twofold: i) bonded hydrogen passi-
vates electrically-active defects such as dangling bonds and weak
molecular bonds, and ii) the chemical bonding of the alloy *per se*
creates a new electronic material. The resulting improvement in
optoelectronic quality relative to pure a-Si permits systematic
electronic doping of the material (1-3) and the fabrication of
developmental solar cells (4).

   The demonstration of photovoltaic feasibility was preceded
by the evolution of several seminal concepts in noncrystalline
semiconductor theory. These developments include: i) localiza-
tion of electronic states in (substitutionally) disordered sys-
tems (5,6); ii) the proof that local chemical bonding, i.e.,
short-range structural order alone, is sufficient to predict the

existence of the fundamental semiconductor bandgap (7); and iii)
the formulation of the mobility edge concept, together with the
idea that overlapping tails of states (albeit disorder-induced)
pin the Fermi level in the bandgap (8,9). Since the first suc-
cessful fabrication of solar cells in 1976, a veritable explosion
in experimental information has resulted from renewed interest in
the characterization of a-Si:H materials. In particular, the
following features have been elucidated: silicon-hydrogen bond-
ing configurations as a function of deposition conditions (10-
12); the nature of defect states responsible for the recombina-
tion of photo-generated carriers (13-15); modifications in opto-
electronic properties of films via impurity incorporation (16,
17); the growth of potentially interesting related alloys such as
a-Si:(F,H) (18); and the influence of gap states upon diode char-
acteristics and device performance (19-23).

In this Chapter we shall selectively review progress that has
been made in advancing an understanding of the materials proper-
ties of plasma-deposited a-Si:H alloys. Therefore, an emphasis
will be placed upon the basic aspects of such materials, but with
a focus toward photovoltaic conversion. In developing the sub-
ject, our philosophy is to take an integrated approach in which
are interwoven discussions of: i) the plasma chemistry respon-
sible for film growth, ii) the crucial effects of plasma process-
ing conditions upon both chemical bonds in the plasma and in
synthesized alloys, and iii) optoelectronic film properties and
device characteristics. Accordingly, in Sect. II we begin by
discussing the nature of the plasma, proceeding from preliminary
concepts of the rf glow discharge (Sect. II.*A*) to a more detailed
description of the plasma chemistry in the silane glow discharge
(Sect. II.*B*). Experience with plasma etching is briefly reviewed
as a paradigm for plasma deposition (Sect. II.*B.1*). We then dis-
cuss emitting reactive species that are identified in plasma
deposition using optical emission spectroscopy (Sect. II.*B.2*),
and end with a summary of electron-impact processes that are

pertinent to the silane glow discharge (Sect. II.*B.3*).

In Sect. III we discuss the characterization of plasma-deposited silicon-hydrogen alloys. The introduction to chemical bonding in Sect. III.*A* consists of discussions on short-range structural order (Sect. III.*A.1*), the role of hydrogen in the alloy (Sect. III.*A.2*), and the influence of residual gap states upon diode characteristics (Sect. III.*A.3*). In Sect. III.*B* we explore the following dilemma: From measurements of quenched photoluminescence efficiency (and of degraded device performance), electronically doped alloys unfortunately exhibit reduced minority-carrier transport. As a consequence, highly conductive, efficiently doped alloys are relegated the menial role of effecting Ohmic contacts. Finally, in Sect. III.*C* we discuss the effects of nitrogen and oxygen impurities with regard to: i) the optoelectronic properties of a-Si:H alloys; and ii) the photovoltaic conversion efficiencies of diagnostic devices that are fabricated using such materials. It follows that an ambiguity arises in the definition of the nominally intrinsic silicon-hydrogen alloy a-Si:H. Indeed, the usual alloy should more accurately be regarded as the alloy a-Si:(H,O,N,C,...). The Chapter is concluded by an expanded discussion of anomalous behavior in photoconductivity (Sect. III.*C.2*). Such behavior involves new recombination processes in alloys prepared under certain low impurity conditions.

II. NATURE OF THE PLASMA

Many deposition techniques now exist for the growth of thin-film a-Si:H materials: rf or dc glow-discharge decomposition of silane (SiH_4); rf reactive sputtering of a silicon target in an atmosphere of argon and hydrogen; low-temperature chemical vapor deposition; e-beam evaporation of silicon into atomic hydrogen; electrodeposition; etc. So far, the most efficient solar cells have been fabricated from a-Si:H alloys grown via the glow-

discharge (plasma deposition) technique. Therefore, we will dis-
cuss the deposition chemistry specifically in the context of pro-
cesses characteristic of plasma deposition. Moreover, we will
mainly confine our remarks to plasma processes that occur for
the rf glow-discharge decomposition of silane in a capacitively-
coupled system. In this case, alloys are typically produced
under the following operating conditions: chamber pressure p =
= 0.1-1.0 Torr, substrate temperature T_s = 225-400°C, and rf
power density = 0.01-0.3 W cm^{-2}.

   Glow discharges ignited in hydride or halide gases create a
dilute plasma state that consists of electrons and many differ-
ent, mostly neutral, radical species. For example, the silane
glow discharge (Sect. II.B) is a metaphorical "zoo" of reactive
species that contains SiH, SiH^+, SiH_2, SiH_3, SiH_3^+, Si_2H_6, H, H_2,
etc. The nature and concentrations of such species vary sensi-
tively with the processing conditions. Now it is possible that
a particular composition of radical species in the plasma (and
in the "sheath" regions) may be correlated with specific bond-
ing patterns in films, and thence with distinct optoelectronic
and microstructural properties of such films. Thus, the plasma
processing conditions play a key role in determining film prop-
erties. Of course, the specific correspondences between molec-
ular bonds of reactive species in the plasma and chemical bonds
in as-deposited films may not be especially simple. Indeed,
complex electron-impact processes create reactive species in the
plasma, while subsequent gas-phase (homogeneous) and $surface$
(heterogeneous) reactions promote film nucleation and growth on
substrates. As a consequence, for example, it may be naive to
expect that concentrations of the radical SiH_2 (detected in the
plasma by molecular absorption techniques) could be correlated
with dihydride chemical bonding $=SiH_2$ (detected in films by
vibrational spectroscopy).

   We again emphasize that the basic plasma chemistry is impor-
tantly influenced by the variation of the processing parameters

in deposition. Moreover, these parameters constitute a rather
large multidimensional space: substrate temperature (T_s); rf
power (P); chamber pressure (p); concentrations of hydrides or
halides in carrier gases; flow rates; electrode biases; impurity
levels; etc. Therefore, a detailed understanding of the rela-
tionship between the plasma processing conditions and the plasma
chemistry would greatly facilitate the optimization of a-Si:H
materials intended for photovoltaic conversion as well as for a
host of other photoelectronic applications.

A. *Preliminary Features of the RF Glow Discharge*

Historically, it was Faraday who first discovered the (dc)
glow discharge by initiating luminous zones in air with a 1000 V
power source at the Royal Institution (1831-1835). The striking
feature of the discharge, namely the visible luminosity, mainly
results from the de-excitation of emitting molecular and atomic
species contained in the plasma. However, as we indicated pre-
viously, a plasma chemistry of considerable complexity belies the
beauty of the glow discharge.

The rf glow discharge in a gas is sustained by inelastic
electron-impact processes that are initiated by electrons which
have acquired sufficient energy from rf fields as a result of
successive elastic collisions with gas molecules. In principle,
ion-molecule reactions also play an important role in the kinet-
ics of the discharge. An electron loses an infinitesimal frac-
tion ($\sim m_e/M$) of its kinetic energy in elastic collisions, but
such collisions provide a random component to the electron veloc-
ity that allows the particle to absorb net power. As we men-
tioned above, when a glow discharge is ignited in a molecular gas
such as silane, the resulting plasma "zoo" contains a wide vari-
ety of species: electrons, excited neutrals (free radicals and
gas molecules), ions, and photons. All of these species partic-
ipate in the plasma chemistry in varying degree.

Equations 1-6 summarize general aspects of typical rf glow-discharge plasmas:

$$n_e \sim 10^8\text{-}10^{12} \text{ cm}^{-3} \qquad (\sim \text{cation density}) \tag{1}$$

$$<E> \sim 0.5\text{-}5 \text{ eV} \qquad (T_e \sim 10^4\text{-}10^5 \text{ K}) \tag{2}$$

$$E_e = \frac{e^2}{2m}\left(\frac{F_o^2}{\omega_c^2 + \omega^2}\right) = \frac{1}{2}m\omega^2 A^2 \tag{3a}$$

$$\sim (F_o/p)^2 \qquad (\omega_c \gg \omega) \tag{3b}$$

$$\text{Ions} \sim 10^{-4}\cdot\text{Neutrals} \tag{4}$$

$$V_{dc} \simeq -\left(\frac{3}{2\varepsilon}\frac{\omega_p^2}{\omega^2}\right)\frac{E_e}{e} \tag{5}$$

$$T_{gas} \ll T_e \quad , \qquad T_{gas} \sim T_s = 300\text{-}650 \text{ K} \tag{6}$$

Equations 1 and 2 list ranges of values for the electron density n_e in the plasma, and for the average electron energy $<E>$, or equivalently, the electron temperature ($\frac{3}{2}kT_e = <E>$). The electron energy distribution, which is only approximately Maxwellian, has an extended tail that, as will be discussed later, is responsible for high-lying excited and ionized states of atoms and molecules in the plasma. It is interesting that the solar corona is another example of a plasma for which the electron density is lower ($n_e \sim 10^7 \text{ cm}^{-3}$) but for which, as anticipated, the average energy is higher ($<E> \sim 100$ eV).

Equation 3a expresses the average electron energy E_e acquired between successive elastic collisions in terms of the rf electric field amplitude F_o and the collision frequency ω_c. Since ω_c is proportional to the gas pressure p, the quantity E_e scales with

the ratio (F_o/p), as shown in Eqn. 3b. This simple result also suggests that the electron temperature, hence the rates of electron-impact processes, should approximately depend upon the ratio P/p^2, where P is the rf power. The electron component of the plasma oscillates in space with rf frequency ω and amplitude $A = \mu_e F_o/\omega$ owing to the high electron mobility $\mu_e = e/m\omega(\omega_c^2+\omega^2)^{\frac{1}{2}}$ compared to that of the ions $(\mu_i/\mu_e \sim m_e/M)$. Indeed, neglecting ambipolar diffusion, all electrons that are within a distance A of a surface are removed from the plasma in each half cycle, leaving a positive space-charge region of width $\sim A$ near the surface. (This region is often referred to as a "dark space", or "sheath".) It is for this reason that ungrounded electrodes in a capacitively-coupled plasma deposition system acquire a negative potential relative to the plasma. Equation 3a also shows that the electron in the plasma behaves like a harmonic oscillator with force constant $m\omega^2$, driving frequency ω, and amplitude A.

The dilute plasma condition expressed by Eqn. 4 is easily understood on the basis of available low-lying excited states relative to high ionization potentials for atomic and molecular species in the plasma. For example, consider the case of the molecule SiH in the silane glow discharge. In the plasma it is more probable that electron-impact processes lead to a low-lying excited state of the neutral molecule, e.g., the state $A^2\Delta - X^2\Pi$ (3 eV above the ground state), than that ionization of the SiH molecule (ionization potential of 8 eV) is effected by the tail of the electron energy distribution. The influence of ions and electrons upon film growth and film properties, however, may be rather greater than suggested by cursory deduction from Eqn. 4.

Equation 5 gives a relation for the negative dc bias V_{dc} that develops between either electrode of a symmetric system and the plasma owing to oscillation of the electron component (see, e.g., Eqn. 3a). V_{dc} is expressed in terms of the "potential drop" E_e/e, multiplied by a dimensionless factor that contains the plasma frequency $\omega_p^2 = n_e e^2/m\varepsilon_o$ and the relative permittivity ε of

the plasma ($\varepsilon \approx 1$). For a typical plasma, the condition that rf
radiation is absorbed, namely $(\omega^2 + \omega_c^2) > \omega_p^2$, is indeed satisfied.
(Otherwise, radiation would be reflected, as with radio waves
that bounce off the ionosphere.) Equation 5, which must be re-
garded as a crude approximation, was derived under the following
assumptions: i) diffusion by electrons to chamber surfaces could
be neglected; and ii) the cation space charge density is constant
in space and equal to n_e. Precisely because of the existence of
the space charge region, the flux of positive ions onto an un-
grounded electrode (cathode) is high relative to the concentra-
tion of cations in the discharge expressed in Eqn. 4. Moreover,
the bias accelerates cations onto the cathode with mean energy
$\sim e|V_{dc}|$ that greatly exceeds thermal energies for neutrals.
Therefore, it is possible that properties of alloys grown on the
cathode are influenced by energetic cation bombardment that, e.g.,
alters existing bonding arrangements, incorporates new bonding
patterns, and influences the rates of gas-surface reactions. A
flux of electrons and anions may also influence the properties of
films grown on the grounded electrode (anode).

    For a numerical example using Eqns. 3 and 5, we assume typ-
ical processing conditions such that $n_e = 10^9$ cm^{-3}, $\omega = 13.56$ MHz,
$\omega_c = 5 \times 10^9$ s^{-1}, and $F_o = 10$ V cm^{-1}. Then we obtain the repre-
sentative values $E_e = 0.035$ eV, $A = 0.26$ cm (a measure of the
"dark space" width), and $V_{dc} = -9.3$ V (the potential drop across
the dark space).

    Equation 6 summarizes a fundamental feature of the rf plasma:
the decoupling of the two characteristic temperatures of the
plasma, i.e., the decoupling of the gas temperature T_{gas} and the
electron temperature T_e. We previously cited the origin of this
circumstance. Namely, in elastic collisions very little kinetic
energy is transferred from the energetic electrons to the mol-
ecules. Moreover, the inelastic collisions of electron-impact
processes predominantly lead to *internal* excited states of
product species, i.e., to excited electronic states of atoms, and

to excited electronic, vibrational, and rotational states of
molecules. The net result is that the kinetic energy (transla-
tional energy) of molecules, hence T_{gas}, is not significantly
increased in the plasma which contains the coexisting hot elec-
tron component.

B. Plasma Chemistry of the Silane Glow Discharge

In order to achieve an understanding of the basic plasma
kinetics and surface reactions encountered in plasma deposition,
a variety of complementary techniques must be employed to study
reactive radical species. Such techniques include optical emis-
sion spectroscopy, molecular absorption spectroscopy, mass spec-
trometry, and novel laser techniques with good spatial resolu-
tion for investigating the gas-solid interface of nascent films.
We will begin this Section with a brief discussion of plasma
etching, a dry etching process of silicon (or SiO_2, Si_3N_4, etc.)
for which complementary plasma techniques have already given
considerable insight. The specific interest in the chemistry of
plasma *deposition*, however, is more acute than in the case of
plasma etching. The ultimate objective in deposition is to find
correspondences between chemical bonds in the plasma and chem-
ical bonds in the condensed state, i.e., in films with desired
optoelectronic properties. In the case of etching, material is
ablated, and chemical bonds simply vaporize into the reactor
effluent. Later in the Section we explore optical emission
spectroscopy as a technique for the identification of emitting
reactive species in the plasma deposition of a-Si:H alloys. The
Section ends with a partial list of possible electron-impact
processes that occur in the silane glow discharge.

1. Plasma Etching Paradigm. The etch rate of silicon in a CF_4
plasma is known to increase with the addition of oxygen to the
plasma. This problem was solved in general terms using both op-
tical emission spectroscopy (OES) and mass spectrometric

techniques (24-26). Since the first technique may be less famil-
iar to the reader, we note here that the de-excitation of atoms
and molecules in the plasma gives rise to photons that (in the
visible part of the spectrum) constitute the luminosity of the
"glow discharge". Spectral analysis of the emission from the
discharge (using a monochromator) allows the identification, in
principle, of the subset of *emitting* reactive species in the
plasma. Using OES, the high etch rate for $\sim$ 15-25% O_2 in the
CF_4 gas stream was correlated with a high emission intensity
from both atomic F and molecular CO, and with suppressed emis-
sion from atomic O. In addition, mass spectrometry of the re-
actor effluent, downstream of the reaction chamber, showed that
the stable end products of the etching are SiF_4, CO, CO_2, and
COF_2. It was therefore concluded that: i) the oxidation of
carbon-bearing species releases atomic F; and ii) F is respon-
sible for etching the silicon and produces only one stable
species, namely SiF_4. Since it is known that CF_4 does not
directly react with atomic O, the radical CF_3 is suspected as a
reaction intermediate that is oxidized. Subsequent reactions
then lead to free atomic F. The recombination of fluorine with
adsorbed carbon may be strongly suppressed owing to the presence
of atomic O. This would be an additional mechanism that aids
the etching.

It is also of interest that in plasma etching the etch rate
is suppressed by the presence of impurity H_2O ($\lesssim$ 20%). Using
OES in a diagnostic mode, this effect can be correlated with
quenched emission from atomic F, and with enhanced emission
from atomic hydrogen that is produced via the decomposition of
H_2O in the plasma (25).

   2. *Toward the Identification of Species in Plasma Deposition
      of a-Si:H Alloys Using Optical Emission Spectroscopy*. Fig-
ure 1 illustrates part of an optical emission spectrum for a
silane glow discharge with 600 ppm added N_2 impurity (17). Since
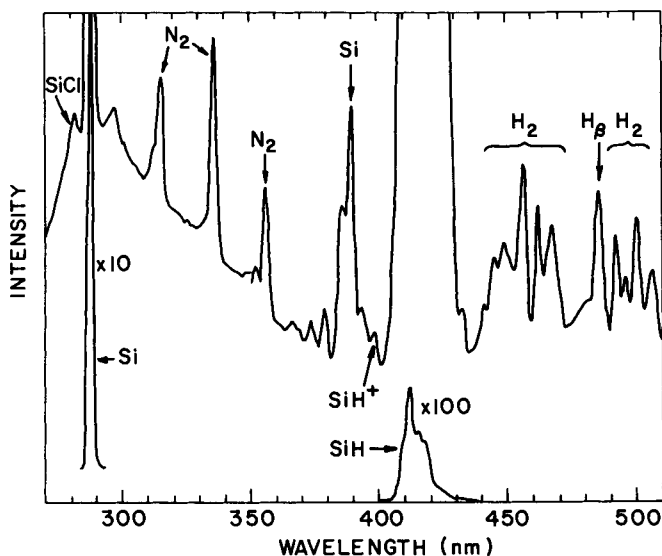
FIGURE 1.   Optical emission spectrum of plasma with 600 ppm
N_2 *added.   (50 W, 250 mTorr, $T_s = 270°C$.)*

optical emission spectroscopy (OES) does not perturb the dis-
charge, this technique is routinely used by our group to monitor
the plasma during film deposition. The particular deposition
conditions used here were: $P = 50$ W rf power, $p = 250$ mTorr,
100 scc min^{-1} silane flow rate, and substrate temperature $T_s =$
$= 270°C$. The following emitting reactive species were detected
in the plasma: Si, SiH, SiH$^+$, H_2, H, and the impurities SiCl and
N_2. Moreover, when oxygen is intentionally added to the silane
gas stream, or when a sizable airleak occurs in the deposition
system, weak emission from the molecule SiO is also observed
(27). Figure 2 shows an emission spectrum for an oxygenated dis-
charge (1000 ppm added O_2) scanned at higher resolution and sen-
sitivity.

The silicon multiplets of Fig. 1, Si(288 nm) and Si(391 nm),
or those of Fig. 2, arise from distinct electronic transitions
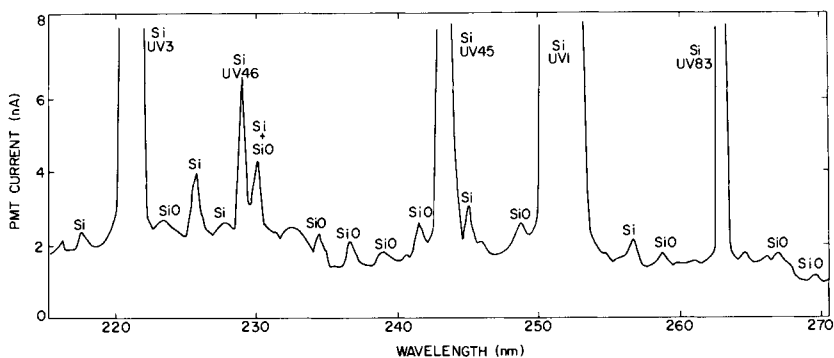
FIGURE 2. *Optical emission spectrum of plasma with 1000 ppm* O_2 *added.* (15 W, 100 mTorr, $T_s = 270°C$.)

of atomic silicon. Some of these Si lines, such as Si UV1 (251-253 nm) in Fig. 2, consist of several components owing to fine structure effects (spin-orbit coupling). By contrast, the prominent SiH band (413-428 nm), together with weaker bands between 386-396 nm (not explicitly identified in Fig. 1), correspond to the *same* electronic transition. This transition, $A^2\Delta - X^2\Pi$, is due to de-excitation from levels that lie ∿ 3 eV above the electronic ground state. Each band, however, comprises distinct vibronic bands (i.e., specific vibrational transitions with unresolved rotational structure). The SiH band (413-428 nm) contributes to the rather striking deep violet appearance of the silane glow discharge. Bands from the electronic transition $A^2\Delta - X^2\Pi$ are also observed in sunspots and weakly in the solar disc. As we mentioned in Sect. II.A, the weak emission in Fig. 1 from the cation SiH[+] (399 nm) can easily be explained: The probability is higher for exciting low-lying levels of the neutral molecule SiH than for ionizing this species with an ionization potential of 8 eV. Another possible source of SiH[+] is the dissociative ionization of SiH_4.

Emission from molecular hydrogen, H_2 (450-630 nm), is also evident in Fig. 1. Moreover, the continuum in Fig. 1 below approximately 400 nm is due to H_2 emission. The extent of the tail for the electron energy distribution can be appreciated by noting that initial energies for the emitting state in the H_2 spectra lie as high as 14 eV above the ground state. Emission from H_β (486 nm) in the Balmer series signals the presence of reactive hydrogen in the plasma. The dark red emission of H_α (656 nm) is also observed (not shown), while under some processing conditions H_γ (434 nm) can be detected. Besides hydrogen impurity in silane tanks, sources of H_2 in the plasma include: i) subsequent gas-phase reactions of primary products of the silane decomposition; and ii) surface reactions at the gas-solid interface of the growing a-Si:H alloy for which the strong bond of H_2 is energetically favored (4.5 eV).

The observed emitting species Si and SiH could arise directly from the decomposition of excited (and unstable) silane molecules SiH_4^*, or via the decomposition of SiH_2 and SiH_3. Unfortunately, these last species have no known emission spectra. Therefore, using the OES technique alone, it is not possible to study such species in the silane glow discharge. On the other hand, the importance of SiH_2 and SiH_3 to the growth of a-Si:H alloys may be inferred from a mass spectrometric study (28) of the 147 nm photolysis of silane (photon energy $h\nu = 8.4$ eV). In that case the two reactions[2]

$$h\nu + SiH_4 \rightarrow SiH_4^* \rightarrow SiH_2 + 2H \quad , \tag{7}$$

$$\rightarrow SiH_3 + H \tag{8}$$
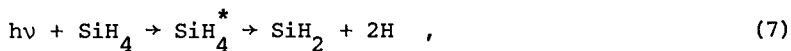
were calculated to have quantum yields of 0.83 and 0.17, respectively. From the study it was also concluded that wall reactions

---

[2] *In photolysis, the threshold for the formation of SiH_4^* is $h\nu = 7.5$ eV. Electron energies >11.7 eV are required for ionization of SiH_4.*

of SiH_3 and SiH_2SiH_2 radicals led to film formation. For proc-
essing conditions that are more appropriate to the plasma deposi-
tion of a-Si:H alloys, film growth may instead proceed from com-
plex surface reactions that involve the gas phase species H, SiH,
SiH_2, and SiH_3 (and perhaps certain ions as well). It is clear
that in order to extract the maximal information about the plasma
chemistry in film deposition, OES must be complemented by ad-
ditional techniques.

Pursuing our analogy with the plasma etching paradigm of
Sect. II.$B.1$, we now turn to the impurities that were detected in
plasma deposition, namely $SiCl(281 nm)$ and $N_2(C^3\Pi_u - B^3\Pi_g)$ of Fig.
1, and $SiO(A^1\Pi - X^1\Sigma^+)$ of Fig. 2. The high sensitivity of OES for
the first two impurities suggests that this technique may play a
useful diagnostic role in the routine monitoring of the plasma.
The presence of oxygen, however, is more easily detected by in-
frared transmission spectroscopy of vibrational modes, such as
the Si-O-Si stretch modes, in as-deposited films. (See Sect.
III.)

At higher resolution, the emission from SiCl can be resolved
into at least two components, i.e., vibronic bands that belong
to the common electronic transition $B^{-2}\Delta - X^2\Pi$. The presence of
this molecule in the plasma can be attributed to the decomposi-
tion of trace chlorosilane impurities originally contained in
the silane process gas. Analysis by secondary-ion-mass-
spectrometry (SIMS) showed a qualitative correlation between the
concentration of Cl incorporated in a-Si:H alloys and the emis-
sion intensity of SiCl in the plasma when using different silane
tanks. However, for 2-600 ppm incorporated chlorine, no obvious
correlation was found between the chlorine concentration and the
electrical properties of a-Si:H alloys, although an inverse rela-
tion with photoconductive response is possible. One difficulty
is that the effects of chlorine are masked by the presence of
other impurities in silane tanks. If the chlorine acts to pas-
sivate defects by participation in bonds such as $\equiv SiCl$ and

=SiHCl, it is conceivable that a small concentration would not have an appreciable effect upon electrical properties. The efficiency for defect passivation by chlorine, compared to that by hydrogen (or fluorine), is presumably influenced by the relatively large covalent radius $\simeq 0.99$ Å for this element.

   The molecule N_2 is a ubiquitous impurity of the usual plasma deposition system. The high sensitivity of OES for emission from N_2 (second positive system) allows quantitative calibration of the N_2 content in the plasma. This feature is quite useful since concentrations of N_2 as low as several hundred ppm in the plasma can affect the electrical properties of a-Si:H alloys. As will be amplified in Sect. III, the modification of film properties is related to the ability of incorporated N to introduce shallow defects, or to act as a donor, i.e., an electronic dopant, in the amorphous network.

   The small relative emission intensity of SiO with respect to atomic Si is apparent from Fig. 2. Each SiO peak, nestled among the "sequoia trees" that are the Si multiplets, corresponds to a distinct vibrational-rotational transition. The common electronic transition $A^1\Pi-X^1\Sigma^+$ involves a de-excitation from an initial state ~ 5.3 eV above the ground state. Since oxygen exhibits extreme reactivity toward silicon hydrides, a-Si:(H,O) alloys are deposited under the processing conditions of Fig. 2. Because SiO is intrinsically a good emitter, the weak relative emission of SiO in Fig. 2 implies that the observed SiO was not a reactive intermediate in the incorporation of oxygen in the a-Si:(H,O) alloy. Instead, this emitting species must be a byproduct of that incorporation. As a consequence, the SiO emission is not expected to be a quantitative measure of oxygen in the plasma that could be used to calibrate oxygen incorporation in films.

   3. Electron-Impact Processes. We review typical processes that in principle give rise to the primary species and major

reactive intermediates engaging in the plasma chemistry of a
silane glow discharge. Some of the reactions are proven on the
basis of the preceding results, but the importance of others can
only be speculative at this stage, pending innovative experiments
for their elucidation.

   a. Electron-molecule (-atom) reactions.

Excitation: $e + Si \rightarrow Si^* + e$ (5.0–6.8 eV)

                   $e + SiH \rightarrow SiH^* + e$ (3.0 eV)

                   $e + SiH^+ \rightarrow (SiH^+)^* + e$ (3.1 eV)

                   $e + H \rightarrow H^* + e$ (12–13 eV)

                   $e + H_2 \rightarrow H_2^* + e$ (11.9–14.0 eV)
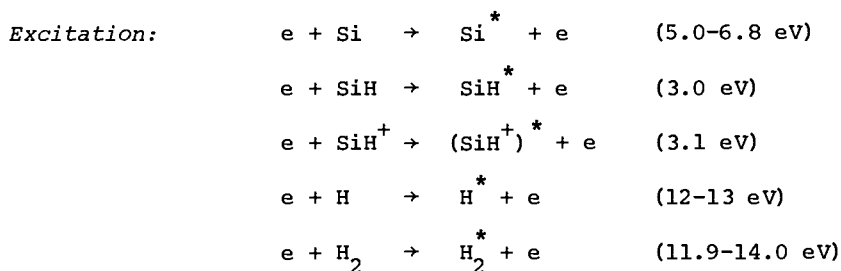
The energies in parentheses refer to measurements by OES in Ref.
27 and denote the positions of the initial emitting states above
the ground state. Of course, the reactions themselves are more
general, and different levels of excitation would depend upon
the particular plasma processing conditions involved.

Dissociation: $e + SiH_4 \rightarrow SiH_3 + H + e$

                     $\rightarrow SiH_2 + 2H + e$

                     $\rightarrow SiH + 3H + e$

                     $\rightarrow Si + 4H + e$
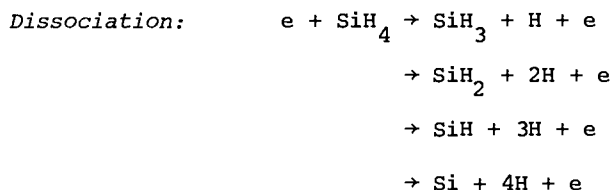
These equations are the analogs of Eqns. 7 and 8 for photolysis
in which the threshold for absorption and dissociation of SiH_4
is 7.5 eV (165 nm). Of course, the silicon-hydride products in
these reactions can be further dissociated by subsequent
electron-impact processes, e.g., $e + SiH_3 \rightarrow SiH + 2H + e$. One
may naively expect that each successive reaction above requires
an additional increment in electron energy equal to the Si–H

bond energy, i.e., equal to 3.06 eV (29) or perhaps 3.6-4.1 eV
(30). On such a model, Eqn. 3b would imply that higher rf power
and lower silane pressure would favor the production of SiH, Si,
and H_2 (H) primary products in the gas phase.

Ionization: $e + SiH \rightarrow SiH^+ + 2e$ (IP = 8 eV)

                      $e + SiH_4 \rightarrow SiH_4^+ + 2e$ (IP = 11.7 eV)

Dissociative $e + SiH_4 \rightarrow SiH_2^+ + H_2 + 2e$ (AP = 11.9 eV)
Ionization:
                                $\rightarrow SiH_3^+ + H + 2e$ (AP = 12.3 eV)
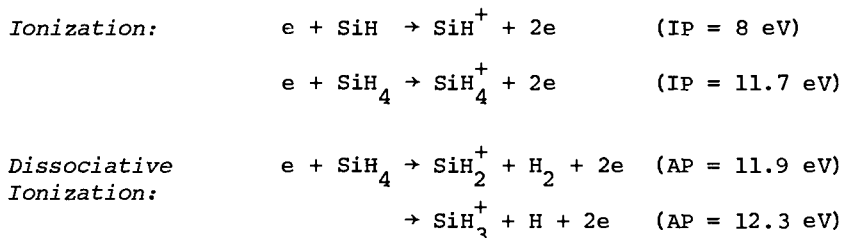
The appearance potential for the cation SiH_2^+ shows that the
cation SiH_4^+ itself is unstable, i.e., the reaction $SiH_4^+ \rightarrow$
$\rightarrow SiH_2^+ + H_2$ is endothermic by only 0.2 eV (30). These ioniza-
tion processes replenish the plasma with electrons and thereby
sustain the discharge. Such "breeder" reactions compete with
electron attachment, certain electron-cation reactions, and the
loss of electrons from the plasma by diffusion and drift to
walls and electrodes.

Attachment: $e + H \rightarrow H^-$ (affinity = 0.75 eV)

                      $e + SiH_4 \rightarrow (SiH_4^-)^*$

Dissociative $e + SiH_4 \rightarrow SiH_3^- + H$
Attachment:
                                $\rightarrow SiH_2^- + H_2$
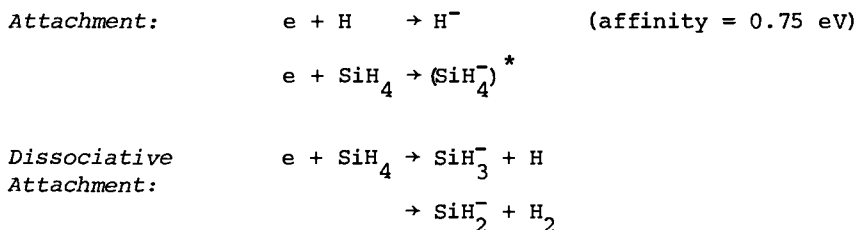
The dissociative attachment reactions could involve *low energy*
resonances between electrons and gas molecules (31). In this
regard, recall that the average electron energy <*E*> of Eqn. 2 is
rather low. A steady state could rapidly be attained for the
anion population as a consequence of competing anion destruction
processes such as associative detachment.

b. Electron-cation reactions.

Recombination: $e + SiH_2^+ \rightarrow SiH_2$

Dissociative $e + SiH_2^+ \rightarrow SiH + H$
Recombination:
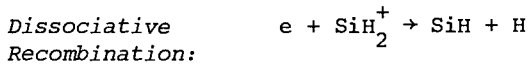
Other processes will now be listed that are *a priori* of con-
siderable importance to film growth.

c. Surface reactions (at electrodes).

$$SiH_2 \underset{s}{\rightarrow} Si(film) + H_2$$

$$SiH_3 \underset{s}{\rightarrow} SiH(film) + H_2 \quad , \text{ etc.} \tag{9}$$

$$SiH^+ + SiH_3(film) \underset{s}{\rightarrow} SiH_2^+(film) + SiH_2(film)$$

$$Si^+ + SiH_2(film) \underset{s}{\rightarrow} SiH^+(film) + SiH(film) \tag{10}$$
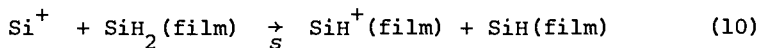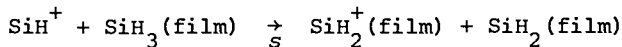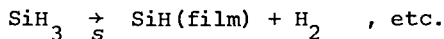
(cation bombardment of films)

As discussed in Sect. II.*A*, the small relative population of
ions in the plasma may be a poor measure of the importance of
ions to film growth that proceeds by surface reactions. Indeed,
the effects of energetic ion bombardment may be twofold: i) a
direct influence on the conversion and incorporation of chemical
bonds in films (Eqn. 10); and ii) the stimulated increase in the
reaction rate of other gas-surface interactions, e.g., those of
Eqn. 9. Finally, we mention that catalytic effects of chamber
surfaces can even alter gas-phase reactions.

d. Ion-molecule reactions.

$$SiH_2^+ + SiH_4 \rightarrow SiH_3^+ + SiH_3$$

$$\rightarrow Si_2H_4^+ + H_2 \quad , \text{ etc.}$$
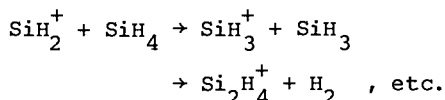
In contradistinction to the surface reactions involving ions, these gas-phase reactions are restricted by Eqn. 4 and may not play a large role in plasma deposition at lower power and pressure.

III. CHARACTERIZATION OF PLASMA-DEPOSITED SILICON-HYDROGEN ALLOYS

Evaporated and sputtered films of pure a-Si exhibit a large density of gap states $\sim 10^{20}$ cm^{-3} eV^{-1}, a large electron-spin-resonance (ESR) signal $N_s \sim 10^{19}$-10^{20} spins cm^{-3}, high dark conductivity, poor photoconductivity, and little or no photoluminescence at low temperatures. By contrast, a-Si:H alloys can be deposited with a low density of gap states ($\sim 10^{15}$-10^{16} cm^{-3} eV^{-1} near midgap), low spin density $N_s \sim 10^{14}$-10^{15} spins cm^{-3}, high resistivity, high photoconductivity, and nearly 100% efficient peak photoluminescence. As a consequence, a-Si:H alloys can be electronically doped (1-3) and used to fabricate promising photovoltaic devices (4,23). It is interesting to note that these alloys are still not completely well-characterized materials. Nonetheless, certain salient materials properties have been established, including features of the silicon-hydrogen bonding (Sect. III.*A*) and many optoelectronic properties (Sect. III.*B*). In addition, in Sect. III.*C* we shall explore the evolving chemical definition of the nominally intrinsic silicon-hydrogen amorphous alloy a-Si:H. Indeed, it has been found that the distribution of gap states for "a-Si:H" alloys may sensitively depend upon the degree of incorporation of common atmospheric impurities encountered in plasma deposition (17). In fact, the more correct designation for the usual a-Si:H alloy should perhaps be a-Si:(H,O,N,C,...), where concentrations of the impurities can be typically as high as $\sim$ 0.1-1%.

A. *Introduction to Silicon-Hydrogen Bonding in the Alloy*

   1. Short-Range Structural Order. Radial distribution func-
tions from electron diffraction data for evaporated films of
pure a-Si show that: i) the first and second coordination
shells are nearly identical with those of the ideal diamond lat-
tice; but ii) the third-neighbor coordination does not exist
(32). Hence, whereas a-Si lacks the long-range structural order
of the perfectly periodic crystal, this noncrystalline phase re-
tains *short-range* structural order. That is, the classic tet-
rahedral bonding of nearest neighbors depicted in Fig. 3a is ap-
proximately preserved for a-Si. In contrast to random network
models for a-Si that are consistent with the diffraction data,
structural models for the alloy a-Si:(H,O,N,C,...) are quite
complex and depend on the degree and kind of alloying involved.
(See Fig. 3b.) An important principle to note for both mate-
rials, however, is that most fundamental semiconductor concepts
follow from short-range structural order alone in a covalently-
bonded solid, i.e., from the local chemical bonding. In partic-
ular, the existence of characteristic energy bands separated by
a "gap" in electron energy is independent of whether the lattice
is ordered (crystal), or disordered (amorphous substance). In-
deed, this fact was always implicit in the chemists' picture of
a semiconductor as a giant molecule in which the conduction band
is composed of "anti-bonding" states and the valence band is
composed of "bonding" states.
   An important theorem due to Weaire and Thorpe (7) proved
that the infinite-range correlation of a perfect lattice is not
required to predict the existence of a bandgap. In order to ap-
preciate this assertion, we first sketch the usual argument that
is employed to predict energy bands for the crystal phase in the
tight-binding approximation. In this case, a Wannier expansion
of the electron wavefunction that embodies Bloch symmetry is in-
serted into Schrödinger's equation for the crystal. The
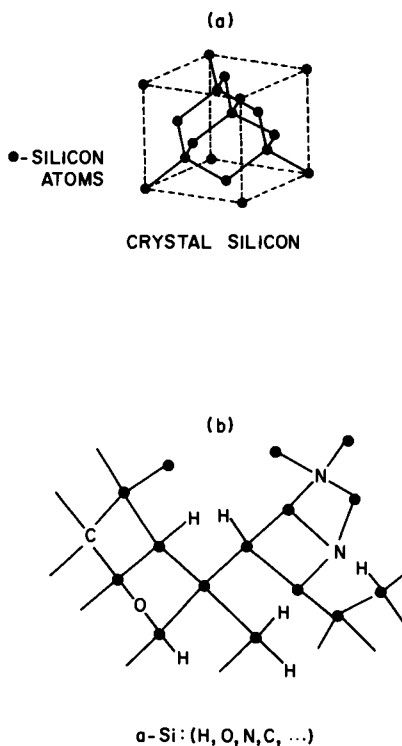
FIGURE 3.   Comparison of crystal structure with that of amorphous "silicon-hydrogen" alloy: (a) unit cell of c-Si; (b) schematic planar representation of the alloy a-Si:(H,O,N,C,...).   In (b) the concentrations of contaminants in the alloy relative to hydrogen have been exaggerated for the purpose of illustration.

retention of nearest-neighbor non-diagonal matrix elements of the
Hamiltonian then gives the elementary energy eigenvalue spectrum
for bands found in textbooks.   The bandgap itself emerges from
consideration of the first Bragg reflection at the boundary of
the first Brillouin zone.   In other words, the crystal bandgap
is derived by initially assuming an exact Bloch wavefunction, and

then approximating the Hamiltonian with nearest-neighbor (and
diagonal) interactions between atomic lattice sites. By con-
trast, on the model of Ref. 7 one *begins* with a Hamiltonian $\hat{H}$
that incorporates overlapping bonding orbitals between nearest-
neighbor atomic sites, and then one solves for the exact energy
eigenvalue spectrum. Topological disorder is thereby implied.
In the simplest formulation,

$$\hat{H} = V_1 \sum_{n,a,a'} |n,a\rangle\langle n,a'| + V_2 \sum_{(n,a),(m,b)} |n,a\rangle\langle m,b| \quad (11)$$

$$\qquad\qquad \text{(atomic sites)} \qquad\qquad \text{(overlapping bonding orbitals)}$$

$$\equiv zV_1\hat{H}_1 + V_2\hat{H}_2 \quad . \tag{12}$$

In Eqn. 11 the state $|n,a\rangle$ represents the orbital a at atomic
site n; V_1 is the self-energy, i.e., the interaction energy be-
tween orbitals at the same site; and V_2 is the interaction energy
for all overlapping orbitals (n,a) and (m,b) that constitute two-
center bonds. In Eqn. 12, z is the coordination number. The
operators $\hat{H}_{1,2}$ have simple interpretations: $\hat{H}_1$ takes the orbital
at any site and averages it over all orbitals at that site, and
$\hat{H}_2$ transforms any orbital into the nearest-neighbor orbital that
shares the common bond. Making use of these properties, and em-
ploying operator algebra manipulations, one can solve for the
eigenvalues of $\hat{H}_1$, $\hat{H}_2$ and, hence, of $\hat{H}$. The result is that $\hat{H}$ is
a two-band Hamiltonian, and that the bands are separated by an
energy gap of width $|zV_1 - 2V_2|$. Of course, $z = 4$ for the sp^3
orbitals of silicon. Thus, the existence of short-range struc-
tural order alone is sufficient to guarantee the existence of a
bandgap for a topologically disordered semiconductor.

   2. Role of Hydrogen in a-Si:H Alloys. The demonstration that
hydrogen is indeed bonded in plasma-deposited materials is best
provided by measurements of infrared transmission spectroscopy

on as-deposited films. Figure 4 illustrates the characteristic
vibrational modes due to silicon-hydrogen bonding in a film pro-
duced at medium-high substrate temperature (T_s = 270°C) and rela-
tively low pressure (p = 250 mTorr). For this alloy with pre-
dominant monohydride bonding, the stretch mode of the complex
$\equiv$SiH is readily identified at $\tilde{\nu}$ = 2000 cm^{-1}. The degenerate wag
and rock modes of this singly hydrogen-bonded complex lie at $\tilde{\nu}$ =
= 630 cm^{-1}. Calibration of the integrated absorption with anal-
yses by SIMS indicates that $\sim$10% hydrogen is incorporated in this
film. Assuming that the mild absorption at $\tilde{\nu}$ = 880 cm^{-1} can be
identified with the bend-scissors and twist modes of the di-
hydride bonding =SiH$_2$, it can be estimated that the proportion
of dihydride modes in this particular alloy is only $\sim$4%. By
comparison, this proportion can be reduced below detectability
for alloys grown at lower rf power (15 W) and pressure (100
mTorr). As first pointed out by Brodsky, *et al.* (10), low sub-
strate temperature and high pressure are processing conditions
that conspire to give a larger proportion of polyhydride bonding
in alloys. Examples are dihydride and trihydride bonding, and
(SiH$_2$)$_n$ polymer bonds that are associated with electrically-
active defects (11). The non-controversial signature of di-
hydride or (SiH$_2$)$_n$ polymer bonding is a bend scissors mode at
$\tilde{\nu}$ = 880-890 cm^{-1}. In the case of (SiH$_2$)$_n$, a wag mode at $\tilde{\nu}$ =
= 845 cm^{-1} is also observed. Both complexes may exhibit a
stretch mode at $\tilde{\nu}$ = 2090 cm^{-1}. However, it has recently been
suggested that this 2090 cm^{-1} absorption may require a more com-
plex interpretation (33). Evidence is mounting that alloys with
predominant monohydride bonding, i.e., no 880-890 cm^{-1} modes,
exhibit better optoelectronic response (photoconductivity,
photoluminescence), thereby resulting in improved device charac-
teristics.

By comparing film properties of pure a-Si with those of the
a-Si:H alloy, it is concluded that the role of hydrogen in the
alloy is twofold: i) hydrogen passivates electrically-active
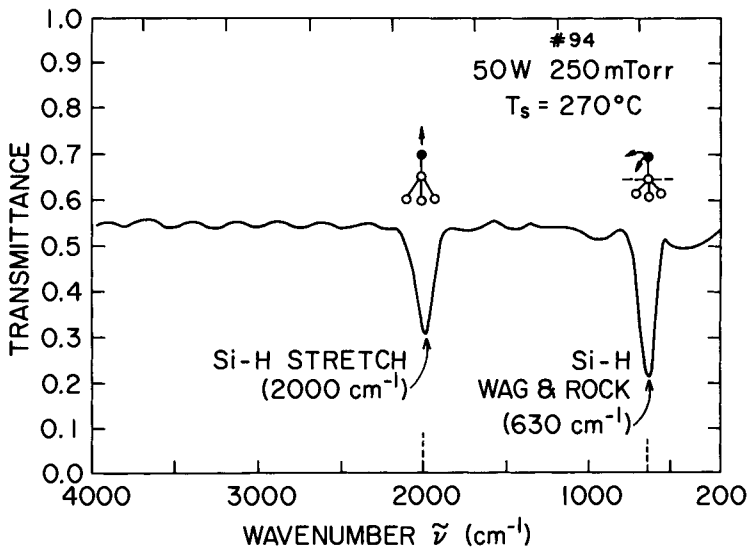
*FIGURE 4.   Infrared transmittance spectrum of predominantly
monohydride a-Si:H alloy.   Film thickness is 4 μm.*

defects in the amorphous network[3]; and ii) the silicon-hydrogen
bonding *per se* modifies the distribution of bonding and anti-
bonding states of otherwise pure silicon, creating a new elec-
tronic material.   To illustrate the first role, the minimal dens-
ity of spins in a-Si:H films ($N_s \sim 10^{14}$-10^{15} cm^{-3}) is consistent
with the idea that hydrogen passivates a whole class of defects
with positive correlation energy[4] $U > 0$, namely, the dangling
bond states ($\equiv$Si·).   By contrast, we noted before that $\sim 10^{20}$

---

[3]*Although in large concentrations, perhaps >25%, hydrogen
incorporation may actually create new defects.   As an example,
dangling bonds could be created in voids associated with $(SiH_2)_n$
polymer chains (11).*

[4]*The electron-electron correlation energy U may be thought of
as the energy needed to add an extra electron to the defect; it
contains the Hubbard energy of Coulombic repulsion.*

paramagnetic states cm^{-3} ($g \simeq 2.0055$) exist in pure a-Si (34,35).
It is therefore reassuring to observe that the spin density of
ultrahigh-vacuum-evaporated a-Si is quenched below $N_s = 10^{17}$ cm^{-3}
when the material is subsequently exposed to a hydrogen plasma at
400-500°C (36). Now in a typical a-Si:H alloy with monohydride
bonding the concentration of hydrogen is ∿5-10%. However, the
concentration of paramagnetic centers in a-Si is only a maximum
of ∿0.2%. Therefore, even if some minimum concentration of hy-
drogen (∿1%?) were consistent with the best electronic properties
of a-Si:H alloys, hydrogen would still be expected to passivate
other, more numerous, defects. One obvious candidate is the
class of defects with paired electron spins. For such localized
states, an energy-dependent and negative correlation energy
U(E) < 0 could imply a *spectrum* of weak molecular bonds in the
amorphous network[5]. Thus the class of spin-paired defects spans
weakly reconstructed Si-Si bonds, divacancies, etc. Incorporated
hydrogen may convert, for example, a reconstructed bond into
≡SiHHSi≡, a broken Si-Si bond with two H atoms inserted.

The second role of hydrogen is suggested by measurements of
both photoemission spectroscopy (PES) and optical absorption.
For example, using PES it was found that the valence band edge
recedes up to 1 eV relative to a-Si as a function of hydrogena-
tion in sputtered and plasma-deposited a-Si:H (37). That is,
Si 3p states that constitute the leading edge of the a-Si valence
band were chemically modified by the silicon-hydrogen bonding.
Since the leading edge of the Si-H bonding states would be ex-
pected[6] to lie below the top of the distribution of Si-Si

---

[5]*However the detailed role of the electron-phonon interaction
in promoting spin-pairing is not well understood at present*

[6]*Because of the small covalent radius of hydrogen, the Si-H
bond strength, 3.06 eV, exceeds the Si-Si bond strength, 1.94 eV
(29).*

bonding states, the valence band should indeed recede and the
energy gap should widen. Using the PES technique (37), states
that arise from the overlap of Si 3s, 3p orbitals and the H ls
orbital can be identified with the bonding configurations ≡SiH,
=SiH$_2$, -SiH$_3$, and (SiH$_2$)$_n$. Consistent with the findings of PES,
the optical bandgap also widens with increasing hydrogenation
(38). For the same kind of alloy depicted in Fig. 4 ([H] = 10%),
Fig. 5 shows the determination of the effective optical gap
$E_O \simeq 1.65$ eV from reflection and transmission measurements at
visible and near-infrared wavelengths. E_O was extrapolated from
a linear fit to the quantity $(\alpha h\nu)^{\frac{1}{2}}$, where $\alpha(\nu)$ is the funda-
mental optical absorption coefficient and $h\nu$ is the photon energy
(39). By comparison, the optical gap for a pure a-Si film, also
prepared at $T_S \simeq 270°C$, lies in the range $E_O = 1.20-1.35$ eV.
Consistent behavior is found when alloys are annealed at
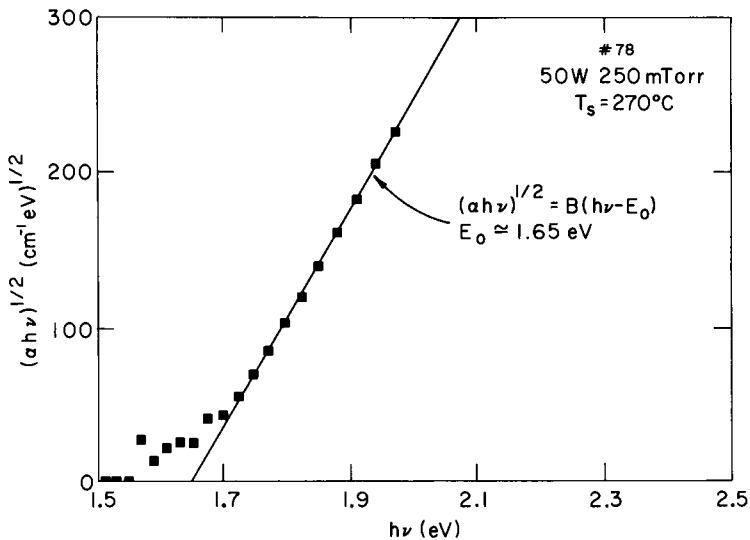
FIGURE 5. *Optical bandgap E_O deduced from plot of $(\alpha h\nu)^{\frac{1}{2}}$
versus photon energy $h\nu$ at room temperature.*

450–600°C: hydrogen effuses, N_s increases owing to the regenera-
tion of dangling bond defects, and E_o decreases toward values
characteristic of pure a-Si (40).

It is evident that the density and distribution of gap states
should have a profound effect upon the optoelectronic properties
of the material. As previously discussed, the incorporation of
hydrogen in a-Si:H alloys significantly decreases the density of
gap states relative to the case of pure a-Si. To illustrate this
feature, Fig. 6 shows the density-of-states distribution $n(E)$
for an a-Si:H film deposited at about T_s = 250°C (41). Also
shown is the density of states in the upper half gap for an
a-Si:(F,H) alloy that was plasma deposited with a gas ratio
$[SiF_4]/[H_2]$ = 5 at the nominal substrate temperature T_s = 380°C
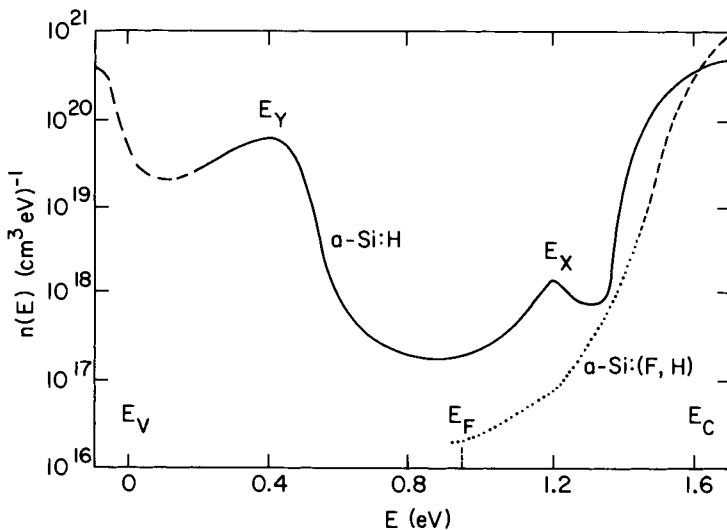
*FIGURE 6.   One-electron density-of-states distribution n(E)
for a-Si:H at $T_s \approx 250°C$ (Ref. 41), and for a-Si:(F,H) at nominal
$T_s = 380°C$ (Ref. 18).*

(18). For both alloys $n(E)$ was deduced from field-effect-conductance measurements. The energies E_C and E_V denote the "mobility edges" of the conduction band and valence band, respectively. These edges are sharp demarcations between free-carrier states and band-tail states that are localized owing to random fluctuations in bond angles and bond lengths. The energies E_Y and E_X refer to peaks in the gap state density that are widely disparate in magnitude. Because of the large difference in magnitude of these peaks, donor-like and acceptor-like states of the *same* defect cannot be invoked to explain their origin. It should be pointed out, however, that the specific presence of two peaks in $n(E)$ invites controversy since the analysis of field-effect-conductance data is subject to many assumptions. Foremost among these limitations is the neglect of surface or interface states that leads to an overestimation of gap state density. Other techniques, in particular deep-level-transient-spectroscopy (42), appear to be promising alternatives for the determination of $n(E)$. A less controversial feature can be abstracted from Fig. 6, namely, that overlapping tails of defect densities pin the Fermi level E_F near the minimum in $n(E)$. ·On this model (41), donor-like states that are neutral when occupied lie mostly in the lower half of the gap; acceptor-like states that are neutral when unoccupied lie mostly in the upper half gap. (See also Sect. III.*A.3.*) Near the Fermi level, unoccupied donor defects (occupied acceptor defects) then give rise to positive (negative) charge distributions. Without invoking structure such as peaks in $n(E)$, the density of donor-like states may be an order-of-magnitude larger than for the acceptor-like states. The high proportion of hole-trapping states in the lower half of the gap *must fundamentally limit minority-carrier transport* in these materials.

    3. Influence of gap states on diode characteristics. The degree to which gap states affect device properties is well

illustrated by the case of the dark forward current $J =$
$= J_o\{\exp(eV_F/nkT) - 1\}$ for Pt/a-Si:H Schottky diodes. (Films
of a-Si:H are "n-type" when not intentionally doped, hence such
diodes are n-type Schottky devices.) Both the diode quality
factor n and the saturation current J_o are found to be sensitive
functions of the alloy preparation conditions (21). In partic-
ular, ideal diode rectification characteristics, namely $n \simeq 1$
and small values $J_o \sim 10^{-11}$ A cm^{-2}, are obtained for low deposi-
tion pressure p, high substrate temperature T_s, high flow rates
of silane, and post-anneal of the Pt contact. For example, Fig.
7 shows the deviation from diode perfection at $T_s = 300°C$ as a
function of increasing chamber pressure from $p = 60$ mTorr to
$p = 300$ mTorr (21). As discussed previously, the processing
conditions that result in more ideal diode parameters are
consistent with a higher proportion of monohydride bonding $\equiv$SiH
versus polyhydride bonding in the bulk of the a-Si:H alloy.
These results suggest that the recombination current[7] increases
relative to the usual injected current with increasing poly-
hydride content. Therefore, polyhydride bonding is correlated
with defects in the bulk of the alloy that, in turn, lead to
poor diode characteristics. Now because of band bending, the
Fermi level lies lower in the gap toward E_v as a function of
position nearer to the metal-semiconductor interface. Hence on
Spear's model (41), deep-lying unoccupied defect donors: i) con-
tribute to the net positive charge of the space-charge region;
ii) self-consistently help to pin E_F; and iii) act as recombina-
tion centers that affect transport. The insensitivity of the
open-circuit voltage V_{oc} to preparation conditions is taken as

---

[7]*For the n-type Schottky diode, recombination in the space-
charge region near the metal-semiconductor interface gives rise
to a current that behaves as $J_r \sim J_{or}\exp\{(\phi_n-\phi_p)/mkT\} \sim$
$\sim J_{or}\exp(eV_F/mkT)$, $m \simeq 2$, compared to the usual injection cur-
rent $J_i \sim J_{oi}\{\exp(eV_F/kT)-1\}$.*
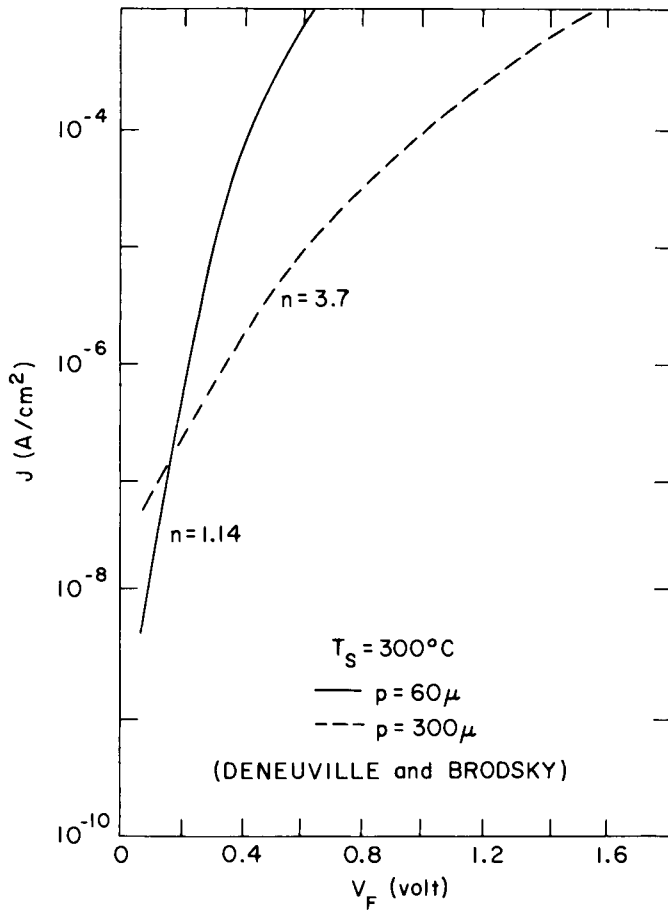
FIGURE 7. Dark current versus forward bias for two dif-
ferent silane pressures, showing deviation from diode perfec-
tion with increasing polyhydride bonding (Ref. 21).

evidence that E_F is pinned by bulk states in the alloy (21). On

the other hand, interface states may also be insensitive to

preparation conditions. Such states with density $\sim 10^{13}$ $cm^{-2} eV^{-1}$

(43) may assist in pinning E_F and in determining the barrier

height ϕ_{Bn}. In either case, bulk states in the alloy strongly

influence recombination rates and therefore affect the transport parameters n and J_o.

Another interesting example of the influence of gap states on device measurements is the following: these states lead to a more complicated interpretation of the differential barrier capacitance C for Schottky diodes. As a consequence, the usual expressions for C in crystalline diode theory cannot naively be applied to the present case. There are two major aspects that must be taken into account for a description of C in the case of amorphous-semiconductor Schottky diodes (19,20): i) the character of the density-of-states distribution $n(E)$ will determine C, and ii) this relationship will be dependent upon the measuring frequency ν of the applied potential. Conversely, with regard to aspect i), we initially note that measurements of C may, in principle, help determine general features of $n(E)$. It is not clear, however, whether detailed structure, such as the peaks E_X and E_Y in Fig. 6, could be proven or disproven by this means. With regard to aspect ii), if states deep in the gap do not have time to respond during the variation of an applied potential, characterized by period $\tau \equiv 1/\nu$, then such states cannot contribute to the space-charge density that determines C. In order to arrive at a relation that crudely quantifies this statement, we proceed as follows (19). Thermal equilibrium is established between the conduction band and an energy level E in the gap with the characteristic thermal response time:

$$\tau_E = (v\sigma_{nE}N_C)^{-1}\exp\{(E_C-E)/kT\} \sim 10^{-13}\cdot\exp\{(E_C-E)/kT\} \text{ s} \quad , \quad (13)$$

since $(v\sigma_{nE}N_C) \sim (10^7 \text{ cm s}^{-1})(10^{-15} \text{ cm}^2)(10^{21} \text{ cm}^{-3}) = 10^{13} \text{ s}^{-1}$.

For states at E to make a contribution to C, we then require that

$$\tau \equiv 1/\nu > \tau_E \quad . \quad\quad\quad (14)$$

For example, for states located near the midgap, $(E_C-E) \simeq$
$\simeq 0.80$ eV, Eqn. 13 implies that $\tau_E \sim 2.3$ s at $T = 300$ K. Hence,
$\nu < 1$ Hz is required from Eqn. 14 -- tantamount to a dc mea-
surement!

Returning now to the behavior with bias of the differential
barrier capacitance C (per unit junction area) we note that for
n-type c-Si Schottky diodes the presence of *shallow* donors sim-
ply implies a constant charge density N_D in the space charge
region. (Donor states of phosphorous in c-Si lie 45 meV below
the conduction band edge.) The solution of Poisson's equation
for the barrier profile potential $\Psi_b(x)$ then results in the
usual linear relation between the quantity C^{-2} and the bias V
($V > 0$ for forward bias):

$$C^{-2} = 2(V_O-V)/\varepsilon\varepsilon_O eN_D \quad \text{(Crystal Case),} \quad (15)$$

where V_O is the "built-in voltage" of the barrier[8]. Extrapola-
tion of Eqn. 15 to large forward bias then yields V_O whereas
the slope determines N_D.

By contrast, in the case of the metal/a-Si:H diode, Ψ_b will
be self-consistently determined by the gap state density. Mea-
surements of C at $\nu \simeq 0$ Hz then probe all states in the gap. In
order to obtain an *exact* analytic result for C that illustrates
this circumstance, we make a simplifying assumption. Namely, we
assume that overlapping *exponential* tails of donor/acceptor de-
fect states pin E_F in the gap as a function of position through-
out the space-charge region. On this model, $n(E) = n_D(E) + n_A(E)$,
where $n_D(E) = N_O\exp\{-\beta_O(E-E_O)\}$, for $E > E_O$, and $n_A(E) =$
$= N_O'\exp\{-\beta_O'(E_O'-E)\}$, for $E < E_O'$. In addition we assume that the
slopes satisfy $\beta_O = \beta_O'$, but this is not an essential assumption

---

[8]*We use the convention for the space charge region that $V_O =$
$= \Psi_b(x)+\Psi(x)$ where $\Psi(x)$ is the true potential difference, i.e.,
$\Psi(0) = 0$ and $\Psi_b(0) = V_O$ at the metal-semiconductor interface
$(x=0)$.*

for the basic result. As a consequence, the space-charge density may be expressed as:

$$\rho(x) = \rho[\Psi_b] = \rho_o \sinh\{e\beta_o \Psi_b(x)\} \qquad (\nu = 0), \qquad (16)$$

where $\rho_o \equiv en(E_{FO})\beta_o^{-1} \equiv en(E_{FO})kT_o$ and E_{FO} is Fermi level in the bulk (quasi-neutral region). Solving for C^{-2}, we receive instead of Eqn. 15:

$$C^{-2} = 2/\varepsilon\varepsilon_o e^2 n(E_{FO})\{\cosh\{e\beta_o(V_o-V)\} + 1\} \qquad (\nu = 0) . \qquad (17)$$

An immediate consequence of Eqn. 17 is the behavior $C^{-2} \sim$ $\sim \exp\{-e\beta_o(V_o+V_R)\}$ that results for increasing reverse bias $V_R = -V > 0$. This (exponential) decrease with reverse bias is obviously completely opposite to the linear increase with V_R that would be predicted by Eqn. 15.

   Figure 8 shows data at $\nu \simeq 0$ Hz (19) that does indeed confirm a rapid decrease in C^{-2} with increasing V_R. On the other hand, measurements at $\nu = 10$ Hz (20) probe states slightly nearer to the conduction band: For increasing V_R, the behavior in Fig. 8 appears more representative of Eqn. 15. Data is also shown in Fig. 8 for measurements of C^{-2} at $\nu = 100$ Hz on a Pt/a-Si:H diode (44). At this frequency, states nearer to E_C presumably dominate the behavior of C^{-2}. However, if Eqn. 15 were literally applied to this case, the physical interpretation of the extracted parameters N_D and V_o would be somewhat dubious. We therefore provisionally note that the two straight line segments of the 100 Hz data yield "densities" $N_{D1} = 5 \times 10^{15}$ cm^{-3} and $N_{D2} = 1.4 \times 10^{16}$ cm^{-3}. Under 0.02 sun illumination, measurements at $\nu = 100$ Hz on the same n-type Schottky diode also gave linear behavior for C^{-2} with V_R. The extracted density parameter $N_L = 3.8 \times 10^{16}$ cm^{-3} exceeds the densities N_{D1}, N_{D2} obtained in the dark (44). Provided that Eqn. 15 could at least be used as a relative measure of space charge densities in the dark and under illumination, it is possible to conclude the existence of: i) a sizable optically-induced space-charge
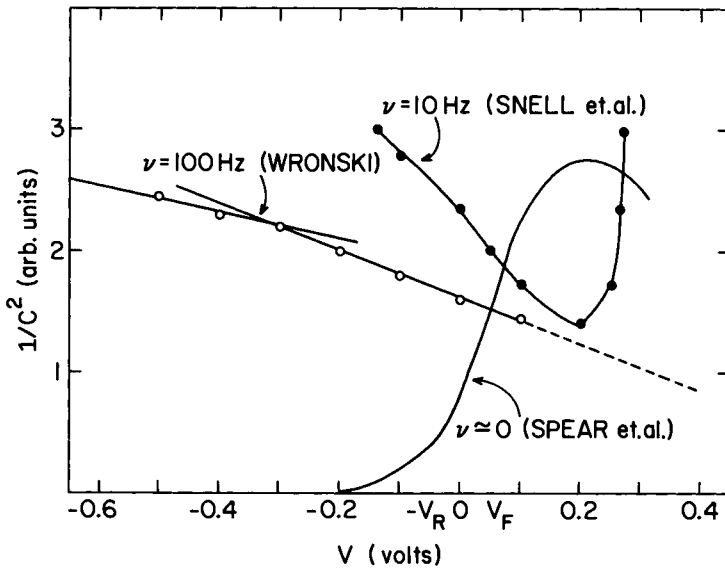
FIGURE 8. C^{-2} plots versus bias V for Schottky diodes mea-
sured at indicated frequencies: a) Au/a-Si:H at ν ≃ 0 Hz (Ref.
19); b) Au/a-Si:H at ν = 10 Hz with upturn for increasing V_F due
to equivalent circuit assumed for bulk corrections (Ref. 20);
and c) Pt/a-Si:H at ν = 100 Hz, bulk corrections unspecified
(Ref. 44).

density, and/or ii) a (reversible) photostructural-induced
change in n(E) itself (45,46). For measurements of C at ν ≃ 0 Hz
that probe deep gap states, it is interesting to speculate about
the first possibility. For example, would optically-induced
states in the space-charge region of the illuminated Schottky
diode share common origins with the optically-induced spin res-
onances detected for doped and undoped alloys (14,47-49)? In
that event, the positive space charge would be enhanced under
illumination by contributions from holes that condense into
various defect states. Hole polarons may also play a role (50),
i.e., free-carrier holes could subsequently self-trap (broad
line in ESR centered near g ≃ 2.01). Hole polarons may be

linked as well to recombination in photoluminescence (15).

Finally, we mention that preliminary studies have been carried out in which solar cell efficiency is correlated with substrate temperature and other processing variables, hence, in principle, with different gap state densities (51).

B. *The Dilemma of Efficient Doping but Reduced Minority-Carrier Transport*

1. Electronic Doping and Increased Conductivity. The first systematic substitutional doping of a-Si:H alloys demonstrated remarkable changes in dark conductivity (1) and in photoconductivity (52,53) as functions of concentrations of the dopant gases phosphine (PH_3) and diborane (B_2H_6). For example, n^+-type films were prepared at $T_s \simeq 250°C$ for which the dark conductivity increased by seven orders of magnitude relative to the undoped state: $\sigma_d(300 \text{ K}) \simeq 10^{-2} \ (\Omega \cdot cm)^{-1}$ for 2000 ppm PH_3 added to the silane gas stream. It was estimated that the substitutional doping efficiency is roughly 15% of the PH_3 concentration in the silane gas stream, and that a maximum of ∿200 ppm P atoms can be incorporated as donors in the a-Si:H network (1). To illustrate these remarks, we show our own data in Figs. 9 and 10 for films doped by phosphorous under various processing conditions (54). Figure 9 shows that at room temperature, $\sigma_d \simeq \ \simeq 10^{-2} \ (\Omega \cdot cm)^{-1}$ was attained with 300 ppm PH_3 dopant. It is probable that the high-temperature activation energy (E_σ) in Fig. 9 pertains to free electron transport. Hence $E_\sigma = (E_C - E_F) = \ = 0.28$ eV, the distance of the Fermi level from the mobility edge of the conduction band. In the absence of intentional doping $E_\sigma \simeq 0.77$ eV under the same processing conditions. Following Ref. 52 the shallower slope in Fig. 9, namely 0.16 eV, may be due to electron hopping in the donor band, or the explanation may require "polaronic" concepts (55). Figure 10 illustrates classic behavior in photoconductivity for a doped film produced under the indicated processing conditions. The room-temperature
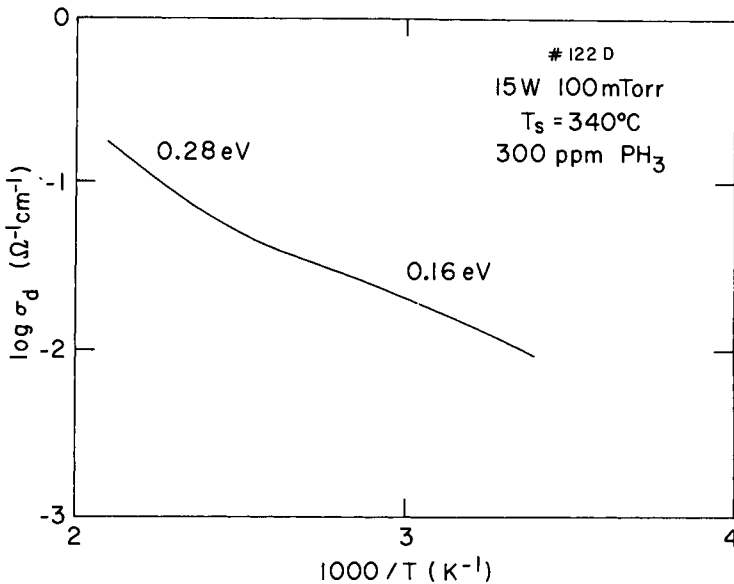
FIGURE 9.   Dark conductivity versus reciprocal temperature for phosphorous-doped a-Si:H alloy.

photoconductivity dramatically increased from σ_p = 1.8 x 10^{-8} $(\Omega \cdot cm)^{-1}$ for the undoped material to σ_p = 4.8 x 10^{-6} $(\Omega \cdot cm)^{-1}$ at a flux of 10^{14} γ's cm^{-2}s^{-1} for material doped by 600 ppm PH$_3$ in the plasma. For this material, the doping reduced the high-temperature activation energy of σ_d from E_σ = 1.05 eV to E_σ = = 0.34 eV: a movement of E_F by ≃ 0.7 eV.[9] Of course, photo-conductivity is a measure of *majority-carrier* transport, in this case by electron carriers. Therefore, high photoconductivity is only one figure-of-merit in selecting candidate materials for photovoltaic conversion. Another, more critical factor is the

___

[9]*On quite general grounds one can understand that as E_F approaches E_C, more and more recombination centers by definition become electron occupied. This situation persists under illumination (quasi-equilibrium), so that recombination is decreased and photoconductivity is increased.*
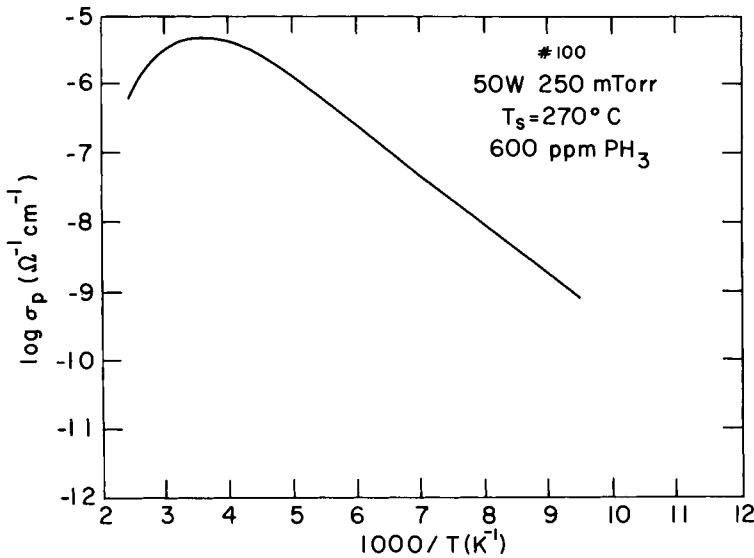
FIGURE 10. Photoconductivity versus reciprocal temperature for phosphorous-doped a-Si:H alloy. Flux $f_\lambda = 10^{14}$ γ's $cm^{-2}s^{-1}$ at $\lambda = 600$ nm.

quality of minority-carrier transport (Sect. III.*B.2)*.

An obstacle to increased doping efficiency of a-Si:H alloys is, of course, the residual gap states shown in Fig. 6. In this regard, it is instructive to compare the relative doping efficiencies of a-Si:H and single crystal silicon. For example, in the case of c-Si, $\sigma_d(300$ K$) = 1$ $(\Omega \cdot cm)^{-1}$ is typically attained with only 0.1 ppm P dopant (n-type) or with 0.3 ppm B dopant (p-type). Moreover, minority-carrier diffusion lengths in these doped c-Si materials are very large, approximately $L \sim$ ~ 100 µm.

Higher *n-type* doping efficiency with phosphorous or arsenic has been reported for a-Si:(F,H) alloys prepared at nominal substrate temperature $T_s = 380°C$ (18). For example, $\sigma_d(300$ K$) \simeq$ $\simeq 5$ $(\Omega \cdot cm)^{-1}$ and $E_\sigma \simeq 0.05$ eV resulted from adding only 500 ppm PH_3 to the $SiF_4 + H_2$ gas stream. This doped material would

appear to be degenerate in the sense that E_F penetrated the bandtail. By contrast, p-type doping with B_2H_6 is no more efficient than found for a-Si:H alloys, i.e., E_σ is limited to $\simeq 0.20$ eV. From these results it is possible to conclude that the density of states for a-Si:(F,H) is lower in the upper half gap relative to the usual a-Si:H alloy (e.g., as suggested in Fig. 6), but that the density of states in the lower half gap is comparable for both materials.

However, it is interesting to note that extremely conductive, σ_d(300 K) $\sim$ 100 $(\Omega\cdot cm)^{-1}$, phosphorous-doped silicon-hydrogen alloys have been grown at high power density and $T_s =$ = 300°C (56). But from X-ray diffraction studies it was determined that these films had, in fact, a *microcrystalline* structure. Moreover, very conductive polycrystalline films with σ_d(300 K) $\sim$ 5 $(\Omega\cdot cm)^{-1}$ result from high temperature anneals of doped a-Si:H alloys (57). From these two studies on a-Si:H alloys it can be concluded that: i) The degree of incorporation of P atoms and the efficiency of conversion to substitutional sites both *increase* with the degree of crystallinity[10]; ii) For high doping levels of PH_3 in the plasma, the crystallization temperature decreases (to $\simeq$ 510°C at $\simeq$ 2400 ppm); and iii) The "sign anomaly" for the Hall mobility of doped a-Si:H is removed for both partially-crystallized (56) and fully-crystallized films (57). On the basis of these results for a-Si:H, it would perhaps be enlightening to carry out measurements of Raman scattering and X-ray diffraction in order to test the amorphicity of doped (and undoped) a-Si:(F,H) alloys. Even the high mechanical stress found for a-Si:(F,H) films might be correlated with the possible appearance of microcrystalline structure.

[10]*From Ref. 56 as many as $\sim$ 2000 ppm P atoms can be incorporated. From Ref. 57 the conversion to substitutionality was 100% for completely crystallized material.*

2. *Quenched Photoluminescence Efficiency*. Since a-Si:H al-
loys can be electronically doped, it might appear possible to
fabricate reasonably efficient p-n homojunctions, and other de-
vices, using such doped materials for the active layers. Un-
fortunately, this expectation has not yet been fully realized[11],
and intentionally doped materials, such as n^+-type a-Si:H al-
loys, are essentially relegated the role of effecting Ohmic con-
tacts (4,58,59). The reason for this situation is qualitatively
the following. Under illumination a solar cell is a "minority-
carrier device", i.e., the photocurrent is carried by minority
carriers. But doping increases the recombination rate for
minority carriers in a-Si:H alloys by: i) introducing addi-
tional defects into the gap; and ii) increasing the occupation
of gap states by majority carriers. As a consequence, minority-
carrier transport is suppressed relative to the case of the un-
doped a-Si:H material. This statement can be appreciated by
noting that even for undoped a-Si:H (or a-Si:(F,H)), minority-
carrier transport is already a limiting factor for solar cells.
In particular, hole diffusion lengths in some "intrinsic" (n-
type) a-Si:H materials were estimated to be only L_p < 400 Å
(60). Small diffusion lengths $L_p \sim$ 1000 Å appear likely for
even the best materials prepared to date. Again, this feature
is a consequence of the high density of states in the lower
half gap (see Fig. 6). Thus the photocurrent of solar cells
based on a-Si:H is composed essentially of carriers that were
generated in the depletion region alone and that are subse-
quently swept out by the drift field. On such a model, the
internal spectral response (for the Schottky diode) can be
crudely approximated by the expression $SR(\lambda) \simeq \eta_\lambda \{1-\exp(-\alpha_\lambda w)\}$,
where w is the width of the space-charge region and $\eta_\lambda \lesssim 1$

---

[11]*For example, in Ref. 4 it was found that the short-circuit
current was reduced if the "intrinsic" layer in a p-i-n cell
were doped.*

denotes the quantum efficiency for carrier creation and separa-
tion in that region.

For undoped films, the efficiency of low-temperature "band-
tail" photoluminescence (PL) peaking at the canonical value
~ 1.3 eV (61,62) has often been taken as a measure of the defect
density that limits minority-carrier transport at room tempera-
ture. For this purpose, it must be assumed that deep-lying de-
fect states in the gap increase the non-radiative recombination
rate that directly competes with the radiative recombination
rate, i.e., with the photoluminescence. A connection then has
to be established between the defect states and minority-carrier
recombination processes at $T = 300$ K. For example, material
produced at low substrate temperatures contains a higher pro-
portion of dangling bond states that is correlated with reduced
PL intensity and hence with a higher non-radiative recombination
rate via paramagnetic defects. Indeed, it was found that the
spin density at $T_s = 25°C$ increased to $N_s \sim 10^{18}$ cm^{-3}, while the
PL intensity was reduced by a factor of 10^{-3}-10^{-2} (63). Such
material, like pure a-Si, presumably exhibits poor minority-
carrier transport.

The effect of doping upon the PL emission spectrum is two-
fold: i) The overall PL intensity is quenched as a function of
increasing dopant incorporation (apparently independent of the
chemical nature of the dopant); and ii) a low-energy spectral
component emerges at 0.8-1.0 eV that grows relative to the
canonical component and dominates the latter over a wide tem-
perature range. This quenching behavior is consistent with a
qualitative connection of photoluminescence efficiency with
minority-carrier transport. The low-energy component was first
noted in the case of phosphorous doping (64). It may well be
related to defects in c-Si introduced by ion implantation (65)
and to defects in "poor" undoped a-Si:H materials (61). Fig-
ure 11 illustrates this circumstance in the case of substitu-
tional doping by nitrogen (17). In this figure PL emission
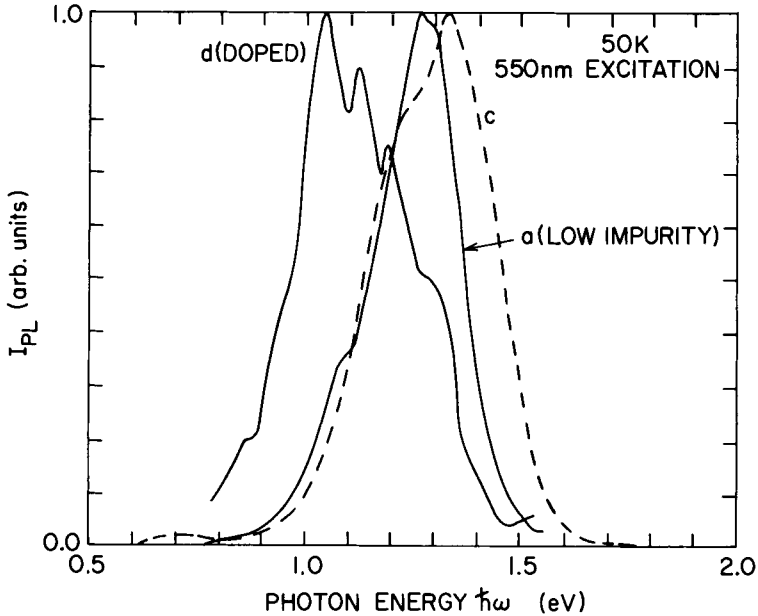
FIGURE 11. Photoluminescence emission spectra at 50 K for a-Si:H alloys with different impurity levels. Film d is electronically doped by nitrogen. (Fringes due to interference effects.)

spectra at 50 K are compared for films prepared at 15 W, 100 mTorr with varying levels of incorporated nitrogen and oxygen impurities. For film a produced under low impurity conditions, the spectrum is dominated by the canonical peak at $\sim$ 1.3 eV. Film c was produced by adding 1200 ppm N_2 and 700 ppm O_2 to the silane gas stream, but from the dark conductivity data, little or no movement of E_F indicates the lack of pronounced doping. The PL spectrum for this film may be slightly shifted to higher energy. Film d was plasma-deposited in the presence of an air leak. The electronic doping of this film by active nitrogen is manifested by: i) the small activation energy of the dark conductivity, $E_\sigma = (E_C - E_F) \simeq 0.5$ eV; and ii) extremely high "classic" photoconductivity that exceeds the photoconductivity

of the P-doped film in Fig. 10 by over an order-of-magnitude at
$T = 300$ K.

The PL spectrum for this particular film is dominated by a
low-energy component at $\sim$ 1.0 eV. In fact, Fig. 12 shows that
the low-energy component d(1.0 eV) dominates the high-energy
component d(1.2 eV) for all temperatures $\gtrsim$ 4.2 K. This tem-
perature dependence is also consistent with behavior found for
the low-energy component in phosphorous- and boron-doped alloys
(64). One effect of doping is therefore to introduce (or acti-
vate) a shallow defect (radiative recombination center) that
traps electrons which subsequently recombine with trapped holes
(perhaps self-trapped holes) to give the low-energy spectral PL
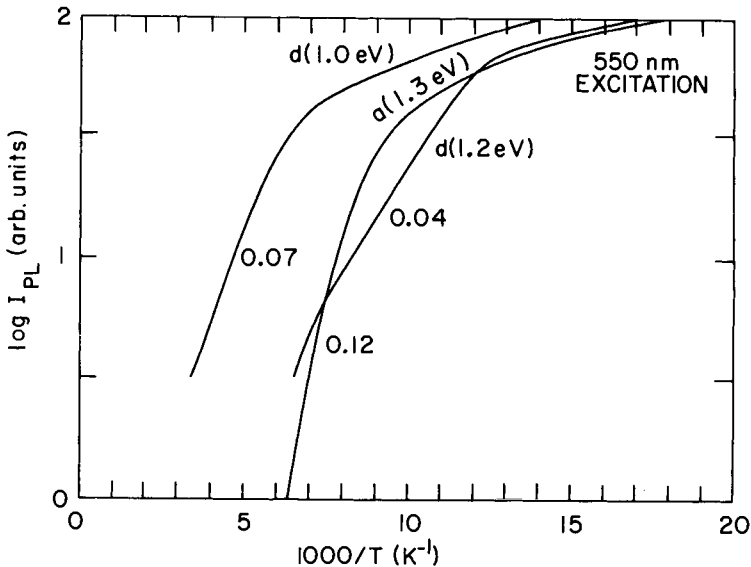
*FIGURE 12. Temperature dependence of PL spectral components
for doped film d. Also shown is canonical component of film a
produced under low impurity conditions. (Arbitrary normaliza-
tion.)*

component. Evidently competitive, non-radiative recombination
centers are also introduced that can be associated with para-
magnetic centers (63). These centers must be responsible for
the overall quenching of the PL intensity, the increased
minority-carrier recombination, and ultimately for degraded
minority-carrier transport in doped junction layers of devices.
Finally, we point out that the degree of the aforementioned ef-
fects in nitrogen-doped alloys seems to be a very sensitive
function of plasma processing conditions, and hence of the level
and efficiency of doping. Preliminary data (54) indicate that
doped alloys can be deposited that do not exhibit significant
quenching of the PL spectrum or the emergence of a low-energy
component at $T = 50$ K even though the Fermi level has shifted
by as much as 0.4 eV from the undoped state (Sect. III.$C.1.b$).

C. The Effects of Incorporated Atmospheric Impurities: The Alloy a-Si:(H,O,N,C,...)

1. Modifications in Optoelectronic Behavior. Many sources
of common atmospheric impurities (nitrogen and oxygen) are en-
countered in the plasma deposition of a-Si:H alloys: ubiquitous
airleaks in the system; backstreaming from the pumping system;
outgassing of adsorbed chamber air and moisture; impurities in
process and carrier gases, etc. It is little wonder, then, that
the optoelectronic properties of films reported in the litera-
ture to date reflect in varying degree the unintentional in-
corporation of such impurities as nitrogen, oxygen, carbon, and
other elements. Indeed, for otherwise fixed processing condi-
tions in a given deposition system, the proverbial irreproduc-
ibility of materials properties may well be ascribed to variable
sources and concentrations of impurities from one deposition run
to the next.

At the time of writing, the effects of impurities upon the
photovoltaic quality of a-Si:H alloys have barely been explored.
In any definitive study, the solar cell conversion efficiency,

the open-circuit voltage, and the short-circuit current would
all need to be correlated with calibrated concentrations of im-
purities contained in the alloy layers of a diagnostic device.
Of course, as a function of impurity content, it may also be
useful to test the hypothesis that measurements of low-
temperature photoluminescence could provide a guide to minority-
carrier transport properties that relate to solar cell effi-
ciencies. The systematic effects of nitrogen and oxygen im-
purities upon both solar cell efficiency and relative photo-
luminescence efficiency are topics of a current comparative
investigation (66).

Accordingly, we first discuss the documented effects of
atmospheric impurities upon majority-carrier transport (Sect.
III.*C.1.a*) and then briefly note trends that are emerging with
regard to the effects of such impurities upon solar cell con-
version efficiency (Sect. III.*C.1.b*). In Sect. III.*C.2* we ex-
plore in more detail the nature of anomalous photoconductivity,
including the universality of such behavior.

a. Majority-carrier transport. Rather striking modifica-
tions of dark conductivity and especially of photoconductivity
are found as the result of the incorporation of nitrogen and
oxygen impurities in a-Si:H alloys (17). The separate effects
of each impurity have already been studied in the case of reac-
tively sputtered a-Si:H alloys (16,67). The details of pre-
paring materials under low impurity conditions, or with cali-
brated concentrations of impurities in the plasma, are discussed
elsewhere (17,27,54). We simply note here that the phrase "low
impurity" specifically pertains to minimizing sources of im-
purities during plasma deposition, hence the resulting alloys
will be produced with a minimal level of incorporated atmo-
spheric impurities *for a given set of processing conditions.*
Varying the processing conditions clearly alters the film depo-
sition rate, the relative concentrations of reactive species

in the plasma due to residual impurities, etc. Therefore actual concentrations of contaminants in "low-impurity" materials vary from one processing condition to the next.

Figure 13 shows the effects upon the dark conductivity of adding 1000 ppm N_2 to the silane gas stream at $P = 50$ W, $p =$ $= 250$ mTorr, and $T_s = 260°C$. As illustrated in Fig. 1, the N_2 impurity in the plasma can easily be detected by optical emission spectroscopy. In Fig. 13 the dark conductivity for the low-impurity material is (approximately) singly-activated with slope $E_\sigma = 1.02$ eV. From an extrapolation of the quantity $(\alpha h\nu)^{\frac{1}{2}}$, the optical gap for the same material is found to be $E_o \simeq 1.65$ eV. (See also Fig. 5.) Hence, E_F lies below midgap for this low-impurity alloy produced at medium-high substrate
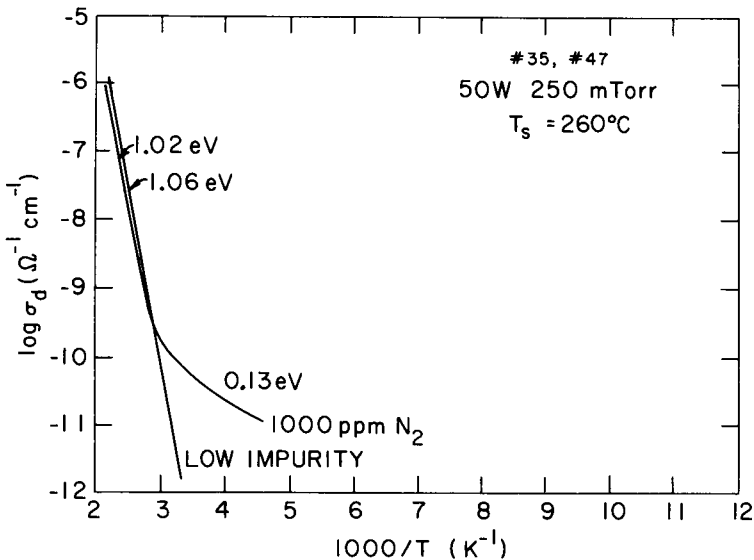
FIGURE 13. Dark conductivity versus reciprocal temperature for a-Si:H alloy produced under low impurity conditions, and for alloy grown with 1000 ppm N_2 in the silane gas stream.

temperature. By contrast, the film with the nitrogen impurity
exhibits phonon-assisted hopping transport below about $T \simeq 360$ K.
Depending upon the processing conditions, as little as several
hundred ppm N_2 can introduce shallow defects that engender hop-
ping in dark transport. The relevance of this observation is,
of course, that N_2 is a ubiquitous impurity encountered in
plasma deposition. In fact, despite manufacturers' specifica-
tions, such levels of N_2 contamination are occasionally found in
silane tanks.

Figure 14 illustrates modifications in photoconductivity
versus reciprocal temperature owing to the incorporation of
oxygen and nitrogen impurities in a-Si:H alloys. Alloys that are
deficient in both impurities, or in either impurity, exhibit
anomalous behavior in photoconductivity. In particular, the
phenomenon of thermal quenching (peaks near room temperature or
below) is apparent for Film a (low impurity conditions), and for
Films b (1000 ppm N_2) and c (1000 ppm O_2). Anomalous photocon-
ductivity in these alloys is actually characterized by as many
as three phenomena: i) the thermal quenching; ii) supralinear
dependence upon illumination intensity; and iii) infrared
quenching (68). By contrast, *synergistic effects* of oxygen and
nitrogen impurities restore classic behavior in photoconductiv-
ity as illustrated for Film d (540 ppm N_2 and 1000 ppm O_2).
Analyses by SIMS show that the transformation $a \rightarrow d$ in Fig. 14
is effected by a twentyfold increase in the *incorporated* im-
purity content: from 0.2% O and 20 ppm N to 4% O and 400 ppm N.

The anomalous thermal quenching phenomenon occurs in regions
of temperature for which the excess majority carriers far out-
number the dark carriers. (See Fig. 14.) On the other hand,
the thermal quenching behavior at *high* temperature in the clas-
sic photoconductivity of Film d is easily understood by noting
that at this flux, the number of dark carriers now exceeds the
excess carrier density. Under these circumstances, the density
of hole-occupied recombination centers for free-carrier
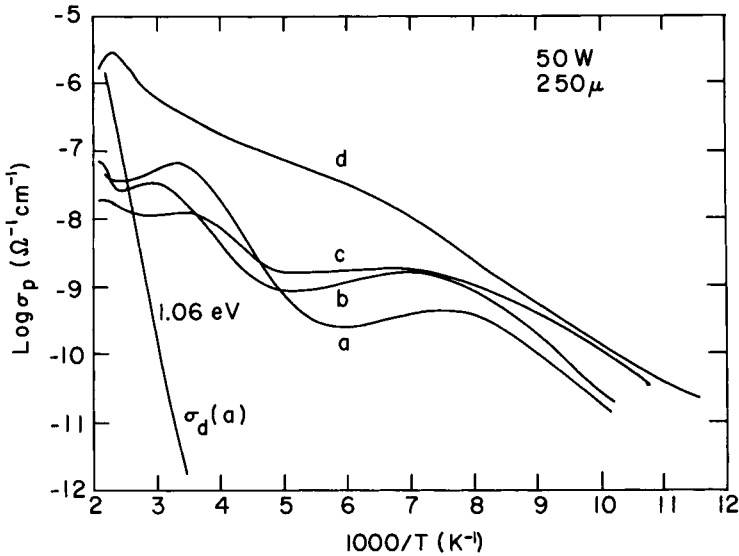
FIGURE 14.   Photoconductivity versus reciprocal temperature as a function of impurity content in the silane gas stream (50 W, 250 mTorr, T_s = 260°C). Low impurity Film a was deposited with no intentional impurities; Film b with 1000 ppm N_2; Film c with 1000 ppm O_2; and Film d with 540 ppm N_2 and 1000 ppm O_2. Flux f_λ = 10^{14} γ's $cm^{-2}s^{-1}$ at λ = 550 nm.

electrons is nearly the same as in thermal equilibrium: the quasi-Fermi levels are not displaced far from the dark Fermi level. Consequently, raising the temperature has the effect of: i) thermally exciting additional holes into the centers; ii) increasing the recombination rate of majority-carrier electrons; and thereby iii) quenching the electron photoconductivity as observed. As a function of illumination intensity, monomolecular recombination $\sigma_p \sim f_\lambda$ is consistently found in this region of temperature.

It is interesting that the introduction of calibrated air-leaks directly into the plasma deposition chamber exactly confirms the aforementioned modifications of film properties for medium-high substrate temperature, e.g., $T_s \simeq 270°C$. At rather

higher substrate temperatures, alloys produced in this manner
exhibit more pronounced effects of electronic doping by nitro-
gen. For example, Fig. 15 shows the photoconductivity and dark
conductivity of an alloy deposited at $T_s \simeq 370\,°C$ in the presence
of $\sim$3000 ppm air. The high-temperature activation energy is
only $E_\sigma \simeq 0.4$ eV, whereas an optical gap of the normal size,
namely $E_o = 1.7$ eV, was found from extrapolation of the quantity
$(\alpha h\nu)^{\frac{1}{2}}$. Consistent with the doping of this material, unusually
high photoconductivity was also attained: $\sigma_p(300\ K) = 4\times10^{-5}$
$(\Omega\cdot cm)^{-1}$ at a flux of 10^{14} γ's cm^{-2} s^{-1}. Thus, depending upon
the processing conditions, nitrogen has the ability to introduce
shallow defects (Fig. 13), or to act as a fourfold-coordinated
substitutional donor in the amorphous network (Figs. 15 and 3b).

Even in the absence of an airleak, high substrate tempera-
tures $T_s \simeq 325$-$375\,°C$ may be expected to promote impurity in-
corporation in materials by at least two mechanisms. Firstly,
high T_s significantly increases the outgassing rate of atmo-
spheric (and other) impurities from chamber surfaces into the
plasma where active species are created. Of course, this par-
tial chamber "bakeout" prior to deposition may actually decrease
certain residual impurity levels, notably water vapor that is
one source for oxygen. Secondly, the effect of high T_s is to
heal the amorphous network (provided that sufficient hydrogen
is incorporated), thereby decreasing the gap state density and
permitting more efficient substitutional doping by impurity
nitrogen in particular. Both mechanisms will be enhanced for
materials grown at low deposition rates. The first mechanism
can be illustrated by comparison with an example taken from a
different deposition process: For pure a-Si that is evaporated
at ultrahigh-vacuum with a low deposition rate ($\lesssim 1$ Å s^{-1}),
enough contamination was found to occur at $T_s = 380\,°C$ that ap-
proximately 5×10^{18} spins cm^{-3} were quenched in the in situ
ESR signal (35). Both mechanisms appear to be illustrated by
the case of an alloy that was plasma-deposited at a low
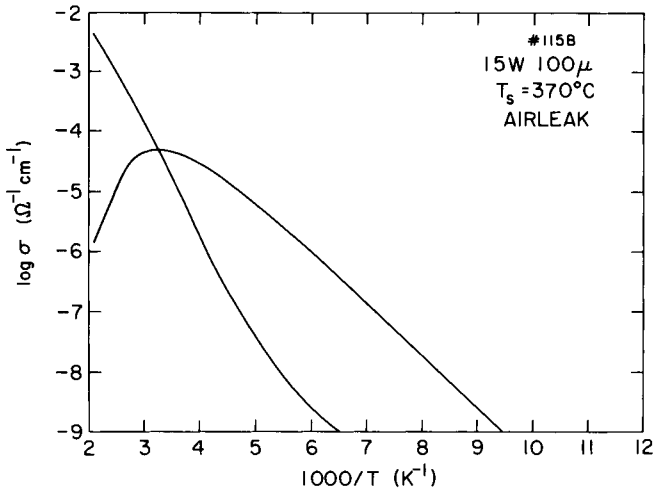
FIGURE 15.   Dark conductivity and photoconductivity versus reciprocal temperature for n^+-type, nitrogen-doped film produced in presence of airleak (15 W, 100 mTorr, $T_S = 370°C$). Flux $f_\lambda = 10^{14}$ γ's $cm^{-2}s^{-1}$ at $\lambda = 600$ nm.

deposition rate under conditions similar to those shown in Fig. 15, but with no intentional airleak. Depending upon illumination intensity, this material exhibited classic behavior in photoconductivity versus reciprocal temperature. The dark activation energy for this alloy, $E_\sigma \simeq 0.77$ eV, and the photoconductivity, $\sigma_p(300$ K$) \sim 10^{-6}$ $(\Omega \cdot cm)^{-1}$ at 10^{14} γ's $cm^{-2}s^{-1}$, are more representative of values found in the literature. Of course at high T_s, both impurity incorporation and altered intrinsic Si-H bonding may be responsible for this behavior.

In order to illustrate an extreme example of impurity incorporation, 1000 ppm O_2 was added to the silane glow discharge at low pressure, i.e., no premixing of oxygen and silane occured in the gas manifold. Whereas only weak emission was observed from molecular SiO in the plasma (Fig. 2), the resulting film was a true alloy with oxygen, a-Si:(H,O). As shown in the infrared transmission data of Fig. 16, the effects of the oxygen
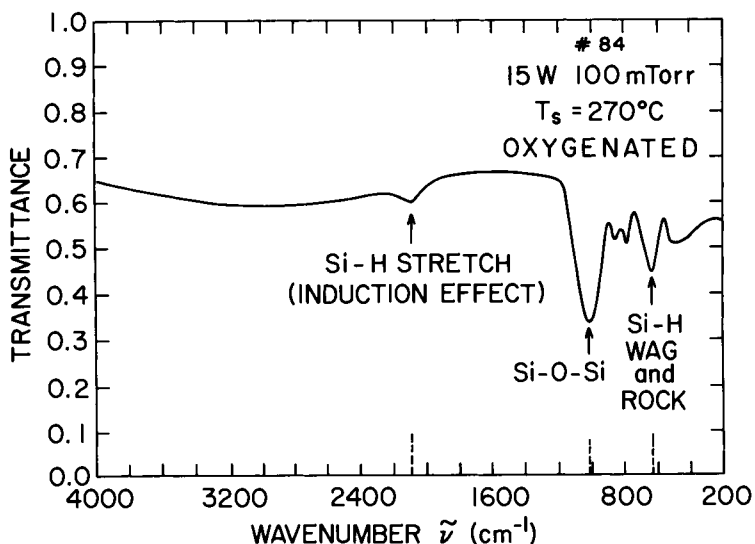
FIGURE 16. Infrared transmission spectrum of oxygenated alloy a-Si:(H,O).

impurity upon the chemical bonding of this alloy are manifested by two features: i) the Si-O-Si asymmetric stretch mode at $\tilde{v} \sim$ $\sim 1000 \text{ cm}^{-1}$ (16); and ii) the "induction effect" in which the monohydride $\equiv$SiH stretch mode at 2000 cm^{-1} has been displaced to $\sim 2100 \text{ cm}^{-1}$ owing to the backbonding of oxygen in the configuration =SiHO (69). (Films produced at 15 W, 100 mTorr contain nearly 100% monohydride bonding.) Using the integrated absorption of the Si-O-Si stretch mode alone, it was estimated that the a-Si:(H,O) alloy contained $\sim$ 15% oxygen, whereas calibration with analyses by SIMS indicates $\sim$ 37% incorporated oxygen. Optical and electrical parameters for this highly oxygenated alloy were typical of a dielectric, e.g., the wider optical gap E_o = 2.0 eV and excessively low photoconductivity σ_p(300 K) = = 6×10^{-11} $(\Omega \cdot \text{cm})^{-1}$ at a flux of 10^{14} γ's $\text{cm}^{-2}\text{s}^{-1}$. For smaller concentrations of incorporated oxygen, the presence of the Si-O-Si bridging configuration suggests that oxygen may

passivate various defects, such as weak molecular bonds. (As depicted in Fig. 3b, the stable complex $\equiv$Si-O-Si$\equiv$ is formed in that case, bound by perhaps $\sim$ 7 eV relative to $\equiv$Si-Si$\equiv$.) Indeed, several hundred ppm O_2 added to the silane gas stream removes the hopping transport depicted in Fig. 13 and results in dark conductivity identical with the low impurity alloy in that figure.

   b. Minority-carrier transport. As a function of impurity incorporation, preliminary correlations were made between the relative photoluminescence efficiency of alloys and the solar cell efficiency of diagnostic Schottky devices in which such alloys constitute the bulk layers (66). For this purpose, a typical device structure was chosen to be

$$\text{SiO/Pd/a-Si:(H,O,N)/n}^+\text{a-Si:H/Mo}$$

in which the bulk layer is either an a-Si(H,O,N) alloy or a-Si:H material produced under low-impurity conditions. No attempt was initially made to optimize the efficiency of this structure since the relative conversion efficiency was of interest for various alloys.

   Relative photoluminescence efficiency was measured at low temperatures for alloys deposited at several processing conditions[12]. As one example, emission spectra were compared at 50 K for alloys produced under low-impurity conditions versus controlled impurity conditions at $P = 15$ W, $p = 100$ mTorr, and $T_s = 370°$C. The highest photoluminescence efficiency was attained for the material deposited under low-impurity conditions. The relative peak photoluminescence efficiency was found to decrease by only 15% for an alloy prepared by admitting 3000 ppm air directly into the plasma deposition chamber. In addition to the lack of significant spectral quenching, no low-energy

---

[12]*Excitation of photoluminescence was accomplished using a low-power He-Ne laser with a diffuse beam (2 mW, hv = 1.96 eV).*

spectral component was observed at 50 K despite the evidence of
fairly pronounced impurity doping by the airleak as illustrated
in Fig. 15.

By contrast, the solar cell efficiency dramatically de-
creased owing to the same airleak rate during the growth of the
bulk alloy layer. In particular, the efficiency was reduced by
51% at 100 mW cm^{-2} illumination relative to the solar cell fab-
ricated with the alloy produced under low-impurity conditions.
This decrease is mainly attributed to a reduction in the short-
circuit current J_{sc}. Therefore, solar cell efficiency (and
particularly J_{sc}) is *a more sensitive measure* of impurity in-
corporation than that provided by the low-temperature photo-
luminescence efficiency. Now according to Fig. 15, very high
photoconductivity was exhibited by the alloy produced in the
presence of the airleak. In fact, $\sigma_p(300$ K$) \sim 10^{-3}$ $(\Omega \cdot cm)^{-1}$ for
AM1 sunlight implies a small bulk series resistance, perhaps
$R_s = 0.1-1$ $\Omega \cdot cm^2$. This improvement is probably masked, however,
by other series resistances. Evidently, minority-carrier re-
combination is increased owing to impurity incorporation so that
better majority-carrier transport is not a guarantee of improved
solar cell efficiency.

The illuminated $J-V$ characteristics of Fig. 17 confirm these
trends at a lower substrate temperature, namely at $T_s = 270°C$.
Again, the performance of two Schottky devices is compared as a
function of impurity incorporation in the bulk alloy layer. For
Fig. 17a, the alloy was produced under low-impurity processing
conditions. For Fig. 17b, the a-Si:(H,O,N) alloy was deposited
in the presence of 3000 ppm air. The indicated efficiency for
each characteristic is an external efficiency for the active
area. It was measured with a tungsten lamp for which the spec-
tral distribution is shifted to the red compared to AM1 sunlight.
In true sunlight (100 mW cm^{-2}), the current J_{sc} and the ef-
ficiency are roughly doubled. Figure 17 shows that the solar
cell efficiency decreased by 43% as a consequence of increased

J (mA cm^{-2})

#140CI/ss
15W 100mTorr 270°C
SiO/Pd/a-Si:H/n$^+$/ss
AREA 0.1188 cm^2
T=300.0K
I (mW cm^{-2})   = 100.2
V$_{OC}$ (V)   = 0.466
J$_{SC}$ (mA cm^{-2}) = 3.462
FF   = 0.527
Eff(%)   = 0.849

-0.8   0.8V

-5

(a)

J (mA cm^{-2})

#141C3/glA
15W 100mTorr 270°C
AIRLEAK
SiO/Pd/a-Si:H/n$^+$/Mo
AREA 0.1188 cm^2
T=300.0K
I (mW cm^{-2})   = 95.0
V$_{OC}$ (V)   = 0.446
J$_{SC}$ (mA cm^{-2}) = 1.930
FF   = 0.538
Eff (%)   = 0.487

-0.6   0.6V

-5
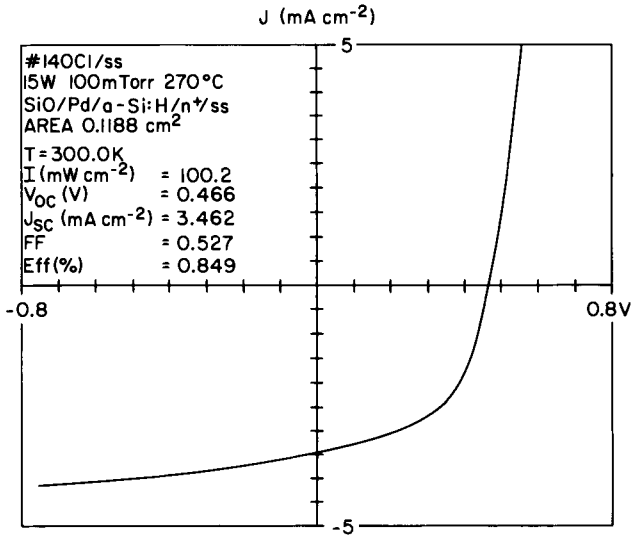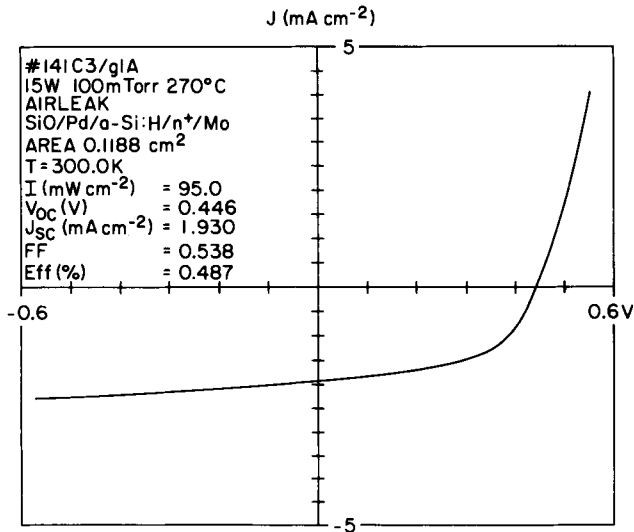
(b)

FIGURE 17.   Effects of impurity incorporation on illumi-
nated J-V characteristics for Schottky solar cell structure
SiO/Pd/a-Si:(H,O,N)/n$^+$a-Si:H/substrate.   Bulk alloy layer is
produced: a) under low-impurity processing conditions; b) in
the presence of 3000 ppm air.

impurity incorporation in the bulk alloy layer. It is also of interest that the more efficient solar cell was fabricated with an alloy that exhibits an anomalous peak in photoconductivity at low temperature ($T \simeq 160$ K) because of the low-impurity processing conditions.

2. *Expanded Discussion of Anomalous Behavior in Photoconductivity*. In order to explore the nature of anomalous photoconductivity further, we proceed to examine the illumination dependence of the anomalous peaks. Figure 18 shows two anomalous peaks in photoconductivity versus reciprocal temperature for an alloy produced at 50 W, 250 mTorr, and $T_s = 270°C$[13]. This particular data was obtained at the flux $f_\lambda = 10^{14}$ γ's cm^{-2}s^{-1} for wavelength $\lambda = 550$ nm ($h\nu = 2.25$ eV). For the thermal quenching side of the T_A peak (high-temperature side), Fig. 19 now illustrates the novel phenomenon of supralinearity in photoconductivity as a function of illumination intensity. For reference, the dashed line in this figure denotes exact monomolecular behavior, i.e., the linear growth $\sigma_p \sim f$. Figure 19 therefore shows that there is a region of illumination intensity for which $\sigma_p \sim f^\nu$ where the power ν *exceeds unity*. Supralinear behavior with a power as large as $\nu \simeq 1.6$ is attained for the thermal quenching side of the T_A peak. A similar plot for the T_B peak reveals more moderate supralinear behavior with $\nu \simeq 1.2$. With increasing monochromatic intensity f_λ, this peak shifts to higher temperature. Infrared quenching of photoconductivity is also exhibited in the region of the T_B peak, i.e., this peak is reduced when a broad spectrum of sub-bandgap radiation is simultaneously imposed (68). The recombination kinetics tends toward bimolecularity with $\nu \simeq 0.5$ for phototransport on the low-temperature side of this anomalous peak (Fig. 18).

[13]*A concentration of 100 ppm N_2 impurity was incidentally present in the silane gas stream.*
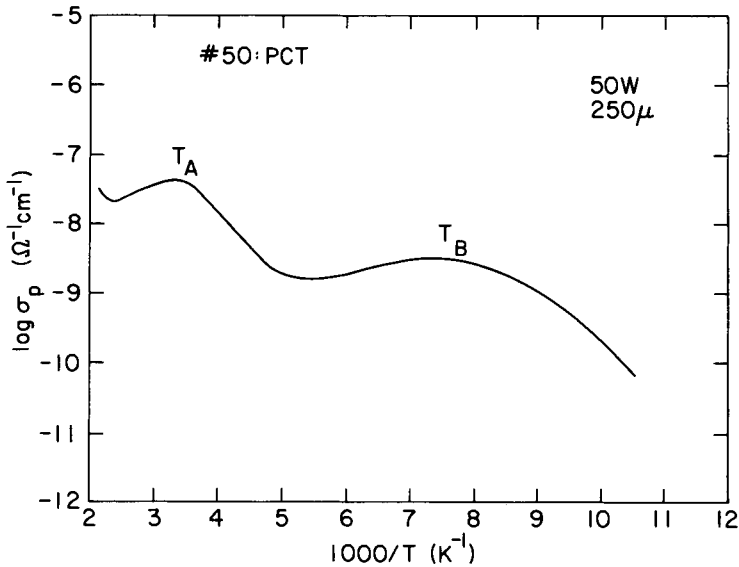
FIGURE 18.   Anomalous peaks with thermal quenching in photo-conductivity versus reciprocal temperature. Flux $f_\lambda = 10^{14}$ γ's $cm^{-2}s^{-1}$ at $\lambda = 550$ nm.

Anomalous behavior in photoconductivity is observed over a wide range of processing conditions (under appropriate impurity controls, as discussed): $p = 30\text{-}500$ mTorr, $P = 15\text{-}100$ W, and a range of substrate temperatures up to at least $T_s \simeq 300°C$. More-over, this behavior is independent of: i) the type of substrate (7059 glass, quartz, or sapphire); ii) contacts on top, or under-neath, the film in a gap cell geometry; iii) the nature of the Ohmic contact (e.g., Mo versus Ag); and iv) film thickness over the range 0.1-10 μm (true bulk effect). The anomalous peaks are also observed to persist under the following conditions: i) broadband illumination (450-650 nm); ii) dc measurement (no chop-ping of illumination); and iii) heating versus cooling cycles for the measurement (implying no thermally-stimulated currents).

The universality of condensed matter science is again dem-onstrated by the observation of anomalous photoconductivity in a
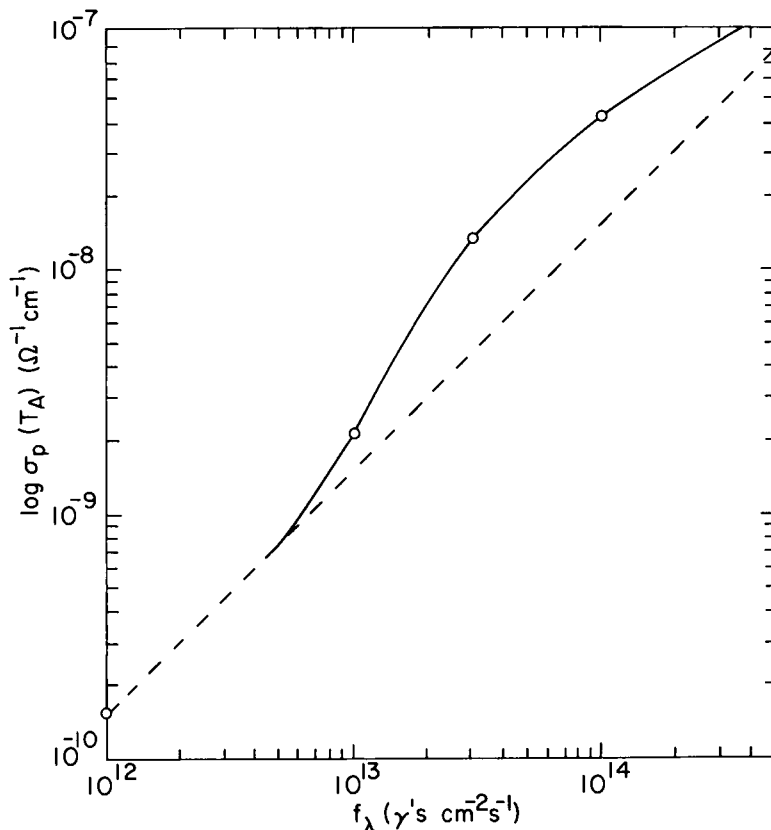
FIGURE 19. Supralinearity in photoconductivity as a function of illumination intensity (λ = 550 nm). Dashed line is monomolecular (linear) growth.

wide variety of materials. The phenomena of thermal quenching, supralinearity, and infrared quenching have been observed for both amorphous and crystalline semiconductors, as well as for certain insulators. For example, Fig. 20 illustrates thermal quenching of photoconductivity (and in some cases, supralinearity) for materials as diverse as: c-CdSe:I:Cu (70), c-Ge:Mn (71), a-ZnSe (72), a-Se (73), and the single-crystal insulator β-AgI (74). Together with related results for a-Si:H alloys,
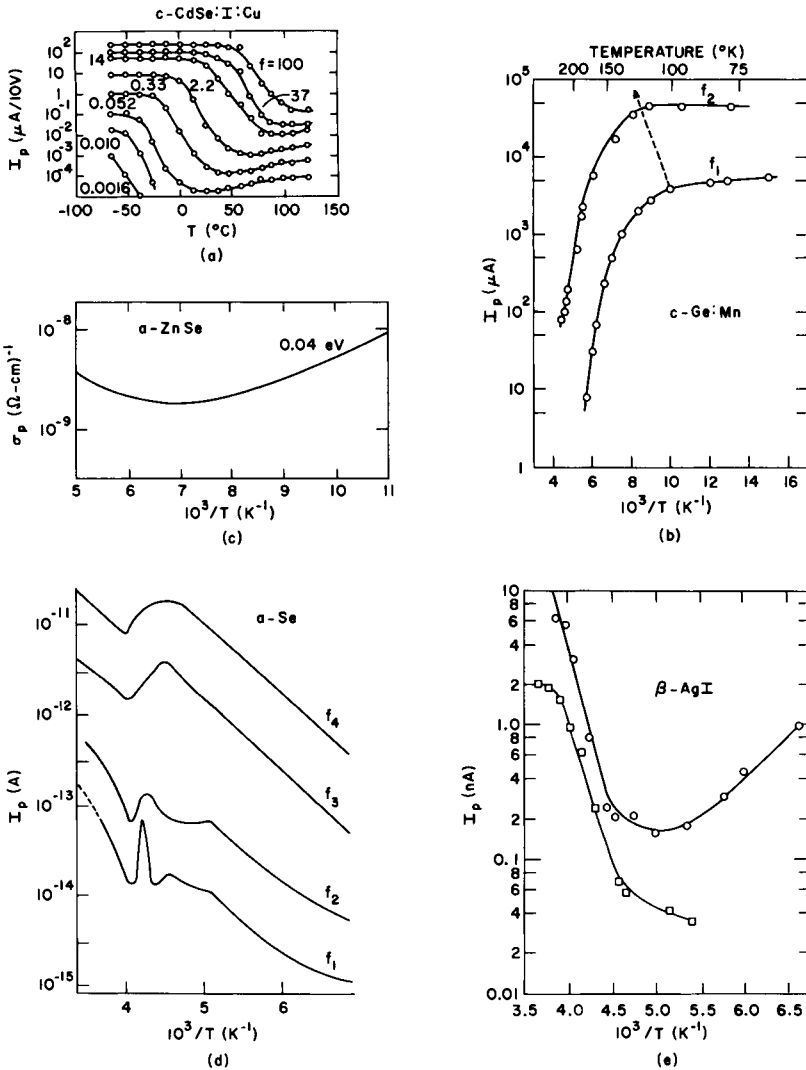
FIGURE 20. Anomalous photoconductivity for different mate-
rials: (a) c-CdSe:I:Cu (Ref. 70), (b) c-Ge:Mn (Ref. 71), (c)
a-ZnSe (Ref. 72), (d) a-Se (Ref. 73), and (e) β-AgI (Ref. 74).

this universality of behavior does not, of course, suggest pre-
cisely the same chemical and physical origins for states that
are responsible for the phenomena.   For example in the case of

c-Ge (or c-Si), substitutional double-acceptor transition metals
such as Mn, Co, Ni, Fe, and Zn have been indicted as sources of
recombination centers in the crystal bandgap that give rise to
anomalous photoconductivity.

In the case of a-Si:H alloys, there are several open pos-
sibilities for such recombination centers, including: i) certain
intrinsic states of the silicon-hydrogen alloy, and ii) centers
due to extrinsic trace elements that are somehow incorporated
during plasma deposition. With regard to concentrations of
transition metals that could conceivably contribute to the sec-
ond possibility, analyses of our alloys by SIMS reveal the pres-
ence of several ppm Cu and several tens ppb Cr. But the ele-
ments Fe, Ni, and Zn are all essentially undetectable in the
bulk of the films. Whatever the nature of the centers, a syn-
ergism of incorporated nitrogen and oxygen effects the trans-
formation to classic behavior in photoconductivity, e.g., the
transformation $a \rightarrow d$ at T_s = 260°C in Fig. 14. Such transforma-
tions at medium-high T_s may be caused by a chemical modification
of the centers *per se*, and/or by displacements (however slight)
of the Fermi level from the vicinity in the gap of the sensitiz-
ing energy levels. The absence of anomalous photoconductivity
at very high T_s may not, at this stage, be taken as unambiguous
evidence for intrinsic centers due to silicon-hydrogen (or even
silicon-silicon) bonding. As we discussed in Sect. III.*C.1.a*,
even though the effect of high T_s is to reduce the overall den-
sity of gap states, chamber impurities (except, perhaps, H_2O)
are less controlled in this case. These questions are currently
being addressed (54).

Despite the fact that the specific chemical bonds responsible
for anomalous photoconductivity have not yet been identified, the
essence of such behavior can be understood on the basis of an
adaptation of a simple two-level model (75). As illustrated in
Fig. 21, it is assumed on the model that there exist two levels
of recombination centers, levels "*1*" and "*2*", located at
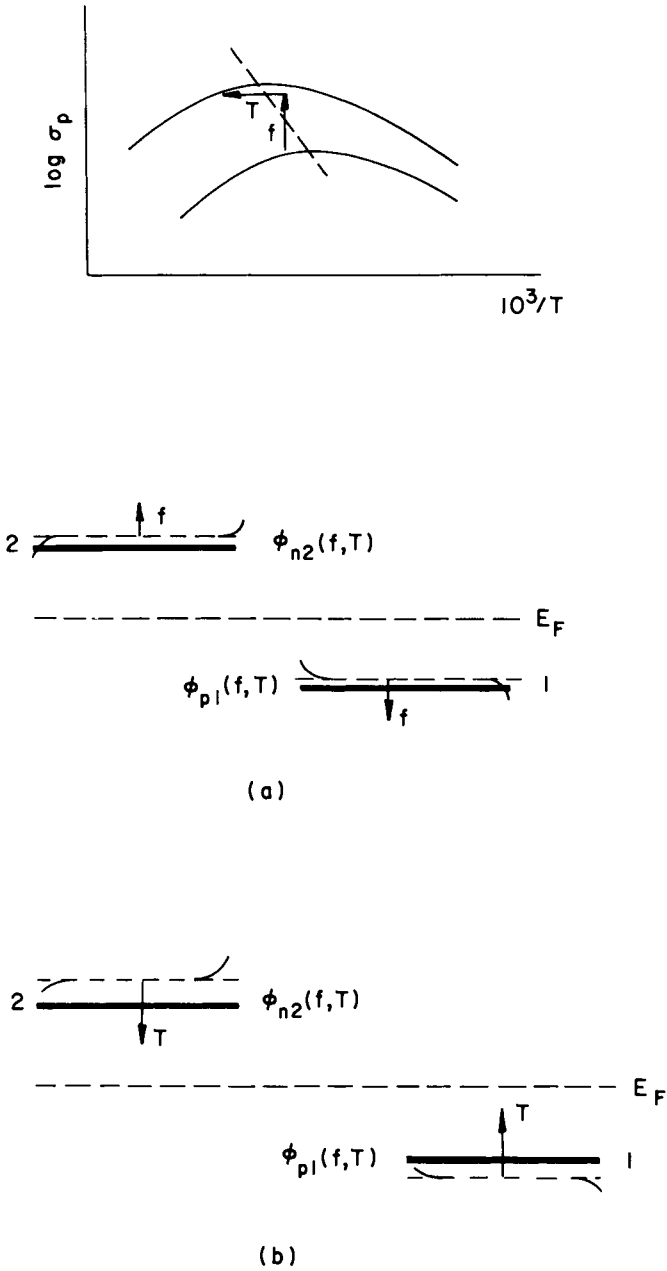
FIGURE 21.   Simple two-level model for explaining anomalous
photoconductivity (top figure): (a) supralinearity (increasing
f); (b) thermal quenching (increasing T).

$E_2 > E_F > E_1$ with respect to the dark Fermi level. (Presumably
these centers help to pin E_F.) For the case of majority-carrier
electron phototransport, it is then essential that these levels
have *widely disparate* kinetic-capture cross sections for elec-
trons:

$$\sigma_{2n} \gg \sigma_{1n} \quad . \tag{18}$$

Let us denote the excess carrier density for electrons by $\Delta n =$
$= f/(\omega_1 + \omega_2)$, where $\omega_i \equiv \tau_i^{-1} \equiv v\sigma_{in}p_{ri}$ ($i = 1,2$) is the recombi-
nation rate per electron by the hole-occupied recombination cen-
ter of density p_{ri}. For specificity we shall also consider an
anomalous peak at low temperature, such as peak T_B of Fig. 18
that lies at $T_B \sim 130$ K. Then, as appropriate for low-
temperature photoconductivity $\sigma_p = e\Delta n\mu$, the density Δn pertains
to low-mobility electrons that carry the photocurrent by phonon-
assisted hopping. Hence mobility μ is thermally activated.

   We shall firstly explain the phenomenon of supralinearity
with reference to Fig. 21. At a given level of illumination,
initially consider a value of σ_p on the thermal quenching side
of the anomalous peak (high-temperature side). Recombination in
this region is dominated by states 2 with the larger capture cross
section for electrons. If we now imagine that the flux f is in-
creased at fixed temperature, then, as depicted in Fig. 21a, the
quasi-Fermi level for trapped electrons $\phi_{n2}(f,T)$ and the quasi-
Fermi level for trapped holes $\phi_{p1}(f,T)$ depart more and more from
the thermal equilibrium position E_F. In this configuration for
which $\phi_{n2}(f,T) \gtrsim E_F$, level 2 is being depopulated of holes. In-
versely, level 1 is acquiring additional holes. Now in a re-
stricted region of the flux f, $\omega_2 \gg \omega_1$ is still satisfied pre-
cisely because of the relatively large capture cross section
σ_{2n}. That is, the recombination rate for photocarriers is still
determined by states 2 so that $\Delta n \simeq f/\omega_2$. But the recombination
rate decreases for increasing f, following the rate of decrease
in the number of holes $p_{r2} = (\omega_2/v\sigma_{2n})$. Hence, $\omega_2 \sim 1/f^\alpha$,
where α is some power. Therefore in that region of flux (and

temperature) we have $\Delta n \simeq f/\omega_2 \sim f^{1+\alpha}$, i.e., supralinear behavior $\sigma_p = e\Delta n\mu \sim f^{1+\alpha}$ is obtained.

For a large enough increase in flux, a point is attained on the low-temperature side of the anomalous peak (see Fig. 21). The capture kinetics on this side proceeds via bimolecular recombination. If this transition to bimolecularity were taken as evidence for a change in dominant recombination path, then the recombination rate by states 1 would finally exceed that by states 2, i.e., $\omega_1 > \omega_2$ and $\Delta n \simeq f/\omega_1$. On this scenario, accurately bimolecular recombination is consistent with $\Delta n \sim p_{r1} \sim$ $\sim (f/v\sigma_{1n})^{\frac{1}{2}}$. Hence, the activation energy of σ_p at sufficiently low temperatures is equal to the thermal activation energy of the mobility μ. Depending upon the exact relative sizes of σ_{2n} and σ_{1n}, and of the densities for states 2 and 1, it is conceivable instead that states 2 could dominate recombination over the entire temperature range of an anomalous peak. (Of course, at high enough flux and low enough temperatures, states 1 would finally have to dominate.) As in the case of c-Si, however, this situation would probably require a different (more positive) charge state for hole-occupied states 2 versus states 1 so that $\sigma_{2n}/\sigma_{1n} \sim 10^6$. This condition would not be met if, for example: i) hole-occupied states 1 were identified with numerous self-trapped holes below E_F, and ii) hole-occupied states 2 were identified with some positive, hole-occupied donor defects lying above E_F. (It can be argued that hole polarons have a smaller capture cross section for electrons than positive, hole-occupied donors, but a larger capture cross section than neutral centers.) Subject to further experimental tests, we shall merely assume for definiteness (and consistency) that states 1 do indeed dominate recombination on the low-T side of the peak.

Proceeding now to an explanation of the thermal quenching phenomenon, we note that an increase in the temperature T at fixed illumination intensity acts to restore thermal equilibrium: i) the quasi-Fermi levels for trapped carriers, $\phi_{n2}(f,T)$ and

$\phi_{pl}(f,T)$, retreat toward E_F , and ii) the Fermi-Dirac distribu-
tions become more extended. (See Fig. 21b.) The net effect is
to increase the population of holes in level 2, and inversely to
decrease the population of holes in level 1. For a large enough
increase in temperature, $\omega_2 > \omega_1$ is restored and recombination
is again dominated by states 2 that thermally quench the photo-
conductivity as depicted in Fig. 21. The shift in the maximum of
the anomalous peak to higher temperature with increasing flux is
implicit in our discussion. Namely, the interplay of flux and
temperature influences the relative populations of hole-occupied
states 1 and 2. An increase in the flux shifts holes away from
states 2, tilting the balance in favor of states 1 (low-T side
of peak). A subsequent increase in the temperature repopulates
states 2 with holes at the expense of states 1, restoring the
thermal quenching. As a consequence, the maximum in the peak
moves to higher temperature for a higher flux. It should be
noted that if phototransport were bipolar at low temperatures,
then anomalous photoconductivity can be explained by an exactly
symmetrical argument for hole-carrier recombination in which
$\sigma_{1p} \gg \sigma_{2p}$ is now assumed to be valid.

    Finally, as shown in Fig. 10, anomalous behavior disappears
when the dark Fermi level is displaced in the gap by intentional
doping with phosphorous (or boron). Presumably, in the absence
of significant chemical modification of the material by the
dopant itself, the effect of doping has simply been to vitiate
the condition $E_2 > E_F > E_1$ that is necessary for anomalous be-
havior. In principle, this situation may be contrasted with the
synergistic incorporation of nitrogen and oxygen in alloys. In
the latter case, new chemical bonds (e.g., "bridging" or "back-
bonding" configurations) could be formed that eliminate either
states 1, 2 or both. Now the classic photoconductivity depicted
for the "airleak" alloy in Fig. 15 certainly was accompanied by
movement of E_F (to within 0.4 eV of E_C). On the other hand,
results have been obtained in which the transformation from

anomalous to classic photoconductivity has been accompanied by little, if any, change in dark conductivity activation. These results could suggest chemical modification of the centers responsible for anomalous behavior. Studies of very lightly doped alloys are currently in progress to test this idea (54).

ACKNOWLEDGMENTS

The Brookhaven data discussed in this Chapter is the result of a group effort, and I gratefully acknowledge in this regard the outstanding contributions by P. E. Vanier (electrical measurements on films), F. J. Kampas (optical studies of the plasma), A. E. Delahoy (device measurements), and M. D. Hirsch (optical measurements on films). I would also like to acknowledge R. Gremme for his technical assistance with film preparation, and L. C. Arns for her very fine typing skills.

REFERENCES

1. Spear, W. E., and Le Comber, P. G., *Sol. Sta. Comm. 17*, 1193 (1975).

2. Chittick, R. C., Alexander, J. H., and Sterling, H. F., *J. Electrochem. Soc. 116*, 77 (1969).

3. Knights, J. C., *Phil. Mag. 34*, 663 (1976).

4. Carlson, D. E., and Wronski, C. R., *Appl. Phys. Lett. 28*, 671 (1976).

5. Anderson, P. W., *Phys. Rev. 109*, 1492 (1958).

6. Ziman, J. M., *J. Phys. C2*, 1230 (1969).

7. Weaire, D., *Phys. Rev. Lett. 26*, 1541 (1971); Weaire, D., and Thorpe, M. F., *Phys. Rev. B4*, 2508 (1971).

8. Mott, N. F., *Adv. Phys. 16*, 49 (1967).

9. Cohen, M. H., Fritzsche, H., and Ovshinsky, S. R., *Phys. Rev. Lett. 22*, 1065 (1969).

10. Brodsky, M. H., *Thin Solid Films 40*, L23 (1977); Brodsky, M. H., Cardona, M., and Cuomo, J. J., *Phys. Rev. B16*, 3556 (1977).

11. Lucovsky, G., Nemanich, R. J., Knights, J. C., *Phys. Rev. B19*, 2064 (1979).

12. Freeman, E. C., and Paul, W., *Phys. Rev. B18,* 8 (1978); Connell, G. A. N., and Pawlik, J. R., *Phys. Rev. B13*, 787 (1976).

13. Spear, W. E., Loveland, R. J., and Al-Sharbaty, A., *J. Non-Crys. Sol. 15*, 410 (1974).

14. Knights, J. C., Biegelsen, D. K., and Solomon, I., *Sol. Sta. Comm. 22*, 133 (1977).

15. Tsang, C., and Street, R. A., *Phil. Mag. B37*, 601 (1978).

16. Paesler, M. A., Anderson, D. A., Freeman, E. C., Moddel, G., and Paul, W., *Phys. Rev. Lett. 41*, 1492 (1978).

17. Griffith, R. W., Kampas, F. J., Vanier, P. E., and Hirsch, M. D., *J. Non-Crys. Solids 35/36, Part I,* 391 (1980).

18. Madan, A., Ovshinsky, S. R., and Benn, E., *Phil. Mag. B40,* 259 (1979).

19. Spear, W. E., Le Comber, P. G., and Snell, A. J., *Phil. Mag. B38*, 303 (1978).

20. Snell, A. J., Mackenzie, K. D., Le Comber, P. G., and Spear, W. E., *Phil. Mag. B40*, 1 (1979).

21. Deneuville, A., and Brodsky, M. H., *J. Appl. Phys. 50*, 1414 (1979).

22. Wronski, C. R., *Sol. Energy Mat. 1*, 287 (1979).

23. Carlson, D. E., *J. Non-Crys. Solids 35/36, Part II*, 707 (1980).

24. Mogab, C. J., Adams, A. C., and Flamm, D. L., *J. Appl. Phys. 49*, 3796 (1978).

25. Harshbarger, W. R., Porter, R. A., Miller, T. A., and Norton, P., *Appl. Spectrosc. 31*, 201 (1977).

26. Winters, H. F., Coburn, J. W., Kay, E., *J. Appl. Phys. 48*, 4973 (1977).

27. Kampas, F. J., and Griffith, R. W., *J. Solar Cells* (to be published).

28. Perkins, G. G. A., Austin, E. R., and Lampe, F. W., *J. Amer. Chem. Soc. 101*, 1109 (1979).

29. Pauling, L., and Pauling, P., "Chemistry", p. 740, W. H. Freeman, San Francisco, (1975).

30. Potzinger, P., and Lampe, F. W., *J. Phys. Chem. 73*, 3912 (1969).

31. Cottrell, T. L., and Walker, I. C., *Trans. Faraday Soc. 63*, 549 (1967).

32. Moss, S. C., and Graczyk, J. F., *Phys. Rev. Lett. 23*, 1167 (1969).

33. Paul, W., Harvard preprint (1979).

34. Brodsky, M. H., Title, R. S., Weiser, K., and Pettit, G. D., *Phys. Rev. B1*, 2632 (1970).

35. Thomas, P. A., Brodsky, M. H., Kaplan, D., and Lépine, D., *Phys. Rev. B18*, 3059 (1978).

36. Kaplan, D., Sol, N., Velasco, G., and Thomas, P. A., *Appl. Phys. Lett. 33*, 440 (1978).

37. von Rödern, B., Ley, L., Cardona, M., and Smith, F. W., *Phil. Mag. B40*, 433 (1979).

38. Griffith, R. W., in "Sharing the Sun! Vol. 6, Photo-voltaics and Materials" (K. W. Böer, ed.), p. 205, Amer. Sect. Int. Sol. Energy Soc. (1976).

39. Tauc, J., Grigorovici, R., and Vancu, A., *Phys. Stat. Sol. 15*, 627 (1966).

40. Fritzsche, H., in "Amorphous and Liquid Semiconductors" (W. E. Spear, ed.), p. 3. University of Edinburgh, Edinburgh, (1977).

41. Madan, A., Le Comber, P. G., and Spear, W. E., *J. Non-Crys. Sol. 20*, 239 (1976); Spear, W. E., and Le Comber, P. G., *Phil. Mag. 33*, 935 (1976).

42. Cohen, J. D., *J. Solar Cells*, to be published.

43. Wronski, C. R., and Carlson, D. E., *Sol. Sta. Comm. 23*, 421 (1977).

44. Wronski, C. R., *IEEE Trans. Elec. Devices ED-24*, 351 (1977).

45. Jousse, D., Viktorovitch, P., Vieux-Rochaz, L., and Chenevas-Paule, A., *J. Non-Crys. Solids 35/36, Part II*, 767 (1980).

46. Staebler, D., and Wronski, C. R., *Appl. Phys. Lett. 31*, 292 (1977).

47. Pawlik, J. R., and Paul, W., in "Amorphous and Liquid Semi-conductors" (W. E. Spear, ed.), p. 437. University of Edinburgh, Edinburgh, (1977).

48. Stuke, J., *ibid.* p. 406.

49. Biegelsen, D. K., and Knights, J. C., *ibid.* p. 429.

50. Emin, D., in "Electronic and Structural Properties of Amorphous Semiconductors" (P. G. Le Comber and J. Mort, eds.), p. 261. Academic Press, London and New York, (1973).

51. Hanak, J. J., Korsun, V., and Pellicane, J. P., to be published.

52. Anderson, D., and Spear, W. E., *Phil. Mag. 36*, 695 (1977).

53. Rehm, W., Fischer, R., Stuke, J., and Wagner, H., *Phys. Stat. Solidi (b)79*, 539 (1977).

54. Brookhaven Group, to be published.

55. Emin, D., in "Amorphous and Liquid Semiconductors" (W. E. Spear, ed.), p. 249. University of Edinburgh, Edinburgh, (1977).

56. Usui, S., and Kikuchi, M., *J. Non-Crys. Solids 34*, 1 (1979).

57. Reilly, O. J., and Spear, W. E., *Phil. Mag. B38*, 295 (1978).

58. Carlson, D. E., Wronski, C. R., Triano, A. R., and Daniel, R. E., *Proc. 12th IEEE Photo. Spec. Conf.*, p. 893. IEEE, New York, (1976).

59. Wilson, J. I. B., McGill, J., and Robinson, P., *Proc. 13th IEEE Photo. Spec. Conf.*, p. 751. IEEE, New York, (1978).

60. Staebler, D. L., *J. Non-Crys. Solids 35/36, Part I*, 387 (1980).

61. Engemann, D., and Fischer, R., in "Structure and Excitations of Amorphous Solids" (G. Lucovsky and F. L. Galeener, eds.), p. 37.   Amer. Inst. Phys., New York, (1976).

62. Street, R. A., *Phil. Mag. B37*, 35 (1978).

63. Street, R. A., Knights, J. C., and Biegelsen, D. K., *Phys. Rev. B18*, 1880 (1978).

64. Nashashibi, T. S., Austin, I. G., and Searle, T. M., in "Amorphous and Liquid Semiconductors" (W. E. Spear, ed.), p. 392.   U. of Edinburgh, Edinburgh, (1977).

65. Pankove, J. I., and Wu, C. P., *Appl. Phys. Lett. 35*, 937 (1979).

66. Delahoy, A. E., Griffith, R. W., and Vanier, P. E., to be published.

67. Baixeras, J., Mencaraglia, D., and Andro, P., *Phil. Mag. B37*, 403 (1978).

68. Vanier, P. E., and Griffith, R. W., *Bull. Amer. Phys. Soc. 25*, 330 (1980); and to be published.

69. Lucovsky, G., *Sol. Sta. Comm. 29*, 571 (1979).

70. Bube, R. H., *J. Phys. Chem. Solids 1*, 234 (1957).

71. Newman, R., Woodbury, H. H., and Tyler, W. W., *Phys. Rev. 102*, 613 (1956).

72. Brodie, D. E., in "Amorphous and Liquid Semiconductors" (W. E. Spear, ed.), p. 472.   U. of Edinburgh, Edinburgh, (1977).

73. Viger, C., Lefrancois, G., and Fleury, G., *J. Non-Crys. Solids 33*, 267 (1979).

74. Govindacharyulu, P. A., and Bose, D. N., *Phys. Rev. B19*, 6532 (1979).

75. Rose, A., *Phys. Rev. 97*, 322 (1955).
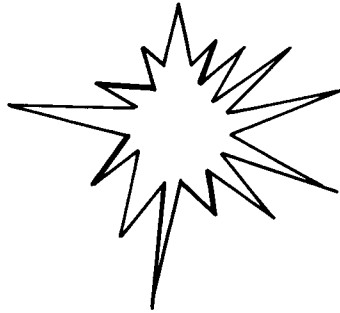
PROBLEMS and References

*The mysteries of matter have stimulated the great intellectual
exploration of our time. There are two reasons why we should
share in its excitements. One is for the sheer fun, the esthetic
pleasure, call it what you like, of reaching deeper into the un-
known. The other is for the understanding to be gained as a
result.*

—————— C.P. Snow

CHAPTER 20

PROBLEMS AND REFERENCES

L.E. Murr

Department of Metallurgical and Materials Engineering
New Mexico Institute of Mining and Technology
Socorro, New Mexico

(1) About 1855 James Clerk Maxwell discovered equations which

govern the behavior of electromagnetic oscillations, and

showed that they were applicable to light. In their (scalar)

integral form, Maxwell's equations can be written

$$\int E_s \, ds = - \int \int \mu \frac{\partial H_n}{\partial t} \, dS$$

and

$$\int H_s \, ds = \int \int (\rho V_n + \sigma E_n + \varepsilon \frac{\partial E_n}{\partial t}) \, dS.$$

The integrals of the tangential components of the electric

and magnetic field intensities, E_s and H_s on the left are

taken around the peripheries of the surfaces over which are

integrated the corresponding normal surface components, E_n

and H_n, respectively on the right; V_n is the velocity of

moving charge; ρ is the density of electric charge; σ is the

conductivity; μ is the permeability; and ε is the permittiv-

ity (or dielectric constant). We see that in these two

fundamental equations, the propagation not only of light,

but all electromagnetic radiation is dependent upon materials

properties: σ, μ, and ε.

In homogeneous, nondissipative media (defined by $\rho = 0$

in the second equation above), the velocity of light is

given by $C = 1/\sqrt{\mu\varepsilon}$, and a plane wave incident at a plane
interface between two *different* homogeneous nondissipative
media is partially "reflected" into the first medium (1),
and partially "refracted" into the second medium (2). If
the incident wave angle relative to the interface is denoted
I_1, the reflected angle R_1 and the angle of refraction r_2,
then $I_1 - R_1$ and Snell's law

$$\cos r_2/\cos I_1 = C_2/C_1$$

govern the angle of refraction. It is perhaps obvious that
if a third medium (3) is added, the initially refracted wave
acts as the incident wave upon the interface between medium
(2) and medium (3).

Considering these very basic, historical wave optics
phenomena, discuss the important features which must be con-
sidered in the design of "idealized" reflectors, absorbers,
and coatings for photoconversion devices, etc. That is,
using some simple sketches, show the effects of various
overlays of say three different optically "transparent"
materials (which can include air as a "layer"). Show all
the angles of incidence, reflection, and refraction and
write the appropriate equations for the angles at the inter-
faces. Indicate what portion of the "initial" wave is
finally "transmitted" through the three layers and what
portion is emitted or re-radiated back. Is there a depen-
dence of the transmitted and emitted portion on the "initial"
angle of incidence? If "yes", then show it. Finally, brief-
ly describe the dependence of ε and μ for materials in
general on such features as crystal structure and composi-
tion and give some examples, using optically "transparent"
single crystals which could ideally be used to construct a
three-layer regime alluded to above. How is the index of
refraction related to either ε or μ?

REFERENCES

Born, M., "Principles of Optics: Electromagnetic Theory of Propa-
    gation, Interference, and Diffraction Light", Pergamon Press,
    New York, (1959).
Carlson, F.P., "Introduction to Applied Optics for Engineers",
    Academic Press, New York, (1977).
Glazebrook, R.T., "James Clerk Maxwell in Modern Physics",
    MacMillan and Co., New York, (1896).
Knittil, Z., "Optics of Thin Films: An Optical Multilayer Theory",
    Wiley-Interscience, New York, (1976).
Weast, R.C. (ed), "Handbook of Chemistry and Physics", The
    Chemical Rubber Co. (CRC), (1978).

(2) Many excellent materials available for solar applications -

     reflectors, absorbers, conversion devices, storage devices,

     etc. - are in such short supply, or are otherwise so expen-

     sive to produce, that their use is virtually untenable, and

     this feature is an important motivating feature in solar

     materials research and development. Compare two typical

     (common) materials in each category for use as reflecting

     surfaces, absorbers, and photocells or photovoltaic mater-

     ials and describe the annual production, production cost,

     and show a projection of costs likely to occur in the next

     decade (1980-1990). Discuss some recycling or other produc-

     tion alternatives which may help alleviate some of the

     critical supply-cost problems, or alternatives which might

     be pursued with regard to new materials development. You

     should specifically describe the development of silicon

     technology in some historical perspective (indicating if

     possible advances or variations in production costs, mater-

     ial purity and perfection, etc. over the past 2-3 decades)

     and discuss how this might be transferred to a new material

     development, or how it may be indicative of current feelings

     of the futility in seeking alternative material development

     in the context of photocells or photovoltaic materials.

     Speculate on breakthroughs which could conceivably alter

     this attitude.

REFERENCES

Halacy, D.S., "The Coming Age of Solar Energy", Harper and Row,
    New York, (1973).
McVeigh, J., "An Introduction to the Applications of Solar
    Energy", Pergamon Press, New York, (1977).
Merrigan, J.A., "Sunlight to Electricity: Prospects for Solar
    Energy Conversion by Photovoltaics", MIT Press, Cambridge,
    Mass., (1975).
Palz, W., "Solar Electricity: An Economic Approach to Solar
    Energy", Butterworths, London, (1977).
Stein, C. (ed), "Critical Materials Problems in Energy Produc-
    tion", Academic Press, New York, (1976).

(3) Referring to Fig. 1 of Chapter 2, show in a geometrical

     sketch that the face-centered tetragonal lattice shown is

     equivalent to a body-centered tetragonal lattice unit cell

     in which the side of the unit cell base is $1/\sqrt{2}$ times that

     for the fct cell. Show the (111) plane in the fct unit cell

     and calculate the spacing between (111) planes if $c/a = 1.95$.

     (Make a sketch of this cell to scale.) If a vacancy were

     formed in every other unit cell center of the bct lattice

     above, what is the density compared to a perfect material?

     Make a two-dimensional sketch of this structure and comment

     upon the microstructure created. If an edge dislocation

     were associated with every four unit cell basal planes, cal-

     culate the dislocation density. In other words a disloca-

     tion line terminates on the basal plane corresponding to

     every four unit cells. Discuss how this compares with

     measured dislocation densities in deformed metals and alloys.

     Finally, show the pseudomorphic, epitaxial growth of a cubic

     deposit upon this tetragonal (fct) substrate material in

     two-dimensions (the substrate is viewed along c and a).

REFERENCES

Barrett, C.S. and Massalski, T.B., "Structure of Metals", 3rd
    Edition, McGraw-Hill Book Co., Inc., New York, (1966).

Buerger, M.J., "Elementary Crystallography", J. Wiley and Sons,
   Inc., New York, (1960).
Guy, A.G., "Introduction to Materials Science", McGraw-Hill Book
   Co., Inc., New York, (1972).
Hirth, J.P. and Lothe, Jens, "Theory of Dislocations", McGraw-Hill
   Book Co., Inc., New York, (1968).
Kuhlmann-Wilsdorf, D., "Workhardening", J.P. Hirth and J.
   Weertman (eds), Gordon and Breach, New York, (1968).
Pearson, W.B., "A Handbook of Lattice Spacings and Structures of
   Metals and Alloys", Pergamon Press, New York, (1958).
Richman, M.H., "An Introduction to the Science of Materials",
   Blaisdell Publishing Co., Walthan, Mass., (1967).
Rigney, R.A., *Scripta Met.*, Vol. 13, p. 353 (1979).

(4)   Optical absorptance is related to the complex dielectric

constant by $\alpha = |\underset{\sim}{k}|\varepsilon''$, where $\underset{\sim}{k}$ is the wave vector (having a

magnitude of $2\pi/\lambda$), and ε'' is the dielectric loss factor.

Optical properties in general are related to the complex

index of refraction. In transparent materials the dielec-

tric constant can be measured optically. Describe how (con-

sider Prob. 1 in retrospect). Another more general method

for measuring the dielectric constant of a medium would be

to utilize a parallel-plate capacitor. For example, a

coating or deposit of a medium of interest could be grown

upon a flat metal substrate to a thickness d. A metallic

layer could then be deposited upon the medium, or another

flat metal plate could be placed upon the medium forming a

simple, parallel, flat-plate capacitor. Describe how the

dielectric constant could be measured.

In a two-layer dielectric or a Maxwell-Wagner two-layer

capacitor as shown below, the optical dielectric constant

is given by

$$\varepsilon'' = \frac{d/\varepsilon_o}{d_1/\varepsilon_1 + d_2/\varepsilon_2} \ .$$
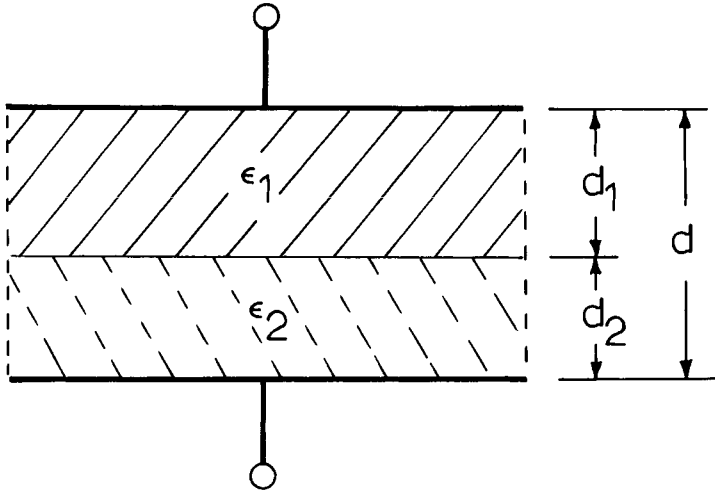
Describe how you would measure this dielectric constant in an experiment identical to the one above. If it can be assumed that this model is applicable to a dielectric layer or a bi-layer upon a metal plate, describe how a flat-plate absorber can be made more efficient (characterized by an increase in absorptance). If the absorber layer were composed of two media of thickness d with one component suspended in the other (for example, spheres of one in the other) how could you approximate the dielectric constant if the dielectric constants of the two component media were known? [As a practical example see Niklasson, G.A. and Granqvist, C.G., *J. Appl. Phys.*, 50(8), 5500, (1979).] From this analysis, what kinds of materials would seem to be the best optical absorbers?

REFERENCES

Condon, E.U, and Odishaw, Hugh (eds), "Handbook of Physics", McGraw-Hill Book Co., Inc., New York, (1958).
Harrop, P., "Dielectrics", Wiley, New York, (1972).
Kaminow, I.P., "An Introduction to Electrooptic Devices", Academic Press, New York, (1974).

Winch, R.P., "Electricity and Magnetism", Prentice-Hall, Inc.,
  New York, (1955); or related text in the general area.

(5) Figure P. 5 below shows vacuum vapor-deposited tin formed on
     the surface of and ionic crystal. Such a thin layer can be
     used to monitor the selective effects of particle size dis-
     tributions on the selective optical response of a surface.
     Make a plot of the particle size from the transmission elec-
     tron microscope view in Fig. P. 5(b) and describe the dis-
     tribution. Comment upon the possibility of selective
     absorption or reflection associated with the particle size
     distribution. If the particle size distribution were natural
     dust or related environmental particulates, would you expect
     the particles to have settled out or to have been attracted
     by static charge differences (surface accumulation); or to
     be a residue in moisture drops? Discuss these options.

REFERENCES

Friedlander, S.K., "Smoke, Dust and Haze: Fundamentals of Aerosol
  Behavior", Wiley Interscience, New York, (1977).
Green, H.C. and Lane, W.R., "Particulate Clouds: Dusts, Smokes
  and Mists; Their Physics and Physical Chemistry and Industrial
  and Environmental Aspects", 2nd Edition, Van Nostrand, Prince-
  ton, New Jersey, (1964).
Murr, L.E., "Electron Optical Applications in Materials Science",
  McGraw-Hill Book Co., New York, (1970).
Powell, C.F., Oxley, J.H., and Blocher, Jr., J.M., "Vapor Deposi-
  tion", J. Wiley and Sons, Inc., New York, (1966).

(6) Figure P. 6 shows two typical aerosol particles attached to
     a float glass protective layer on a flat-plate silver re-
     flector. Which particle would be the more easily removed?
     Show, using simple surface tension relationships which
     particle has the highest surface tension? If a detergent
     were used in removing the particles in Fig. P. 6(b), what
     must the detergent do, in principle, in order to aid the
     efficient particle removal? Show this effect schematically.
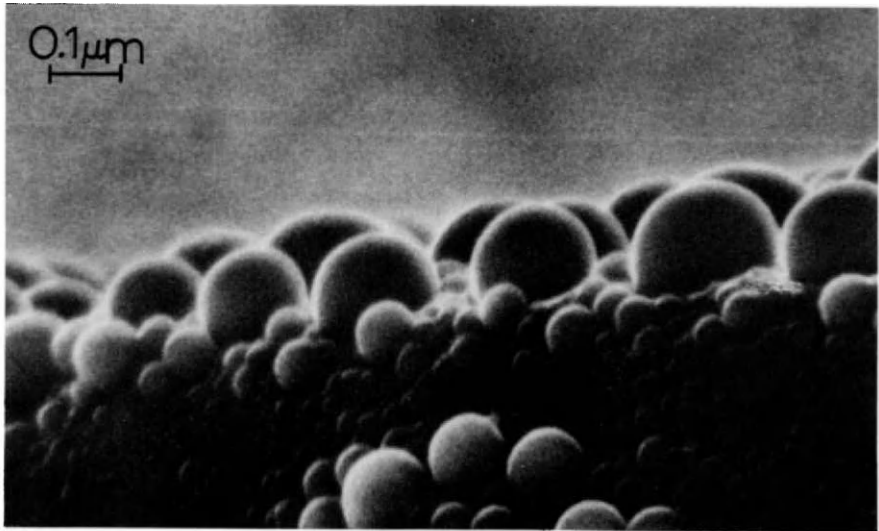
(a)
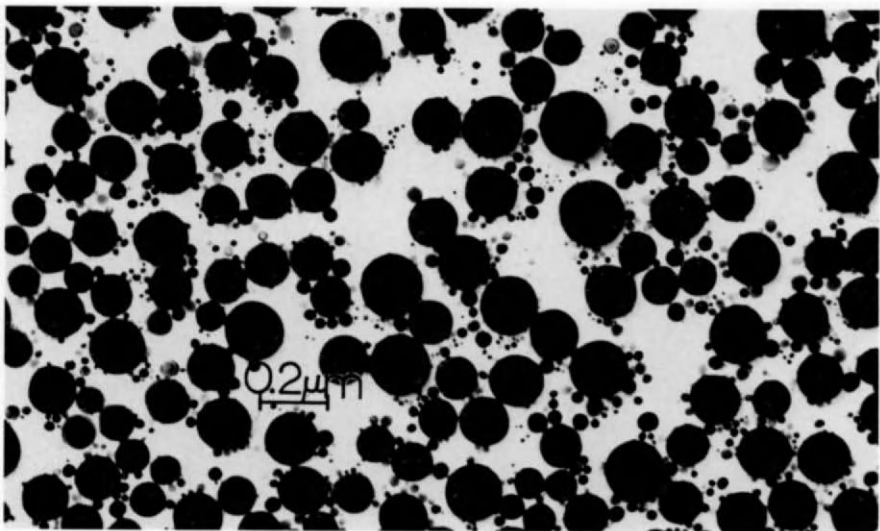
(b)

FIGURE P.5.   (a) SEM view of tin particles.   (b) TEM view of
same particles.

(a)   *(b)*
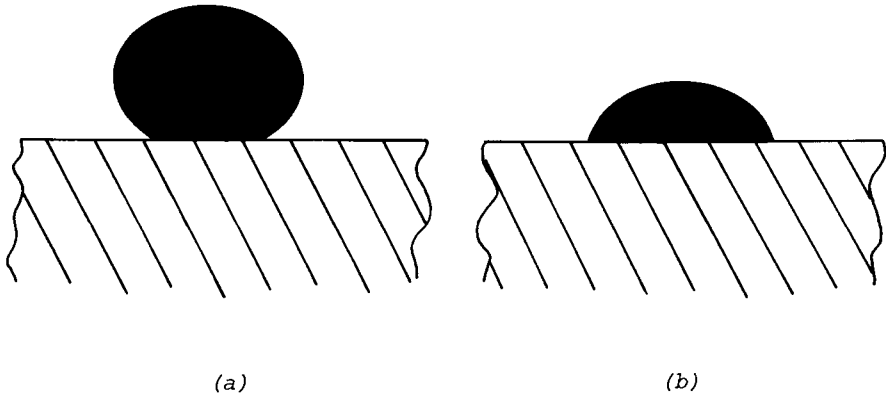
FIGURE P.6.

Describe how the adsorption or affinity for adsorption and
the adhesion "strength" of particles could be reduced by
changing the protective coating material. If the accumula-
tion of dust or aerosol particles on a reflector/protector
layer develops and is not removed, show the effects on the
reflectivity and discuss the difference which could be ex-
pected if the initial silver reflectivity were 0.95 as
compared to 0.90 as a result of differences in, for example,
deposition characteristics. What structural or microstruc-
tural features of the silver reflecting layer could account
for these initial reflectivity differences?

REFERENCES

Adamson, A.W., "Physical Chemistry of Surfaces", Wiley-Intersci-
    ence, New York, (1960).
Bikerman, J.J., "Physical Surfaces", Academic Press, New York,
    (1970).
Murr, L.E., *Mater. Sci. Engr.*, Vol. 12, 3277 (1973).
Murr, L.E., "Interfacial Phenomena in Metals and Alloys", Addison-
    Wesley Publishing Co., Reading, Mass., (1975).
Murr, L.E., ASTM Special Technical Publication No. 640, "Adhesion
    Measurement of Thin Films, Thick Films, and Bulk Coatings",
    K.L. Mittal (ed), Philadelphia, Pennsylvania, p. 82, (1978).

Richman, M.H., "An Introduction to the Science of Materials",
    Ginn/Blaisdell Publishing Co., Waltham, Mass., (1967).
Woodruff, D.P., "The Solid-Liquid Interface", Cambridge University
    Press, London, (1973).

(7)   Total hemispherical emissivity is expressed by

$$\bar{\varepsilon}_H = \int_0^{\pi/2} (\frac{\varepsilon_{TE} + \varepsilon_{TM}}{2}) \cos\theta \sin\theta \, d\theta \cdot \int_0^\infty L_w dw \Big/ \int_0^{\pi/2} \cos\theta \sin\theta \, d\theta$$

$$\cdot \int_0^\infty L_w dw$$

show that $\bar{\varepsilon}_H(TE) = \varepsilon/3$ and $\bar{\varepsilon}_H(TM) = \varepsilon (\varepsilon = \bar{\varepsilon}_N)$; and conse-
quently $\bar{\varepsilon}_H = 4\bar{\varepsilon}_N/3$. (TE and TM refer to the electric and
magnetic wave components, respectively; $\varepsilon_{TE} = \varepsilon \cos\theta$,
$\varepsilon_{TM} = \varepsilon/\cos\theta$.) Discuss how the hemispherical emissivity
can be decreased by altering the crystal structure of a
material. Under what conditions would the emissivity of a
metal approach zero?

REFERENCES

Condon, E.U., and Odishaw, H. (eds), "Handbook of Physics",
    p. 4-75 and 6-14, McGraw-Hill Book Co., New York, (1958).
Goodenough, J.B., and Whittingham, M.S. (eds), "Solid-State
    Chemistry of Energy Conversion and Storage", (Adv. in Chem.
    Serier 163, Amer. Chem. Soc.), 1977.
Guy, A.G., "Introduction to Materials Science", p. 371, McGraw-
    Hill Book Co., New York, (1972).
Müller, W.M. (ed), "Energetics in Metallurgical Phenomena",
    Vol. 1, Gordon and Breach, Science Publishers, New York,
    (1965).

(8)   Referring to the tin vapor deposit of Fig. P. 5(b) above,
       show that the absorptivity in the U.V. will be essentially
       the same as that for a continuous film having an absorptiv-
       ity of $2/\omega \tau$ if the principles of geometrical optics are
       assumed to apply for the range of larger particle sizes

shown. Would the emissivity of a thick tin film on a tungsten surface increase or decrease the room temperature emissivity? By how much? If the absorptivity of a black-chrome electrodeposit is 0.97 and the emissivity is measured to be 0.12 at 100°C, what must be done in order to maintain the same $\alpha_s/\overline{\varepsilon}_H$ ratio at 400°C?

REFERENCES

Heavens, O.S., "Optical Properties of Thin Solid Films", Dover, New York, (1965).

Kerker, M., "The Scattering of Light and Other Electromagnetic Radiation", Academic Press, New York, (1969).

Pramanik, D., Sievers, A.J., and Silsbee, R.H., "The Spectral Selectivity of Conducting Micromeshes in Solar Energy Materials", in press, (1979).

Seraphin, B.O. (ed), "Solar Energy Conversion-Solid State Physics Aspects, Topics in Applied Physics", Vol. 31, Springer-Verlag, Berlin, (1979).

(9) Given the following data for a composite absorber coating, make a plot of optical extinction coefficient versus wavelength and briefly discuss the merits of the composite as an optical absorber:

λ (μm)	ε (total relative dielectric constant)	R (reflectivity)
0.3	9	0.30
0.6	16	0.40
1.4	25	0.45
2.6	16	0.36

All data apply at 500 K.

Is it sufficient to consider absorptivity of such a composite independent of other properties? Discuss your answer. That is, discuss what features are important in good optical absorbers.

REFERENCES

Craighead, H.G., Bartynski, R., Buhrman, R.A., Wojcik, L., and
    Sievers, A.J., *Sol. Energy Mater.*, 1, 105 (1979).
Fulrath, R.M., and Pask, J.A. (eds), "Ceramic Microstructures,
    1976, with Emphasis on Energy-Related Applications", Proc.
    6th Int. Mater. Symposium, Westview Press, Boulder, Colorado,
    (1977).
Heavens, O.S., "Optical Properties of Thin Solid Films", Dover,
    New York, (1965).
Kerker, M., "The Scattering of Light and Other Electromagnetic
    Radiation", Academic Press, New York, (1962).

(10) Describe an efficient method for fabricating Au-Al$_2$O$_3$ selec-

      tive absorbers, including the choice of a substrate. Dis-

      cuss how the absorptivity and emissivity can be controlled

      by the adjustment of fabrication parameters. What two

      fabrication parameters can be most effectively controlled to

      produce selective absorptivity and emissivity, and how can

      these be changed? On considering the reference to work of

      Murr and Bitler listed below, is there any evidence of

      intrinsic structural effects on the optical response of thin

      Au films in the solar portion of the spectrum? Discuss your

      answer. (Note the effect of temperature on the grain size

      in evaporated Au.) Recall that in Chapter 2 it was noted

      that reflectivity at $\lambda = 10.6$ μm was influenced by grain

      size in silver films, while in the reference cited above

      there is no evidence of similar microstructural influence.

      Discuss this apparent discrepancy.

REFERENCES

Abeles, F. (ed), "Optical Properties and Electronic Structure of
    Metals and Alloys", North-Holland, Amsterdam, (1966).
Chopra, K.L., "Thin Film Phenomena", McGraw-Hill Book Co., New
    York, (1969).
Craighead, H.G., Bartynski, R., Buhrman, R.A., Wojick, L., and
    Sievers, A.J., *Sol. Energy Mater.*, 1, 105 (1979).
Craighead, H.G., and Buhrman, R.A., *Appl. Phys. Lett.*, 31, 423
    (1977); *J. Vac. Sci. Technol.*, 15, 269 (1978).

Murr, L.E., and Bitler, W.R., *Mater. Res. Bull.*, 2, 787 (1967).
Szilva, W.A., and Murr, L.E., *Phys. Stat. Sol. (a)*, 40, 211
    (1977).

(11) Many simple solar collection schemes can be envisioned as
      being composed of a variety of materials, and of course many
      indeed are. Early collectors and many contemporary designs
      use a variety of metals and alloys which are somewhat in-
      compatible in terms of corrosion. The case in point would
      be copper tubing connected to iron or iron alloy hot-water
      units, which can be prone to galvanic corrosion. In general,
      galvanic corrosion for a single electrode process can be
      characterized by

$$E = E^{\circ} + \frac{RT}{ZF} \ln K,$$

      where E is the electrode potential, E° is the metal elec-
      trode potential (standard electrode potential), R is the
      gas constant, T is the absolute temperature, F is the Fara-
      day constant [23,600 cal/volt (gram equivalent)], Z is the
      metal (ion) charge, and K is the equilibrium constant for
      the single electrode process (or activity of the metal in-
      volved). In effect, this expresses the theoretical limit of
      oxidation of a metal (at equilibrium) in contact with the
      standard hydrogen electrode (SHE). Find the activity of
      copper and iron separately, and then find the ratio of
      activities ($K_{Fe}/K_{Cu} = a_{Fe^{2+}}/a_{Cu^{2+}}$). Discuss the implica-
      tions of these results. (Hint: E in the equation will be
      the hydrogen electrode potential.) What could happen if the
      system were aluminum and copper rather than iron and copper?
      What would the potential (emf) be if a zinc-copper cell were
      created somewhere in the system, i.e., what would the dif-
      ference be?

REFERENCES

Evans, U.R., "The Corrosion and Oxidation of Metals: Scientific
    Principles and Practical Applications", St. Martin's Press,
    New York, (1960); plus supplement, (1968).
Fontana, M.G., and Greene, N.D., "Corrosion Engineering", McGraw-
    Hill Book Co., New York, (1967).
Guy, A.W., "Introduction to Materials Science", McGraw-Hill Book
    Co., New York, (1972).
Uhlig, H.H., "Corrosion and Corrosion Control: An Introduction to
    Corrosion Science and Engineering", Wiley, New York, (1971).
Weast, R.C. (ed), "Handbook of Chemistry and Physics", The
    Chemical Rubber Co., Cleveland, Ohio, (1978).

(12) A heat transfer tube in a solar furnace is subjected to a

      maximum stress (tensile) of 20 Ksi. The tube alloy has a

      yield stress of 50 Ksi and an ultimate tensile stress (UTS)

      of 110 Ksi. The tube is 20 cm in outside diameter and has

      a 1 cm wall thickness. Because of chloride-ion contamina-

      tion in the heat-transfer fluid, the inside tube wall is

      observed to corrode away at a rate of 0.1 mm/month. If a

      safe system design were to consider a safety factor of 2

      based upon the UTS, when would the tube have to be consid-

      ered for replacement, if the maximum load never changes?

      During a focusing accident, the load is removed on an iden-

      tical tube in a similar furnace and the tube wall is rapidly

      annealed, resulting in a grain size in a circumferential

      section which is a factor 10 greater than the initial grain

      size. What effect would you expect this to have on the

      yield stress in this region when normal operation resumes?

      That is, what change, if any, would occur in the yield

      stress? (Hint: Consider a Hall-Petch relationship applies.)

REFERENCES

Ailor, W.H. (ed), Symposium on the State of the Art in Corrosion
    Testing, "Handbook on Corrosion Testing and Evaluation",
    Wiley, New York, (1971).

Berry, W.E., "Corrosion in Nuclear Applications", Wiley, New
   York, (1971).
Cernica, J.N., "Strength of Materials", Holt, Rinehart and
   Winston, Inc., New York, (1966).
Guy, A.W., "Introduction to Materials Science", McGraw-Hill Book
   Co., New York, (1972).
Tegart, W.M.M., "Elements of Mechanical Metallurgy", The MacMil-
   lan Co., New York, (1966).

(13) Compare the thermal energy (heat) which can be stored on
      melting 1 ft^3 (0.029 m^3) of sodium chloride, sodium sulfate,
      sodium hydroxide, silicon, sodium, and gallium. Which of
      these materials would you choose for a solar home heating
      system? Discuss your choice based upon efficiency, econ-
      omics, and materials availability, compatibility and other
      environmental considerations. Compare the difference in
      energy required in a solar-industrial recycling operation
      for reprocessing iron and aluminum scrap. (Assume the
      metals are melted for pouring into ingots and consider their
      temperature must be raised from room temperature, i.e.,
      20°C.)

REFERENCES

Duffie, J.A. and Beckman, W.A., "Solar Energy Thermal Proces-
   ses", J. Wiley and Sons, New York, (1974).
Telkes, M., *ASHRAE Journal*, September, 40 (1974).
Telkes, M., "Critical Materials Problems in Energy Production",
   C. Stein (ed), Chap. 14, Academic Press, New York, p. 440,
   (1976).
Ubbelohde, A.R., "Melting and Crystal Structure", Clarenden
   Press, Oxford, (1965).
Weast, R.C. (ed), "Handbook of Chemistry and Physics", Chemical
   Rubber Co., Cleveland, Ohio, (1978).

(14) A small industrial photoprocess plant measures 200 ft
      (61.5 m) and 100 ft (30.8 m) (wide). The exterior walls have
      no windows and are 6 inches (15.24 cm) thick. The flat
      ceiling and roof of the single-level building is 14 inches
      (35.56 cm) thick, and has a height of 15 ft (4.6 m). The

walls and ceiling have the same (or uniform) average thermal
conductivity, K = 0.05 (in units of BTU/ft^2 $hr/°F/ft$). If
the building is solar heated, what is the minimum storage
volume of sodium sulfate decahydrate to offset the heat loss
in a 12 hour period when the collector is not operating if
the average inside temperature is to be maintained at 68°F
and the average outside temperature is 0°F during this
period? What percent of the heat lost can be saved if
another 0.5 ft of insulation is added to the ceiling area?
(Assume the thermal conductivity of the insulation is the
same as noted.) What type of energy resource does this con-
stitute?

REFERENCES

Bayley, F.J., Owen, J.M., and Turner, A.B., "Heat Transfer",
    Barnes and Moble, New York, (1972).
Chapman, A.J., "Heat Transfer", 3rd Edition, MacMillan Publish-
    ing Co., Inc., New York, (1974).
Duffie, J.A., and Beckman, W.A., "Solar Energy Thermal Processes",
    Wiley, New York, (1974).
Ozisik, M., "Basic Heat Transfer", McGraw-Hill Book Co., New York,
    (1977).
Telkes, M., "Critical Materials Problems in Energy Development",
    Chap. 14, C. Stein (ed), Academic Press, New York, (1976).
Young, H.D., "Fundamentals of Mechanics and Heat", McGraw-Hill
    Book Co., New York, (1974).

(15) Consider the thermal decomposition reaction: $CaCO_3$(solid) =
      CaO(solid) + CO_2(gas). Illustrate how this reaction can be
      utilized in the storage of solar heat at high temperature.
      Calculate the standard free energy of dissociation at 937°C.
      Show how the associated entropy change and enthalpy change
      could be calculated for $CaCO_3$.

REFERENCES

Darken, L.S. and Gurry, R.W., "Physical Chemistry of Metals",
    McGraw-Hill Book Co., New York, (1953).

Gaskell, D.R., "Introduction to Metallurgical Thermodynamics",
   McGraw-Hill Book Co., New York, (1973).
Hammes, G.G., "Principles of Chemical Kinetics", Academic Press,
   New York, (1978).
Huang, F.F., "Engineering Thermodynamics", MacMillan Publishing
   Co., Inc., New York, (1976).

(16) Describe the principal contemporary thermochemical reactions

      of interest for solar energy storage and give some examples

      of each. Consider the reversible reaction $CH_4 + H_2O \longrightarrow$

      $CO + 3H_2$. Make a sketch of the complete reactor system and

      describe any special materials problems attendant to this

      system.

REFERENCES

Duffie, J.A., and Beckman, W.A., "Solar Thermal Processes", J.
   Wiley and Sons, New York, (1974).
Guy, A.G., "Introduction to Materials Science", McGraw-Hill Book
   Co., New York, (1972).

(17) A critical feature in semiconductor junction devices, in-

      cluding solar cells, is the metal/semiconductor junction

      response. That is, depending upon the type and chemistry of

      semiconductor and the type of contact metallization, the

      junctions can respond as either rectifying junctions or

      ohmic junctions. Consider the p-n junction device config-

      uration shown below. Draw the energy band diagram for the

      complete device system shown and an equivalent circuit,

      thereby indicating whether the junctions are ohmic or rec-

      tifying. What determines the nature of the junction, i.e.,

      what are the conditions for p- or n-type materials joined

      to a metal which make it ohmic or rectifying? What can you

      say about the metal/metal junctions? (Hint: The p-Si

      and n-Si work functions are 3.6 and 3.7 eV, respectively.)
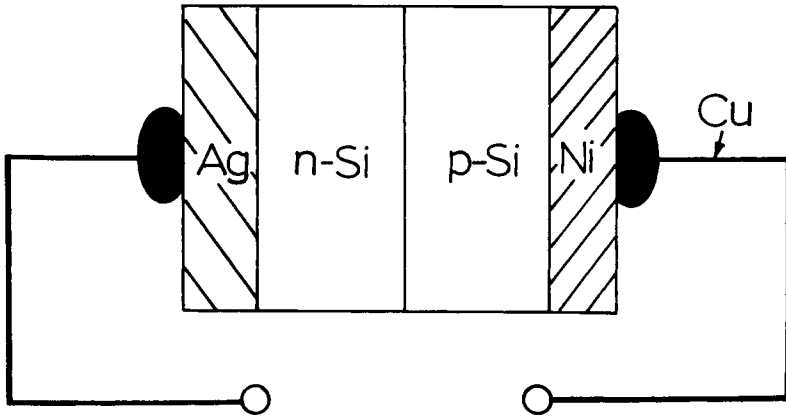
FIGURE P.17.

REFERENCES

Deboo, G.J. and Burrous, C.N., "Integrated Circuits and Semi-
   conductor Devices: Theory and Applications", 2nd Edition,
   McGraw-Hill Book Co., New York, (1977).
Driscoll, F.F. and Coughlin, R.F., "Solid-State Devices and
   Applications", Prentice Hall, Inc., Englewood Cliffs, New
   Jersey, (1975).
Fan, John C.C., "Solar Cells: Plugging Into the Sun", Technology
   Review, August/September, 14 (1978).
Merrigan, J.A., "Sunlight to Electricity: Prospects for Solar
   Energy Conversion by Photovoltaics", MIT Press, Cambridge,
   (1975).
Murr, L.E., "Solid-State Electronics", Marcel Dekker, Inc., New
   York, (1978).
Tickle, "Thin Film Transistors", J. Wiley and Sons, Inc., New
   York, (1969).

(18)   A feature of interest in contemporary devices such as sili-
       con solar cells is the so-called grain boundary passivation.
       Some polycrystalline silicon, when specially solidified,
       contains a multitude of boundaries which appear to be twin
       boundaries. How could one unambiguously identify twin
       boundaries in silicon? If passivation is associated with
       segregation of hydrogen along grain boundaries at 500°C, and
       this is induced by high interfacial energies, what can you

say about twin boundaries in silicon with regard to segregation if the twin boundary/grain boundary (high-angle) energy ratio is the same as that in indium? [Assume the grain boundary energy in silicon to be 0.3 F_S, where F_S is the surface energy given by $F_S = 1.2 (\gamma_{LV})_m + 0.45 (T_m - T)$; where $(\gamma_{LV})_m$ is the liquid (liquid/vapor) surface free energy at the melting point, T_m is the melting temperature (°C), and T is the temperature in the solid state.] Are there other types of grain boundaries which could have special energies (and structures)?

REFERENCES

Azaroff, L.V., "Introduction to Solids", McGraw-Hill Book Co., New York, (1960).

Chalmers, B., "The Photovoltaic Generation of Electricity", Scientific American, November (1976), p. 34.

Murr, L.E., "Interfacial Phenomena in Metals and Alloys", Addison-Wesley Publishing Co., Reading, Mass., (1975).

Seager, C.H. and Ginley, D.S., *Appl. Phys. Letters*, 34(5), 337 (1979).

(19) Consider the idealized case of a Cu_2S/CdS single-crystal heterojunction. Make a sketch of the associated energy-level diagram and discuss how this is characteristic of a junction (P/n) device. Show the lattice mismatch associated with this junction and make a sketch indicating how this mismatch can be accommodated by the formation of interfacial dislocations. Describe the mismatch at ZnO/Cd Te junctions for the idealized case of single crystal films. (Hint: Consult the ASTM X-ray Card Fild and associated references. Do not consider epitaxial growth. The junctions are directly bonded.)

REFERENCES

Bube, R.H., Chap. 16 in "Critical Materials Problems in Energy
    Production", C. Stein (ed), Academic Press, New York, (1976),
    p. 486.
Bube, R.H., "Photoconductivity of Solids", J. Wiley and Sons,
    New York, (1960). (Reprinted by Krieger, New York, 1978).
Larach, S., "Photoelectronic Materials and Devices", Van Nostrand,
    Princeton, New Jersey, (1965).
Milnes, A.G., and Feucht, D.L., "Heterojunctions and Metal-Semi-
    conductor Junctions", Academic Press, New York, (1972).
Murr, L.E., "Interfacial Phenomena in Metals and Alloys",
    Addison-Wesley, Reading, Mass., (1975).
Seraphin, B.O. (ed), "Solar Energy Conversion", Springer-Verlag
    New York, Inc., New York, (1979).

(20) Dislocations in or near a bonded Cu_2S/CdS heterojunction

        interface can be associated with three different regimes:

        Cu_2S, the interfacial plane, or CdS. What types of Burgers

        vectors would you expect for the dislocations in the Cu_2S

        and CdS? Discuss your response. What effect would you

        expect dislocation density to have? Make a sketch of open

        circuit current versus dislocation density at some constant

        solar flux. (Hint: In addition to the general references

        suggested below you should search the journal and periodical

        literature.)

REFERENCES

Bube, R.H., "Electronic Properties of Crystalline Solids: An
    Introduction of Fundamentals", Academic Press, New York,
    (1974).
Guy, A.G., "Introduction to Materials Science", McGraw-Hill Book
    Co., New York, (1972).
Hirth, J.P., and Lothe, J., "Theory of Dislocations", McGraw-Hill
    Book Co., New York, (1968).
Milnes, A.G., and Feucht, D.L., "Heterojunctions and Metal-Semi-
    conductor for Junctions", Academic Press, New York, (1972).
Murr, L.E., "Interfacial Phenomena in Metals and Alloys",
    Addison-Wesley Publishing Co., Reading, Mass., (1975).
Sharma, B.L., and Purohit, R.K., "Semiconductor Heterojunctions",
    Pergamon Press, New York, (1974).

(21) Describe the zeta potential and its measurement. How does
the zeta potential determine the dlotation characteristics
of inorganic minerals? How does the zeta potential influ-
ence the operation of the wet photovoltaic cell, and how is
this concept related to the zeta potential role in mineral
flotation?

REFERENCES

Adamson, A.W., "Physical Chemistry of Surfaces", Interscience
   Publishers, New York, (1967).
Bockris, J. O'M., and Drazic, D.M., "Electrochemical Science",
   Barnes and Noble, New York, (1976).
Bockris, J. O'M., and Reddy, A.K.N., "Modern Electrochemistry",
   Vols. 1 and 2, Plenum Publishing Corp., New York, (1970)
   (Second Reprint in paperback, 1976).
Gaudin, A.M., "Flotation", McGraw-Hill Book Co., New York, (1957).
Holmes, J.P. (ed), "The Electrochemistry of Semiconductors",
   Academic Press, New York, (1962).
Osipow, L.I., "Surface Chemistry", Reinhold Publishing Corp., New
   York, (1962).

(22) Grain boundary passivation in polycrystalline silicon occurs
for diffused hydrogen and magnesium, but not for N, F, or
atomic oxygen. Show the possible effect of all these ele-
ments adsorbed along a grain boundary in silicon and their
passivation or non-passivation role using simple sketches or
atomic models. Make a model of a simple symmetric grain
boundary between two (010) silicon grains having a misorien-
tation of $5°$ and another having a misorientation of $15°$.
If hydrogen passivation by bond satisfaction occurs, how
much more hydrogen is contained in the $15°$ boundary than the
$5°$ boundary?

REFERENCES

Gleiter, H., and Chalmers, B., "High-Angle Grain Boundaries",
   Pergamon Press, New York, (1972).
McLean, O., "Grain Boundaries in Metals", Clarenden Press, Oxford,
   (1957).

Murr, L.E., "Interfacial Phenomena in Metals and Alloys",
    Addison-Wesley Publishing Co., Reading, Mass., (1975).
Read, W.T., "Dislocations in Crystals", McGraw-Hill Book Co.,
    New York, (1953).

(23) Figure P.23 below shows black-chrome surface topography
      after argon ion bombardment. Note that the surface appears
      to be composed of tiny spheres or sphere-like "particles".
      What additional techniques could be used to determine the
      structure of the layer shown in Fig. P.23? Refer to Chap. 3
      and discuss the techniques available for examining the
      chemical composition of the layer. How could you determine
      whether the layer was a composite of Cr or Cr-rich "parti-
      cles" within a Cr_2O_3 matrix?
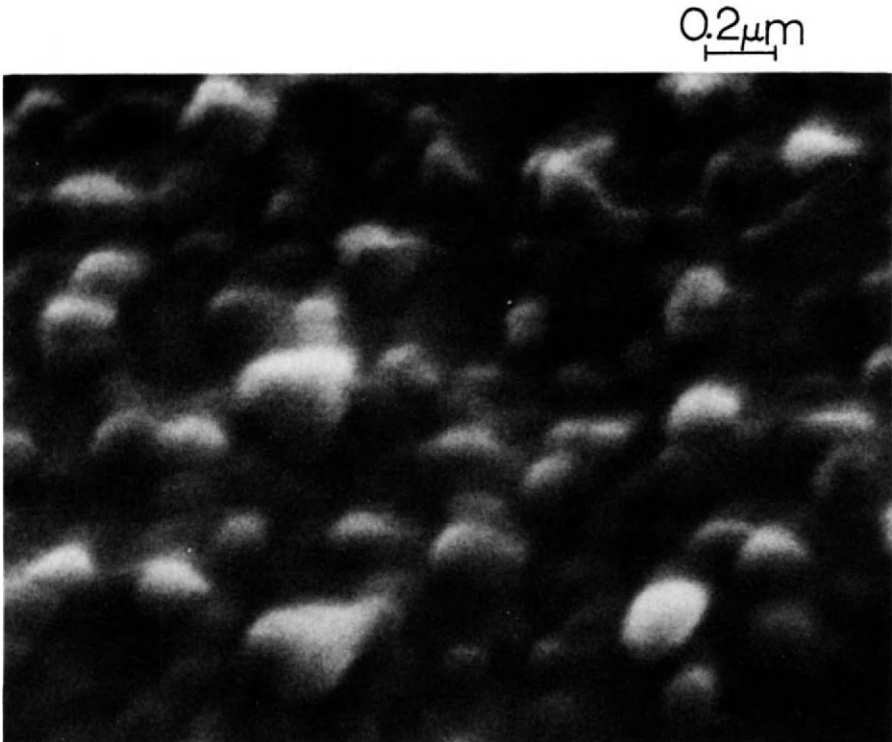
FIGURE P.23.   Scanning electron micrograph showing ion-etched
black-chrome coating electrodeposited onto nickel.

REFERENCES

Buck, Otto, Tien, J.K., and Marcus, H.L. (eds), "Electron and
   Positron Spectrocopies in Material Science and Engineering",
   Academic Press, Inc., New York, (1979).
Czanderna, A.W., and Vasofsky, R., *Progress in Surface Science*,
   9, 43 (1979).
Czanderna, A.W. (ed), "Methods of Surface Analysis", Elsevier,
   Amsterdam, (1975).
Murr, L.E., "Electron Optical Applications in Materials Science",
   McGraw-Hill Book Co., New York, (1970).

(24) Is it possible to examine amorphous silicon structure?

   That is, can the atomic structure in amorphous silicon be

   directly observed? How? Describe the technique. What has

   already been learned about the "structure" of amorphous

   materials, including metals and alloys? Is hydrogen passi-

   vation effective in amorphous silicon? Why?

REFERENCES

Buck, Otto, Tien, J.K., and Marcus, H.L. (eds), "Electron and
   Positron Spectroscopies in Material Science and Engineering",
   Academic Press, Inc., New York, (1979).
Goldstein, J.I., Hren, J.J., and Joy, D.C. (eds), "Introduction
   to Analytical Electron Microscopy", Plenum Press, New York,
   (1979).
Howie, A., *J. Non-Crystalline Solids*, 31, 41 (1978).
Valdre, U., and Ruedl, E. (eds), "Electron Microscopy in Materials
   Science", Parts I-IV, Commission of the European Communities,
   Luxembourg, (1975).

(25) Discuss the current efforts to understand materials problems

   associated with the development of a viable solar technology.

   Do you envision changes in the traditional approaches to

   materials science and engineering in regard to future solar

   technology developments? If so, describe them and discuss

   their possible consequences.

REFERENCES

Cohen, M. (ed), "Materials Science and Engineering: Its Evolution,
    Practice, and Prospects", Special Issue of *Materials Science
    and Engineering,* 37(1), (1979).
Roller, D.H.D. (ed), "Perspectives in the History of Science and
    Technology", Univ. of Oklahoma Press, Norman, (1971).
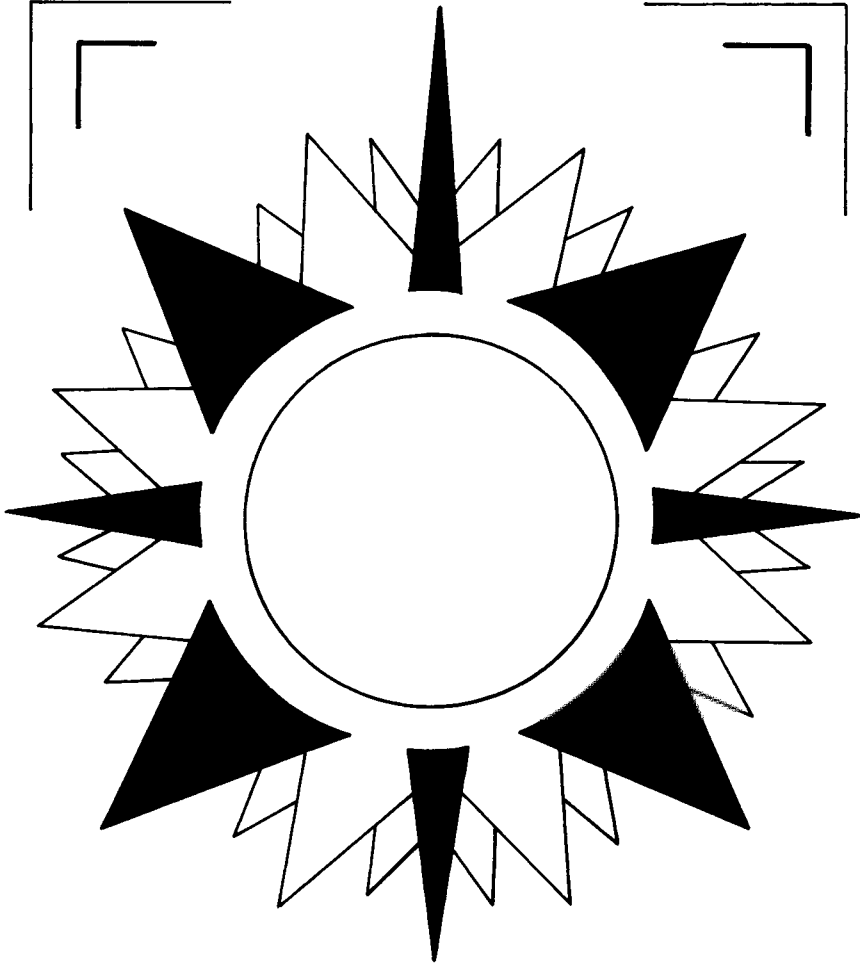
PROBLEM
SOLUTIONS
and Discussion

I give you now Professor Twist,
A conscientious scientist.
Trustees exclaimed, "He never bungles!"
And sent him off to distant jungles.
Camped on a tropic riverside,
One day he missed his loving bride.
She had, the guide informed him later,
Been eaten by an alligator.
Professor Twist could not but smile.
"You mean," he said, "a crocodile."

———— The Purist, by Ogden Nash

760

PROBLEM SOLUTIONS AND DISCUSSION

L.E. Murr

Department of Metallurgical and Materials Engineering
New Mexico Institute of Mining and Technology
Socorro, New Mexico

(1) As shown below, plane waves incident upon a plane interface
are related by the angles shown: $90° - I_1$, $90° - k_1$,
$90° - r_2$, and

$$\cos r_2/\cos I_1 = \sqrt{\mu_1 \varepsilon_1 / \mu_2 \varepsilon_2}$$

since $C_j = 1/\sqrt{\mu_j \varepsilon_j}$; $j = 1, 2, \ldots$
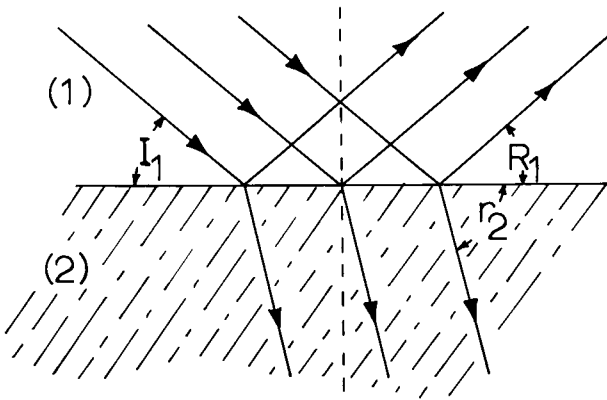
If we add a third medium (3) we have the following:

761
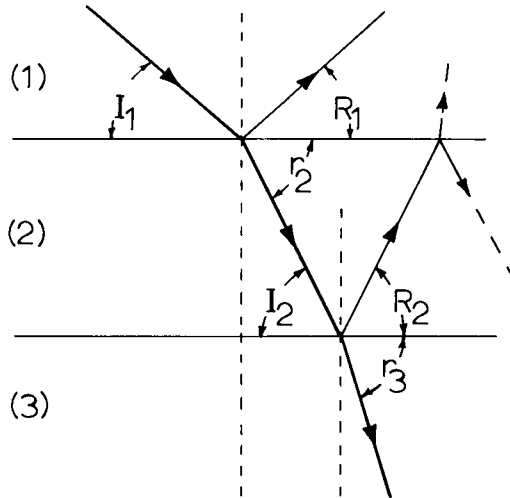
From the three-medium sketch above showing the angles of the incident, reflected, and refracted wave portions in (1), (2), and (3), it can be observed that all angles depend upon the properties of the media, and all are interconnected. Thus, it is apparent that any transmitted portion and reflected portions of the wave are dependent upon the angle of incidence in medium (1), I_1. The angles in all media show a dependence on μ or ε which are dependent upon the particular kinds of atoms composing the media, the way in which they are bound, and the crystal structure. Furthermore, the media may be composites or aggregates which could alter μ and ε (especially ε) depending upon the aggregate size and distribution. The effects leading to variations in μ or ε occur mainly in response to magnetic or electric polarizabilities. Polarization of either magnetic or electric dipoles and indeed the creation of such dipoles is dependent upon the atomic structure, the electronic structure, the crystal structure, and on a larger scale, the microstructure. The index of refraction, n, is strongly coupled to the dielectric constant through a relationship of the form $n = \sqrt{\varepsilon_r \mu_r}$ where

ε_r is referred to as the relative dielectric constant and defined by the ratio of permittivity in a particular medium to that of free space, denoted ε_o. Thus $\varepsilon_r = \varepsilon/\varepsilon_o$; and correspondingly $\mu_r = \mu/\mu_o$. For nonmagnetic material, $\mu \cong \mu_o$ and $n = \sqrt{\varepsilon_r}$.

(2) Two prominent reflector materials would of course be silver and aluminum. Silver is becoming increasingly expensive. For example, the market price of silver has increased nearly by a factor 3 in the period 1976 - 1979. Similarly, aluminum cost has escalated, but aluminum is comparatively cheap. Raw material pricing of aluminum (principally bauxite) has increased more than a factor 4 in the period above. Chromium, another reflecting coating is not even produced in the United States and has not been produced since 1964. Consequently, it is imported. The United States has few large sources of bauxite, so it too is imported. Prominent absorber candidates include black chrome and black nickel, along with other oxide candidates. Most can be considered to be reasonably cheap except when large volumes are required, and for massive solar proliferation this will be the case. For a comparison of metal costs, etc. you might consult "Metal Statistics", American Metal Market, Fairchild Productions Division of Capital Cities Media, Inc., 7 East 12th St., New York for appropriate years, and other related references.

Photovoltaics include of course the common silicon solar cell or metal sulfides, especially sulfide heterojunctions. These are relatively expensive and are at present inefficient. Current costs for silicon cells are roughly $10/watt and this constitutes a size of roughly 0.01 m^2. Historically, silicon technology in America has accelerated steadily since about 1950, and very standard techniques are utilized in producing very pure, defect free, oriented single crystal chips or slices which are routinely ~ 0.01 m^2 in disc form, grown from boules in continuous growth processes.

Polycrystalline materials are also rapidly grown with a high
degree of quality control. New photovoltaic technology must
face the quality control problem, the production of large-
area arrays, and a host of complex technological and produc-
tion-related problems. The issue is really how long would
it take to develop such a manufacturing capability for a
new photovoltaic scheme? In some cases the projections are
decades. Consequently, a current principal thrust is to
alter current manufacturing processes to improve contempor-
ary device efficiencies. The cost to do this could be far
cheaper than a massive redevelopment program. However, new
concepts such as the improvement of efficiency in so-called
amorphous semiconductors could provide a breakthrough be-
cause such devices do not require rigid quality control,
grain boundary passivation (because they do not in principal
have grain boundaries), or related process controls, and
they could be manufactured like sheet glass or plastics in
enormous areas in very little time.

(3)   As shown below a single bct cell (heavy lines) can be drawn
within two fct cells, where it can be readily observed that
the a and b unit cell dimensions of the bct cell differ by a
factor $\sqrt{2}$ from those of the fct cell since they are half-
diagonals of the fct cell.
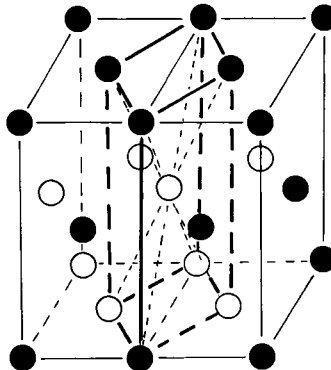
The distance between planes in a tetragonal lattice is given by the general equation for orthogonal unit cells:

$$d = 1 \Big/ \sqrt{(h/a)^2 + (k/b)^2 + (\ell/c)^2}$$

where h, k, and ℓ are the Miller indices for the plane (hkℓ), and a, b, and c are the lattice parameters. Since in a tetragonal cell, a = b, and given c/a = 1.95, d can be calculated for (111) to be a/1.5. If a vacancy were formed in every other cell center in the bct cell above (composed within the fct cells), the number of atoms per unit cell would be reduced by twenty-five percent. The structure created would be a vacancy defect structure and a vacancy sublattice (or superlattice) will occur.

If an edge dislocation intersects, or is associated with, every four unit cell basal planes, we would have one in an area of $4a^2$ and the density would be $(4a^2)^{-1}$. Assuming a value of a of say 4Å, this would give a dislocation density of 1.6×10^{14} cm^{-2}, which is about two orders of magnitude higher than normally measured or expected as a limiting value in deformed metals and alloys.

A deposit layer grown pseudomorphically upon the basal plane of an fct substrate would be cubic because the dimensions in the plane of the overgrowth would be a, and would assume an epitaxial (001) orientation.

(4) In optical materials where the relative permeability is unity ($\mu = \mu_o$), the index of refraction, n, equals the square root of the relative dielectric constant. Consequently ε can be measured by measuring n.

In a parallel plate capacitor the capacitance is given by $C = C_o K_r$ where $\varepsilon_r \equiv K_r = \varepsilon/\varepsilon_o$. So $K_r = C/C_o$. We need only measure the capacitance of an identical parallel-plate capacitor in air for comparison. The same is true of a two-layer dielectric or a complex dielectric, i.e., the same

parallel plate set-up is used, with the same plate spacing,
etc. If a flat-plate absorber is increased in thickness the
dielectric effect will increase or if the absorber is a bi-
layer, the more efficient layer can be increased in thick-
ness or occupy a greater percentage of the total layer
thickness. For complex mixtures of two different dielec-
trics, a logarithmic mixing rule is commonly used in the
form $\log K_m = \theta_1 \cdot \log K_1 + \theta_2 \cdot \log K_2$ where K_m is the
dielectric constant of the mixture; K_1 and K_2, the dielec-
tric constant of the components, and θ_1 and θ_2 are the
volume ratios of the respective components.

Since dielectric constants are important in optical ab-
sorption, it would seem that materials with high dielectric
constants and especially high dielectric loss factors would
be the better absorbers or absorber complexes. Consequently,
oxide systems would be the best absorbers, including perhaps
ferroelectric materials such as $BaTiO_3$ or other materials
having highly polarizable crystal structures embedded in
materials of lower or different dielectric constants.

(5) A plot of particle size in Fig. P. 5(b) will show a bimodel
size distribution with two average particle sizes less than
0.2 μm diameter. This size is below the solar (optical)
portion of the spectrum and as a consequence there will be
no absorption because the surface will be technically "re-
flecting" because even the spaces between the particles are
in this range, and the surface will be absorbing only in the
U.V. part of the spectrum. Since the size distributions are
below 0.2 μm, such particulates in the natural environment
could certainly not settle out because only particles greater
than about 50 μm readily settle out. Such small particu-
lates could be deposited in rain, and could more easily be
attached electrostatically to the surface.

(6)   The easiest particles to remove from a surface are those
      least attached.   Consequently particles in Fig. P. 6(a)
      would probably be the easiest to remove.   Removal really
      depends upon the adhesive strength or adhesive energy, and
      this depends upon the balance of interfacial energies in
      the system:
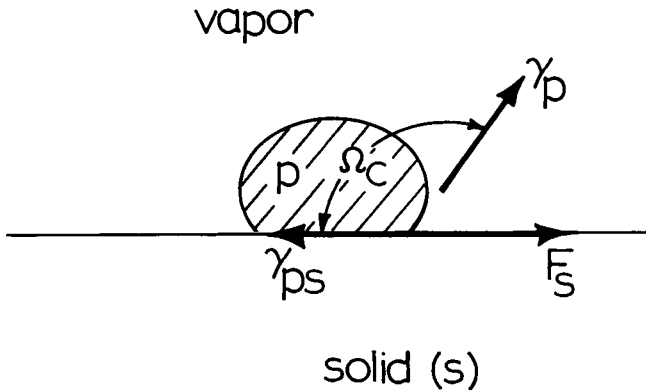
In the notation shown

$$\gamma_{ps} = \gamma_p \cos(180 - \Omega_c) + F_s$$

where γ_{ps} is the particle substrate interfacial free energy,
γ_p is the particle surface free energy (or surface tension)
and F_s is the substrate surface free energy (or surface ten-
sion).   We see that when the contact angle, $\Omega_c < 90°$, the
particle tends to "wet" the substrate or spread over the
substrate while for $\Omega_c > 90°$ the particle tends to loose
such a tendency.   If the particles in Fig. P. 6 are attached
to the same substrate, the particle in Fig. P. 6(a) would
have the highest surface tension.   Consequently, a detergent
must increase the particle surface tension or lower the
interfacial free energy in order to reduce the wetting, and

thereby decrease the contact angle. Ideally, a particle
which is completely non-wetting and therefore not techni-
cally in contact with the surface is one where $\Omega_c = 180°$,
while complete wetting occurs when $\Omega_c = 0°$. By changing the
substrate, the interfacial free energy can be changed because
F_s will change. Consequently the contact angle can be
altered. A practical example is the application of a wax
layer to prevent water wetting of a surface, e.g., the bead-
ing of water on a freshly polished automobile.

If dust accumulation produces a plateau of optical re-
sponse, then the effect performance might be characterized
by, say the difference from the initial conditions to the
plateau. Consequently, for a reflectivity plateau, the
better performance would result from a higher initial re-
flectivity. Reflectivity in certain parts of the spectrum
is highly dependent upon grain size of a reflecting coating
as well as porosity. These could account for reflectivity
variations in silver reflecting coatings. This is at
present a somewhat hypothetical situation in the solar
spectrum.

(7) Assuming either ε_{TM} or ε_{TE} to be zero, respectively, or
simply integrating the entire equation, using standard
integral tables we find:

$$\frac{\varepsilon}{2} \int_0^{\pi/2} \cos^2 \theta \sin \theta \, d\theta = \varepsilon/6; \quad \frac{\varepsilon}{2} \int_0^{\pi/2} \sin \theta \, d\theta = \varepsilon/2$$

and
$$\int_0^{\pi/2} \cos \theta \sin \theta \, d\theta = \frac{1}{2} \int_0^{\pi/2} \sin 2\theta \, d\theta = 1/2.$$

Since $\overline{\varepsilon}_H = 4\overline{\varepsilon}_N/3$, and $\overline{\varepsilon}_N \alpha \rho_{d.c.} \cdot (T)$ it is possible to alter
the emissivity by altering the resistivity. For example, it
is known that resistivity increases with a significant

increase in crystal defects such as point defects and dislo-
cations.   There is also a rather abrupt change in resistivity
when an order-disorder transition occurs.   Consequently, when
the resistivity approaches zero the emissivity will also
approach zero.   This occurs in metals at very low tempera-
ture, or ideally where a metal becomes superconducting
$(\sigma \rightarrow \infty; \rho \rightarrow 0)$.

(8)   When geometrical optics apply (as in the visible portion of
the spectrum) Kirchoff's law states that absorptivity =
emissivity; consequently absorptivity of a continuous film =
$2/\omega \tau$.   Similarly, the absorptivity of a micromesh, which
the vapor deposit in Fig. P. 5(b) might be considered to
represent, is given by $(2/\omega \tau)(d/2a)$, where d is the distance
between the particles and a is their diameter.   It can be
observed (by direct measurements) in Fig. P. 5(b) that the
distance between the larger particles is approximately twice
the particle diameter.   Consequently the factor (d/2a) = 1,
and the absorptivity will be essentially the same as a con-
tinuous tin film.   Since the emissivity is in proportion to
the resistivity, and since the room temperature resistivity
of tungsten is about 5.5 microhm-cm as compared to 11.5
microhm-cm for tin, (c.f. Handbook of Chemistry and Physics),
the emissivity would increase by nearly a factor 2.   Since
the emissivity increases with temperature if a black-chrome
coating is to maintain a constant ratio $\alpha_s/\overline{\varepsilon}_H = 0.97/0.12$ the
absorptivity will have to be increased because the emissiv-
ity at 400°C will increase over that at 100°C.

(9)   Consider

$$R = \left[\frac{(n-1)^2 + k^2}{(n+1)^2 + k^2} \right] \; ; \quad n = \sqrt{\varepsilon}$$

and solve for

$$k = \frac{\sqrt{R(n+1)^2 - (n-1)^2}}{(1-R)} \; .$$

We can then plot values for k versus λ as shown below, where it can be observed that the composite is a somewhat selective absorber in the solar spectrum ($0 < \lambda < 2$ μm), but is characterized by a large thermal broadening.
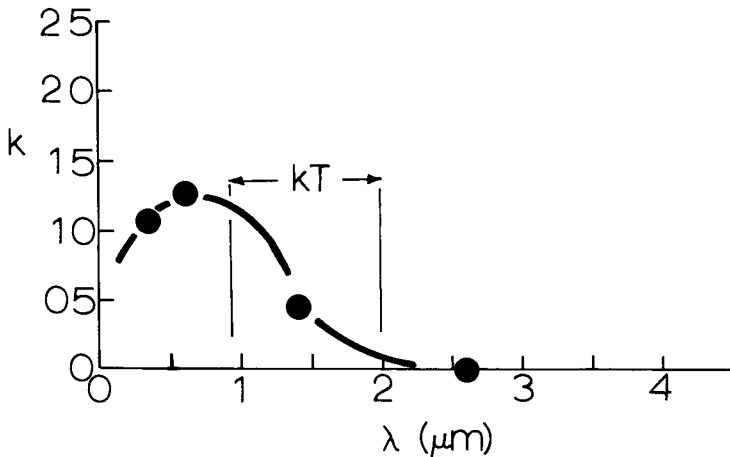
It is well established that variations in high values of absorptivity usually involve variations in emissivity. Both absorptivity and emissivity are important. Ideally one strives to achieve the highest absorptivity and a correspondingly low emissivity. For example, $\alpha_s > 0.95$, $\varepsilon_H < 0.1$.

(10) Selective composite (cermet) absorbers can be fabricated by co-evaporation or sputtering of Au and Al_2O_3 in vacuum or inert atmosphere upon a reflecting substrate providing good adhesion for the composite overgrowth. The substrate must be heated to provide for a specific size of Au particles and the evaporation rates can be systematically adjusted to allow for a gradient in the metallic fraction with overgrowth thickness. Absorptivity and emissivity can be most effectively controlled by varying the metal (Au) fill fraction

and/or film thickness. The thickness is simply adjusted by
evaporation rate or sputtering time and the fill fraction
can be varied by varying the ratio of deposition rates for
metal and ceramic, or by varying the temperature and thereby
increasing (with increasing temperature) or decreasing (with
decreasing temperature) the mean particle (metal inclusion)
size.

   In the case of vapor-deposited gold films there is no
evidence of variations in grain size having a measurable
effect on optical properties (absorption) in the visible
portion of the spectrum for grain sizes greater than about
0.01 μm. The same was observed for silver. While an effect
of grain size has been observed in silver films at 10.6 μm,
this is more than an order of magnitude greater wavelength
and the electromagnetic interactions would be expected to be
considerably different.

(11) In the single electrode process for iron we have

$$0 = -0.41 + \frac{0.0592}{2} \log a_{Fe^{2+}}$$

where -0.41 is the electrode potential (from the electro-
motive or electrochemical series) for iron (Fe^{2+}), $2.3\,RT/F =$
0.0592, and the denominator represents the charge. Solving
for $a_{Fe^{2+}}$ we find $\sim 10^{15}$ (an impossibly large activity).
Conversely, solving for copper (Cu^{2+}) we find $a_{Cu^{2+}} \simeq 10^{-11}$
(an impossibly small activity). Consequently the ratio
$a_{Fe^{2+}}/a_{Cu^{2+}} \simeq 10^{26}$, indicating an enormous difference in the
theoretical limit of oxidation. Replacing the iron by
aluminum simply changes the electrode potential and the
corrosion characteristics, but there would still be corro-
sion of the aluminum provided an oxide were not formed.
Unlike iron, aluminum normally forms a very tenacious pro-
tective oxide (Al_2O_3). Consequently there may be a signifi-
cant reduction in corrosion even though the electrochemical

conditions are possible. If a zinc-copper cell were formed
in the system, the electrode potential (or potential differ-
ence) would be - 0.763 - (0.337) volts or - 1.1 volts.
(Data from the electrochemical series.)

(12) The initial and constant maximum load is determined from
$P = \sigma A = 20$ Ksi$[\pi(10^2 - 9^2)]/(2.54)^2 = 185$ K. Then for a
safety factor 2 based upon UTS implies a maximum permissible
stress of 55 Ksi (110 Ksi/2). We set this equal to 183
K/$\pi[10^2 - (9 + 0.01$ t$)^2]/(2.54)^2$, and solving for t in
months we find t = 64 months (or 5.33 years). Considering
the annealed tube wall section, the yield stress can be
approximated by a Hall-Petch relationship, $\sigma_y = \sigma_o + KD^{-1/2}$.
If σ_o and K do not change, then σ_y (the yield stress), would
be reduced since the new grain diameter, D' = 10D.

(13) Compare the heats of fusion and melting points as follows:

Material	Heat of fusion	Melting point	Heat storage
Sodium chloride	124 cal/g	800°C	30,551 BTU/ft^3
Sodium sulfate (anhydrous)	41 cal/g	884°C	12,432 BTU/ft^3
Sodium sulfate decahydrate	60 cal/g	32°C	10,476 BTU/ft^3
Sodium hydroxide	50 cal/g	322°C	11,790 BTU/ft^3
Silicon	337 cal/g	1427°C	88,015 BTU/ft^3
Sodium	27 cal/g	98°C	2,989 BTU/ft^3
Gallium	19 cal/g	29°C	12,716 BTU/ft^3

The heat storage is obtained by converting heat of fusion in
cal/g to BTU/ft^3, considering the density for each material.
It can be observed that the only practical materials for
home solar heat storage are sodium sulfate decahydrate,
sodium, and gallium since their melting points are in the
range of such systems. But sodium melts a bit too high and

stores little heat. It is also more expensive and difficult
to store. Sodium sulfate decahydrate is similar to gallium
in melting point and heat storage but it is roughly a factor
10^3 less expensive. Sodium sulfate decahydrate is therefore
the logical choice. It is plentiful and easily stored in
plastic containers, etc.

The heat energy required to melt aluminum is about the
same as that required to melt iron (since the specific heats
for Al and Fe are 0.250 cal/g and 0.150 cal/g, respectively,
and the heats of fusion are 96 cal/g and 64 cal/g for Al and
Fe, respectively); even though the melting point for Fe is
more than twice that for Al.

(14) For steady-state heat transfer through plane walls and
ceilings

$$Q = - KA \frac{dT}{dx} \text{ (BTU/hr)}$$

where A is the area through which the heat flows, T is the
temperature, x is the wall or ceiling thickness. Since heat
flows from higher to lower temperature we can solve the above
for

$$Q = \frac{KA(T_1 - T_2)}{x_2 - x_1} = \frac{KA\Delta T}{\Delta x}$$

So, for the walls, Q_1 = (0.05)(9000)(68)/0.5 = 61200 BTU/hr.
and for the ceiling and roof, Q_2 = (0.05)(20000)(68)/1.17 =
58120 BTU/hr. Since the heat of fusion of sodium sulfate
decahydrate is 108 BTU/lb, and since its density is 97 lb/ft^3,
the minimum volume of salt storage will be 137 ft^3. If an
extra 6 inches of insulation are added, it can be observed
that the savings will be around 17000 BTU/hr. or 14%. This
is of course an important part of energy conservation, some-
times referred to as an energy resource.

(15) At any temperature

$$\Delta G^\circ(T) = - RT\ln K_{eq}(T)$$

where for the dissociation of $CaCO_3$

$$K_{eq} = \frac{a_{CaO}^{Solid} \, a_{CO_2}^{Gas}}{a_{CaCO_3}^{Solid}} = P_{CO_2}; \ \text{(P in atmospheres)}$$

Therefore we can write

$$\Delta G^\circ(1210^\circ K) = - R(1210^\circ K)\ln(1.77) = - 1373 \ \text{cal/mole}$$

Since $\Delta G^\circ(T) = \Delta H^\circ - T\Delta S^\circ$, we could compare the standard free energies at two different temperatures:

$$\Delta G^\circ(T_1) = \Delta H^\circ - T_1\Delta S^\circ$$

$$\Delta G^\circ(T_2) = \Delta H^\circ - T_2\Delta S^\circ$$

So $\Delta S^\circ = - \left[\Delta G^\circ(T_2) - \Delta G^\circ(T_1)\right]/(T_2 - T_1)$, etc.

(16) Principal thermochemical systems include catalyzed reactions such as $2SO_3 \longrightarrow 2SO_2 + O_2$ and $CH_4 + H_2O \longrightarrow CO + 3H_2$; thermal decomposition reactions such as $CaCO_3 \longrightarrow CaO + CO_2$ and $Ca(OH)_2 \longrightarrow H_2O$; solution-dissolution reactions such as the mixing of water with acid (H_2SO_4) to generate exothermic reaction heat. In the methane cycle, hydrogen embrittlement must be considered a serious potential materials problem especially because of the high temperatures involved.

(17) For the device in equilibrium as shown, the energy-level diagram is depicted below along with the equivalent-circuit junction components. Note that the first feature of any energy-level system is to draw the Fermi level. This never varies. Biasing causes band bending (conduction and valance bands).
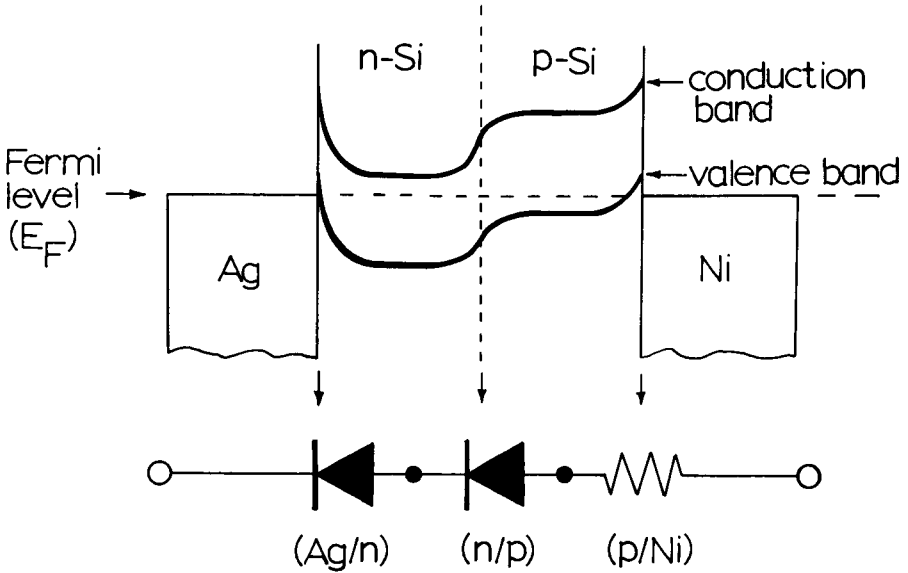
The metal work functions are larger than the semiconductor work functions (4.8 eV and 4.6 eV, respectively for silver and nickel). The rules for contacts are as follows: ($E_{w(m)}$, $E_{ws(n)}$, and $E_{ws(p)}$ refer to the metal, n-type semi-conductor, and p-type semiconductor work function, respectively).

$E_{w(m)} > E_{ws(n)}$ ➤ RECTIFYING

$E_{w(m)} < E_{ws(n)}$ ➤ OHMIC

$E_{w(m)} < E_{ws(p)}$ ➤ RECTIFYING

$E_{w(m)} > E_{ws(p)}$ ➤ OHMIC

The metal junctions can also become active as voltage generators because of work function differences, i.e., consider the Peltier effect.

(18) If the boundaries are twin boundaries they would lie pre-
      dominantly along {111} plane directions. This could be
      verified by either transmission electron diffraction for
      very small grain sizes or X-ray diffraction for very large
      grain sizes. If the twin boundaries have energies given by
      γ_{tb}/γ_{gb} = 0.055 (ratio of twin to grain boundary free energy),
      then the twin boundary energy is very low since $(\gamma_{LV})_m$ =
      730 ergs/cm^2 and at 500°C, $F_S \simeq$ 1.2 (730) + (1410 - 500)(.45)
      $\simeq$ 1286 ergs/cm^2. So for γ_{gb}/F_S = 0.3 we have γ_{gb} = 386
      ergs/cm^2 and γ_{tb} = 21 ergs/cm^2. This is a very low energy
      indicating the twin boundaries are very well ordered, and
      certainly not conducive to accepting adsorbed hydrogen
      atoms. Other similar coincidence boundaries could have the
      same effect since they are by their nature of low energy.
      Even coincidence boundaries having energies twice the
      coherent (111) twin boundary energy would still be low
      energy since the grain boundary (high-angle) energy would
      be an order of magnitude larger.

(19) The normal form (crystal structure) for Cu$_2$S is orthorhombic
      (a = 11.9 Å, b = 27.3 Å, c = 13.5 Å) while CdS can have
      cubic (sphalerite) (a = 5.8 Å), or wurtzite structure. It
      is therefore not possible to develop a coherent interface
      through structural accommodations by dislocations except
      through epitaxial growth on specific orientations. This is
      also the case for ZnO/CdTe junctions since ZnO is hexagonal
      (wurtzite structure with a = 3.2 Å and c ~ 5.2 Å) and CdTe
      is cubic (sphalerite structure with a ~ 6.5 Å). A coherent
      interface can, however be created at the P-CdTe/n - CdS
      junction interface if CdS is cubic. The misfit here, defined
      by 100[a(CdTe) - a(CdS)]/a(CdTe), in percent, will be
      100(6.5 - 5.8)/6.5 = 11%. This very large mismatch can be
      accommodated by creating dislocations in the (001) plane
      interface after every nine {010} planes in the CdS. That is,
      an extra-half plane will be an (010) plane in the CdS.

(20) Since Cu_2S is orthorhombic, dislocations can occur on several
      different slip planes and will have a variety of Burgers
      vectors. This is a large lattice and dislocations will be
      influenced by temperature, stress, etc. If the CdS is cubic
      (sphalerite) the slip plane will be {111} and the Burgers
      vectors will be of the form $\frac{a}{2}$ <110>. If the CdS has the
      wurtzite structure, the slip plane will be (00.1) and slip
      directions (Burgers vectors) will have a form <110>. Since
      the c/a ratio is > 1.6, slip is restricted to (00.1). Dis-
      locations at the interface or within the matrix can cause
      recombination and trapping and as a consequence the greater
      the density the lower the device efficiency. A simple plot
      could be made of open circuit current versus dislocation
      density at some constant solar flux which would show current
      decreasing as dislocation density increases. The curve
      would probably be different depending upon whether disloca-
      tions were being measured in the junction interface or in
      the matrix on either side of the junction (in the Cu_2S or
      the CdS).

(21) The zeta potential or electrokinetic potential (ζ), in
      millivolts, is related to the electric double layer capaci-
      tance associated with a surface: $\zeta = \sigma/C$; where σ is the
      charge per unit surface and C is an equivalent capacitance.
      Such a double layer exists between any solid surface and an
      ionic liquid. It can be measured by several electrokinetic
      methods and at the point of zero zeta potential obviously
      $\sigma = 0$. This means that the solid surface will be uncharged.
      At this point mineral floculation will occur which can pro-
      mote settling. On the otherhand, by adjusting the magnitude
      and sign of ζ (or σ) dispersion of particles can be induced.
      The zeta potential influences wet photovoltaic cell biasing
      through the effect of hydrogen ion (pH) on the photoelec-
      trodes. In CdS/sulfide electrolyte wet cells there is a

dependence of the point of zero zeta potentia. .PZZP) on
S^{2-}. In general pH changes are zero at the PZZP. Conse-
quently, zeta potentials and their relationship to pH are
somewhat critical in determining wet photocell operation as
well as the flotation features for many minerals.

(22) While it is not known with any certainty how passivation
occurs, the most obvious mechanism involves bond satisfac-
tion. Consequently, hydrogen would be most effective
because of its valence and its small atomic size. While
magnesium is small, its valence would require it to satisfy
two dangling Si bonds simultaneously. This is certainly a
possibility but this mechanism is probably not as effective
as with atomic hydrogen. The sizes of N, F, and O are
somewhat larger and the electronic structure is not condu-
cive to the type of favorable electron sharing provided by
H. However F could be effective because of its valence
although it is roughly four times larger than H. On con-
sidering the symmetric tilt boundary shown below, the
boundary dislocations are observed as sites of unsatisfied
Si bonds. Consequently, hydrogen would be expected to
selectively and chemically attach to these sites as shown.
The spacing of dislocations in the boundary, d, and there-
fore the number per unit length of boundary is related
approximately by $d = |\underset{\sim}{b}|/\Theta$, where $|b|$ is the magnitude of
the Burgers vector and Θ is the misorientation (in radians).
Since the hydrogen in the boundary will be associated with
individual dislocations, the difference in concentration
will simply be the ratio of dislocation spacings or
$\Theta_{15}/\Theta_5 = 3$. Consequently, the $15°$ boundary would have
roughly 3 times the hydrogen as the $5°$ boundary.
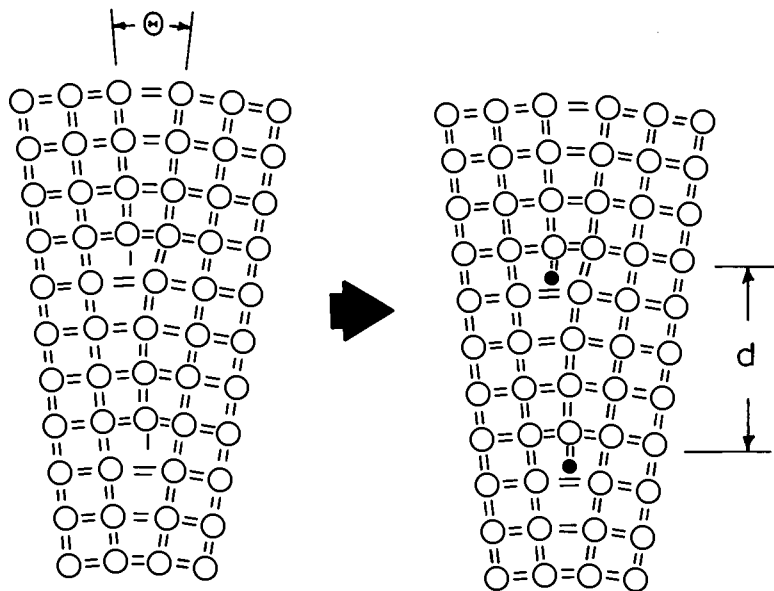
(23) It must be recognized in Fig. P.23 that the topography is
      exaggerated by the ion etching which is more rapid within
      the grain boundaries. This effect produces a "particle"-
      like typography. Careful inspection will indicate that the
      "particles" are not spheres but have in some cases well-
      defined facets. By thinning the substrate from the reverse
      side a thin film could be made of the black chrome. This
      would allow one to determine that the "particles" are
      actually contiguous grains. Auger electron or other surface
      analytical techniques could be employed in determining the
      composition of individual "particles". This could also be
      accomplished in the electron microscope (TEM) if instrumen-
      tal attachments are available. This mode of analysis is
      referred to as analytical electron microscopy (AEM).

(24) High-resolution (lattice-imaging) transmission electron
      microscopy techniques are allowing for the direct observation

of amorphous structures, where it has been observed that in
some cases the "amorphous" structure is really a micro-micro
crystalline regime. (See for example the article by M.
Fukarrachi, K. Hashimoto and H. Yoshida, *Scripta Met.*, 13,
807 (1979).) Since amorphous silicon could be considered
a micro-micrograin regime, hydrogen passivation can be
effective by satisfying the multitude of unsatisfied bonds
in the microcrystallite "boundaries". Furthermore, the
large "grain boundary" area in such a micrograin regime
would be conducive to rapid diffusion of hydrogen through-
out. Dangling bonds are reduced in hydrogenated amorphous
silicon by roughly a factor 10^4.

(25) Some particular, contemporary insight can be gained especial-
ly from part II of the first reference [R.S. Claassen and
A.G. Chynoweth, *Mater. Sci. Engr.*, 37(1), 31 (1979)]. A
very extended historical perspective with regard to metal-
lurgical technology and its very early development can also
be gleaned from "De Re Metallica" (translated by H.C. Hoover
and L.H. Hoover and published by Dover Publications, Inc.,
New York, 1950). This work describes very early metallur-
gical technology up to the 16th Century. While this may
seem remote in the context of modern times and future needs,
the importance lies in an understanding of the connection
between the needs of a period, the existing social and
economic systems, and the availability of materials and
methods of production, etc.

INDEX